Menzies, Ryan D.D. (2002) *Investigation of S-shaped intake aerodynamics using computational fluid dynamics.* PhD thesis.

http://theses.gla.ac.uk/1440/

Copyright and moral rights for this thesis are retained by the author

A copy can be downloaded for personal non-commercial research or study, without prior permission or charge

This thesis cannot be reproduced or quoted extensively from without first obtaining permission in writing from the Author

The content must not be changed in any way or sold commercially in any format or medium without the formal permission of the Author

When referring to this work, full bibliographic details including the author, title, awarding institution and date of the thesis must be given

Glasgow Theses Service
http://theses.gla.ac.uk/
theses@gla.ac.uk

Investigation of S-Shaped Intake Aerodynamics Using Computational Fluid Dynamics

Ryan D. D. Menzies, M.Eng

Dissertation submitted to the Faculty of Engineering,
University of Glasgow, for the Degree of Doctor of Philosophy

University of Glasgow
Department of Aerospace Engineering

October 2002

© 2002 Ryan D. D. Menzies

Abstract

Flows in the s-shaped intake (Royal Aircraft Establishment intake model 2129 - M2129) have been simulated and analysed using Computational Fluid Dynamics (CFD). Various flows have been simulated from steady through-flow for validation and verification, steady flows at a variety of angles of pitch and yaw, and the unsteady flow of surge wave propagation following the application of surge signatures at the engine face. Reynolds Averaged Navier-Stokes (RANS) simulations have been considered using the SA, $k - \omega$ and SST turbulence models where possible. The freestream Mach number was fixed at 0.21 and the Reynolds number based on the non-dimensional engine face diameter was $777,000$ for all cases.

The Glasgow flow solver PMB was used and second order accuracy was achieved in both space and time. Grid and time step convergence studies verified the numerical method, the grids being of the structured multi-block type. A comprehensive validation study was undertaken on the steady through-flow problem. Previously examined low and high mass flow cases were studied. It was found that the low mass flow results compared well with previous computational solutions. Problems however were encountered in the quantitative prediction of the secondary flow when compared with experiment however the SST model did qualitatively predict this. The high mass flow case proved more challenging. Solutions predicted two different flow regimes depending on the turbulence model used. It was found that the SST model provided a good match with the primary set of experimental data. Confidence in this result was gained as it also performed well in the low mass flow case and also as it has shown previous improvements in the prediction of separation in flows with strong adverse pressure gradients.

The M2129 intake was then examined at various angles of pitch and yaw for the same low and high mass flow cases using the SST turbulence model. Positive angles of yaw reduced the effect of the offset causing lower values of distortion and better pressure recovery. Negative angles of yaw accentuated the effect of the offset and caused significantly poorer pressure recovery and distortion coefficients. Flow control strategies are suggested to alleviate these problems. Although the predicted flows appear plausible it is stressed that confidence in the results cannot be gained without validation with experimental data.

Surge propagation was simulated in the M2129 duct. No experimental data was available for validation. Instead the classic inviscid shocktube was examined computationally as a straightforward shock propagation problem, as the inviscid analytical (1-D) solution is available. Experimental data was also made available for a shock propagation study performed by the Royal Military College of Science on a straight pipe. Although not an ideal case, this was modelled computationally. In both cases numerical solutions compared reasonably with available data.

Following these validation studies, surge was then modelled in the M2129. Attention was concentrated on the propagation of a surge wave through the duct and this was achieved by applying a pre-determined surge pressure/time history at the downstream boundary. A variety of surge signatures were applied and compared for the high and low mass flow cases described above. It was found that the consequent propagation of the surge wave through the duct demonstrated a complex flow with an interaction with the natural separation of the flow from the starboard side first bend, more especially at high mass flow conditions. The duct offsets induce an over-pressure on the port side of the duct at the first bend that can peak at a value of around 3 with respect to the downstream boundary steady-state pressure in extreme cases.

Predictions of over-pressures associated with engine surge are important and are used as peak loads for the design of intake structures. Traditional methods have relied on empirical techniques to predict such loads. It is hoped that the current computational surge work will help to understand some of the flow mechanisms involved, and serve to promote further studies in areas such as hot surge modelling and resonance in s-shaped intakes. It is also hoped that this work will encourage further studies, particularly experimental, as validation data is currently not available for such intakes.

Acknowledgements

I would like to thank Dr. Ken Badcock and Prof. Bryan Richards for their continuous support, encouragement, and enthusiasm throughout the course of this work. Thanks are also expressed to Dr. George Barakos for his help and suggestions at important phases in the study. Without their help and patience this thesis would certainly not have been possible and to them I am deeply indebted.

I would like to thank the CFD group as a whole within the Aerospace Engineering Department for their contributions, particularly Mark Allan, Iain McPherson, Daniel Feszty, and Jason Henderson (now at Imperial College, London), who were more than happy to assist with a range of problems and queries and showed a lasting interest in my work.

This work is supported by sponsorship from QinetiQ (formerly DERA) Bedford. My gratitude is expressed to Mark Jackson for his assistance and also for providing some experimental and computational results. I also wish to extend my thanks to Dr Kevin Knowles at the Royal Military College of Science for providing useful experimental data.

Last, but certainly not least, there are numerous others who have helped me in so many different ways, in particular my loving and supportive friends and family, and especially my parents. They provide motivation and encouragement in so many forms, lift my spirits when needed, and they are all an inspiration to me.

Contents

List of Tables

List of Figures

Nomenclature

a	Speed of sound
A	Area
D	Diameter
D	Dissipation
e	Energy
E	Total energy
$\mathbf{F}, \mathbf{G}, \mathbf{H}$	Flux vectors
h	Enthalpy
H	Total enthalpy
i, j, k	Cartesian unit vectors
$\mathbf{I}$	Identity matrix
J	Jacobian matrix of transformation
k	Turbulent kinetic energy
L	Duct length
L	Reference length
M	Mach number
P, P^*	Non-dimensionalised (reduced) pressure, dimensional pressure
P	Production
P_r	Prandtl number
ρ	Density
q	Dynamic pressure
q	Heat flux component
R	Effective radius normal to centreline at longitudinal location, X

R	Gas constant
$\mathbf{R}$	Vector of residuals
Re	Reynolds Number
Re_T	Turbulent Reynolds number (μ_T/μ)
S	Entropy
t, t^*	Non-dimensionalised (reduced) time, dimensional time
T	Temperature
u, v, w	Cartesian velocity components
U_∞	Freestream velocity (in x-direction only)
V	Velocity magnitude
V_p	Shock propagation velocity
$\mathbf{W}$	Vector of independent flow variables
x, y, z	Cartesian coordinate system
X	Distance from highlight leading edge

Greek Symbols

δ	Boundary layer thickness
Δ	Change in a variable
Δt	Time step
$\Delta\mathbf{W}$	Vector of conservative updates
γ	Ratio of specific heats
μ	Molecular viscosity
μ_T	Turbulent eddy viscosity
ω	Specific dissipation rate
θ	Sector angle
ρ	Density
τ	Shear stress
τ	Pseudo time
ξ, η, ζ	Curvilinear coordinates

Subscripts

$cent$	Centrifugal quantity
cl	Quantity relating to intake centreline
ef	Condition at the engine face
hl	Condition at engine highlight
i	Quantity relating to intake
i	Inviscid value
k	Kinetic energy
l	Quantity relating to left hand side of system
L	Characteristic length
r	Quantity relating to right hand side of system
s	Static value i.e. static pressure, P_s
$shock$	Quantity relating to shock wave front
S	Freestream static value i.e. static pressure, P_S
t	Throat value i.e. throat area, A_t
t	Local total value i.e. total pressure, P_t
T	Total value i.e. total pressure, P_T
v	Viscous value
ω	Dissipation
0	Reference to freestream value
0	Reference value
∞	Freestream value, i.e. P_∞

Superscripts

m	Pseudo time index
n	Time index

$*$	Dimensional quantity
$\bar{\ }$	Time averaged component i.e. $\bar{\rho}$
$\bar{\ }$	Mean value of component i.e. $\bar{P}$
$'$	Turbulent fluctuation component i.e. ρ'
$\hat{\ }$	Vector of variables in conservative form i.e. $\hat{\mathbf{F}}$

Acronyms

AGARD	The Advisory Group for Aerospace Research and Development
AIP	Aerodynamic interface plane
AoA	Angle of attack
ARA	Aircraft Research Association
CFD	Computational Fluid Dynamics
CFL	Courant-Friedrichs-Levy
CFR	Capture flow ratio
CR	Contraction ratio
DC	Distortion coefficient
DERA	Defence Evaluation and Research Agency
DNS	Direct numerical simulation
GCG	Generalised conjugate gradient
HMFR	High mass flow ratio
IGV	Intake guide vane
LEVM	Linear eddy viscosity model
LMFR	Low mass flow ratio
LO	Low Observability
MFP	Mass flow parameter
MFR	Mass flow ratio/rate
NACA	National Advisory Committee for Aeronautics
NASA	National Aeronautics and Space Administration
NLEVM	Non linear eddy viscosity model

$N-S$	Navier-Stokes
OPR	Over-pressure ratio
PMB	Parallel multi-block
PR	Pressure recovery
RAE	Royal Aircraft Establishment
$RANS$	Reynolds-Averaged Navier Stokes
RCS	Radar cross-section
$RMCS$	Royal Military College of Science
SWG	Surge wave generator
WCH	Wall clock hour

Chapter 1

Introduction

This chapter gives a background on CFD and intake aerodynamics and reviews previous work.

1.1 Historical

Since the 1960's improvements in intake design have largely come from wind tunnel test data. Any problems that occurred, such as damage to intake structures as a result of engine surge, tended to be detected only after prototype testing and flying. The late 1960's and early 1970's featured comprehensive reviews of airframe/engine integration understanding. Extensive intake/airframe experimental studies were undertaken as a result of problems arising from highly integrated intake positions.

From the early 1970's wind tunnel testing methods have improved considerably and there has also been a much greater understanding of some important characteristics of intake flows. During this time computational techniques have also become widely used. Successful (and indeed unsuccessful) CFD simulations of aircraft intake flows also added to the understanding of the intake flow physics. CFD methods have advantages over experimental techniques in that they are generally cheaper in terms of cost, time and resources. Good agreement with experiment can now be obtained, but CFD should be thought of as an aid to experimental studies rather than a replacement as full confidence in results cannot be guaranteed. However there are problems that are difficult to examine experimentally, often at great expense and requiring a full scale facility to do so, and in such circumstances CFD could be thought of as a viable alternative. CFD can also assist with the understanding of experimental problems providing validation of the results has been done.

1.2 The Design and Role of an Air Intake

Intakes are a very important component of an aircraft. The efficiency of such devices is crucial in that they make major contributions to the performance and handling attributes of the aircraft. At least as important is the need for intake and engine compatibility. Engine surge can be induced if factors such as cowl lip shape and subsonic diffuser shape are not considered in the design process.

The primary purpose of the intake is to offer the compressor face a uniform stream of air (from freestream conditions) at specific conditions required by the engine whilst maximising efficiency. This uniform stream of air is defined as the internal flow and can be described as one in which pressure, temperature, and density are uniform in the radial direction (a direction normal to the centreline of the intake). External flow does not enter the air intake but is affected by the presence of the intake and so is still of vital importance as factors such as aerodynamic drag will be influenced.

The design of an aircraft intake generally depends on the conditions within which the aircraft will operate but can also depend on the specific role of the aircraft, the placement of store bays, and location of undercarriage wells. For example low observability (LO) aircraft tend to have intakes that hide the compressor face in some way to reduce the radar cross-section (RCS) of the aircraft. This can be done in a number of ways such as using radar absorbing materials for the intake surfaces. Another method is to design the intake to eliminate a line of sight view from the intake to the compressor face since it is a strong source of radar reflection. External surfaces can be shaped so that all radar reflections get diverted away from the direction of the threat.

Engine intakes should be designed to minimise total pressure loss. Intake performance can then be characterised by high total pressure ratio, good uniformity of flow (across the engine plane), low installation drag (drag due to the presence of the intake), low signatures (LO as described in the previous paragraph), and low weight. These factors should all be considered and yet the final intake design must still meet longevity and reliability targets.

Subsonic and supersonic intakes tend to vary considerably. Subsonic intakes usually have fixed geometries (i.e. no moving parts). Due to the low speeds encountered it is possible for subsonic intakes to draw in air from a greater area than the highlight area. Thus, a variable intake geometry is not required. The diffusing part of the intake tends to be shorter in length due to the lower speeds. However, longer diffuser parts are sometimes needed (as on the RAE intake model 2129). This, for example, may be because of the need to bend the intake round an undercarriage well or weapons bay or for stealth reasons. Splitter plates are sometimes also used to help obscure the engine face for stealth reasons. Some well known examples of aircraft that utilise s-shaped intakes include the F16 and Eurofighter Typhoon. The proposal by Boeing Aircraft Corporation for a Sonic cruiser has the engines at the rear of a diamond/delta shaped wing with s-shaped intake ducts supplying the compressor with air.

Supersonic intakes need to take account of the complex shock patterns that form as a result of slowing the freestream to subsonic speeds for entry to the compressor. These shock patterns are designed to compress the incoming flow. Moving ramps are required to alter the position of the shock depending on the speed of the aircraft.

The final aspect of an aircraft intake is the downstream compressor face. The primary purpose of the compressor is to draw and compress air into the engine core. Pressure rise is in the direction of flow for a compressor (an adverse pressure gradient) and hence this increases the likelihood of boundary layer separation. Compressor stall leads to a rapid drop in the performance of the compressor and the possibility of engine surge or rotating stall. This is described in more detail in chapter 5.

1.3 Diffusing S-Duct Flows

1.3.1 Terminology

Experimentally, it is generally difficult to take measurements at a compressor face when an engine is running. The aerodynamic interface plane (AIP) is a plane forward of the compressor face but sufficiently close to the compressor face to have a very similar flow field. For example, an important parameter in duct flow is the pressure recovery (PR). This can be defined as the ratio of the total pressure at the engine face to freestream total pressure (as described later in this section). The total pressure at the compressor face is actually taken at the AIP during wind tunnel testing.

Common terminology for describing intake flow is illustrated in Figure 1.1. The freestream area, A_∞, is the area enclosed between the dividing streamlines (the envelope of the streamlines), i.e. it is the freestream air that actually gets drawn into the engine. The highlight area, A_{hl}, is the area of the disc that is created from the furthest protruding point of the cowl into the freestream (the leading edge). The throat area, A_t, is simply the area of the intake at its narrowest cross-sectional location. Finally, the engine face area, A_{ef}, is the area of the plane lying where the first row of compressor blades would lie.

The capture flow ratio can be defined as

$$CFR = \frac{A_\infty}{A_{hl}}. \tag{1.1}$$

The CFR helps describe the extent of the engine demand.

The Contraction Ratio (CR) is defined as

$$CR = \frac{A_{hl}}{A_{ef}}. \tag{1.2}$$

This is an important geometrical definition used when considering engine demand and relates directly to intake highlight area and intake engine face area.

1.3.2 Distortion

Engine/intake compatibility is purely concerned with the quality of the airflow that is delivered by the intake to the engine and how the engine is effected. This process should ideally be accomplished with the minimum total pressure loss and the flow distribution should be as uniform as possible. Distortion is the term given to the variation of total pressure across the engine face. Many aircraft have experienced intake compatibility problems due to the effects of distortion. It has been shown that a high degree of distortion can induce engine surge.

As previously mentioned air intakes must limit the possibility of compressor surge and stall. This can be done by eliminating non-uniformities in pressure across the engine face although total elimination is not possible in real flows. Sources of distortion include wall separation due to high diffusion rates, shock/boundary layer interaction and inadequate boundary layer bleeds. Any non-uniform loss in total pressure across the intake entrance results in a degree of distortion of the flow and this will progress to the compressor face although a degree of attenuation is likely. Local degradation in total pressure leads to changes in the velocity vector orientation at the compressor face which can cause compressor stall and possible surge.

Distortion is quantified by a number of parameters and equations. The most popular descriptor used in the United Kingdom and introduced by Rolls Royce is the coefficient

$$DC(\theta) = \frac{\bar{P}_{t_{ef}} - \bar{P}_{t_\theta}}{\bar{q}_{t_{ef}}}. \qquad (1.3)$$

Here, P_{t_θ} corresponds to the mean total pressure in the sector θ. The sector is chosen relating to the area with the worst distortion. The most common coefficients are DC(60), DC(90) and DC(120).

1.3.3 Mass Flow and Pressure Recovery Definitions

The Mass Flow Parameter (MFP) is a convenient term and can be defined, noting that the equation is a unique function of M (the local Mach number) only in a calorifically perfect gas, as

$$MFP = M\sqrt{\frac{\gamma}{R}}\left(1 + \frac{\gamma-1}{2}M^2\right)^{-\frac{1}{2}\frac{\gamma+1}{\gamma-1}}. \qquad (1.4)$$

The value of the MFP peaks at around 0.0485 for a Mach number of 1.0 and falls thereafter in the supersonic regime. It is also useful to note that the formula for the MFP can be manipulated to give

$$MFP_1 = \frac{(MFP_2)(MFR)(CR)}{PR}, \qquad (1.5)$$

where, in this case[1]

$$PR = \frac{\bar{P}_{T_1}}{\bar{P}_{T_2}}. \qquad (1.6)$$

The Mass Flow Rate, MFR, can be defined as

$$MFR = \frac{A_\infty}{A_{hl}}. \qquad (1.7)$$

---

[1] Here subscripts 1 and 2 simply refer to two different states

The MFR is also known as the Capture Flow Ratio, CFR. When considering low speed subsonic cases this number is greater than one as the intake can draw air in from an area greater than the highlight area (i.e. the intake is not being supplied with sufficient air to meet demand). High speed supersonic intakes tend to have a MFR less than one as the intake draws in air from an area less than the highlight area (i.e. the intake is being supplied with more air than it requires). The MFR is a parameter that can be used to quantify engine demand.

The Pressure Recovery, PR, is defined as

$$PR = \frac{\bar{P}_{t_{ef}}}{P_{T_\infty}}. \tag{1.8}$$

In high speed flight the intake slows the airflow down for entry into the compressor and produces a corresponding increase in pressure. This is a form of ram compression. The pressure recovery factor is a measure of the efficiency of the intake and is a significant design parameter as a loss in total pressure can be directly related to a loss in engine thrust. Clearly a value of pressure recovery as close to unity as possible is desirable and would indicate an efficient intake with a low distortion across the compressor face and hence low susceptibility to engine surge.

At low Mach numbers air is generally being 'sucked' into the intake and so static pressure tends to suffer an overall drop. Therefore, for practical reasons, the total pressure is used in the definition even though it only drops in relation to the freestream value. Also total pressure falls when there are losses in the flow that could occur as a result of boundary layer build up, shock waves, and separation. These losses can also be responsible for distortional effects across the compressor face and surge generation. Hence by quantifying these losses we have an effective way of describing the flow.

1.3.4 The Fluid Mechanics of Diffusing S-Duct Flows

The fluid mechanics of the airflow within an intake vary with the geometry of the intake. The RAE intake model 2129 is a diffusing s-duct, that is the cross-sectional area increases as you travel through the duct. There is also an offset in the y-plane between the highlight plane of the intake and the plane on which the compressor face lies creating an s-shaped type centreline. As a result there are a number of interesting characteristics that these flows exhibit.

After the first bend in the diffuser there is an interaction between the centrifugal pressure gradient and low energy region (such as that found in a boundary layer or separation region). If the air is to travel in a curved trajectory this requires a centrifugal force. As the air is turned, static pressure and velocity distributions change. The centrifugal pressure, P_{cent}, can be written as

$$P_{cent} \propto \frac{\rho V^2}{R}, \tag{1.9}$$

where V is the mainstream velocity and R relates to the curvature of the bend in question. Due to the fact that the outer wall has a greater radius than the inner wall then from equation 1.9 the inner wall has a greater centrifugal pressure. For ideal fluid with a uniform energy distribution the static pressure increases with radius to balance the centrifugal force. The sum of the velocity and static pressures is the same everywhere. Hence the velocities decrease from the inside to the outside of the bend as shown in figure 1.2.

Real flows involve non-uniform energy distributions. Velocity distributions change from zero at the duct walls to a maximum in the core flow. Centrifugal and pressure forces acting on the faster moving core flow cause it to move towards the outside of the bend. However, there is an adverse pressure gradient created on the outside of the bend (region of increasing pressure). Near wall fluid that is energy deficient and approaches this adverse pressure gradient cannot pass through it. Instead, the flow moves round the walls towards the low static pressure on the inside of the bends. This movement of the low energy region towards the inside of the bend combined with the movement of the core flow towards the outside of the bend sets up two cells of swirling secondary flows as seen in figure 1.3.

For the second bend the low energy flow is largely on the outside wall as a result of the first bend and is not driven back circumferentially by the method described previously. Hence the swirl pattern experienced at the engine face in a double bended intake is in the direction from the first bend and not the second bend.

This swirling flow can change the flow angle of attack on the compressor blades which can then lead to stall. Intake guide vanes (IGV) are fitted to some engines to combat this problem. Swirl is particularly susceptible in offset diffusers such as the one being considered in this thesis. Here the airflow is being delivered to the engine through a double bend (s-bend) as found on aircraft such as the F16.

Compressor blade stalling can act like a solid wall at the compressor face and can result in an engine surge. A resulting shock wave, often referred to as a 'hammershock', travels forwards out of the engine. A more in-depth discussion of engine surge can be found in chapter 5. Some common causes of compressor stalling are high distortion, cowl lip separation, and general flow unsteadiness. The distortion was described as the maldistribution of flow in terms of total pressure at the compressor face. Historically this has generally been a sufficient description of distortion although there have been a few notable exceptions. In one such case the failure to fully understand the nature of the intake flow field and the sensitivity of the engine to it led to some major problems. Swirling flow aggravated the effect of total pressure distortion and surge was encountered when the swirl was contrarotational to the direction of the fan rotor blades.

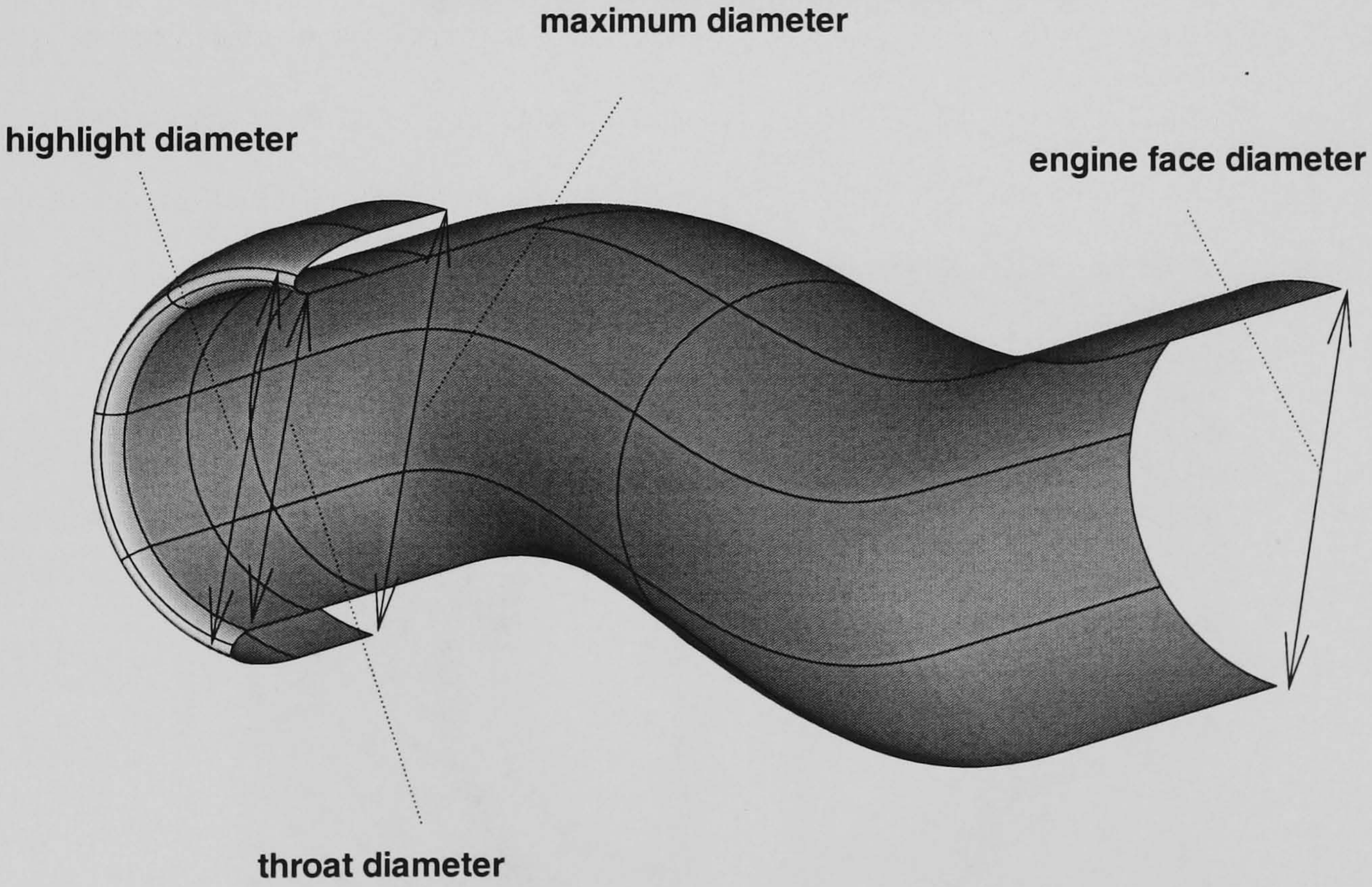

Figure 1.1: *Area definitions*

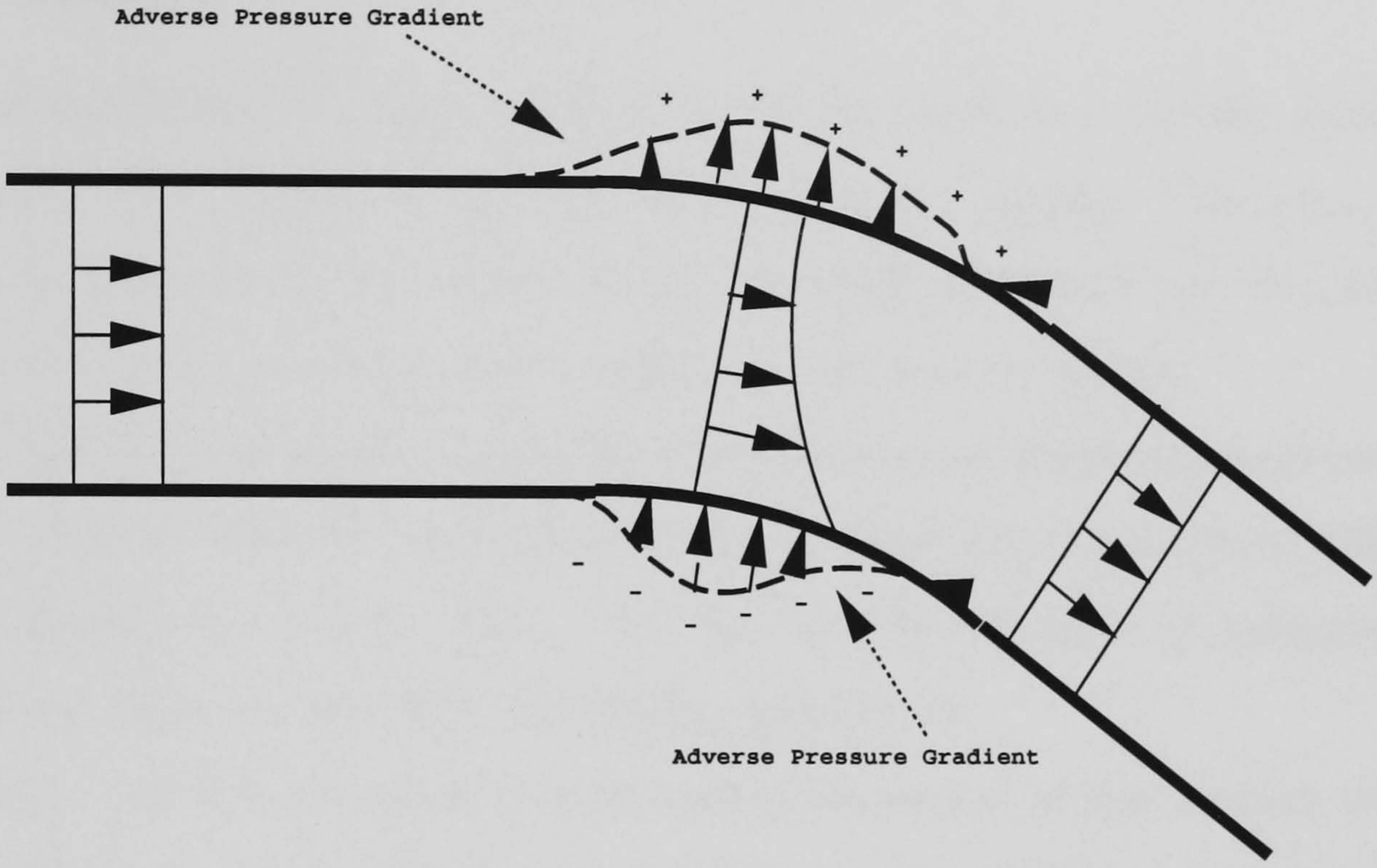

Figure 1.2: *Ideal flow around a bend*

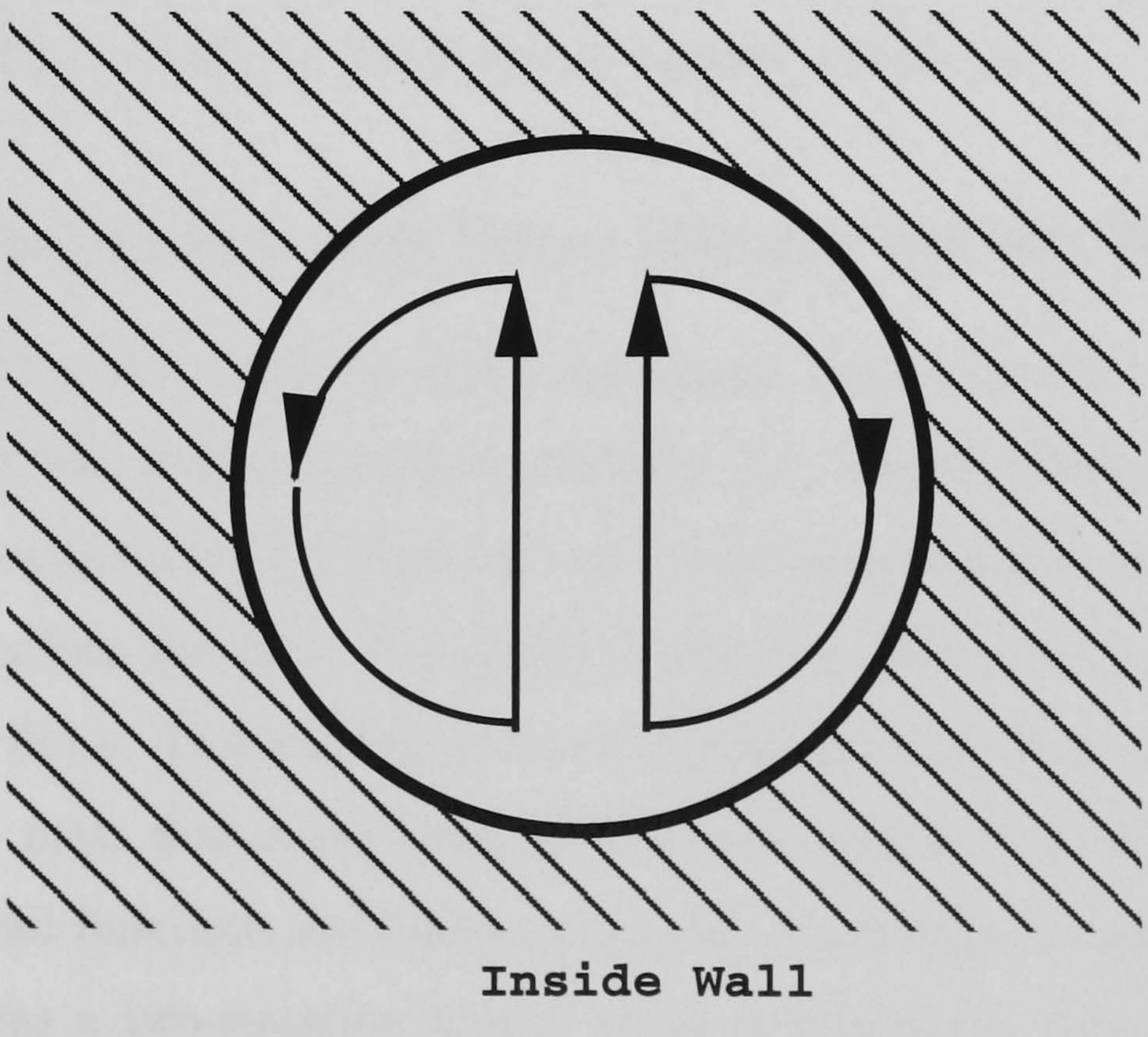

Figure 1.3: *Secondary flow*

1.4 Review of Previous Work

1.4.1 Intake Design, Flow Mechanics, and Compressor Blade Theory

Goldsmith and Seddon [7, 8] provided a detailed introduction to intake aerodynamics. These books cover intakes at subsonic and supersonic speeds. Distortion, pressure recovery, lip separation, and incidence are discussed and there are also sections on wind tunnel testing, computational techniques, and various designs.

Miller [9] has given a good description of the mechanics of flow in an enclosed curved geometry. This includes the forces that act on the fluid and the resultant effect on the fluid flow downstream of the offset. This has obvious relevance to s-shaped intakes. The book also looks at the effect of diffusing geometries.

Mattingly [10] has provided a fundamental discussion of gas turbine propulsion. The book covers a variety of topics, first giving a review of thermodynamics and compressible flows, before looking into gas turbines in more detail. Of specific interest is the section on component performance, turbomachinery, and nozzles.

Dardis and Mayhew [11] have developed a definitive process for determining intake pressure distortion data between test methods and facilities. There is useful information on experimental techniques for determining flow distortion.

1.4.2 Computational and Experimental Intake Work

Computational Euler and Navier-Stokes calculations were sought for the two standard high and low mass flow rate test cases in reference [12]. The flow features are described thoroughly and comparisons are made to two sets of experimental data.

May [13] describes the first of a series of Aircraft Research Association (ARA) reports on s-duct flows. This particular report investigates the flow in the M2129 duct for high and low mass flow rates using several two-equation turbulence models. It was found that wall functions are inappropriate for modelling the secondary flow and separation, whereas a two-equation model which is integrated through the sub-layer provides a qualitative prediction in the separated region. It is then postulated that a further improvement may be obtained by including non-linear eddy viscosity terms and modifications to sensitise the model to adverse pressure gradients. The report found that, for the low mass flow case, all the turbulence models used failed to predict any secondary flow.

May et al [14] advanced work carried out in reference [13] into the study of flow in the M2129 diffuser. Euler calculations were performed that included an experimentally determined displacement surface that was incorporated into the geometry. It was found that surface pressure predictions agree well following this modification. Turbulent Navier-Stokes simulations are presented that used an automatic procedure for updating the outflow boundary condition according to boundary layer development. The predicted results compare very well with experiment.

May [15] again examines the M2129 geometry for low and high mass flow demand. It was found that the two-equation model results for the low mass flow rate case are very similar to the results obtained using the algebraic turbulence model (reference [14]).

Abrahamsen et al [16] looked at the flow in an s-shaped intake (M2129) using experiments and computations and the results are compared with available experimental data (reference[12]). It is concluded that a low cost experimental method and improved computational method seem to be viable. The improved computational method consists of a non-linear numerical modelling approach to improve the predictive capability of CFD. The results obtained appear good although the paper only examines the relatively simple low mass flow case.

Kral [17] investigated the flow in a highly serpentine duct using various turbulence models. It is concluded that the two-equation models better predict the flow than the algebraic and one-equation models when compared with experimental data.

Anderson et al [18] applied a 3D Full Navier-Stokes (FNS) analysis and a 3D Reduced Navier-Stokes (RNS) technique to examine the flow separation in diffusing offset intakes. The RNS approach uses an initial value space marching solution technique to achieve a level of approximation that will yield accurate flow predictions, while reducing the computational time of the FNS approach. The FNS implicit approach solves the full 3D RANS equations in a strong conservative form. Both methods were able to capture the overall flow physics of vortex lift-off but more consideration to the development of turbulence models for the prediction of separation and reattachment points is needed.

Harloff et al [19] computed three-dimensional Navier-Stokes solutions for diffusing and non-diffusing s-shaped intakes. In the calculations both H-grids and polar grids are used. Both grids give similar results but the polar grid provided smoother turbulent eddy viscosity due to the lack of 'corner effects'. These corner effects on the H-grid cause excessive grid skewness and lead to non-orthogonal grids, causing some discrepancies. Euler solutions showed that the development of secondary flow was mainly driven by inviscid effects. It was finally concluded that perhaps the realism could have been improved by using adaptive gridding and more advanced turbulence models.

Town and Schum [20] carried out a three-dimensional investigation of complex intake designs using a parabolic Navier-Stokes code. The effect of curvature of the diffuser centreline and transitioning cross-sections is studied. The primary source of engine face distortion is centreline offset and not transitioning diffuser cross-sections. The thickness of the boundary layer at the diffuser intake should be as thin as possible in order to minimise total pressure losses in the duct.

Zhang and Assanis [21] set out to evaluate the performance and accuracy of a three-dimensional Navier-Stokes flow code using the $k-\epsilon$ turbulence model. The benchmark used is an S-duct of circular cross-section. They concluded that, given the limitations of the turbulence model in use, the numerical method yields satisfactory results giving a good qualitative description of the pressure field and quantitative prediction of the velocities.

Wendt and Reichert [22] investigated, using experimental techniques, the effects of vortex ingestion in a diffusing s-shaped intake. The study looked at different locations of vortex ingestion and compares the results with a 'clean' intake flowfield. Little effect was found to occur as a result of vortex ingestion, except in the case where the ingested vortex interferes with the region of flow separation on the starboard side of the intake. The vortex appeared to promote stronger regions of transverse flow.

Harloff et al [23] compared three-dimensional Navier-Stokes computational results with new experimental measurements. A previous study had indicated inadequacies in either the grid resolution or algebraic turbulence model used. This study used a finer grid and the $k-\epsilon$ turbulence model. The results are in reasonable agreement but both turbulence models under-predict the length and angular extent of boundary layer separation and in both cases initiated further downstream than witnessed in experiment. They concluded that neither turbulence model adequately accounts for strong secondary flows with separation.

Saterskog et al [24] detailed computational work carried out on the SAAB 105 intake. The main aim was to investigate the possibility of using CFD to determine intake flow characteristics affecting the engine functions. As a result the work has focused mainly on flow quality at the engine face by determining engine face distortion and pressure recovery. They determined that for mainly attached flow the comparison with experiment tends to be very good. However, in cases where the flow is highly distorted (which tends to be associated with separated flow) there are regions with larger losses than experiment. They mentioned that the tendency was to overpredict the pressure recovery in such regions and that other authors have found this too.

Van Deusen and Mardoc [25] discussed a method of evaluating intake pressure defects and random pressure fluctuations on supersonic aircraft. A review was made of the development of a distortion factor for steady state intake pressure distortion. It concluded that, as well as distortion, turbulence is a prime variable in assessing the compatibility of an engine/intake combination. The authors also discussed several methods of assessing turbulence levels to this effect.

1.4.3 Computational Surge Work

There has not been a great deal of computational work into the study of surge and surge wave propagation and what work that has been done does not relate to diffusing s-duct intakes. The subject area is relatively unresearched and has been mainly tackled using experimental approaches.

Ytterstrom and Axelson [26] were mainly concerned with the evaluation of a new time stepping scheme. However the application used for this evaluation was the hammershock phenomena that can occur in air intakes as the engine stalls. The authors used a sample uniform surge signature (one which is applied across the whole compressor face) and measured pressure/time histories through the duct. There was unfortunately no experimental data with which to compare the results. The paper also gave the case of a reflected shock in a shock tube as a test case.

Hsieh et al.[27] looked at two different signatures applied to an aircraft intake and it's corresponding response. It was found that at higher levels of pressure fluctuation, the viscous flowfield bore little resemblance to the inviscid one. They state that the flowfields obtained are plausible but the accuracy remains to be determined since there is no experimental data available for comparison.

Causon and Ingram [28] used computational techniques to study the flow in a twin side-by-side intake system using the Euler equations. The modelling of the surge was done by prescribing a pressure disturbance at the exit plane of one of the intakes, the strength of which was between 100% and 200% of the mean exit static pressure. The results obtained appear to indicate that the static pressure attenuation of a propagating surge wave in the prescribed conditions occurs upstream of the intake entry plane and thus a weak rarefaction wave travels down the adjacent intake. However there was no evidence that this rarefaction wave induced sufficient dynamic distortion to induce a complementary surge.

Goble et al [29] also employed computational techniques to the study of engine surge propagation. The study was done on the ATF F-22 aircraft intake at supersonic speeds. Again, an unsteady engine back pressure boundary condition was introduced and some time appears to have been spent on accurately modelling an engine surge. They suggested that the simplest method - an instantaneous peak pressure known as the 'guillotine' method - is not a realistic representation and that the actual form of a surge is more akin to a sinusoidal pattern with a gradual (but rapid relative to global time scales) build up in peak pressure. The results presented included a time-history of the forces in the duct.

Miller and Hamstra [30] described how ultimate loads for intake structures are set by peak pressures associated with hammershocks induced by engine surge. Existing techniques for predicting peak pressure loads were based on an empirical approach using flight test data for the F-111 aircraft but the paper went on to mention that this would no longer be suitable given the changes to intake designs. It was mentioned that a new approach to the prediction is required and that CFD could be developed as a cost-effective alternative. Computational work was done on the F-16 NSI (normal shock intake) and steady state computations were used as a starting solution to the unsteady problem. An ultimate over-pressure ratio of 1.69 was set based on guillotine analysis with a rise and fall time of 10 milliseconds . A physical time step of 13 microseconds was chosen with the calculation continued until the shock was fully expelled from the intake system. The hammershock took three quarters of the duct length to develop to peak strength as opposed to the guillotine method which generated a hammershock immediately upstream of the engine face.

Mays [31] looked at a numerical solution of the one-dimensional, unsteady, inviscid flow equations in a variable area duct. Again the simulation of the engine face during surge modelling was considered. One attempt was to set the Mach number at the engine face to zero which is similar to the guillotine method, but ultimately a corrected weight flow parameter was used to describe dynamic engine behaviour. The authors found that the peak pressure experienced by the intake during compressor surge was sensitive to the intake contraction ratio and also to the presence of auxiliary air systems.

Hindash et al [32] looked at the two-dimensional computations to evaluate the prediction capabilities of the intake duct pressure rise during engine surge. The results obtained were compared with analytic shocktube work and flight test data. Similar to previous work, a starting steady state solution was obtained and initial unsteady work was done by assuming a solid wall at the engine face (in essence flow stagnates across the entire engine face simultaneously). The authors point out that this is not truly representative of the real aircraft intakes that can sometimes develop backflow during a stall/hammershock event to release high pressure within the compressor. The authors detail their difficulty in finding experimental information about backflows and instead use engineering judgement to make assumptions. They add a small addition to the grid downstream where a uniform backflow Mach number is assigned. The resultant hammershock was found to be expelled from the geometry faster than the hammershock created by the closed end method. Subsequent work then looked at partial blockage which rapidly progressed to complete blockage. Oblique shocks were found to be generated and they coalesce into a normal hammershock that travels out of the intake. The shock orientation matched that of an inclined closed end and this was used to model other complex flows that have non-uniform stall events. Overall they conclude that the hammershock event is characterised by the coalesced waves. The wave continues to grow stronger by overtaking weak oblique shocks in front of it and soon becomes normal to the incoming flow.

1.4.4 Experimental Surge Work

In comparison to computational work, there is more experimental work available in the study of surge and surge wave propagation. However none relate directly to the modelling of surge in diffusing s-duct intakes.

Evans and Truax [33] presented basic data and procedures used to calculate structural loads due to engine surge. The work was based on a correlation between transient pressure and engine-compressor pressure ratio. The paper also contained an excellent summary of engine surge theory. Lotter et al [34] emphasised that accurate knowledge about pressure and its amplification/attenuation (which is essential for accurate determination of the structural requirements) is difficult to obtain by purely theoretical means. A surge wave generator (SWG) was created and placed downstream of the AIP. By blowing air upstream intermittently through a rotating hollow cylinder and varying blowing speed, area and the rotational speed of the cylinder allowed for the creation of very accurate surge signatures. Work was done on a twin side-by-side intake system and it was found that the peak pressure level is attenuated in the intake where the surge is initiated but it did propagate into the adjacent intake.

Marshall [35] derived a semi-empirical method that had been developed for predicting the peak surge-induced overpressures in the vicinity of the engine face. The method was found to be applicable to long intakes such as those found on military aircraft, and particularly supersonic aircraft. Auzins [36] described the structural effects of engine stall while maintaining required structural margins. It was found that hammershocks can impose significant loads on external stores as well as the intake structure itself. Luber and Becker [37] examined the effect of dynamic loads such as bird strike, gun fire, buffet and landing on aircraft carriers and how to approach the problem of integrating all aspects into an optimum design. Dynamic hammershock effects on intake design were summarised.

Bellman and Hughes [38] described information on flight tests conducted on the F-111 aircraft that had dynamic and steady state pressure sensors in the left intake. Many surges were encountered in the trials due to increasing the angle of attack. The data showed that steady state distortion was the primary cause of compressor stall and that there was a generally low level of turbulence (as opposed to static distortion where increases in the angle of attack lead to corresponding increases in the level of turbulence). High turbulence levels were found to be associated with areas of low pressure recovery and, following a compressor stall, a rotating stall is almost always experienced.

Burcham and Hughes [39] carried out an experimental investigation of an F-111A aircraft in an effort to determine the dynamic nature of intake pressure fluctuations which can lead to compressor surge. A series of compressor surges were studied over a wide range of Mach numbers from subsonic to supersonic. The conditions of the intake prior to surge were investigated using statistical techniques and high response distortion factor calculations. Combining the steady state distortion patterns obtained from low response pressure instrumentation with the dynamic sensor data gives a distortion factor that always shows a peak prior to the occurrence of surge. The peak value was found to increase with increased airflow, with non-afterburning engines among other things.

Becker et al [40] offers good background information on hammershock loading. Comparison was also made of local dynamic stress calculations obtained from NASTRAN using static stress calculations using assumed constant dynamic load factors. It was demonstrated that the dynamic tools could be used for verification purposes and interestingly also to minimise structural weight. Breuer and Servaty [41] detailed the results of experimental and numerical studies to examine the inception process of rotating stall and surge. Unsteady pressure measurements carried out on a 3-stage high speed compressor revealed characteristic features of the instability onset. The data obtained suggested that the instability started from small amplitude disturbances rotating in the 'rotor' direction which finally led to rotating stall or surge. With regard to the numerical work the author used an inviscid model and the influence of the blade rows was accounted for by source terms to account for pressure loss and energy input. However it is concluded that the model does not predict pre-stall waves as witnessed in experiments. This was attributed to an overall lack of knowledge regarding the nature and cause of the pre-stall waves and more detailed experimental work was suggested.

Cousins et al [42] presented unique high response measurements that show the characteristics of post stall behaviour. Comparisons of compressor stall and surge with and without a centrifugal stage highlighted the advantages of using centrifugal technology in gas turbine engines. Borys and Moffatt[43] described how rotating stall is a viscosity-related phenomenon whose effects are well understood but whose origins are less well understood. The paper presented the results of several studies in rotating stall. The main conclusions were that the stall tended to be most evident at the tip of the compressor blade and the strength of the stall decreased with successive stages through the compressor.

Finally, Kirkov et al [44] detailed peak static pressure measurements at the intake to an engine (both turbojet and turbofan) during stall. It was found that the highest pressures at the engine intake were obtained as a result of stall caused by intake pressure distortion, a fuel pulse or afterburner transient. For a given compressor pressure ratio, intake pressure distortion induced stall provided the highest pressure at the engine intake and the highest engine face static pressure during stall was around twice the engine intake static pressure.

1.4.5 Review of Turbulence Closures

Past research in relation to steady and unsteady turbulent flow simulations in the context of Reynolds Averaged Navier-Stokes (RANS) equations has shown that the realism of numerical predictions is significantly affected by the turbulence model employed. Experience using zero-equation turbulence models (e.g. Baldwin and Lomax [45]) has shown that these models do not provide satisfactory results, especially in separated flows and their predictions depend upon empirical constants and topographic parameters which are case specific.

Linear eddy-viscosity models (LEVM) assume an explicit algebraic relationship between Reynolds stresses and mean strain, known as the Boussinesq approximation (the principal axis of the Reynolds stress tensor is computed as the product of the eddy viscosity and the mean strain rate-rate tensor). These models provide satisfactory results for attached, fully developed turbulent boundary layers with weak pressure gradients and are also relatively easy to implement into computational fluid dynamics (CFD) codes. However, the predictions deteriorate when all components of the Reynolds-stress tensor become dynamically significant.

Linear low-Re two-equation models seem to offer the best balance between realism and computational cost, but since they employ the Boussinesq approximation for the Reynolds stress tensor, are not able to capture effects arising from normal-stress anisotropy. Second-moment closures offer a more exact representation of the Reynolds stresses but require longer computing times and careful numerical implementation for obtaining stable numerical solutions. Reynolds-stress models have been used in the past to investigate shock/boundary layer interaction (see Davidson [46]; Batten et al [47], amongst others). These studies showed that in certain cases second-moment closures may provide better results than linear models, but in other cases the results are inconclusive. Other approaches in turbulence modelling include the non-linear eddy viscosity models (NLEVM) (Speziale [48]; Craft et al [49]) and explicit algebraic stress models (see Gatski [50]; Abid et al [51, 52]).

Since part of the focus of this work attempts to predict the flow field in an intake under unsteady flow conditions several issues regarding the performance of turbulence models in unsteady flows must be considered.

Previous work by Fan et al [64] found, that since an instantaneous log-law does not in general exist, formulations based on the log-law and the equilibrium assumption are not appropriate for unsteady flow computations. In addition, as the frequency of the unsteadiness increases the turbulence becomes more directly affected by the fluctuating mean flow and non-equilibrium effects become important; this part of the turbulent flow physics is not well represented in most of the available closures. Separation often accompanies the unsteady flow and consequently good prediction of the separated flow region is essential for realistic unsteady flow computations. This is necessary for both internal and external flows.

Looking at published results for unsteady turbulent flow one may conclude that for many cases the obtained results are in qualitative agreement with the experiments but quantitative comparisons indicate that there is significant room for improvement.

Finally, problems arise from the lack of adequate experimental data for comparison, especially for unsteady flow cases. This is mainly due to the difficulties in performing flow field visualisation and measurements under unsteady flow conditions. There is, however, a need for high quality experiments at realistic Reynolds and Mach numbers in order to assess, and possibly "tune" the available turbulence models.

1.5 Overview of Dissertation

From the literature review it is apparent that there has been considerable investigation of the M2129 intake under standard steady conditions. However these studies have raised further questions in many cases. It was therefore felt worthwhile to undertake a thorough investigation of the M2129 at two standard test conditions. Further, there has been no documented information on the investigation of the M2129 at incidence and also the performance of the intake when various surge signatures are applied. These scenarios have also been covered to provide a more complete investigation of the M2129 intake in various flow regimes.

Chapter 2 discusses the numerical techniques used. A summary of the code is given, with details given in appendix A. Turbulence modelling issues are outlined and are described in detail in appendix B. Grid generation and formulation of boundary conditions are discussed.

Chapter 3 examines the operation of an air intake at normal conditions (computationally steady) for a high and low mass flow rate. Before any study can begin into unsteady intake aerodynamics it is vital to validate computational results against any previous computational solutions and experimental data available. Ideally the steady validation should be done against previous experimental data but also against any computational data in order to offer direct comparisons between flow solvers.

Chapter 4 furthers the steady intake study by examining the problem of intakes at incidence. Various angles of yaw (section 4.1) and pitch (section 4.2) are studied, focusing on the effects on pressure recovery and distortion. Both high and low mass flow rates are again examined.

Focus then shifts in chapter 5 to the unsteady problem of surge. The phenomena of engine surge is reviewed. As there is currently no surge validation data (experimental or otherwise) available for the M2129, other cases had to be explored. The first unsteady validation case examined was an inviscid shocktube. Unsteady validation is concluded with a look at a simple surge in a straight pipe for which experimental data is available.

Chapter 6 then looks at the application of surge signatures in the M2129 intake. This work begins with a review of different techniques for simulating an engine surge. Grid and time convergence studies are then undertaken. Four surge signatures are then looked at and applied for the high mass flow rate. The surge work is concluded by applying surge signatures at the low mass flow rate, varying the over-pressure ratio, and applying a surge signature at incidence. Finally, overall conclusions are drawn in chapter 7.

Chapter 2

Numerical Formulation

This chapter describes the computational model used for the study. The code is introduced in the form of a summary of the features and techniques employed. A more detailed description of the code can be found in reference [69] and in appendices A and B.

Following a description of the code grid generation is considered. Finally there is a full description of the boundary conditions used, particularly those at the engine face.

2.1 Flow Simulation Code

2.1.1 Background

PMB, Glasgow University's three-dimensional flow code, has been tested on a range of aerodynamic problems including hypersonic spiked body flows (Feszty et al [70]), rolling pitching and yawing delta wings (Arthur et al [71]) and 2D and 3D cavity flows (Henderson et al [72]).

All flow variables are non-dimensionalised by the following method where variables with an asterisk indicate a dimensional quantity

$$x = \frac{x^*}{L^*}, \qquad y = \frac{y^*}{L^*}, \qquad z = \frac{z^*}{L^*}, \qquad t = \frac{t^*}{L^*/U^*_\infty},$$

$$u = \frac{u^*}{U^*_\infty}, \qquad v = \frac{v^*}{U^*_\infty}, \qquad w = \frac{w^*}{U^*_\infty}, \qquad \mu = \frac{\mu^*}{\mu^*_\infty},$$

$$\rho = \frac{\rho^*}{\rho^*_\infty}, \qquad p = \frac{p^*}{\rho^*_\infty V^{*2}_\infty}, \qquad T = \frac{T^*}{T^*_\infty}, \qquad e = \frac{e^*}{V^{*2}_\infty} \tag{2.1}$$

A cell centred finite volume technique is used to solve the Euler and RANS equations in curvilinear form. The diffusive terms are discretised using a central differencing scheme and the convective terms use Roe's scheme with MUSCL variable interpolation offering second order accuracy. Steady and unsteady flows can be solved. Steady flow calculations can be classified into two different stages, initially running an explicit scheme at a small CFL to smooth out the starting solution and then a switch to a implicit time stepping scheme to obtain rapid convergence. The preconditioning method is based on Block Incomplete Lower-Upper (BILU) factorisation which is also decoupled between blocks which helps reduce computational time. The linear system arising at each implicit step is solved using a Generalised Conjugate Gradient (GCG) method.

The unsteady code uses an implicit unfactored dual time approach and the rate of convergence between the two consecutive real time steps is analysed by the pseudo time tolerance. This pseudo time formulation allows the time step to be chosen for time accuracy, improving the calculation efficiency. Attention is drawn to appendix A for further details on the steady and unsteady flow solvers in PMB.

2.1.2 Turbulence Modelling

One of the aims of this work is to assess the performance of various turbulence closures in modelling complex internal flows. The flow is challenging with complex secondary flows and strong pressure gradients generated by localised acceleration and deceleration, placing high demands on turbulence models. Turbulence is an eddying motion that exists at high Reynolds numbers. Turbulence has a wide spectrum of eddy sizes with a corresponding spectrum of fluctuation frequencies. Turbulence has prevailing rotational motion that can be thought of as a tangle of vortex elements with highly unsteady vorticity vectors that are aligned in all directions. The largest eddies have sizes on the same order of magnitude as the flow domain, have low frequencies, and are effected by the boundaries and the mean flow. The smallest eddies, on the other hand, are determined by the viscosity of the fluid and have high frequency fluctuations. As the

Reynolds number of a given flow increases, the width of the spectrum, or the difference between the largest and smallest eddies, increases.

The large eddies extract kinetic energy from the mean motion and feed it to the large scale turbulent motion. The eddies may be considered as vortex elements that stretch each other. Due to this vortex stretching, energy is passed down the cascade to smaller and smaller eddies until viscosity causes the dissipation of the eddies. Turbulence modelling remains a challenge in CFD. Reynolds (1895) introduced a statistical approach for expressing the flow properties as the sum of mean and fluctuating parts. For example the w-velocity component can be written as

$$w = \bar{w} + w', \tag{2.2}$$

where w is the instantaneous value, $\bar{w}$ is the time averaged component, and w' is the fluctuating component.

Turbulent calculations are permitted by deriving RANS equations for the time averaged values. These are very similar to the N-S equations except they contain terms which are averages of fluctuations that arise from turbulent eddies. As the fluctuations are uncorrelated with the mean flow values they are treated as additional unknowns in the equations which are thus indeterminate. Extra equations must be introduced in order to solve for the mean flow variables. This is known as closure and it is the provision of these equations that is the domain of turbulence modelling. Turbulence closure remains one of the central problems in modern day CFD.

For calculations employing a turbulence model a variety of turbulence closure techniques are available. The two most popular are algebraic (e.g. Baldwin Lomax [45]) and the two-equation model (e.g. $k - \epsilon$ and $k - \omega$). This work has used the $k - \omega$ model as described in Wilcox [65], a hybrid of the $k - \omega$ model called the SST model by Menter [67] and the one-equation Spalart-Allmaras (SA) model [66]. These approaches rely on the Boussinesq eddy viscosity hypothesis where there is the assumption that there is a linear relationship between uncorrelated Reynolds stress terms and strain rate terms. The Boussinesq approximation allows the equations for the mean flow to be obtained simply by re-interpreting the flow variables as being time-averaged values and replacing the molecular viscosity, μ, by $\mu + \mu_T$ where μ_T is the turbulent (or eddy) viscosity. However a method is still required to calculate μ_T.

The $k-\omega$ [65] turbulence model is a two-equation model. The eddy viscosity is determined from the solution of two partial differential equations - one for the turbulent kinetic energy (k) and one for the specific dissipation rate (ω). The rate of dissipation of energy in unit volume and time is related to the external scale of turbulence, l. Consequently two equation models are termed as complete as they can be used to predict turbulent flow without initial knowledge of the turbulent flow structure. In general two-equation turbulence models are preferred, particularly for complex geometries where they usually have the advantage of less dependence on distance from the wall. They are based on transport equations for k and ω. These equations contain additional uncorrelated terms which require modelling in a similar fashion to the Boussinesq approximation. The $k-\omega$ model has been widely used and has been successful, particularly for two-dimensional flows with adverse and favourable pressure gradients. It has also been found [65] that the model appears to match measured properties of recirculating flows with no changes to the basic model and it's closure coefficients. Problems found with the model include an unreliability when used in flows with boundary layer separation induced by an interaction with a shock wave. There has also been reported inaccuracies with flows over curved surfaces in some circumstances.

The shear stress transport (SST) [67] turbulence closure is a two-equation model that is a hybrid of the $k-\omega$ model. Closures that are based on the Boussinesq hypothesis are notoriously unreliable for flows with secondary motions. The SST model was devised in order to improve the prediction of the extent of separation in flows dominated by adverse pressure gradients (Bardina et al. [68] for example). To this end it was expected that SST predictions would show improvements over standard $k-\omega$ predictions for flows in diffusing offset intakes. The eddy viscosity formulation is modified to account for transport effects of the principal turbulent shear stress.

The S-A model [66] is a one equation turbulence model. This sort of model attempts to preserve the evolution advantages of two-equation models while side-stepping some known solution difficulties and is becoming more popular. In this respect it is more straightforward to implement into CFD solvers. However these models also rely on the Boussinesq -hypothesis and so can have limited success in their predictions for a variety of flows. However there are approaches to overcome this. One approach is to assume a non-linear relationship between uncorrelated terms in the RANS equations and the strain rates and can be implemented as an extension of a two-equation model. The model does not require as fine grid resolution for wall bounded flows. The model has been found to give poorer predictions in jet flow, but gives reasonably good predictions of 2D mixing layers, flat plate boundary layers, and wake flows. Importantly, it has shown improvements over the standard $k-\omega$ model for adverse pressure gradient flows, though not to the extent of the SST model (e.g. Bardina et al. [68] amongst others).

All of the above model equations are detailed in appendix B for completeness.

2.1.3 Computational Resource

The Computational Fluid Dynamics group at the University of Glasgow owns a cluster of PC's - known collectively as Jupiter and fully described by Badcock [69]. There are 32 nodes of 750MHz AMD Athlon Thunderbird uni-processor machines with 768Mb of 100MHz DRAM. MPI is used to link up multiple nodes to create a virtual machine and execute demanding problems. PMB distributes the load (the blocks according to size) as evenly as possible amongst the processors to further reduce calculation times. For example, running a turbulent problem on a grid of around 400,000 points and converging to 8 orders of accuracy (around 2000 implicit steps at a CFL of 30) requires 6 hours of computational time from execution to solution output running on 8 processors.

2.2 Grid Generation

Grid generation for the s-duct is challenging due to the nature of the duct and the desire to model an upstream far field to simulate flow from freestream into the duct. This has the advantage that direct comparisons can be made between flow solvers as the problem will be modelled from the same initial conditions and eliminates the difficulty of specifying different entrance conditions to the duct.

The geometry examined in this study is the RAE intake model 2129 (shown in figure 2.1), and was used as test case 3 by AGARD Working Group 13 [12]. The duct geometry consists of a circular intake section, one engine face diameter long and of constant cross section, joined smoothly into an s-bend diffuser of circular cross section. There follows a further constant area axi-symmetric cross sectional piece of one engine face diameter in length that terminates at the downstream boundary. At the upstream section of the intake (at the intake throat) there is an intake cowl which is defined internally by an ellipse and externally by NACA aerofoil section 1-854-35. The duct is circular in cross section throughout its length. The offset of the centreline and the variation of the radius in the diffusing part of the intake can be defined by the following two equations:

$$\Delta Z = \Delta Z_{cl} \left[1 - cos \left(\pi \frac{X_{cl}}{L} \right) \right] \tag{2.3}$$

$$\left(\frac{R - R_i}{R_{ef} - R_i} \right) = 3 \left(1 - \frac{X_{cl}}{L} \right)^4 - 4 \left(1 - \frac{X_{cl}}{L} \right)^3 + 1 \tag{2.4}$$

The dimensions of the model used in wind tunnel tests were:

- Duct length, $L = 18$ inches
- Duct intake throat radius, $R_i = 2.5335$ inches
- Duct engine face radius, $R_{ef} = 3$ inches

As mentioned, a constant area section of one engine face diameter in length was added to this duct length at either end of the diffuser and also a small component equating to about one half inch for the cowl. Hence, after non-dimensionalising with respect to the engine face diameter this leaves a total duct length of approximately 5, a diffuser length of 3, and the constant area sections are one engine face diameter long. The Reynolds number used in the experiments was 129,500 per inch. The Reynolds number used in the simulations of 777,000 was calculated based on the reduced engine face diameter of 1. The offset between the centreline at the highlight plane and the centreline at the engine face plane is 0.3 times the total length of the diffuser, L, which works out as 0.9 when non-dimensionalised with respect to the engine face diameter.

The ICEMCFD [73] commercial package was used to generate the geometry and grid. DDN is the 3D CAD/CAM package supplied with ICEMCFD that allows for all aspects of 3D surface and solid modelling. ICEMCFD HEXA is the 3D multiblock volume mesher that was used. The block topology is generated directly on the underlying CAD geometry. Rapid generation and manipulation of the block structure is possible.

The package is thus useful as it allows a blocking topology to be quickly created, the geometry can be altered, and the blocking strategy re-applied to the modified geometry.

In general, for circular shaped ducts there are two popular blocking strategies employed. The first option is to use a polar grid that has a face collapsed to an edge lying along the centreline of the duct. This method was not used as, invariably, there will be collapsed blocks lying in a region of the geometry where the flow characteristics are very important.

The second option is to use an 'o' grid topology that contains no collapsed faces or edges as shown in figure 2.1. The figure shows that the intake, downstream from the cowl, is split into six blocks through a cross-section. In the region of the cowl, however, problems arise with this blocking method and are due to the cowl interaction with the upstream 'farfield' blocks. This is visible in figure 2.2 (a) and (b). The most suitable method to minimise this problem was to extend the two large centre blocks of the 'o' grid out of the intake and into the farfield block. The four smaller outer blocks used in the intake (the 4 blocks defining the semi-circular shape) were also stretched out of the intake but then swept round to follow the contours of the cowl. This method produced the least skewed cells with good stretching ratios and orthogonality measures. Inevitably, however, there are areas in which 5 blocks join at a point (a line in 3D) and so in this area it is important to ensure that the detrimental effect on the grid is kept to a minimum by maintaining orthogonality as best as possible. In total 66 blocks were used to produce the topologies shown in the figures.

Figure 2.3 (a) and (b) show the blocks used to define the intake and the positions at which cowl block sections were taken for the subsequent figures. Figure 2.3 (c),(d),(e), and (f) then show these extractions. From these figures and referring back to figure 2.2 (b), it can be seen more clearly how the o grid is used to map onto the intake cowl. It is then simply a case of extending the blocks back into the farfield region. This region is large but because of the blocking topology used it is possible to have a coarser mesh in regions where the flow is freestream, keeping the global mesh size to a minimum.

Once a suitable block topology has been generated then dimensions are assigned to the grid and block and mesh smoothing are performed if necessary. Coarse, medium and fine meshes have been generated.

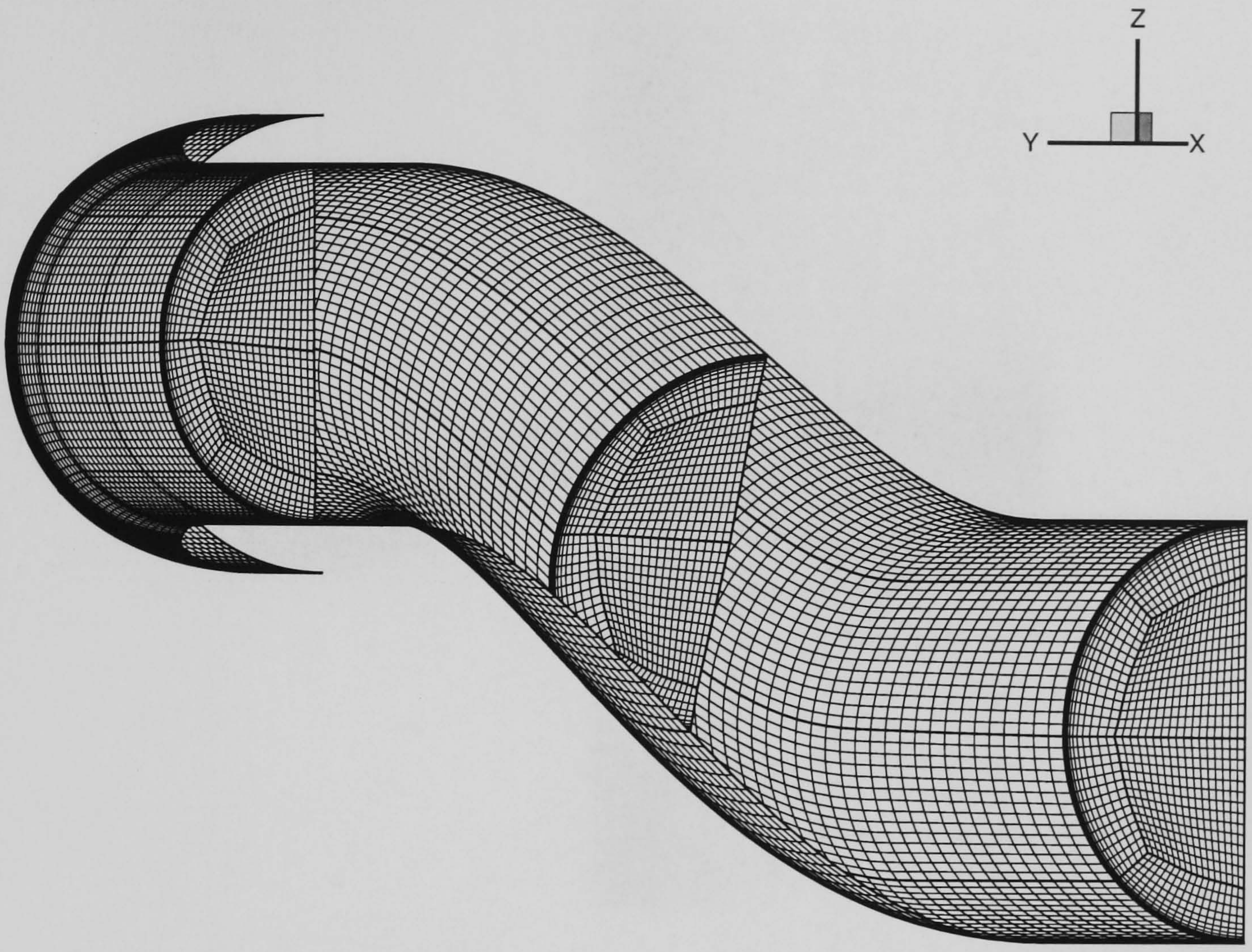

Figure 2.1: *'O' grid topology*

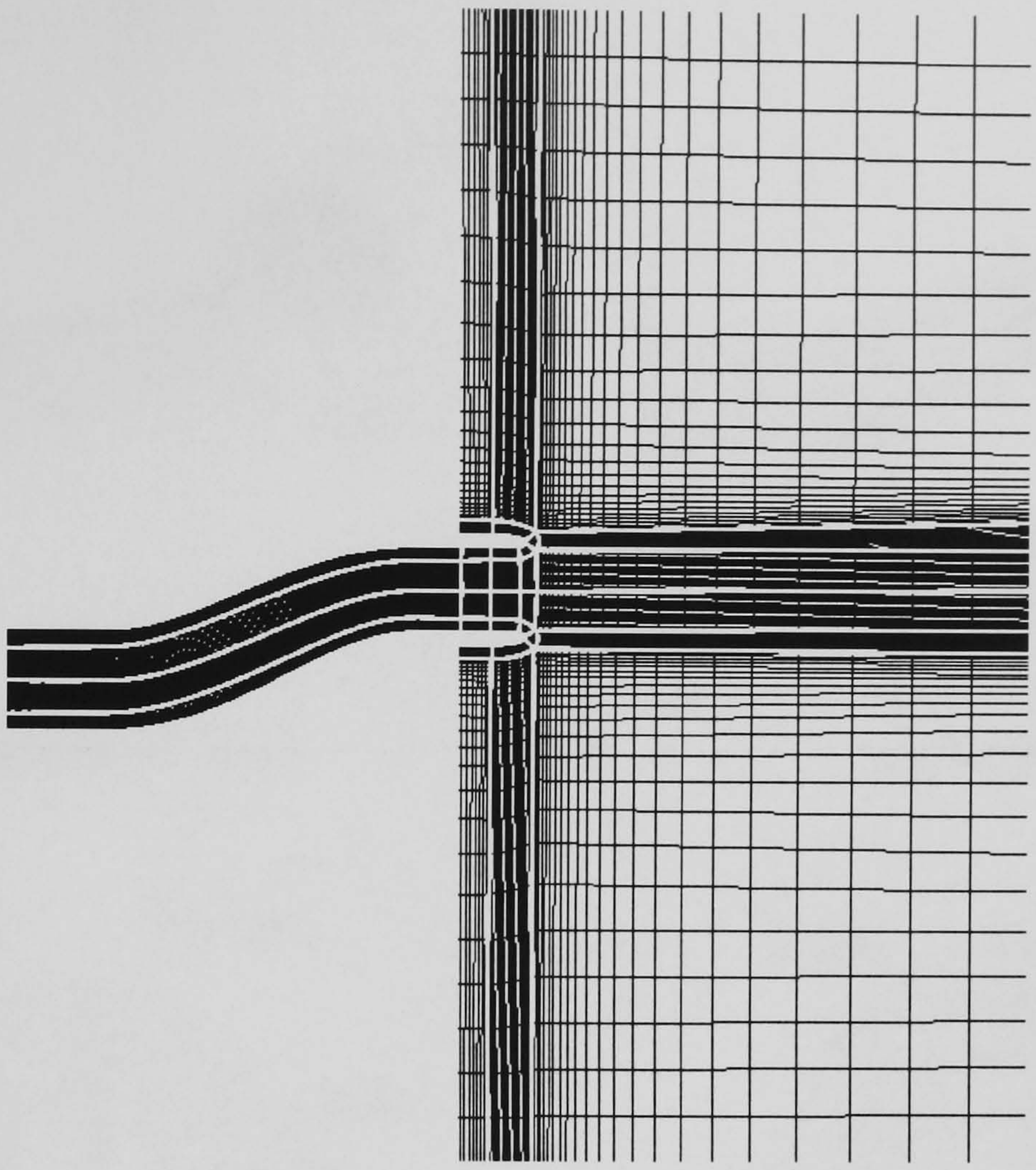

(a) Symmetry plane block boundaries

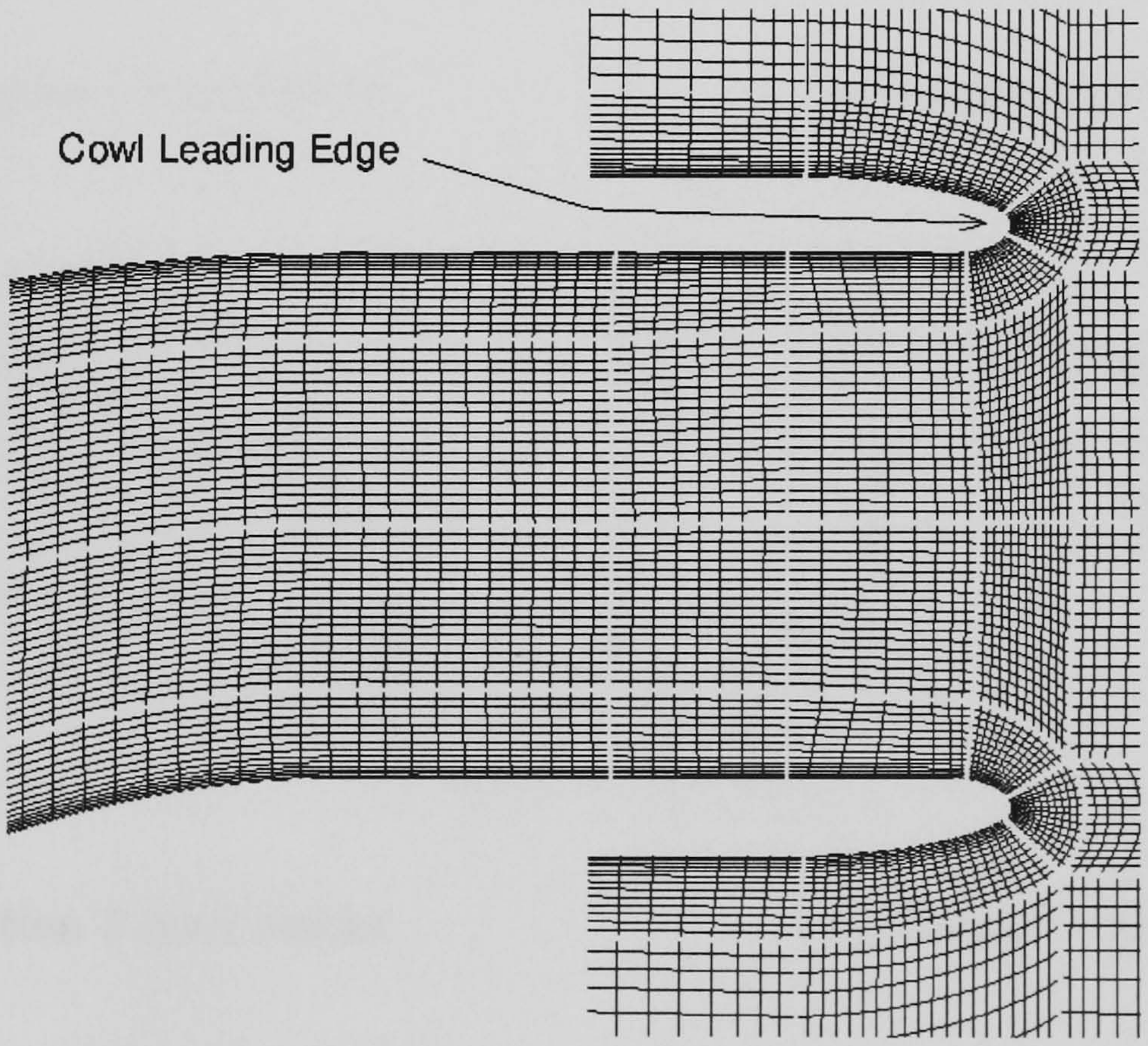

(b) Cowl symmetry plane blocks

Figure 2.2: *Block boundaries*

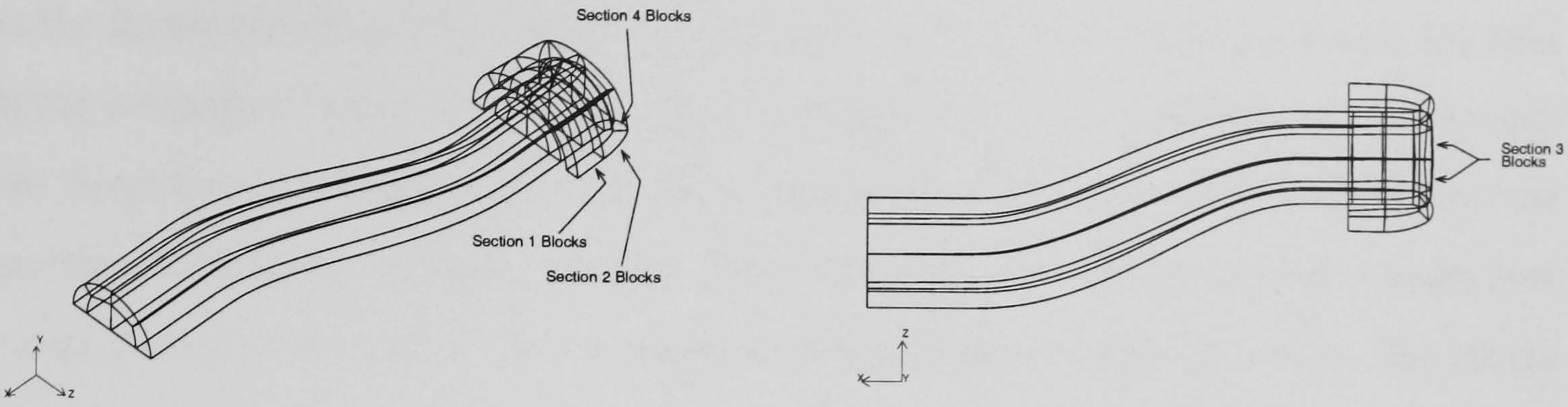

(a) Isometric view

(b) Normal view

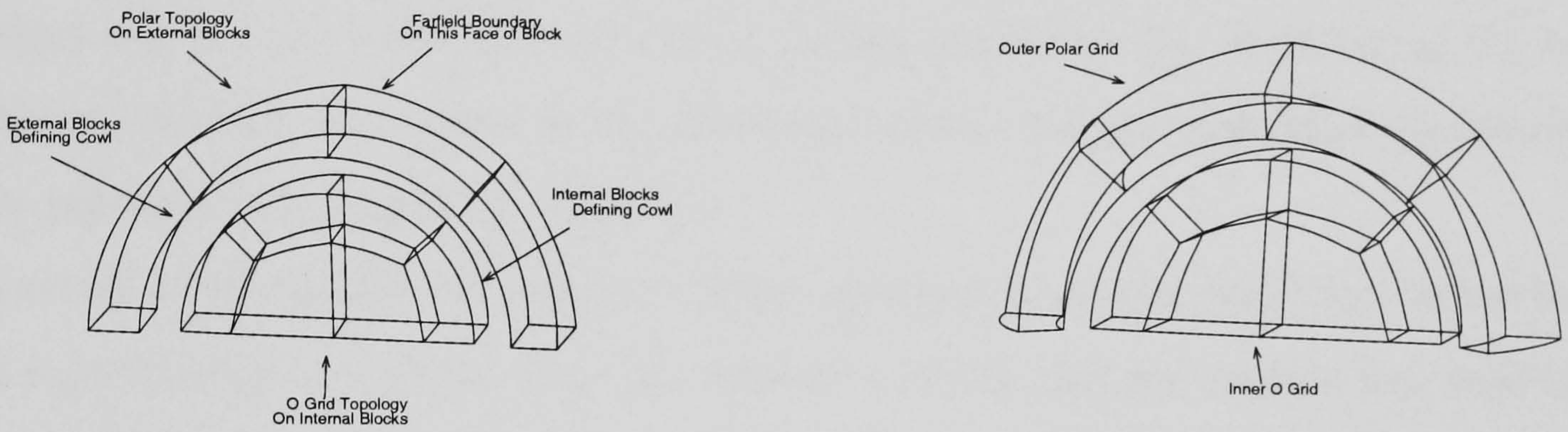

(c) Section 1 cowl blocks

(d) Section 2 cowl blocks

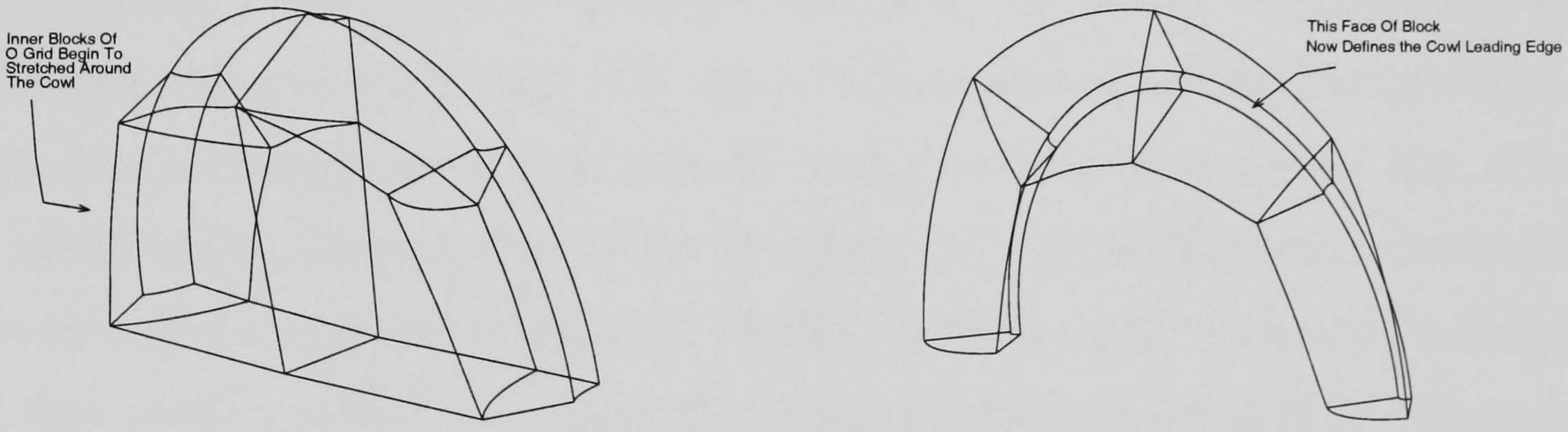

(e) Section 3 cowl blocks

(f) Section 4 cowl blocks

Figure 2.3: *Cowl blocking strategy*

2.3 Engine Face Boundary Conditions

From the literature (May [13], Mayer et al [74], and Chung and Cole [75]) it appears that applying a constant static pressure at the compressor face is a commonly used approach for the boundary condition and is the most straightforward method for simulating the engine face for strictly subsonic outflow. This could be done by specifying a mass flow rate and a contraction ratio. An estimation of the pressure recovery across the intake should also be made along with the knowledge of the freestream Mach number. Using all this input data it is possible to determine an engine face Mach number and from this a pressure ratio that is to be used as the downstream boundary condition.

The application of a constant static pressure for supersonic flow at the downstream boundary can be very reflective, as seen by Chung and Cole [75]. Mayer et al [74] uses a technique which is less reflective but disturbances like vortices travelling downstream can be reflected and propagate upstream.

In terms of the validity of a constant static pressure boundary condition, it has been found experimentally that for diffusing subsonic s-ducts this assumption can hold true [75]. This increases our confidence that this is the best method to tackle the problem while still remaining relatively straightforward. The downstream boundary is usually placed sufficiently far downstream from the aerodynamic interface plane.

A constant value of static pressure is not valid through the s-duct nor is it true for the total pressure at any location (including the engine face plane). Static pressure is only assumed constant at the engine face plane. It should be noted that the boundary condition that is being proposed here does not actually model the fan in any way. It is purely modelling the demand required by the engine (i.e. the fan/compressor rotation is assumed to have no upstream influence). Setting the right engine demand (specifying a mass flow ratio) is sufficient to model the upstream effects of the engine. This is a simplification in that the fan may impose a small amount of bulk swirl into the main flow but this has been found to be negligible.

The first step is to calculate the freestream MFP as

$$MFP_\infty = \sqrt{\gamma} M_\infty \left(1 + \frac{\gamma - 1}{2} M_\infty^2\right)^{-\frac{1}{2}\frac{\gamma+1}{\gamma-1}} . \tag{2.5}$$

Using this it is possible to determine the MFP at the engine face as

$$MFP_{ef} = \frac{(MFP_{\infty})(MFR)(CR)}{PR}. \tag{2.6}$$

It is known that values for the MFP should be less than 0.68461 for conditions we wish to examine (Mattingly [10]) so a check should be made to ensure the value is within suitable limits. The next step is to determine the engine face Mach number. We can use Newton's method to calculate this from equation 2.6.

When M_{ef} is known then the following formula can be used to determine the ratio of $P_{s_{ef}}$ to $P_{s_{\infty}}$

$$\frac{P_{s_{ef}}}{P_{s_{\infty}}} = \frac{P_{T_{ef}} \left(1 + \frac{\gamma-1}{2} M_{\infty}^2\right)^{\frac{\gamma}{\gamma-1}}}{P_{T_{\infty}} \left(1 + \frac{\gamma-1}{2} M_{ef}^2\right)^{\frac{\gamma}{\gamma-1}}}. \tag{2.7}$$

Applying a non-dimensionalisation consistent with the flow code,

$$\frac{P_s}{2q_{\infty}} = \frac{1}{2} \frac{P_s}{P_{s_{\infty}}} \left[\frac{1}{\left(1 + \frac{\gamma-1}{2} M_{\infty}^2\right)^{\frac{\gamma}{\gamma-1}} - 1} \right]. \tag{2.8}$$

This pressure ratio is the value that is used directly at the engine face boundary shown in figure 2.4. The MFR can be adjusted to get the constant static pressure required. When running a test case or comparing results with experiment the MFR is known and is not adjusted to give the constant downstream static pressure. Instead all the inputs would be known and the pressure ratio to be applied could be determined.

Although the pressure ratio derived in equation 2.8 is fixed for each specific test case mass flow at the engine face, the total pressure is not fixed and so the engine face Mach number is also free to vary. Density and velocity components are extrapolated out of the domain as with the extrapolation boundary condition (values on one side of the boundary are extrapolated across to the ghost cells on the other side of the boundary).

The downstream farfield boundary condition shown in figure 2.4 (freestream velocity, pressure, and density are fixed) is switched to an extrapolation boundary condition during the surge calculations in chapter 6 as spillage out of the intake occurs in some circumstances. Imposing freestream condition in this case is not appropriate (unless the boundary is moved sufficiently far downstream) and thus an extrapolation of all variables is set. The conditions at the other boundaries are more straightforward.

Farfield conditions are imposed on the boundaries in the upstream region. Standard symmetry conditions are set on the $y = 0$ plane. Wall boundary conditions are used to model the intake geometry. These boundaries can be seen in figure 2.4, with more details of the boundary conditions used contained in appendix A.5

As an addition, when post processing a parameter frequently examined is P_t/P_{T_∞}. From our pressure data output it is straightforward to determine this from

$$\frac{P_t}{P_{T_\infty}} = \frac{P_s}{P_{T_\infty}}\frac{P_t}{P_s}, \tag{2.9}$$

with the final term in equation 2.9 calculated from

$$\frac{P_t}{P_s} = \left(1 + \frac{\gamma - 1}{2}M^2_{local}\right)^{\frac{\gamma}{\gamma-1}}. \tag{2.10}$$

Another parameter that is important in intake studies is the distortion coefficient. This parameter is defined as

$$DC(\theta) = \frac{P_{t_{ef}} - P_{t_\theta}}{q_{t_{ef}}}. \tag{2.11}$$

Dividing through by the freestream total pressure gives

$$DC(\theta) = \frac{\frac{P_{t_{ef}}}{P_T} - \frac{P_{t_\theta}}{P_T}}{\frac{q_{t_{ef}}}{P_T}}. \tag{2.12}$$

The parameters on the top line are known and hence we only need to calculate the denominator from

$$\frac{q_{t_{ef}}}{P_T} = \frac{P_{t_{ef}}}{P_T} - \frac{P_{s_{ef}}}{P_T}, \tag{2.13}$$

and thus the distortion can be determined.

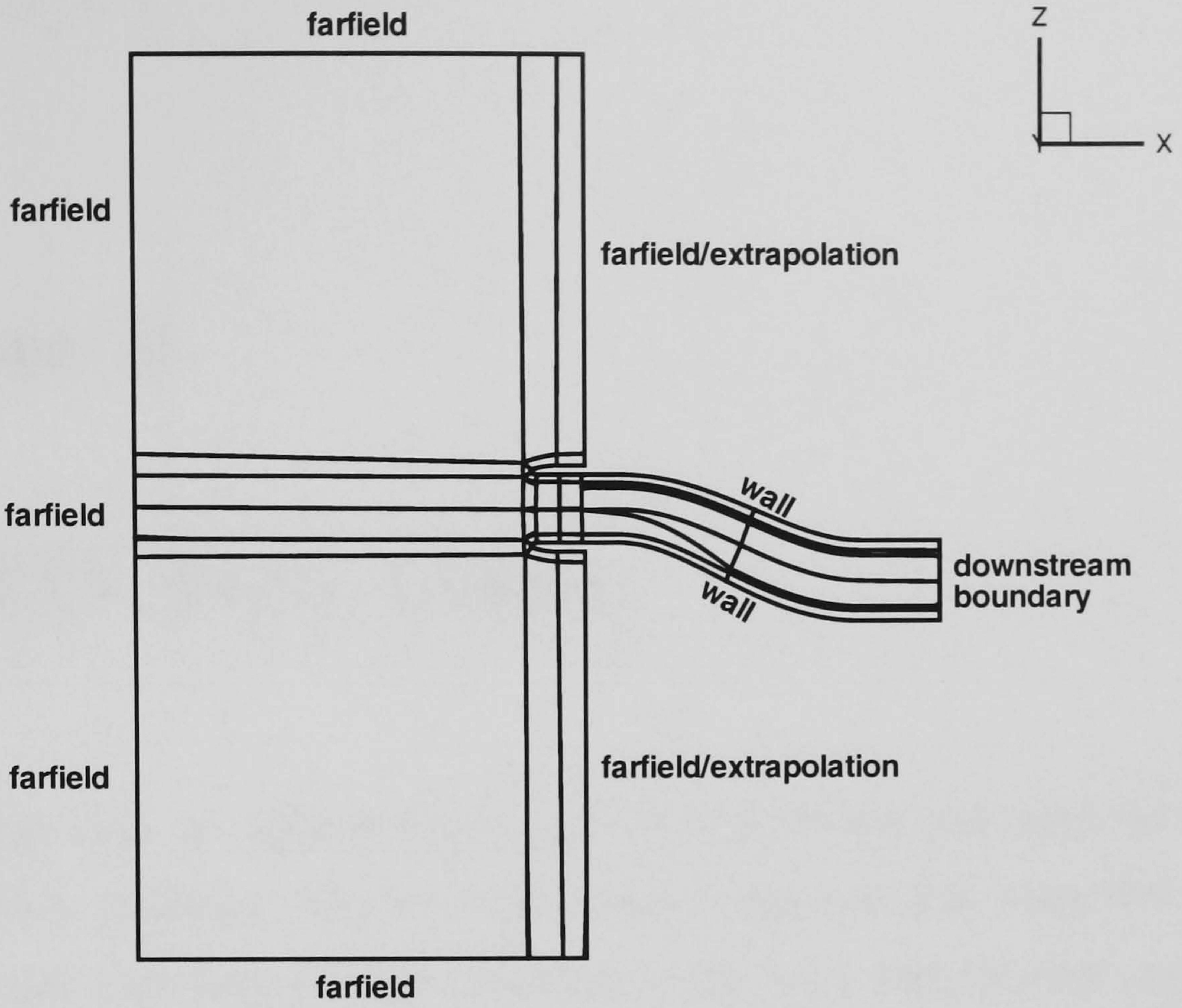

Figure 2.4: *Boundary definitions*

Chapter 3

AGARD Test Cases

This chapter aims to validate results against well known test cases for a steady through-flow problem. The test cases feature high and low mass flow demand by the engine and have been studied previously using both experimental and computational techniques. The experimental Reynolds number was 129,500 per inch. The characteristic length is the engine face diameter (6 inches in the experiments and non-dimensionalised to 1 for the simulations). Thus the Reynolds number used in the calculations was 777,000 for all cases. The case conditions are listed in table 3.1, following the definitions made in chapter 1.

Test Case	Mach Number	Pressure Recovery	Mass Flow Rate	Contraction Ratio
3.1	0.21	0.9280	2.173	0.9312
3.2	0.21	0.9897	1.457	0.9312

Table 3.1: *Summary of test case conditions*

3.1 High Mass Flow Rate - Case 1

RANS calculations were performed on the full geometry and compared with previous experimental and computational data. Comparisons for this type of problem are usually made for pressure data along the intake duct wall from the upstream cowl to the downstream engine face. The data is extracted from constant planes on the intake walls - namely the port, starboard and top/bottom side walls. These locations can be seen in figure 3.1. Because of the symmetry of the problem (the intake is not positioned at an angle of attack to the freestream at this stage) only half of the intake has been examined.

Using the techniques described in section 2.3, it was determined that the high mass flow engine face non-dimensional pressure ($p_s/2q$) should be set to 13.146 for the calculation. Remembering that the freestream Mach number is 0.21, then the freestream pressure will be 16.197 and the pressure ratio between freestream and engine face conditions is 1.232.

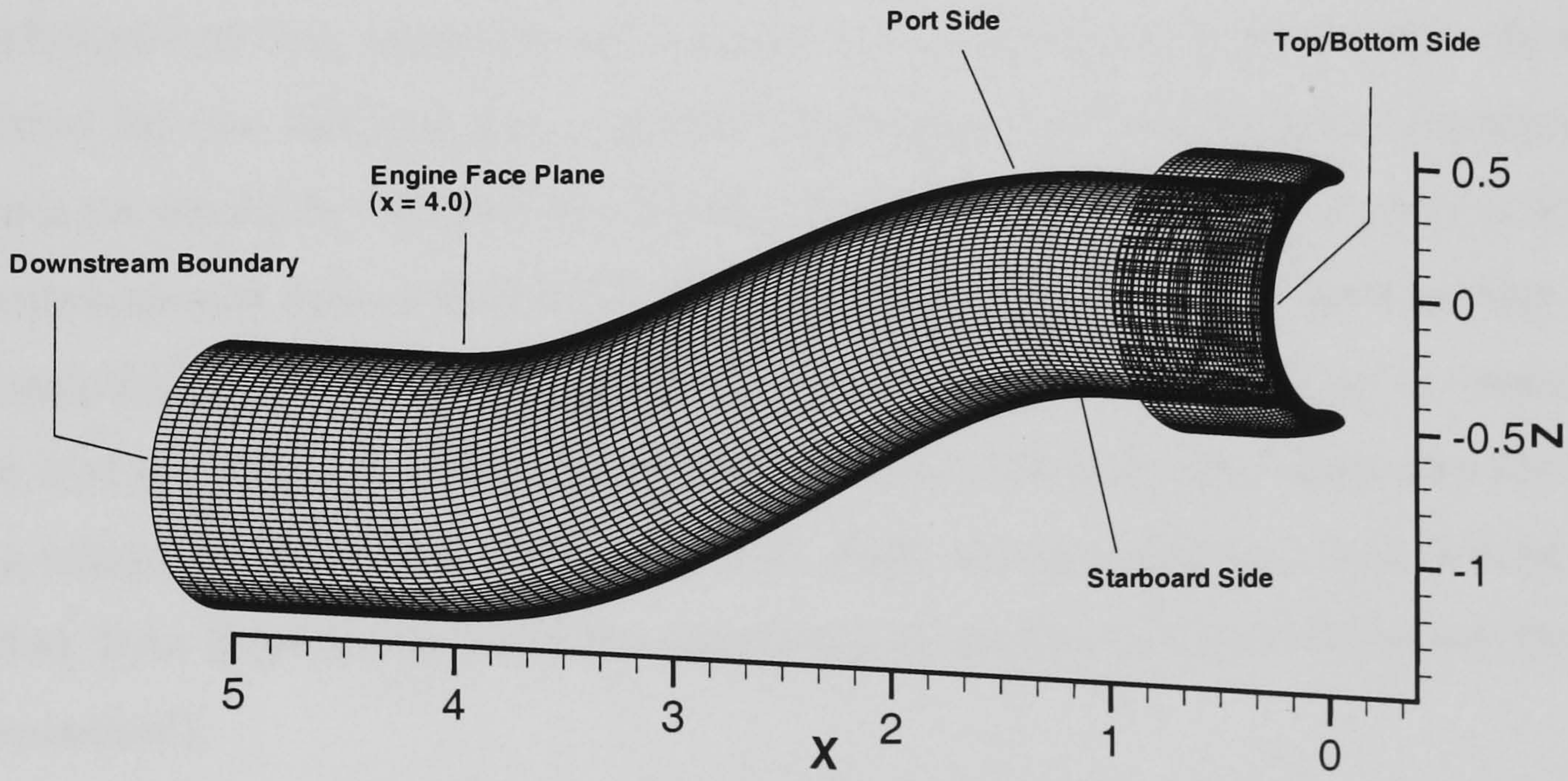

Figure 3.1: *RAE Intake Model 2129 - Wall boundaries including external geometry of cowl showing locations of slice extractions*

3.1.1 Results

A fully RANS converged solution to 8 orders of magnitude was achieved for all turbulence models used. Figure 3.2 shows the convergence details for the SST calculation.

Computations were run on different sized meshes to ensure grid independence. The coarse grid has around $204,980$ points, the medium grid $401,000$ points and the fine grid $830,000$ points. All three grids have the same 66 block topology as described previously. Again, the solutions for all turbulence models were found to be fully grid independent. Figure 3.3 shows extractions of pressure from the starboard and port sides for all three meshes for the $k-\omega$ turbulence model. It is clear that the results are very similar. This is of particular importance in the separated region on the starboard side. It can be concluded that the solutions are fully grid independent and the following calculations have been run on the grid termed 'medium'. Similar results were achieved for the other turbulence models but are not shown.

Static Wall Pressures Along Duct

With the knowledge that the solutions are fully converged and grid independent for all turbulence models, attention can now turn to examination of the results, which are compared for two different sets of previous computational solutions and experiments. The first set available was from the Defence Evaluation and Research Agency (DERA). The experimental data is labelled 'ARA Experiment' and can be found in May [13]. The computational solutions (using the $k - \omega$ model) can be found in the same reference and are labelled 'ARA computation'. The second set was taken directly from results contained in the AGARD report [12]. Here, the experimental data is from BAe (labelled 'BAe Experiment') and the computations are from Dornier (labelled 'Dornier Computation').

Figure 3.4 shows plots of local static pressure (non-dimensionalised with freestream total pressure) extractions from the starboard and port sides of the intake. Comparisons are made with ARA results. Comparison downstream of the first bend ($X/D = 1.0$) shows that all models compare qualitatively. The major differences occur upstream of $x/D = 1$ in the intake cowl region. Here the SST model is closest to previous work. The stagnation point on the outer cowl surface is in approximately the same location for all models. The subsequent acceleration of the flow into the duct from the stagnation point (the first dip on the graphs) is well matched. The $k - \omega$ and SA models both over-predict this acceleration (P_s/P_T values of less than 0.52 approximately indicate supersonic flow) whereas the SST model matches previous computation and experiment very closely.

The $k - \omega$ results do not recover from the over-prediction in flow acceleration. It will be discussed later that a complex shock reflection pattern develops that does not appear to be witnessed in experiments. As the pressure does not recover, the acceleration of the flow around the first bend is also over-predicted. Flow recovery is good following the first bend however and matches experiment better than the other models, particularly on the starboard side. This is probably fortuitous due to the lower pressure levels in the cowl region. As will be seen later, the flow separates from the first bend starboard side. Due to the flow mechanics described in section 1.3.4, a complex secondary flow develops. This can be detected in the graph for the starboard side by a slight dip (or 'saddle') in the pressure trace at around $X/D = 2.25$. The saddle is clearly not as strong as with other turbulence models or experiment. As the flow approaches the engine face ($X/D = 4.0$) the flow accelerates around the second bend on the port side ($X/D = 3.4$). It can be seen that the $k - \omega$ model appears to capture this the closest also but again upstream effects are likely to account for this.

The SA model also shows signs of complex flow in the cowl region. However the shock reflection is not as extensive and the flow recovers prior to the first bend. Acceleration around this first bend is then closely matched. Secondary flow is well predicted and a pronounced saddle dip on the starboard side is clearly evident. This is probably because it is known that the SA model predicts adverse pressure gradient flows more satisfactorily (see section 2.1.2). Subsequent flow acceleration around the second bend port side occurs but is slightly under-predicted.

The SST model gives the closest match to experiment and previous computation. Acceleration from stagnation is closely matched with previous works. Pressure recovery is marginally over-predicted through the cowl on both sides leading to a slight under-prediction of the acceleration of flow round the first bend on the starboard side. Secondary flow is then very well predicted on the starboard side, with a stronger saddle than was seen in the SA result. Flow remains in good agreement on the port side as well and the second bend acceleration on the port side is reasonably well matched.

Figure 3.5 shows plots of local static pressure (non-dimensionalised with freestream total pressure) extractions from the starboard and port sides of the intake. Comparisons are made with results contained in the AGARD report [12]. Previous comparisons in figure 3.4 showed that the $k-\omega$ model performed poorly in the cowl region. However it is clear that comparisons with Dornier calculations show strong similarities. Dornier calculations show some evidence of shock reflection in the cowl region (certainly the flow remains supersonic). On the starboard wall there is a strong shock following the first bend which is well matched in Dornier and $k - \omega$ solutions.

It is also clear that the two experimental data sets differ. BAe pressure levels are lower than those measured by ARA in all areas. Following subsequent discussions (DERA [78]) it was decided that ARA results are probably the most reliable as they are the latest set of experimental data to be obtained. Reference [12] reports sensitivity of the flow to numerical procedures. It concludes that discrepancies probably occur due to turbulence modelling errors, the inaccurate resolution of shock/boundary layer interaction, or missing information on the experimental transition from laminar to turbulent flow. It concludes that more detailed experimental data would be beneficial. This comparison highlights this need.

Symmetry Plane Boundary Layer Profile

An examination of the flow through the boundary layer in the cowl region ($X/D = 0.2$) in figure 3.6 shows that the SST model predicts a small pocket of separation following the initial acceleration into the duct that is probably shock induced. Due to a lack of detailed experimental data it is not possible to tell if a small separation pocket in the cowl region was witnessed in the experiment. The SA and $k - \omega$ models have a more turbulent boundary layer profile. Near wall velocities are much greater and the core velocity is higher. The profile for the SST model is more laminar like, boundary layers are smaller in the cowl region, and induced velocities here are smaller.

Symmetry Plane Flow Features

Symmetry plane Mach numbers and streamlines for all turbulence models are shown in figure 3.7. The problem of shock reflection in the cowl region for the $k - \omega$ and SA models is much clearer. Supersonic flow remains until the first bend for the $k-\omega$ model which has strong similarities with the Dornier computation in figure 3.5. The extent of the supersonic flow for the SA model is not as far-reaching as the $k-\omega$ model and shows a degree of quantitative and qualitative similarities with the experimental data labelled 'BAe' in figure 3.5. Supersonic flow is restricted to pockets for the SST model. These pockets occur when the flow initially accelerates into the intake indicated by the high clustering of iso-Mach lines in figure 3.7, and also as the flow accelerates around the first bend starboard side as previously discussed. This supersonic locations can be cross-referenced with the dips in the SST starboard pressure plots in figure 3.4 where is can be seen that the pressure recovers to subsonic values (P_s/P_T values of less than 0.52 approximately) quickly following the dips.

Acceleration of the flow around the starboard side first bend is also clearer with the $k-\omega$ model predicting the largest Mach numbers. It appears that the size of this region is considerably smaller for the SST model. Separation induced by accelerating flow around the port side second bend is detectable - particularly for the SST model although this can also be seen with the SA model. Separation from the starboard side first bend can be seen in the Mach number plot and more readily in the streamline plots. Here it is clear that the extent is considerable indicating a large distorted region as we shall see in section 3.1.1. The size of the separated region is comparable for all turbulence models, as is the separation and re-attachment locations.

Although all flow regimes are very different, namely in the cowl region, the SST model predicts the best comparison with ARA experimental data which is considered to be the primary set of experimental data. Increased confidence in the SST results can be found after a review of section 2.1.2 where it was predicted that the SST model would perform better due to its improved abilities in simulating separated adverse pressure gradient flow. In the following section, where attention turns to the low mass flow case, it was again found that the SST model performs the most satisfactorily when compared with experiential data. This further increases confidence in the current results.

Engine Face Behaviour

Figure 3.8 shows a plot of engine face total pressures for all turbulence models and includes a plot of total pressures from a previous computation and experiment for comparison. The general size of the distorted region is comparable for all models. Comparison with previous computation is favourable. It would appear that the size of the experimental distorted region is much smaller. However the number of probes used on the rake was small which could account for this. The velocity vectors clearly show the swirling secondary flow at the engine face. It is also clear that there is a circular region missing from the centre of the engine face plane for the previous work. This is where the engine face bullet is located. The engine face bullet was not modelled for the current computations as it will not have a strong influence upstream of this location which is the primary interest.

As mentioned, the generation of secondary flow in the intake has major implications in terms of engine performance. Some quality metrics that give an indication of engine performance are distortion and pressure recovery. Table 3.2 details these metrics for all turbulence models and compares them with previous results. The definitions of these metrics can be found in section 1.3. It can be seen that the pressure recovery data compares well between different turbulence models and is slightly over-predicted when compared with previous computations and experiment. The distortion coefficients are also over-predicted. The experimental rake that is used across the engine face to measure flow variables is not thought to be of a high resolution and this could account for the discrepancies. Another possible reason may be that the engine face bullet has not been modelled in the present computations as the primary interest is upstream of this location and so this could also have had an effect. For all zero incidence cases the 60^o sector chosen was 30^o either side of the starboard side symmetry plane.

Case	Pressure Recovery	Distortion Coefficient (DC(60))
ARA Experiment	0.92798	0.398
ARA Computation	0.92063	0.884
PMB-$k-\omega$	0.94359	0.658
PMB-SA	0.94366	0.651
PMB-SST	0.94117	0.688

Table 3.2: *HMFR distortion and pressure recovery at the engine face*

CFD Flow Field

A plot of surface shear stress on the inside wall of the duct for the *SST* model can be seen in figure 3.9 (a). As the flow approaches the first intake bend on the upper port side, it is swept round the curvature of the bend by the mechanisms described in the introduction. As one moves around the surface of the intake from the port to the starboard side, a point is reached where the flow spirals to a saddle point. It is clear that the whole surface shear stress is affected by the secondary flow motion. Closer examination of the cowl region shows that there is a discontinuity just inside the cowl lip where contours do not flow out and around the outer cowl surface. The reason for this is that there is a very small separation pocket predicted by the SST model in this region and this causes the discontinuity in the stream traces of shear stress.

Figure 3.9 (b) shows a plot of turbulent Reynolds number contours for the *SST* model. The extent of the viscous region is clearly visible. As the flow approaches the engine face this highly disturbed region reaches to the centre-line of the duct. It also extends into the flow considerably as can be seen from the engine face plane which, naturally, lies perpendicular to the symmetry plane.

Finally, figure 3.10 is included as it gives a very clear view of the secondary flow development as one moves through the duct. Intersecting planes are also included periodically. It should be noted that no plane actually lies where the engine face is located ($X/D = 4.0$). The most downstream plane is actually the downstream boundary located at $X/D = 5.0$.

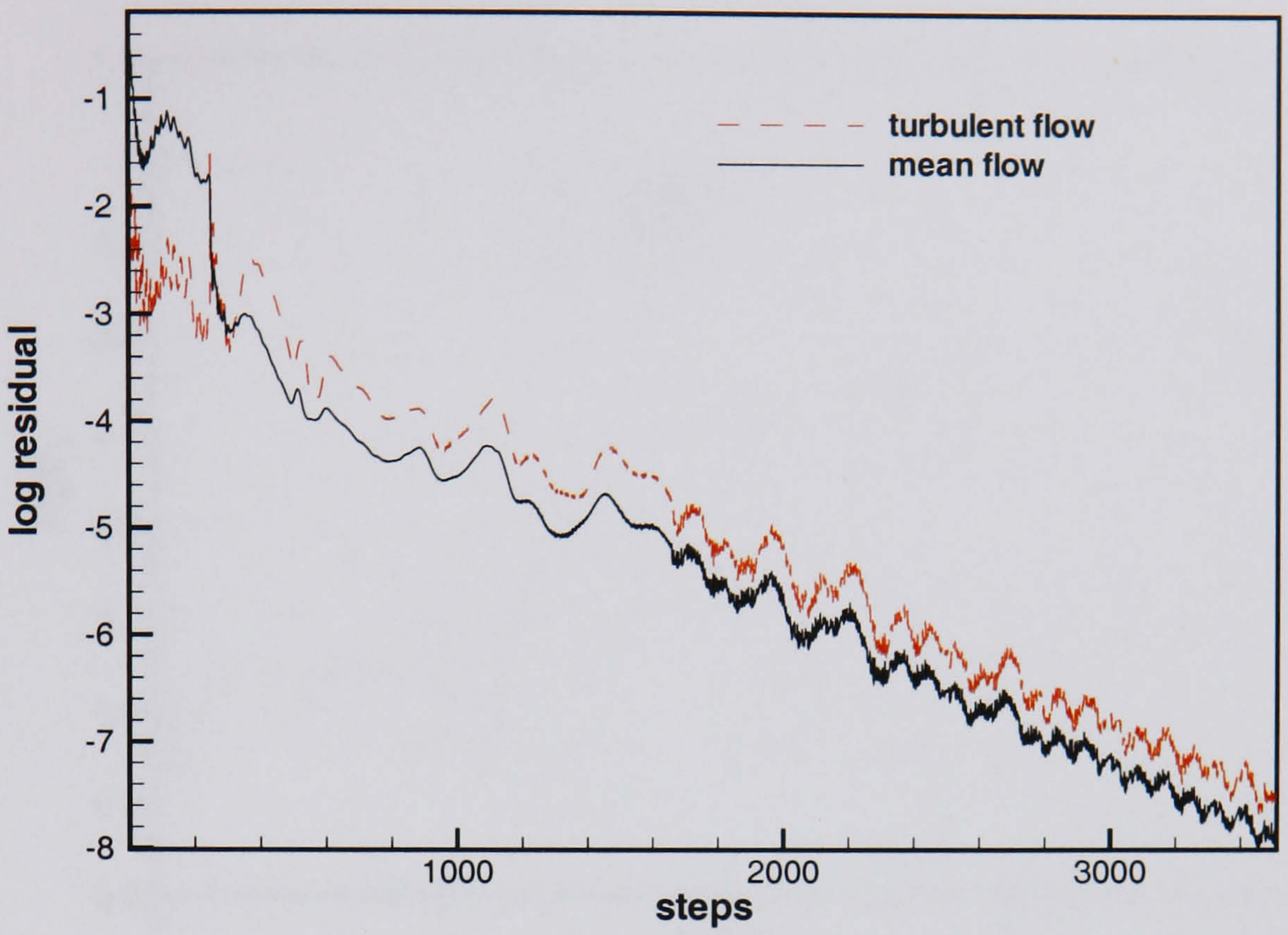

Figure 3.2: *HMFR Turbulent calculation, convergence for SST model*

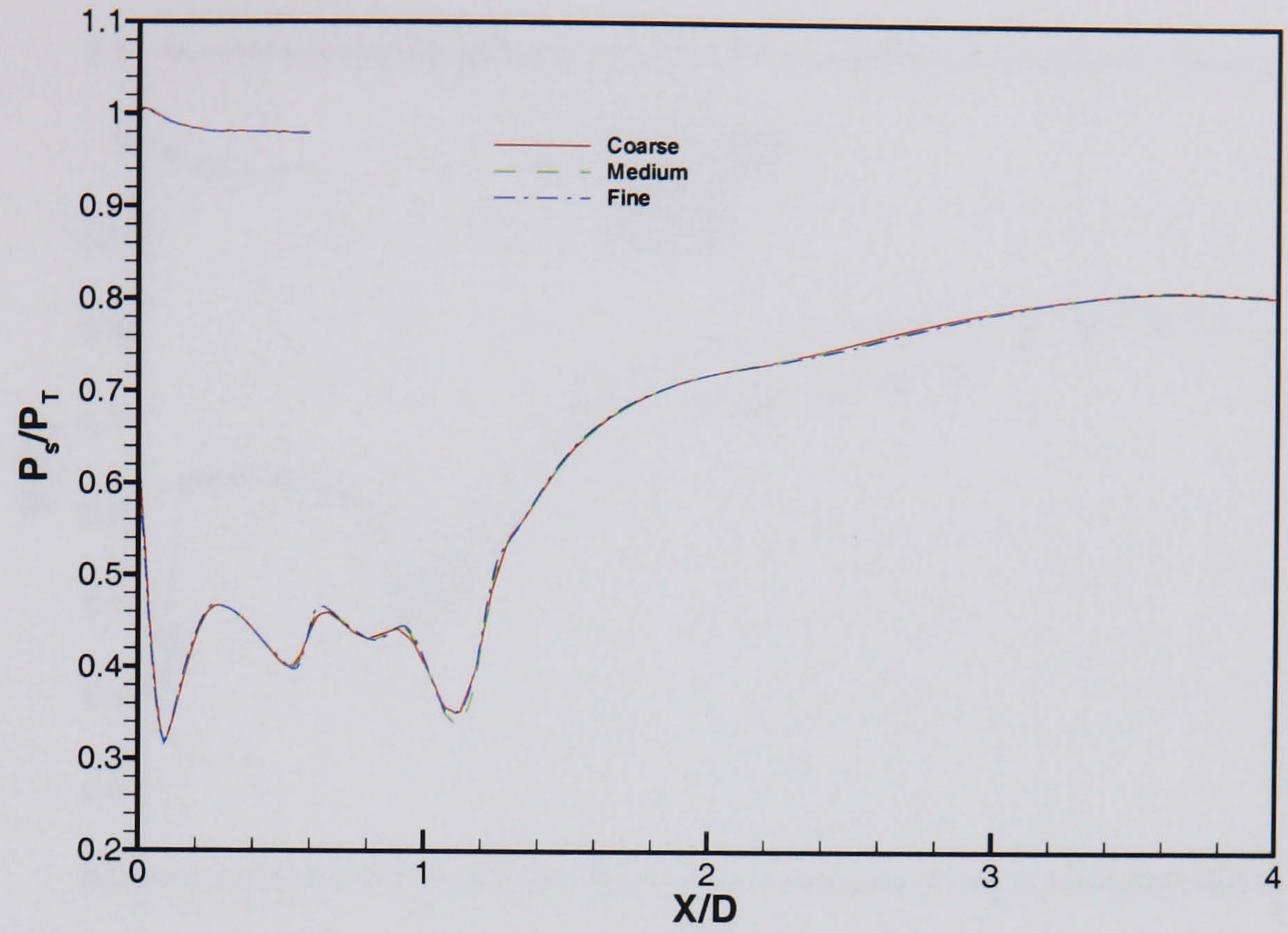

(a) Starboard side

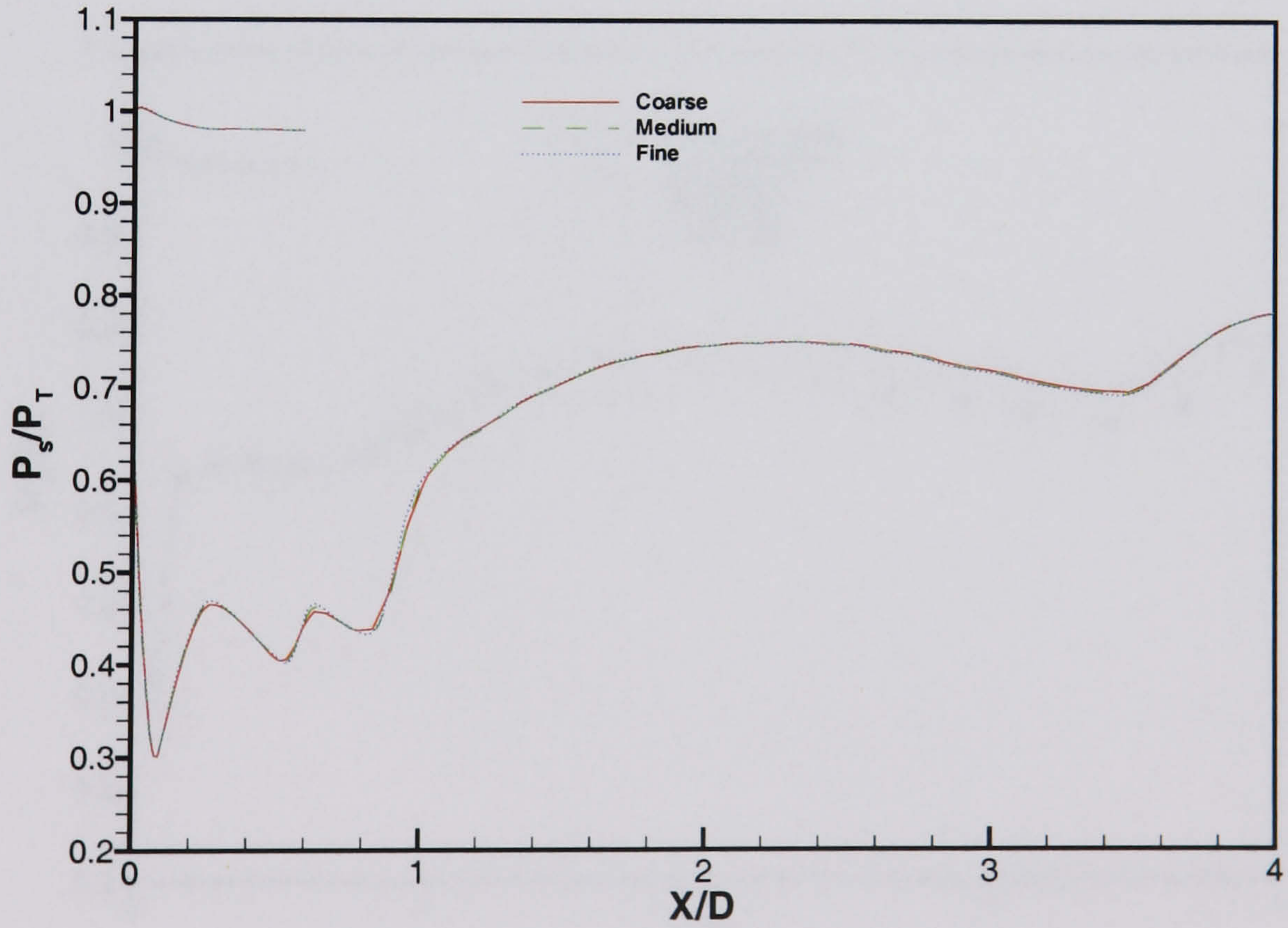

(b) Port

Figure 3.3: *HMFR Turbulent calculation, $k-\omega$ model - grid comparison for port and starboard sides*

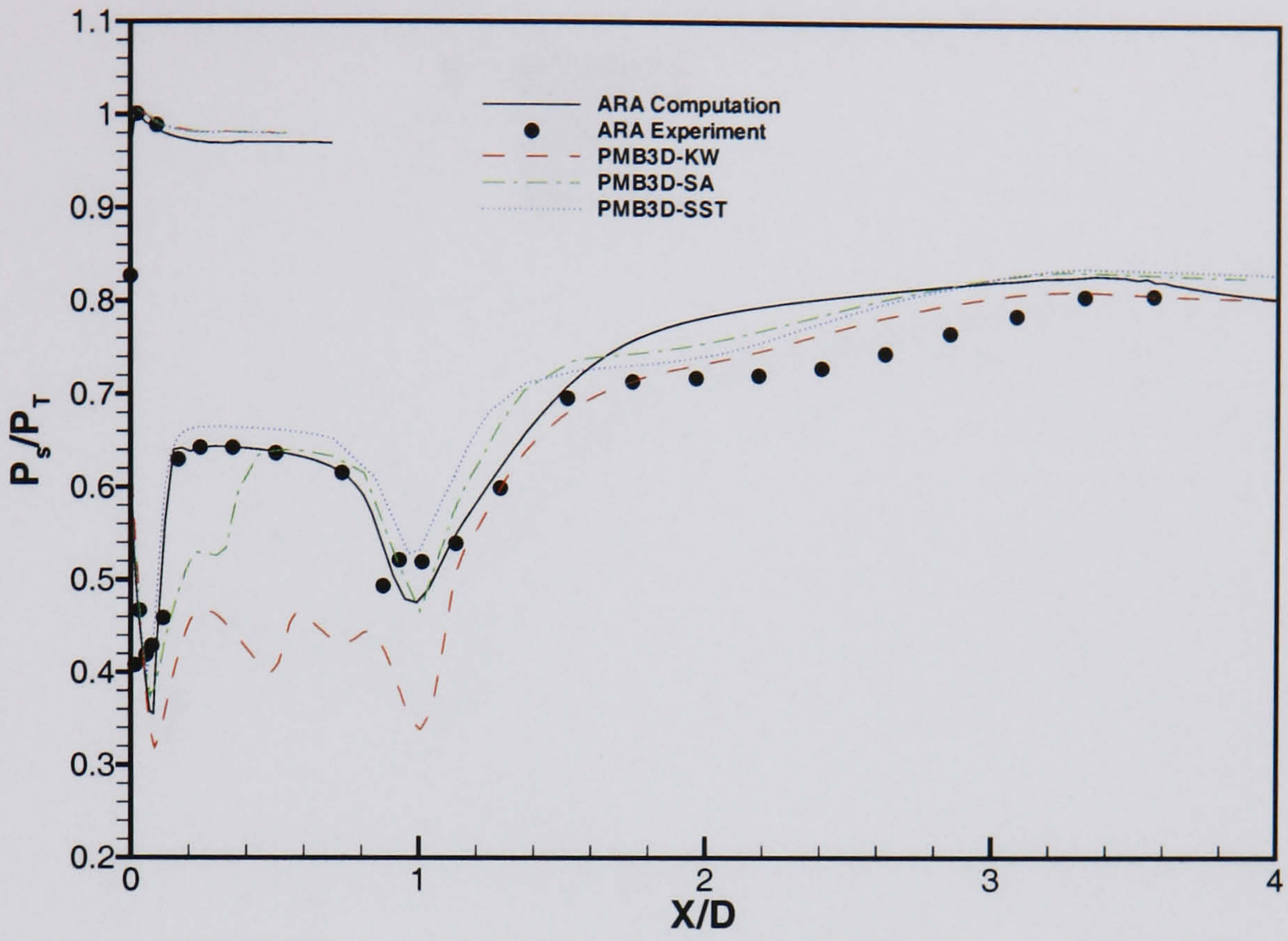

(a) Starboard side

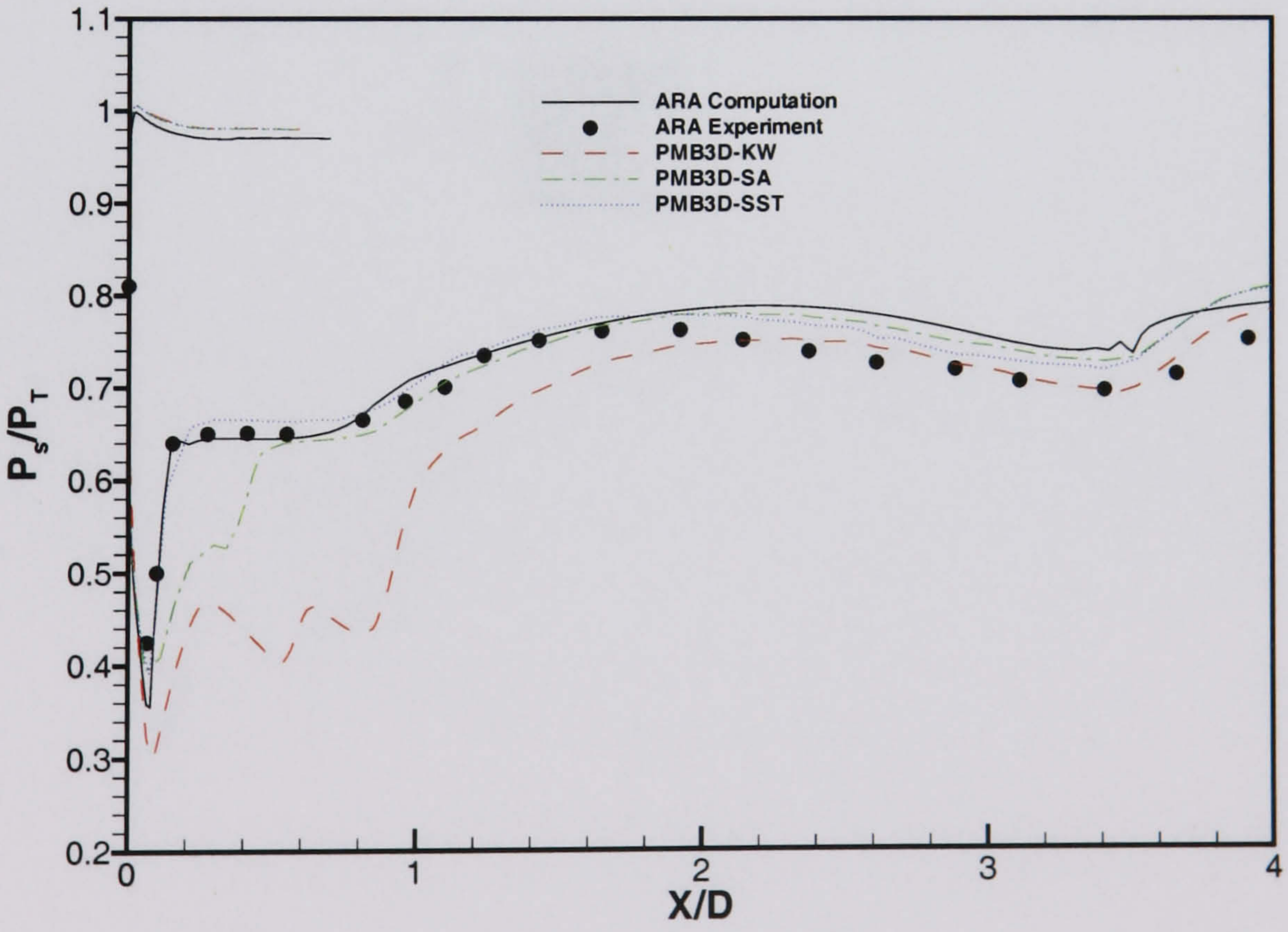

(b) Port side

Figure 3.4: *HMFR Turbulent calculation, port and starboard sides - ARA comparison*

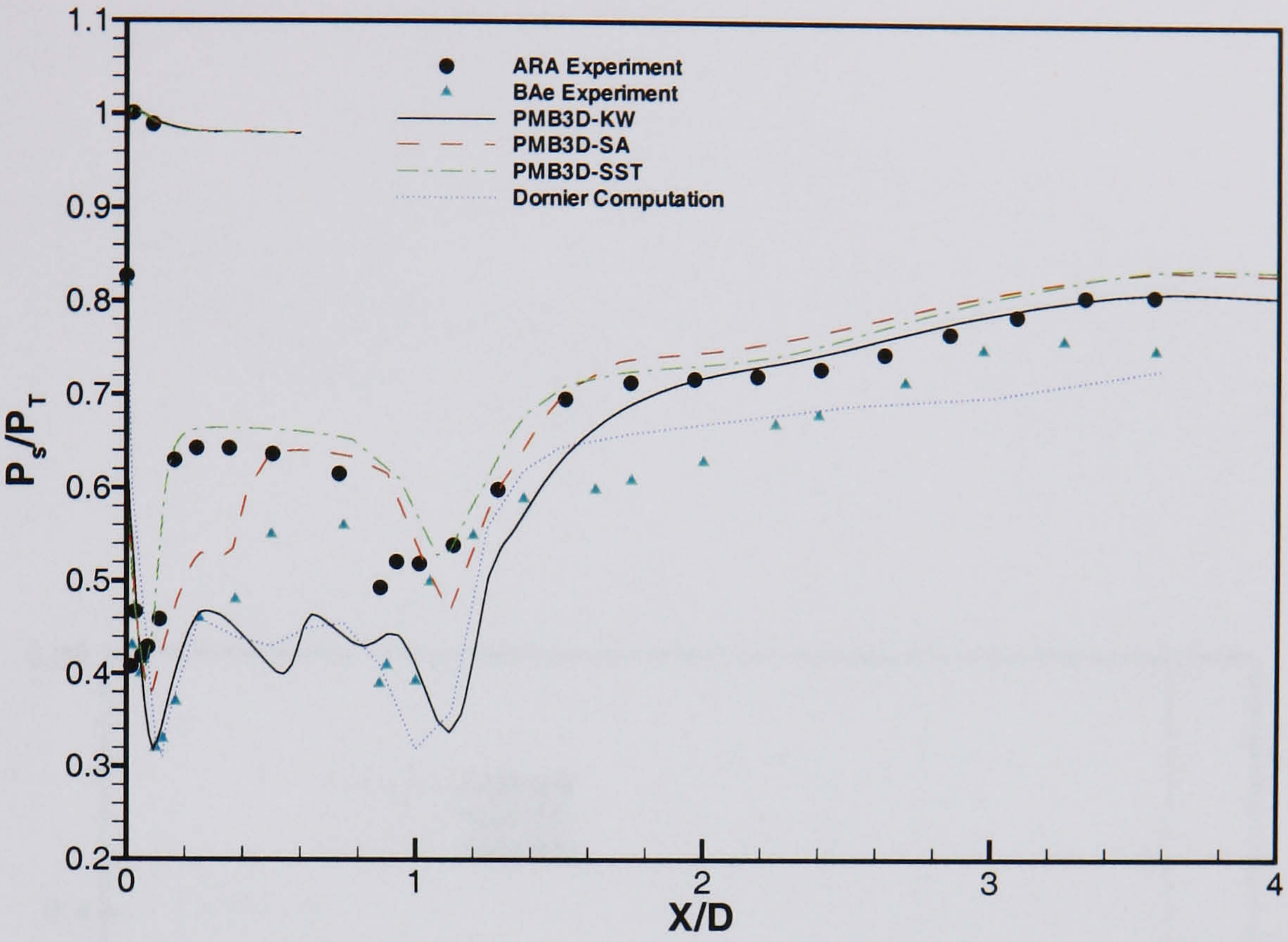

(a) Starboard side

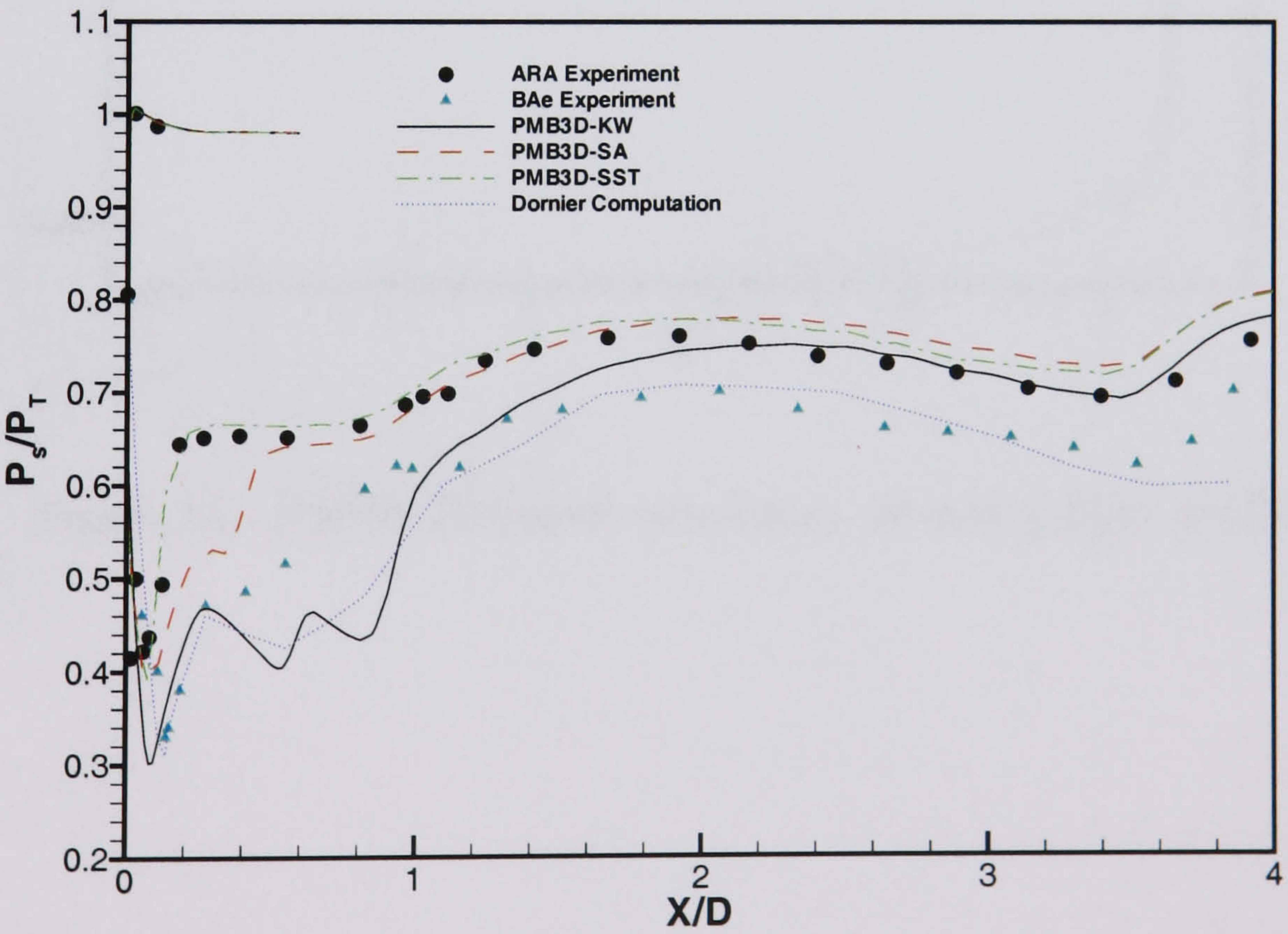

(b) Port side

Figure 3.5: *HMFR Turbulent calculation, port and starboard sides - Dornier comparison*

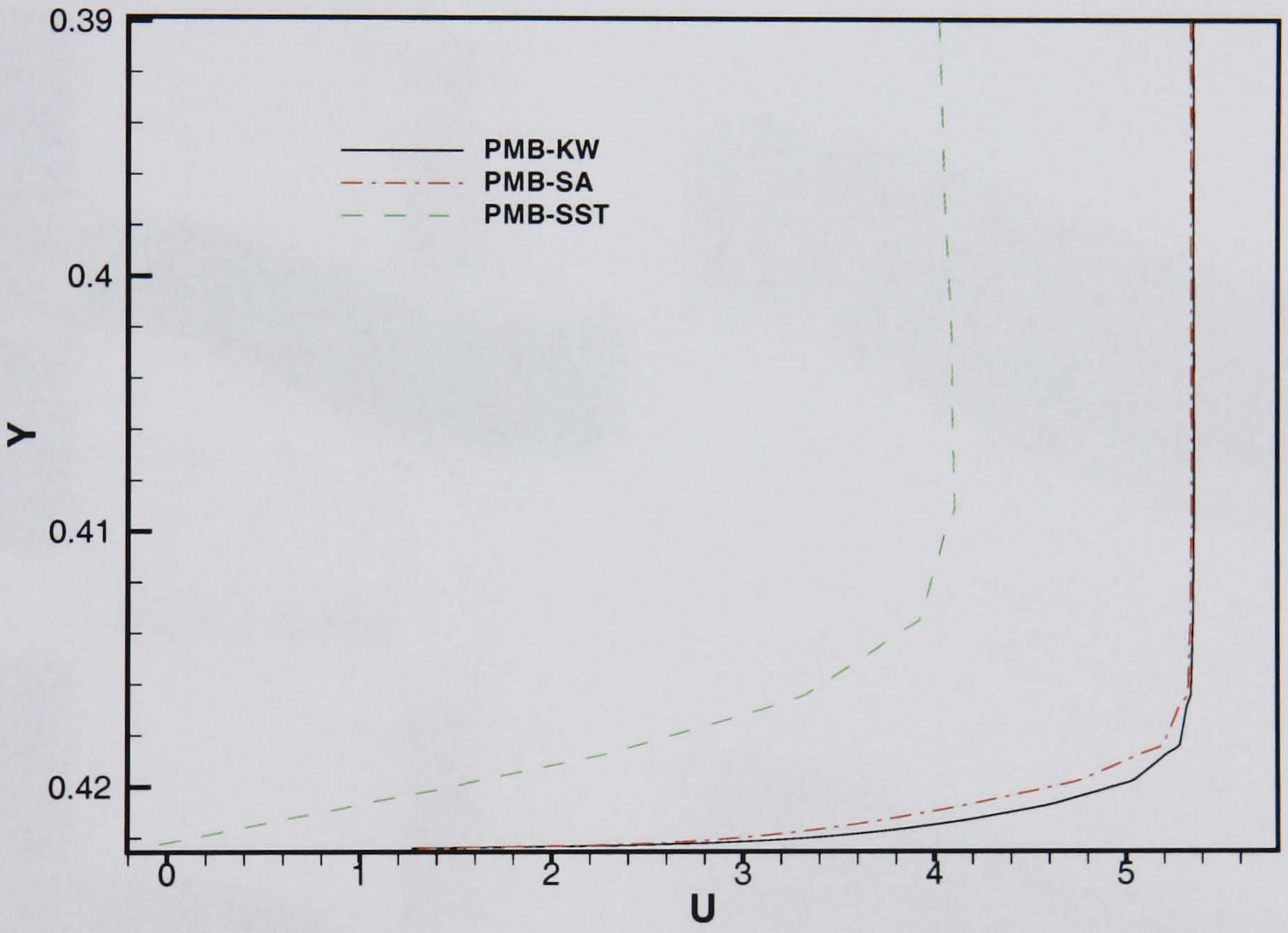

Figure 3.6: *HMFR Turbulent calculation, boundary layer profiles*

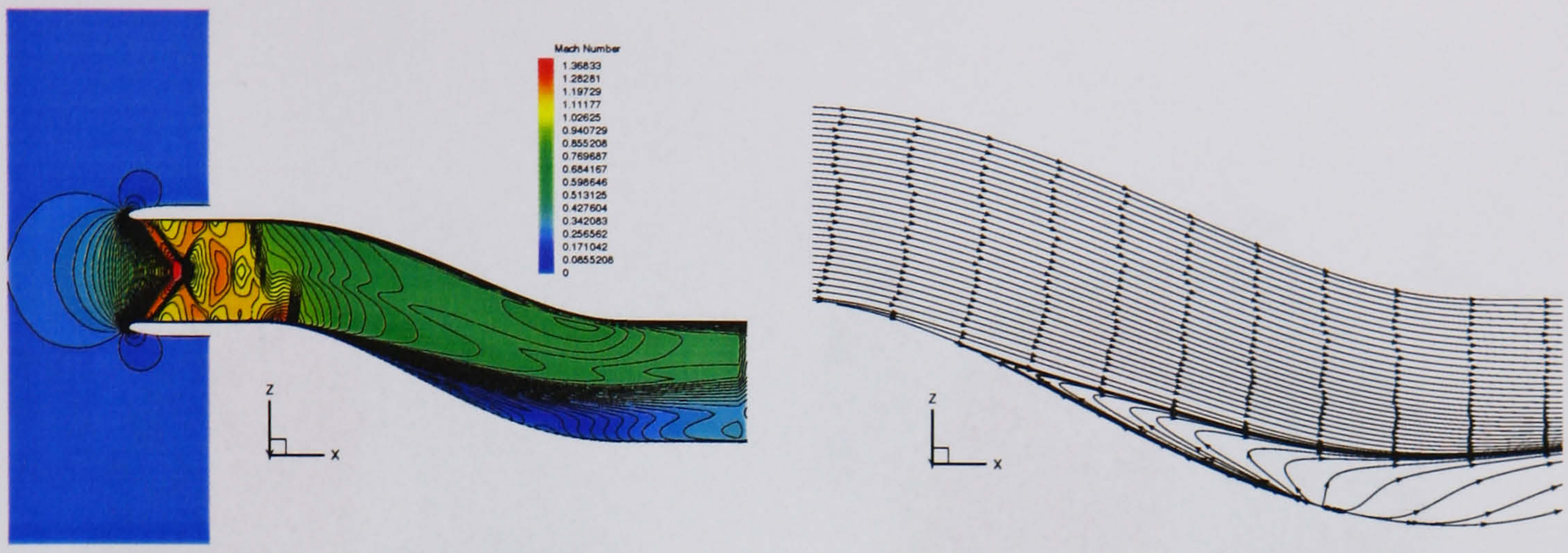

(a) $k - \omega$ model

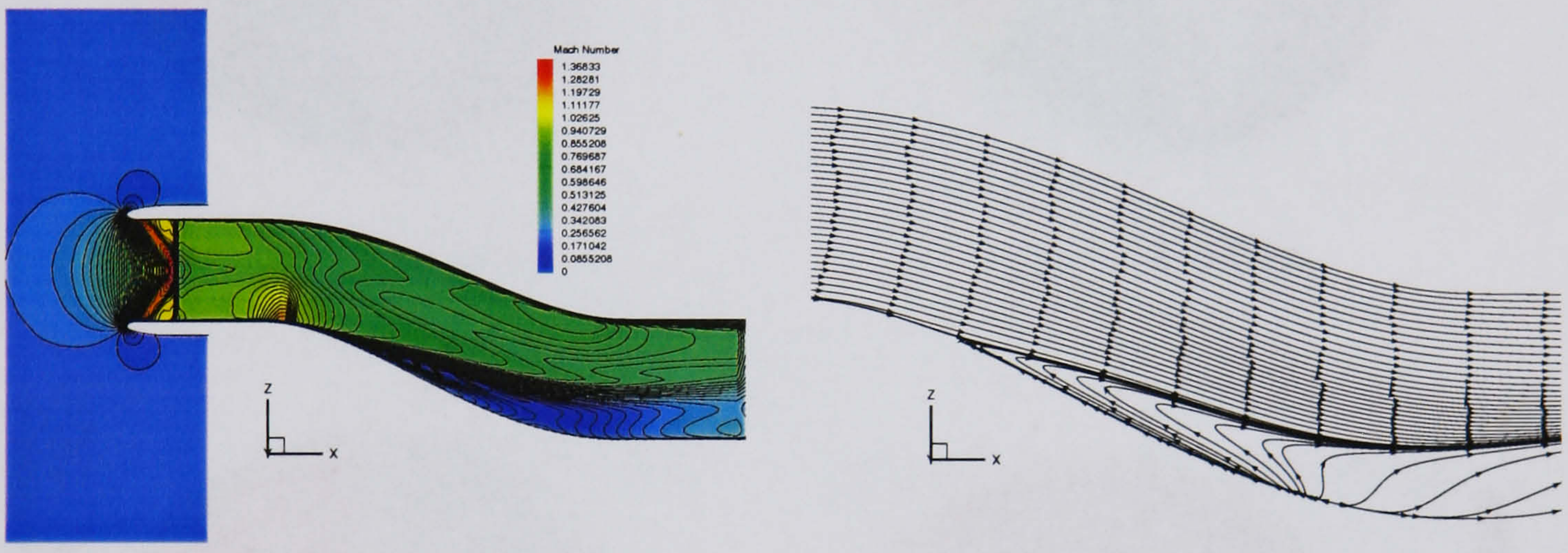

(b) SA model

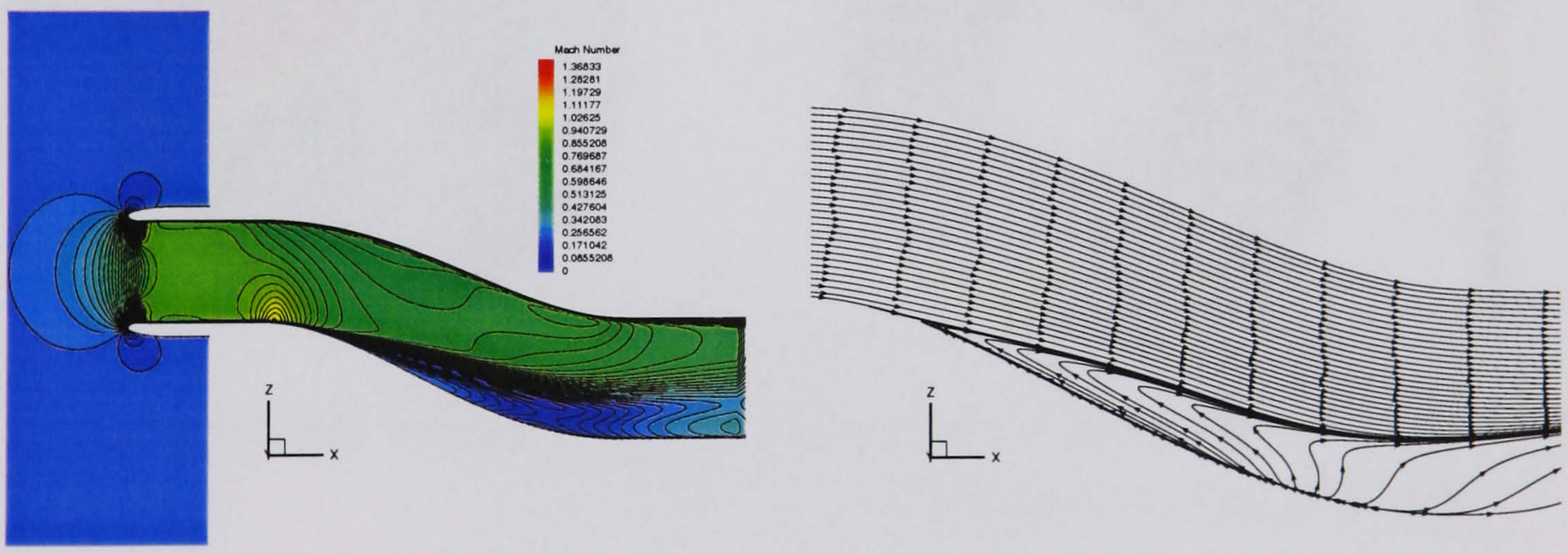

(c) SST model

Figure 3.7: *HMFR Turbulent calculation - Symmetry plane mach number and streamlines*

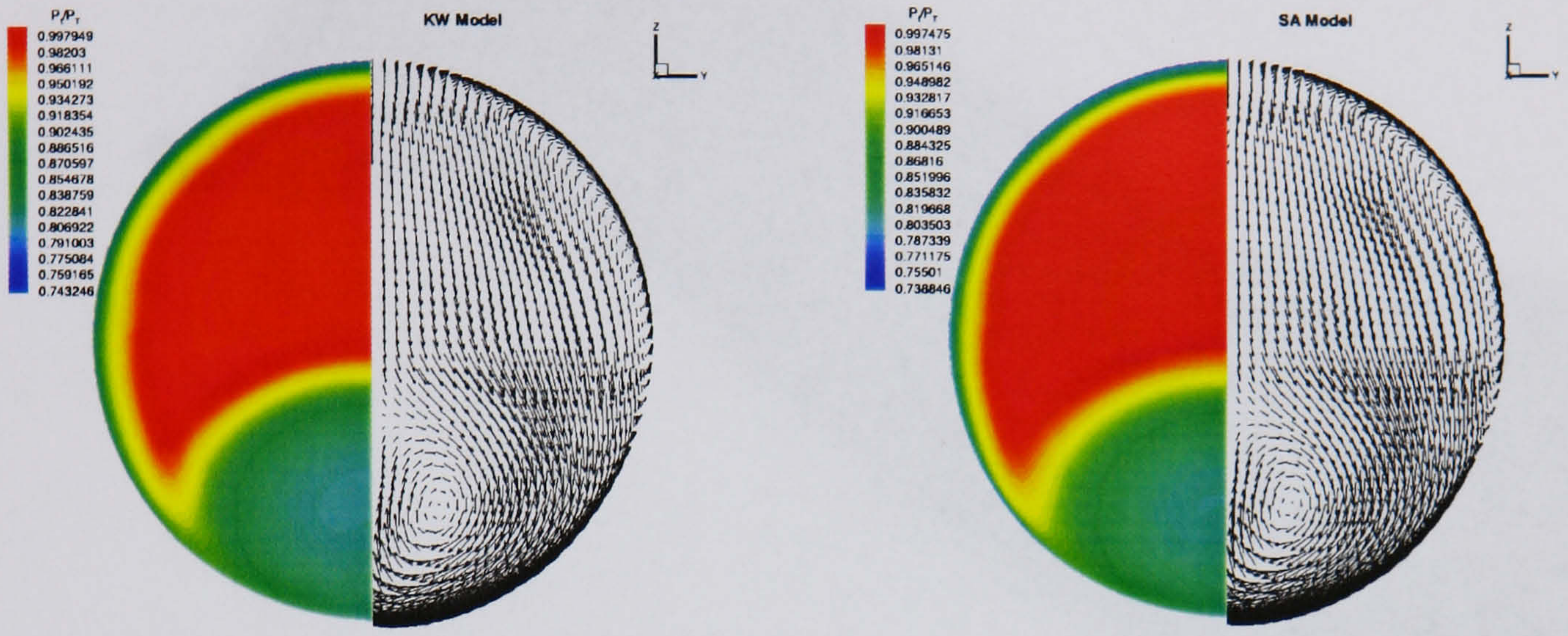

(a) $k-\omega$ model (b) SA model

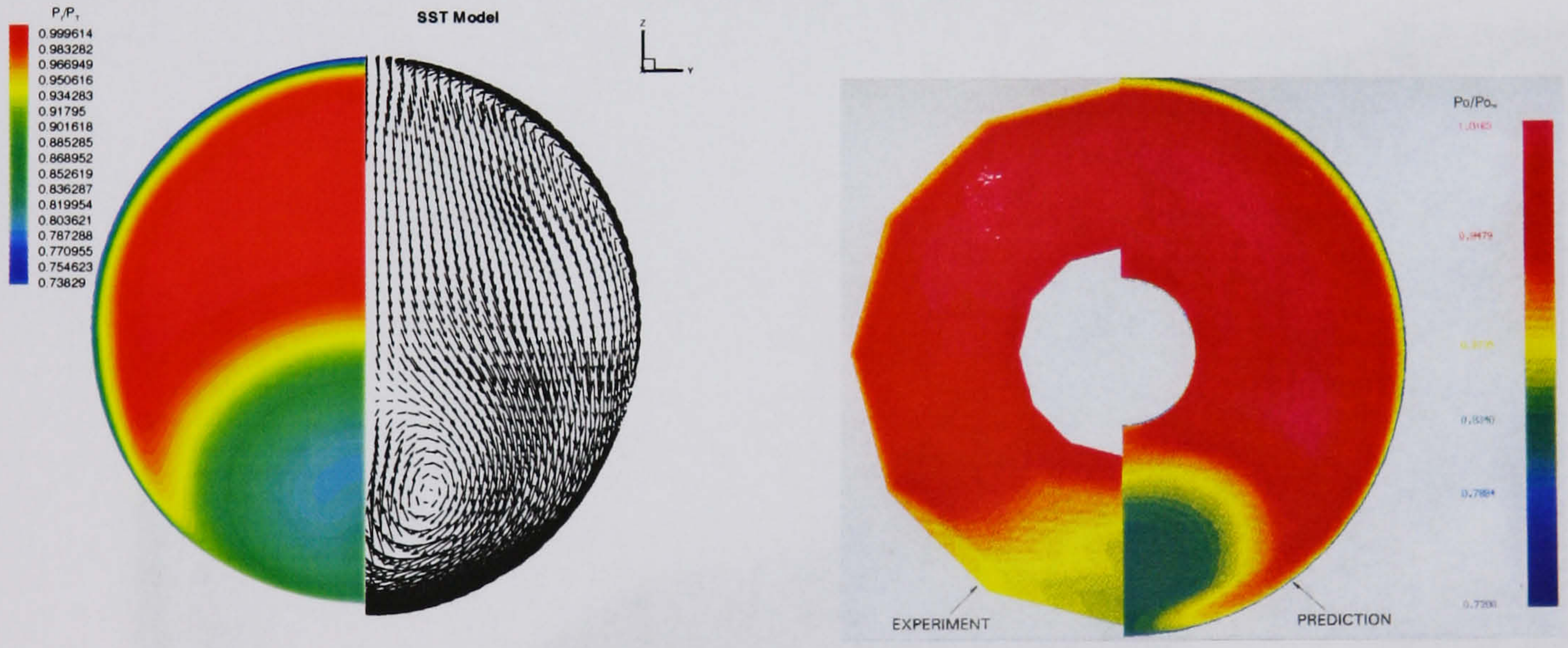

(c) SST model (d) Previous computation and experiment (taken from May [13], Fig. 5(e))

Figure 3.8: *HMFR Turbulent calculation - Engine face plane total pressures and velocity vectors*

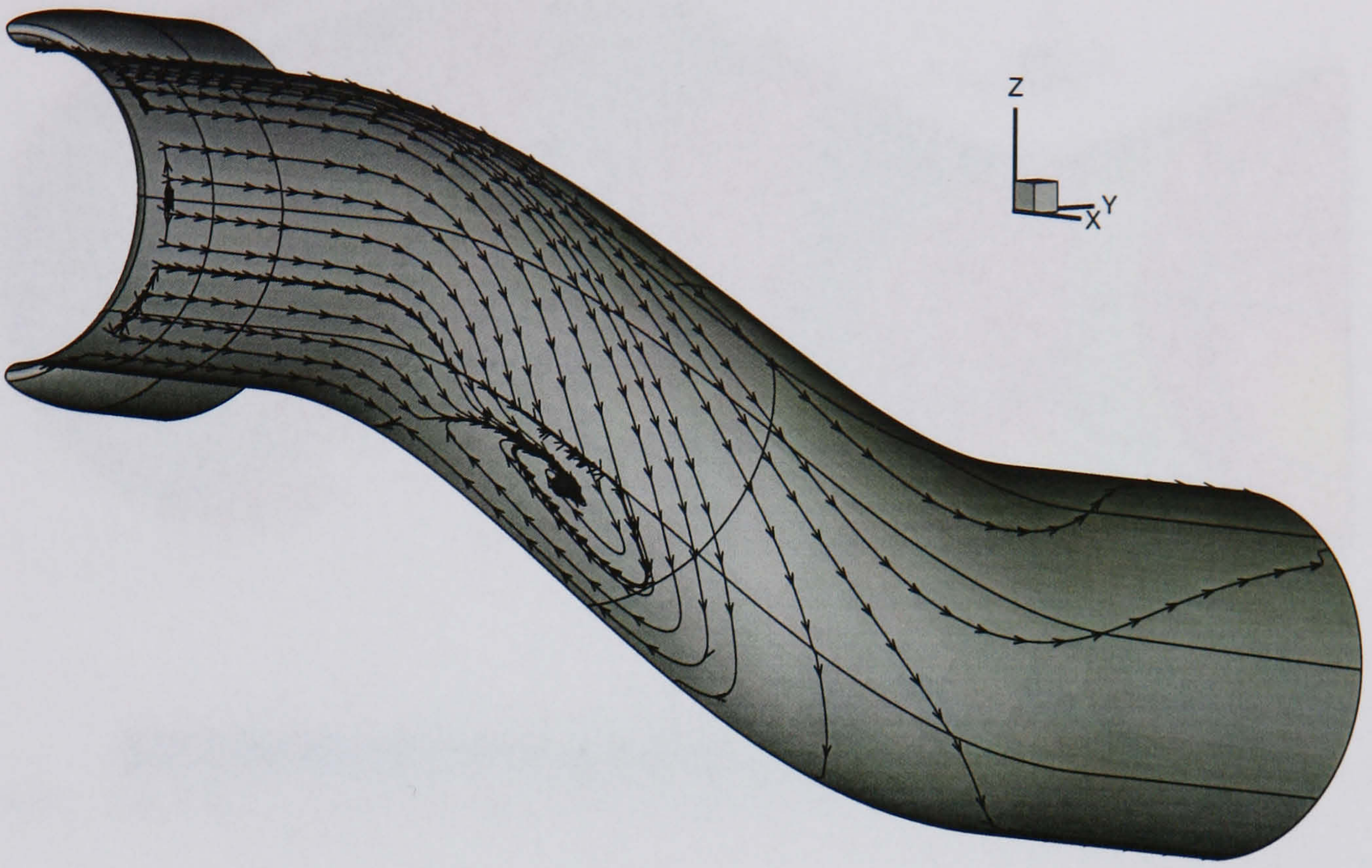

(a) Surface shear stress

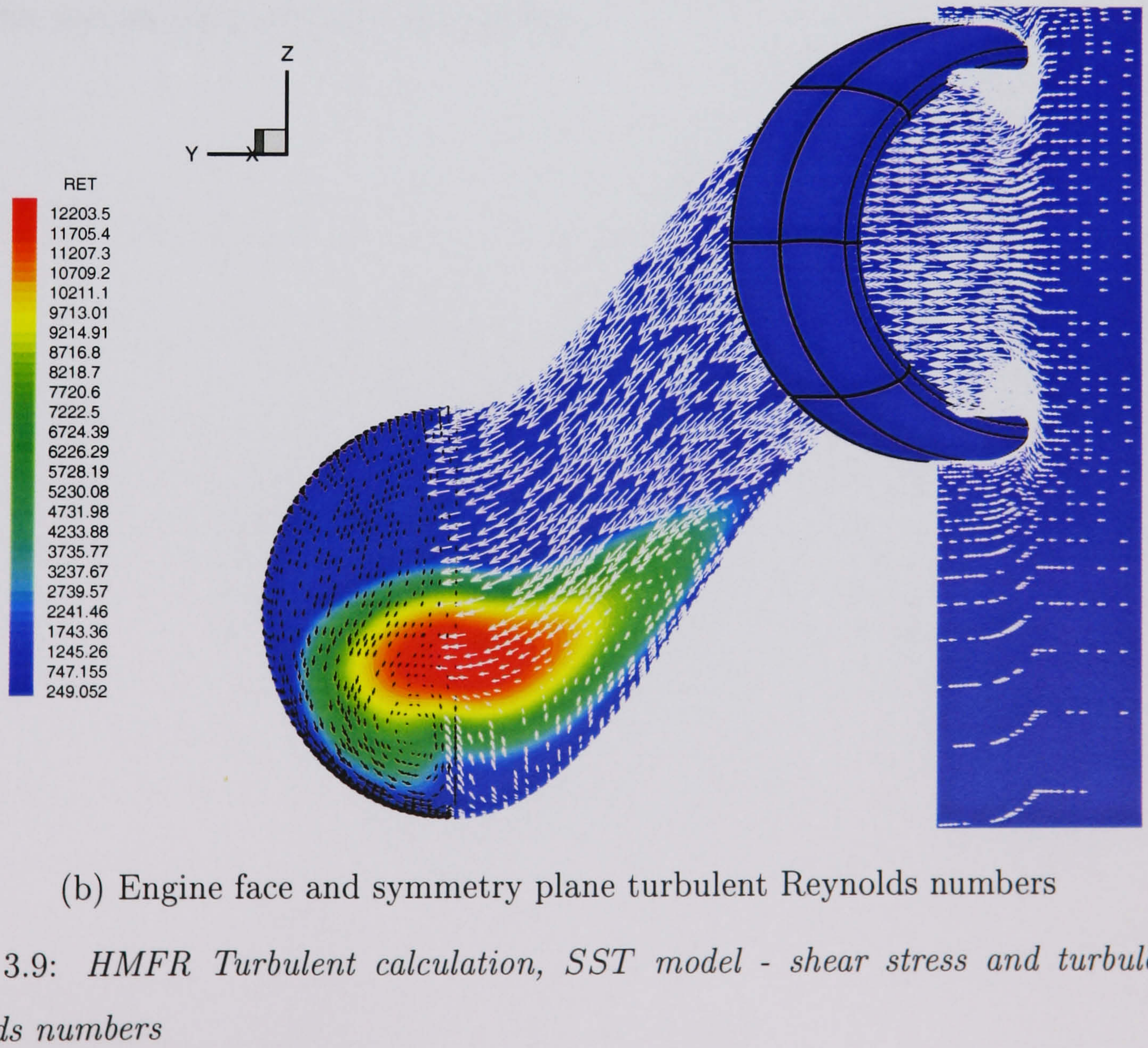

(b) Engine face and symmetry plane turbulent Reynolds numbers

Figure 3.9: *HMFR Turbulent calculation, SST model - shear stress and turbulent Reynolds numbers*

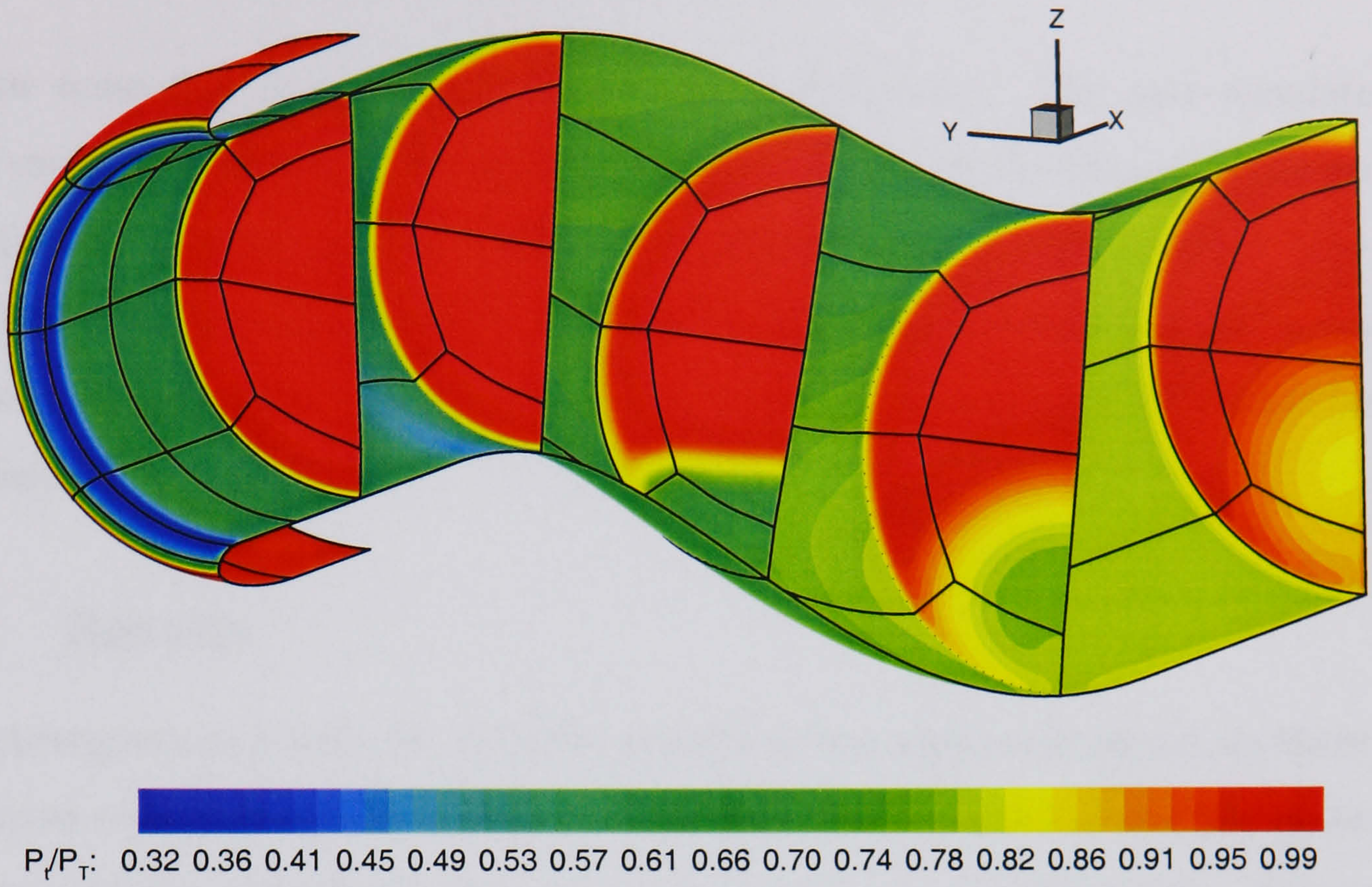

Figure 3.10: *HMFR Turbulent calculation, SST model - wall total pressure through duct with periodic slices through duct volume*

3.2 Low Mass Flow Rate - Case 2

The low mass flow rate test case is more straightforward. The case simulates low engine mass flow demand. As a consequence the ratio of the freestream static pressure to freestream pressure at the simulated compressor face is nearer unity. The non-dimensional engine face pressure is 15.525. This gives a freestream to engine face pressure ratio of 1.043. This is considerably less than for the high MFR case (around 18% less).

3.2.1 Results

The convergence study for the RANS calculations was again carried out on three grids designated coarse, medium, and fine. The coarse grid consists of 204,980 points, the medium grid has 401,020 points, and the fine grid has 830,072 points. Figure 3.12 (a) and (b) show starboard and port pressures respectively for these three grids for the SST turbulence model. It is clear that all three grids offer near identical results. Similar results were obtained for the other turbulence models but are not shown here. Figure 3.11 shows a plot of the convergence history for this calculation. In summary fully converged solutions were obtained for all models and the medium grid was used in the following investigation.

Static Wall Pressures Along Duct

Figure 3.13(a) shows the starboard side pressures compared against a previous computation by the ARA (using a $k - \omega$ model) and experimental data. All computational results are very similar. Flow from stagnation into the duct is well captured by all models and matches previous work satisfactorily. Subsequent pressure recovery is also well matched, with the $k - \omega$ model performing the best. The SA and SST models show a slight over-prediction in pressure recovery. Consequently these models under-predict the acceleration of the flow around the first bend. Again, the $k - \omega$ model captures this best. From the literature ([12, 13]) the most challenging problem with the LMFR case simulation is predicting the secondary flow generation. It can be seen that all models fail to predict the pressure drop that was witnessed in experiment. Closer examination, however, reveals that the SST and SA models do predict a slight drop (or 'saddle') in the trace between $X/D = 2$ and 3. This would perhaps be expected following the findings for the HMFR case. The $k - \omega$ model and ARA computation do not appear to capture this.

Figure 3.13(b) shows the port side pressure over the whole duct length. Initial impressions show a good agreement with the ARA results and also with experiment for flow from stagnation into the duct. As for the starboard side, the pressure recovery is over-predicted for the SA and SST models. The $k - \omega$ model predicts the flow very well in this region. All models and the experiment show pressure steadily rising through the first bend right up to the approaches of the second bend where there is a further acceleration due to the effects of curvature (as discussed in section 1.3.4). This is best matched with experiment by the $k - \omega$ model and the ARA solution, the SA and SST models slightly under-predict this acceleration. After this the flow then decelerates to the engine face.

Symmetry Plane Flow Features

Figure 3.14 shows plots from the symmetry plane of Mach number and streamlines. The Mach contour plots show the basic flow features nicely. Stagnation on the outer cowl lip is clearly visible as is the subsequent high velocity regions on the inside of the cowl lip. The maximum Mach number of 0.57 is at this location for all models. All models predict similar flow up to the first intake bend. It is clear that the $k - \omega$ model predicts a smaller region of separated flow than the SA and SST models. This is clear in the streamline plots on the right hand side of figure 3.14. There is very little, if any flow reversal with the $k - \omega$ model. The SA and more particularly the SST models predict a small amount of flow reversal. This is indicative of secondary flow which is discussed next and compares best with experiment.

Engine Face Behaviour

Figure 3.15 shows plots of total pressure and velocity vectors for all turbulence models with comparisons made with total pressure predicted from previous experimental and computational data. The amount of secondary flow generated is small for all computational models. The SA and SST models clearly show larger regions. This is perhaps unsurprising when correlation is made with the amount of separation experienced (figure 3.14). The previous computation also uses a $k - \omega$ model and it is clear that the amount of secondary flow predicted at the engine face is minimal, if any. The current $k - \omega$ results are a little better. Although the secondary flow is still very small, it is present and can be seen in the velocity vector plot.

The consequence of this secondary flow is the undesirable maldistribution of total pressure across the engine face. This has been quantified in table 3.3. Comparisons of pressure recovery show that the results are very similar for all cases with values close to unity now due to the substantial reduction in secondary flow when compared to the HMFR case. Coefficients for the distortion show a wider spread in values. Comparison of the current results show a significant spread. This spread is predictable, however, considering the amount of secondary flow predicted with each turbulence model. Again the worst distorted 60 degrees sector was 30 degrees either side of the starboard side symmetry plane. It should also be remembered that the current results do not simulate the engine bullet as appears in the previous computations and experiment. This could have a small effect, as discussed in section 3.1.1.

Case	Pressure Recovery	Distortion Coefficient (DC(60))
ARA Experiment	0.98974	0.226
ARA Computation	0.99180	0.157
PMB-$k - \omega$	0.99992	0.229
PMB-SA	0.99990	0.340
PMB-SST	0.99994	0.377

Table 3.3: *LMFR distortion and pressure recovery at the engine face*

CFD Flow Field

Figure 3.16 shows a plot of (a) the surface shear stress and (b) turbulent Reynolds number for the SST model. The surface shear stress for the low mass flow case has similarities with the HMFR case. The flow once more spirals to a saddle point and the whole surface shear pattern is effected by the secondary flow generation. The draw towards the engine face is not as great as for the HMFR case however. There is no longer a discontinuity of shear stress isolines just inside the cowl as the LMFR case does not induce a small separation pocket inside the cowl lip.

Figure (b) shows the extent of the viscous region for the LMFR case using the SST model. Naturally this region is much smaller for the LMFR case but does still effect a significant portion of the intake volume downstream of the first bend and, more particularly, at the engine face. Flow reversal from the first bend and circulation at the engine face can also be seen.

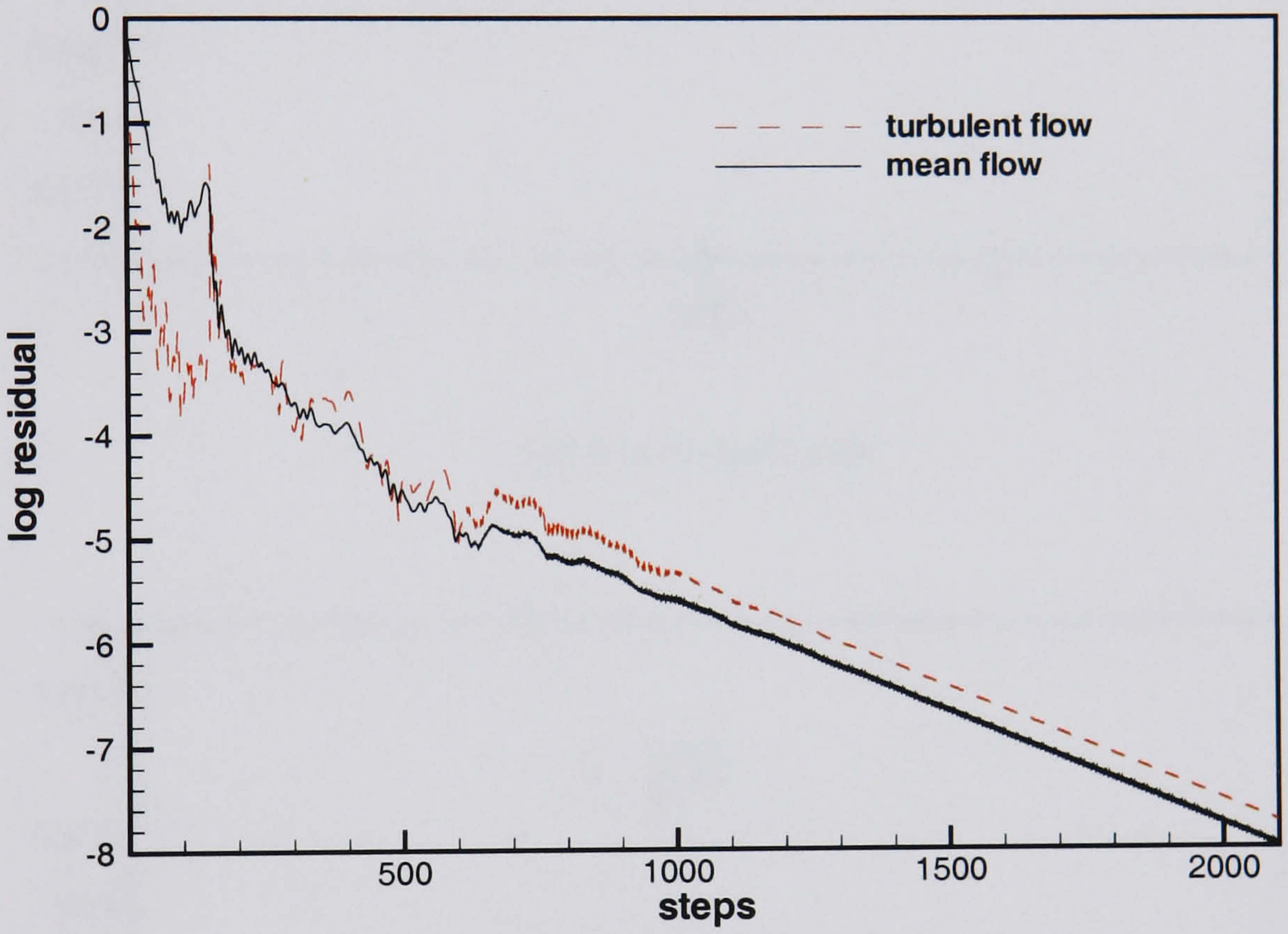

Figure 3.11: *Convergence history for the LMFR medium grid SST calculation*

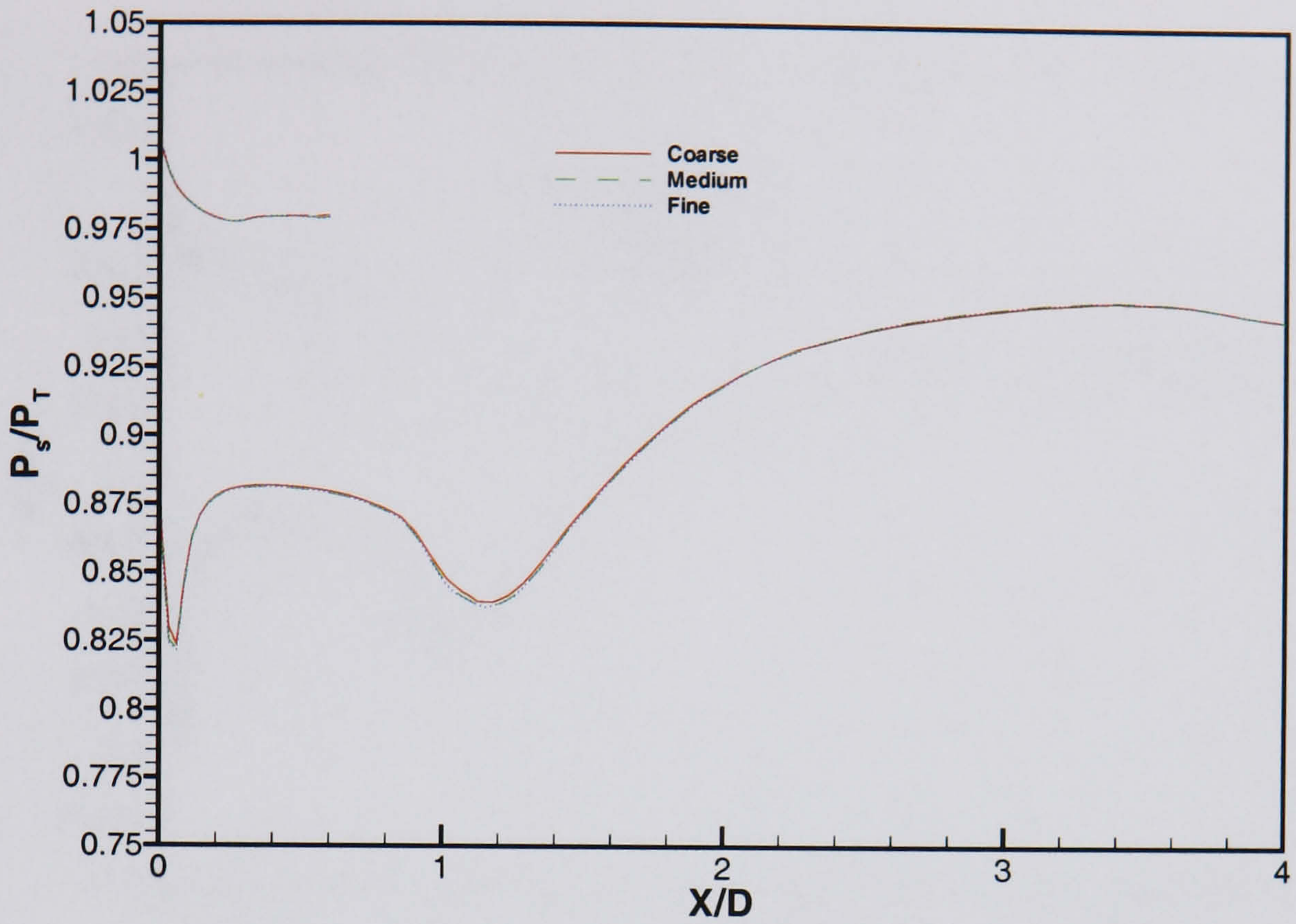

(a) Starboard side

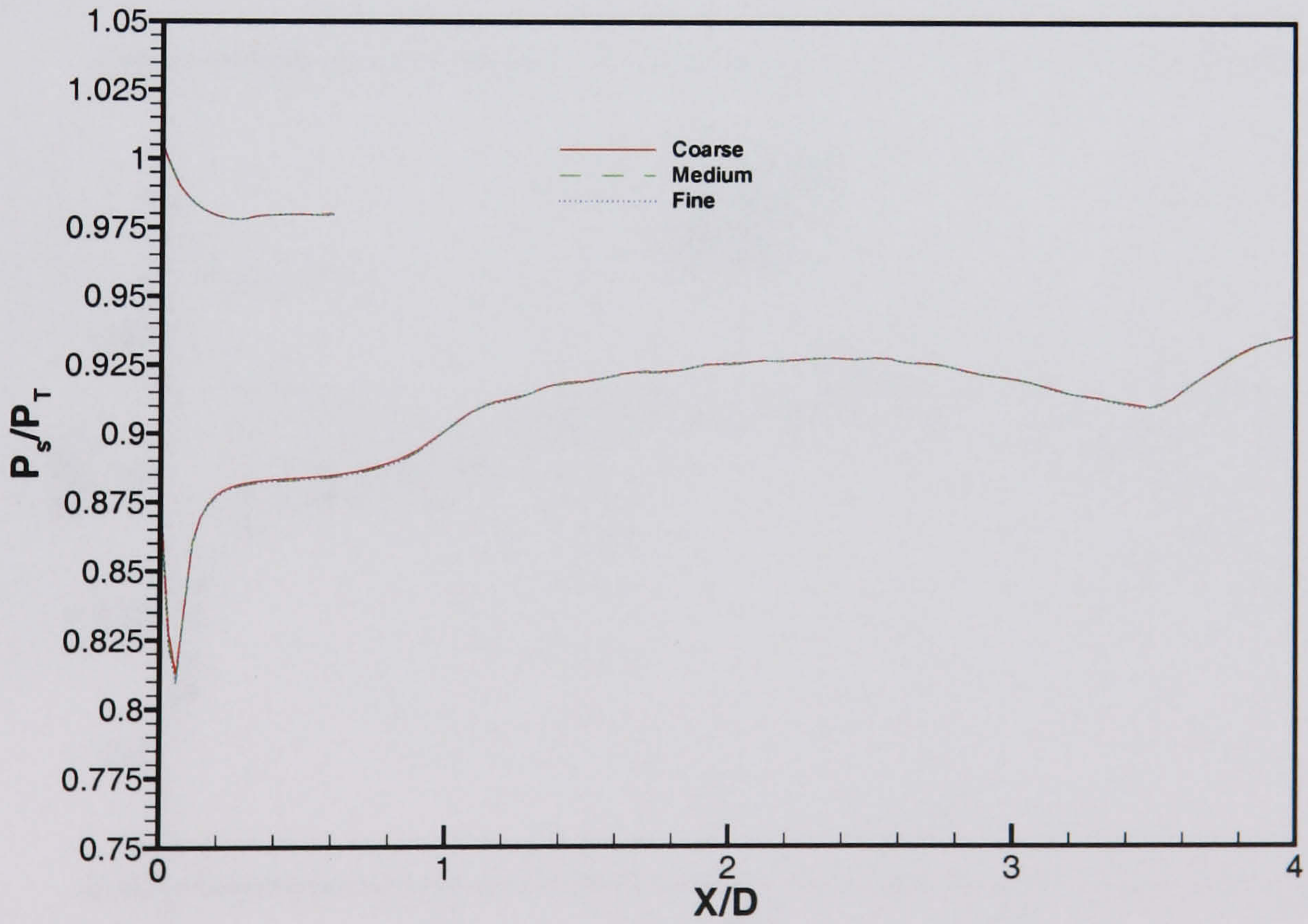

(b) Port

Figure 3.12: *LMFR Turbulent calculation, SST model - grid comparison for port and starboard sides*

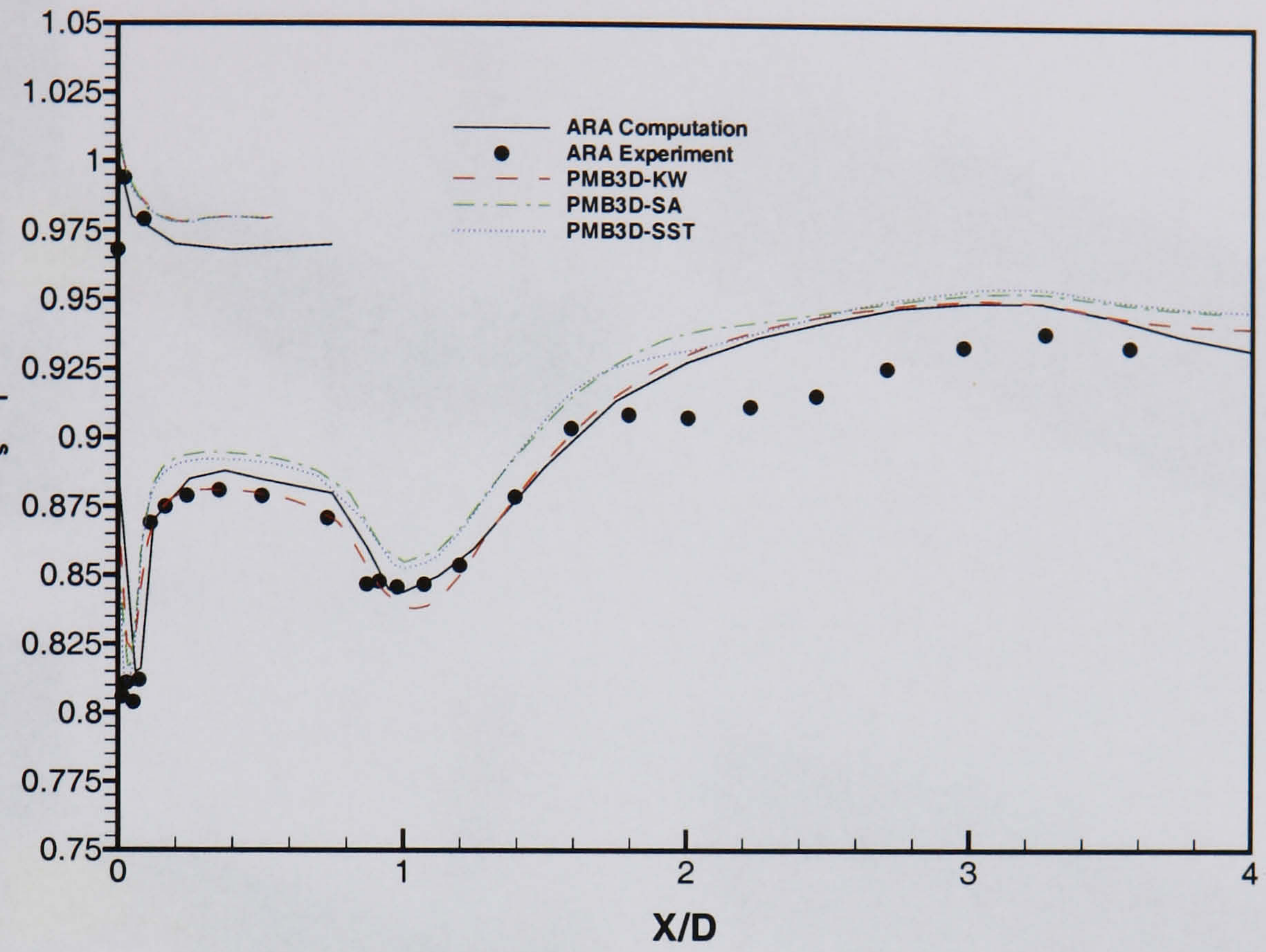

(a) Starboard side

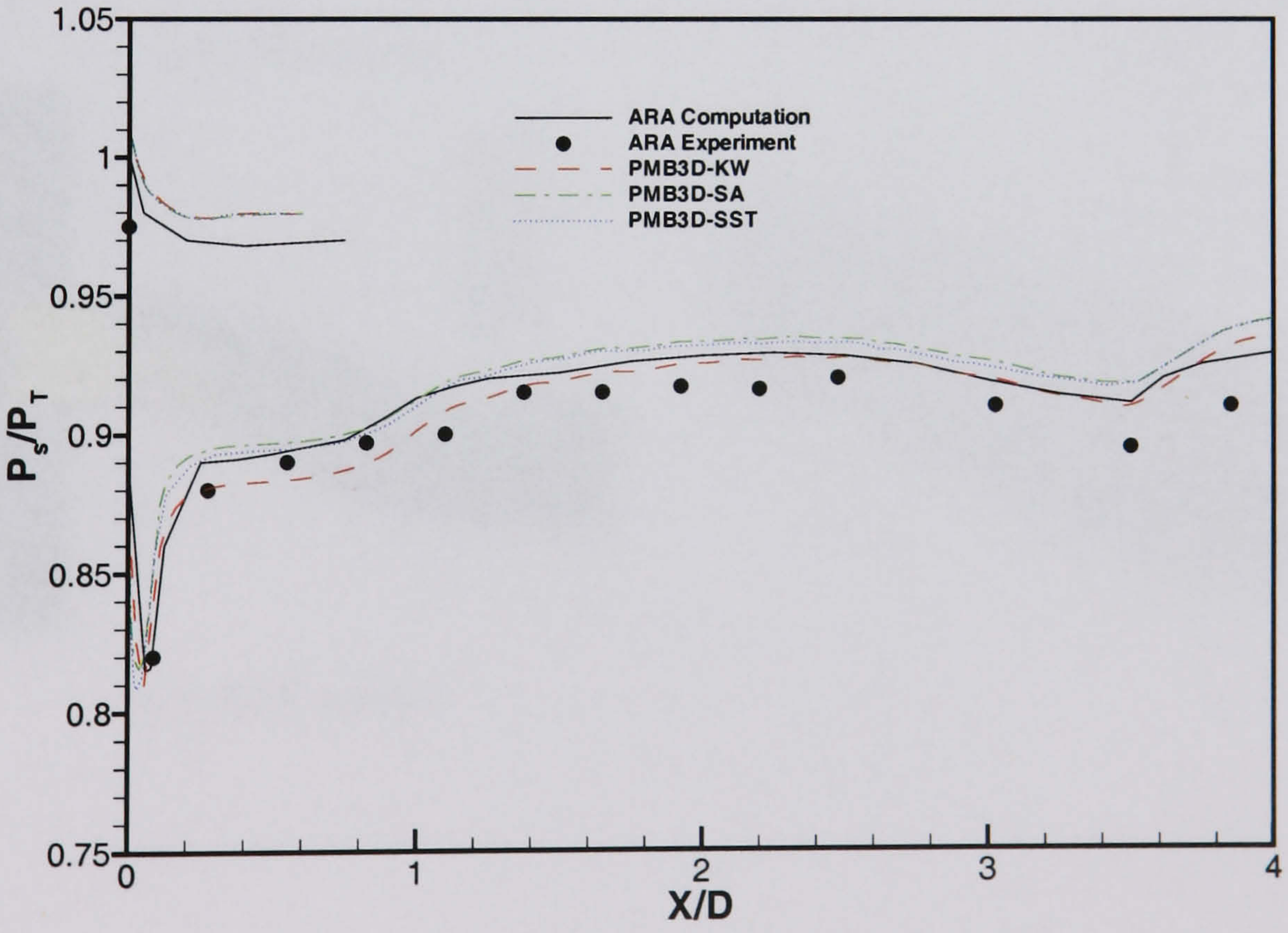

(b) Port side

Figure 3.13: *LMFR Turbulent calculation, port and starboard sides - ARA comparison*

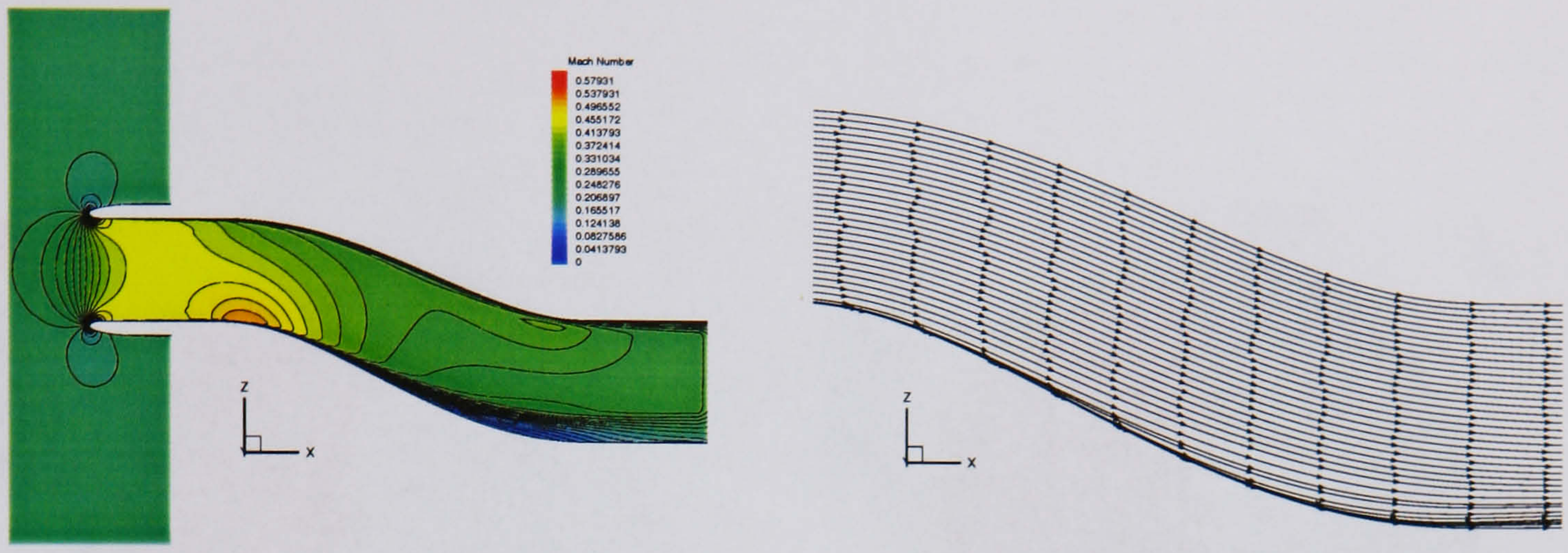

(a) $k - \omega$ model

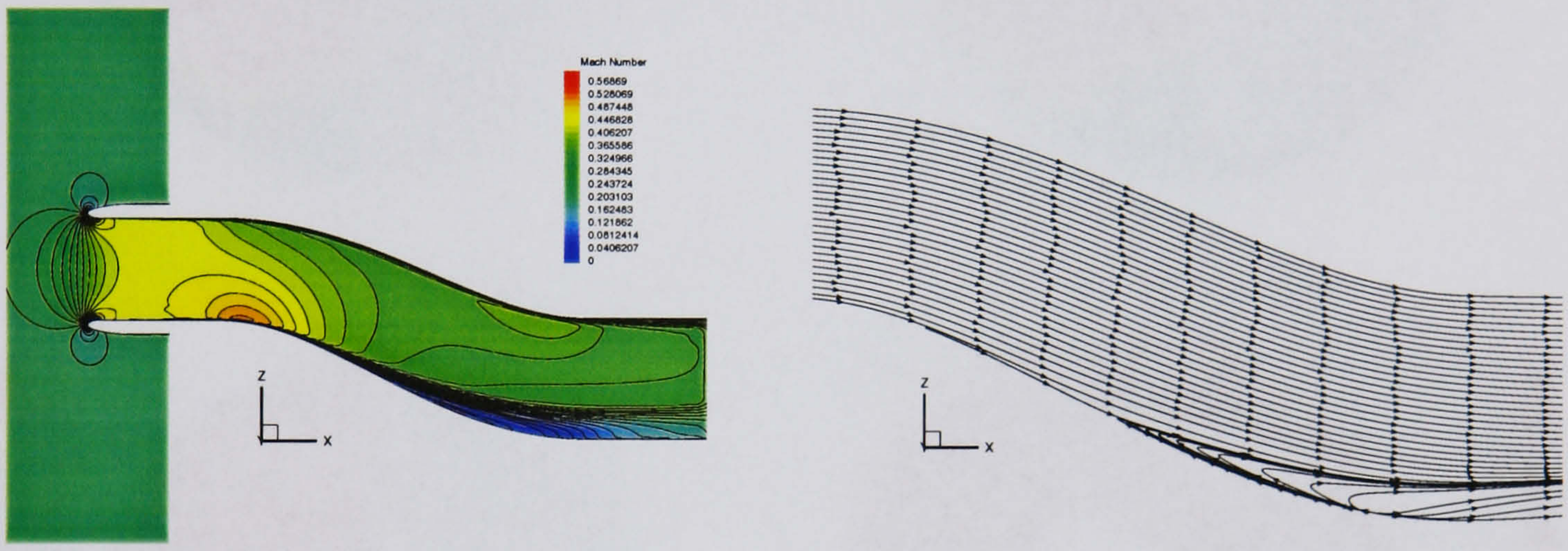

(b) SA model

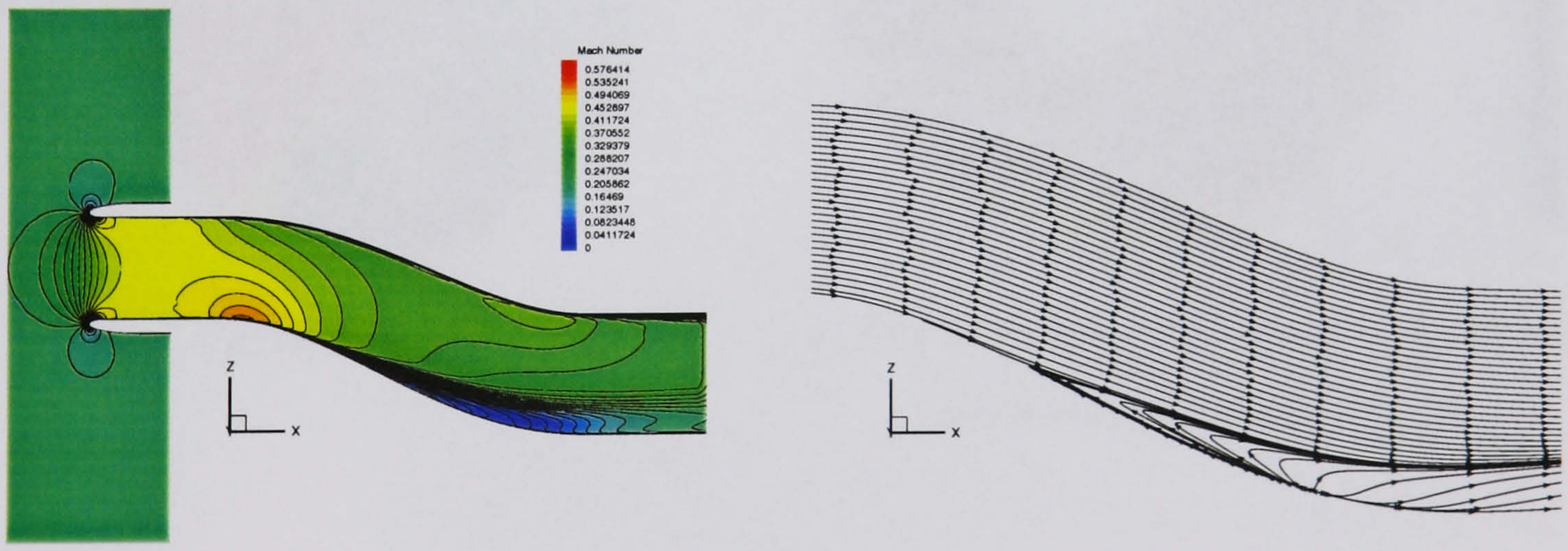

(c) SST model

Figure 3.14: *LMFR Turbulent calculation - Symmetry plane Mach number and streamlines*

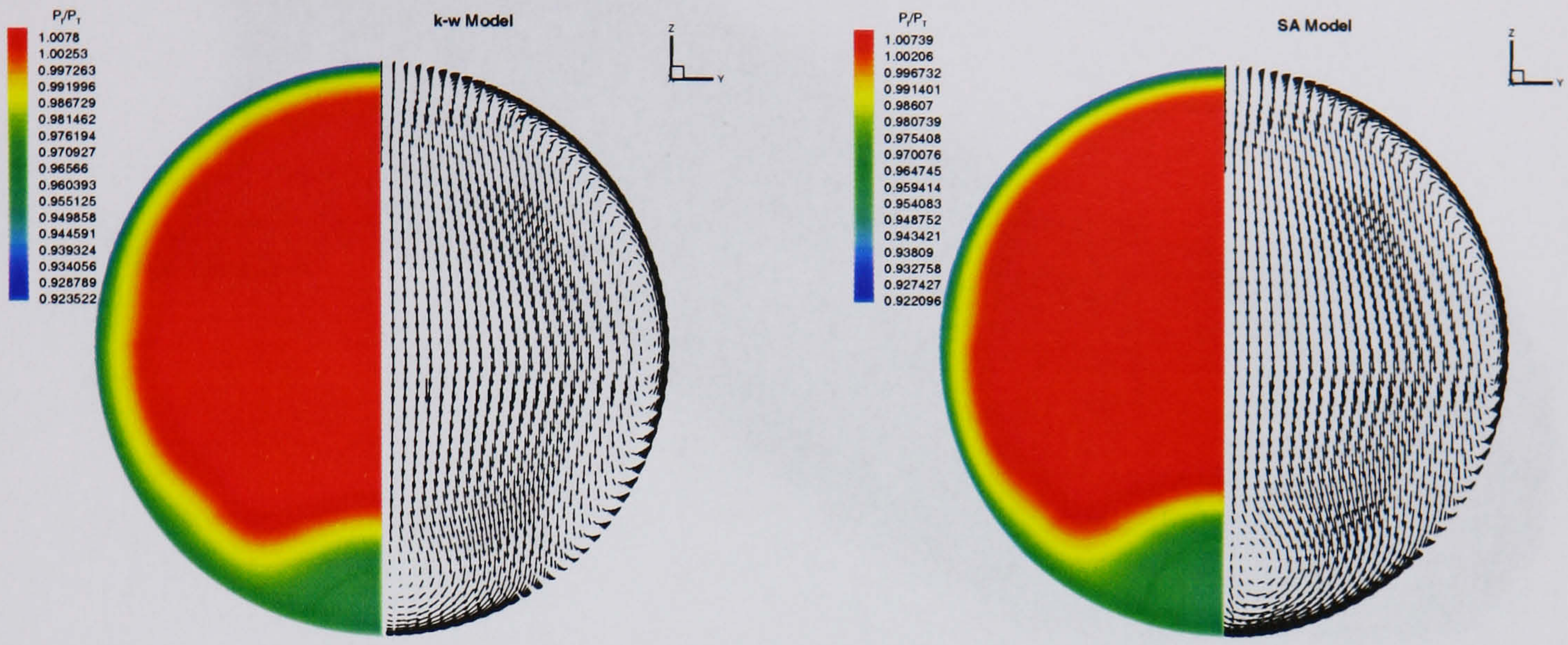

(a) $k-\omega$ model

(b) SA model

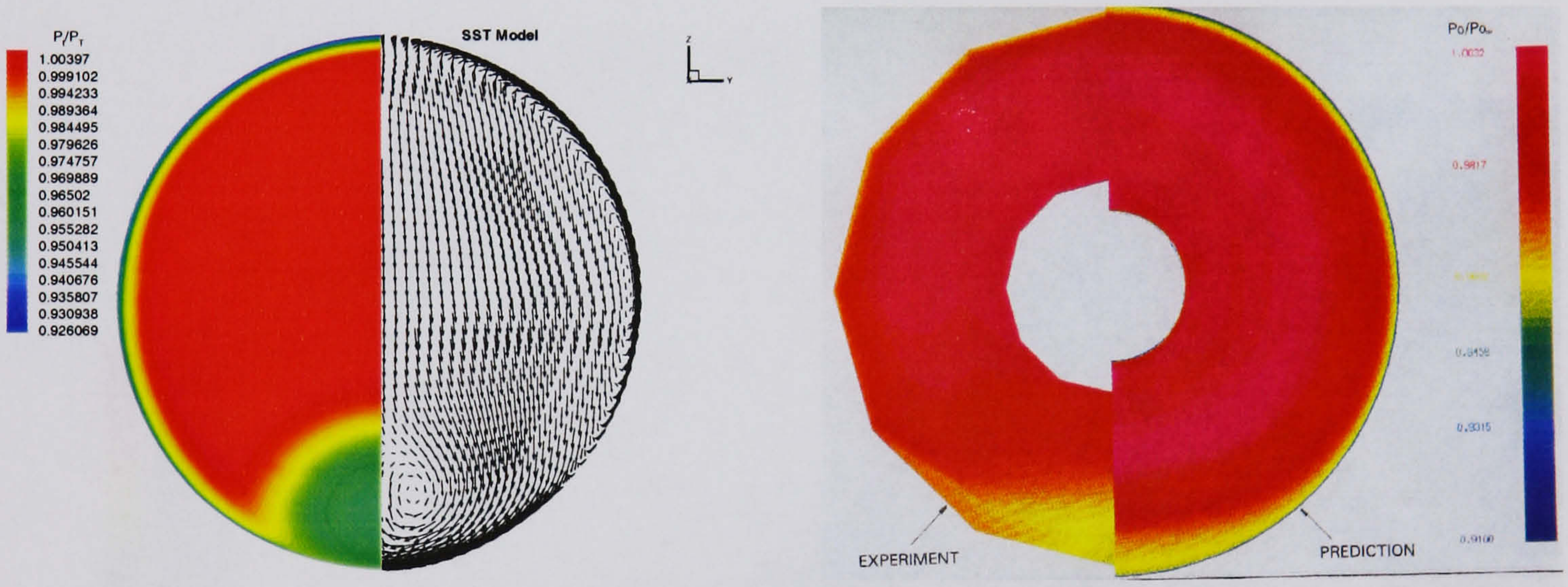

(c) SST model

(d) Previous computation and experiment (taken from May [13], Fig. 8)

Figure 3.15: *LMFR Turbulent calculation - Engine face plane total pressures and velocity vectors*

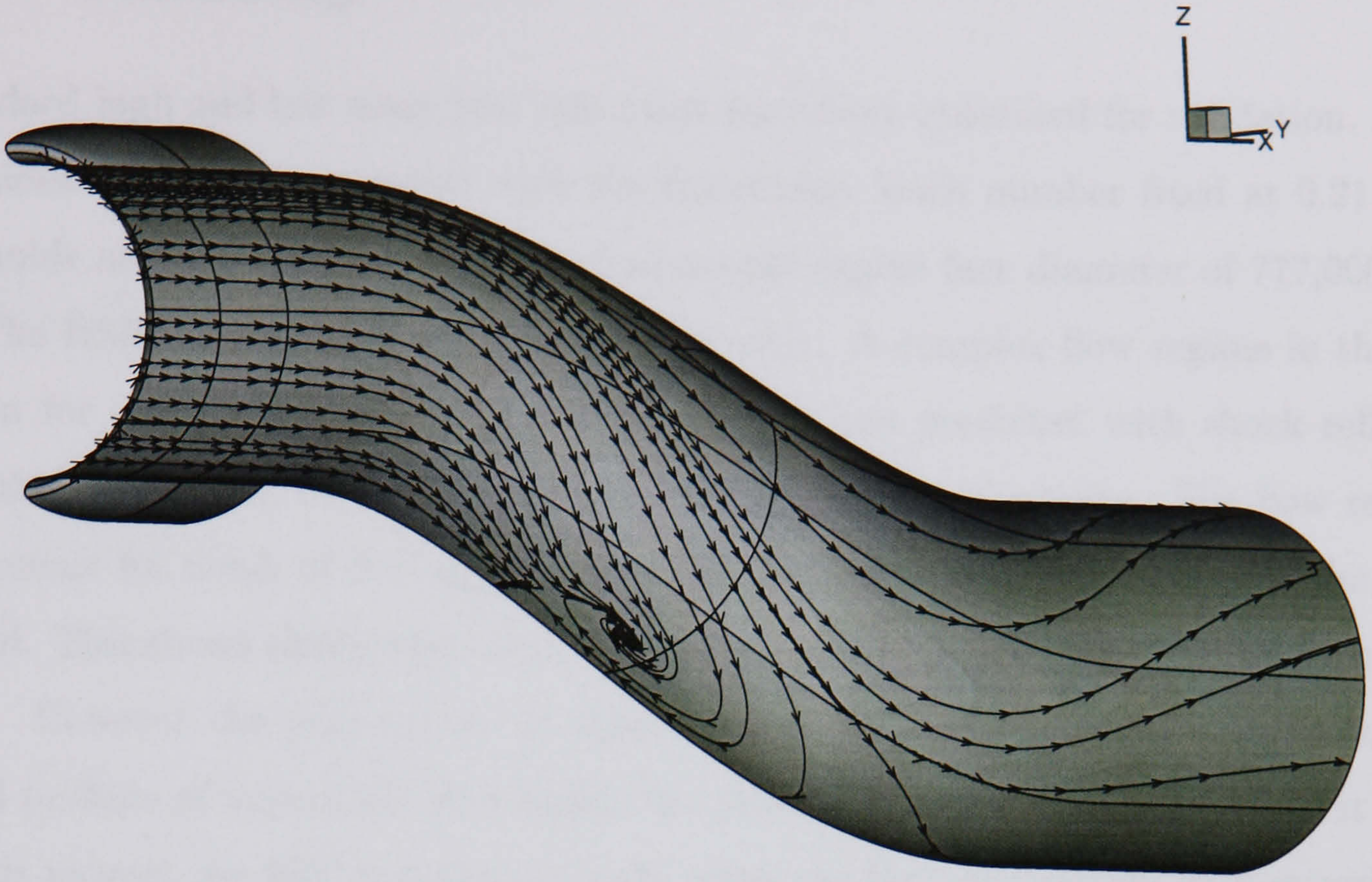

(a) Surface shear stress

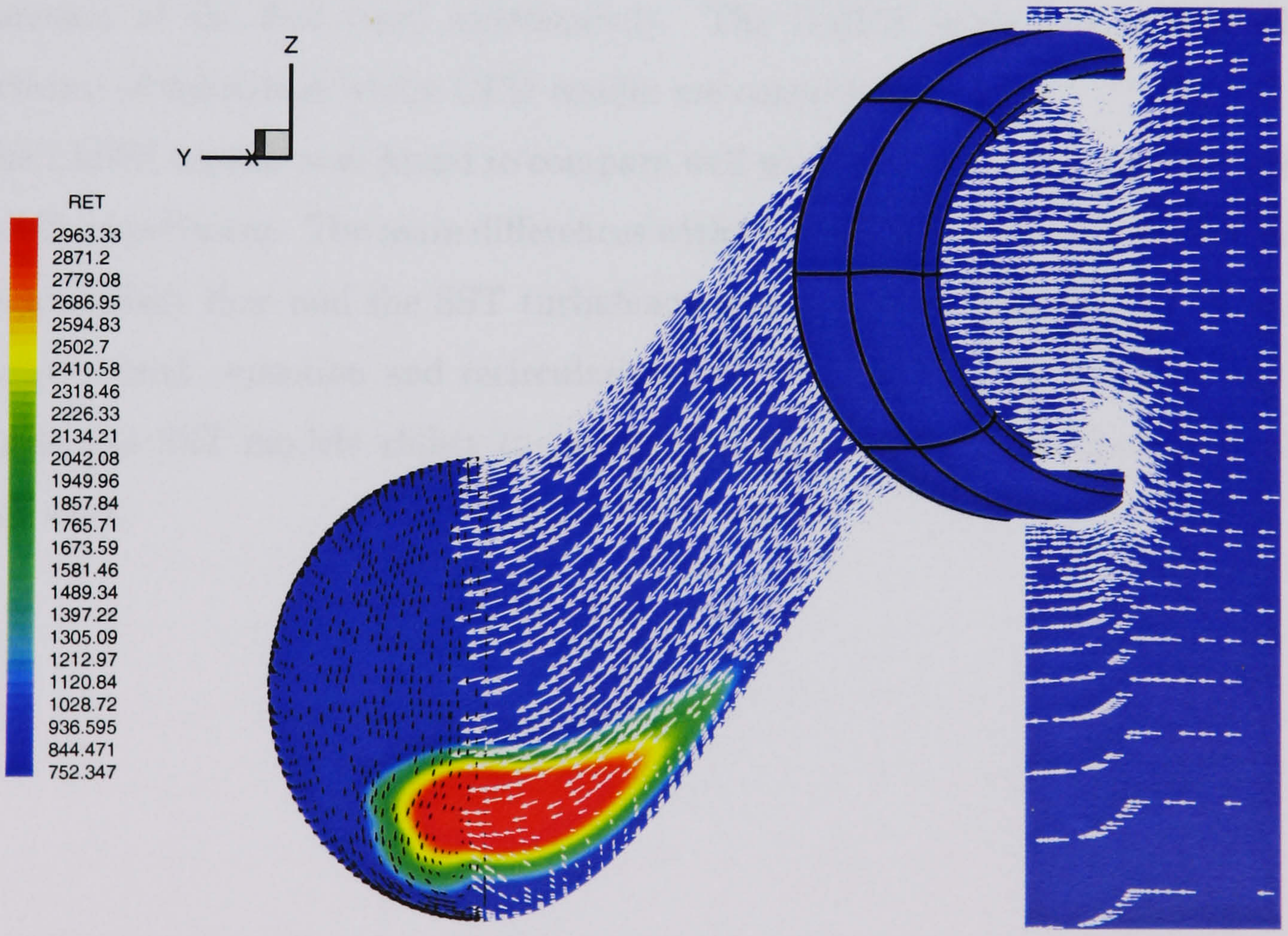

(b) Engine face and symmetry plane turbulent Reynolds numbers

Figure 3.16: *LMFR Turbulent calculation, SST model - shear stress and turbulent Reynolds numbers*

3.3 Summary

Standard high and low mass flow rate cases have been examined for validation. RANS solutions have been computed with the freestream Mach number fixed at 0.21 and a Reynolds number based on the non-dimensional engine face diameter of 777,000.

The HMFR results are challenging to predict. A complex flow regime in the cowl region for the SA and $k - \omega$ turbulence models was predicted with shock reflection and this appears to be contrary to the main experimental results. The flow remains supersonic for much of the region leading to the first bend, particularly for the $k - \omega$ model. This shows similarities with a secondary set of computational and experimental data. However the primary set of experimental and computational data shows only small pockets of supersonic flow inside the cowl and at the starboard side first bend. In this respect the SST turbulence model offers the best comparison with experiment. Confidence can be gained as the SST model is known to improve the prediction of flows with adverse pressure gradients and separated flow. All models predict secondary flow downstream of the first bend satisfactorily. The HMFR study has underlined the importance of validation where CFD results are considered.

The LMFR results were found to compare well with previous computations and satisfactorily experiment. The main differences with experiment occurred in the prediction of the secondary flow and the SST turbulence model provided the best simulation in this respect with sepration and recirculation evident. This further increases the confidence in the SST models ability to predict the high and low mass flow cases in the present work.

Chapter 4

Intakes at Incidence

As a follow on to the validation study in chapter 3, the effects of varying the incidence of the intake to the freestream in both pitch and yaw are examined. Low and high mass flow rates (as previously defined in chapter 3) will again be investigated with a freestream Mach number of 0.21 and Reynolds number of 777,000 based on the non-dimensional engine face diameter. Due to the findings in the previous chapter the RANS calculations will employ the SST turbulence model. The grid used is the 'medium' grid from the previous chapter which has a size of $401,000$ points.

During a flight it is inevitable that the flow entering the intake will be attacking at some angle other than zero. This would typically occur during hard aircraft manoeuvres, or on aircraft that have short-field capabilities, but can also occur due to natural unsteadiness in the atmosphere e.g. updrafts. Under these circumstances it is important that the intake should operate as near to normal as possible and not flame-out or surge. Particular attention will be paid to the flow quality at the engine face.

In order to calculate a geometry at a specified incidence the velocity vector is rotated in the $x-y$ plane. In order to examine yaw and pitch calculations the orientation axis for the grid has to be re-arranged such that rotation about the $x-y$ plane causes an increase or decrease in the yaw or pitch angle. Figure 4.1 shows the surface grid used for the yaw calculations with reference to the orientation axis. The pitched grids were orientated as in the validation study of the 0^o through flow problem. The symmetry plane is the $x-z$ plane as opposed to the $x-y$ plane in the yaw calculations. However due to the nature of the problem a symmetry boundary condition could not be enforced.

This can be seen more clearly in figure 4.10 where flow would be exiting the $x-z$ plane.

4.1 Yaw

Yawed calculations are straightforward with yaw angle defined as positive when the effect of the s-shaped offset is diminished (when the components of velocity are positive in the x and y sense). Low and High mass flow rates have been examined and six different angles examined: ±15, ±30, and ±45 degrees. The effect of positive and negative yaw angles is not the same. The following two sections break down the results into solutions for the low and high mass flow cases.

4.1.1 High Mass Flow Case

Positive angles of yaw

The left hand images in figure 4.2 (a)-(c) show Mach contours with velocity stream traces overlaid for positive angles of yaw of $+15^o$, $+30^o$ and $+45^o$. It can be seen that as the angle of attack increases, flow is concentrated towards the starboard side of the intake. This is most prominent at $+45^o$ where there is considerable separation from the inboard port cowl. The separation off the starboard side first bend is diminished. As the angle of attack is increased the flow has more energy on the starboard side, especially at greater positive yaw angles, and the curvature effects are reduced. This has benefits in terms of pressure distribution at the engine face as we shall see.

The $+15^o$ case is very similar to the case at zero angle of attack. The angle is insufficient to produce any major difference in the flow regime. However the extent of the secondary flow is diminished and hence the distortion is reduced on the starboard side. Although the flow does not actually separate from the inboard port lip, low energy flow develops and Mach numbers remain low towards the port side through the duct. This leads to a slight distorted region towards the port side at the engine face. It should be noted however that the vortical flow is still only present in the usual starboard location.

It is interesting to note from table 4.1 that the amount of distortion for the $+30^o$ case is actually the smallest. With reference to figure 4.2(b), this would appear to be because the angle of the flow attacking the intake causes a reduction in the natural separation off the starboard side first bend as the effect of the offset is diminished. Flow separates from the inboard port side of the duct and leads to low Mach number flow all the way to the engine face. The combination of these actions leads to a channeling of the flow through the centre of the duct and causes two regions of lower total pressure at the engine face towards the port and starboard sides, as seen in the right hand image in (b) (again, the only swirling flow at the engine face is in the starboard side region of low total pressure). Thus there is no single region of low total pressure and so distortion is not as bad as in some other cases. As a note, this leads to a different location for the 60^o worst distorted sector (more towards the port side as opposed to the starboard side for the 0^o and 15^o cases).

The $+45^o$ case has a slightly poorer pressure recovery. The distortion is worse than the $+30^o$ case but is still better than 0^o case because of the diminished effects of the offset (as discussed above) leading to lower pressures across the whole engine face. Swirling secondary flow is maintained towards the starboard side of the engine face at all positive angles of yaw as flow does not separate from the starboard side inner cowl region. However as the angle increases, the size and strength of the swirling secondary flow region decreases.

Figure 4.4 shows the starboard and port side wall pressures in (a) and (b) respectively. It can be seen that the 0^o and $+15^o$ cases are very similar. The $+30^o$ and $+45^o$ cases show major differences, especially on the starboard side. On the starboard side, the pressure gradient is negative in the cowl region (favourable pressure gradient) and then levels off prior to the first bend and separation still occurs. On the port side however there is a slight adverse pressure gradient in the cowl region for all yawed angles (most evident for the 30^o and $+45^o$ where separation occurs). Following the first bend the static pressure recovers well on the starboard side to match the zero degree case towards the engine face. On the port side this is not the case at higher angles of attack where the effects of port side flow being forced out towards the starboard side leading to an adverse pressure gradient and separation. This appears to diminish the effects of flow acceleration around the second bend and eliminate any corresponding static pressure drop prior to the engine face at $x = 4.0$.

Negative angles of yaw

Negative yaw angles have the effect of increasing the amount the flow has to turn to navigate the first bend of the intake forcing the flow towards the port side of the intake. Figure 4.3 shows the flow concentrating towards the port side as the negative yaw angle is increased. This leads to larger regions of low total pressure at the engine face starboard side and consequently significantly higher distortion coefficients and lower pressure recoveries as seen in table 4.1. At 30^o and 45^o the flow also separates from the starboard side inboard cowl. At 30^o there is reattachment prior to the first bend starboard side but at 45^o the flow remains detached and only reattaches just prior to the engine face. Secondary flow at the engine face appears to be strongest when flow remains attached in the cowl starboard side region, as depicted by the streamtrace patterns at the engine face.

Referring to table 4.1, we can see that at all negative yaw angles there is a large difference from the positive yaw angles for the distortion coefficient. The beneficial effects of positive angles in reducing secondary flow are not felt here as the offset is actually increased with reference to the freestream AoA. The largest jump in distortion levels occurs at 30^o. This is most likely due to separation that occurs on the starboard cowl lip that leads to much lower total pressures and stronger swirling flow concentrated on the starboard side of the engine face.

Figure 4.5 shows the starboard and port side wall pressures respectively in (a) and (b). Again, there are major differences in the values in the region of the cowl, more especially for the port side in this case. Port pressures in the cowl region show an increasingly strong favourable pressure gradient on the inside cowl surface and so separation is unlikely here. On the Port outer cowl wall, however, there is evidence of an adverse pressure gradient developing with increasing negative yaw angle and so separation here is probable at higher negative angles of yaw. On the starboard side a strong adverse pressure gradient develops in the cowl region, particularly at 30^o and 45^o where we know significant separation does occur. The adverse pressure gradient on the starboard side leads to a greatly reduced acceleration through the first bend as the flow is very low energy and is actually detached at 45^o.

Yaw Angle	Pressure Recovery	Distortion Coefficient (DC(60))	Yaw Angle	Pressure Recovery	Distortion Coefficient (DC(60))
0	0.94117	0.68818	0	0.94117	0.68818
15	0.94193	0.65904	-15	0.93320	0.73461
30	0.92969	0.60510	-30	0.91614	0.82123
45	0.91304	0.64018	-45	0.89605	0.85863

Table 4.1: *Distortion and Pressure Recovery at engine face for HMFR yawed intake*

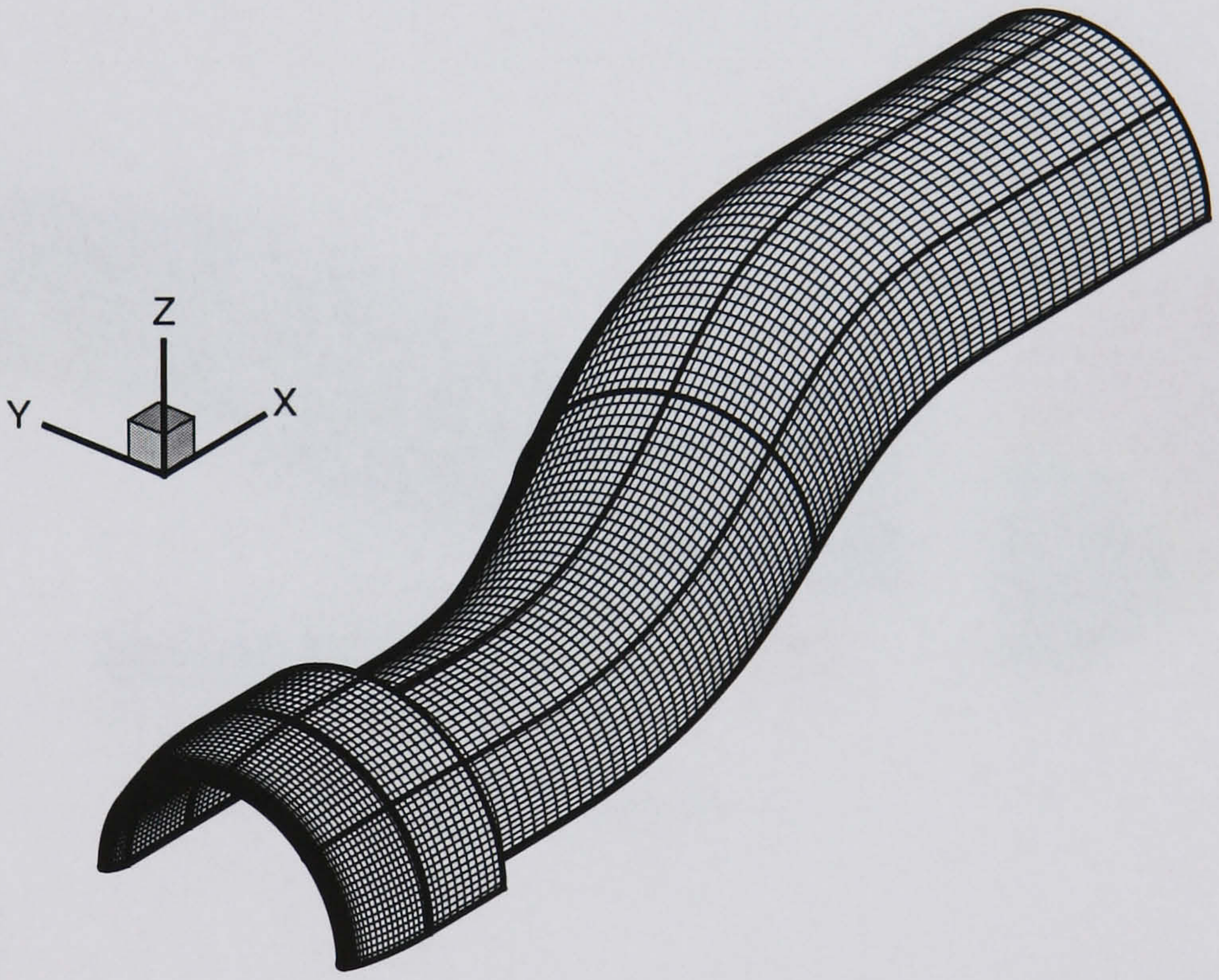

Figure 4.1: *Surface grid of geometry used for yaw calculations*

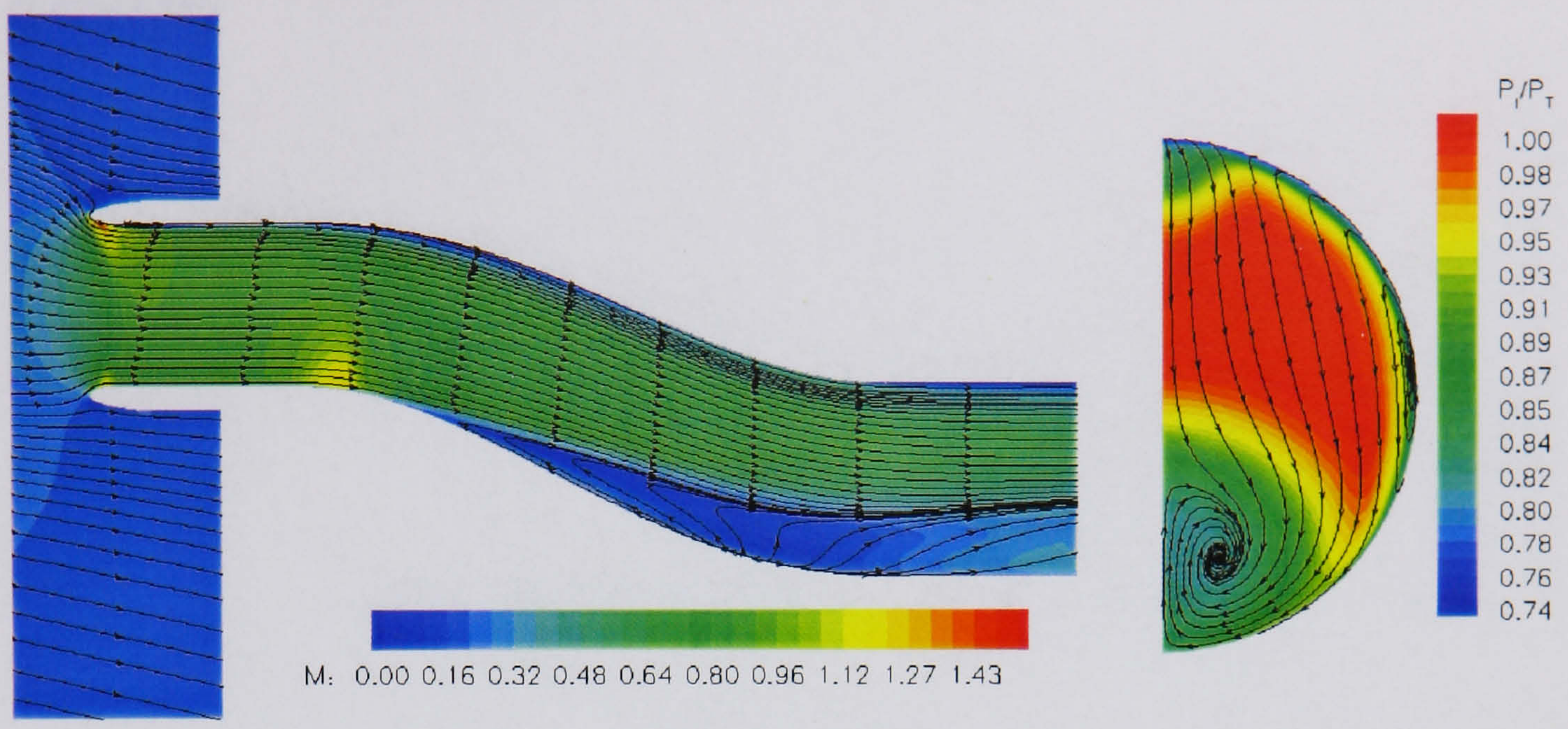

(a) 15 degrees

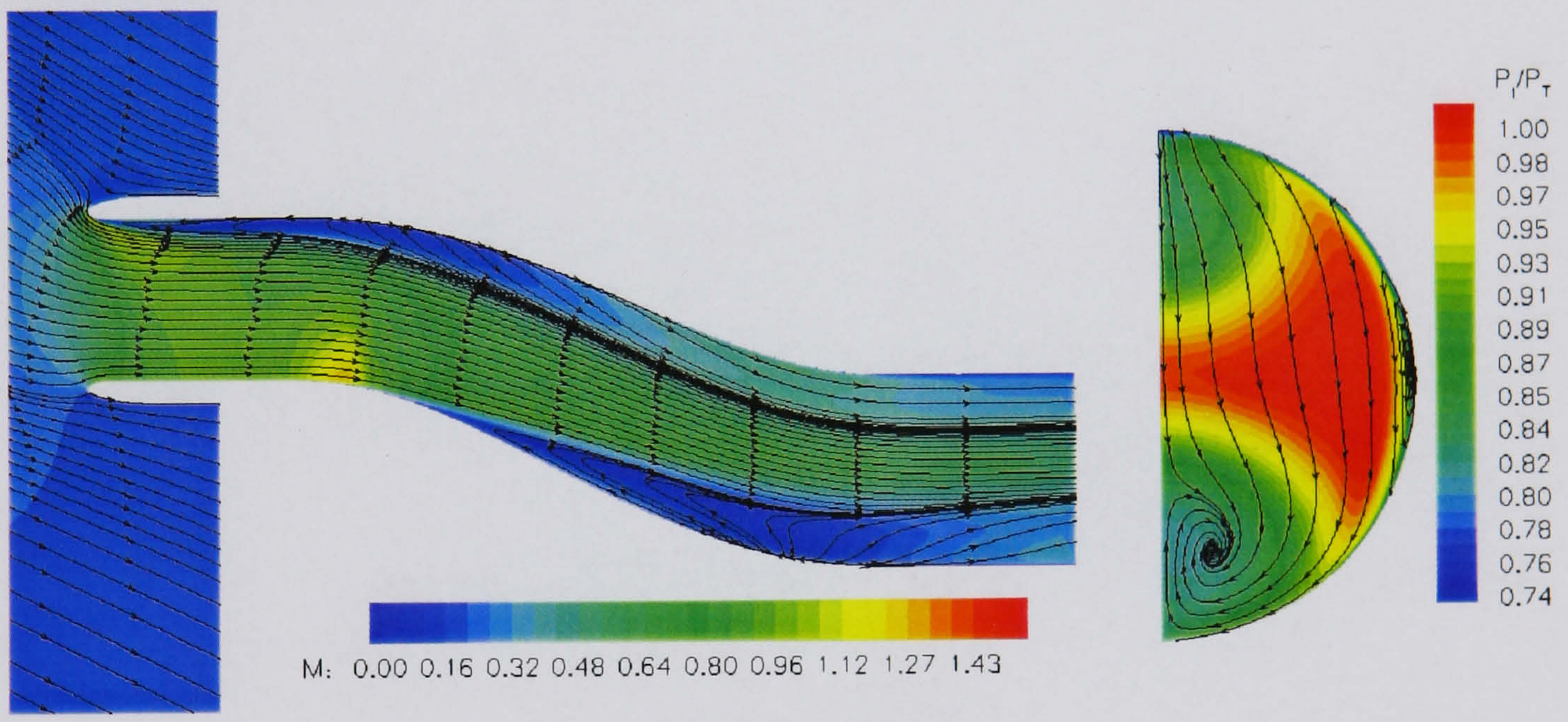

(b) 30 degrees

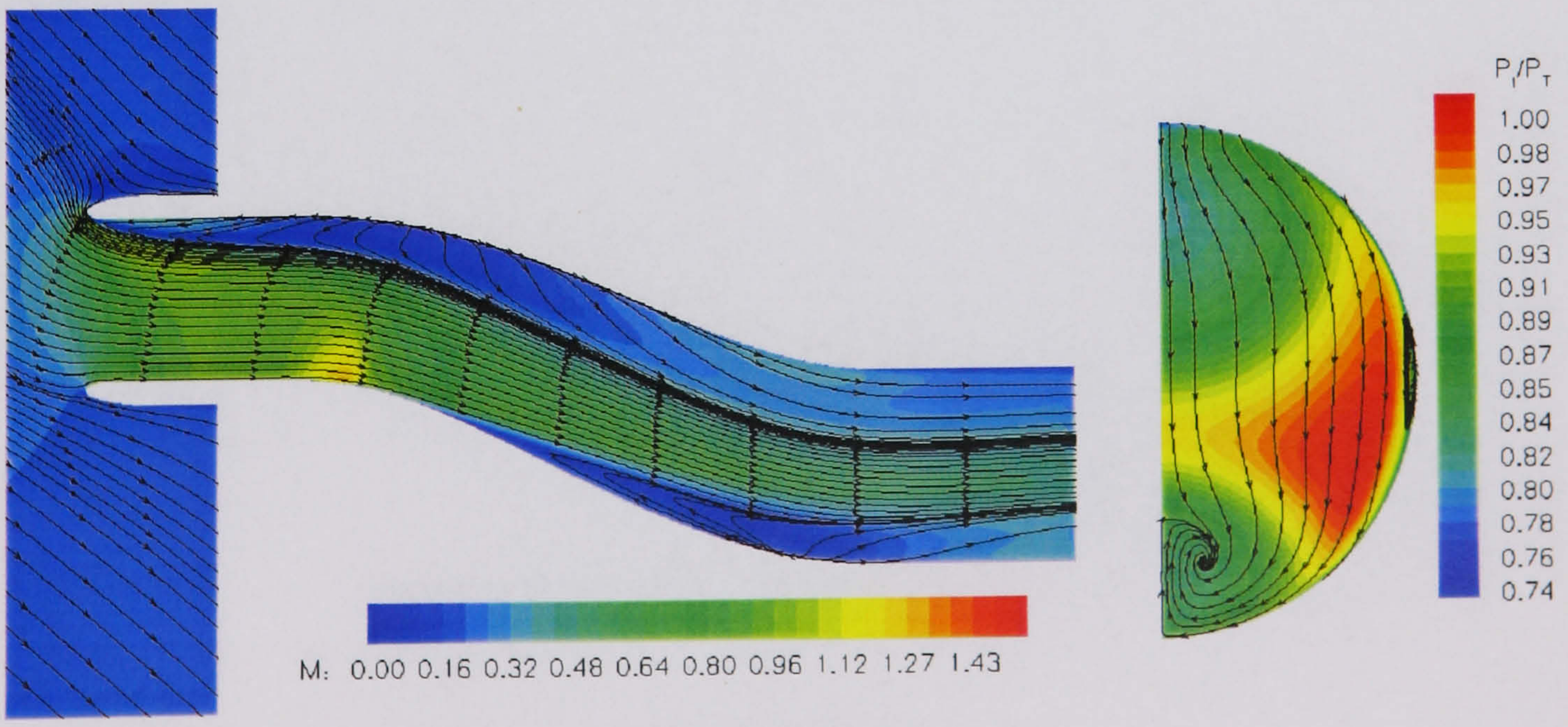

(c) 45 degrees

Figure 4.2: *HMFR SST calculation - Symmetry plane Mach numbers and engine face plane total pressures - positive angles of yaw*

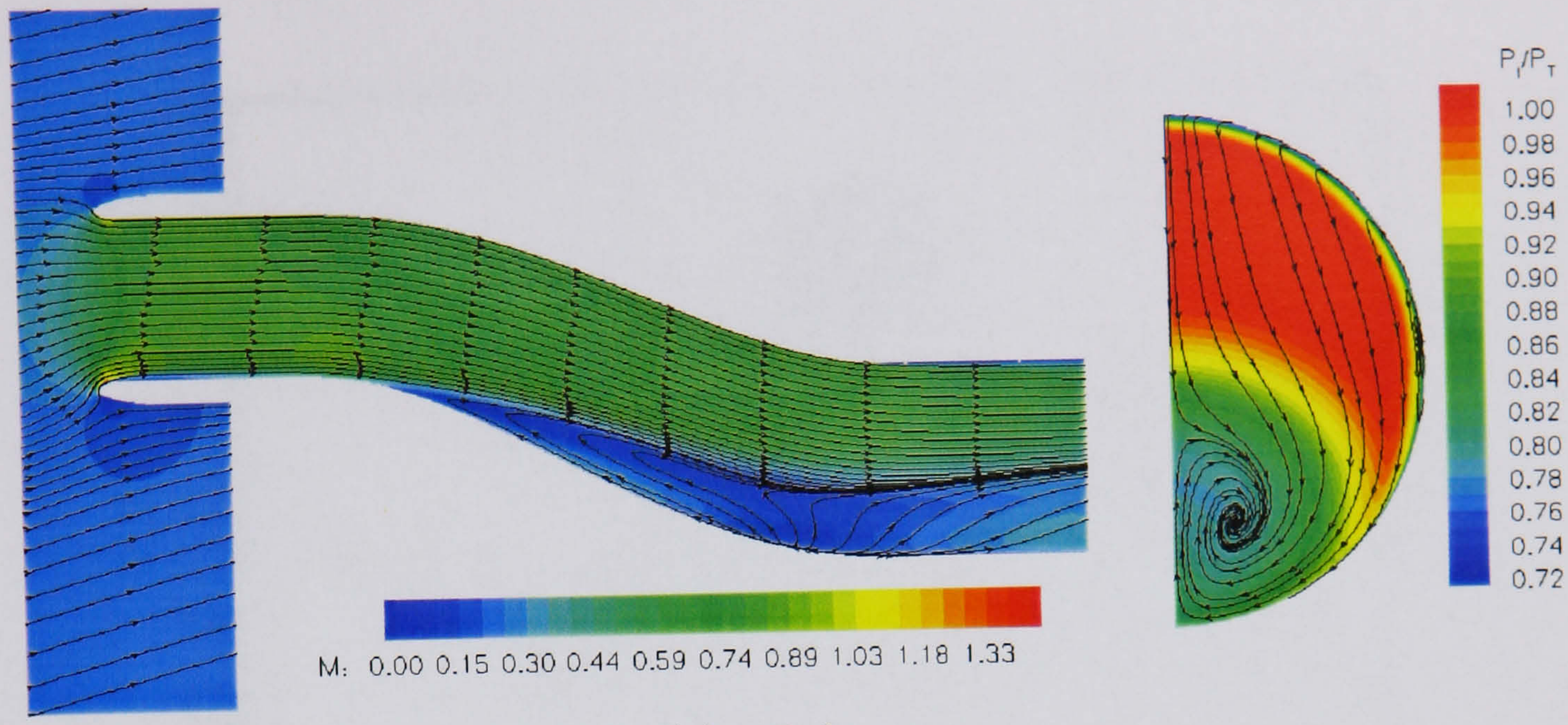

(a) -15 degrees

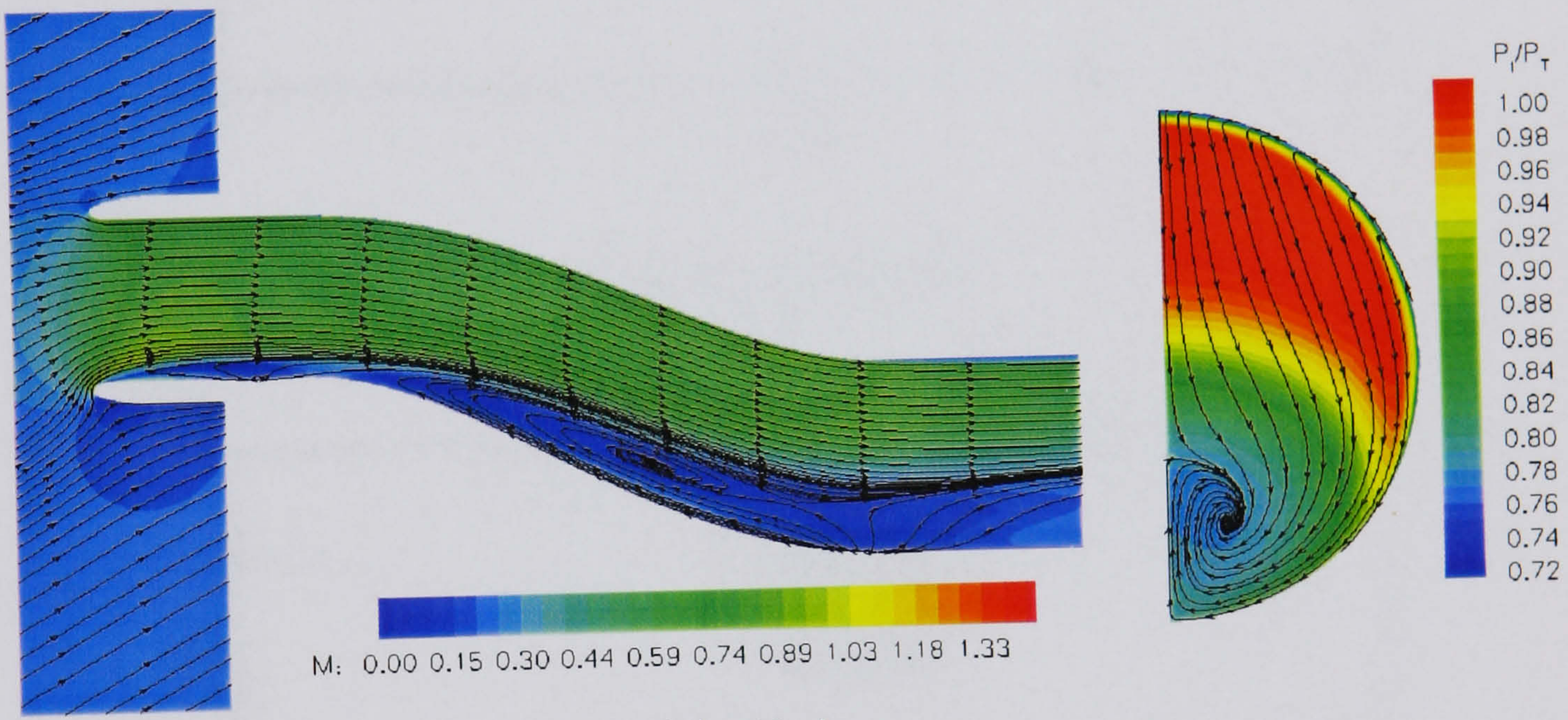

(b) -30 degrees

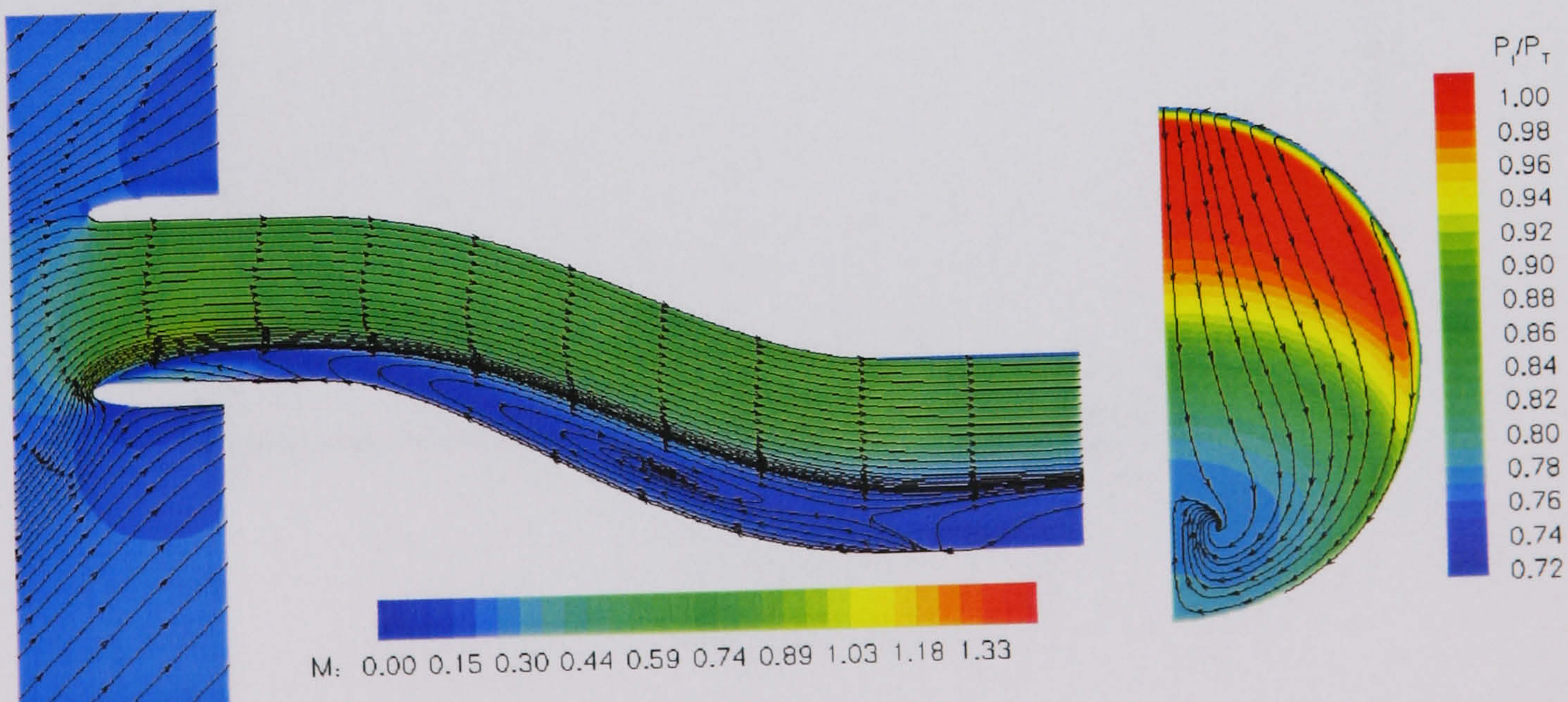

(c) -45 degrees

Figure 4.3: *HMFR SST calculation - Symmetry plane Mach numbers and engine face plane total pressures - negative angles of yaw*

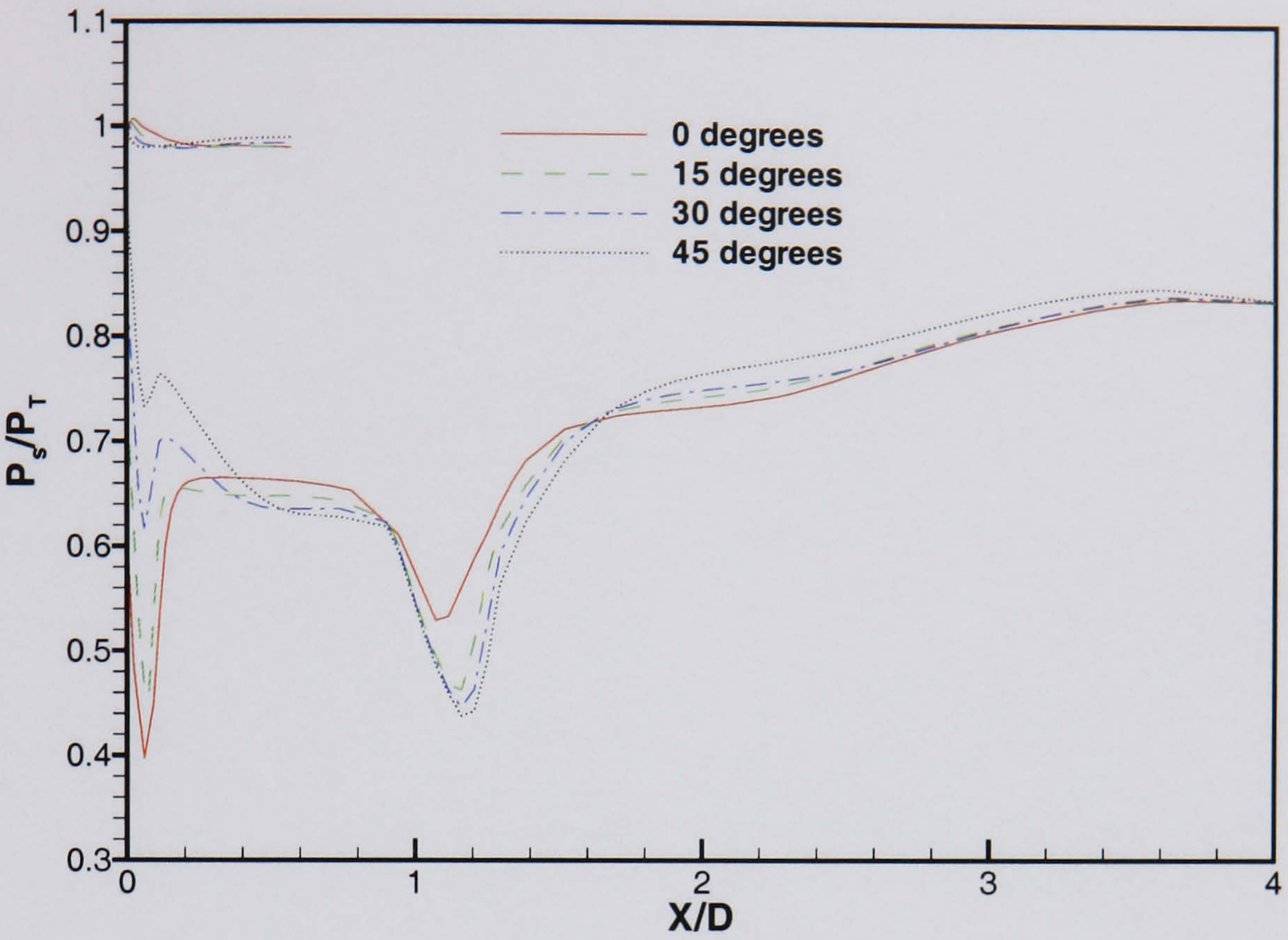

(a) Starboard side

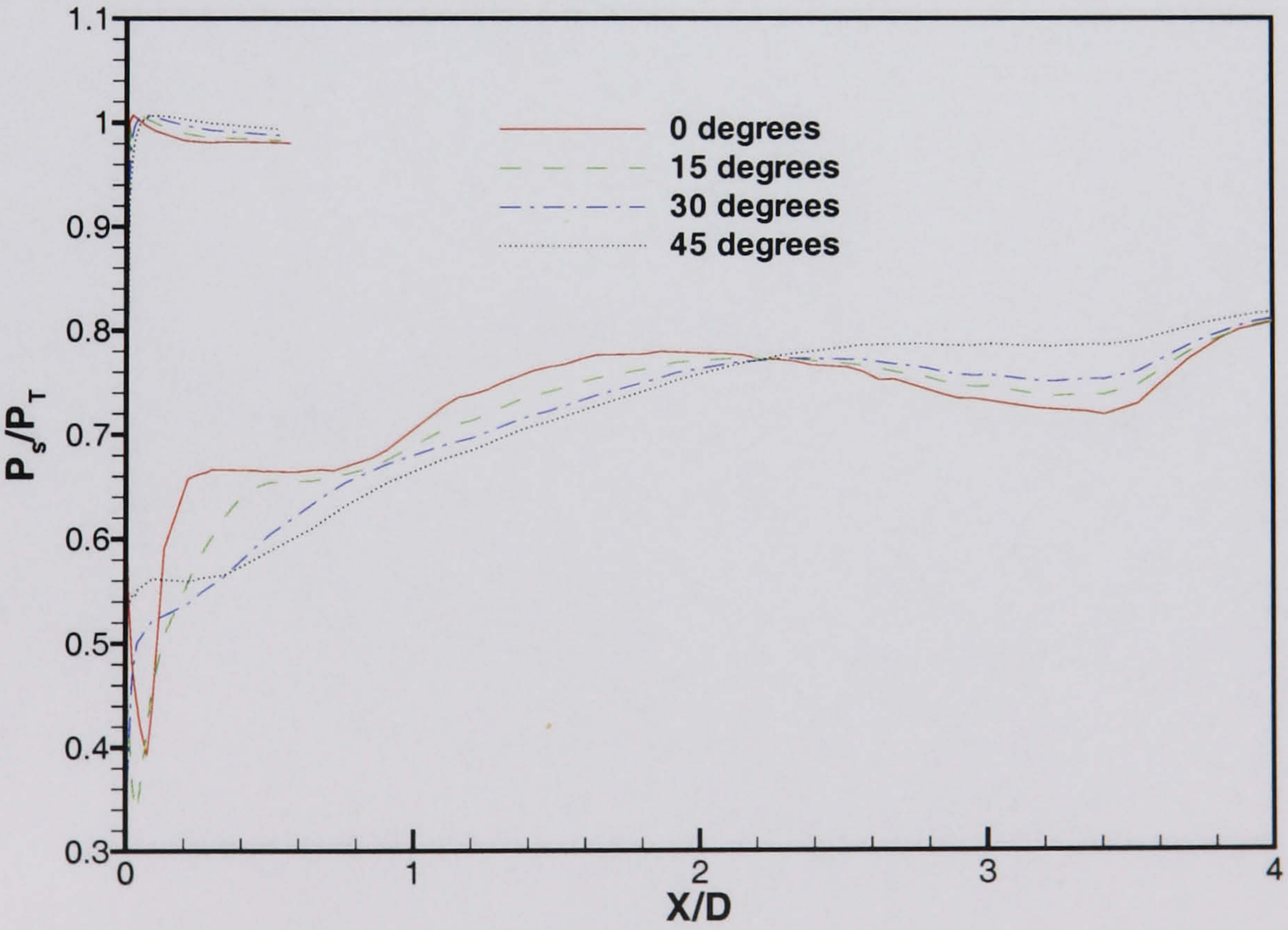

(b) Port side

Figure 4.4: *HMFR Turbulent calculation, SST model - pressure comparison for port and starboard sides for positive angles of yaw*

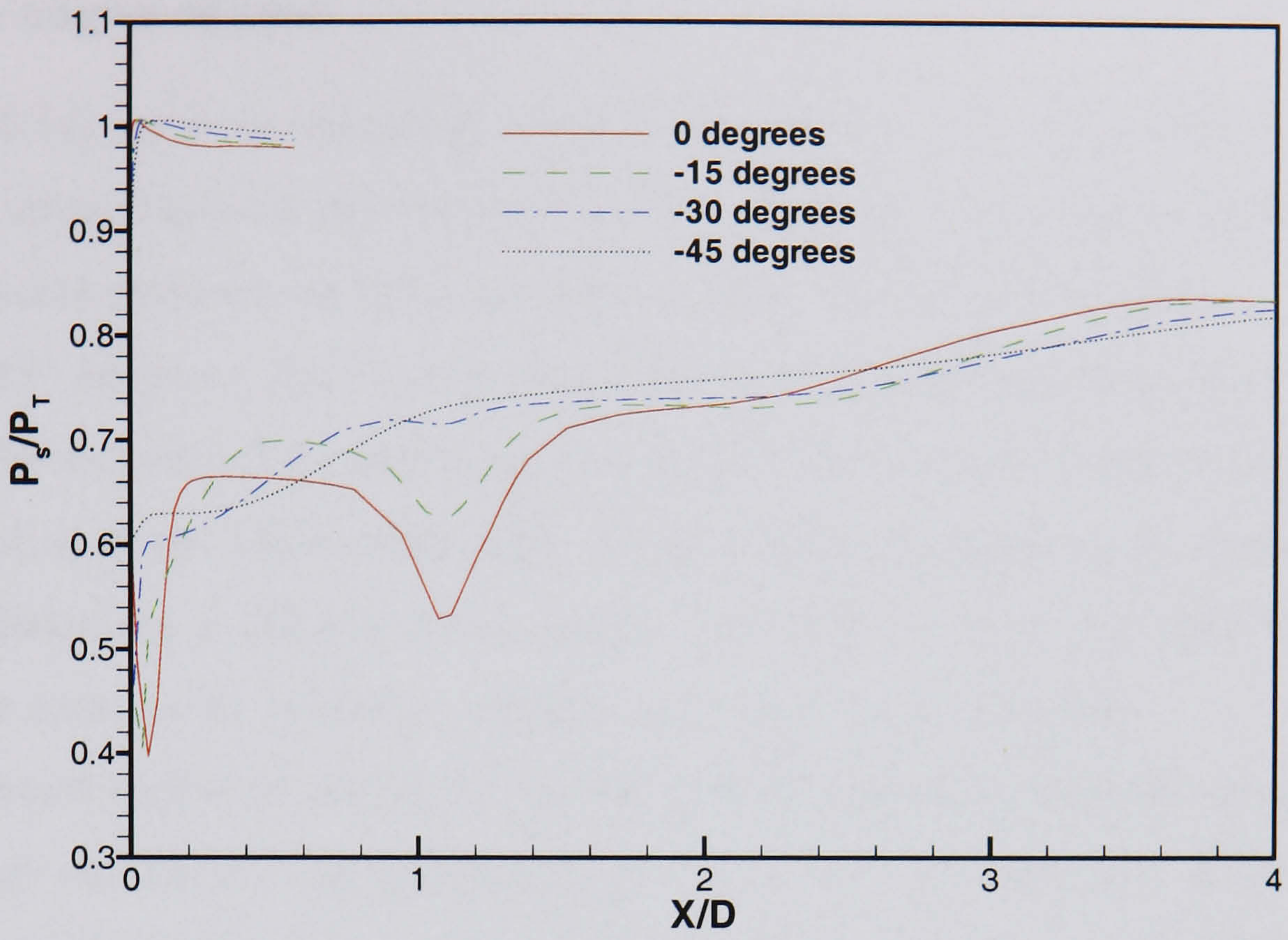

(a) Starboard side

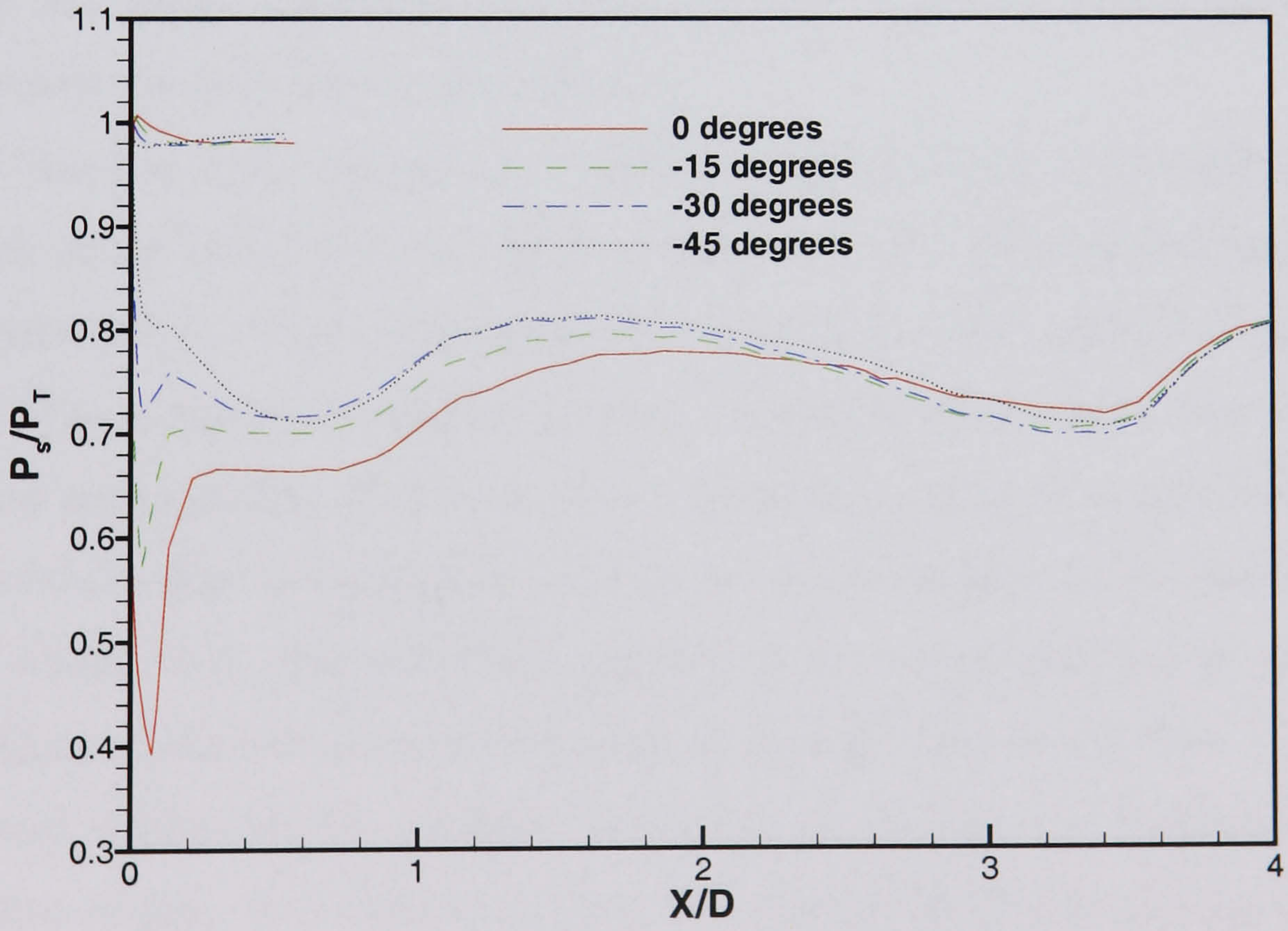

(b) Port side

Figure 4.5: *HMFR Turbulent calculation, SST model - pressure comparison for port and starboard sides for negative angles of yaw*

4.1.2 Low Mass Flow Case

Positive angles of yaw

Figure 4.6 (a)-(c) show symmetry plane Mach contours with streamtraces showing the core flow streamlines for yaw angles of $+15^o$, $+30^o$, and $+45^o$, coupled with engine face total pressure contours on the right hand side for the same yaw angles.

At $+15^o$ degrees it can be seen that there is little difference from the 0^o case - Fig. 4.6(a). The amount of separation and secondary flow from the starboard side first bend is diminished as the effect of the offset is again reduced. However this does not lead to a lower distortion coefficient at the engine face (table 4.2) as was seen with the high mass flow case, as the secondary flow is not as strong in this case.

The worst distorted region for the 30^o case is located towards the port side of the engine face and there is an increase in distortion from the 15^o case. Examining figure 4.6(b), it is clear that the secondary flow is effectively destroyed from the starboard side first bend. Separation now occurs on the inside of the port cowl, which leads to low Mach number and total pressure flow all the way to the engine face. This is the reason for the poorer distortion over previous cases, with the poorer distorted region being towards the port side in this instance.

When the flow angle increases to $+45^o$ these trends continue. Considerable separation occurs on the inside port cowl region. This has severe effects downstream as can be seen in figure 4.6(c). There is separation from the outer cowl surface on the starboard side also. The distortion coefficient is poor. Examining the engine face contours and streamlines explains this. The worst distorted sector is again located towards the port side. Secondary flow at the engine face in the usual location at the starboard side is now now totally lost. Instead, there appears to be a small amount of evidence that some swirling of the flow is occurring towards the port side of the duct.

Port and starboard side pressure extraction can be seen in figure 4.8 for LMFR positive yaw angles. It is clear that there is a strong favourable pressure gradient on the starboard side inside cowl region as expected which is also the case for the port side outer cowl surface to a lesser extent. The port side inner cowl surface shows signs of an adverse pressure gradient for higher angles, as does the starboard side outer cowl surface, promoting separation.

Negative angles of yaw

Figure 4.7 (a)-(c) show symmetry plane Mach contours with streamtraces showing the main core flow path for yaw angles of -15^o, -30^o, and -45^o, coupled with engine face total pressure contours. With reference to table 4.2, the pressure recovery is slightly worse for these cases. The distortion is also worse for the -15^o and -30^o cases as the effect of the offset is again magnified leading to a much greater region of secondary flow. At 30^o there is also separation from the inboard cowl starboard lip. Reattachment is brief prior to the first bend before the flow separates once more. This leads to a very large region of badly distorted flow explaining the factor of two increase in distortion coefficient over the 15^o case. Because of the separation from the starboard lip, the secondary flow is not as strong however.

At -45^o the distortion is not as bad as for the $+45^o$ case since, although the total pressure region is lower, it is spread out over a larger region (high total pressures are limited in extent). This, together with the fact the pressure recovery is lower, leads to a smaller distortion coefficient than would perhaps be expected. There is considerable separation of the flow for the -45^o case from the starboard side inside cowl lip, and there is no re-attachment prior to the first bend. This effectively destroys the creation of secondary flow from the first bend starboard side. As the flow negotiates the first intake bend and approaches the second bend, it is forced back towards the starboard side reducing the separated region on the starboard side. This is another contributing factor as to why the distortion is not as low as may have been expected. This may be because the flow is being forced towards the port side of the intake as it enters due to the major starboard side lip separation. Acceleration around the port side second bend is now stronger than previously seen.

Pressure extractions from the starboard and port sides for negative yaw angles are shown in figure 4.9 (a) and (b) respectively. Adverse pressure gradients can be seen on the inner cowl surface of the starboard side promoting separation. This can also be seen on the outer cowl surface of the starboard side. There is a stronger favourable pressure gradient on the inner port cowl surface than on the outer cowl starboard surface. It can be seen that there is no acceleration of the flow around the starboard side first bend at -30^o and -45^o because of the effects of separation upstream at the cowl.

Yaw Angle	Pressure Recovery	Distortion Coefficient (DC(60))	Yaw Angle	Pressure Recovery	Distortion Coefficient (DC(60))
0	0.99994	0.2085	0	0.99994	0.2085
15	0.99977	0.2872	-15	0.99783	0.4946
30	0.98904	0.5565	-30	0.98106	0.7926
45	0.97048	0.8560	-45	0.96473	0.8304

Table 4.2: *Distortion and Pressure Recovery at engine face for LMFR yawed intake*

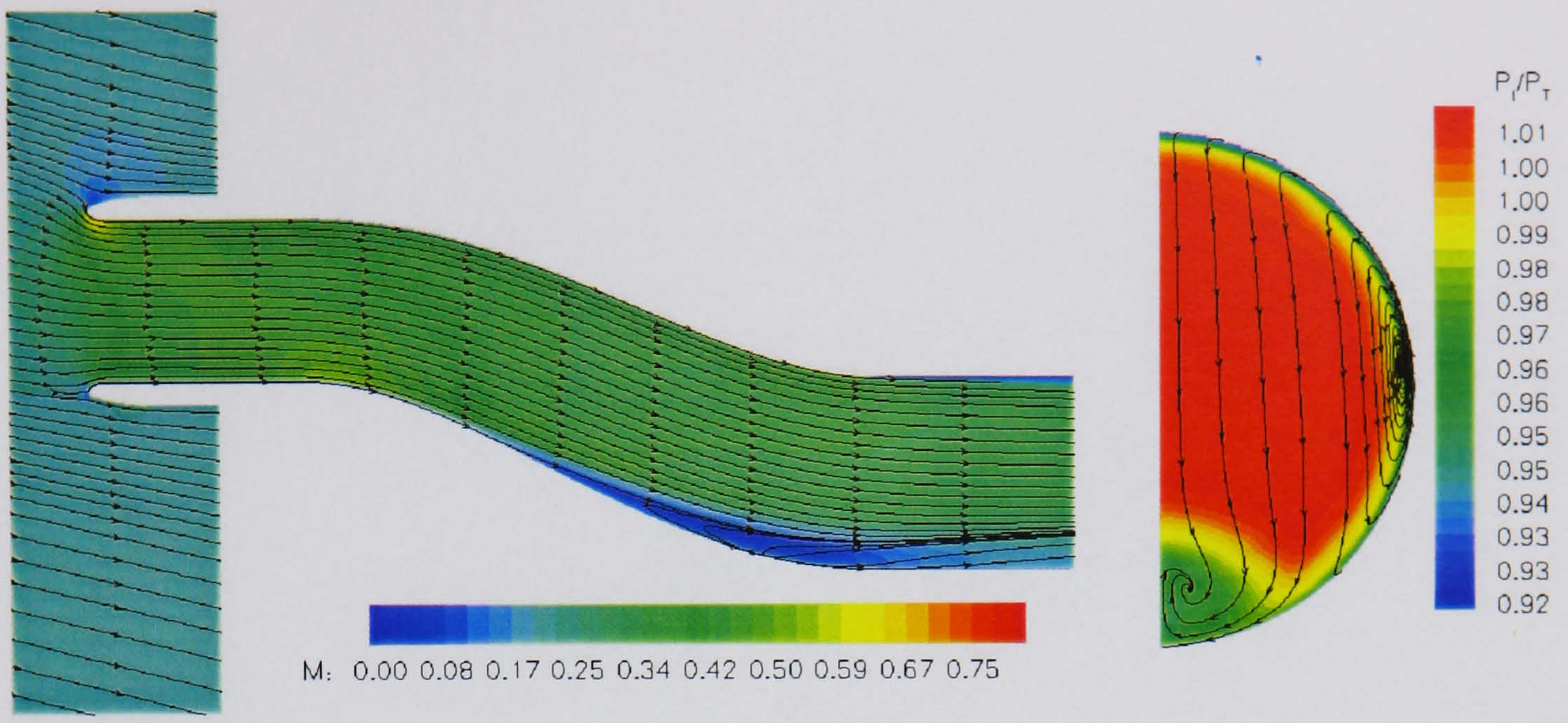

(a) 15 degrees

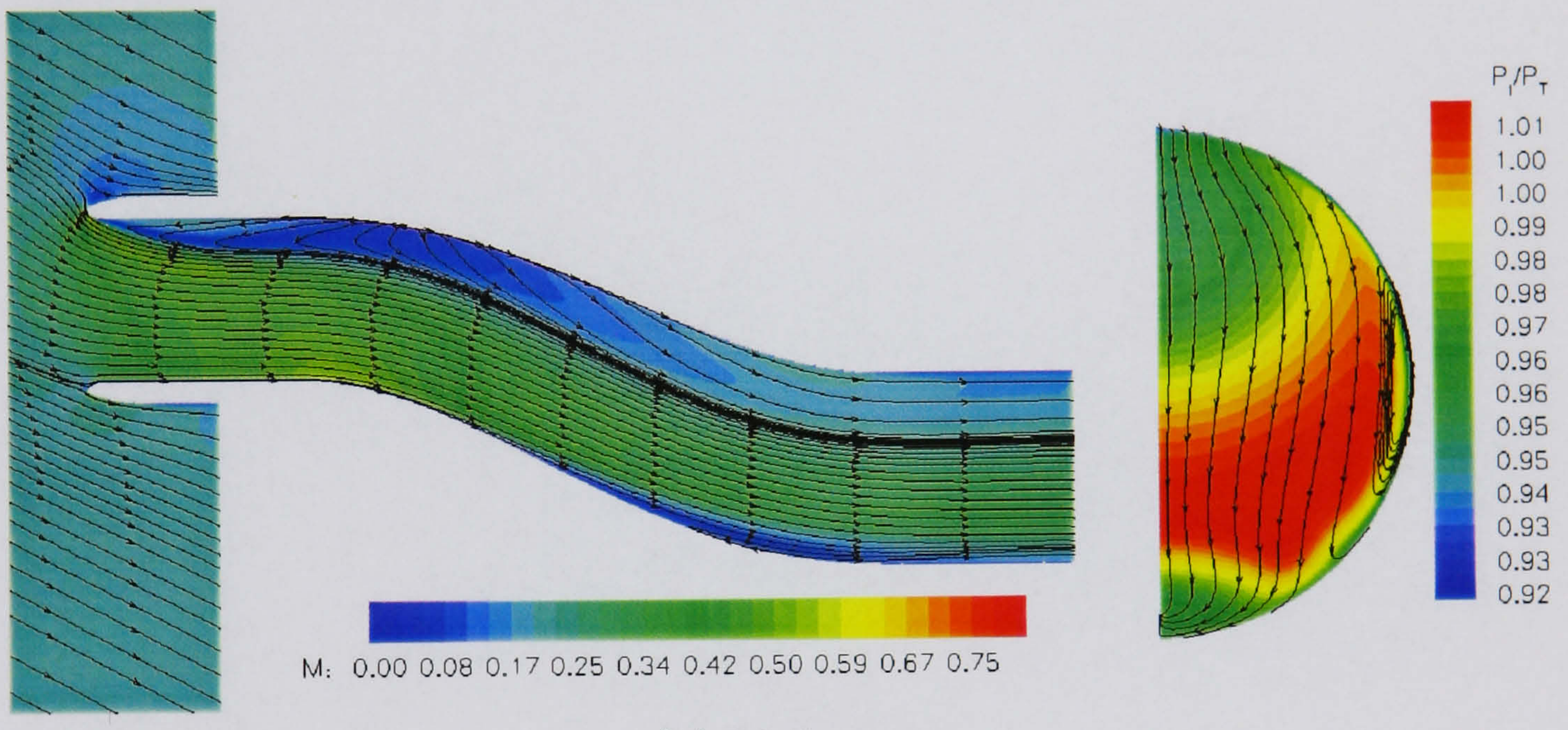

(b) 30 degrees

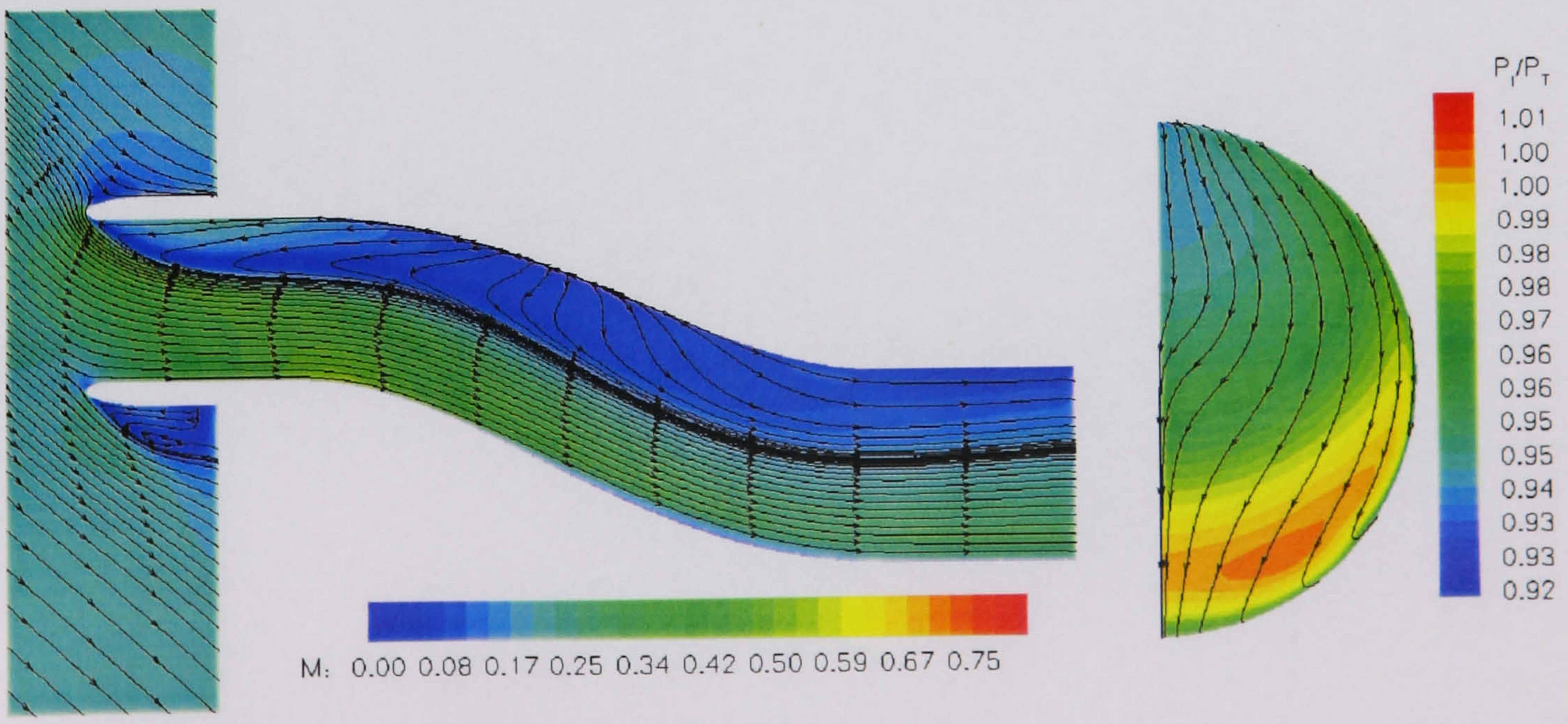

(c) 45 degrees

Figure 4.6: *LMFR SST calculation - Symmetry plane Mach numbers and engine face plane total pressures - positive angles of yaw*

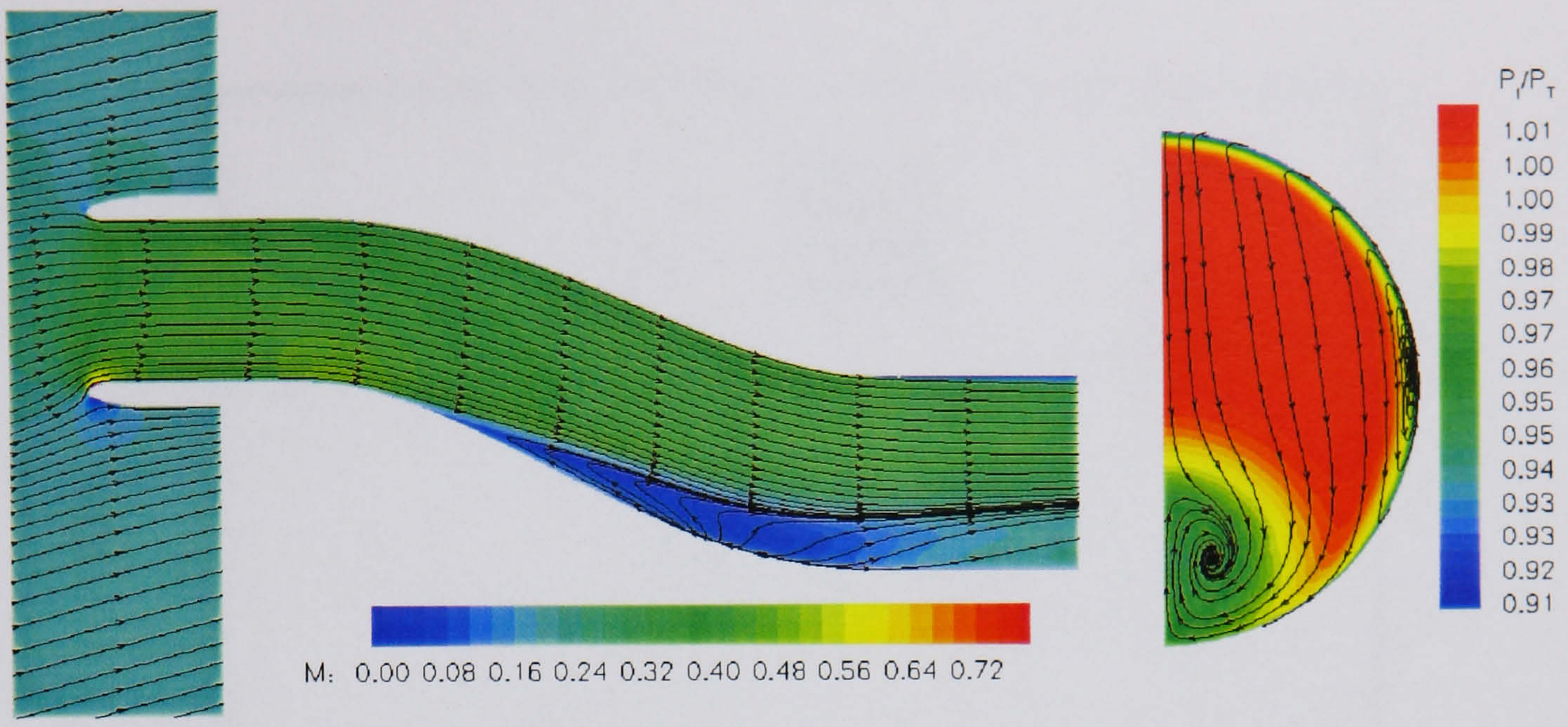

(a) -15 degrees

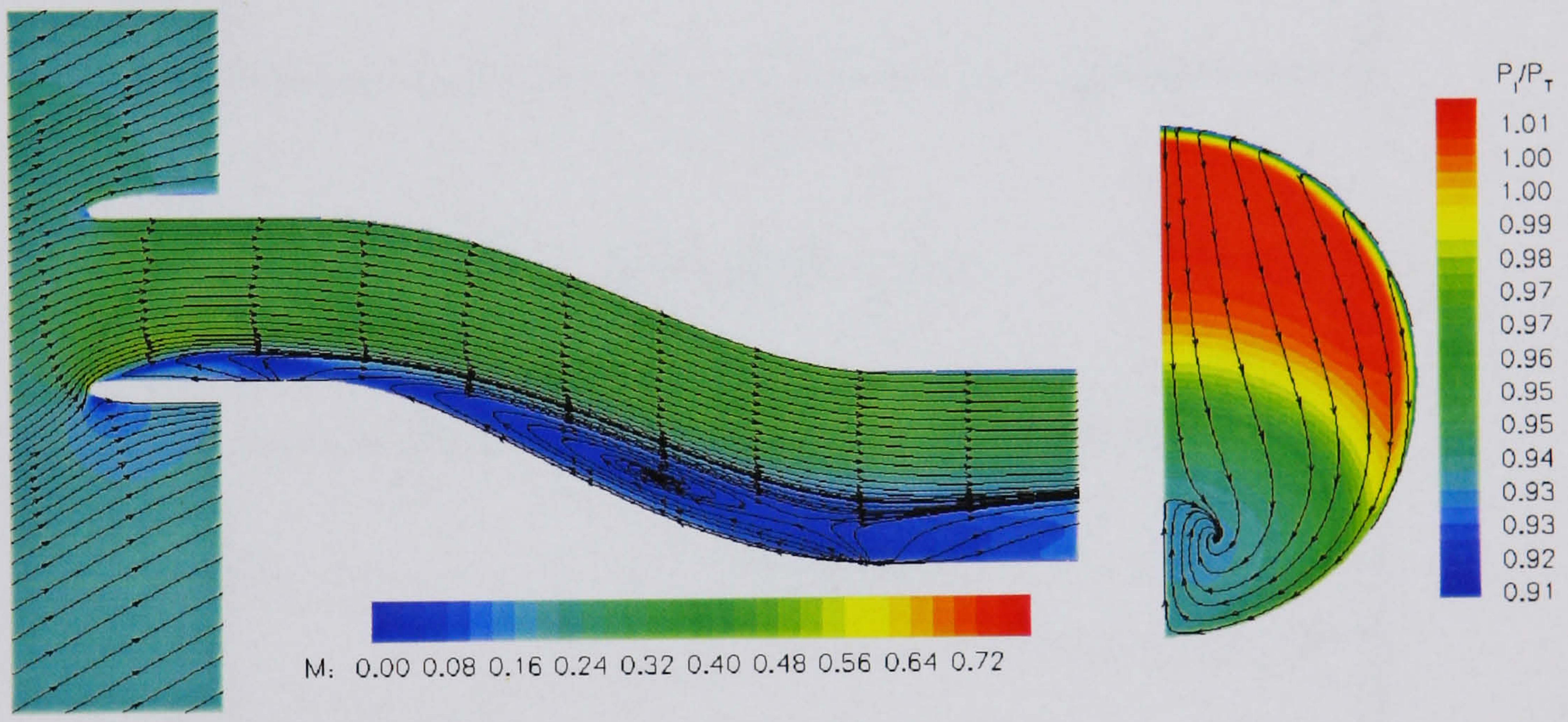

(b) -30 degrees

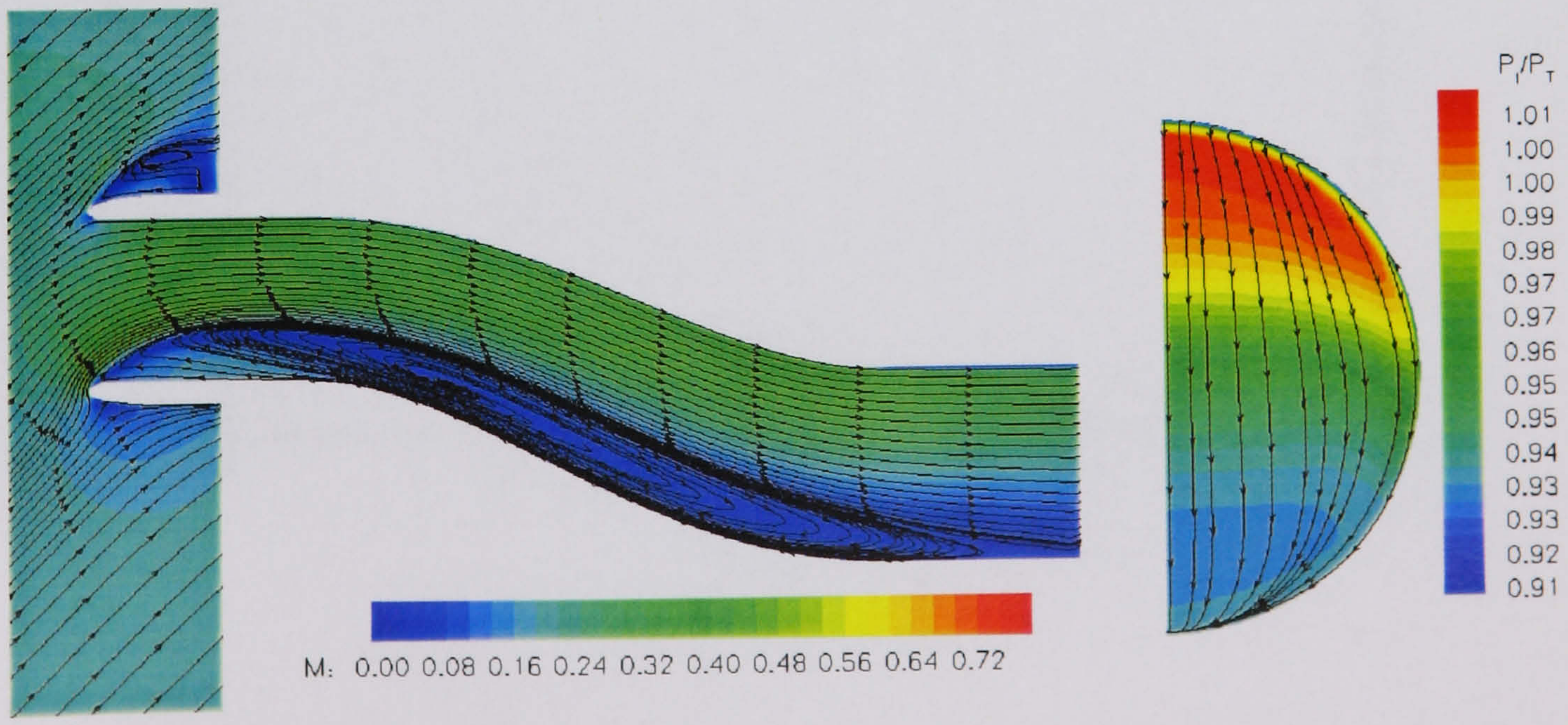

(c) -45 degrees

Figure 4.7: *LMFR SST calculation - Symmetry plane Mach numbers and engine face plane total pressures - negative angles of yaw*

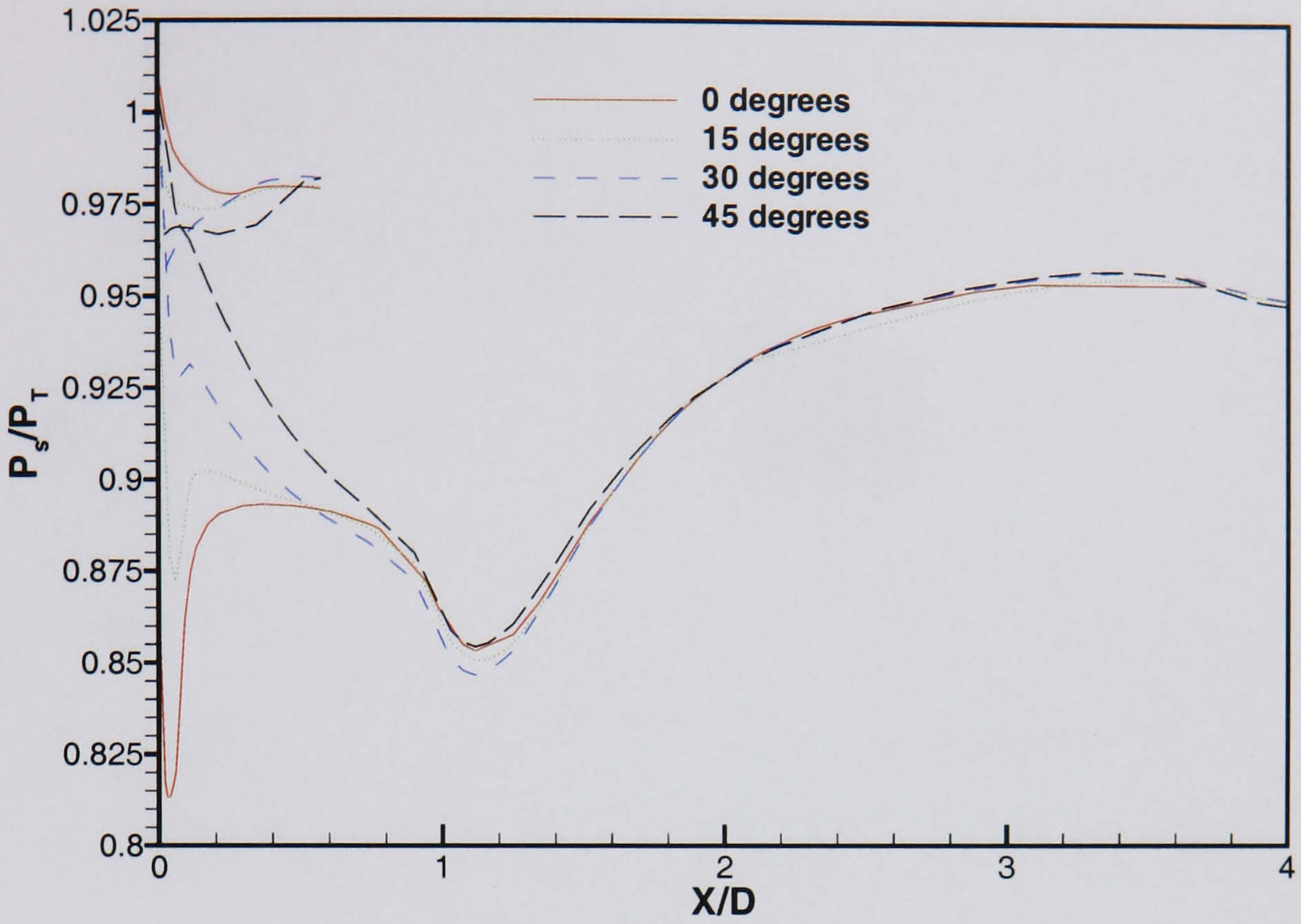

(a) Starboard side

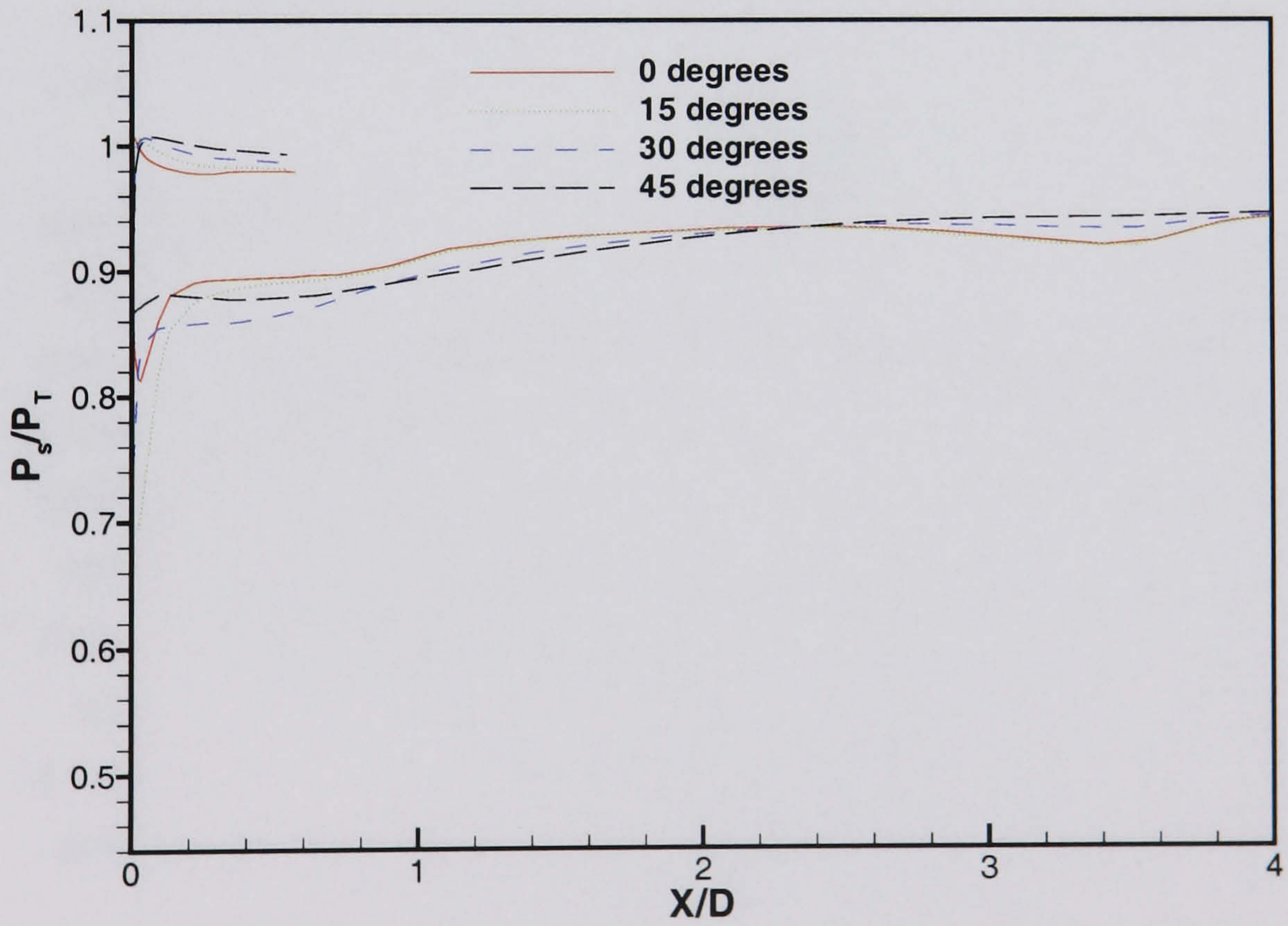

(b) Port side

Figure 4.8: *LMFR Turbulent calculation, SST model - pressure comparison for port and starboard sides for positive angles of yaw*

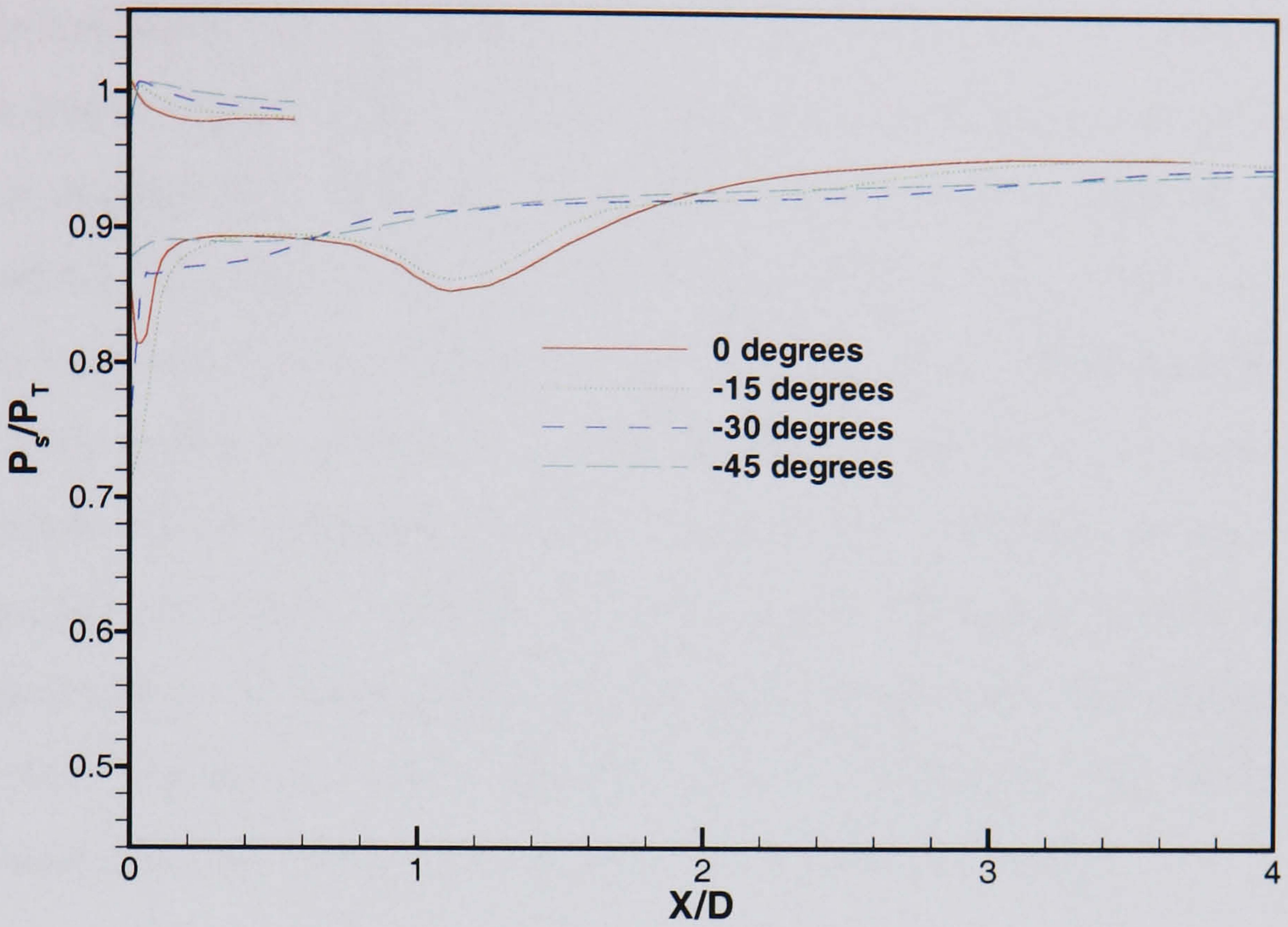

(a) Starboard side

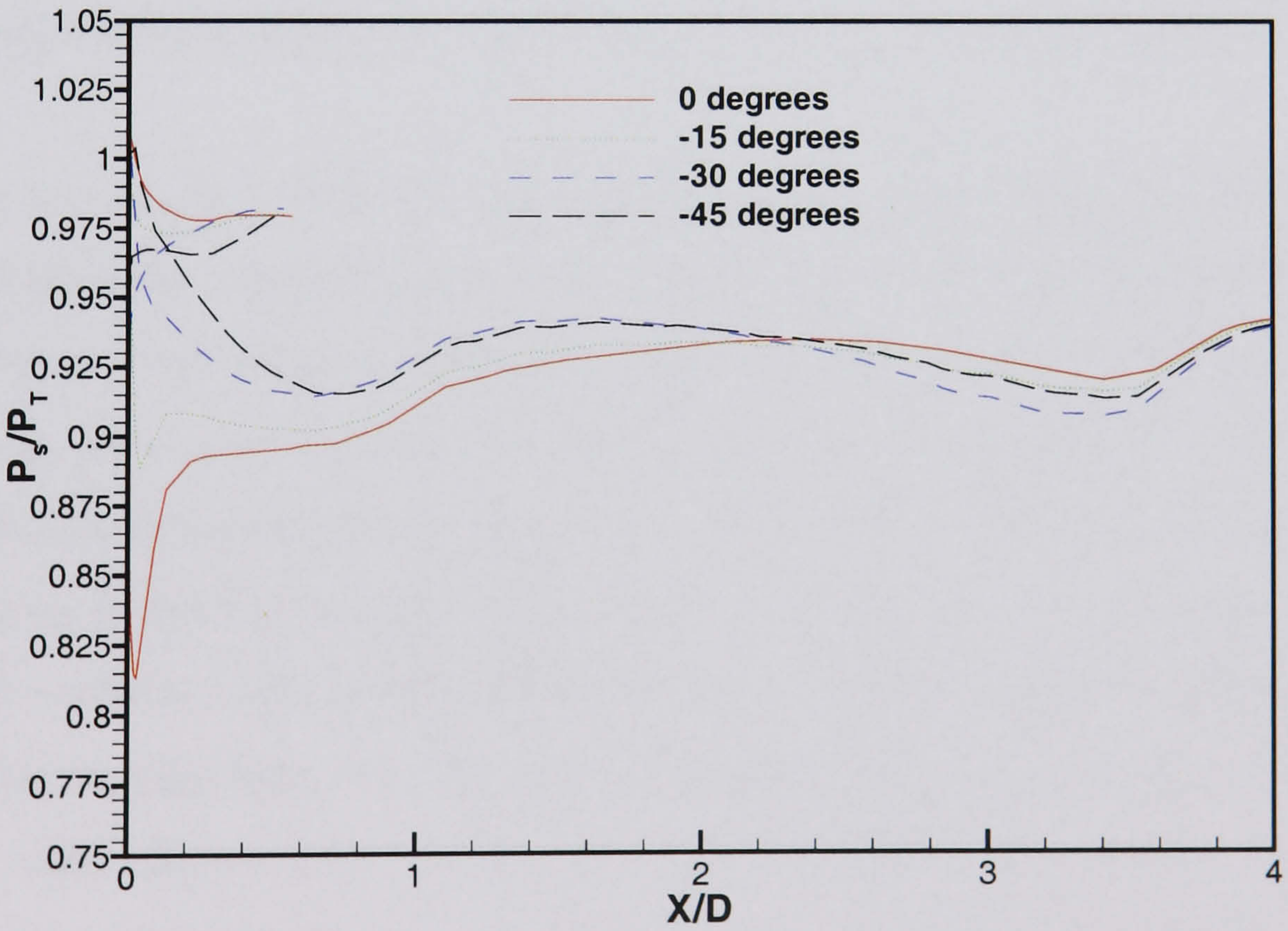

(b) Port side

Figure 4.9: *LMFR Turbulent calculation, SST model - pressure comparison for port and starboard sides for negative angles of yaw*

4.2 Pitch

Due to the orientation of the intake the pitch calculations are not symmetric as in the validation study (figure 4.10). This inevitably leads to computational domains that double the original size. Thus for the medium viscous grid as used in this study the overall domain consisted of around 800, 000 grid points. Again only the viscous case was studied and computations were done for both the high and low mass flow rates. For this case both positive and negative pitch angles are effectively the same and so only positive pitch will be considered at 15^o, 30^o, and 45^o. However, pressure extractions solely from the port and starboard side are no longer adequate to fully appreciate the flow characteristics. Consequently, extractions have also been made from the top and bottom sides. Figure 4.10 shows the full definitions for these new extractions. High and low mass flow rate solutions are again subdivided for clarity.

4.2.1 High Mass Flow Case

Figure 4.11 (a), (b), and (c) shows Mach contour plots through the $Y = 0$ and $Z = 0$ planes, coupled with engine face plane total pressures, for pitch angles of 15^o, 30^o, and 45^o.

It can be seen that with the intake pitched at 15^o (figure 4.11(a)) the results differ very little from the 'normal' case at zero angle of incidence. The slice through the plane at $Z = 0$ shows that there is no separation off the cowl lip. This leads to total pressure contours at the engine face that are nearly symmetric and similar to the zero degree case (although streamtrace patterns show a concentration of the secondary flow on the right portion of the engine face). Indeed table 4.3 shows that the pressure recovery and distortion coefficient (for a 60^o sector) for the 0^o and 15^o cases are almost the same. This is further highlighted in the graphs of static pressure taken from the starboard and port sides (figure 4.12) and top and bottom sides (figure 4.13). One difference appears to be that the pressure recovery, following the initial acceleration of the flow into the intake, is poorer leading to a greater acceleration of the flow on the starboard side around the first bend of the intake.

The main differences, however, occur on the top and bottom sides. As mentioned, only positive angles of pitch are examined as negative angles would show the same results, the top and bottom sides just being swapped. At positive angles the stagnation point on the top side moves towards the inside region of the duct whereas the stagnation point on the bottom side moves more towards the outer cowl region of the duct. It can be seen in figure 4.13(a) that a favourable pressure gradient develops on the top wall cowl inside the duct as the stagnation point shifts further inside the duct and separation does not occur. The size of the flow acceleration into the duct is greatly affected with very little acceleration evident on the top wall at 45^o. On the bottom wall (figure 4.13(b)) an adverse pressure gradient develops at 30^o and 45^o which is conducive to separation, which does occur at these angles.

At 30^o (figure 4.11(b)) it can be seen that separation off the cowl lip is induced. This has the effect of moving the region of low total pressure at the engine face so that there is no longer any symmetry. Lower pressure spreads around towards the $Y = 0$ plane due to the separation at the cowl causing lower energy flow in this location. The disturbed area at the engine face also increases in size which has the effect of lowering the distortion coefficient and causing a poorer pressure recovery. From the slice through the symmetry plane, it can be seen that supersonic flow is still generated in the cowl region. From the slice through the $Z = 0$ plane, the level of the supersonic flow is further increased due to the additional acceleration of the flow around the cowl top side because of the angle of incidence. Pressure traces from the starboard and port sides show that there is not too much difference from the 15^o case. Pressure recovery in the cowl region is poor and remains underestimated (with reference to the 0^o case) all the way to the engine face.

Finally, at 45^o the separation off the cowl lip further increases (figure 4.2.1(c)). This interferes with the natural separation off the intake first bend leading to a large region of low total pressure at the engine face. This low total pressure region is moved further up towards the port side. This gives a poor pressure recovery as expected but gives a comparatively better distortion coefficient level. This is because the poorer pressure levels are covering such a high proportion of the engine face at this stage. Pressure extraction from the port side shows that the pressure recovery in the cowl region has improved. It is also clear that the initial pressure drop into the intake is not as great indicating less acceleration of the flow in this location.

Pitch Angle	Pressure Recovery	Distortion Coefficient (DC(60))
0	0.94117	0.68818
15	0.94002	0.71132
30	0.93358	0.70316
45	0.91221	0.62174

Table 4.3: *Distortion and Pressure Recovery at engine face for a pitched intake at HMFR*

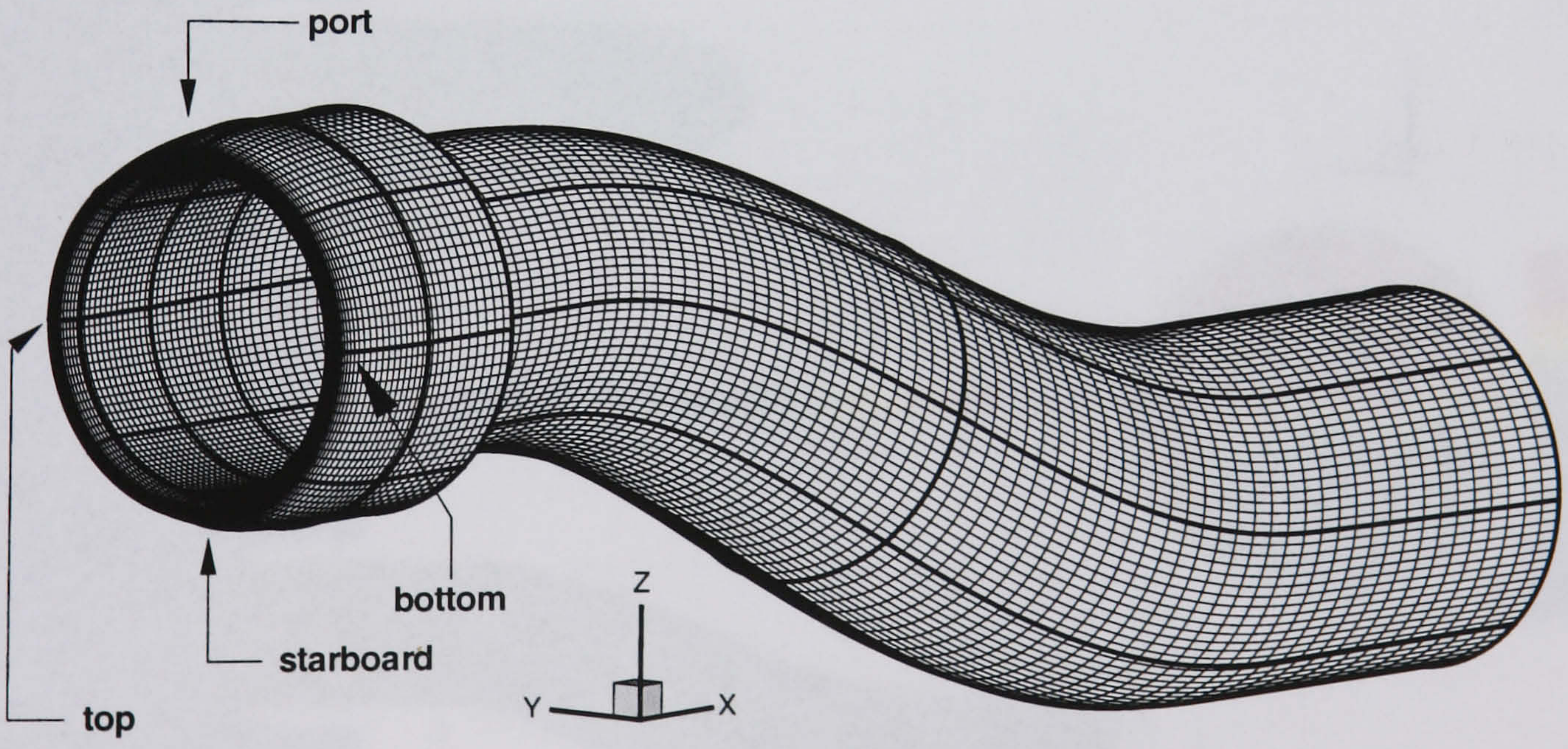

Figure 4.10: *Surface grid of geometry used for pitch calculations*

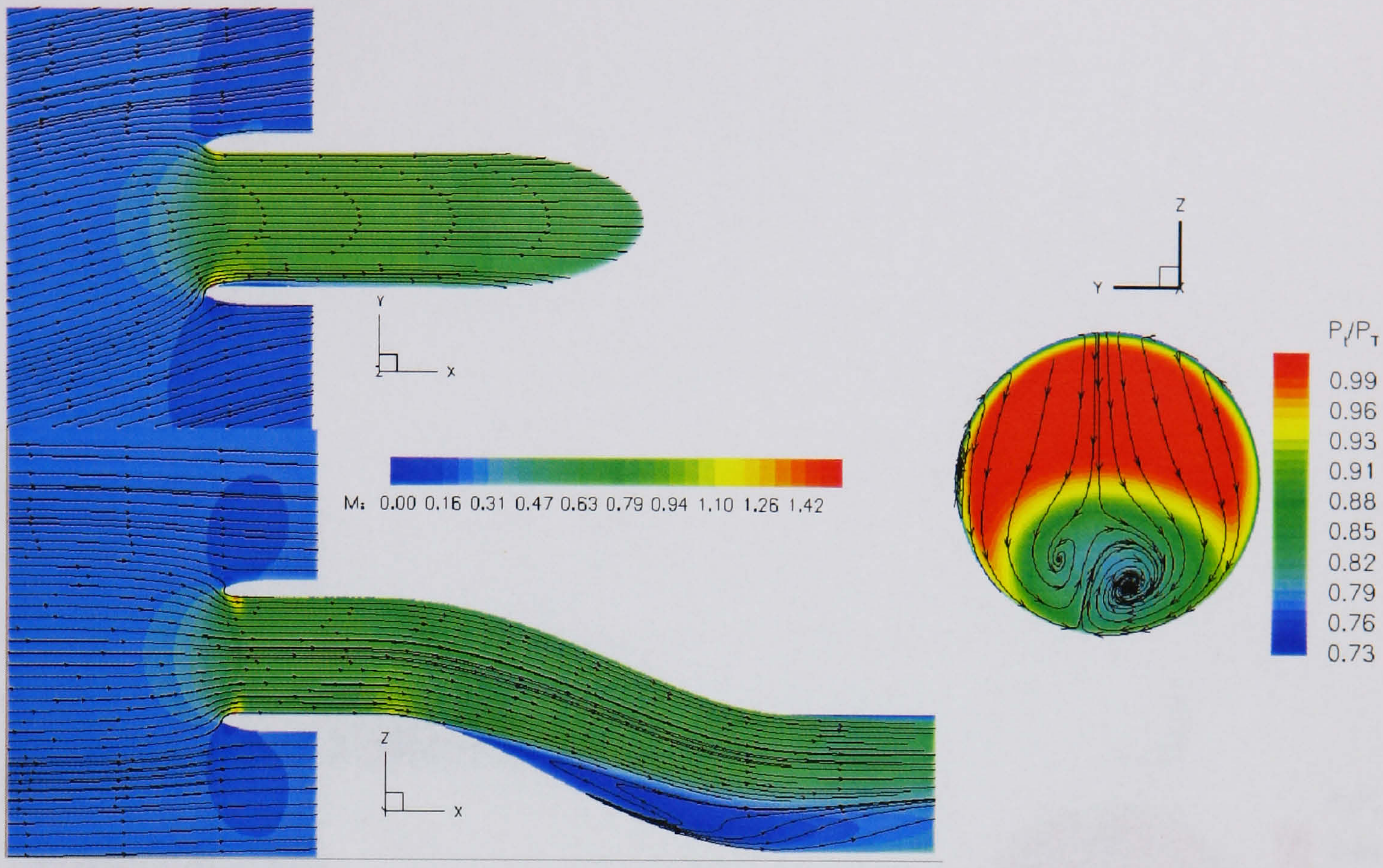

(a) 15 degrees

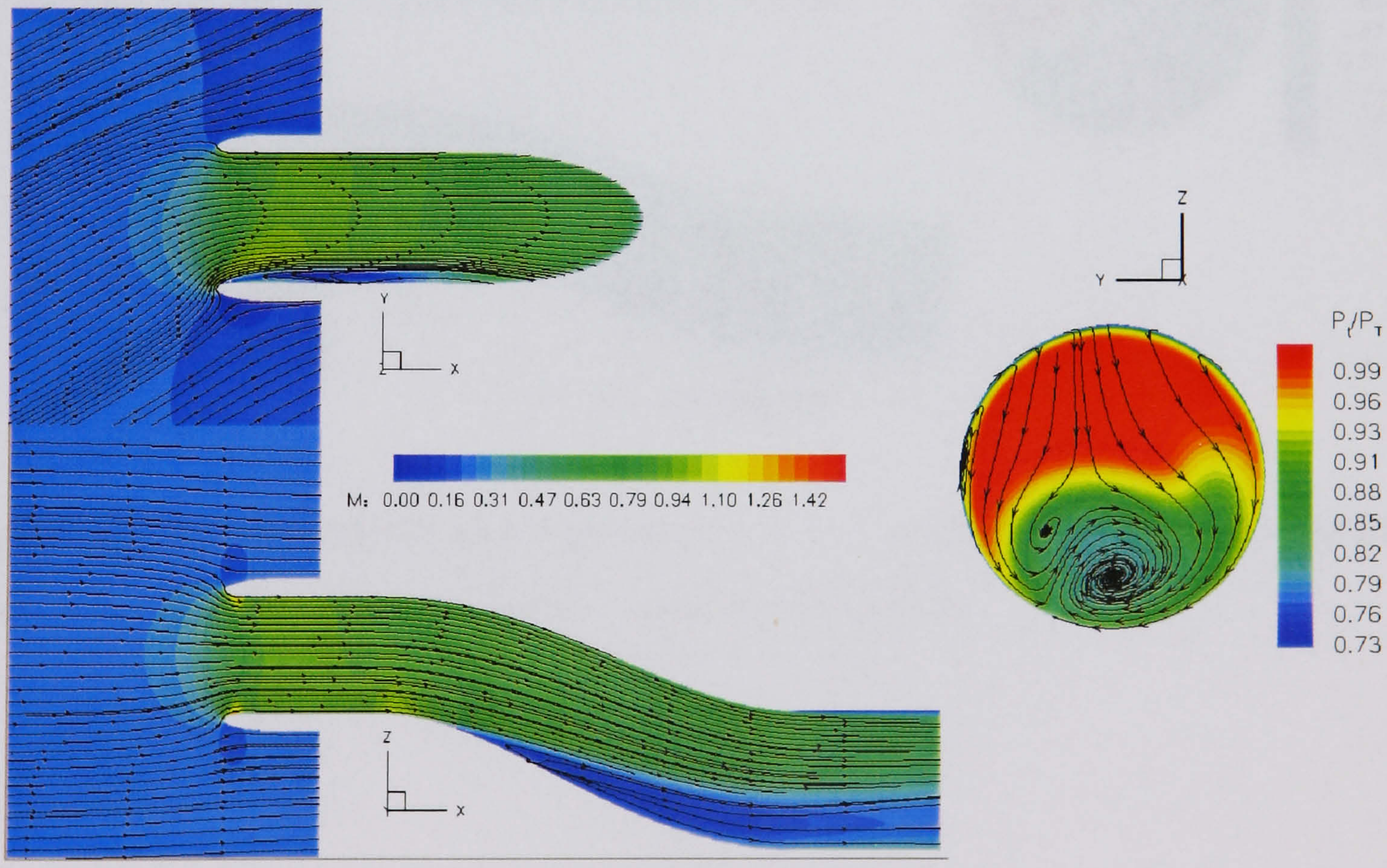

(b) 30 degrees

Figure 4.11: *HMFR SST calculation - $Y = 0$ and $Z = 0$ plane Mach numbers and engine face plane total pressures - various pitch angles*

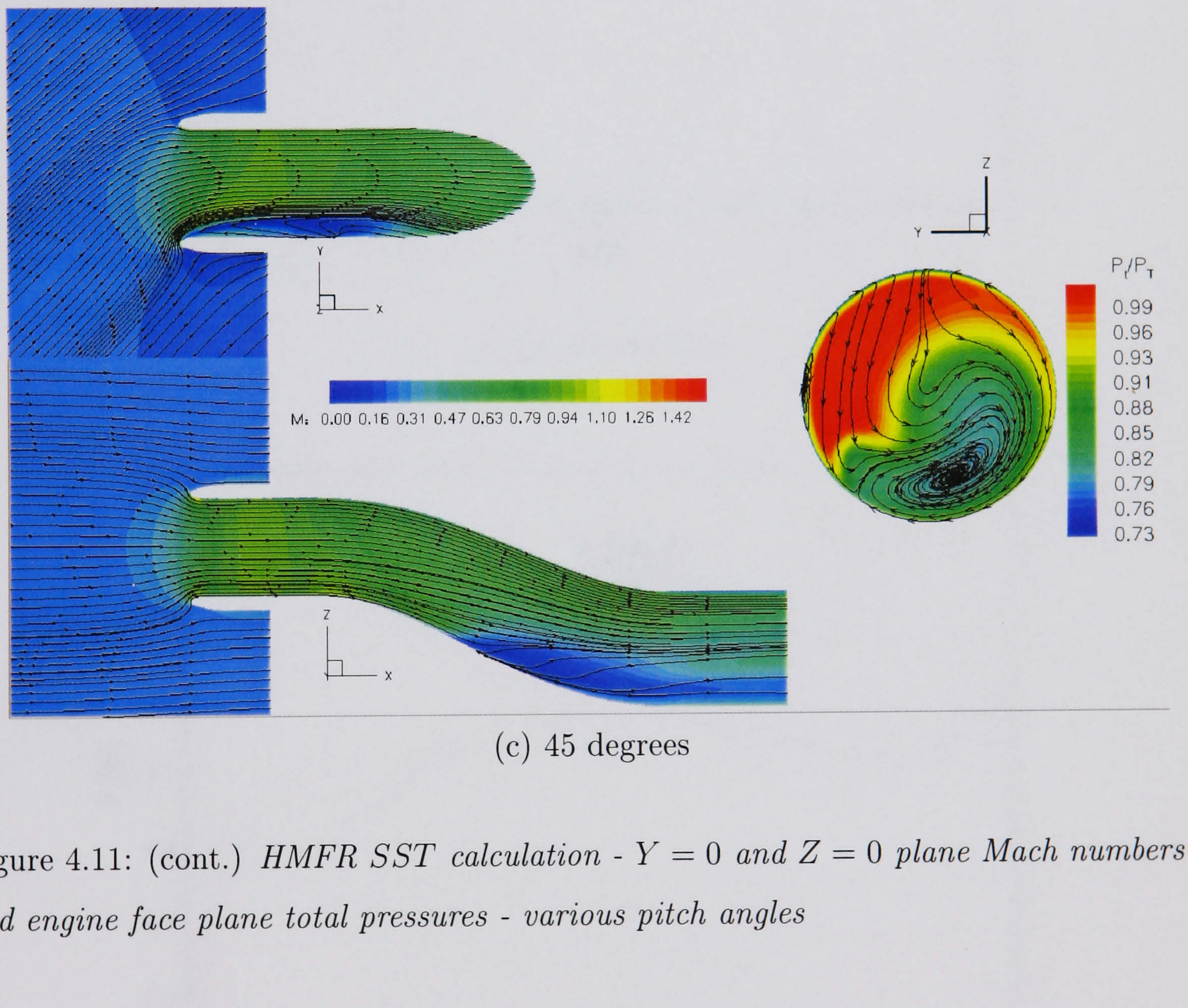

(c) 45 degrees

Figure 4.11: (cont.) *HMFR SST calculation - $Y = 0$ and $Z = 0$ plane Mach numbers and engine face plane total pressures - various pitch angles*

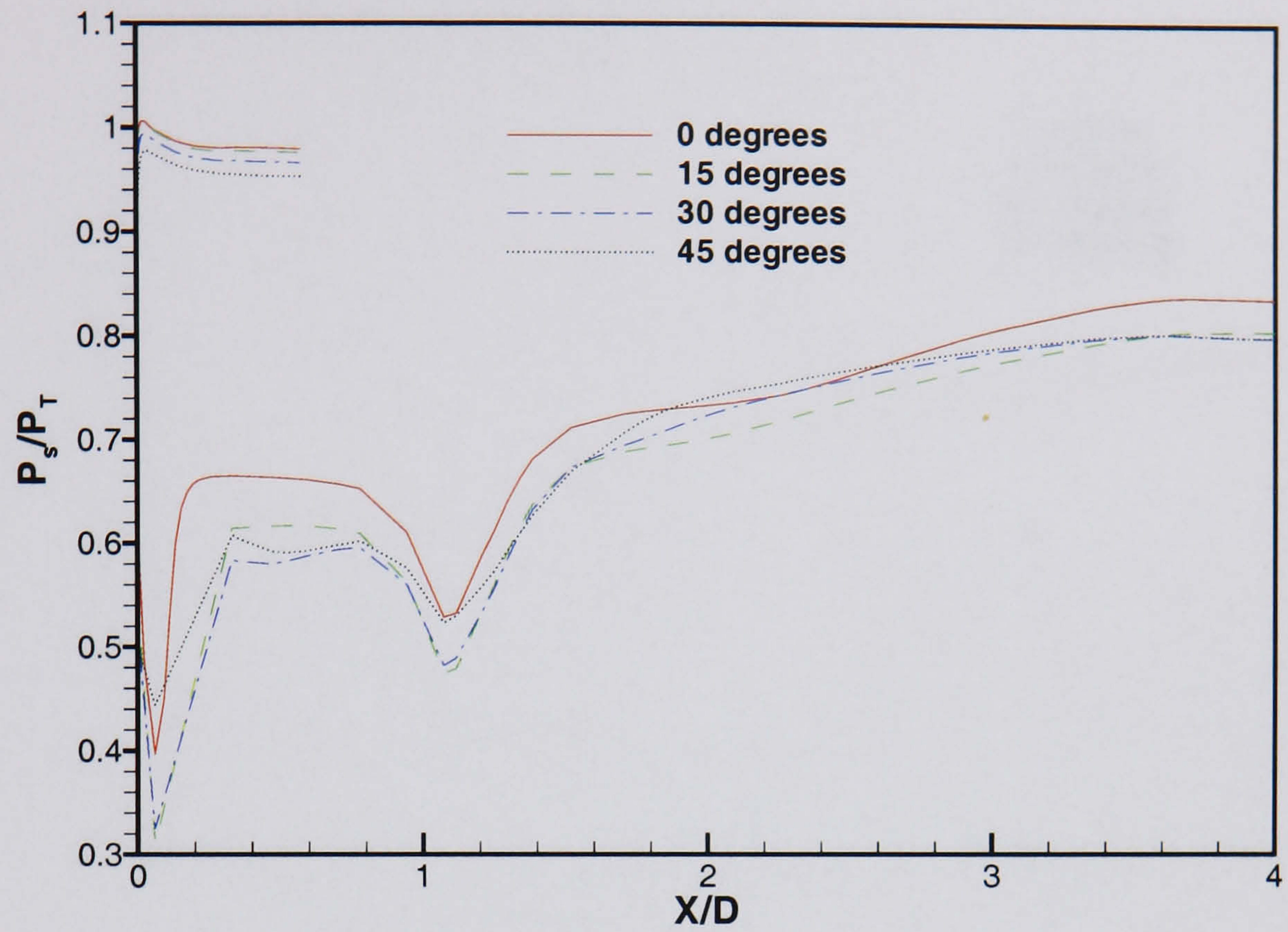

(a) Starboard side

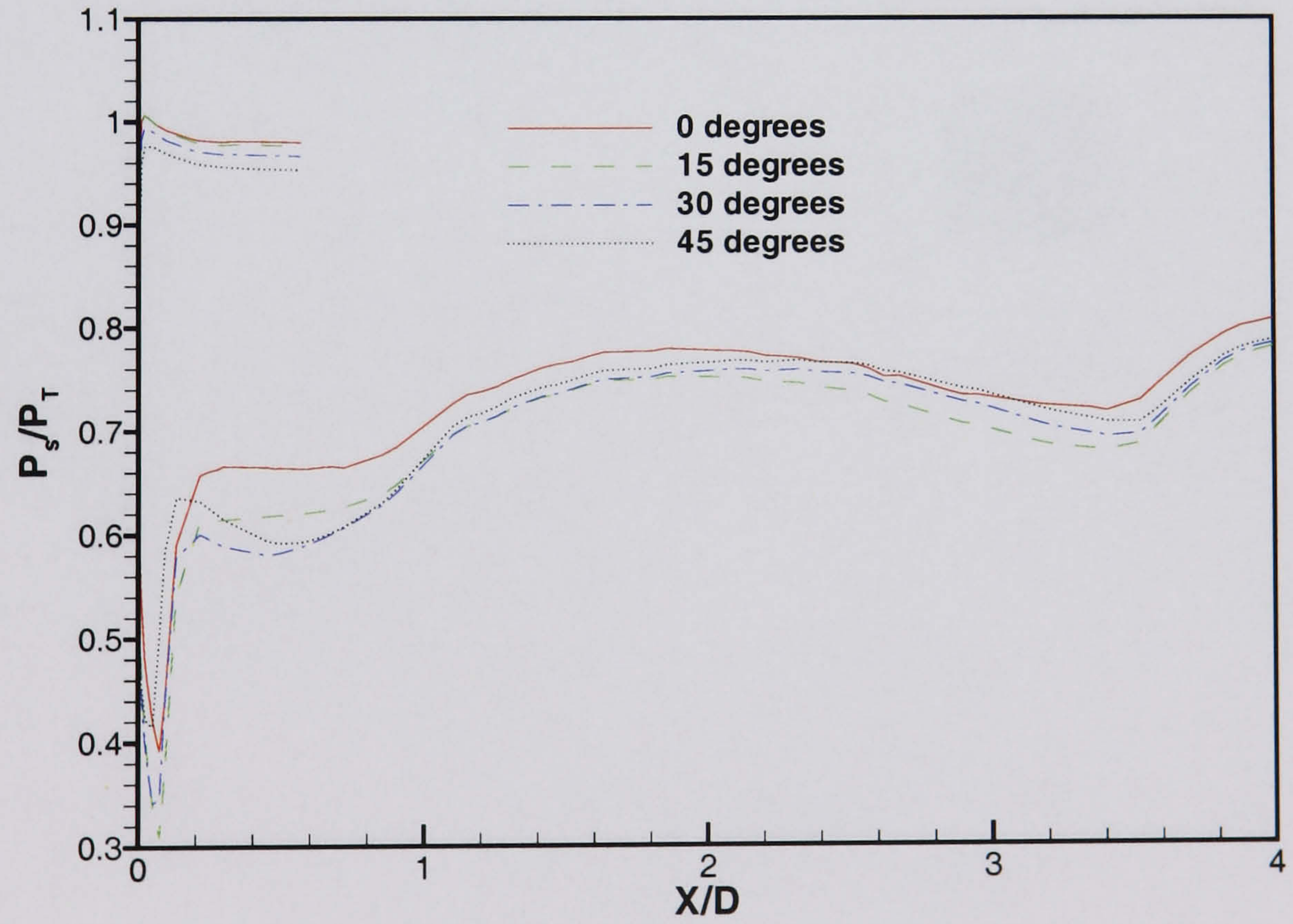

(b) Port side

Figure 4.12: *HMFR Turbulent calculation, SST model - pressure comparison for port and starboard sides for angles of pitch*

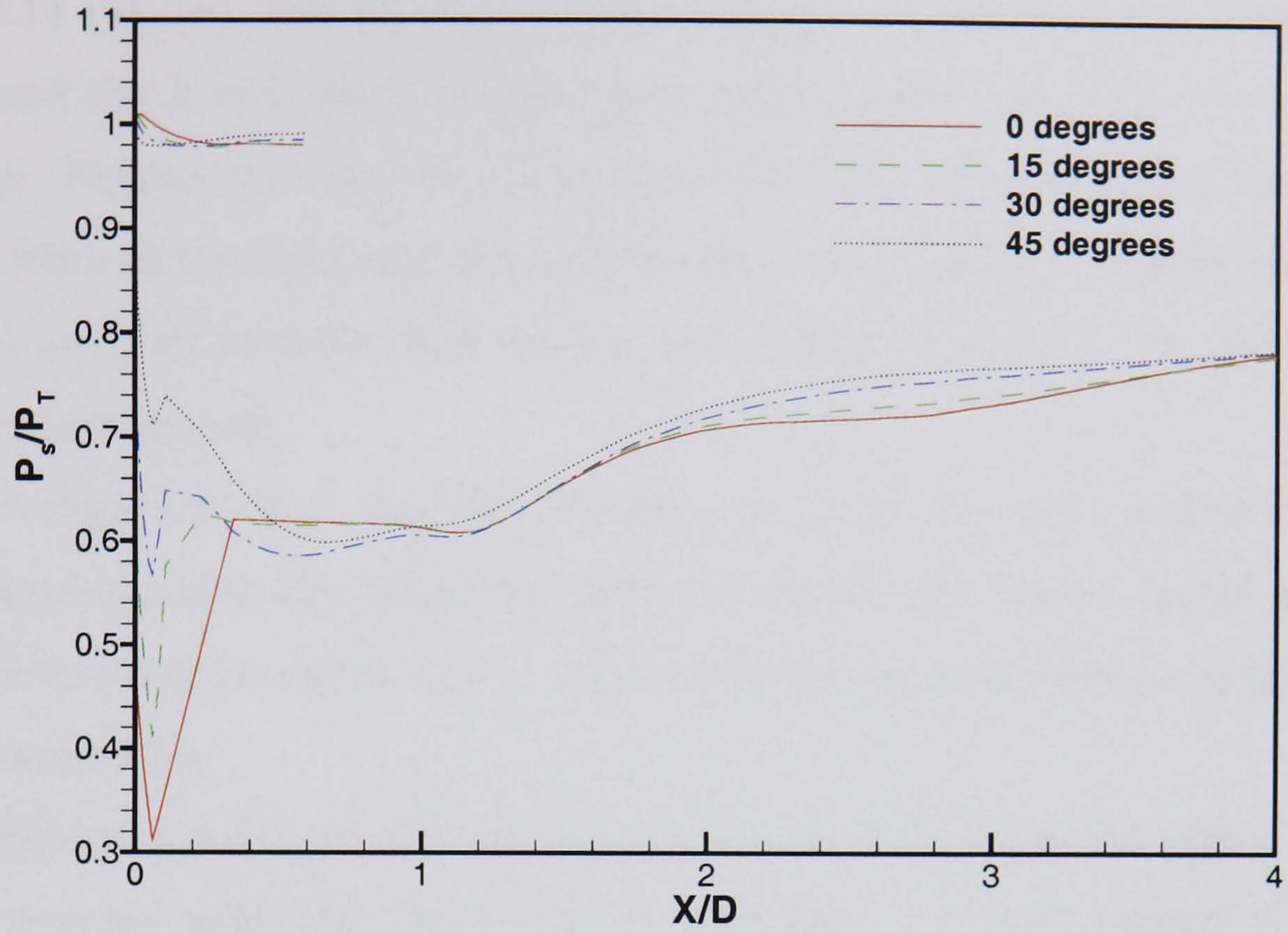

(a) Top side

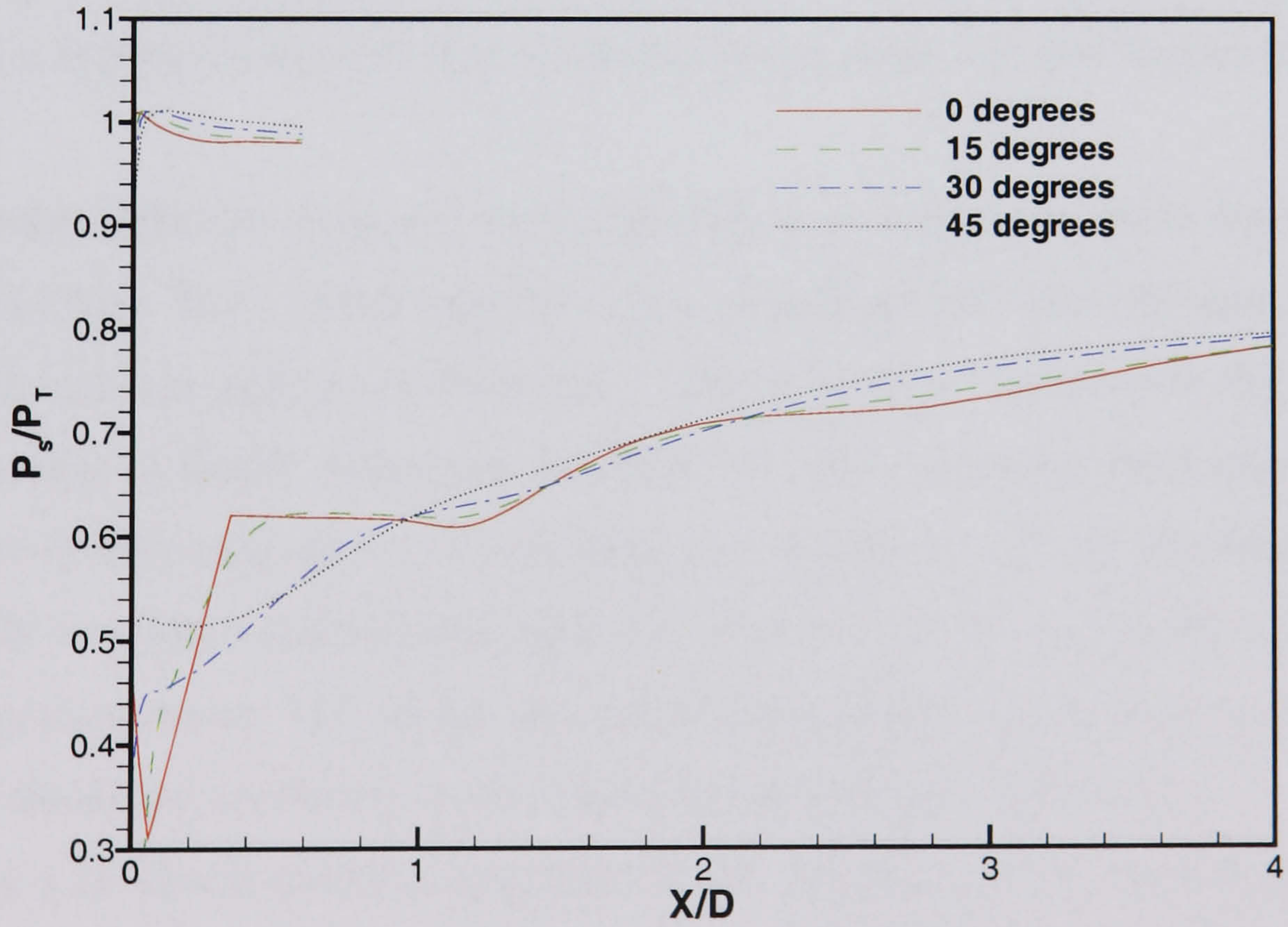

(b) Bottom side

Figure 4.13: *HMFR Turbulent calculation, SST model - pressure comparison for top and bottom sides for angles of pitch*

4.2.2 Low Mass Flow Case

Figures 4.14 (a), (b), and (c) show Mach contour plots through the symmetry plane ($Y = 0$) and the $Z = 0$ plane, coupled with total pressures extracted from the engine face plane. Figures 4.15 and 4.16 also show the static pressures along the starboard and port sides of the duct and top and bottom sides. Table 4.4 shows the distortion levels and pressure recovery data for the cases which were again 15^o, 30^o and 45^o for the low mass flow case.

At 15^o (figure 4.14(a)), the flow features are much the same as the 0^o case. The main difference is that the distortion coefficient for the 60^o 'worst' sector is higher due to the effects of the increased upstream disturbance and its influence on the secondary flow characteristics.

The distortion coefficient for the 30^o case increases again as the region of low total pressure remains relatively local at the engine face. A small amount of separation occurs in the cowl region and also on the outer cowl top side. The stagnation point of the flow on the outer cowl lower side moves further out. It is also worthwhile to note that a small amount of supersonic flow is generated for the 30^o pitched case at the cowl on the $Z = 0$ plane lower side due to the increased angle the flow has to turn to enter the duct.

The main difference from the high mass flow case appears to occur for the 45^o case (figure 4.2.2(c)). Here, there appears to be a much greater cowl lip separation when compared with the high mass flow case. This is likely to be because the engine face static pressure is higher which has the effect of a less powerful draw into the intake. The effect of this separation coupled with the separation off the starboard side first bend leads to a low total pressure across a wide area of the engine face. This gives a poor pressure recovery but, as the low total pressure affects a large area of the engine face, the distortion coefficient is less than for the 30^o case (table 4.4).

Figure 4.15 shows pressure extraction from the port and starboard sides for this case. Results for the 0^o and 15^o cases are essentially the same. The 30^o cases is also very similar although some separation pockets are induced or enhanced on the duct walls. The 45^o degree case again has the main differences unsurprisingly due to severe separation in the cowl region that leads to highly distorted flow downstream on the

Pitch Angle	Pressure Recovery	Distortion Coefficient (DC(60))
0	0.99994	0.2085
15	0.99981	0.2389
30	0.99694	0.4490
45	0.97602	0.3652

Table 4.4: *Distortion and Pressure Recovery at engine face for a pitched intake at LMFR*

duct walls.

Again the main sides of interest when considering the pitched intake case are the top and bottom walls shown in figure 4.16 (a) and (b) respectively. On the top side the location of the stagnation point can be seen to move more inside the intake as the angle of pitch is increased. A strong favourable pressure gradient develops in the inner cowl region which will not promote separation. Again the flow acceleration into the duct is badly affected at higher pitch angles leading to a poorer comparison downstream although the flow appears to recover following the first bend on the top side. On the bottom side at 45^o there are large differences with other angles of attack in the cowl region due to the large extent of the separation witnessed. Flow acceleration from freestream is significant at higher angles (mainly 15^o and 30^o) due to the increased angle through which the flow must turn, and consequently accelerate, to enter the duct.

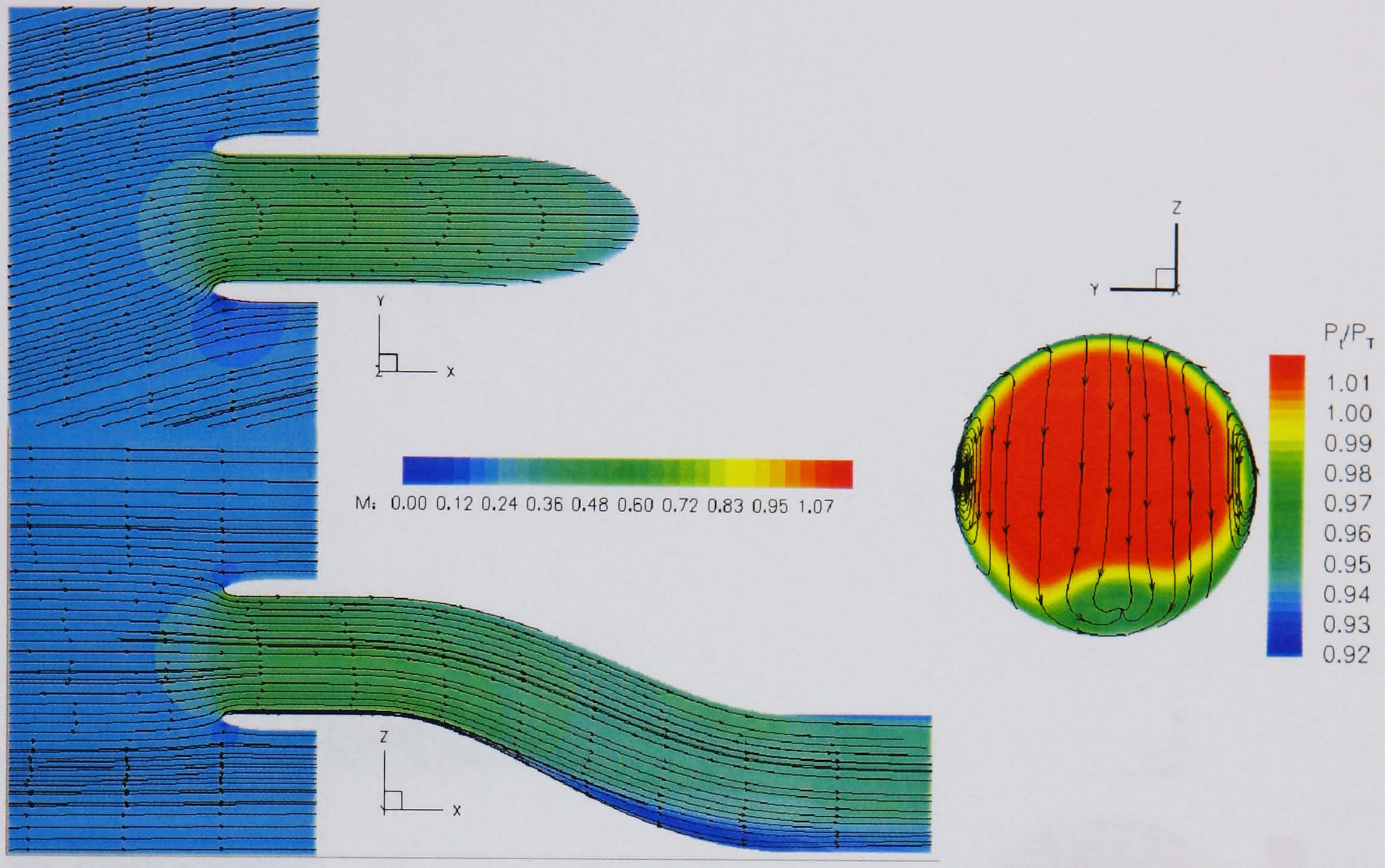

(a) 15 degrees

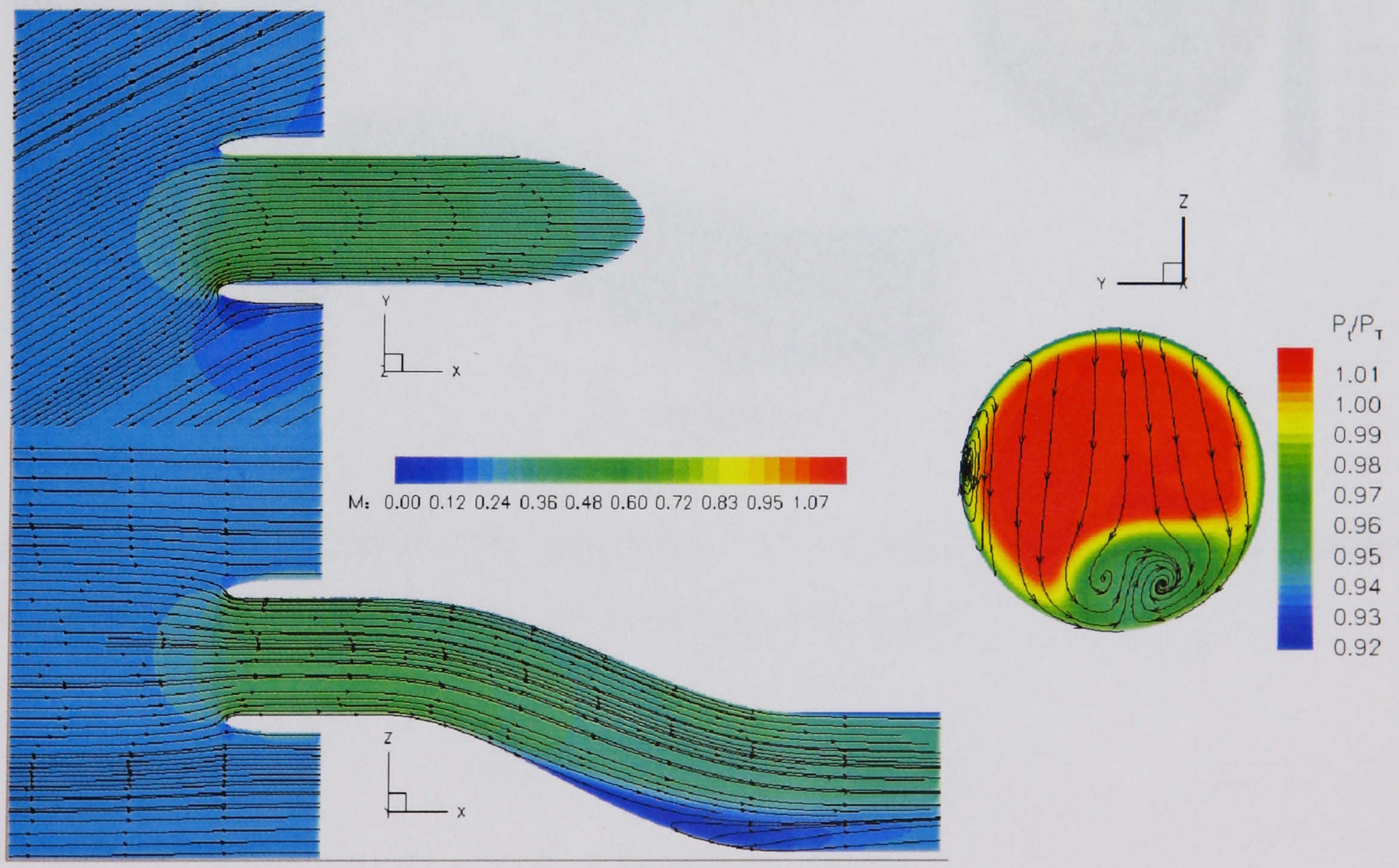

(b) 30 degrees

Figure 4.14: *LMFR SST calculation -* $Y = 0$ *and* $Z = 0$ *plane Mach numbers and engine face plane total pressures - various pitch angles*

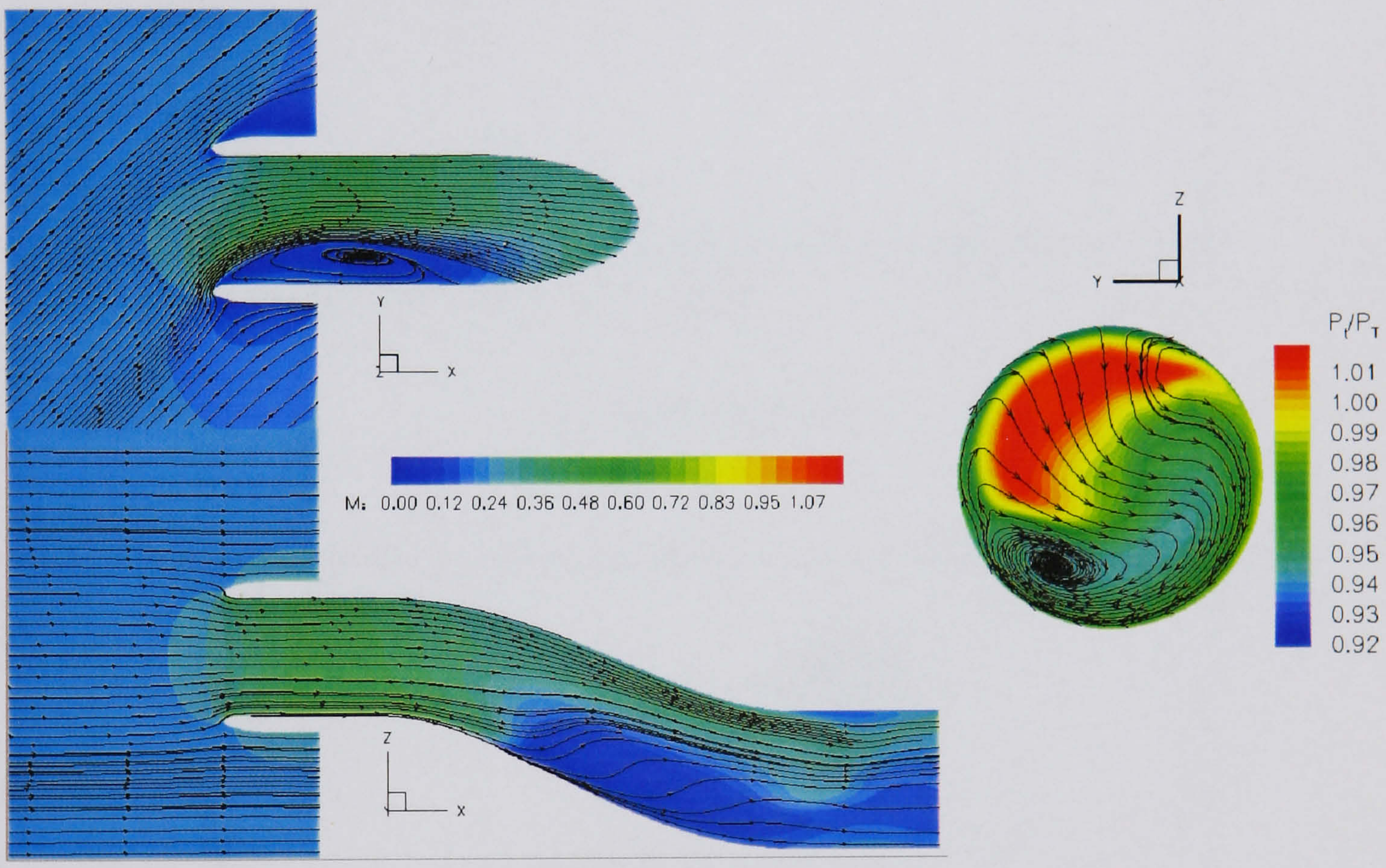

(c) 45 degrees

Figure 4.14: (cont.) *LMFR SST calculation* - $Y = 0$ *and* $Z = 0$ *plane Mach numbers and engine face plane total pressures - various pitch angles*

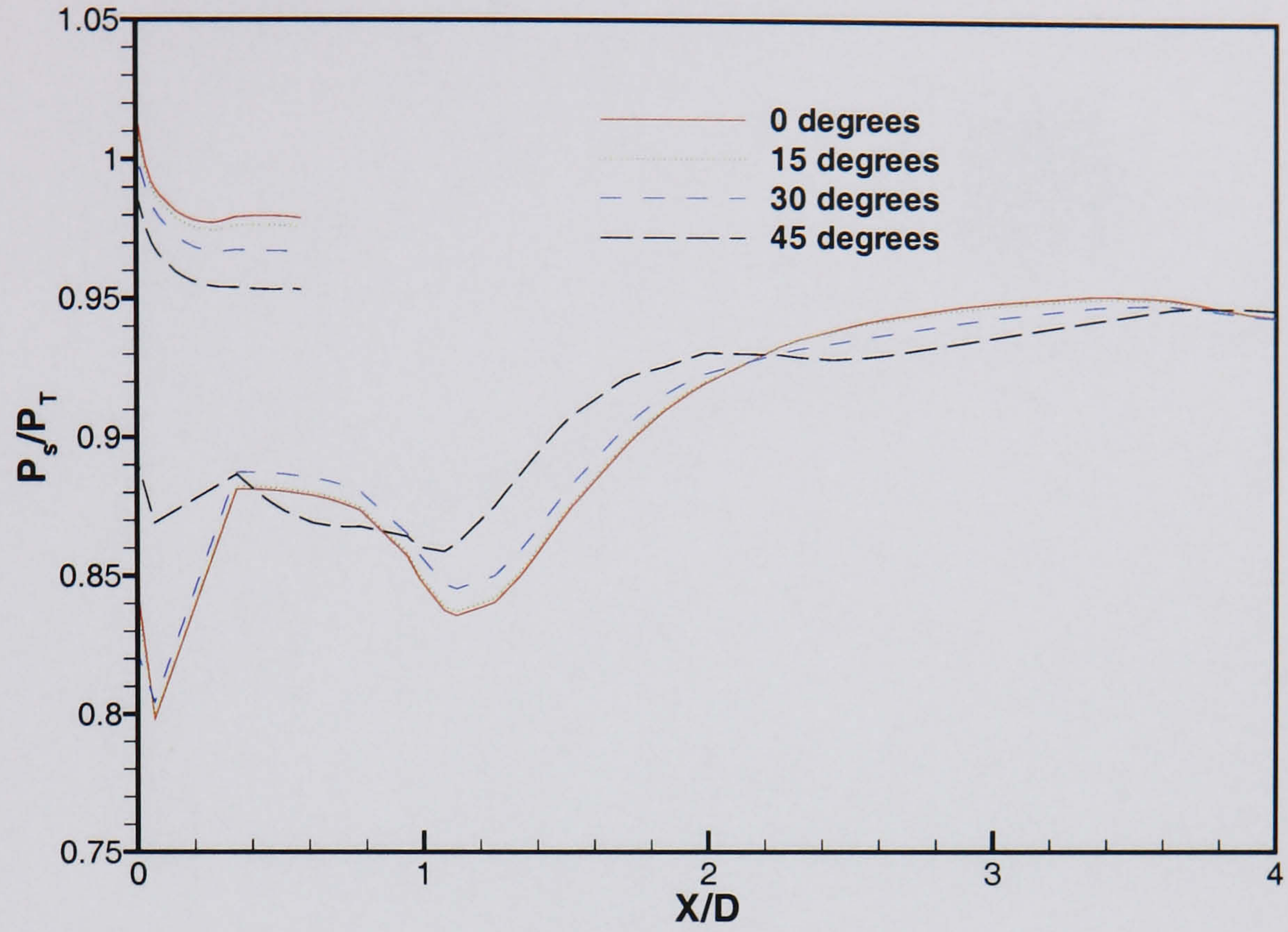

(a) Starboard side

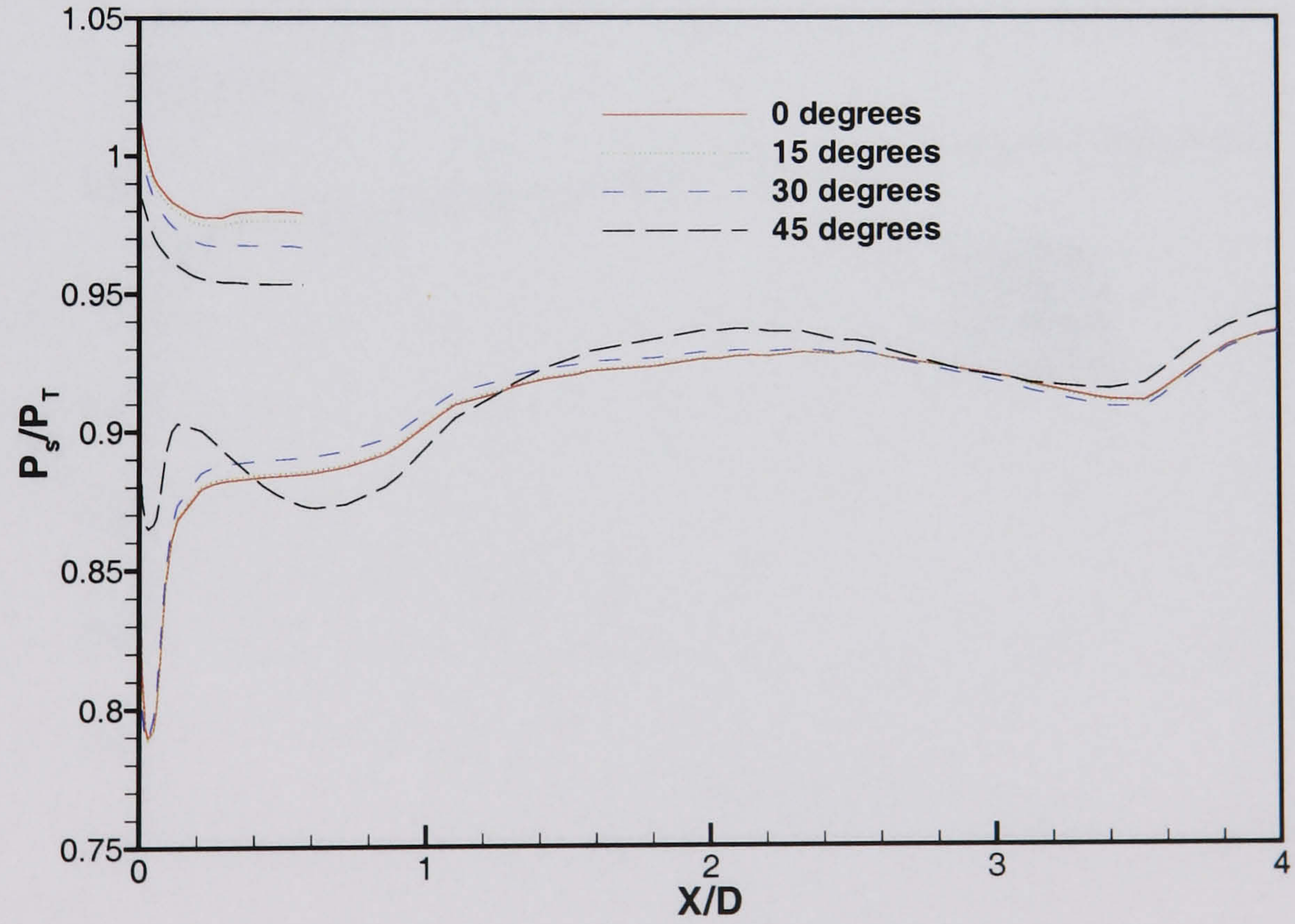

(b) Port side

Figure 4.15: *LMFR Turbulent calculation, SST model - pressure comparison for port and starboard sides for angles of pitch*

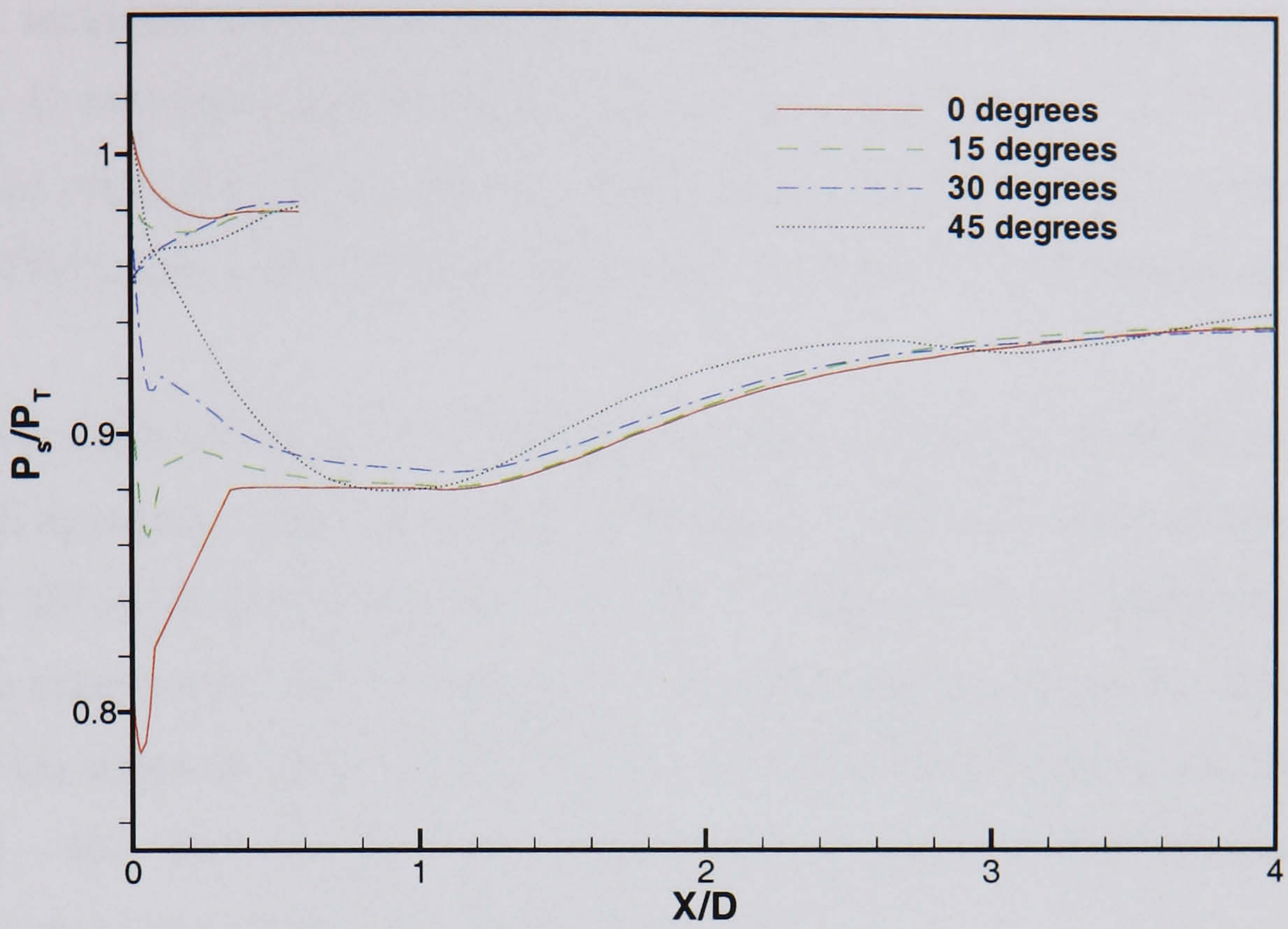

(a) Top side

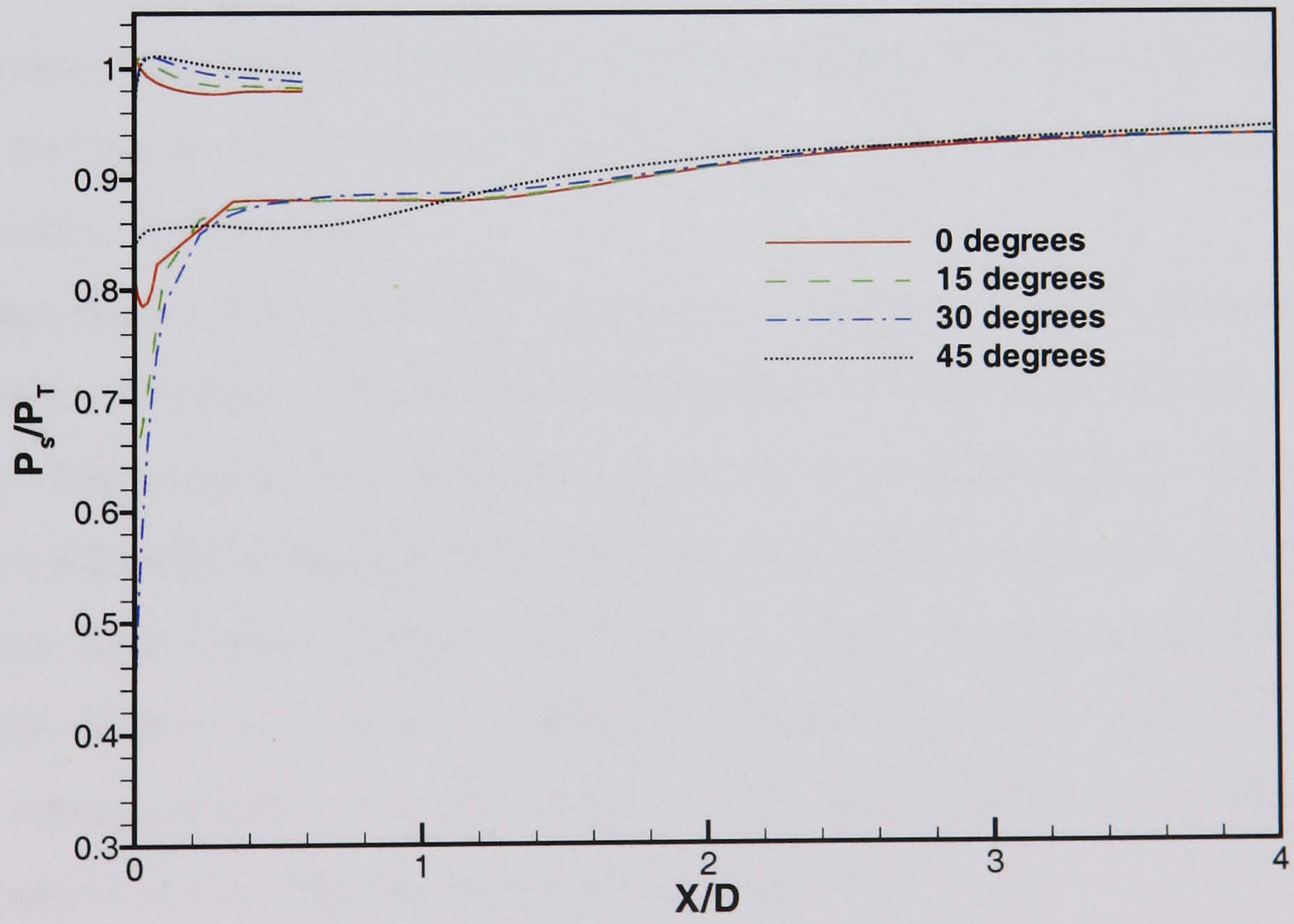

(b) Bottom side

Figure 4.16: *LMFR Turbulent calculation, SST model - pressure comparison for top and bottom sides for angles of pitch*

4.3 Summary

Intakes at incidence were investigated. Both high and low mass flow rates (as defined in chapter 3) were examined for both pitch and yaw angles ($\pm 15^o, \pm 30^o, \pm 45^o$). RANS calculations using the SST turbulence model were performed with a freestream Mach number of 0.21 and a Reynolds number based on the non-dimensional engine face of 777,000.

Positive angles of yaw for the HMFR case have the effect of decreasing the effective offset with increasing angle. A minimum distortion coefficient at 30^o resulted with separation at 45^o on the port side inner cowl region with poorer total pressure distribution across the compressor face. Increasing the negative angles of yaw for the HMFR case increased the effective offset with separation on the starboard side inner cowl region at -30^o and -45^o. At -45^o the flow does not reattach prior to the first bend with the effect that secondary flow generation is destroyed.

With positive angles of yaw at LMFR, as the angle increases the distortional coefficient decreases. However the pressure recovery does get poorer. Negative angles of yaw at LMFR increases the effect of the offset. At -30^o separation occurs from the inner starboard surface but reattaches prior to the first bend. At -45^o the separation from the starboard side lip does not reattach prior to the first bend and so secondary flow generation is destroyed.

Pitching calculations at HMFR found that as pitching angle is increased the pressure recovery decreases. The distortion coefficient is poorest at 15^o but improves by 45^o as the low pressure has affected a majority of the engine face. This is because there is considerable separation from the inner cowl surface upstream. LMFR pitching calculations show similar trends to the HMFR results. Pressure recovery gets poorer as the angle of pitch is increased. Distortion is harder to predict and is poorest at 30^o. At 45^o it again improves as considerable cowl lip separation occurs upstream leading to large regions of low total pressure at the engine face.

Flow control strategies introduced to manage poor distortion and pressure recovery metrics are of current interest in highly offset compact ducts (Hamstra et al. [79], Anderson et al. [80]). Distortion has been reduced by around 50% in some cases with pressure recovery being improved by around 5%. Active flow control through the use of micro air-jets or micro-vanes would perhaps increase efficiency during yawed and pitched manoeuvres.

In conclusion, the SST turbulence model was chosen because of the relative success when examining the 0^o case in chapter 3. Although the flowfields predicted for intakes at incidence in this chapter appear to be plausible, the accuracy of the calculations remains to be determined, as experimental data is not available for comparison. Until such a time when experimental data is available then the overall confidence in the results cannot be exaggerated.

Chapter 5

Engine Surge Review and Unsteady Validation

Following successful work for the M2129 on the AGARD test cases and extending this to examine intakes at incidence, attention now turns to the problem of modelling a surge wave propagating through an intake duct. As previously discussed this is a relatively unresearched area, particularly using computational techniques. This chapter will give a background on engine surge and validate against suitable unsteady cases. Unfortunately there is no experimental surge data available for the M2129 for comparison and so the validation here consists of the well known shocktube problem, and also surge simulations in a straight pipe for which experimental data is available.

5.1 Causes of Engine Surge

Engine surge is a complicated phenomenon that can occur at the compressor face. The causes of surge can be wide ranging, especially when considering the engine systems as a whole (nozzle, turbines, combustion chamber, and compression systems) as each individual component can induce surge. The production of an engine surge is usually the result of some or all of the compressor blades stalling. This stalling can be attributed to many causes dependent on operating conditions, the more common being:

- Naturally occurring transients in the flow;

- Cowl lip separation leading to unsteadiness in the intake flow - perhaps due to hard aircraft manoeuvres or extreme pitch/yaw;
- High engine face total distortions;
- Abrupt breakdown of flow conditions within the intake leading to a sudden reduction in the airflow within the compressor;
- General unsteady freestream conditions.

A recent opportunity the author had to witness a commercial turbofan engine experiencing surge problems at Rolls-Roye in East Kilbride, UK, highlighted this. Mechanics were able to force the engine to surge but were unsure why the engine was surging. The solution in these cases is very often based on 'trial and error', replacing components in an effort to resolve the problem. It is clear that there can be many reasons for the breakdown in flow conditions. An interesting and very relevant reason is poor engine intake distortion as this is very likely to occur on intakes that are highly offset such as in RAE intake model 2129.

5.2 Relation of Distortion with Surge

As previously suggested, the main cause of surge can be attributed to compressor blade stalling and tracking back, poor flow quality across the engine face is indicative of this. This lack of a uniform quality of flow across a plane (in this case the engine face plane which is assumed to be 2D) is quantified by the parameter called distortion. This parameter is usually given for a 60^o 'worst sector' case. However there are many, more complicated descriptors for distortion (Burcham and Hughes [39], Van Deusen and Mardoc [25], and an AGARD report [76]).

A satisfactory quantitative link between unsteady-pressure measurements and the onset of surge was made when it was realised that surge would follow if the critical value of distortion coefficient was to be exceeded for a period of about one engine revolution. One engine revolution can typically take the order of 5 milliseconds (200 Hz). Typical rise times of the surge signatures used in this thesis are typically less than this and so the assumption that the surge is a uniform event across the whole compressor face may be a fair one.

Flow separation is inevitable if the mass flow rate (demand) by the engine is sufficient. Intake flow distortion also manifests itself as secondary flow development travelling to the engine face.

5.3 Relation of the Compressor Face with Surge

The compressor face is a disc of rotating blades whose purpose is to draw and compress air into the engine core and through the bypass - the aim being to have maximum pressure rise and minimum flow velocity at the combustion chamber. Compression is usually done over a large number of stages, each stage consisting of a rotating set of blades (rotors) and a stationary set of blades (stators). The compressor stages are driven by the turbine. Because the pressure is falling with the direction of the flow in the turbine, more overall power tends to be generated when compared with the compressor.

The pressure rise is in the direction of flow in the compressor (adverse pressure gradient) and hence separation is likely with a consequent drop in performance. This separation can also lead to engine surge or a rotating stall. A rotating stall is a situation in which there is a non-uniform flow pattern with reduced flow rate and consequent pressure rise. A rotating stall can also happen if the pressure rise for a particular stage is too large. The boundary where the flow breaks down into a rotating stall or surge is known as the surge line.

In the computations performed for an engine operating normally it was assumed that across the compressor face the static pressure and temperature are constant. This has been found to be a good approximation (AGARD [12]), and implies that the Mach number is now only a function of total pressure. Figure 5.1 shows a typical velocity vector diagram of the compressor. It can be seen that the velocity of a compressor blade is composed of a component due to the circumferential velocity (due to the engine rotation) and an axial component (due to the incoming airflow). The size of these individual components dictates the angle of attack of the flow relative to the compressor blade. A reduction of the total pressure at the compressor face decreases the axial velocity component. Assuming constant engine rotation, this has the effect that the relative velocity vector changes, increasing the angle, and moving the compressor blade further towards the stall limit.

5.4 Consequences of Engine Surge

When the compressor disc as a whole stalls this can have the effect of acting like a solid wall in this unsteady flow. The abrupt complete or partial blockage of the flow is referred to as an engine surge. This engine surge can create a strong shock wave which can propagate up the aircraft intake. This propagating wave is sometimes referred to as a hammershock. The strength of the shock can be significant - at times as much as twice the steady pressure (even though the wave is transient), hence it is not unheard of for such waves to cause structural damage within the duct. Indeed the design of the Tornado took account of hammershock pressures for the aircraft ducts, ramps and linkage systems. In summary we can say that surge is manifested by large scale oscillatory flow instability which can be violent, often with pulsating reversal of flow involving the entire unit. Compressor surge can also produce high noise in the form of violent bangs - a series of surges which is collectively known as cyclic surge. A single surge is known as a pop surge.

By modelling surge propagation under different conditions it is possible to obtain pressure-time histories for intake ducts. This information can be used in conjunction with structural modeling packages to determine loads inflicted on the duct structure. If necessary, re-design or attenuation measures can be taken and further iterations carried out until what is left is an intake that is structurally sound and efficiently supplies the engine face with a minimally distorted flow. Other consequences of surge can be far reaching when considering the case of twin side-by-side intakes common on military aircraft. It has been suggested that surge propagation in one intake can induce flow distortion in the adjacent intake that is sufficient to induce a further surge. This is clearly a highly undesirable situation. Other implications arise when considering intakes with splitter plates for example.

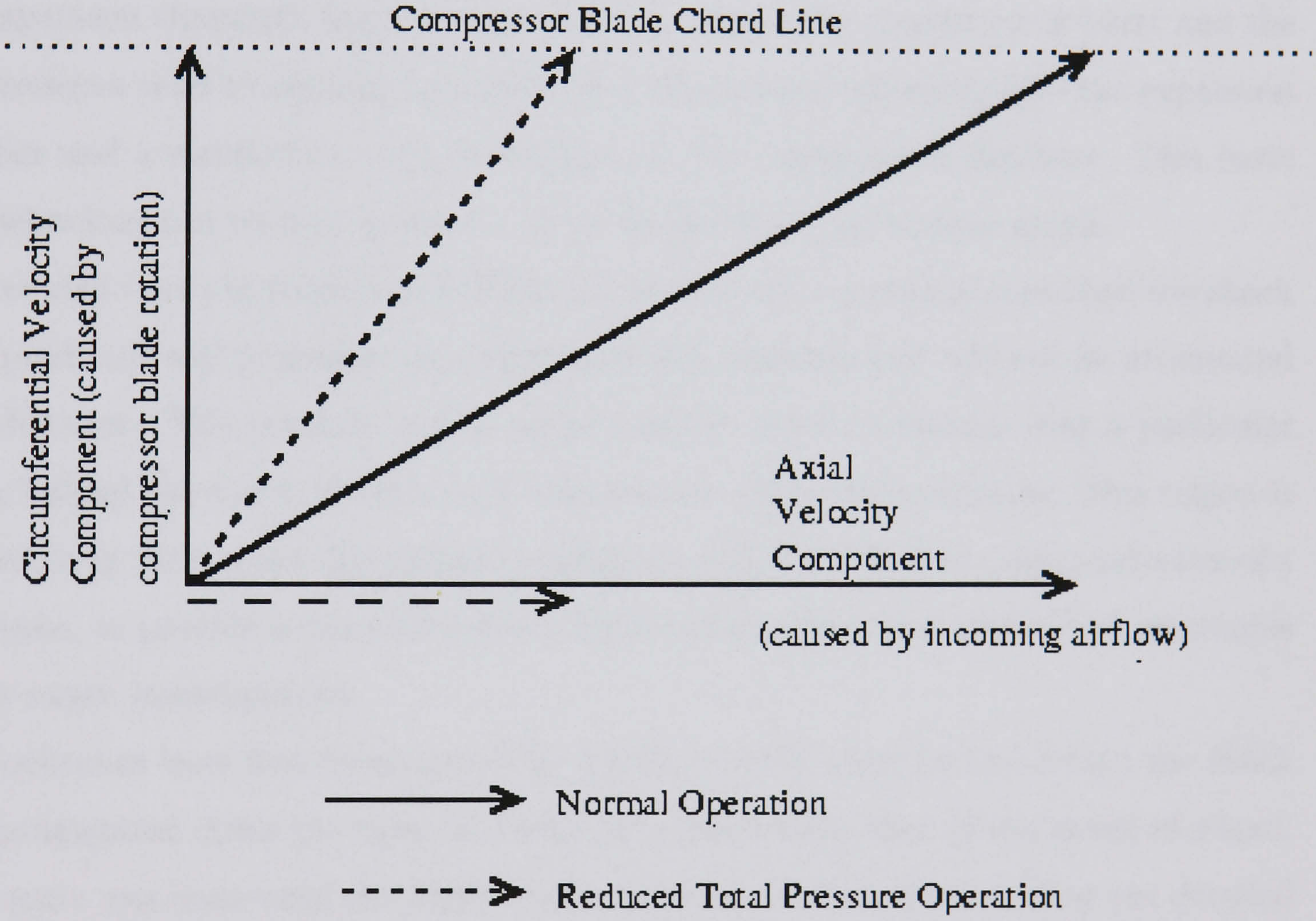

Figure 5.1: *Compressor velocity vector diagram*

5.5 Unsteady Validation

5.5.1 Shocktube Test Case

Background

In its simplest form a shocktube is a rigid cylinder divided into two chambers, each chamber containing gas under different pressures. The gases are separated by an air-tight membrane that is mounted normal to the longitudinal axis - see figure 5.2.

The two regions of high and low pressure are normally referred to as the compression and expansion chambers respectively. At some instant the membrane is burst and the two pressures tend to equalise by means of a shock wave travelling into the expansion chamber and a rarefaction wave travelling into the compression chamber. This basic flow behaviour can be seen in figure 5.3 by means of a time history graph.

Provided that the shocktube exhibits a constant cross sectional area then the shock wave produced will propagate into the expansion chamber and will not be attenuated with distance. The pressure and particle velocity will be constant over a particular region behind the shock, density and temperature being discontinuous. This region is referred to as the contact discontinuity indicated in figure 5.3. It is these properties of a shocktube, to provide a controlled shock wave and gas flow, that make it an invaluable tool in many investigations.

Shocktubes were first investigated by Vieille in 1898 when he found that the shock wave propagated down the tube at a velocity greater than that of the speed of sound. Little more was done until the 1930's when Payman and Shepherd carried out detailed examinations of the structure of the shocks produced in a shocktube. The 1939 - 1946 war brought about the necessity to study blast waves and brought the shocktube into more general use. Later years brought about a rapid increase in the use of the shocktube due to their relative simplicity, versatility and comparative cheapness. Nowadays highly sophisticated shocktubes are in use and, with the modern day computer at our disposal, calculations can be performed easily and quickly. More information is available in references such as Wright [82] and Badcock [83].

Results

The shocktube problem has similarities with the modelling of a surge wave. Although inviscid and viscous solutions were computed the results included here are inviscid with the ratio of the compression chamber to expansion chamber pressure set to 100. The shape of the shocktube is arbitrary and is unimportant for the inviscid case.

In order to analytically determine the speed of the contact discontinuity propagating in a shocktube following the removal of the membrane, the following equation is used from the Navard report [84],

$$\frac{P_l}{P_r} = \left[\frac{2\gamma {M_{shock}}^2 - \gamma + 1}{\gamma + 1}\right] \left[\frac{1}{1 - \left(\frac{(\gamma-1)a_l}{(\gamma+1)a_r}\left(M_{shock} - \frac{1}{M_{shock}}\right)\right)}\right]^{\frac{2\gamma}{\gamma-1}} . \tag{5.1}$$

For a pressure ratio of 100, this gives a predicted shock front propagation Mach number of 2.39. Figure 5.4 shows the pressure/time history computed by the current method for the same initial conditions. By determining the time it takes the shock front to travel a specified distance, and knowing the speed of sound (non-dimensional), we can determine the Mach number of the shock front for the computed case,

$$V_{shock} = \frac{4.7 - 3}{0.7 - 0.1} = 2.8333 \tag{5.2}$$

$$a_{shock} = \sqrt{\gamma} \tag{5.3}$$

$$\Rightarrow M_{shock} = 2.39. \tag{5.4}$$

Therefore the computed and analytical shock propagation speeds match up well. Figure 5.5 shows some other variables that are commonly examined when investigating the shocktube problem. The figure shows that the shock front has reached a location of $x = 4.2$ after a non-dimensional time of 0.5. The graphs of pressure and velocity are continuous over a region behind the shock before returning to static conditions at a far enough distance. However, as previously discussed, temperature and density are discontinuous over this region directly behind the shock front. The exact point of this discontinuity is known as the contact discontinuity and is the location of the membrane prior to removal.

As a conclusion on the shocktube work, it is clear from figure 5.5 that there are some bumps in the solution. This common problem arises from the limiter used. One method of eliminating the problem would be to use a different limiter, for example the Superbee limiter as discussed in Hirsch [85].

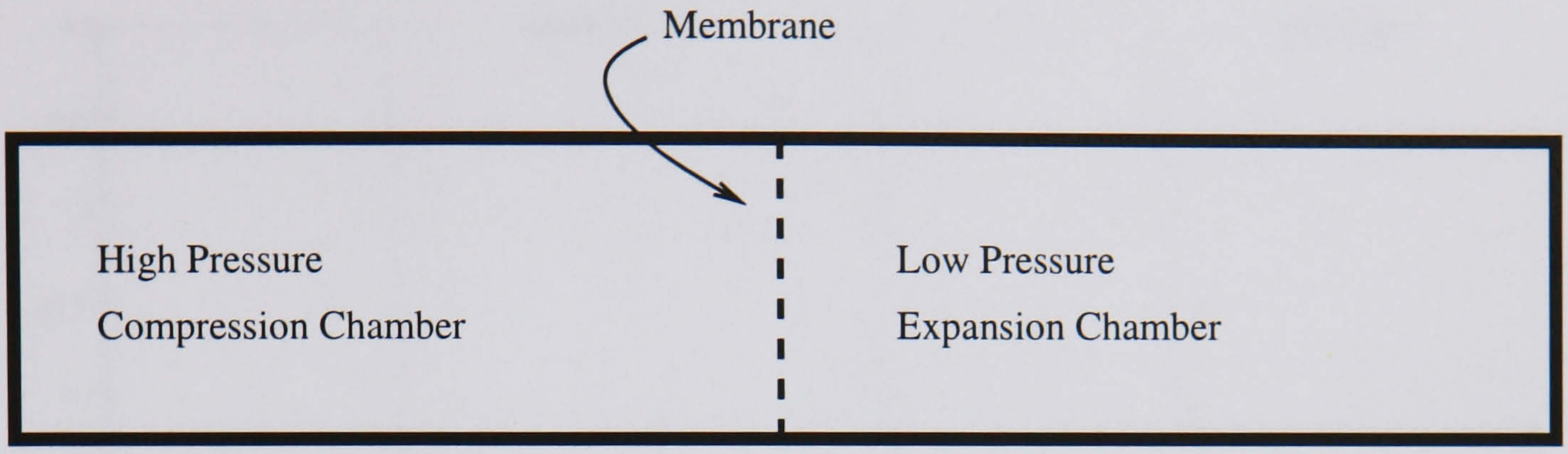

Figure 5.2: *Simple shocktube layout*

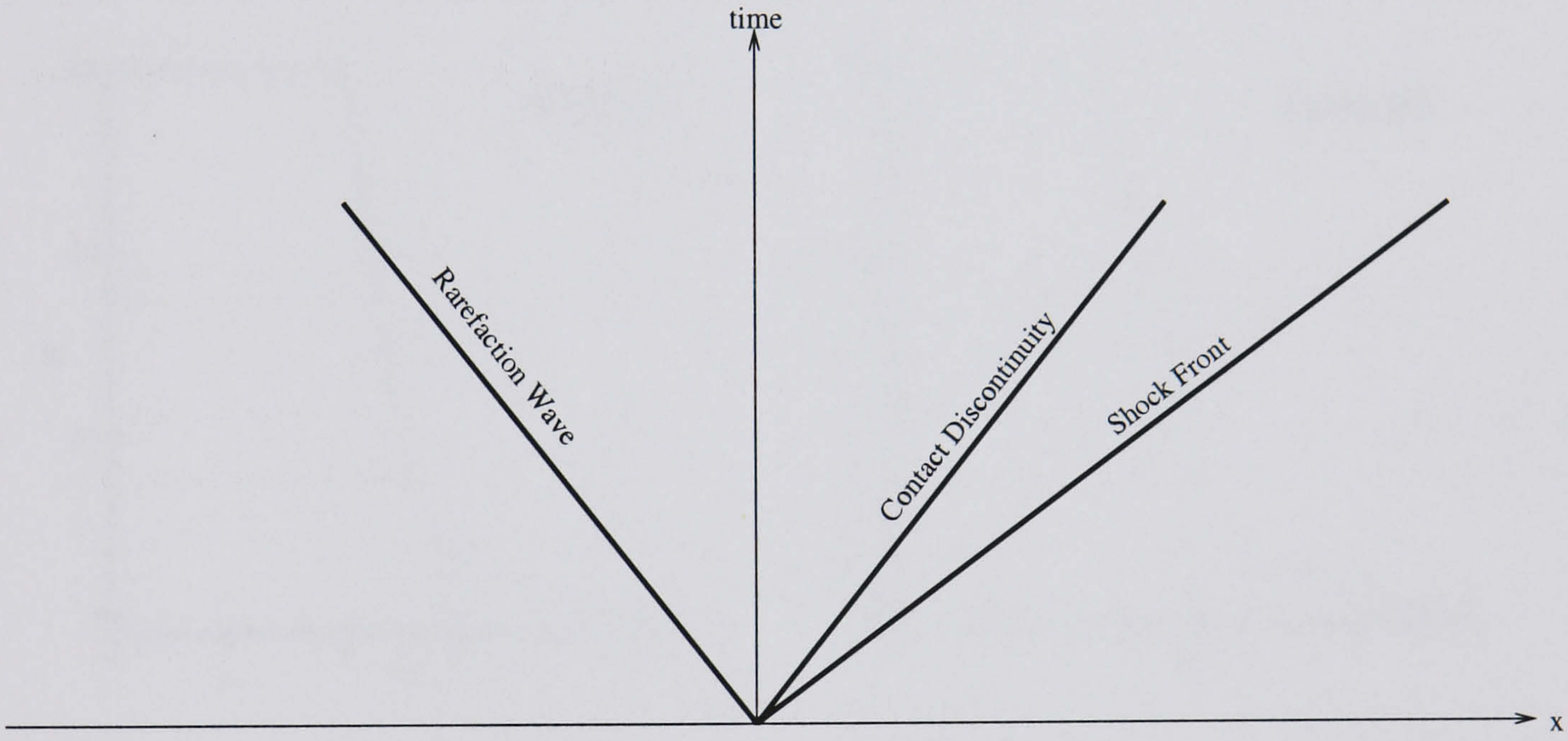

Figure 5.3: *Standard solution to the shocktube problem*

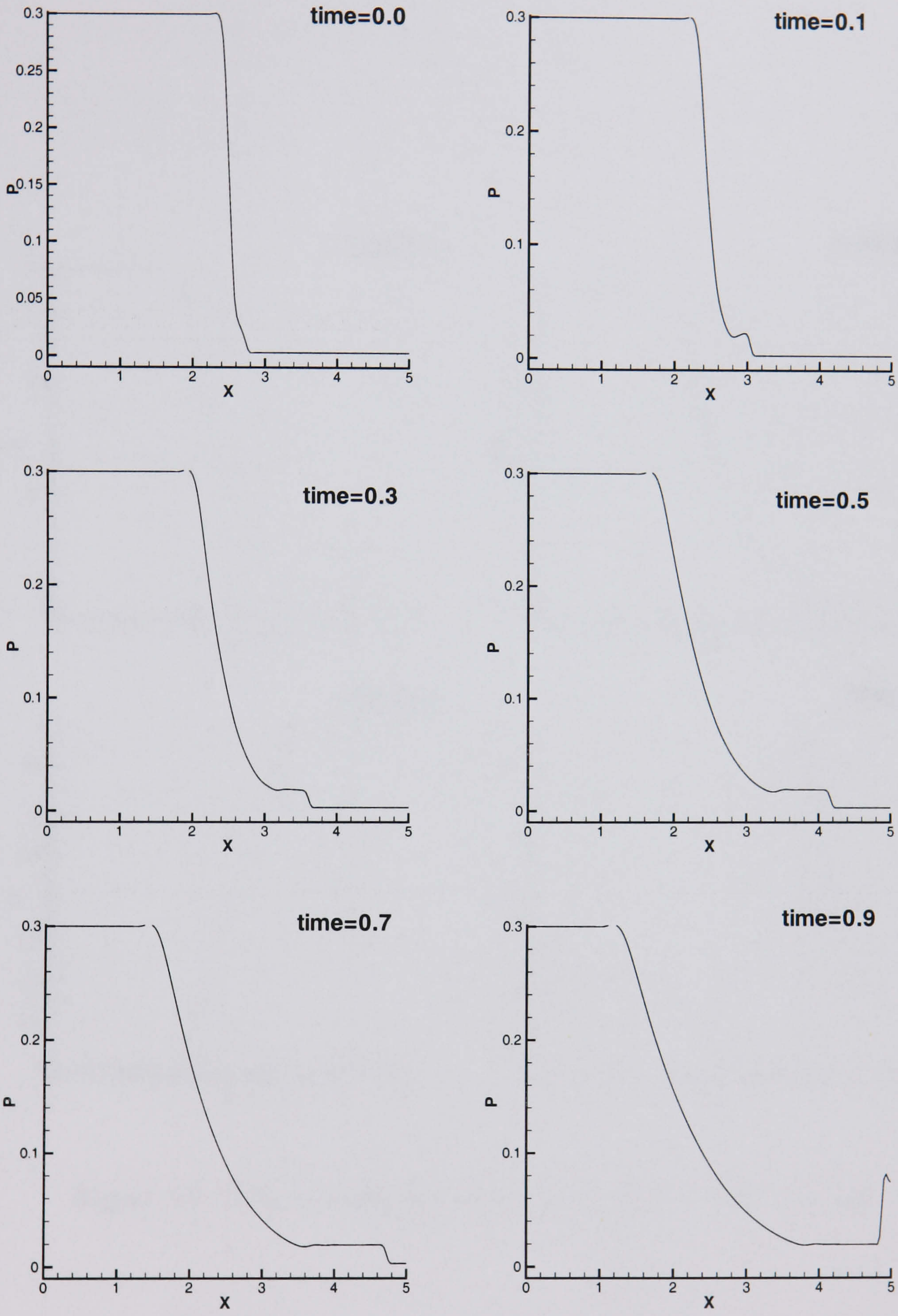

Figure 5.4: *Pressure history showing propagation of shock front into expansion chamber for a PR of 100, inviscid*

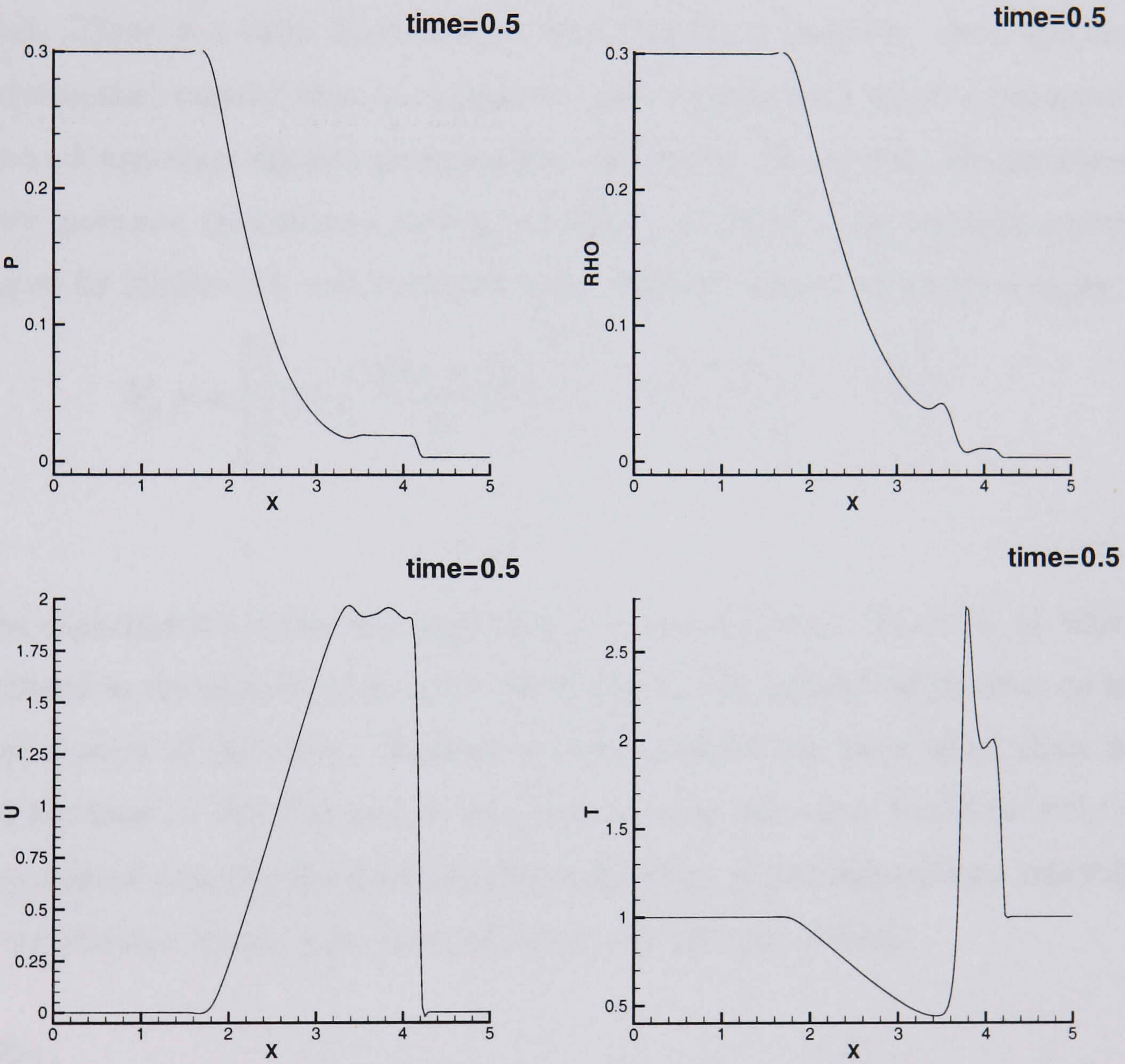

Figure 5.5: *Flow variables at a time of 0.5, PR = 100, inviscid*

5.5.2 RMCS Test Case

Background

Recent work at the Royal Military College of Science (RMCS), at Cranfield University, United Kingdom, has looked at a simplified surge problem experimentally. Air is blown at constant velocity through a straight section of pipe and vented through a nozzle to atmosphere. The pipe section has 10 pressure transducers spaced equally at $0.2778m$ intervals. There is a valve located $0.1m$ from the last transducer. At a specific time the valve is shut rapidly (but not instantly) and a consequent surge is generated that travels back upstream against the mean flow. All results are based on the measurements from the pressure transducers and comparisons are drawn with analytic expressions developed by Kirkov [44] and standard water-hammer theory which gives V_p as

$$V_p = a\left[\left[1+\left(\frac{M(\gamma+1)}{4}\right)^2\right]^{0.5} + M\left(\frac{(\gamma+1)}{4}-1\right)\right] \tag{5.5}$$

$$V_p = a - u. \tag{5.6}$$

The experimental setup was simplified for computations. The rate at which the valve closed in the experiments was undetermined. The simulation assumes an instantaneous closure of the valve. However a hammershock can form when there is only partial blockage of the flow and it was thought that the valve would be fully closed prior to a shock reaching the first transducer location. Experimental data was collected for three different steady pipe flow velocities: 50, 100 and $150m/s$.

Results

All 3 steady state pipe flow velocities were examined computationally. The computational grid only modelled the test section. The computational domain was minimised by assuming two axes of symmetry. RANS calculations using the SST turbulence model were run and grid and time independent solutions were achieved (not shown here). Figure 5.6 shows a comparison of shock propagation speeds for all the methods considered. It can be seen that for a Mach number of 0.145 (steady velocity of $50m/s$) all methods compare favourably, with the predictions based on the Kirkov equation (equation 5.5) being slightly higher then anticipated. Increasing the Mach number to 0.22625 (steady velocity of $100 m/s$) produces similar trends with experiment, the current results, and the two theoretical techniques. The technique of Kirkov is again over-predicted when compared with water hammer theory and experiment. Further increasing the Mach number to 0.64 leads to the water-hammer theory and experiment showing similarities and the current results also agreeing with both. Kirkov's technique again predicts a higher propagation speed.

The variations in the theoretical predictions of Kirkov with water hammer theory are likely to come from compressibility effects, the water hammer theory not accounting for such effects. At lower Mach numbers this will be minimal and so the agreement is closer. At higher Mach numbers the compressibility effects will naturally be greater and so Kirkov's results may be more accurate as they account for such effects, when compared with water hammer theory. With such limited experimental data though, it is hard to conclude which analytical theory is better supported. Additionally, the work by the RMCS was subject to significant error. One such source of error is in the curve fitting that is used to analyse the transient experimental data. The time taken for the wave to pass from one transducer to the next was very small ($0.8 ms$) which is theoretically within the capabilities. However the was significant background noise served to hide such high frequencies. The package used in the experimental analysis allowed for the investigation of such highly complex signals but invariably introduced an element of subjectivity

Further, it should be remembered that the results from Kirkov and water hammer theory are 1D, whereas the experiments and present computations assume fully developed 3D flow. Also, the valve closure times in the experiment is not instant but takes a small, undetermined, time. The valve closure time in the theoretical and computational results was instant. It was known that the theoretical results lie within the error boundary of the experimental data and thus it can be stated that this is also true for the computational solution.

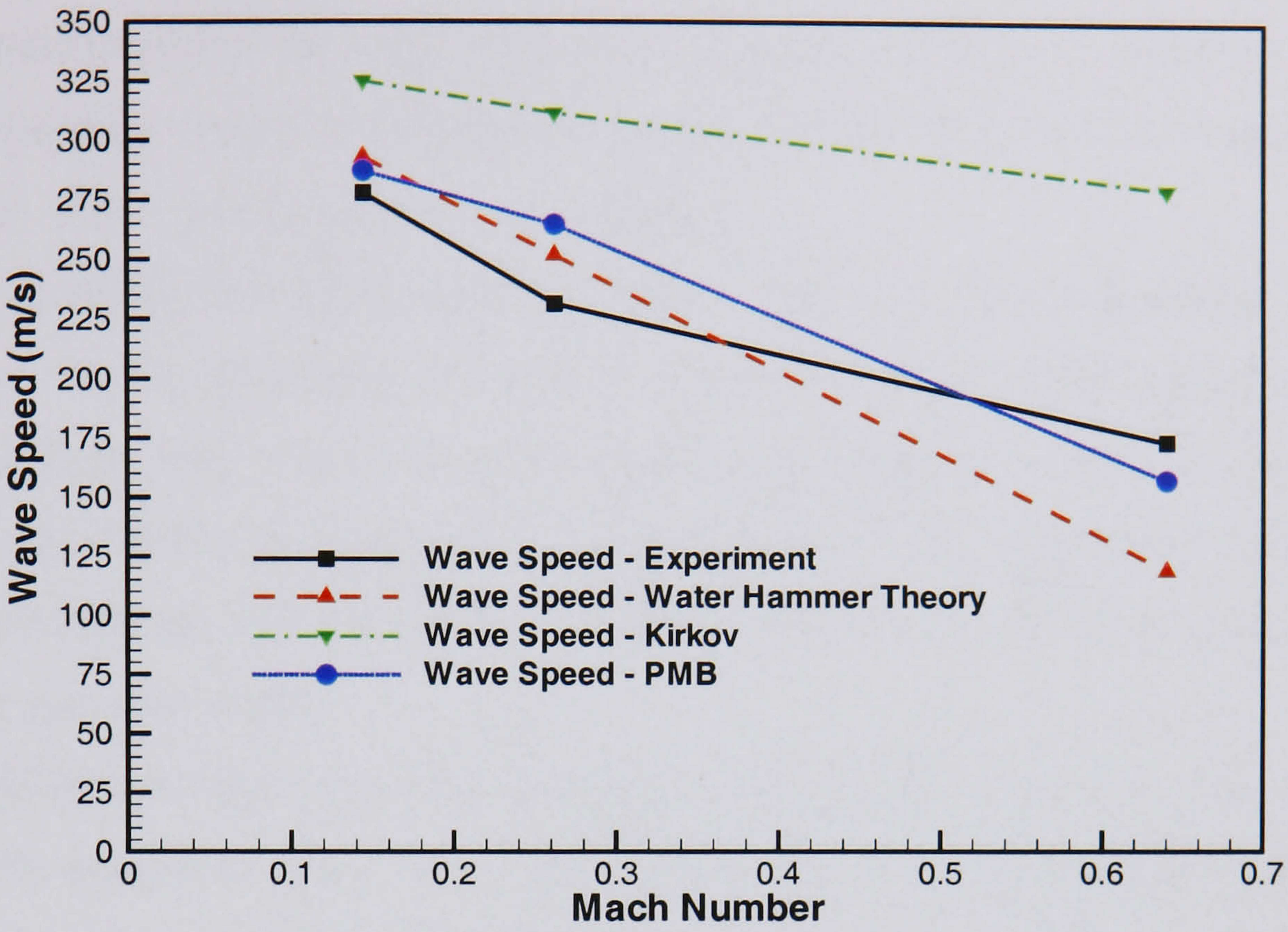

Figure 5.6: *Comparison of shock wave propagation speeds*

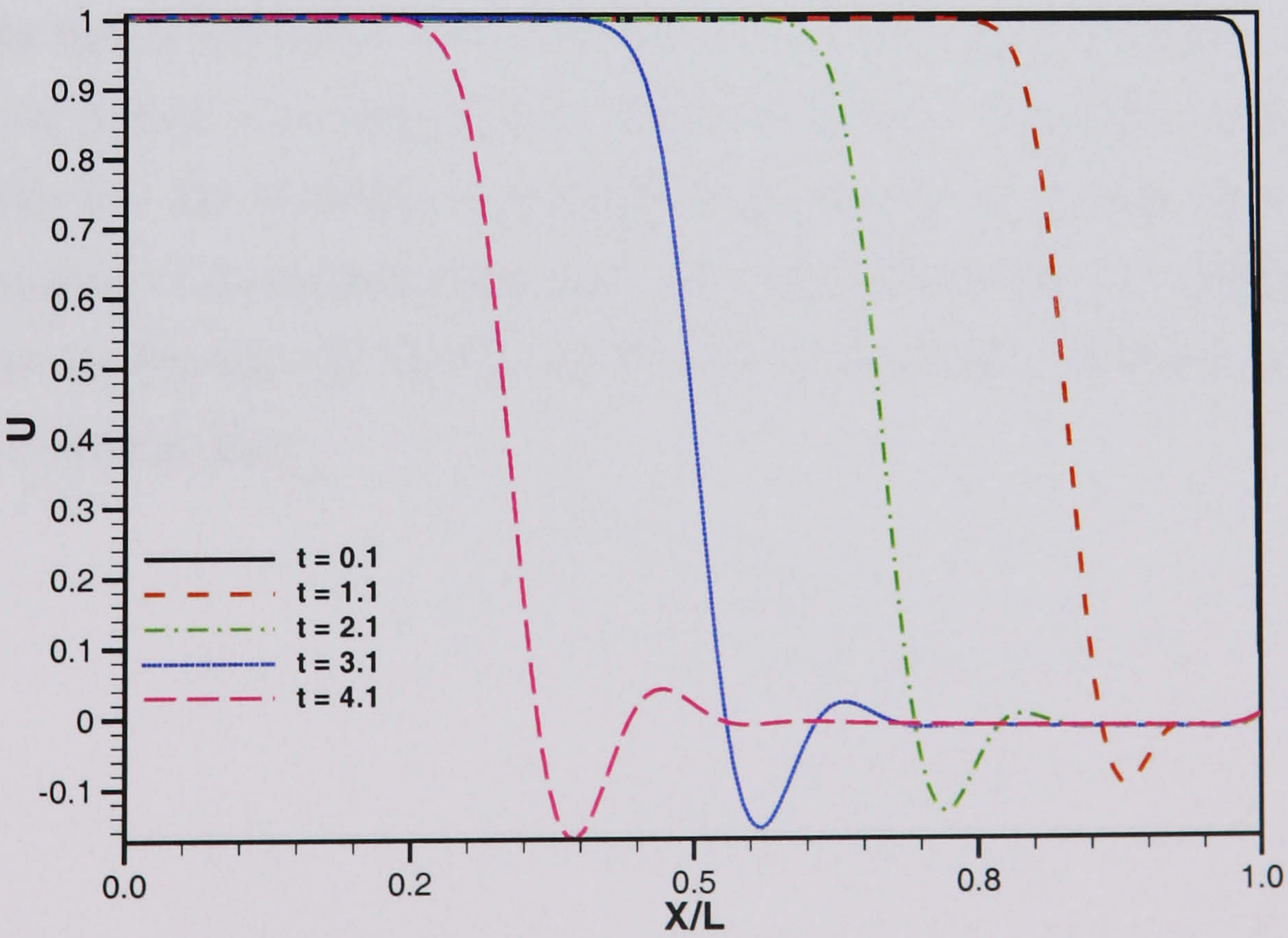

Figure 5.7: *U velocity through the centre of the pipe for the* $M = 0.145$ *case*

5.6 Summary

Direct validation for the surge work is not possible as there is currently no unsteady experimental or computational data available for the M2129 intake model 2129. Consequently other options had to be considered.

The unsteady shocktube problem was chosen as a useful unsteady introductory problem. Shock propagation speeds predicted computationally agreed with results obtained from well known analytical equations. Slight peaks in the computational solution were found in places and were attributed to the limiter used in PMB. It was concluded that the use of an alternate limiter would eradicate these peaks as had been found in previous works.

Experimental data was also obtained from the RMCS for the case of a surge in a straight section of pipe. The surge was simulated by allowing uniform flow of air through a pipe and then abruptly blocking the outflow. The experimental data is limited to pressure recordings from 10 transducers along the pipe length. Shock propagation speeds can be determined from water-hammer theory and from analytical solutions and were found to show reasonable agreement. The experimental results were perhaps slightly low but this is probably due to the fact that closure of the valve that blocks the flow is not instantaneous as assumed in the analytic equations. The error in general was known to be large for the experimental data. Although it was not possible to quantify this the analytic and water hammer theory was thought to be within the error boundary of the experimental data. This case was modelled in PMB assuming an instantaneous blockage of the flow and showed a reasonable agreement with analytic and experimental data.

Chapter 6

Surge in the M2129

Following the validation study in chapter 5, attention now turns to the modelling of surge in the M2129. A variety of signatures have been examined for the standard high mass flow case defined in chapter 3. The low mass flow case was then studied and a different OPR was also computed. Finally surge at incidence was looked at based on the steady results found in chapter 4

6.1 Methods of Modelling Surge

Engine surge is a complicated phenomenon whose origin can be from several sources as discussed in section 5. Consequently, a method that is able to predict the abrupt breakdown of the flow through the engine, the production of an engine surge, and the subsequent modelling of the surge wave as it propagates up the intake duct is beyond the scope of this work. Instead, the focus is on applying a realistic surge signature with emphasis placed on the modelling of the surge propagation, the understanding of the flow physics involved when considering surge propagation, the consequences in terms of over-pressures throughout the duct, and the sensitivity to the surge signature applied.

As previously mentioned, there has been a limited amount of work on the computational modelling of surge. One of the most important aspects is the choice of surge signature. The form of the surge is hard to predict but it is known to be a very rapid event. Computational papers that have examined surge were listed in section 1.4.3. Here, a more detailed look at the techniques of surge modelling and signature selection will be given.

Goble et al.[29] looked at surge in the F-22 intake. The steady flow calculations involved the application of the same boundary calculations as used in the present work (constant uniform static pressure). The importance of the over-pressure waveform for a correct emulation of the engine stall behaviour is discussed. They concluded that a guillotine surge application (instantaneous) does not correctly model the forward expulsion of compressor air into the duct. It is estimated that the guillotine ramp up may only last around t^*=3ms with steady state values returning after around t^*=15ms. Goble had access to data for the YF119 engine which he claimed demonstrated that the duration of a surge was considerably longer with peak engine face pressures not reached for around t^*=15ms. Goble concluded that hard stall events may last for over t^*=60ms and that the ramp up and ramp down are sinusoidal in nature - figure 6.2(a).

Webb and Heron[81] discussed the importance of adequately defining a surge waveform or that, at least, a correctly recorded waveform was available. They said that, in the past, unrealistic surge waveforms have been used. Unrealistic waveforms are defined as rounded and smooth, not unlike the signature used by Goble, with a rise time of around t^*=12ms and a recession phase of around t^*=30ms. The main features of their 'realistic' signature is a sharp initial rise in positive over-pressure to a peak after only around t^*=1ms. There then follows a gradual recession to a pressure below the normal operating pressure before there is a second sharp rise which is sharp but generally less than the first one - figure 6.2(c).

Causon et al.[28] looked at the application of a surge signature to a generic aircraft intake. No detailed information was given on the dimension of the intake although it appears to be around 10m long. The surge takes the form of a linear rise to a peak OPR after t^*=2.5ms followed by a linear recession back to a normal OPR after a subsequent t^*=30ms - figure 6.2(e). Steady state solutions were initially sought. At each engine face boundary condition, a constant static pressure was applied corresponding to an assumed pressure recovery factor. The transient phase then commenced when the pop surge pressure pulse was applied.

Ytterstrom et al[26] discussed engine stall leading to a sudden pressure rise, with the possible production of an upstream travelling shock and usually occuring at supersonic speeds for low throttle settings. The pressure rise can be as much a three times the pressure levels experienced in steady state, and this was used as the design load for an intake duct. They state the phenomenon is similar to the shocktube case and is largely inviscid although factors such as separation and intake design would have an impact.

The computational technique used by Ytterstrom was to obtain a steady state solution in a similar fashion to the steady state solutions achieved in this work in chapter 3. A surge signature was then applied by altering the engine boundary condition from a static pressure to a time-dependent static pressure. The pressure rises to a peak in t^*=20ms (the time required for a hammershock to form) and a subsequent t^*=15ms was needed before the hammershock had travelled upstream through the duct. The pressure rise to a peak was approximately linear, and, once at the peak, droped back to a normal pressure after around t^*=50ms in an approximate linear fashion - figure 6.2(g). An approximation of t^*=33ms for the wave to propagate from the engine face upstream to the duct intake was made. However the paper's main focus was on the time-stepping technique used in the problem and contained little technical surge information and no information on engine face diameter or duct length.

Hsieh et al.[27] examined an intake response to an increase in exit pressure. Two different signatures were used. The first was one in which the pressure was increased linearly by 14% in a time of $t^*=0.2ms$ and was held at this increased pressure. The second signature was a pressure pulse where the pressure again rose 14%. The linear rise time was $t^*=0.2ms$, the pressure was held for $t^*=0.4ms$, and then receded linearly back to the original pressure over a time of $t^*=0.2ms$. The intake diameter used was $67mm$ and the computational upstream and downstream boundaries were $559mm$ apart.

In summary, previous works have used a variety of surge signatures which can be listed as follows (with the numbering of the surge signatures following that used later in the chapter):

1. Sinusoidal function similar to that defined by Goble et al.[29] and Webb and Heron[81] - rise to peak after around $t^*=12ms$ and decay over $t^*=20ms$.
2. Rapid rise in $t^*=1ms$ accompanied by a gradual decay over $t^*=30ms$ - Webb and Heron[81]
3. Rapid linear rise to peak after $t^*=2.5ms$ followed by a linear recession over around

t^*=30ms - Causon et al.[28]

4. Quasi-linear rise to peak after t^*=20ms followed by a recession over a period of t^*=20ms - Ytterstrom et al.[26]

There are certain situations in which it is more likely to encounter engine surge. Flying at high speeds when throttle settings are low is one such scenario, high mass flow demand into the engine another, and also if the air is highly disturbed on reaching the compressor face. Here, the AGARD [12] high mass flow case will be examined. The four different signatures listed above will be studied to assess the sensitivity to the signature applied. Finally, surge at incidence will be looked at as these scenarios tend to produce more disturbed flow into the intake which can be conducive to engine surge.

Due to the three dimensional and unsteady nature of the flow it is challenging to visualise the results by figures alone. Much of the analysis was done using information from probe points located on the port and starboard walls (figure 6.1). There are also slices through the geometry and surface plots of the intake at various instants. Appendix C contains an attachment CD that contains movie clips of these unsteady surge events that will help understand the flow mechanics involved in these events.

Figure 6.2 shows all four signatures and their approximations used in the simulation. The simulation works with non-dimensional quantities. Pressure is non-dimensionalised, or reduced, with respect to the freestream value. Time is reduced as

$$t = \frac{t^*}{L^*/U^*_\infty} \tag{6.1}$$

where * indicates a dimensional quantity. Signatures available from previous work tended to work in dimensional quantities (seconds). This can be non-dimensionalised (reduced) using the above equation assuming the characteristic length and freestream velocity for which the information is available is known. Unfortunately the specific engine type and freestream conditions were not detailed for some signatures and so relevant guesses were made. This is discussed further in the following sections for each signature. It should also be noted that the general result for each surge event analysed is similar. Therefore, signature one (section 6.3) is analysed in detail. Subsequent signatures focus on the differences with signature 1 for brevity.

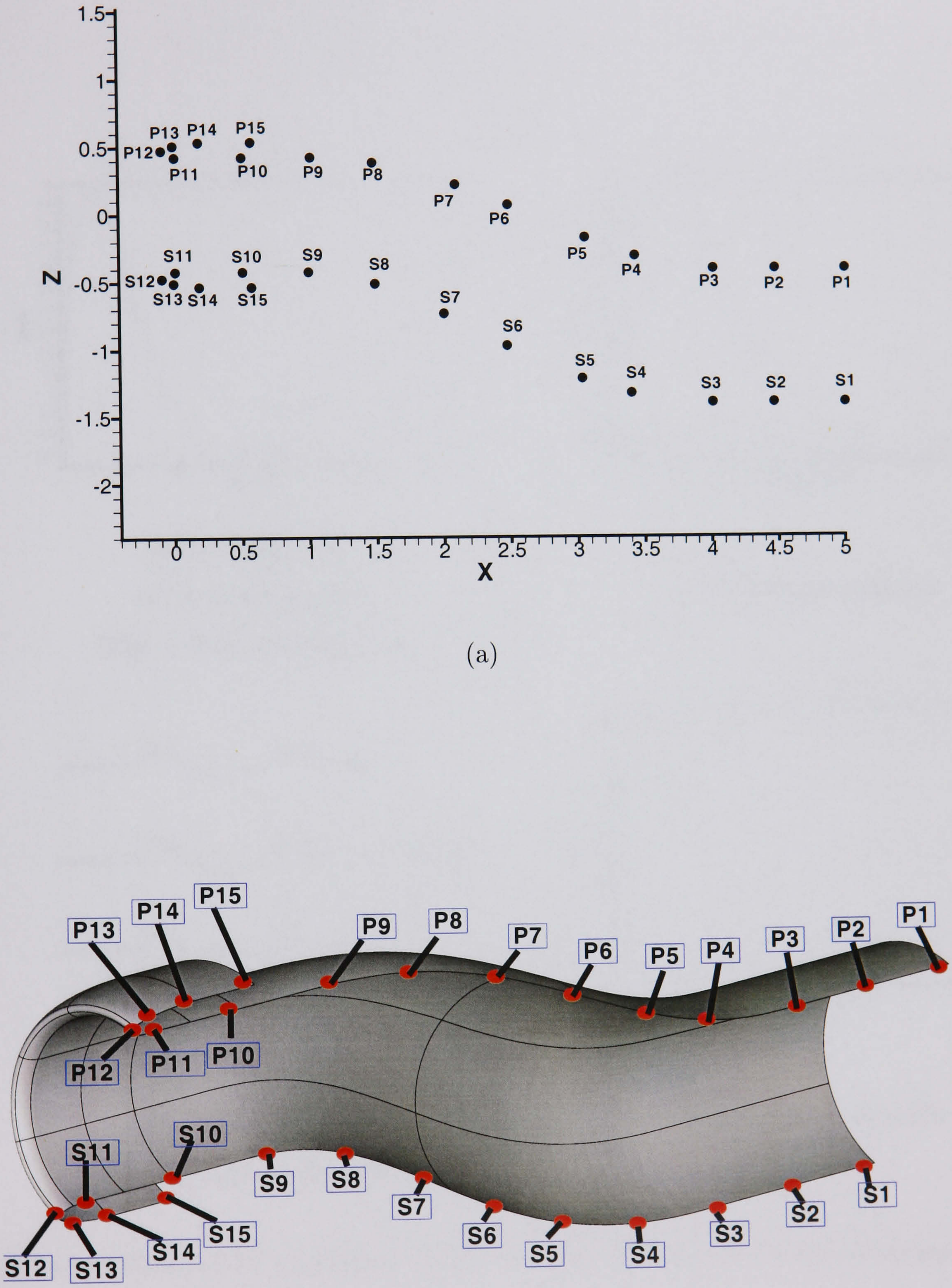

(a)

(b)

Figure 6.1: *Probe locations through the symmetry plane*

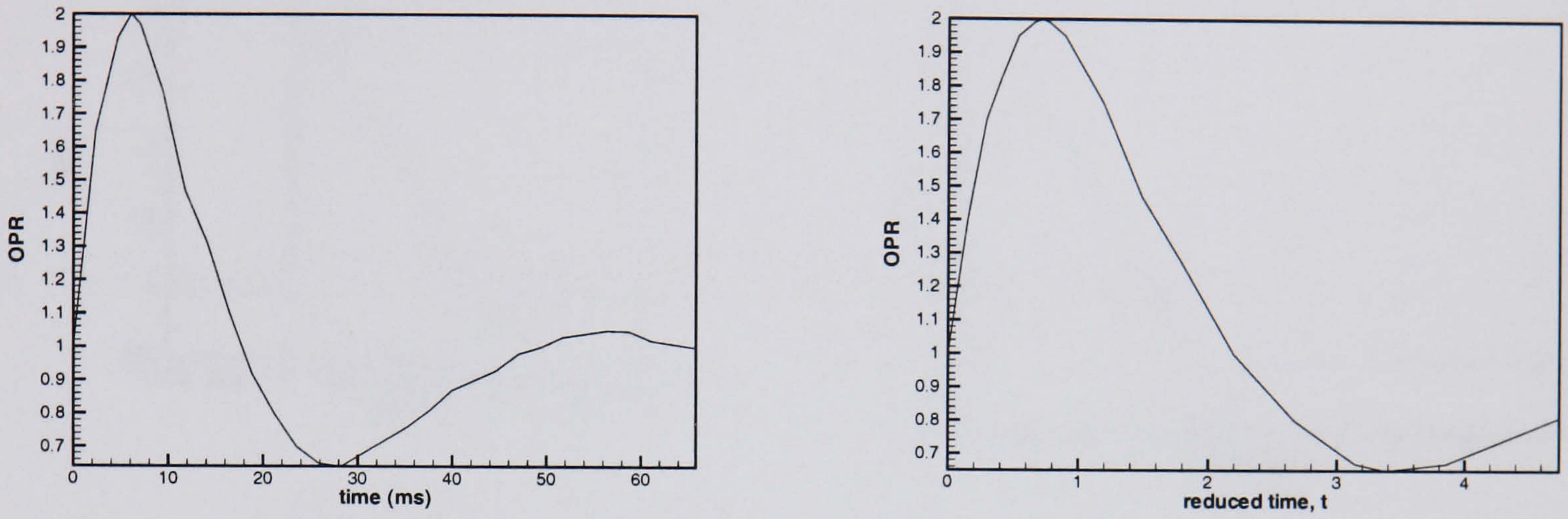

Surge Signature 1

(a) Actual signature

(Fig. 1 from reference [81])

(b) PMB approximation

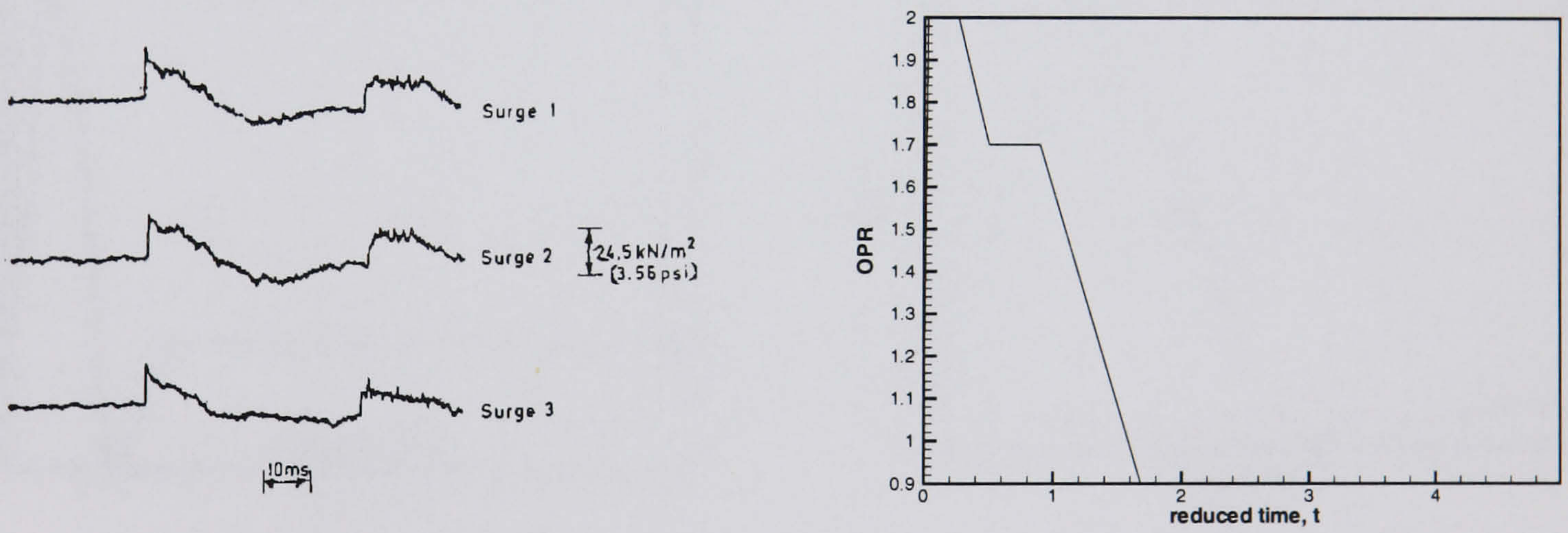

Surge Signature 2

(c) Actual signature

(Fig. 2 from reference [81])

(d) PMB approximation

Figure 6.2: *HMFR SST calculation, OPR = 2, Real and approximate signatures applied*

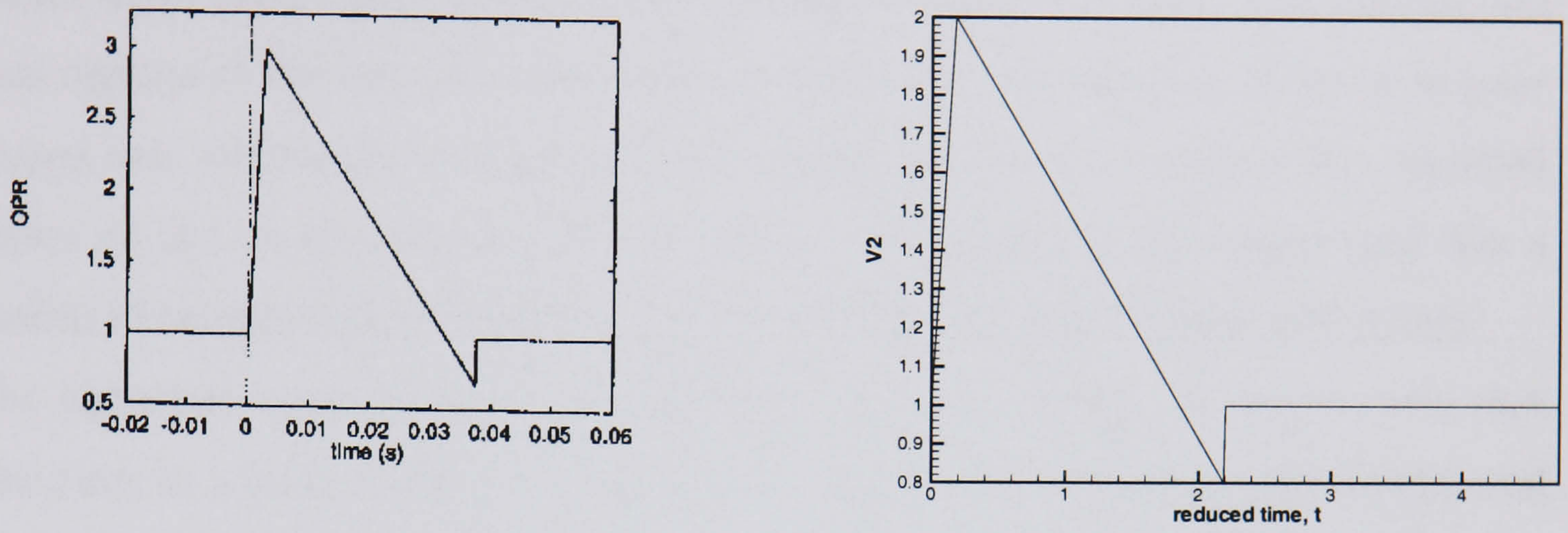

Surge Signature 3

(e) Actual signature

(from reference [28])

(f) PMB approximation

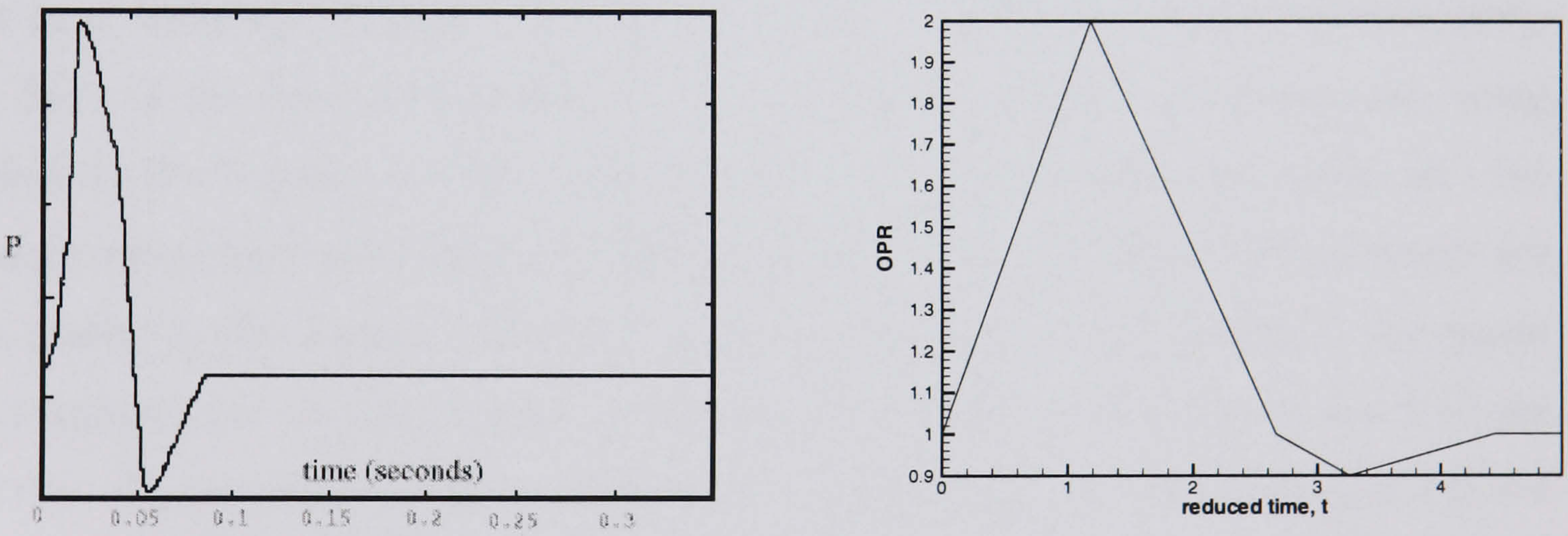

Surge Signature 4

(g) Actual signature

(from reference [26])

(h) PMB approximation

Figure 6.2: (cont.) *HMFR SST calculation, OPR = 2, Real and approximate signatures applied*

6.2 Grid and Time Convergence Study

6.2.1 Grid Convergence Study

Coarse and fine grids are used to run surge signature 1. Probe points on the port and starboard sides (figure 6.1) are used to compare between solutions. The grid for the internal regions of the duct is as used for the steady flow calculations. However heavier clustering was introduced around the cowl region in order to capture the expected expulsion of the surge wave out of the intake. Consequently the coarse grid has a dimension of around 542,714 grid points and the fine grid has 975,386 grid points.

The signature used for this study is shown in figure 6.2(b). It can be seen that the rise time to a peak applied over pressure is just under one unit of non-dimensional time. A time step must be chosen that suitably captures this rise. It was decided that $\Delta t = 0.001$ would be satisfactory giving around 900 time steps during the rise time. It was found that a complete calculation for the coarse grid lasted 85 wall clock hours (WCH) and the fine grid required 224 WCH using 8 parallel computing nodes for this time step. Refering to figure 6.3, probes P4 and S5 lie near the engine face boundary. The form of the pressure recorded is very similar to the form of the pressure being applied at the boundary as the surge front has not encountered duct bends and the pressure waves have not coalesced to form an abrupt pressure front. The solutions are very similar in this location. However small oscillations that are present in the coarse grid computation are not present in the fine grid solution. Probes S10 and P10 are also very similar. Some minor oscillations are again present on the coarse grid that are not seen with the fine grid. Peak reduced pressures predicted are also greater for the fine grid solution by about 5-10% which could be significant.

As the surge front exits the intake (P12 and S12) it can be seen that there are further differences between coarse and fine meshes (however it should also be noted that as the pressure levels are lower in this location, the differences are accentuated when compared with previous probe locations). In both locations the fine mesh predicts slightly higher peak pressure and, similarly, slightly lower minimum pressure. Overall, the differences between the coarse and fine meshes are small and hence the coarse mesh will be used for the consequent time convergence study and also the subsequent surge investigation.

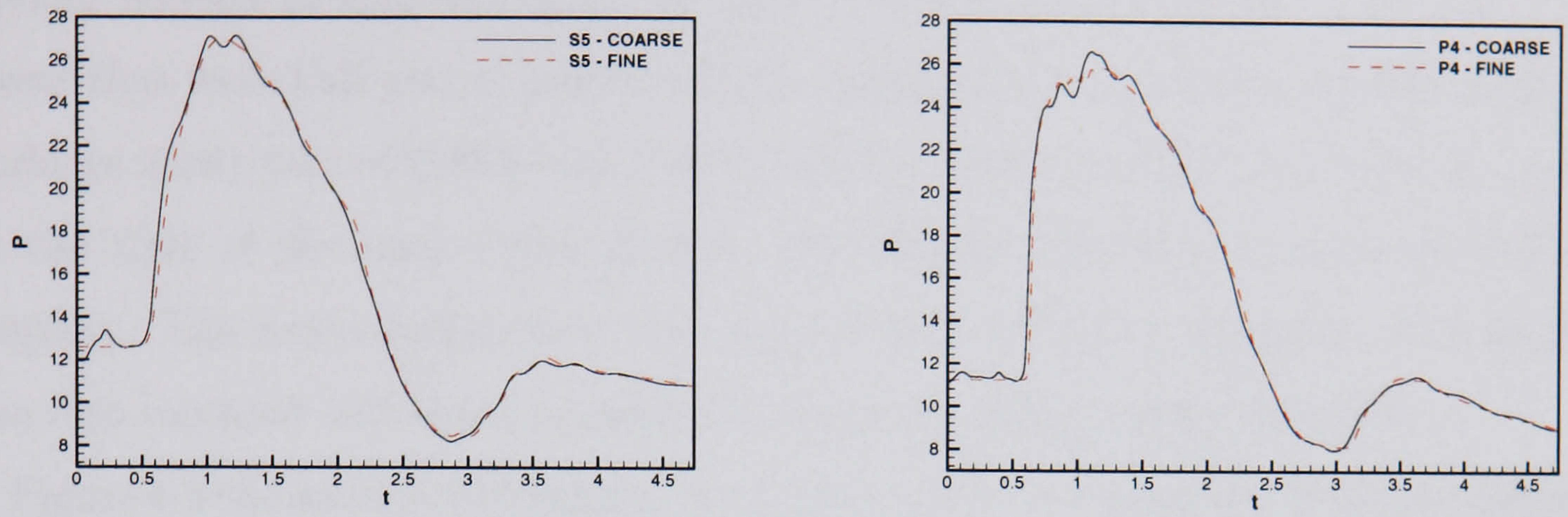

(a) Starboard probe 5

(b) Port probe 4

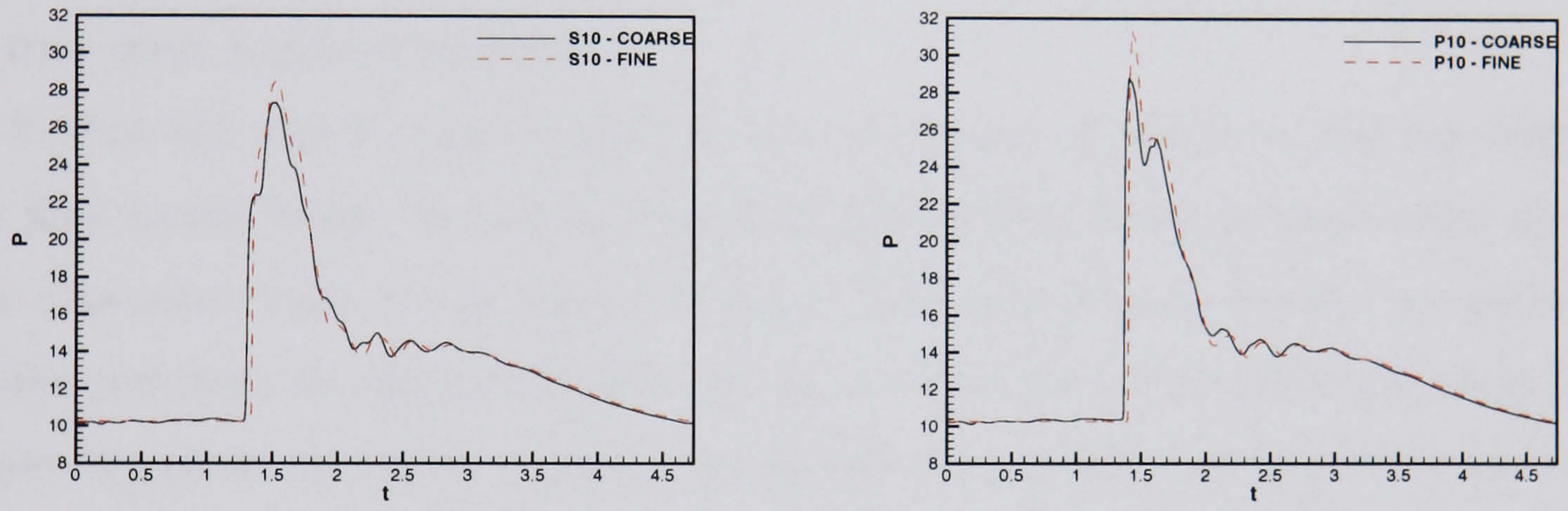

(c) Starboard probe 10

(d) Port probe 10

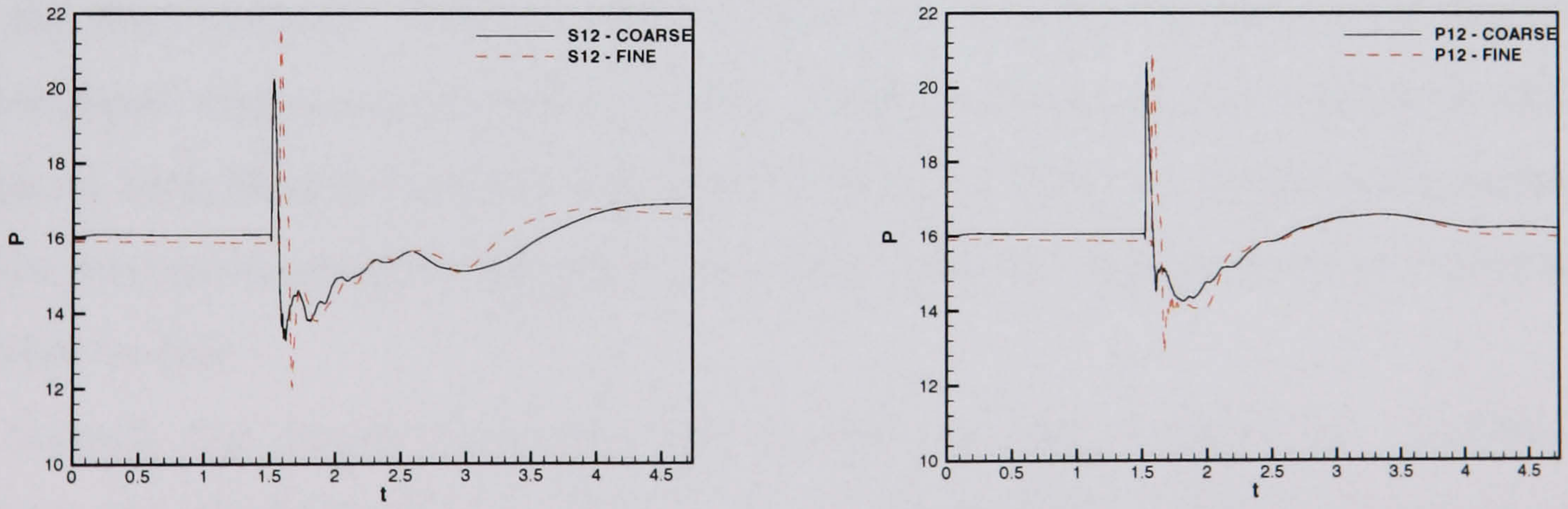

(e) Starboard probe 12

(f) Port probe 12

Figure 6.3: *HMFR SST calculation, OPR = 2, Surge signature 1 - Symmetry plane grid convergence*

6.2.2 Time Convergence Study

The time convergence study was undertaken using the coarse grid as defined in the previous section as this was found to have an adequate resolution. Time steps were chosen that were half and a quarter of the original time step chosen for the grid independence study (Δt of 0.0005 and 0.00025 giving 1800 and 3600 time steps to capture the rise time of the surge respectively). The largest time step required 85 WCH to complete. The intermediate time step required 140 WCH to complete. The smallest time step required 230 hours to complete using 8 parallel computer nodes.

Figure 6.4 shows reduced pressure time histories from a selection of probes following the numbering in figure 6.1. Probes S5 and P4 lie nearest the downstream boundary where the pressure surge signature is applied. It can be seen that the general form for all time steps is almost identical.

Probes S10 and P10 are located in the cowl region of the duct, just upstream of the first intake bend. It can be seen that the pressure front is much more abrupt now (discussed more in the results section). Pressures from both sides are generally similar and there are again oscillations in the solution, particularly after the surge front passes the probe locations. Again it seems that the smaller the time step, the more these oscillations are damped out. Probes P12 and S12 are located on the highlight of the cowl duct on the port and starboard sides respectively (the most upstream point on the duct surface). This location has the largest variations although it should be remembered that pressure levels are lower. Maximum pressures are similar for all time steps on both the port and starboard sides. However there are considerable variations in the minimum pressures following this. There does not appear to be any discernible pattern to this.

Overall, the intermediate time step appears to offer a satisfactory solution and capture all salient features of the flow. There are variations between time steps, more especially once the surge front had propagated the length of the duct and is expelled into the freestream. However these differences are not considered significant. The intermediate time step also provides computationally cheaper solutions when compared with the smallest time step and will be used for all subsequent surge calculations.

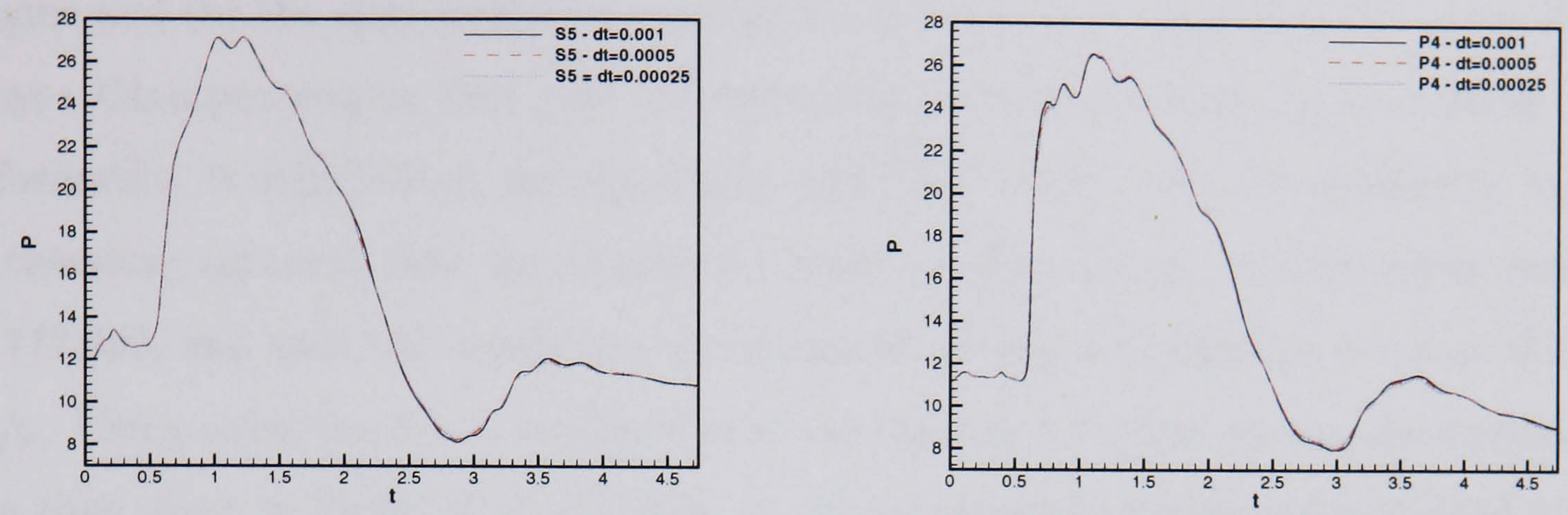

(a) Starboard probe 5

(b) Port probe 4

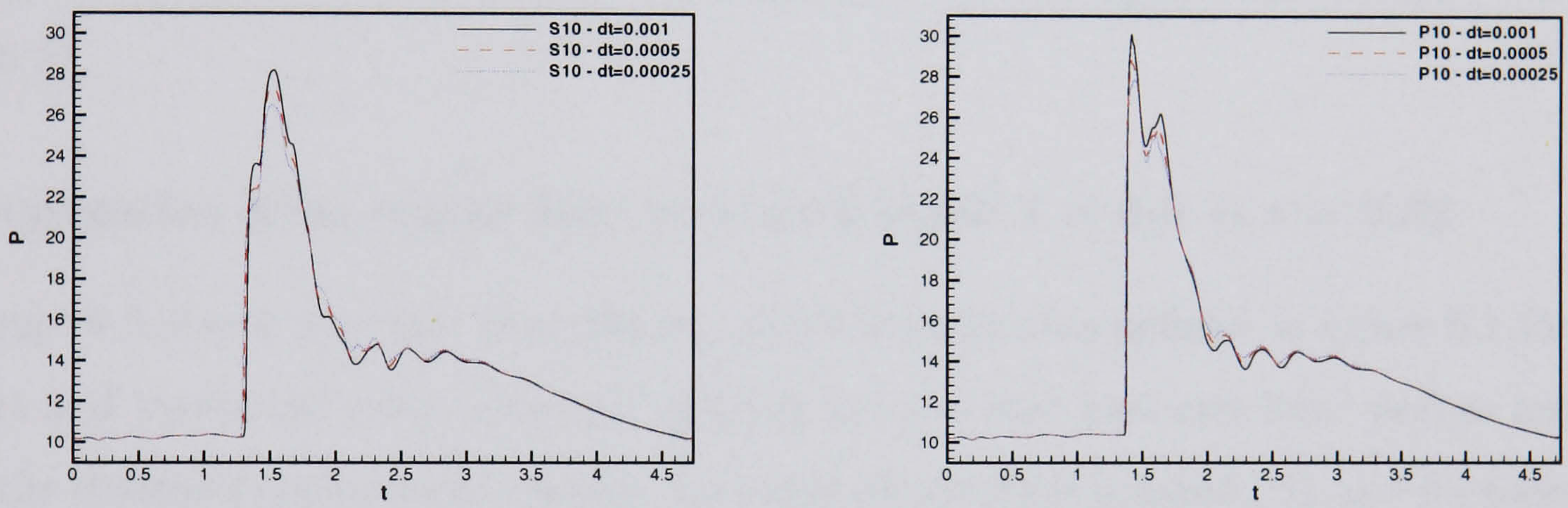

(c) Starboard probe 10

(d) Port probe 10

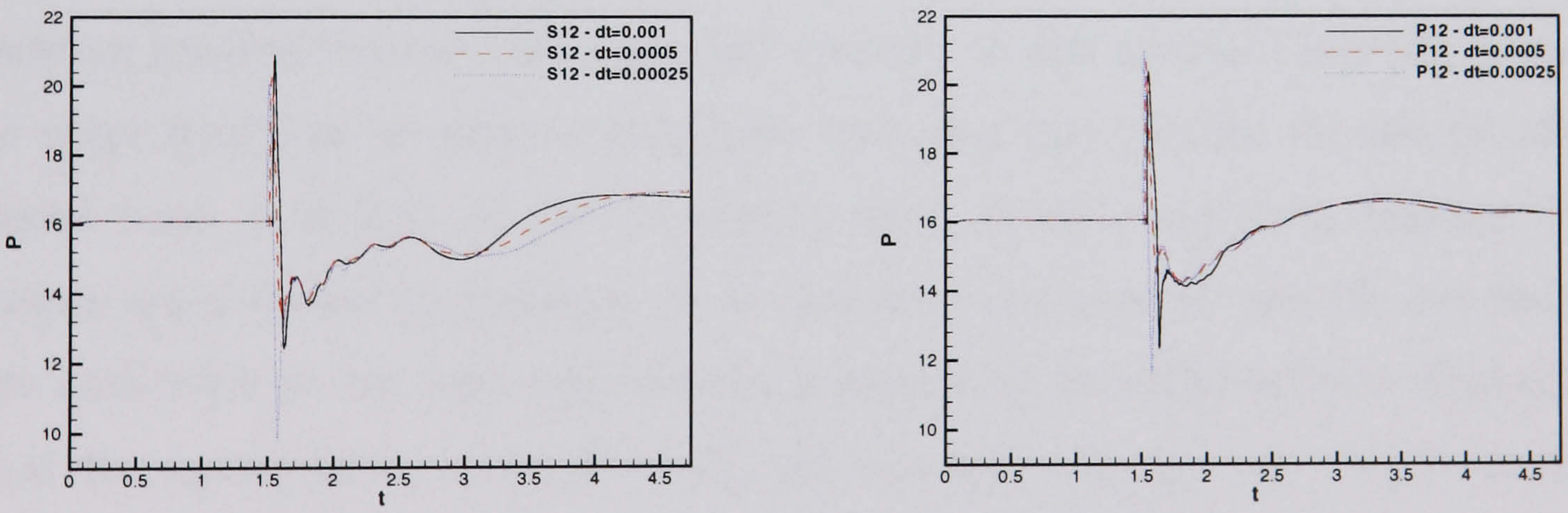

(e) Starboard probe 12

(f) Port probe 12

Figure 6.4: *HMFR SST calculation, OPR = 2, Surge signature 1 - Symmetry plane time convergence*

6.3 Surge Signature 1

Figure 6.2 show the surge signature (a) [81] applicable to the Rolls Royce Olympus engine and (b) the approximation used for the calculations. The diameter of the Rolls-Royce Olympus engine face (the characteristic length) is known to be 1.207m. No information is supplied on the operating conditions that it may be applicable for. It is therefore assumed that the freestream Mach number is 0.21, the Reynolds number is 777,000, and that the conditions are standard, giving a freestream velocity of 71.47 m/s. Using equation 6.1, a scaling factor can readily be found to non-dimensionalise the time given in Webb et al [81], Fig. 1. The maximum over-pressure applied at the downstream boundary is 2. As the high mass flow case is being examined then this gives a maximum reduced pressure of 26.29 (2 x 13.15) applied at a reduced time, t, of 0.71.

Propagation from engine face to second bend: t = 0.0 → t = 0.62

Figure 6.5 shows pressure time history detail from probes defined in figure 6.1 for the port and starboard sides. Here (a) and (b) are pressure histories from probes nearest to the downstream boundary where the surge signature is applied. S1 and P1 basically represent the signature being applied. The signature is sinusoidal in nature. Peak pressure is reached and then there is a decay to a pressure below that of the normal operating pressure followed by a gradual recovery to the normal operating pressure. The surge front can be seen to propagate upstream and reaches P3 and S3 after a reduced time, t, of 0.4. It can be noticed that, as the surge front reaches P3, it becomes much steeper in gradient. As we continue to probes P5 and S5 this becomes more noticeable on the port side probes. It should be remembered that although S5 lies at the second bend, probe P5 is located an equal distance from the downstream boundary but is actually upstream of the second bend as it is on the inside of the second bend. The maximum pressure levels throughout are the similar to those being applied at the engine face for Probes 1-5. Upstream of these probes there is no change from steady state as the surge front has not yet had an effect.

Figure 6.6 (a) and (b) show Mach contours as the surge forms at the engine face (a) and then propagates as far as the second bend (b) (the second bend being defined as that closest to the downstream boundary). We can see that there is an interaction of the surge front with the separated flow from the starboard side first bend. The Mach number is reduced to near zero values. As the surge front reaches the second bend there is a region of higher Mach number that develops near the starboard side that is associated with the recirculating region. Included in these figures are instantaneous graphs of pressure versus duct longitudinal location for port and starboard sides. At t=0.62 it is clear that the surge front is much more pronounced on the port side.

Figure 6.7 (a) and (b) show streamlines from the symmetry plane and give an insight into this interaction. It can be seen that as the surge front passes through the separated region flow reversal is created or enhanced depending on the initial steady state (figure (b)), creating a vortex. Away from the separated region, towards the port side the flow is slowed down dramatically. Upstream of the surge front the flow can be seen to be unaffected.

Figures 6.8 and 6.9 (a) and (b) show that the pressure contours (gradient) are uniform as the surge is applied and forms at the engine face. This is as expected as the flow is similar to that in a straight duct and thus should not lose any uniformity. Once it has propagated to the first bend (t=0.62) however there is a stronger pressure gradient that develops towards the port wall as the flow here does not interact with the separated region. Figure 6.9 (a) and (b) shows the surface pressure for this case at times of 0.24 and 0.62. Again the uniform pressure on the port and starboard sides can be seen at the earlier time. As the wave front reaches the second bend the isolines are more concentrated towards the port side. Towards the starboard side the isolines are less concentrated. However it does appear that the most upstream waves have progressed further on this side. On the port side they appear to coalesce more.

Propagation from second bend to first bend: $t = 0.62 \rightarrow t = 1.26$

Returning to figure 6.5, (c) and (d) show the pressure probe histories in the region from the second bend to the cowl, just upstream of the first bend. On the starboard side it can be seen that the trend of the surge front becoming sharper continues. Probe S6 has a straighter gradient although the peak pressure is much the same as the probes further downstream. Probe S8 lies approximately half way around the starboard first bend. It can be seen that the effects of the applied pressure are first felt just before t=1.0. On the port side the surge front takes slightly longer to reach probe P8 (t=1.2). It can also be seen on the port side that as the wave moves from the second bend through the duct to the first bend, the peak pressure also increases. Following the propagation around the second bend, and just prior to it reaching the first bend, the pressure level has increased from 26 to a maximum of around 32. After the wave has propagated around the first bend it reaches probes P10 and S10 at much the same time. The pressures on the port side decrease a little from the peak pressure experienced, while the pressure on the starboard side increases.

Back at the engine face region (P1-P5 and S1-S5) the pressure being applied begins to enter the recession phase. There is a pattern that, as you move away from the downstream region and towards the upstream cowl, the surge front profile becomes more compact. That is to say, as the surge signature is applied and subsequently propagates upstream, there forms an abrupt surge front with a sharp increase to maximum pressure, followed by an equally abrupt decrease in pressure back to near normal levels. This is particularly apparent when comparing probes S1-S5 with S6-S10.

Figure 6.6 (c) and (d) show Mach contours through the symmetry plane coupled with instantaneous pressure levels along the port and starboard side walls at times of 1.0 and 1.26. This roughly equates to points when the surge front is just before the first bend and when the surge front is in the cowl region respectively. It can be seen that there are further complex flow features as the surge hits the separated flow region from the first bend. A region of higher Mach number develops due to an induced reversal of the flow that is normally low speed and separated. There is a thin streak of low Mach number flow separating this region of reversed flow from the normal flow towards the port side at the first bend. The surge front again appears more distinct on the port side. As the front navigates the second bend (figure (d)), the region of swirling flow reversal set up by the interaction of the propagating surge wave with the separated region also propagates upstream. The surge front propagation on the port side also seems to catch up with the propagation distance reached on the starboard side.

Figure 6.7 (c) and (d) show symmetry plane streamlines at the same instants as the Mach number plots described above. At t=1.0 it can be seen that the circulation after the first bend increases in size and strength and propagates upstream. The high velocity flow at the starboard side first bend is then forced up towards the port side where it meets the surge front and is slowed down dramatically. Upstream the flow is the same as the steady state case. Downstream the flow is very low speed. Towards the starboard side the flow remains against the mean stream and continues to feed the circulation at the starboard side first bend. In (d) it can be seen that the core of the main circulation from the starboard side has moved further upstream. Flow entering the intake towards the starboard side now encounters this region prior to the first bend and is deflected towards the port sides where it meets the port side of the surge front. Again, upstream the flow is steady state and downstream there is a continued reversal of the flow towards the starboard side.

Figures 6.8 and 6.9 (c) and (d) show the symmetry plane and duct surface pressure isolines. Figure (c) shows that the surge wave has reached the first bend on the starboard side and the pressure gradient is now a lot higher (the pressure isolines are packed more closely together). On the port side the surge wave has not as yet propagated so far. The region of higher pressure is clearly visible. Further downstream it can be seen that the region of peak pressure that is applied at the downstream boundary has propagated to the second bend. Figures 6.9 (d) shows the pressure front has navigated the first intake bend. The pressure peak behind the front towards the port side reaches a maximum at this stage. With reference to figure 6.8 (d), it can be seen that the maximum pressure is not actually on the duct surface but a little distance from the wall on the symmetry plane. The strong pressure gradient front to the surge wave is also clear in this figure as the wave begins to propagate along the cowl region of the duct, prior to expulsion.

Propagation from first bend to freestream: t = 1.26 onwards

Figures 6.5 (e) and (f) capture the pressure time history from the port and starboard sides as the pressure waves exits the duct. From figure 6.1 it can be seen that one point is on the inner cowl surface, one point is on the highlight, and the remainder are distributed around the outer cowl surface. Figure 6.5 (a), (b), (c), and (d) then record the subsequent pressure history after the surge wave exits the duct into the freestream.

Probes S11 and P11 show similar forms. There is an abrupt and dramatic increase in pressure from steady state (over-pressure factor of nearly 4) that begins at around a reduced time, t, of 1.5. Probes on the intake highlight (P12, S12) show a less dramatic increase in pressure due to the dissipation of the surge wave at this time into the freestream. Following the small peak there is a drop in pressure below the normal operating level and similar traits can be seen at probes 13. However probes 14 and 15 are located far enough from the duct intake on the outer cowl surface to be almost unaffected.

Figure 6.5 (a) and (b) show pressures back at the engine face following the surge expulsion. Probes S1 and P1 show that the pressure being applied recedes to a minimum at around a time of 3.5. However probes upstream register a dip in the pressure prior to this which indicates an upstream effect. Figure 6.5 (c) and (d) appear to confirm this and closer examination reveals that this is an upstream travelling wave that is probably a reflection of the initial wave back at the downstream boundary. As the wave propagates upstream it gets damped out.

Figures 6.6 and 6.7 (e) onwards shows the Mach number contours and streamlines at various times after the surge exits the intake. It can be seen that there is spillage out of the duct, particularly from the starboard side. Downstream, towards the engine face, the flow begins to accelerate in the normal sense following the second bend. This generates a lower pressure in this downstream area and unchokes the flow upstream which begins to accelerate as normal into the intake.

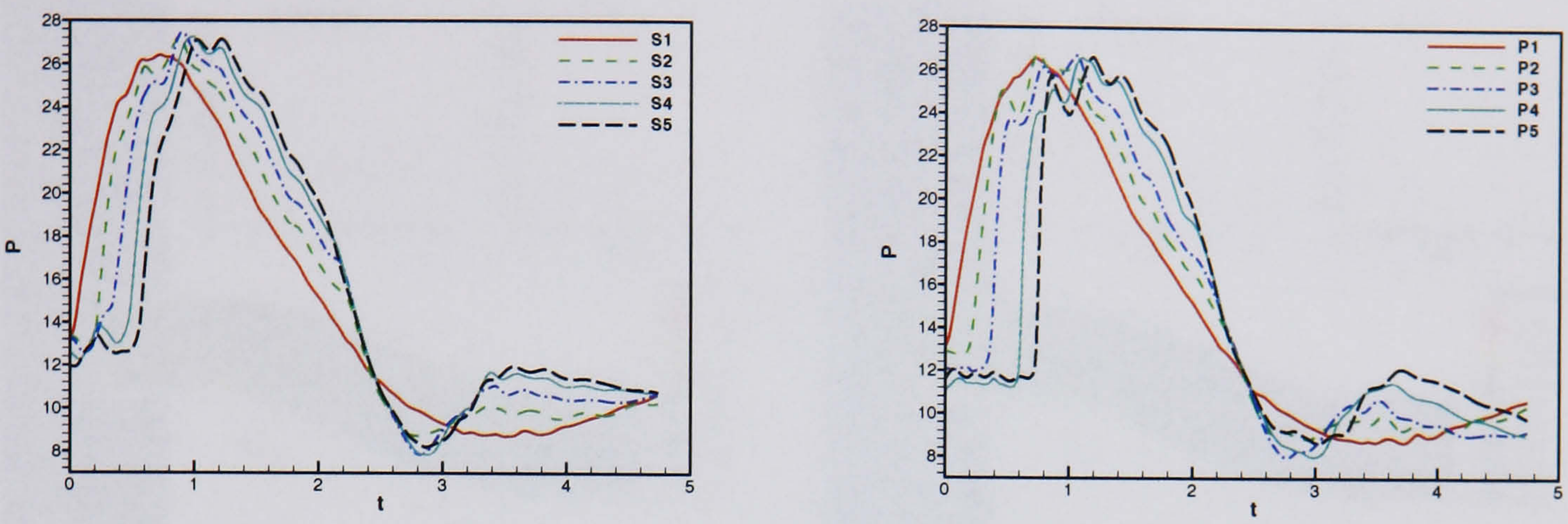

(a) Starboard probes 1 - 5 (b) Port probes 1 - 5

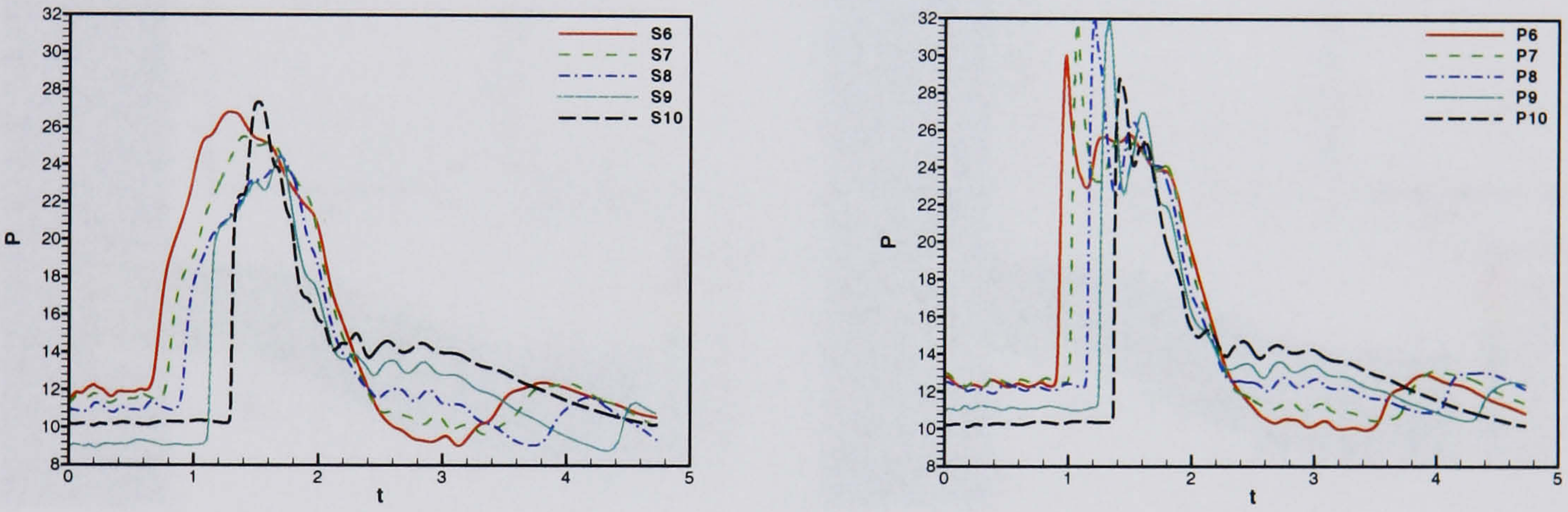

(c) Starboard probes 6 - 10 (d) Port probes 6 - 10

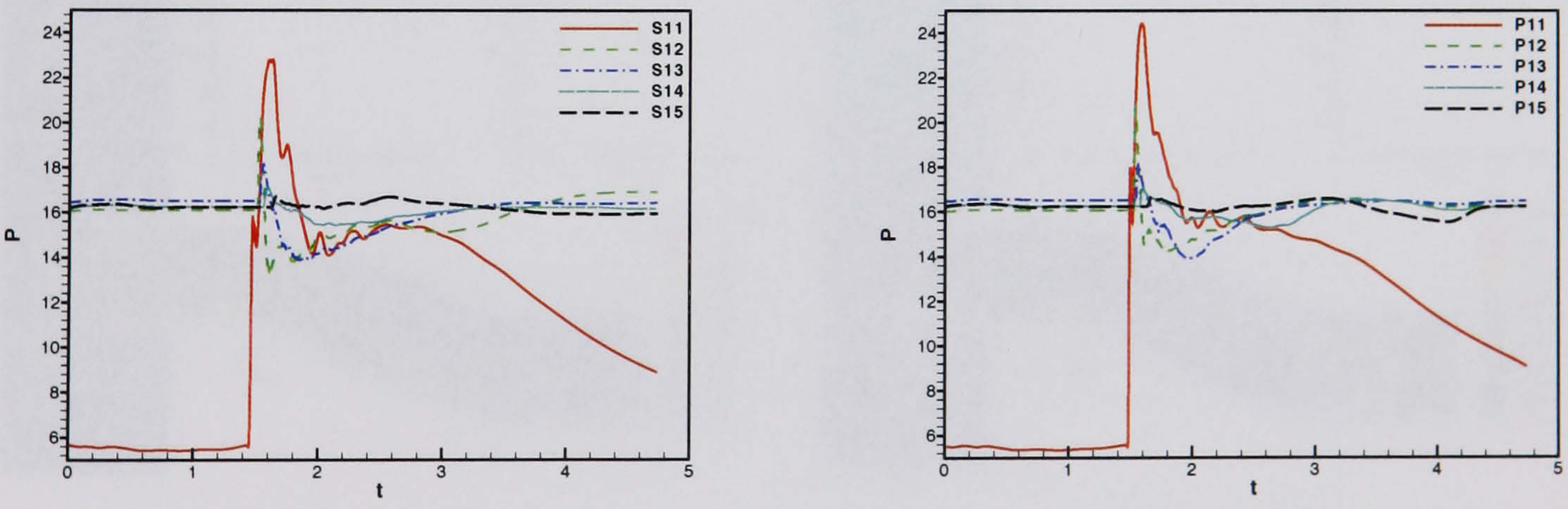

(e) Starboard probes 11 - 15 (f) Port probes 11 - 15

Figure 6.5: *HMFR SST calculation, OPR = 2, Surge signature 1 - Symmetry plane probe data*

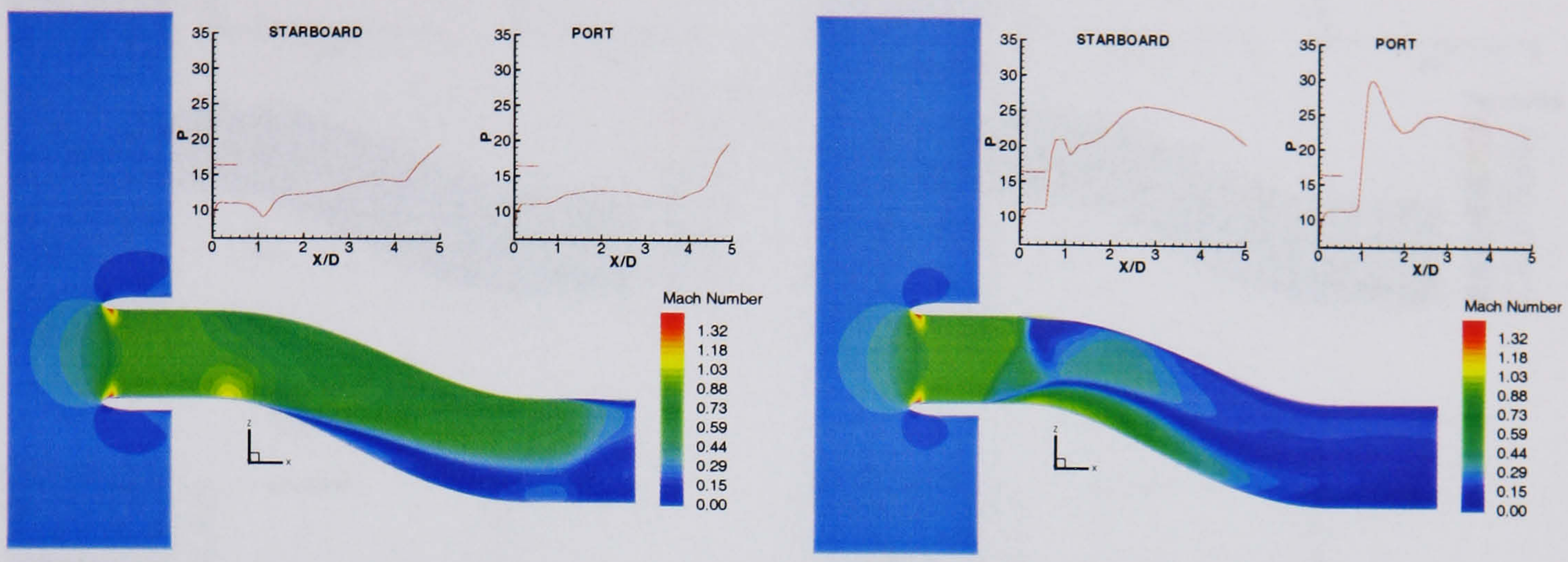

(a) t = 0.24

(d) t = 1.26

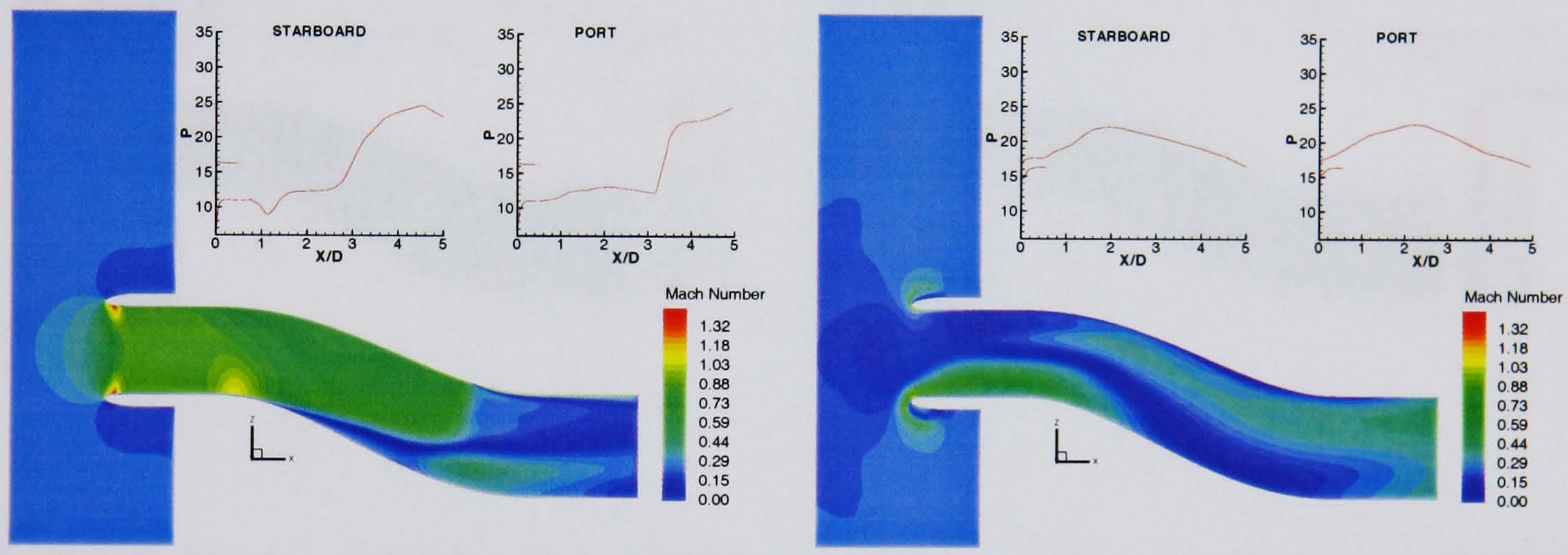

(b) t = 0.62

(e) t = 1.84

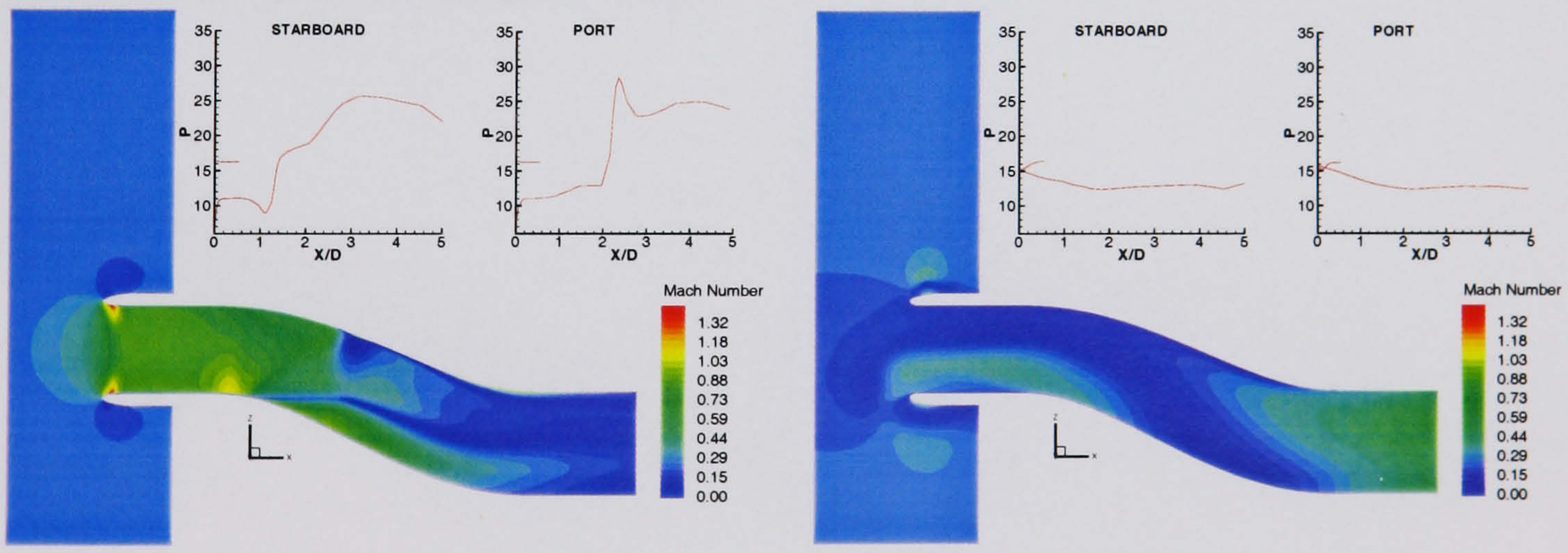

(c) t = 1.00

(f) t = 2.40

Figure 6.6: *HMFR SST calculation, OPR = 2, Surge signature 1 - Symmetry plane Mach number and pressure traces*

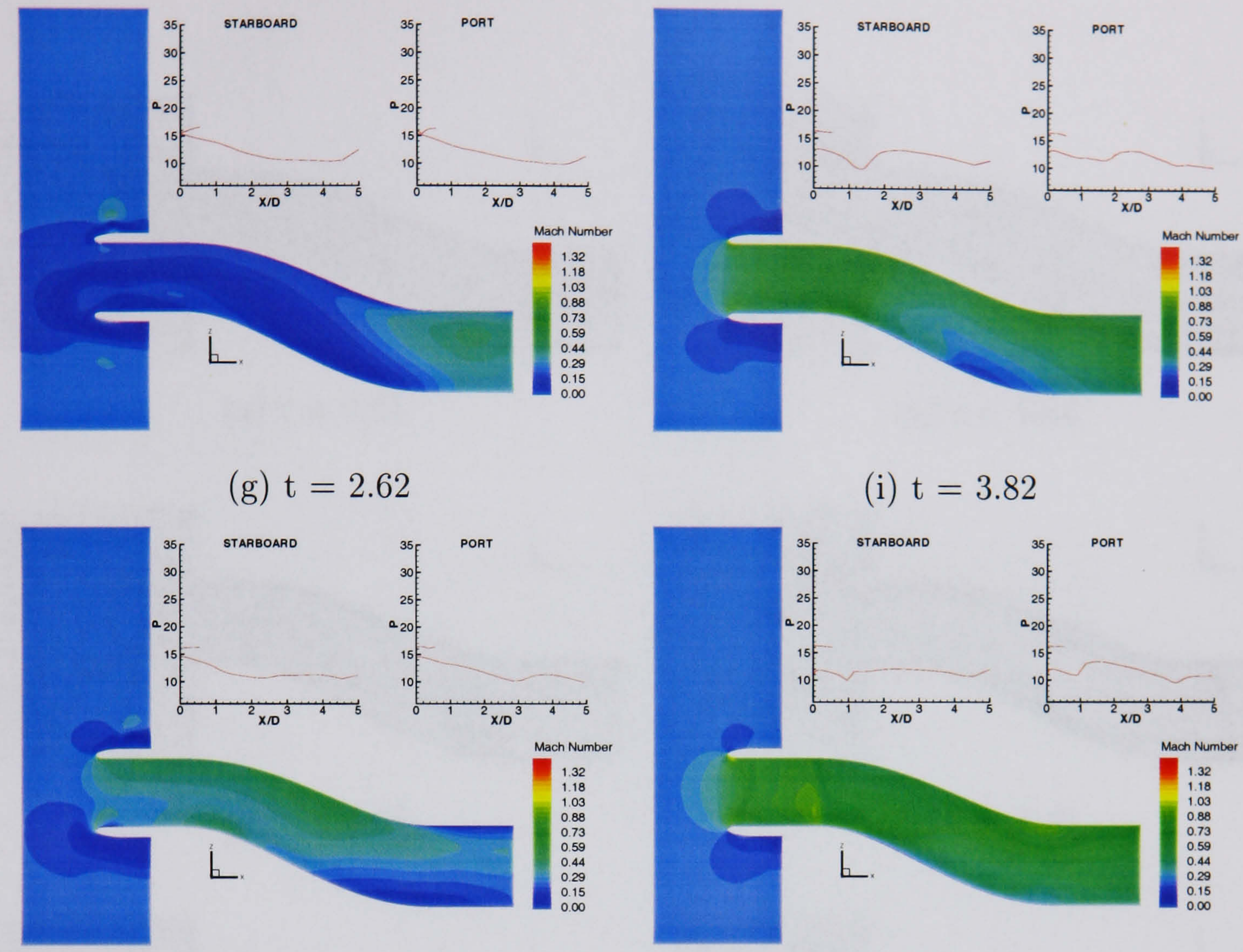

(g) t = 2.62

(i) t = 3.82

(h) t = 3.26

(j) t = 4.38

Figure 6.6: (cont.) *HMFR SST calculation, OPR = 2, Surge signature 1 - Symmetry plane Mach number and pressure traces*

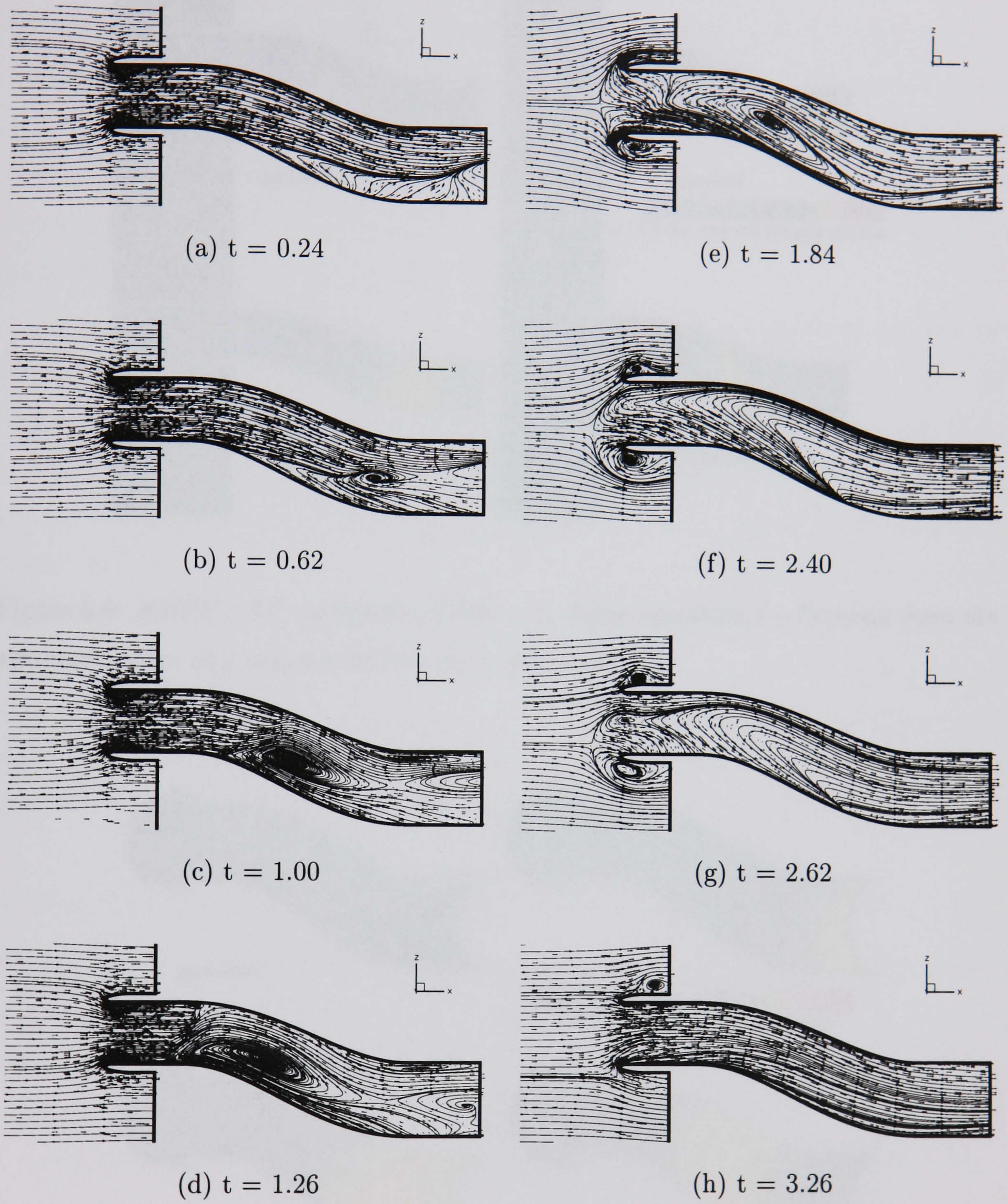

(a) t = 0.24

(b) t = 0.62

(c) t = 1.00

(d) t = 1.26

(e) t = 1.84

(f) t = 2.40

(g) t = 2.62

(h) t = 3.26

Figure 6.7: *HMFR SST calculation, OPR = 2, Surge signature 1 - Symmetry plane streamlines*

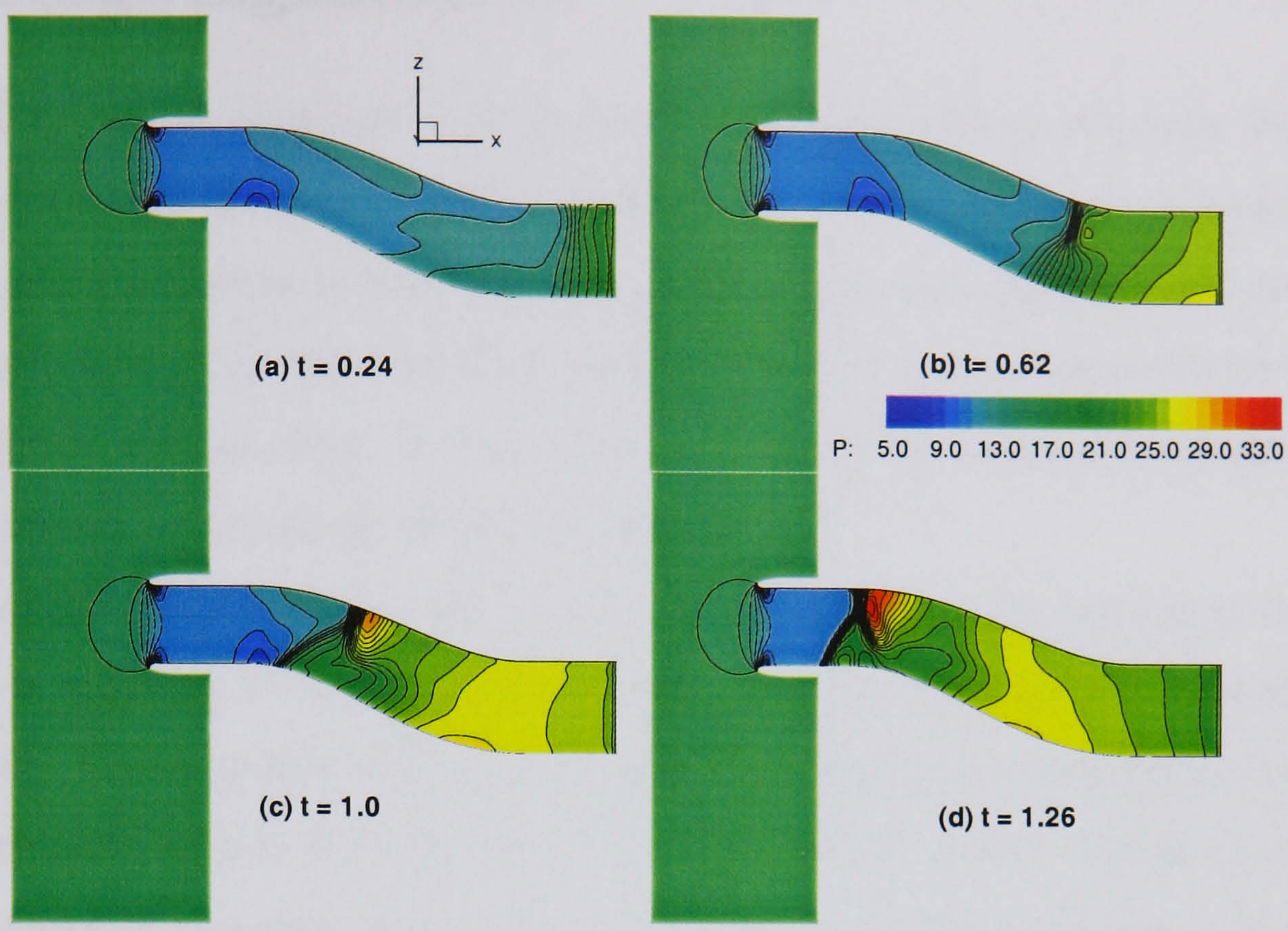

Figure 6.8: *HMFR SST calculation, OPR = 2, Surge signature 1 - Pressure from the symmetry plane at 4 instants leading up to surge exit*

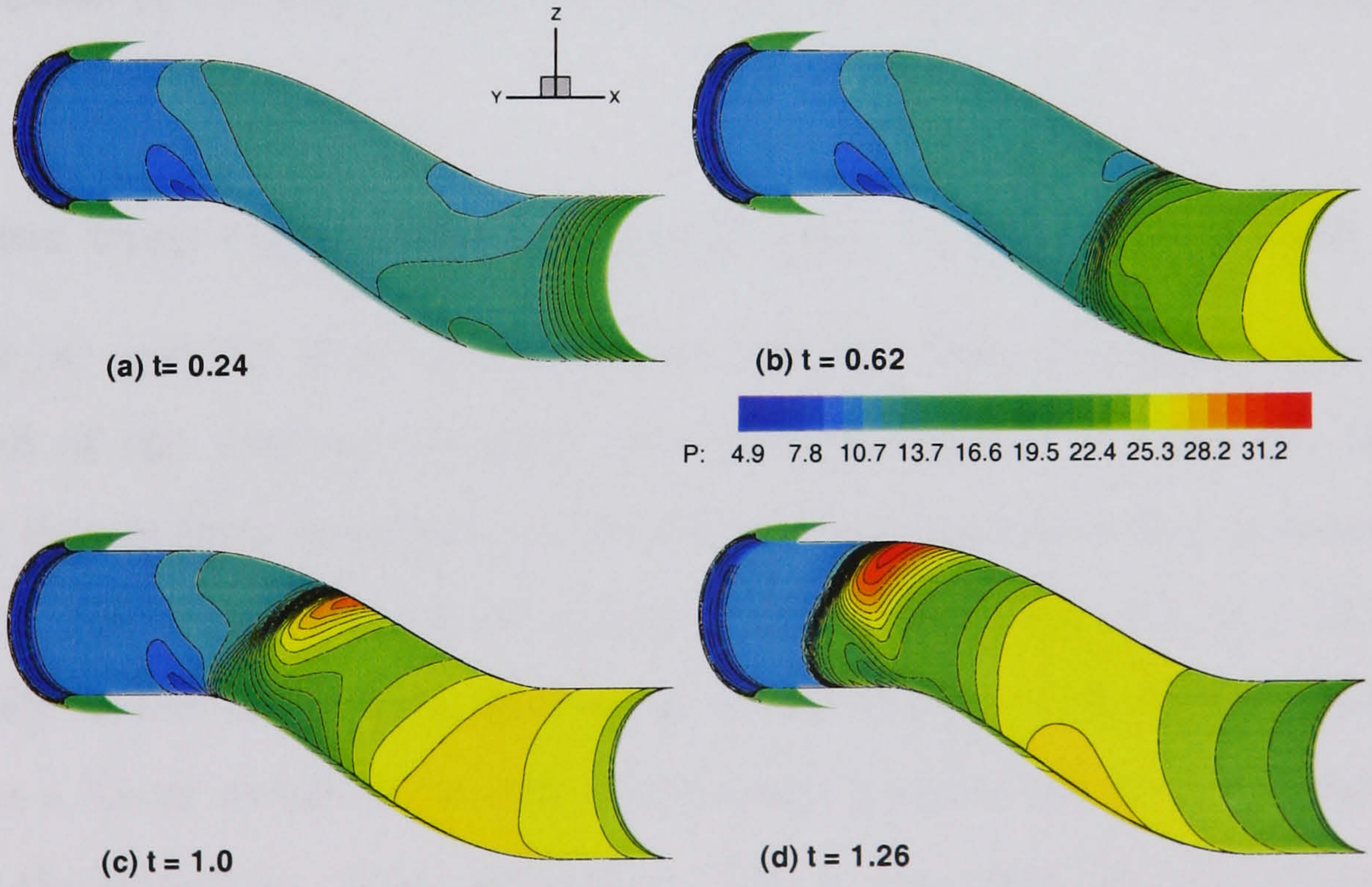

Figure 6.9: *HMFR SST calculation, OPR = 2, Surge signature 1 - Pressure from the duct wall at 4 instants leading up to surge exit*

6.4 Surge Signature 2

Figure 6.2 (c) shows signature 2 as recorded experimentally in reference [81] and the approximation used for the calculations herein (d). The first thing that should be noted about the recorded surge is that it is not possible to extract detailed information from this. No information on the actual engine on which it was recorded could be found and pressure levels are not clear. It was decided to apply the same assumptions used for the previous signature unless otherwise stated here.

Returning to figure 6.2 (c) and (d), it can be seen that the measured rise time of the surge is rapid ($\leq$ 1ms) which equates to a non-dimensionalised (reduced) value of around 0.05. Consequently the time-step also havs to be suitably small to capture this. It was decided in section 6.2.2 to use $\Delta t = 0.0005$. This gives 100 steps to capture the rise time alone in this case. Once the peak pressure has been reached it is held there briefly before dropping down. It is then held again at an OPR of 1.7 before linearly decreasing to 70% of the normal operating pressure. This is held for the remainder of the calculation. Examination of figure 6.2 (a) shows that there is a secondary peak. It is thought that this could possibly be a reflection of the hammershock travelling back down the intake to the engine face, as discussed for signature 1, and so this was not modelled.

Propagation from engine face to second bend: t = 0.0 → t = 0.62

Figure 6.10 (a) and (b) show pressure time histories from the engine face up to the second bend of the duct on the port and starboard sides. P1 and S1, the probes nearest the downstream boundary, show the pressure signature that is being applied. As discussed, the characteristics are a rapid rise to peak OPR of 2 (2 x 13.15) which is held briefly before a recession back to an OPR of 1.7, which again is held. There then follows a linear recession to 90% of the normal operating pressure which is held throughout the remainder of the calculation. Due to the rapid rise time the surge front forms much faster and reaches the first bend quicker than signature 1. Probes S5 and P4 register a rapid rise in pressure at around t=0.5. As the surge propagates around the second bend it can be seen that the pressure begins to rise more on the port side at P5.

Figure 6.11 (a) shows the symmetry plane Mach number with an inset of pressure from the port and starboard sides along the duct. With comparison to the same figure from signature 1 results, it can clearly be seen that the surge front has propagated considerably further upstream in the same time. The pressure along the port and starboard side walls shows a very steep gradient pressure front located at $X/D = 4.0$. It can be determined that the non-dimensional shock front speed equates to 4.17 which, when dimensionalised using equations described in section 2.1.1, and considering a freestream velocity of 71.47m/s, gives a surge speed of 297.8m/s.

Figure 6.12 (a) shows streamlines at the same instant. It can be seen that the rapid application of a surge leads to a much stronger flow stoppage and reversal behind the surge front, especially towards the starboard side, but also very close to the port wall. In this location the flow has a reduced energy after turning through the second bend and thus reversal of flow is possible. At this stage the the surge front has not influenced the separated region in any way.

Figures 6.13 and 6.14 (a) show symmetry plane and duct surface pressures respectively. From the symmetry plane pressures the strong pressure gradient across the surge front is clear and there is evidence of a higher pressure towards the port side. From 6.14 (a) this can be seen to be on the wall surface approximately between the two sides.

Propagation from second bend to first bend: t = 0.62 → t = 1.0

Again, figure 6.10 (c) and (d) show pressure time history from probes between the two bends. On the starboard side a rapid rise in pressure is visible at all probe points. As the surge front approaches the first bend starboard side this appears to have the effect of compacting the surge front. At S10 this is most prominent and the pressure pulse is considerably less full than at S6 for example. On the port side at P6, there is a sharp increase to a pressure that is nearly three times the normal operating pressure. This is an abrupt pulse and does not last long. The pressure then plateaus at a level comparable to that on the starboard side. As we move to probe P10, we see that the pressure pulse is not as full as seen in those probes further downstream and is similar to the starboard side probes.

In figure 6.11 (b), we can see that the surge front has negotiated the second bend.

A large region of high Mach number flow is generated in the normally separated region after the starboard side first bend. Figure 6.12 (b) shows the streamlines and confirms this. There is a strong circulatory motion to the flow in this location. The flow accelerating around the first bend meets this region and is forced towards the port side, around the recirculating region. At the downstream boundary there is still reversal of flow towards the starboard side and close to the port side wall.

Figures 6.13 and 6.14 (b) show that the region of high pressure in the symmetry plane behind the surge front is further developed towards the port side. Figure 6.14 (b) shows that this region must take up most of the port half of the duct and can be seen on the duct wall. These figures also show the distinct boundary between the normal steady flow conditions upstream and high pressure behind the surge front.

Propagation from first bend to freestream: t = 1.0 onwards

Returning to figure 6.10, plots (c) and (d) show the pressure in the cowl region as the surge front passes out of the duct. Again a rapid rise to peak can be seen similar to signature 1 at probes P11 and S11. There then follows a fairly constant pressure before there is a linear drop before a rise again at t=4.4. If we return to plots (a) and (b), we can see this secondary peak develop at probes P2 and S2 at t=2.4, around t=1.2 after the initial surge front exits the duct. It should also be noted that the initial surge front took around t=1.2 to propagate through the duct and so it is likely that this secondary peak is a reflection of the exiting initial surge wave. This secondary peak then starts to propagate upstream, and negotiates the two bends to enter the cowl section at t=4.1. It then exits the duct at t=4.5 and the disturbance can be seen on the external cowl surface at probes P12, P13 and P14 shortly after this (and similarly on the starboard side).

Figure 6.11 and 6.12 (c) shows the pressure front as it enters the cowl region. Downstream of the front the region of high Mach number associated with the recirculating flow is clear and can be seen in the streamlines to be stretched out compared to its size at t=0.62. In (d) we see that the surge front has moved to the highlight of the duct and the maximum pressures in the cowl region have reduced. The recirculating region has stretched out still further and the core appears to begin to be moving back downstream. At this stage flow reversal out of the duct occurs near the port and starboard walls. At (e) we see that the recirculation has almost broken down. There is a significant flow reversal region towards the starboard side at the highlight. Flow begins to recover downstream of the first bend. There is still outflow, particularly on the starboard side, and vortices are created on the outer cowl surface as a result of this outflow (or spillage). As we move on to (f) the spillage out of the duct begins to reduce. Towards the downstream boundary the flow out of the domain begins to reduce once more as the secondary wave forms and begins to propagate upstream. By (g) it has reached the second bend and by (j) it has exited to freestream.

Figures 6.13 and 6.14 again show symmetry plane and surface pressures at t=1.0 in (c) and t=1.26 in (d). At t=1.0 it can be seen that the pressure towards the port side has increased significantly and there is an abrupt change from the low pressure region in the cowl region under normal steady conditions. As the surge front moves on to the cowl highlight (d) the peak pressure moves towards the centre of the duct and pressures on the duct walls drop off.

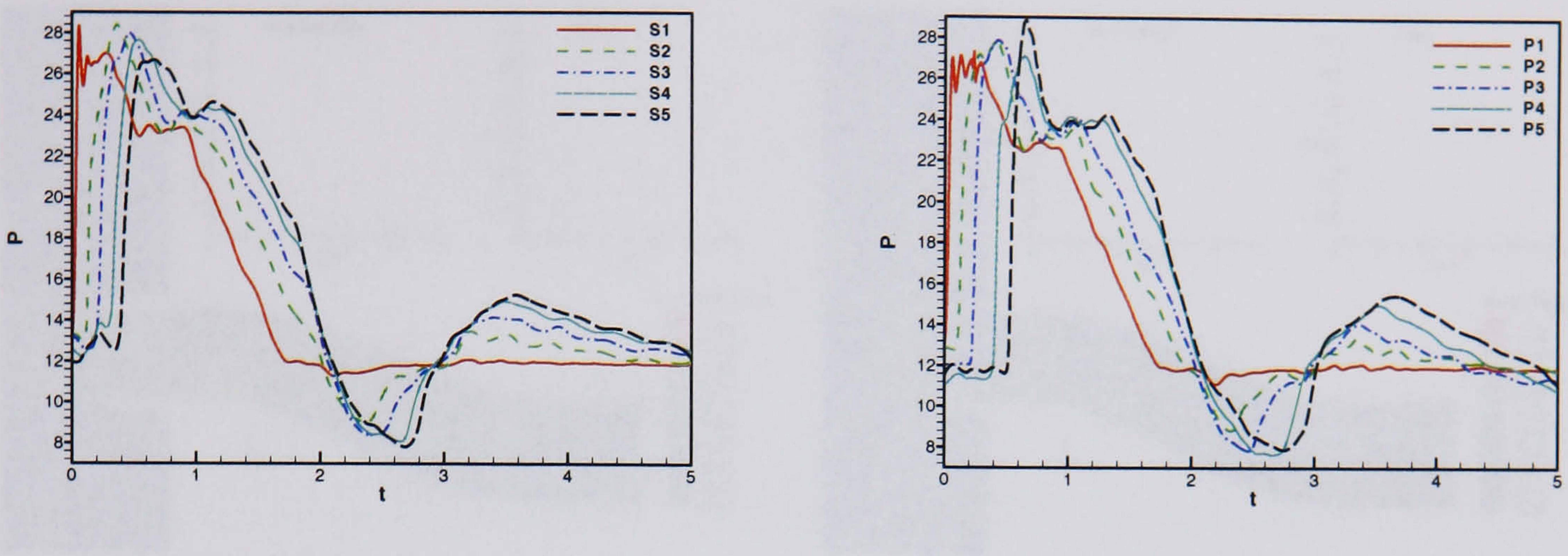

(a) Starboard probes 1 - 5 (b) Port probes 1 - 5

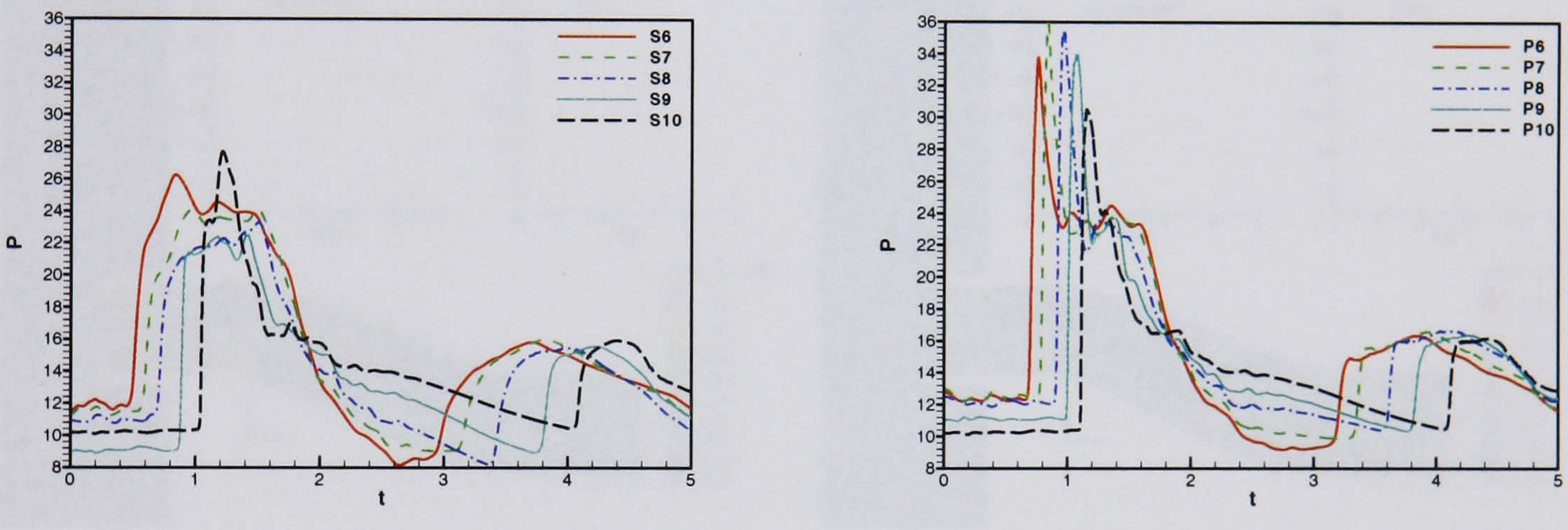

(c) Starboard probes 6 - 10 (d) Port probes 6 - 10

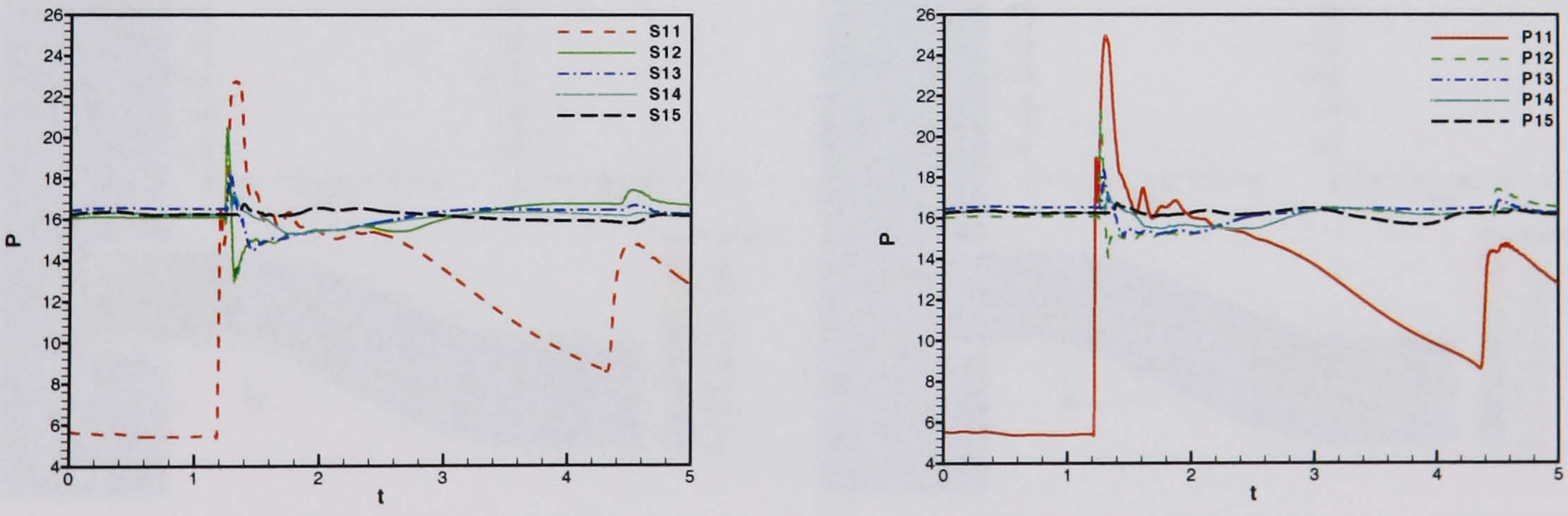

(e) Starboard probes 11 - 15 (f) Port probes 11 - 15

Figure 6.10: *HMFR SST calculation, OPR = 2, Surge signature 2 - Symmetry plane probe data*

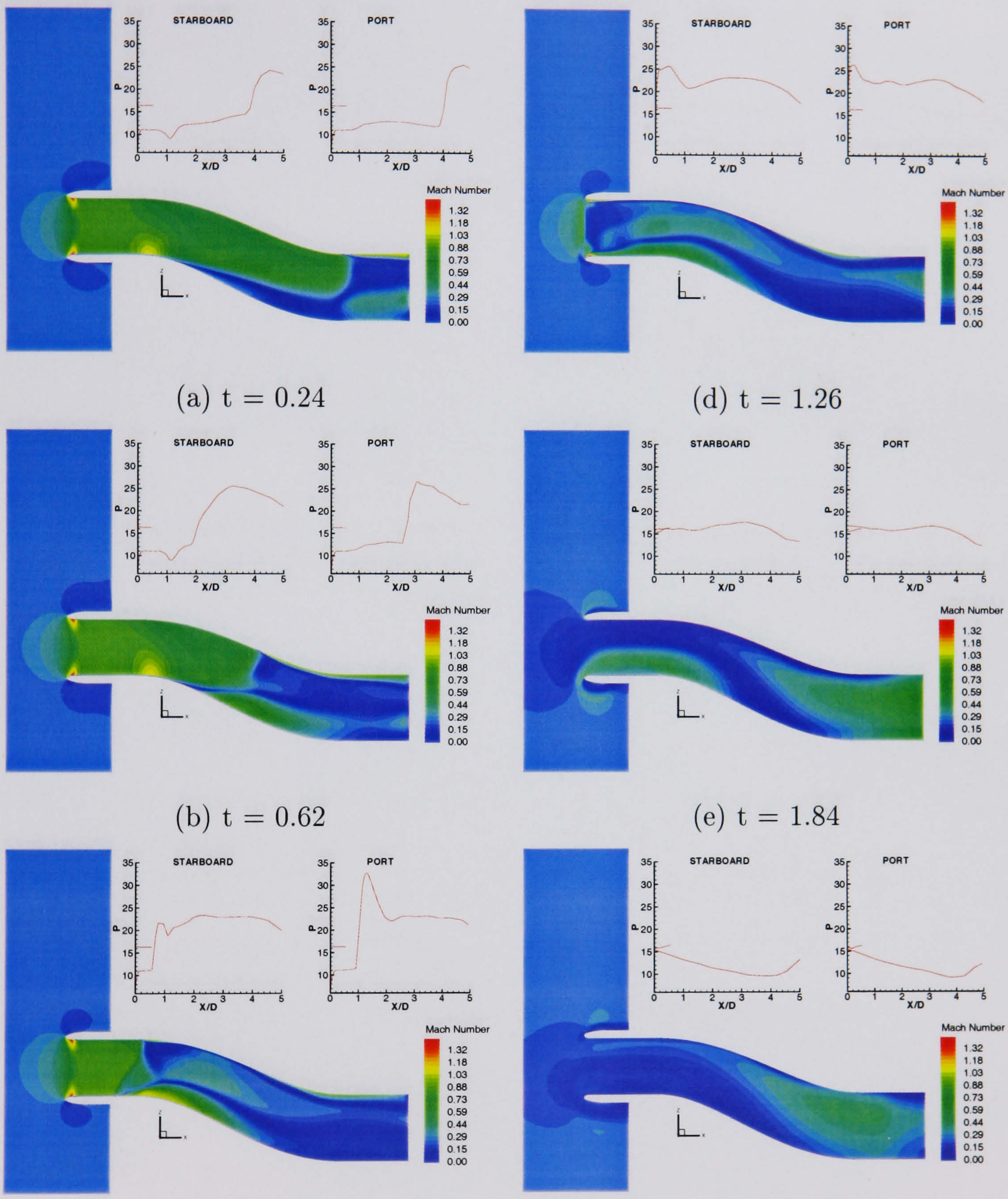

(a) t = 0.24

(d) t = 1.26

(b) t = 0.62

(e) t = 1.84

(c) t = 1.00

(f) t = 2.40

Figure 6.11: *HMFR SST calculation, OPR = 2, Surge signature 2 - Symmetry plane Mach number and pressure traces*

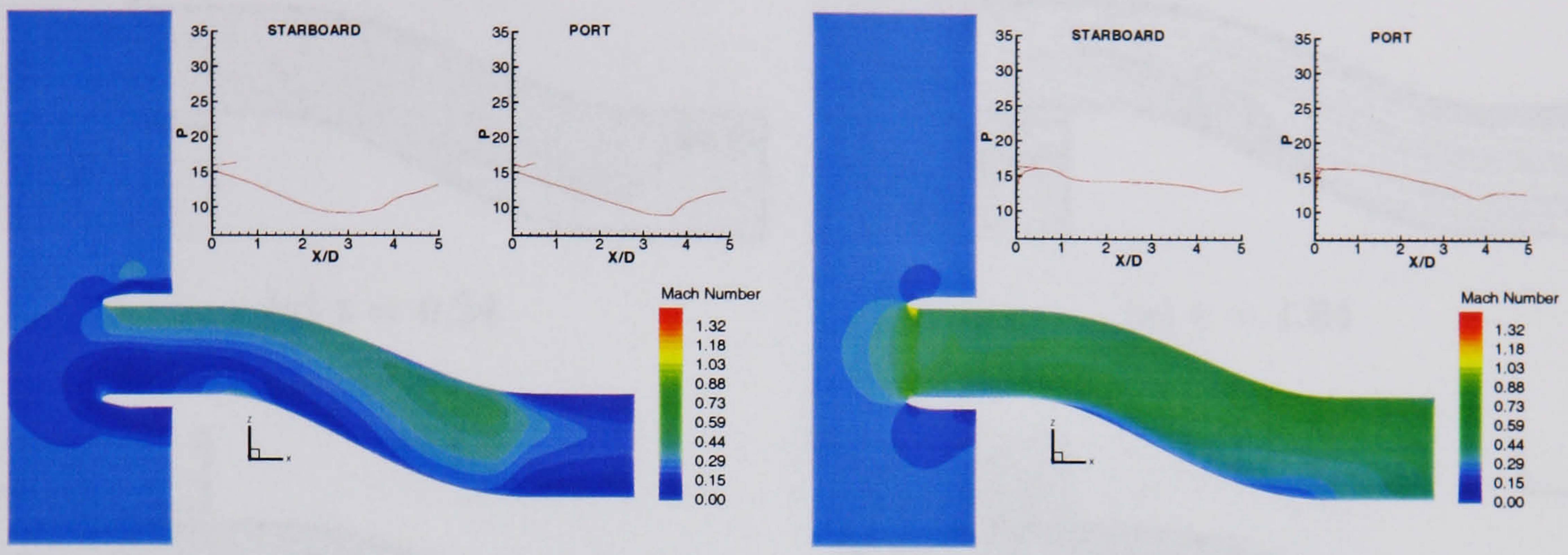

(g) t = 2.62

(j) t = 4.38

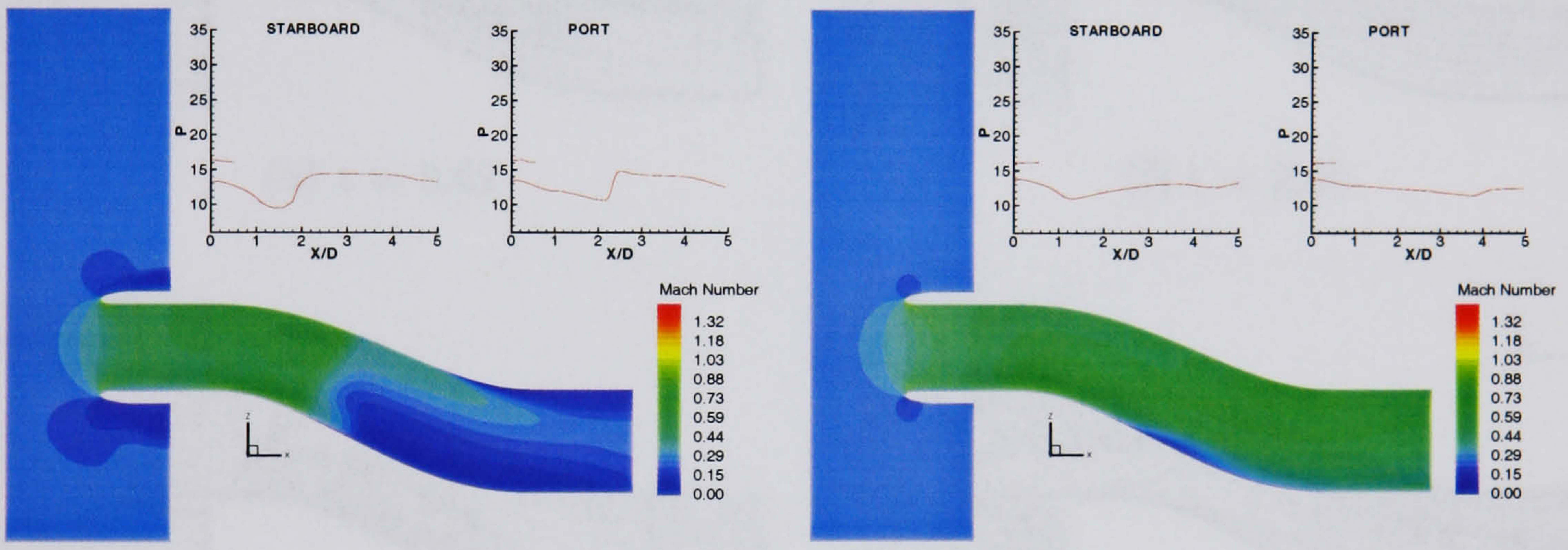

(h) t = 3.26

(k) t = 4.98

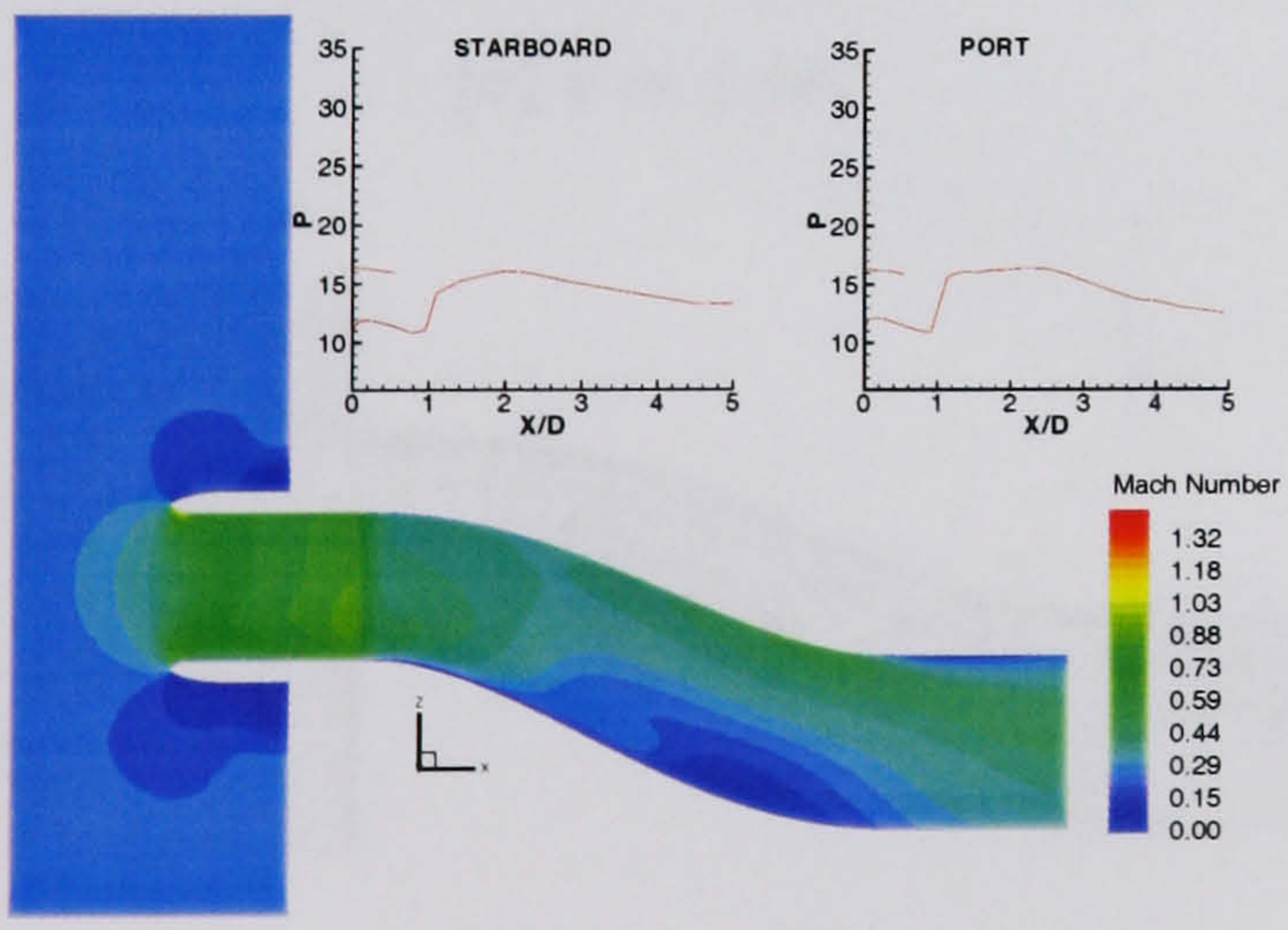

(i) t = 3.82

Figure 6.11: (cont.) *HMFR SST calculation, OPR = 2, Surge signature 2 - Symmetry plane Mach number and pressure traces*

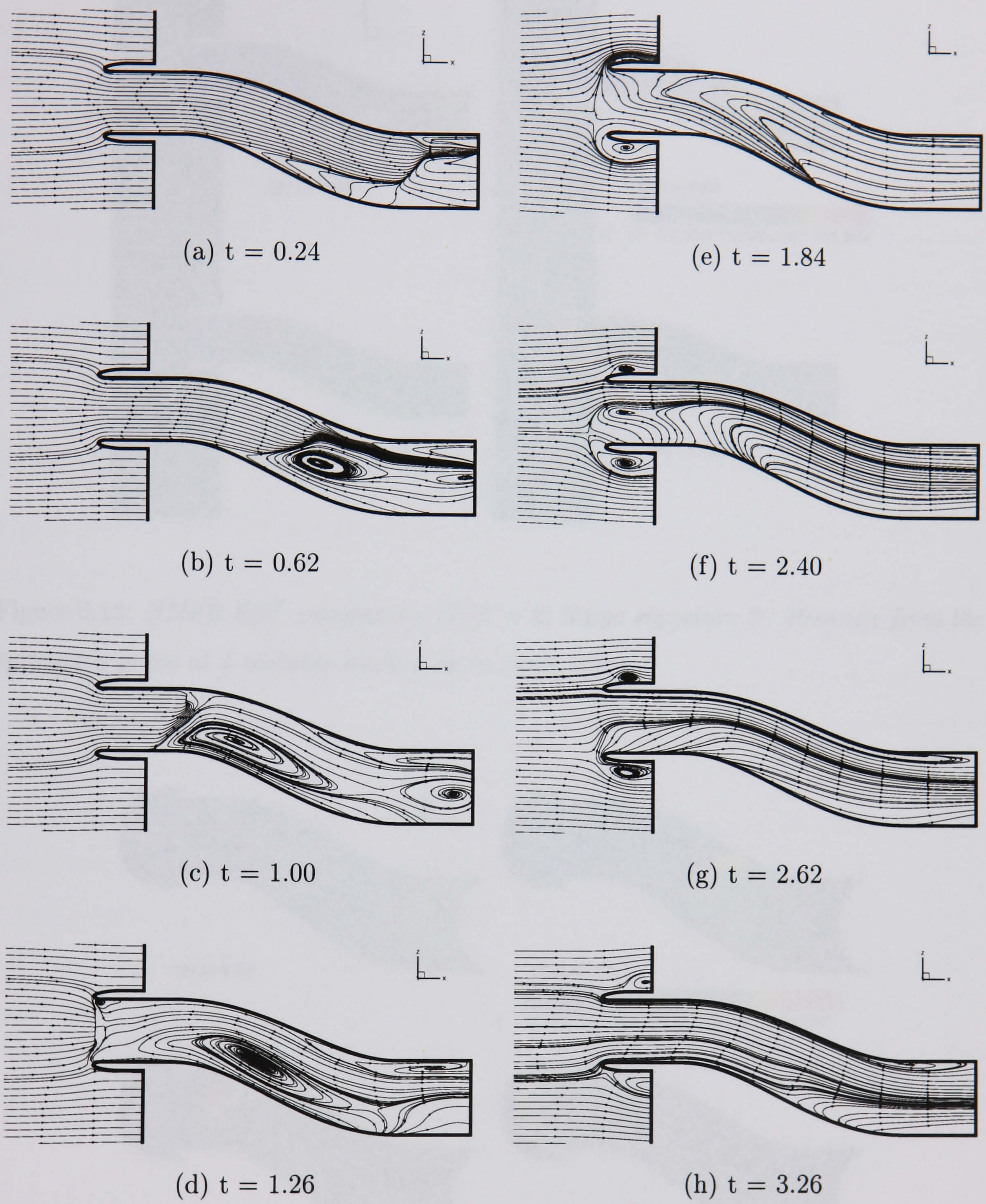

(a) t = 0.24

(e) t = 1.84

(b) t = 0.62

(f) t = 2.40

(c) t = 1.00

(g) t = 2.62

(d) t = 1.26

(h) t = 3.26

Figure 6.12: *HMFR SST calculation, OPR = 2, Surge signature 2 - Symmetry plane streamlines*

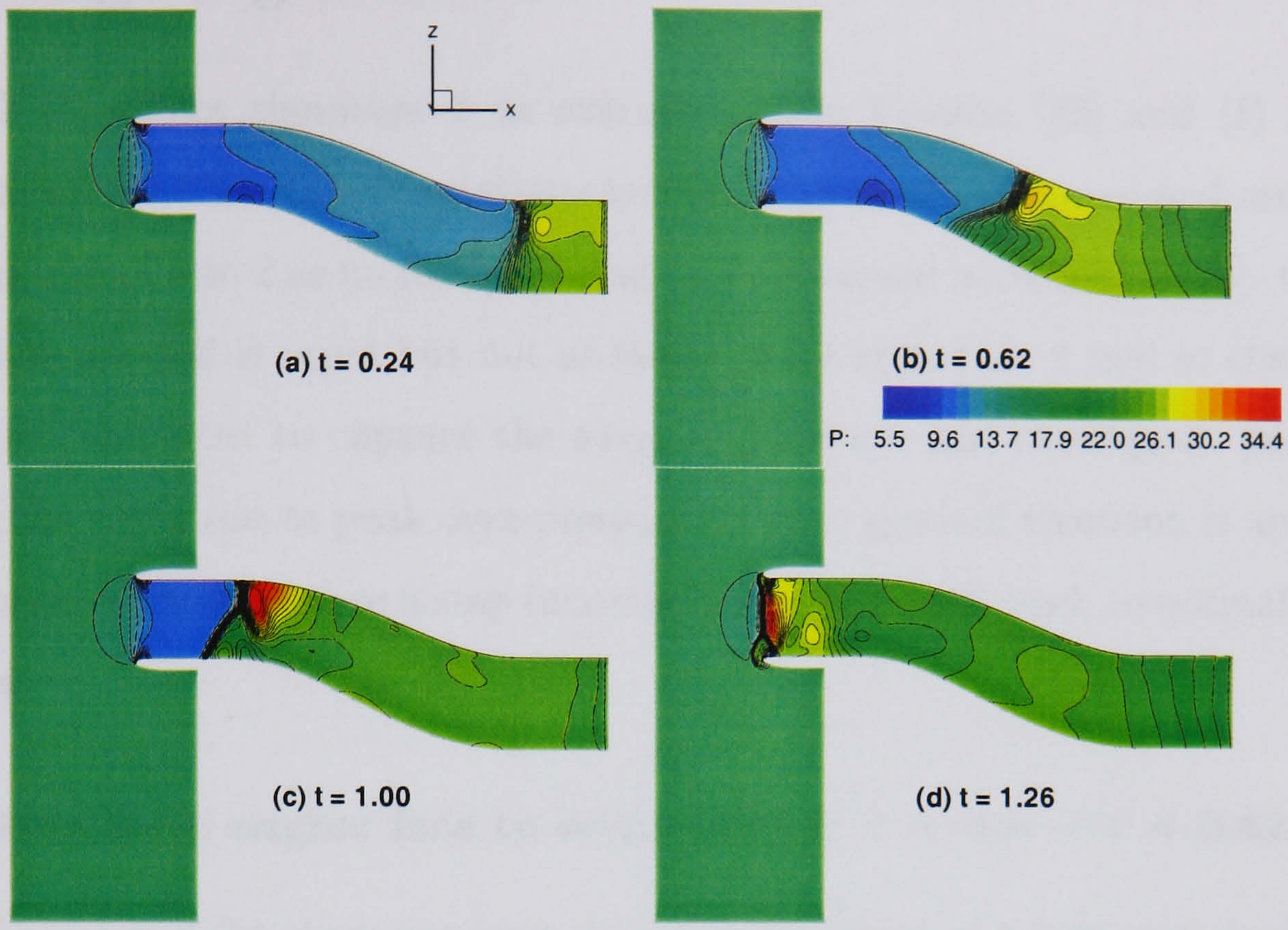

Figure 6.13: *HMFR SST calculation, OPR = 2, Surge signature 2 - Pressure from the symmetry plane at 4 instants leading up to surge exit*

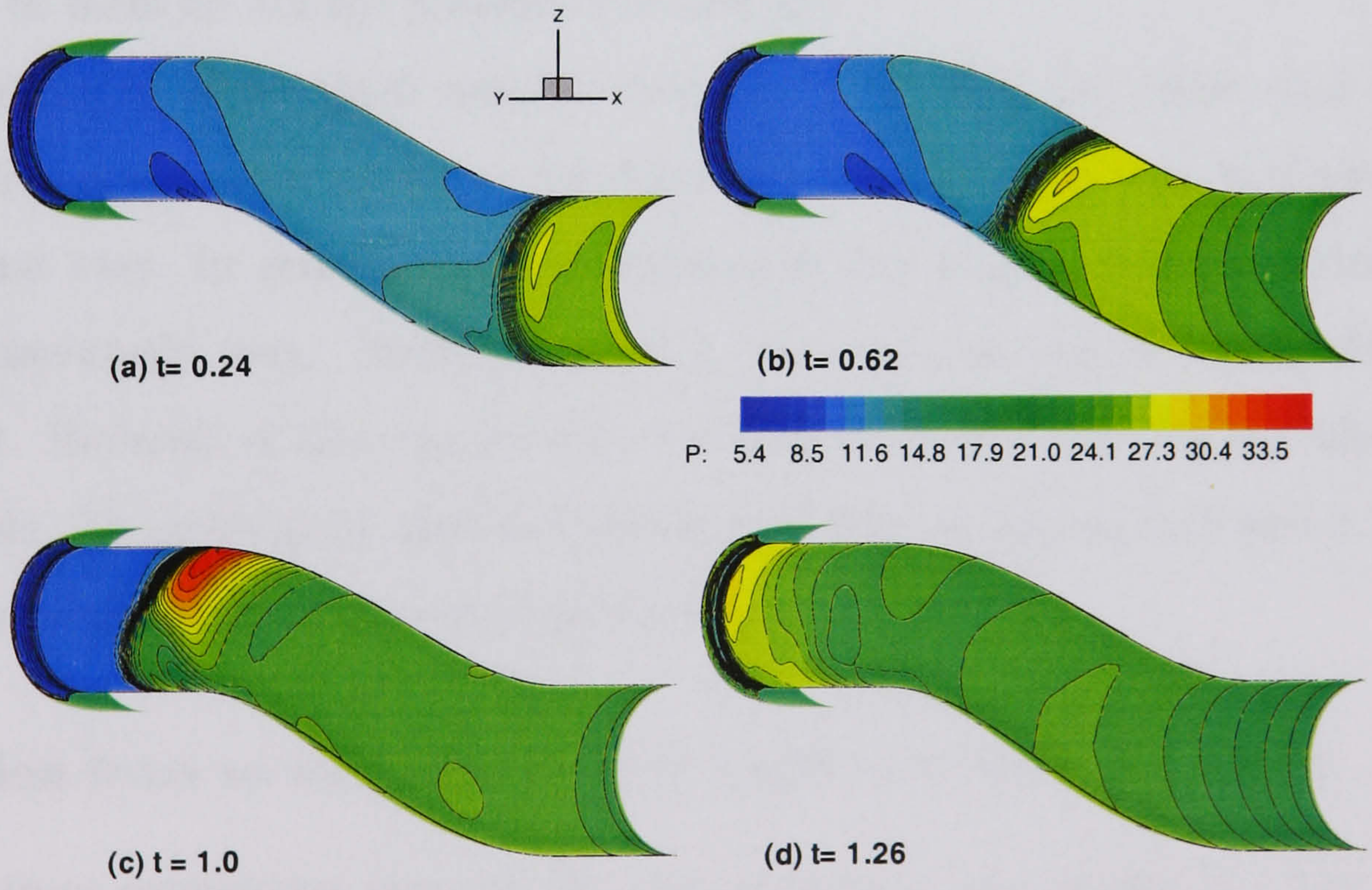

Figure 6.14: *HMFR SST calculation, OPR = 2, Surge signature 2 - Pressure from the duct wall at 4 instants leading up to surge exit*

6.5 Surge Signature 3

Figure 6.2 (e) shows signature 3 as extracted from Causon [28] and (f) shows the approximation used for the calculations herein. The conditions assumed are the same as for signatures 1 and 2 as no further details are contained in reference [28]. Once more the rise time applied is rapid but not as much as for signature 2 and so the time step is considered sufficient to capture the surge application and consequent propagation. Following the rapid rise to peak over-pressure, a more gradual recession is applied back to a minimum pressure before a step increase brings the OPR back to normal operating conditions.

Propagation from engine face to second bend: t = 0.0 → t = 0.62

Figure 6.15 (a) and (b) show pressure time histories from the port and starboard side walls from the downstream boundary to the second bend. Again this signature features a rapid rise to peak over pressure after t=0.2. As the surge wave propagates towards the second bend the pressure increases towards the port side, as seen in the previous surge signatures examined. As we move from P1 to P5, the peak pressure can be seen to develop to form an abrupt pressure rise and fall.

The symmetry plane Mach number contours (Fig. 6.16 (a)) show that the surge front has not propagated as far as for signature 2 as the rise time is slightly slower than for that case. In general the flow features at this stage are very similar to what has been previously seen. Streamlines (Fig. 6.17 (a)) also show similar features to signature 2. Reversal of flow can be seen towards the starboard side but also close to the port side. The symmetry and wall pressure isolines in figures 6.18 and 6.19 (a) are also similar to signature 2 described previously.

Propagation from second bend to first bend: t = 0.62 → t = 1.0

The surge front propagates through the second bend in the intake in much the same fashion to signature 2. Figure 6.15 (c) and (d) show that the pressure levels generated are not as high as seen for signature 2. This is most likely because signature 2 features a faster rise time to peak, and this peak pressure is help for a short period. In signature 3, once the peak OPR is reached, there follows an immediate linear recession. The fullness of the pulse reduces as it propagates through the duct. Once the surge front approaches the first bend the duration of the high over pressure is only of the order of t=0.2 on the port side.

The Mach number contours from the symmetry plane in figure 6.16 (b) and (c) show that the leading edge of the surge front goes past the second bend creating a strong circulating region that propagates upstream, close to the starboard side behind the surge front, as we have previously seen. This is also visible in figure 6.17 (b) and (c). With reference to signature 2, it can be seen in figures 6.18 and 6.19 (b) and (c) that the surge front from signature 3 does not propagate as far due to the reduced time that the peak pressure is applied. It can also be seen that the pressure levels are less on the duct surface and do not cover as large an area as for signature 2.

Propagation from first bend to freestream: t = 1.0 onwards

Returning to figure 6.15, (e) and (f) show the pressure probes at the cowl. The surge exits the duct at about t=1.3. The form is very similar to what has been previously seen, particularly in signature 2 which features a similarly rapid rise to peak. Again there appears to be a reflection of the surge exit felt at the downstream boundary. The time taken for the surge to exit the duct, and a similar time taken for a reflection to travel back down the intake equates to a reflection at the downstream boundary at about t=2.6 which is around the time that probes S2 and P2 record a pressure rise. It should be remembered that a feature of this signature is a sharp rise from an OPR of 0.8 (following the recession from peak OPR) to an OPR of 1 that is held for the remainder of the calculation. The sharp rise to OPR=1 coincides with the reflection captured at the downstream probes. This probably has the effect of increasing the strength of the reflection as it can be seen to be stronger than witnessed in signature 2 for example.

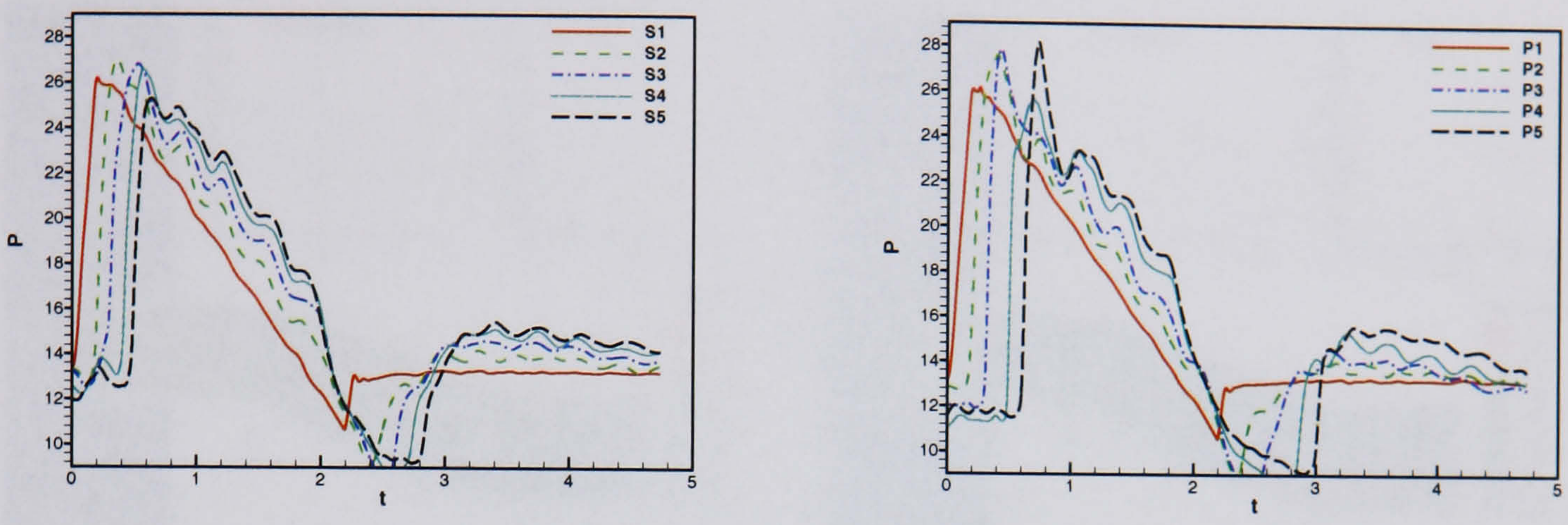

(a) Starboard probes 1 - 5

(b) Port probes 1 - 5

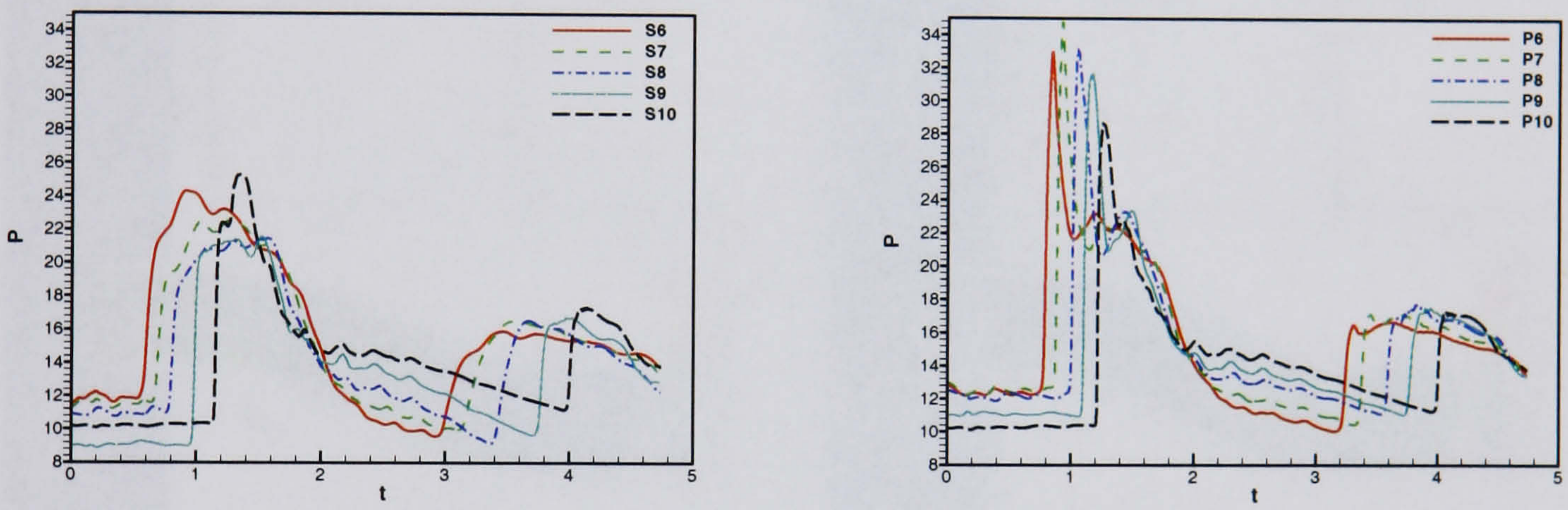

(c) Starboard probes 6 - 10

(d) Port probes 6 - 10

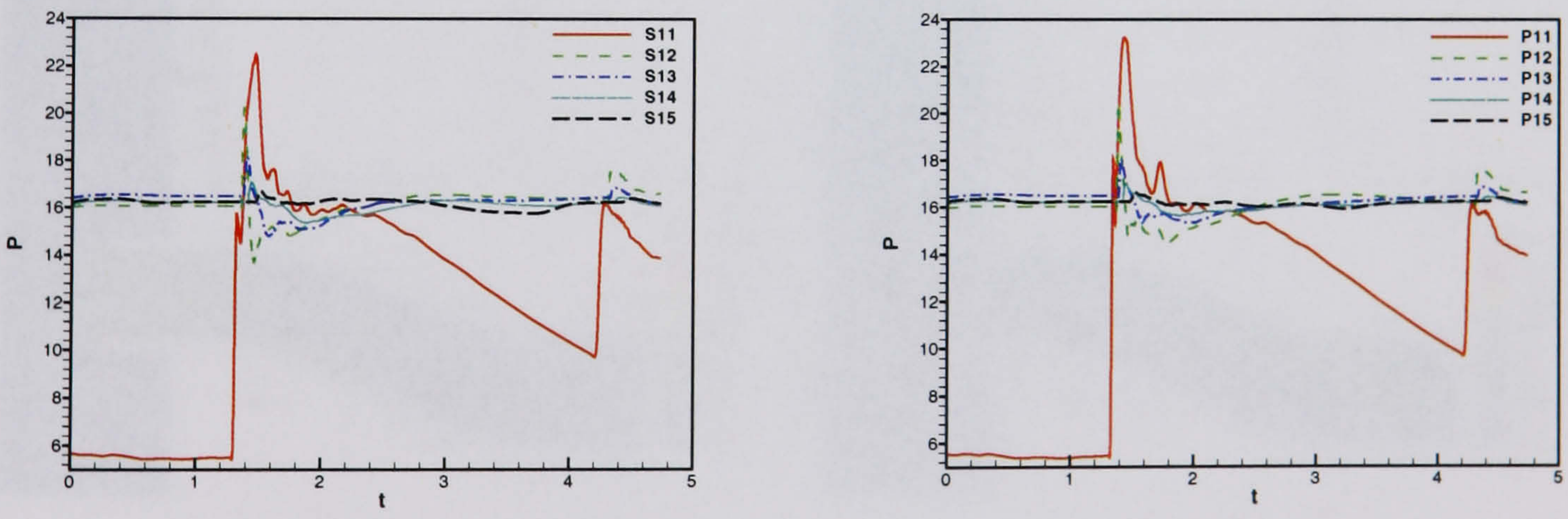

(e) Starboard probes 11 - 15

(f) Port probes 11 - 15

Figure 6.15: *HMFR SST calculation, OPR = 2, Surge signature 3 - Symmetry plane probe data*

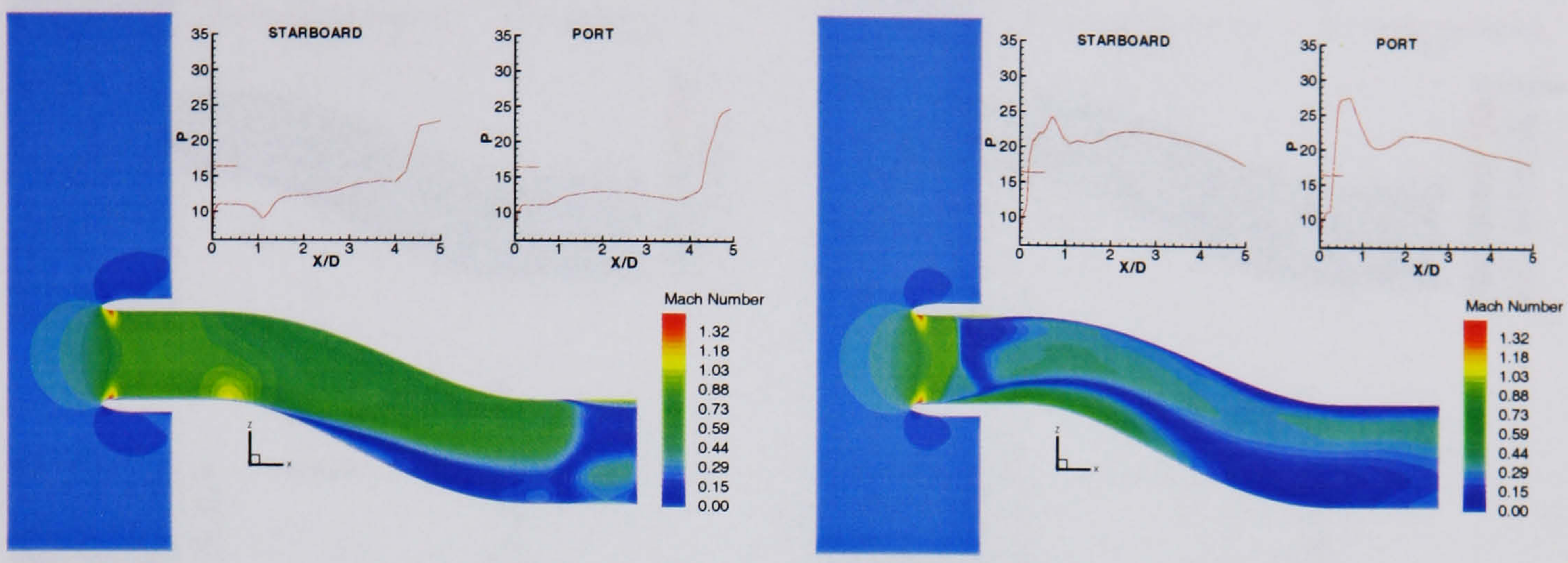

(a) t = 0.24

(d) t = 1.26

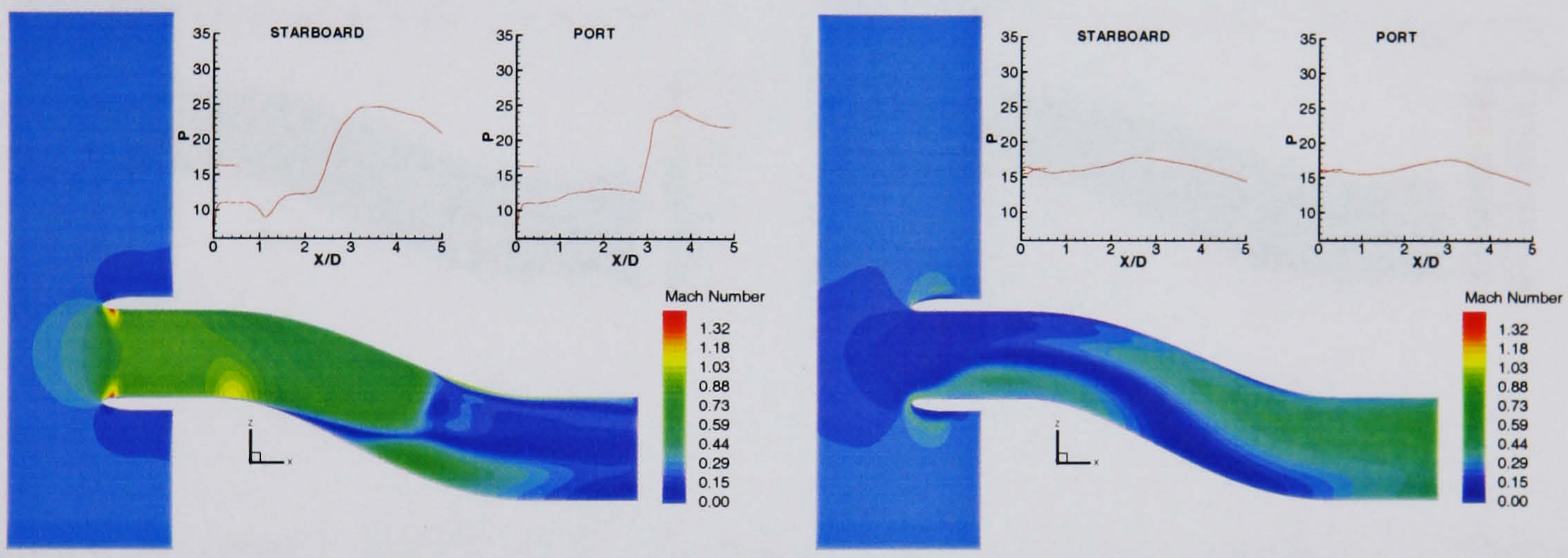

(b) t = 0.62

(e) t = 1.84

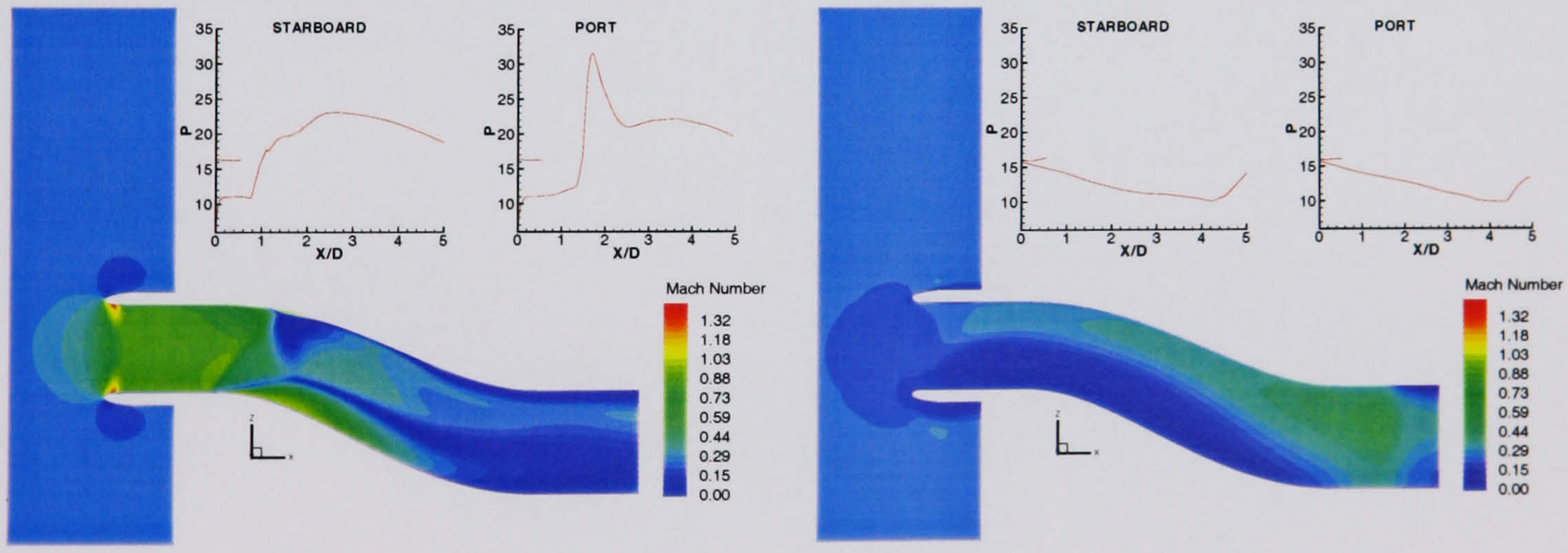

(c) t = 1.00

(f) t = 2.40

Figure 6.16: *HMFR SST calculation, OPR = 2, Surge signature 3 - Symmetry plane Mach number and pressure traces*

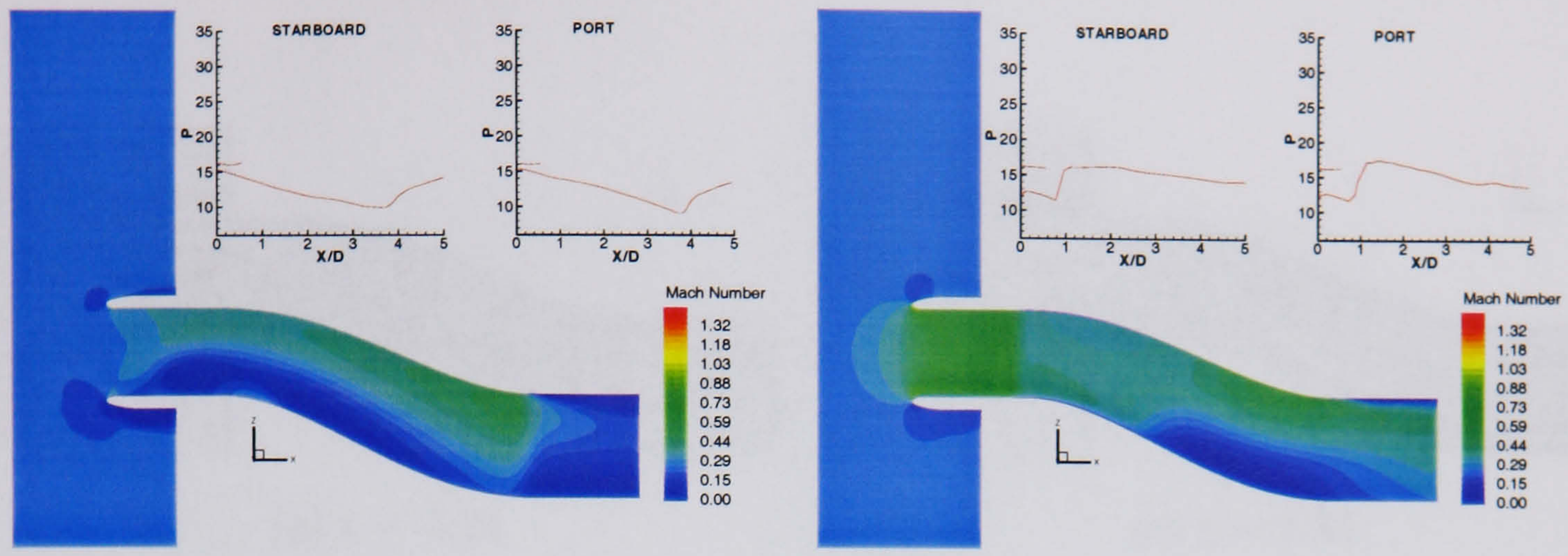

(g) t = 2.62

(i) t = 3.82

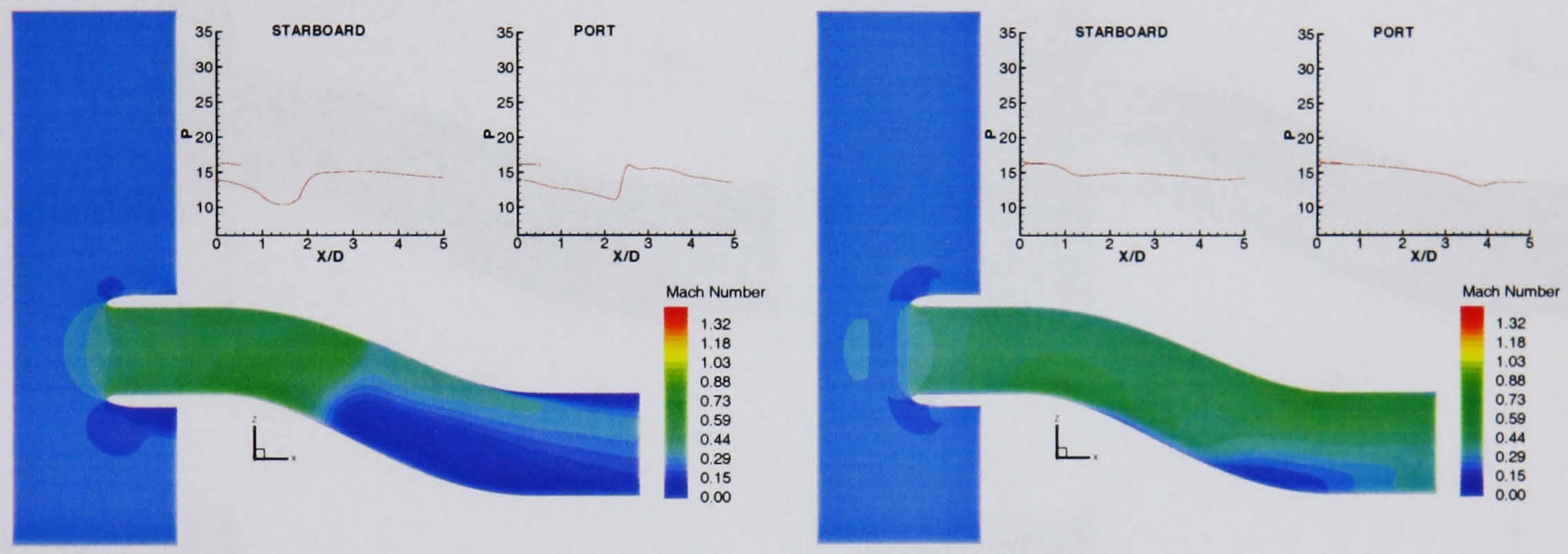

(h) t = 3.26

(j) t = 4.38

Figure 6.16: (cont.) *HMFR SST calculation, OPR = 2, Surge signature 3 - Symmetry plane Mach number and pressure traces*

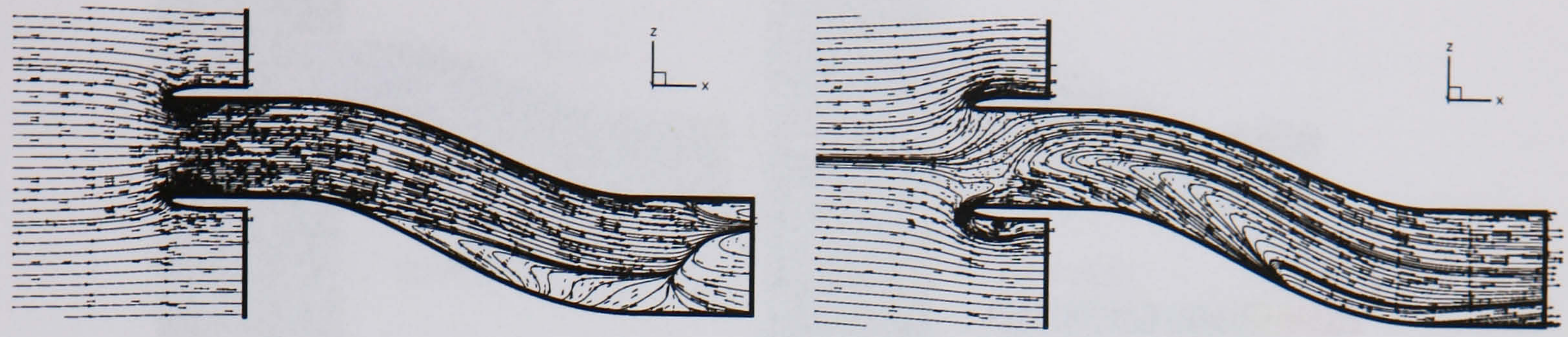

(a) t = 0.24

(e) t = 1.84

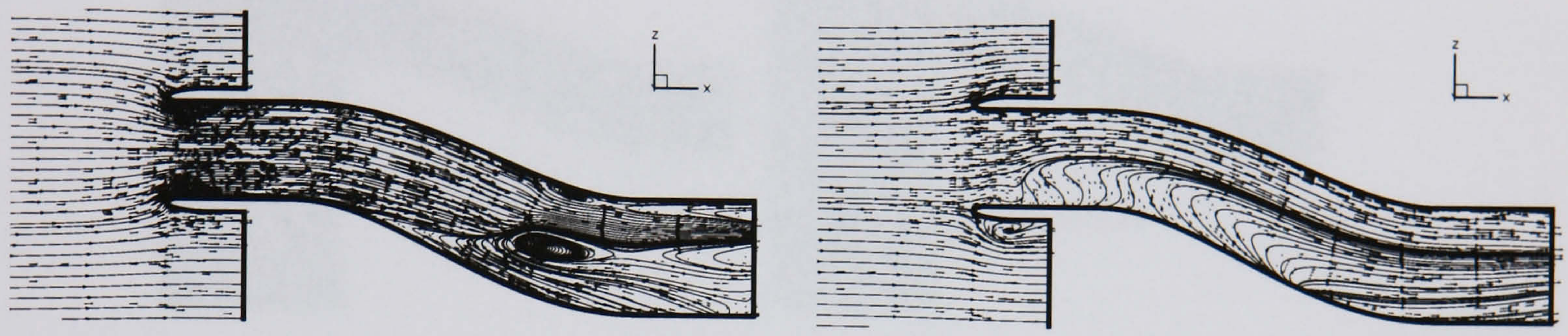

(b) t = 0.62

(f) t = 2.40

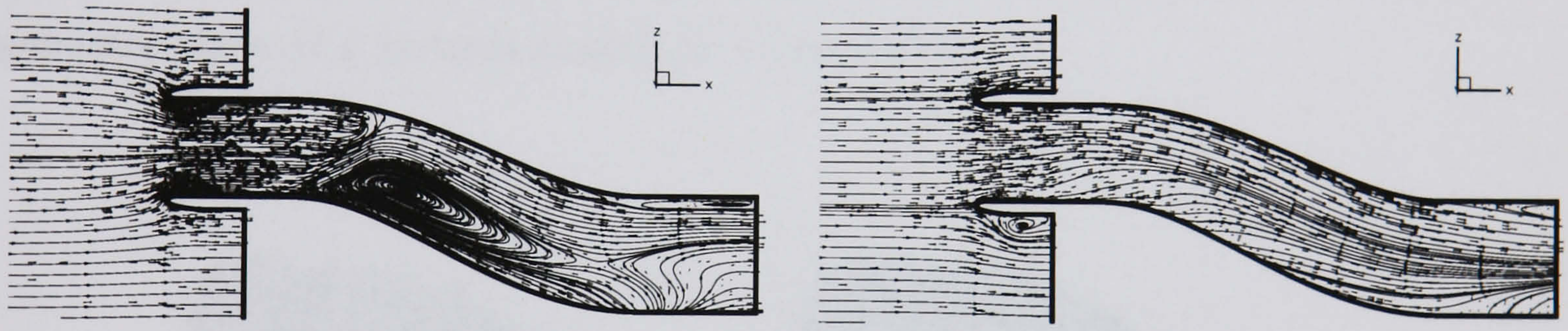

(c) t = 1.00

(g) t = 2.62

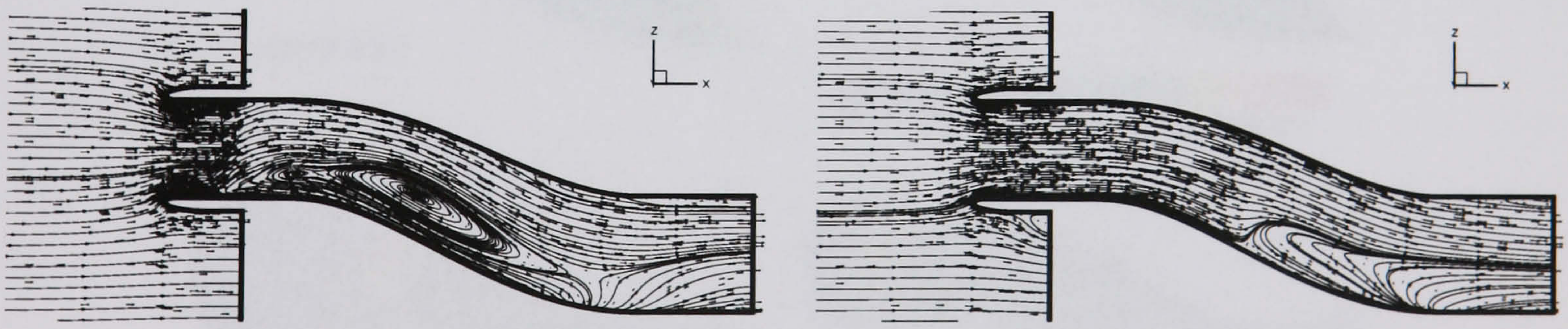

(d) t = 1.26

(h) t = 3.26

Figure 6.17: *HMFR SST calculation, OPR = 2, Surge signature 3 - Symmetry plane streamlines*

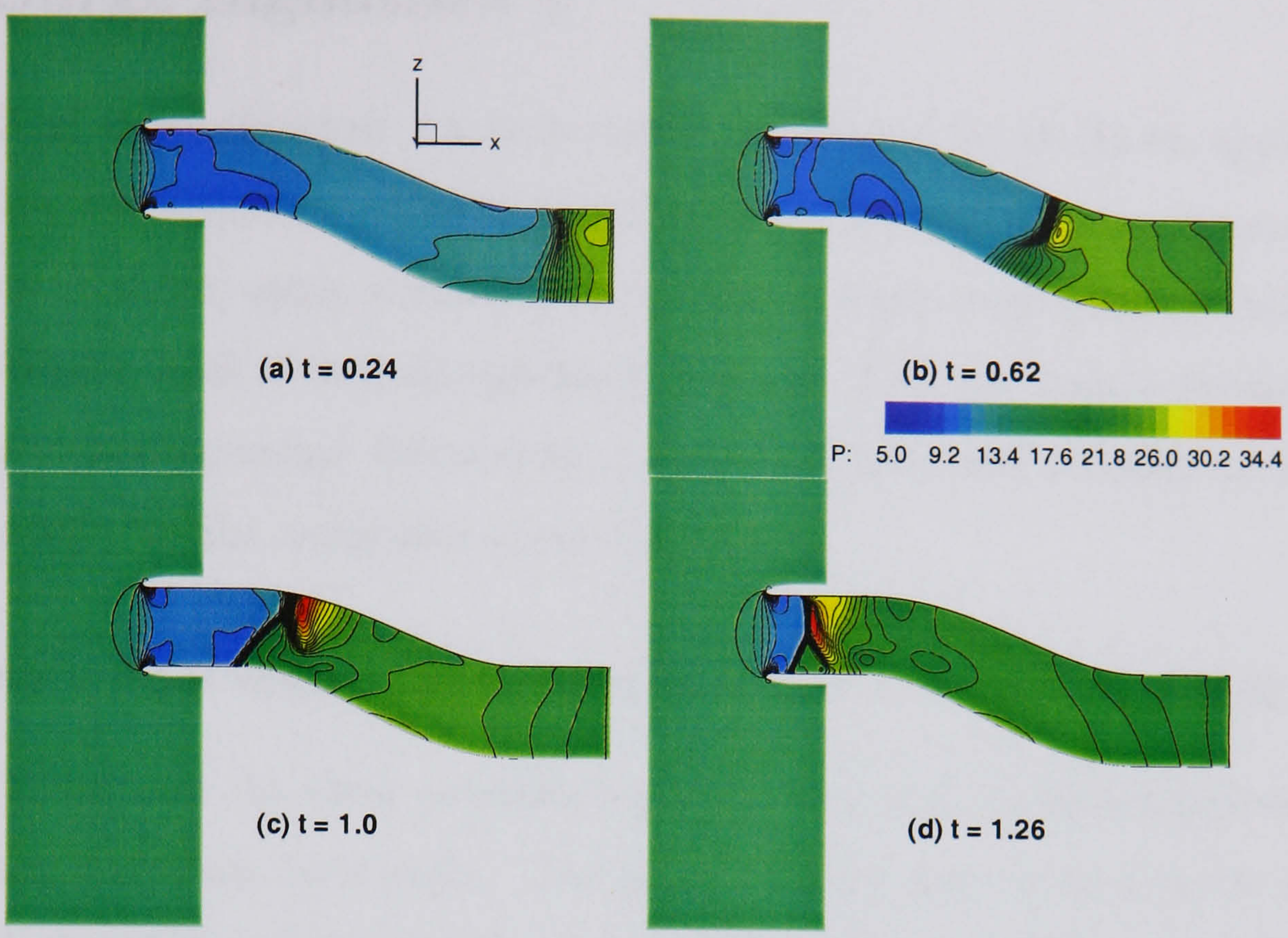

Figure 6.18: *HMFR SST calculation, OPR = 2, Surge signature 3 - Pressure from the symmetry plane at 4 instants leading up to surge exit*

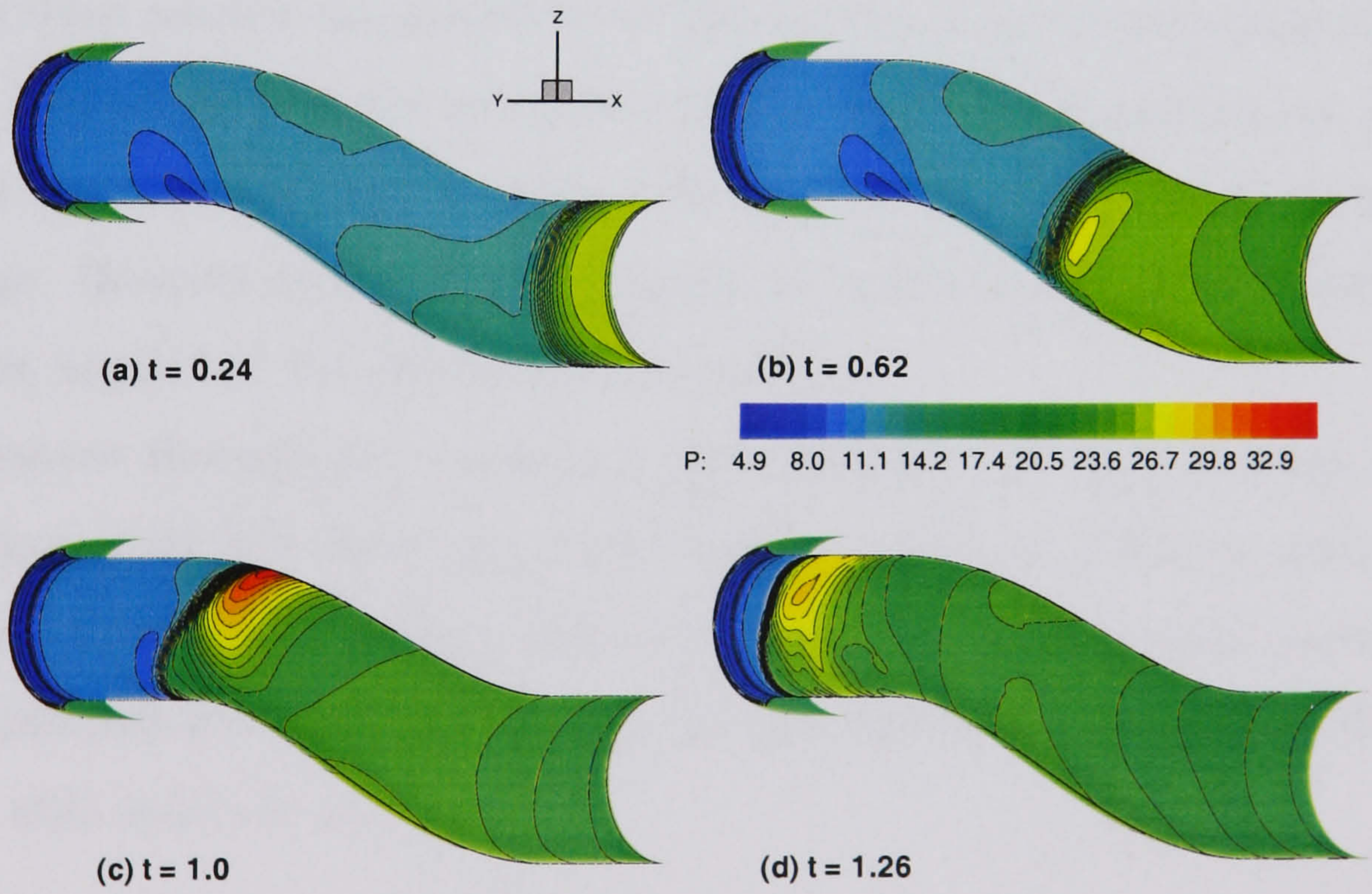

Figure 6.19: *HMFR SST calculation, OPR = 2, Surge signature 3 - Pressure from the duct wall at 4 instants leading up to surge exit*

6.6 Surge Signature 4

Figure 6.2 (g) shows signature 4 as extracted from [26] and (h) shows the approximation used for the calculations. Assumed conditions are the same as for signatures 1 - 3. Ytterstrom et al [26] apply a much greater time to reach peak pressure followed by a similar recession back to normal operating pressure. This has been approximated as a linear rise to peak pressure followed by a linear recession and recovery to an OPR of 0.7 that is held for the remainder of the calculation.

Propagation from engine face to second bend: t = 0.0 → t = 0.62

Figure 6.20 (a) and (b) show pressure from the port and starboard probes near the downstream boundary once more. The peak pressure can be seen to be applied at P1 and S1 at t=1.2 and the pressure gradient is gentle compared to previous applied signatures. As the surge propagates towards the second bend the pressure gradient increases, particularly on the port side.

The symmetry plane Mach number contours shown in figure 6.21 show that the propagation of the surge front is slower than for signatures 2 and 3. As the leading edge of the front reaches the second bend (figure (b)) it can be seen that there is not significant interaction with the secondary flow as yet. The streamlines in figure 6.22 (b) confirm that no significant reversal of flow has occurred behind the pressure front at this stage. However at this stage it should be remembered that the peak pressure has not been applied at the downstream boundary.

The pressure through the symmetry plane (Figure 6.23 (a)) and the duct wall pressure (figure 6.24 (b)) show that a high pressure gradient develops much faster on the port side of the duct (pressure waves coalescing) compared to the starboard side. Pressures upstream are unaffected at this stage and downstream boundary OPR's being applied are still relatively low.

Propagation from second bend to first bend: t = 0.62 → t = 1.26

Returning to figure 6.20 (c) and (d), it can be seen that the development of the steep pressure gradient across the surge front continues on both sides of the duct. Peak pressures generated are considerably less than witnessed for other signatures, even signature 1 which also has a slower rise time. The maximum pressure appears to occur on the port wall between probes 8 and 9 at the first intake bend where an abrupt rise in pressure occurs similar to previous signatures.

The Mach number contours from the symmetry plane show that interaction of the propagating surge front with the secondary flow region occurs a lot later in this case. The secondary recirculating flow can be seen to propagate upstream in figures 6.22 (c) and (d). Figure 6.23 (c) shows the pressure through the symmetry plane and features a clustering of the isolines on the port side that has developed. At t=1.26 the peak pressure has eventually been applied at the downstream boundary. It can be seen that the leading edge of the surge front is already approaching the first bend at this stage.

Propagation from first bend to freestream: t = 1.26 onwards

Returning to figure 6.20, the surge front can be seen to exit the intake duct at about t=1.9. Spillage is induced behind the surge front as it exits, primarily on the starboard side as seen in the Mach contour plots and streamlines of figures 6.21 and 6.22. A reflection is again induced that reaches the downstream boundary at about t=3.3. This propagates upstream and exits the duct at around t=4.9 (in comparison to about t=4.1 for signature 3).

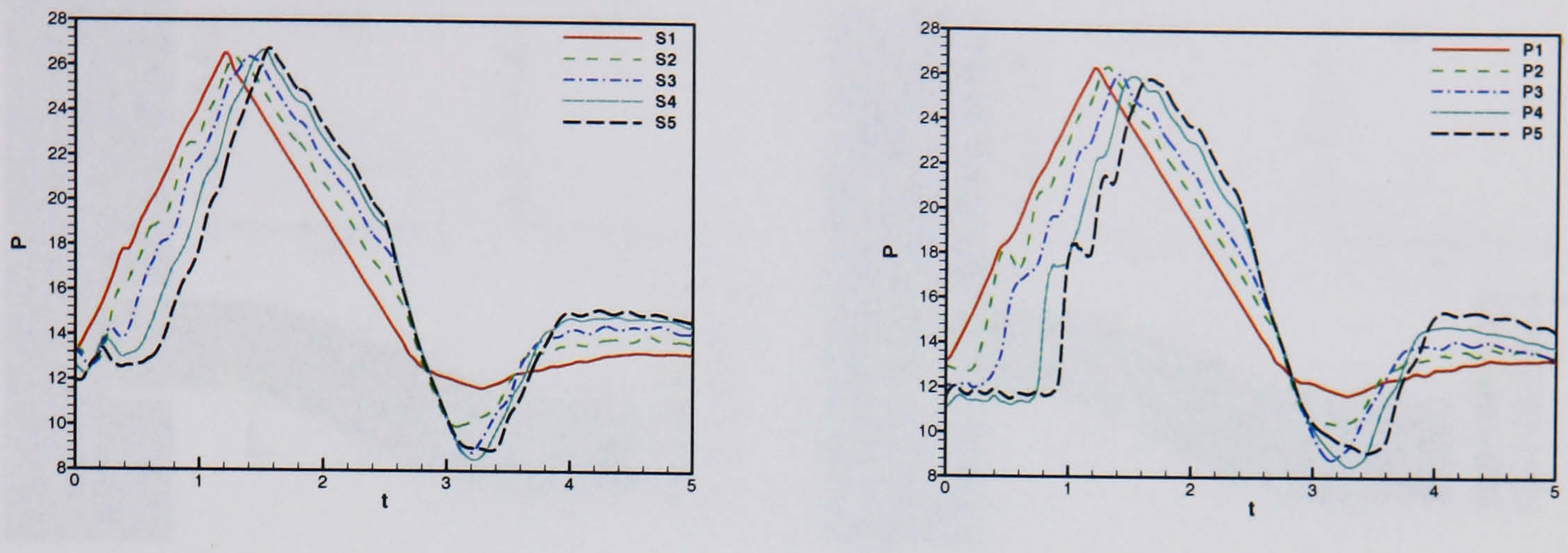

(a) Starboard probes 1 - 5

(b) Port probes 1 - 5

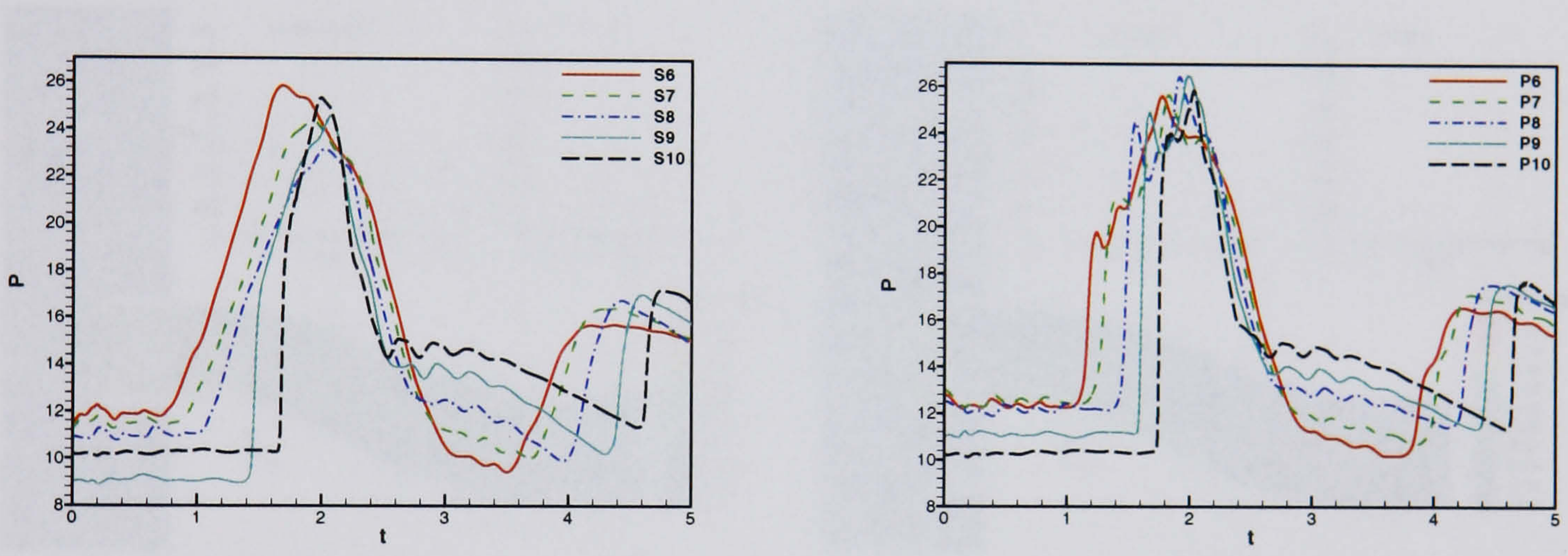

(c) Starboard probes 6 - 10

(d) Port probes 6 - 10

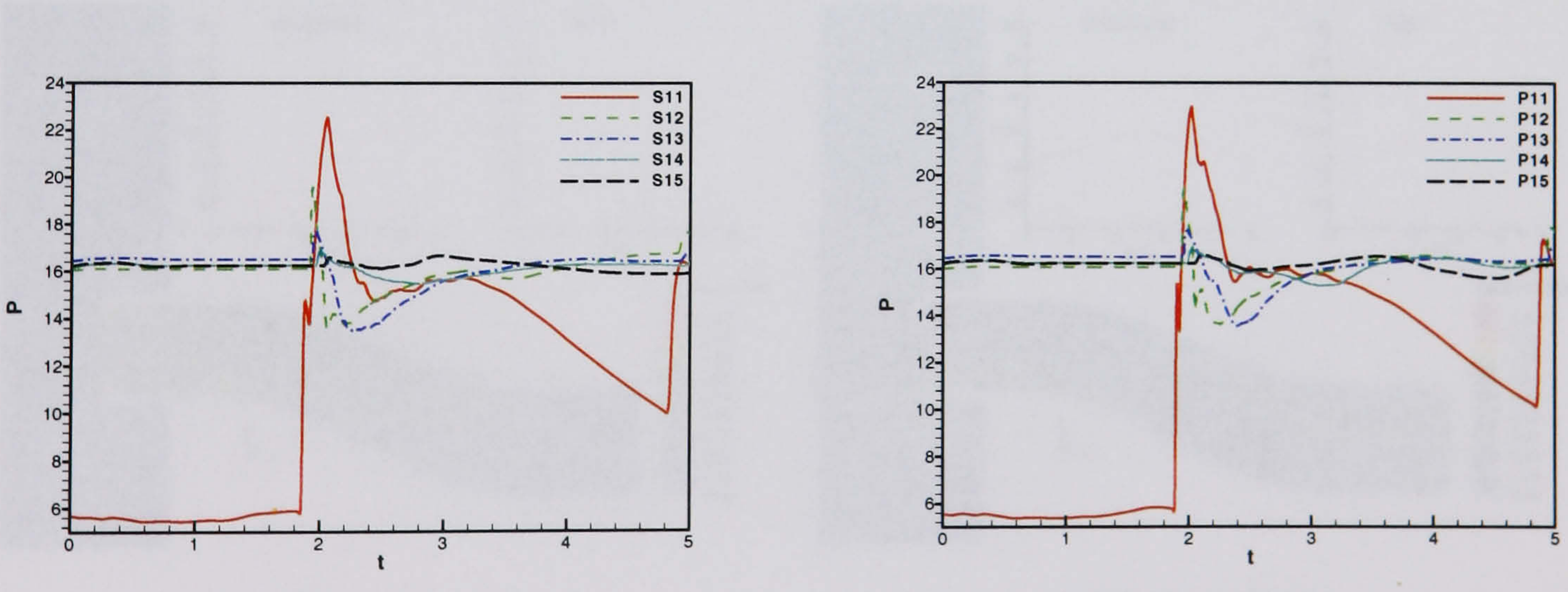

(e) Starboard probes 11 - 15

(f) Port probes 11 - 15

Figure 6.20: *HMFR SST calculation, OPR = 2, Surge signature 4 - Symmetry plane probe data*

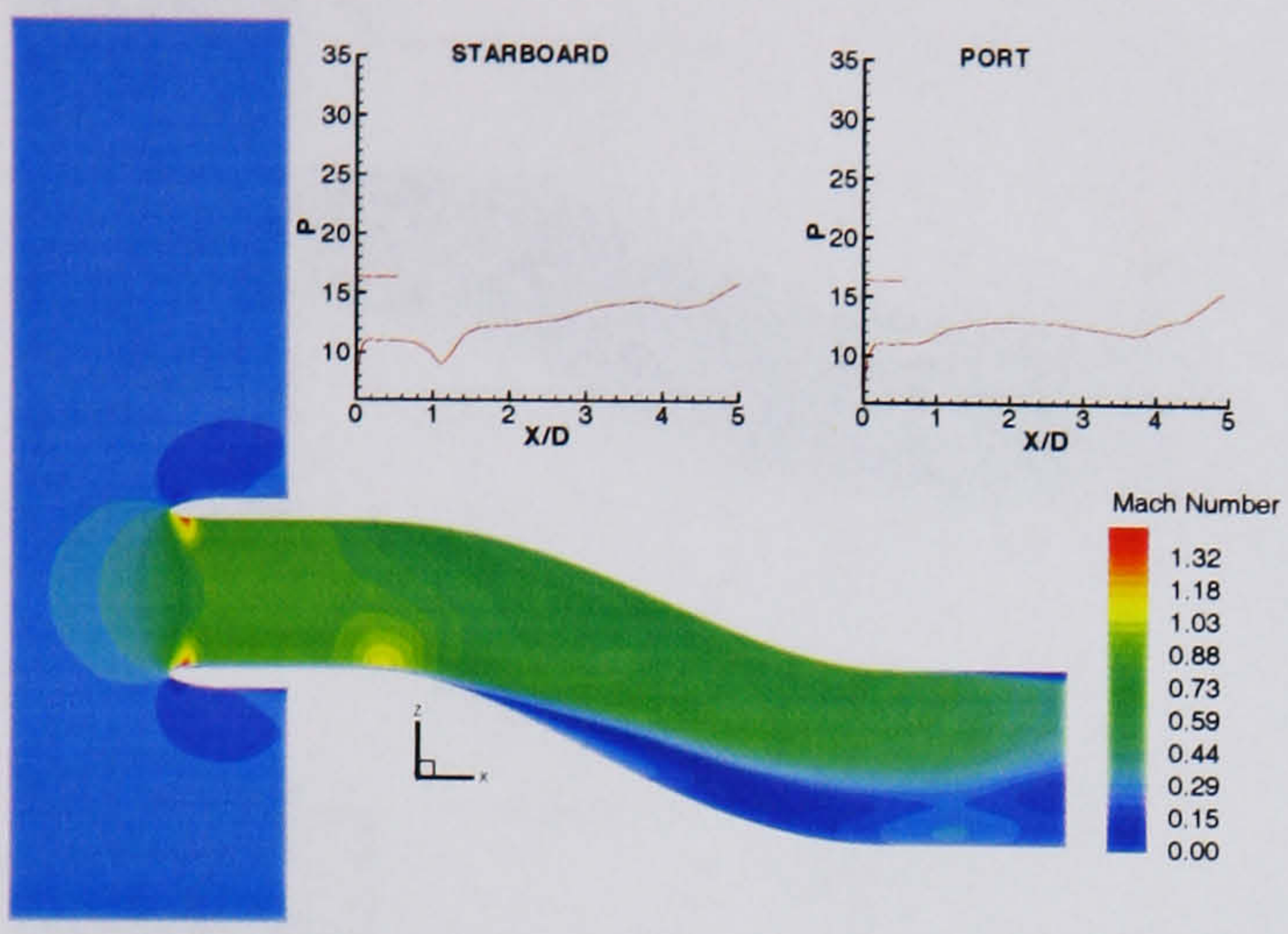

(a) t = 0.24

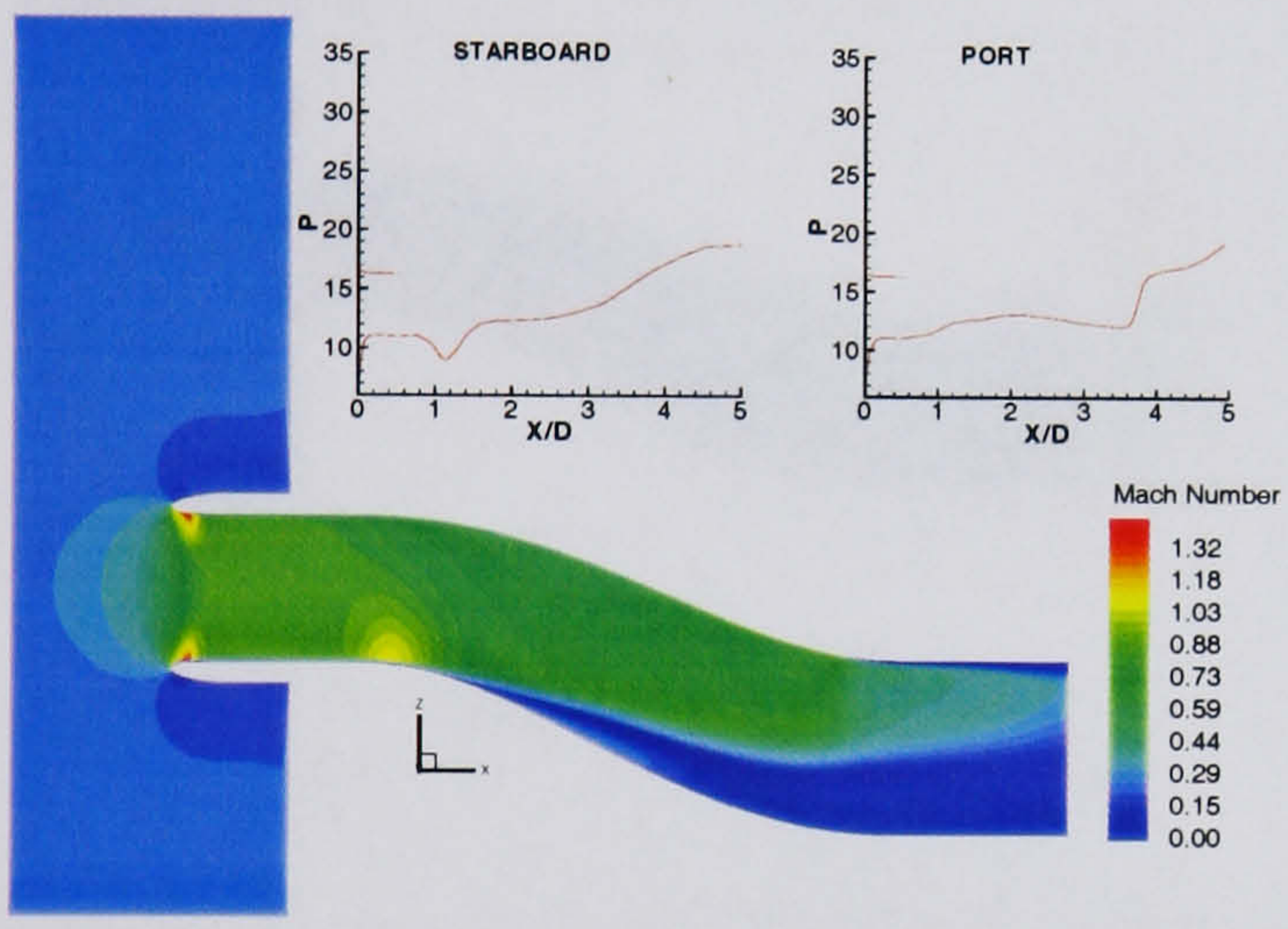

(b) t = 0.62

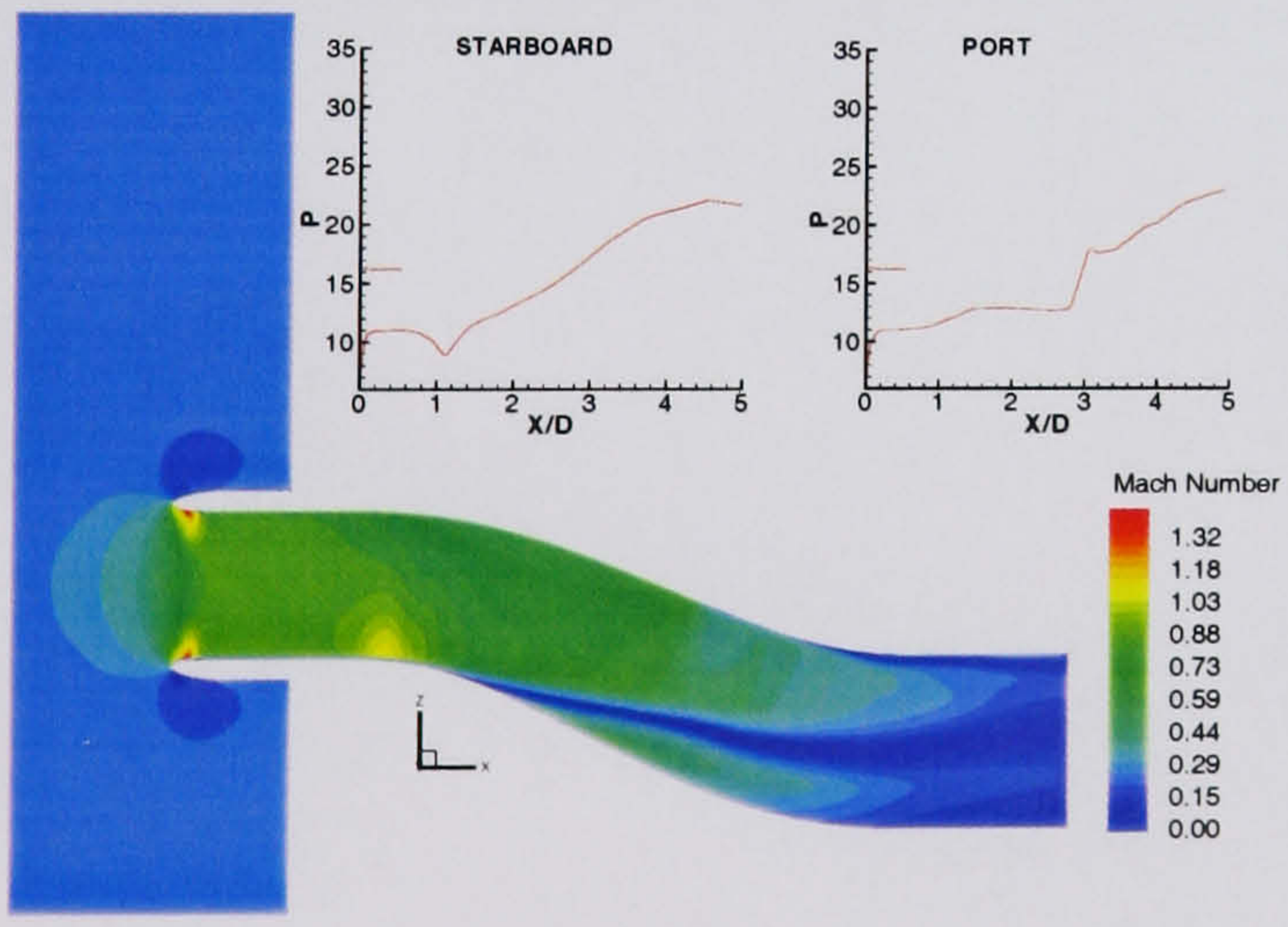

(c) t = 1.00

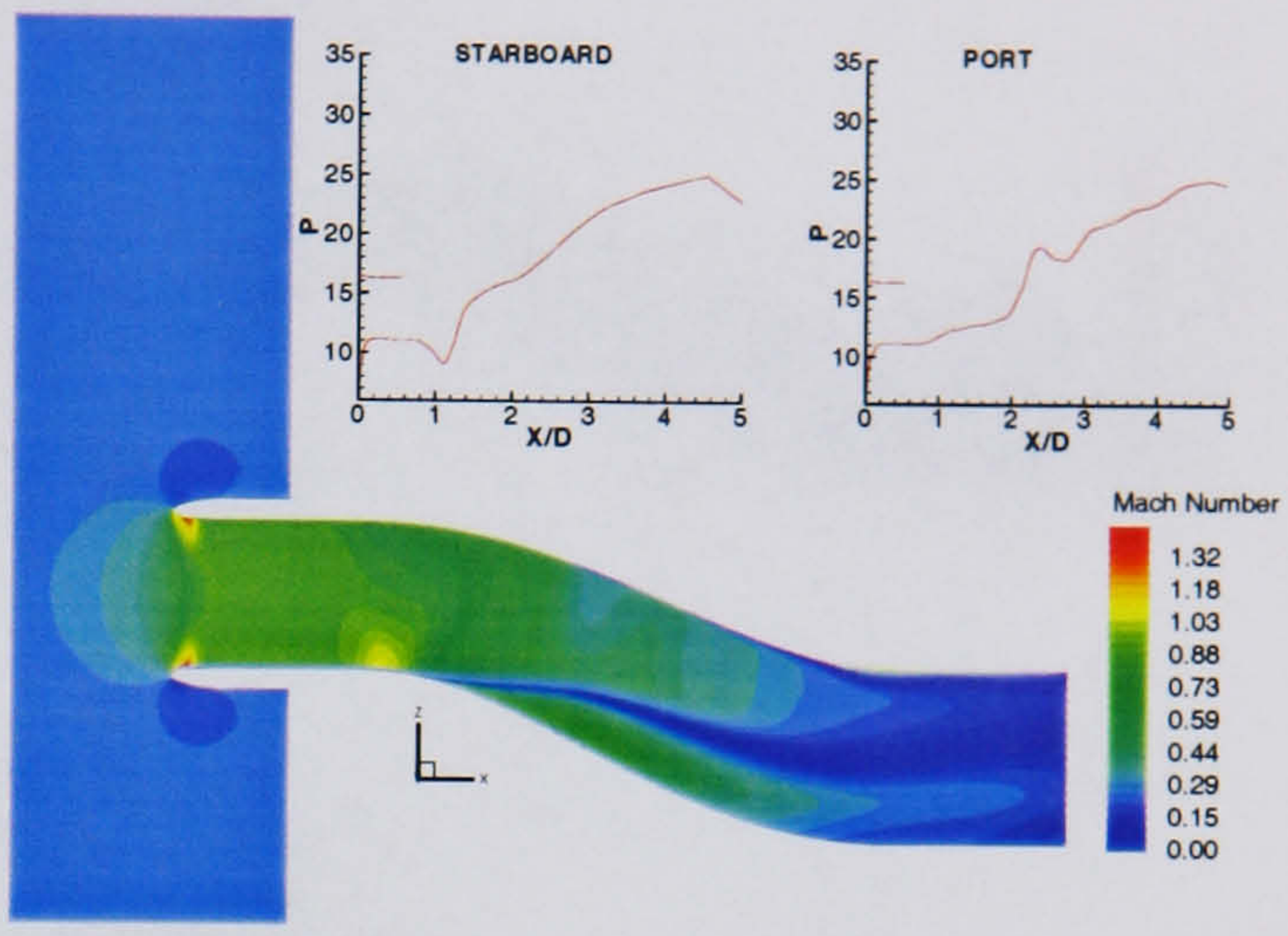

(d) t = 1.26

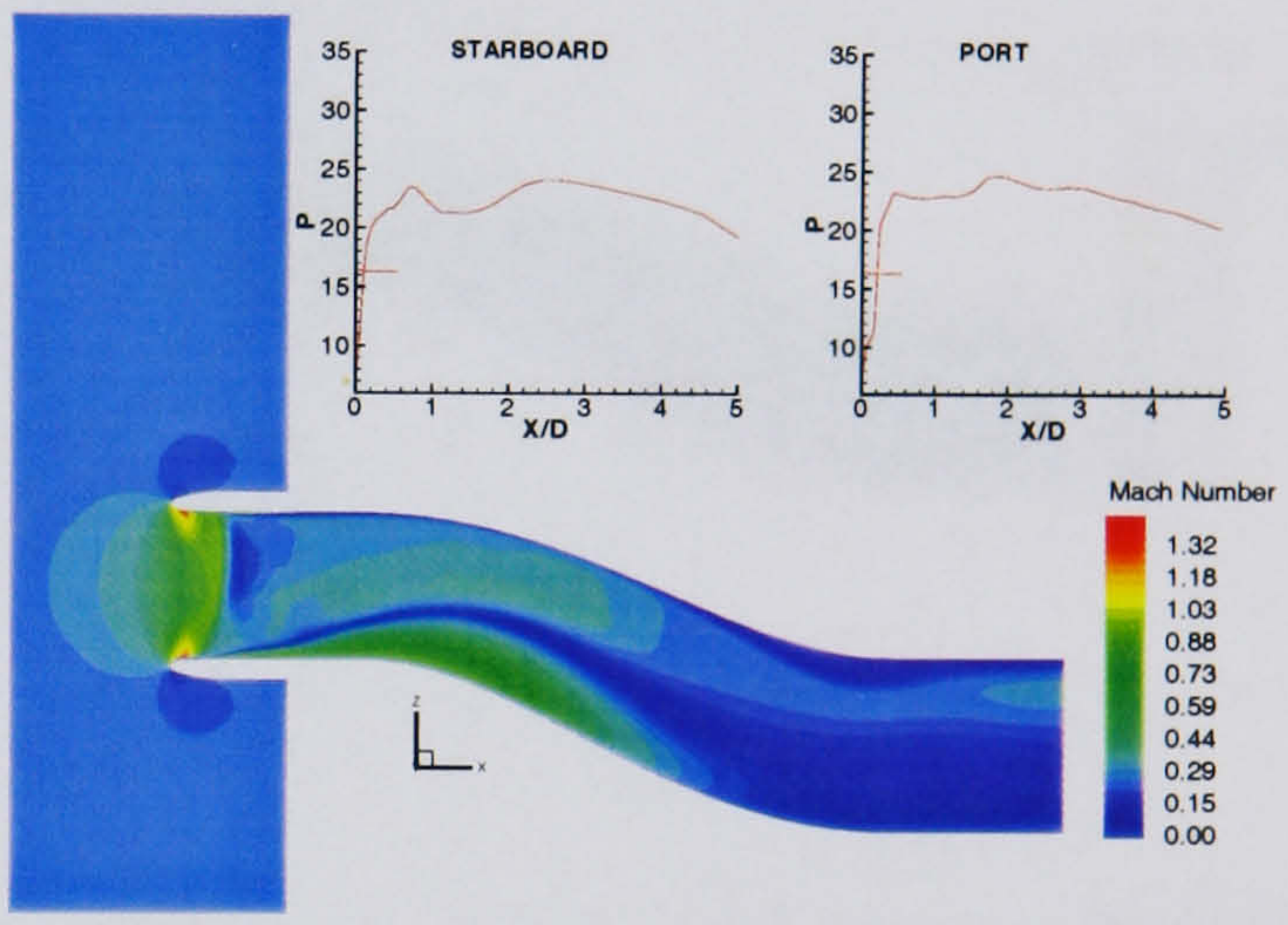

(e) t = 1.84

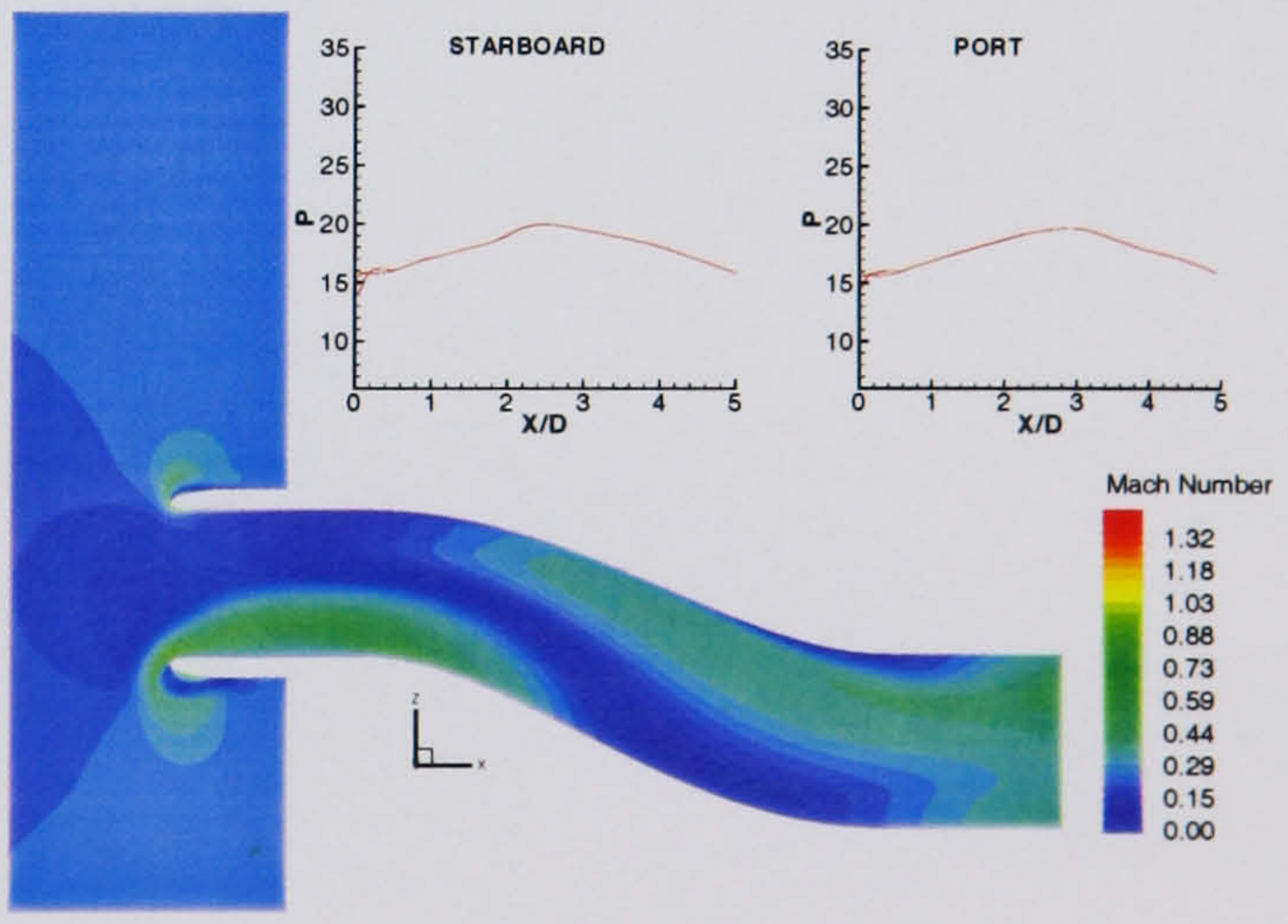

(f) t = 2.40

Figure 6.21: *HMFR SST calculation, OPR = 2, Surge signature 4 - Symmetry plane Mach number and pressure traces*

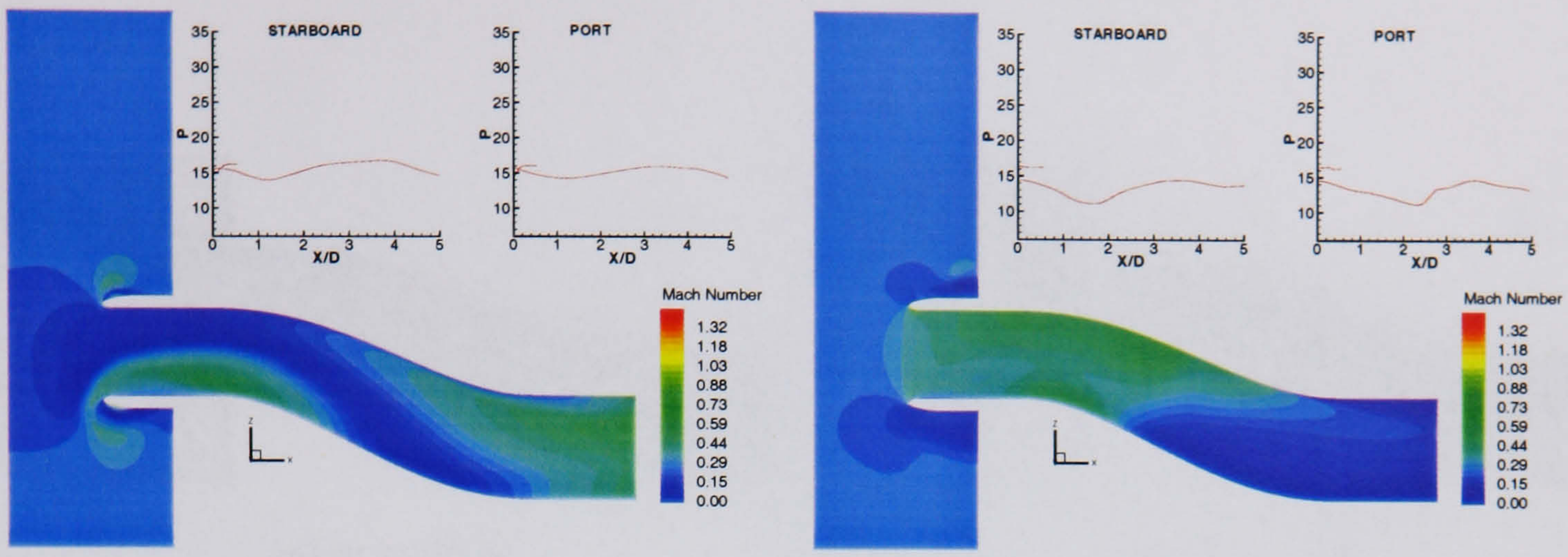

(g) t = 2.62

(i) t = 3.82

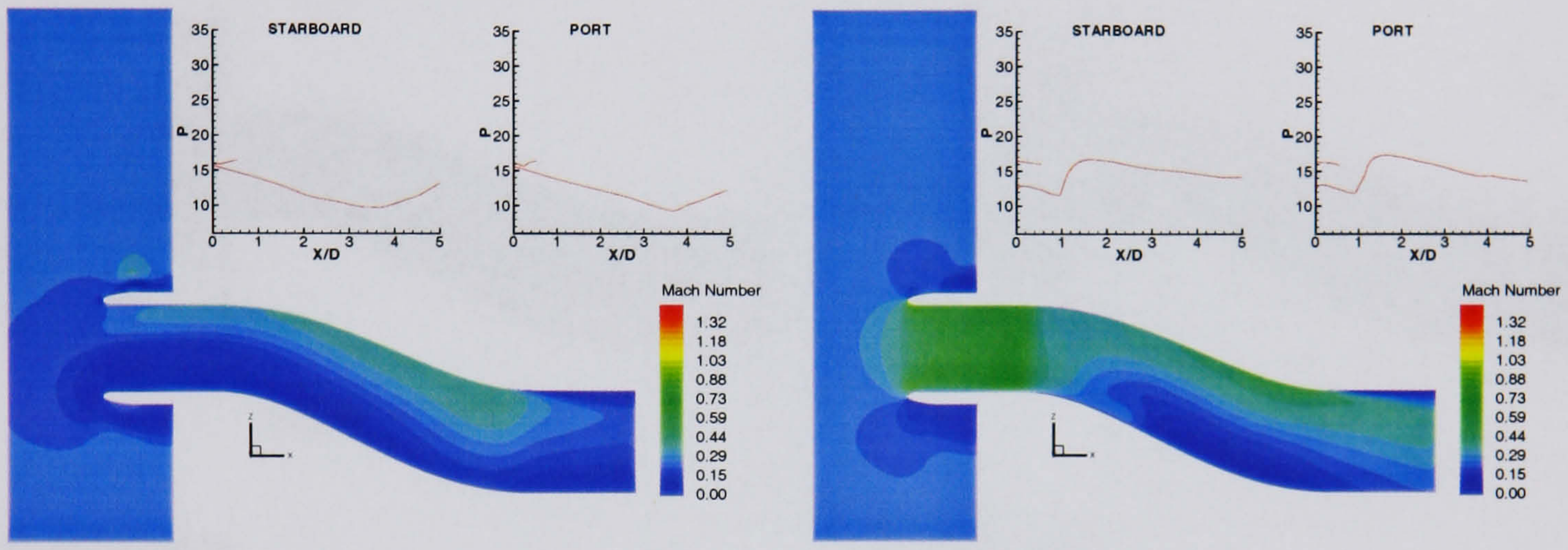

(h) t = 3.26

(j) t = 4.38

Figure 6.21: (cont.) *HMFR SST calculation, OPR = 2, Surge signature 4 - Symmetry plane Mach number and pressure traces*

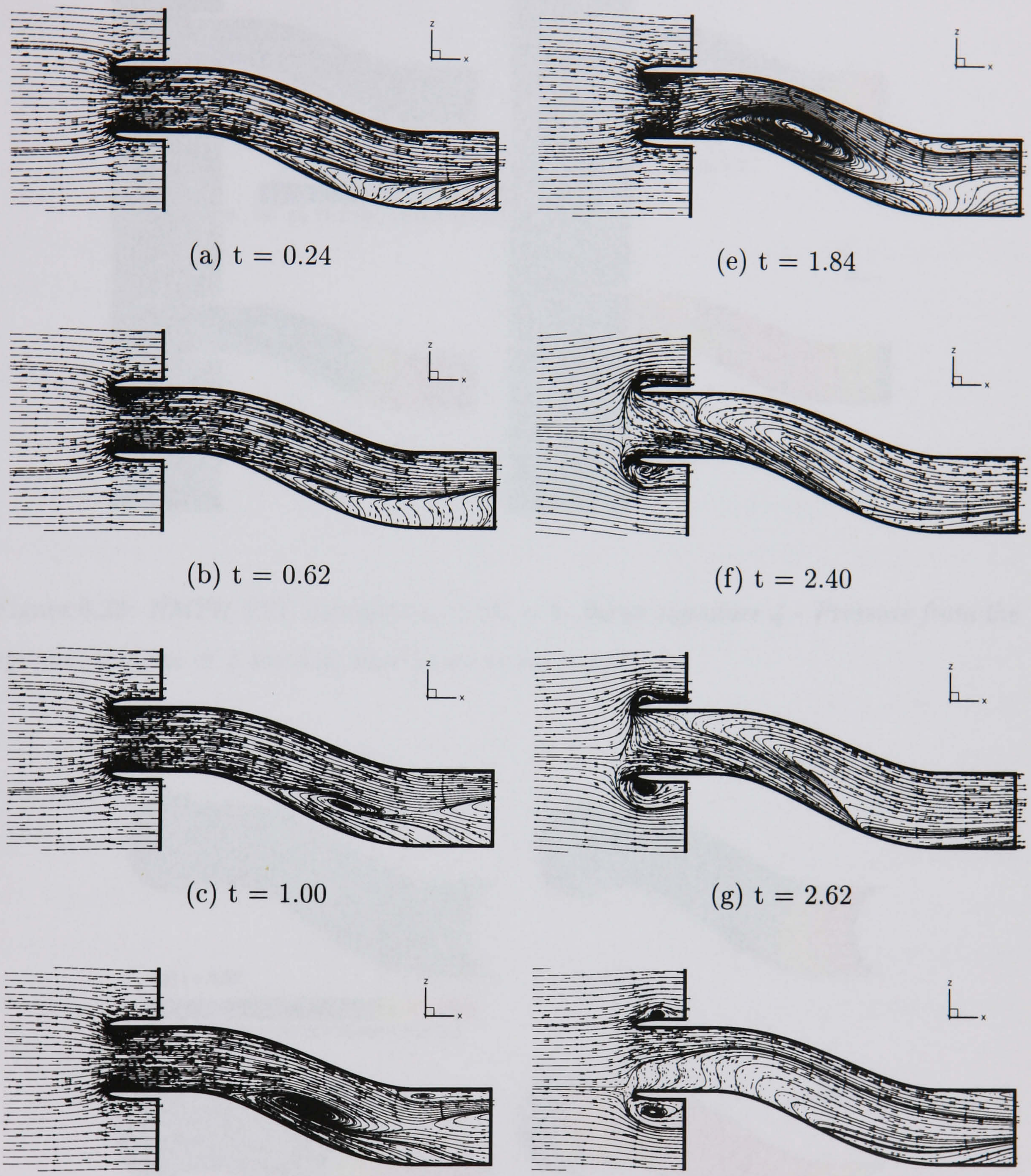

(a) t = 0.24

(b) t = 0.62

(c) t = 1.00

(d) t = 1.26

(e) t = 1.84

(f) t = 2.40

(g) t = 2.62

(h) t = 3.26

Figure 6.22: *HMFR SST calculation, OPR = 2, Surge signature 4 - Symmetry plane streamlines*

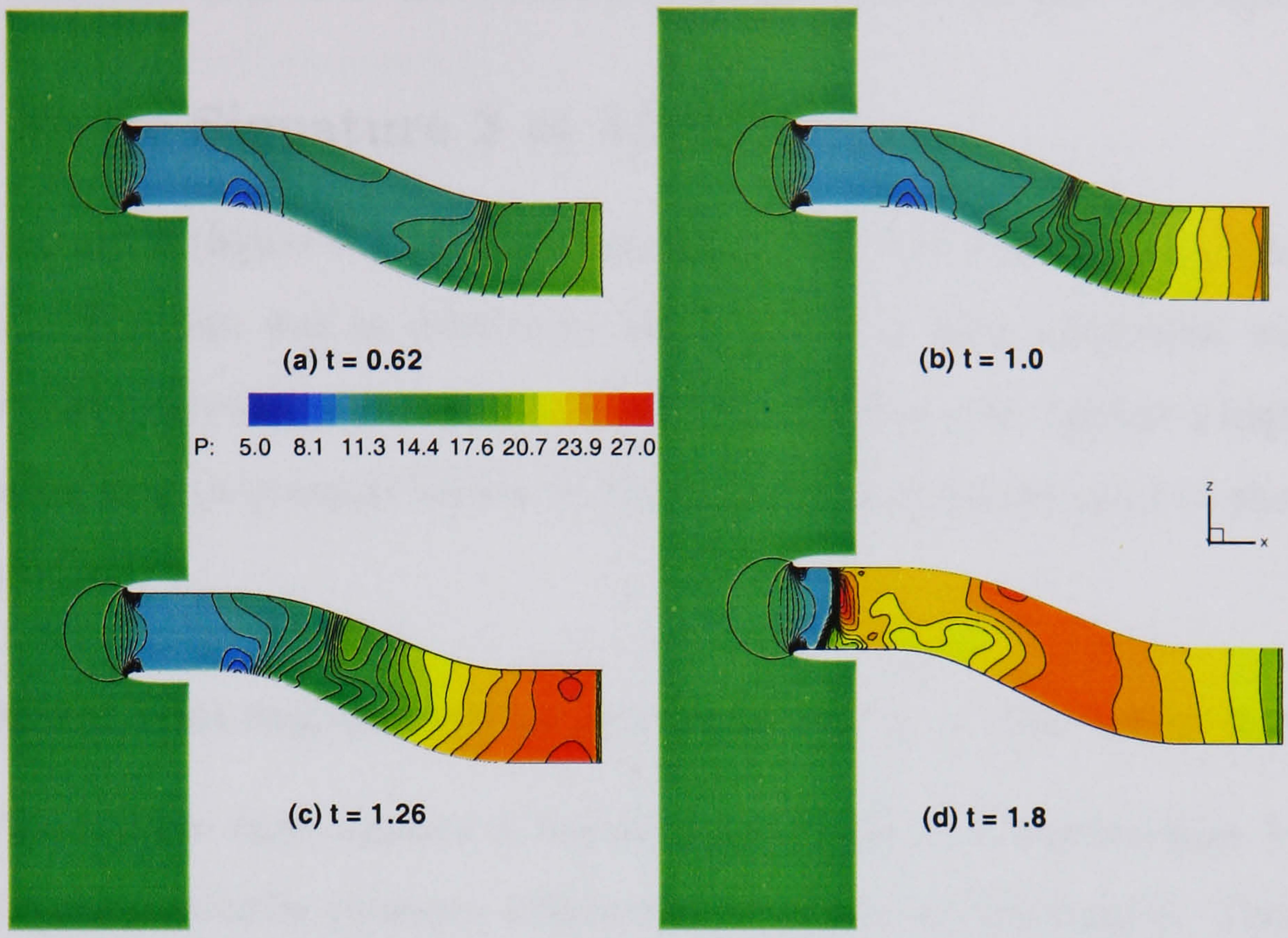

Figure 6.23: *HMFR SST calculation, OPR = 2, Surge signature 4 - Pressure from the symmetry plane at 4 instants leading up to surge exit*

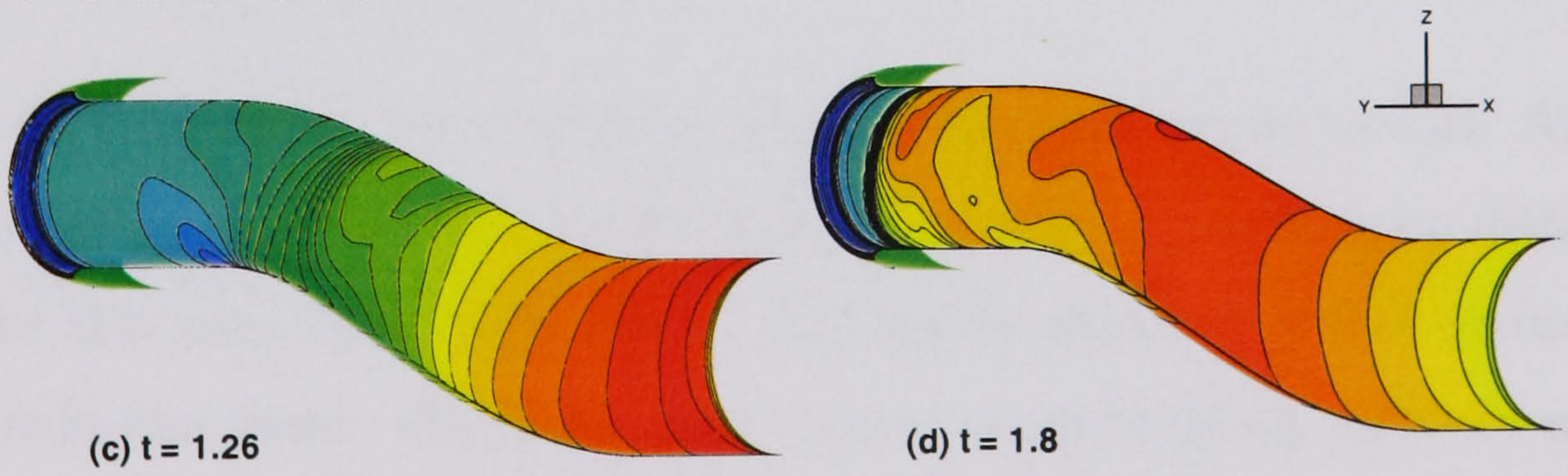

Figure 6.24: *HMFR SST calculation, OPR = 2, Surge signature 4 - Pressure from the duct wall at 4 instants leading up to surge exit*

6.7 Effect of OPR and MFR on Surge Propagation

6.7.1 Surge Signature 2 at LMFR

Surge signature 2 (figure 6.2 (d)) was applied to the low mass flow case as defined in section 3.2. The aim was to determine the differences when compared with the high mass flow case analysed in section 6.4. The low mass flow case applies a higher pressure at the engine face (a pressure closer to the freestream pressure) and so the peak OPR will be greater.

Propagation from engine face to second bend: t = 0.0 → t = 0.24

The low mass flow case applies a higher pressure at the downstream boundary in order to create a smaller pressure differential between the freestream. Thus, the peak overpressure of 31.05 (2 x 15.525) is applied after around t=0.05. Figure 6.25 (a) and (b) show pressure time history data from probes in the straight section of the duct leading to the downstream boundary. Overall pressure levels are much higher as higher pressure is being applied in the LMFR case. However the general form as the surge forms and propagates as far as the first bend is very similar. With reference to probe P6, it appears that the surge front reaches this probe slightly faster than for the HMFR case. Also, as the surge front reaches the first bend and begins to propagate through the separated region on the starboard side, the pressure levels on the starboard side probes remain comparable to the port side probes. For the HMFR case the starboard probes near the second bend record a lower pressure than the equivalent probes on the port side.

Figure 6.26 (a) shows the symmetry plane Mach numbers at t=0.24. At this time the surge front has reached the second bend. The front is much more distinct across the duct for this case, most likely due to the smaller separation that occurs from the starboard side first bend. The same figure shows pressure along the duct wall at this time. The surge front can be seen to be much more abrupt on both sides of the duct when compared with the HMFR case. Figure 6.27 (a) shows the streamlines through the symmetry plane at the same instant. It is immediately apparent that flow reversal is predicted to a much greater degree and is again stronger in the separated region towards the starboard side.

Figure 6.28 (a) shows the pressure isolines from the symmetry plane. The uniform surge front across the symmetry plane is clear. Figure 6.29 (a) also shows this although the pressure is still slightly higher towards the port side. At this stage the pressures are still the maximum applied at the downstream boundary.

Propagation from second bend to first bend: t = 0.24 → t = 0.62

Figure 6.25 (c) and (d) cover probes from the second bend to the first bend. Again the general trends are similar to what has been seen previously for other signatures. The surge wave forms into a more abrupt rise and fall in pressure on both the starboard and port sides. Peak pressure is generated on the port side as the surge front reaches the first bend although in this case it is not proportionately higher than on the starboard side, due to the reduced natural steady state separation for this case.

Figure 6.26 (b) shows that the Mach contours are not as complex as those for the surge signatures in the HMFR case. As there is only a very small amount of recirculating flow and steady state separation at the starboard side first bend the propagating surge front moves through this region in a less complex manner to what has been seen previously with no upstream propagating recirculating flow. Figure 6.27 (b) shows the streamlines at the same instant and confirms this. It also shows that the flow reversal is strongest towards the starboard side where lies the limited steady-state separation.

The pressure isolines from the symmetry plane and duct wall in figures 6.28 and 6.29 (b) again show the more uniform leading edge to the propagating surge wave across the duct. Behind the initial front the pressure levels induced do begin to build but in this case they are not as localised towards the port side as in previous cases.

Propagation from first bend to freestream: t = 0.62 onwards

Figure 6.25 (e) and (f) cover probes in the inner and outer cowl regions. The sharp pressure front can be seen to pass probes S11 and P11 and exit to freestream just after t=1.0. The same signature for the HMFR case shows the surge front to exit after t=1.2. The peak pressure is still high and it is interesting to note that it is recorded on the starboard side rather than the usual port side. The maximum pressure recorded for the case is still on the starboard side first bend however at t=0.9.

Figure 6.26 (c) and (d) show the pressure front just before and just after expulsion into the freestream. The pressure traces along the duct walls in figure (c) show a near identical form on the port and starboard walls. As we move to (d) we can see the surge front exits the duct into the freestream. The pressures along the duct walls begin to drop and there appears to be considerable outflow, especially towards the duct walls. Figure 6.27 (d) shows the streamlines and velocity vectors and confirms this. This flow spillage, on meeting the freestream, creates two large vorticies on the port and starboard sides. Due to the size of the vorticies, questions are raised relating to their proximity to the downstream freestream boundary. This boundary is switched to an extrapolation type boundary for the surge simulations to better handle any spillage out of the duct. However in this instance it would most probably be a better solution to move the downstream freestream boundary further downstream.

Finally, figures 6.28 and 6.29 (c) and (d) show the symmetry plane and duct wall pressure isolines once more. The uniform surge front at this stage is clear to see and the peak pressures develop just before the surge exits to freestream. Peak pressures are greater than those seen for the surge signatures at a high mass flow rate as the pressure being applied at the engine face is greater for the low mass flow case.

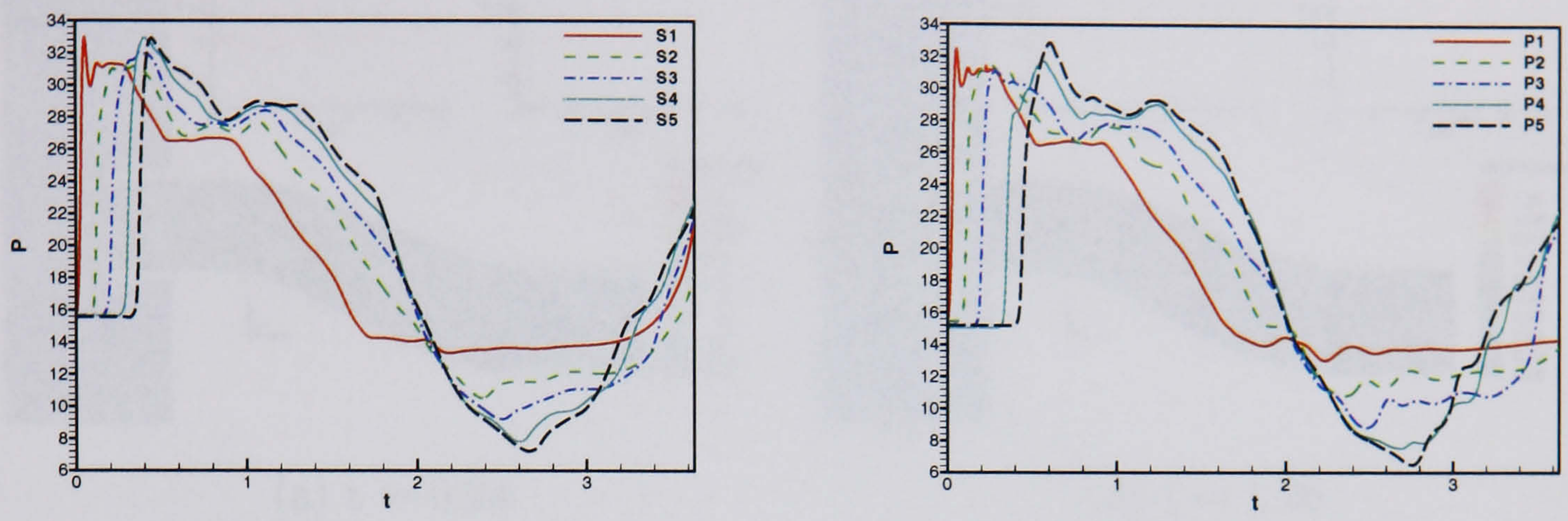

(a) Starboard probes 1 - 5

(b) Port probes 1 - 5

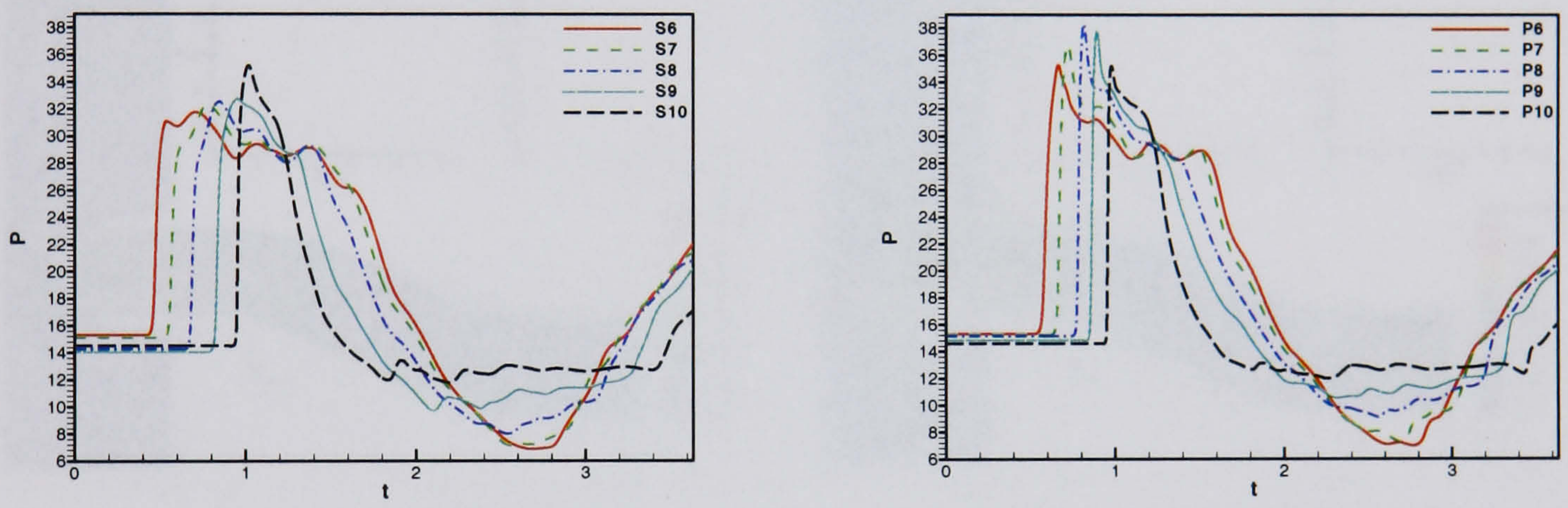

(c) Starboard probes 6 - 10

(d) Port probes 6 - 10

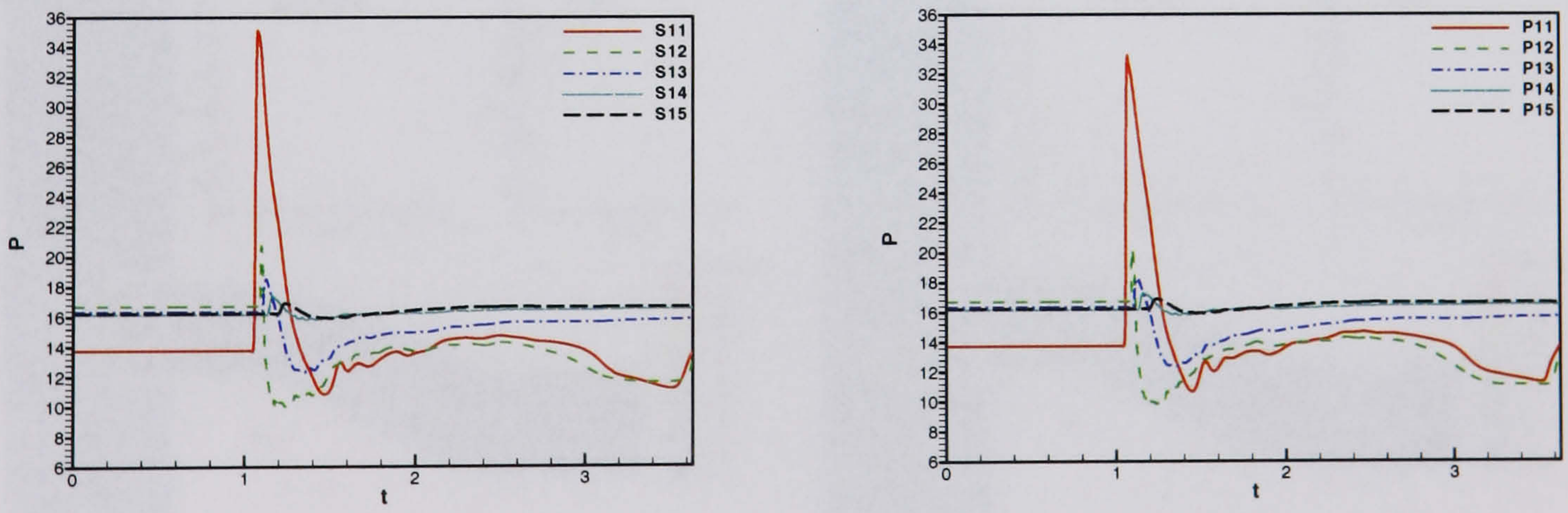

(e) Starboard probes 11 - 15

(f) Port probes 11 - 15

Figure 6.25: *LMFR SST calculation, OPR = 2, Surge signature 2 - Symmetry plane probe data*

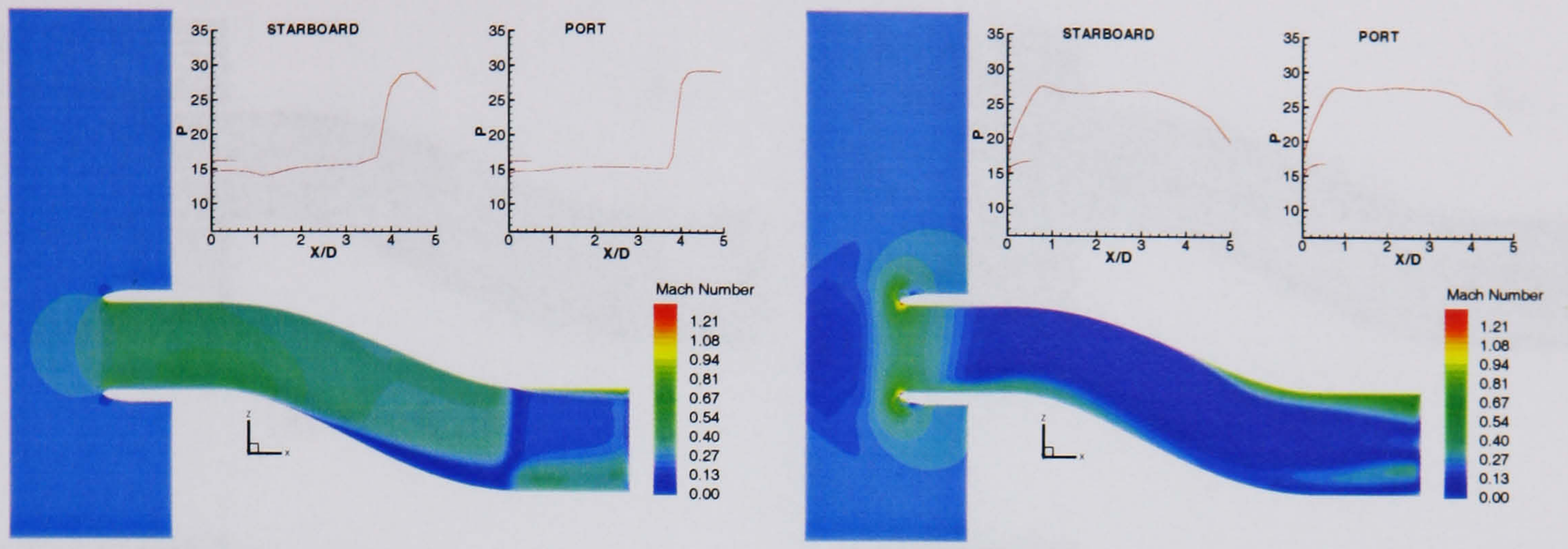

(a) t = 0.24

(d) t = 1.26

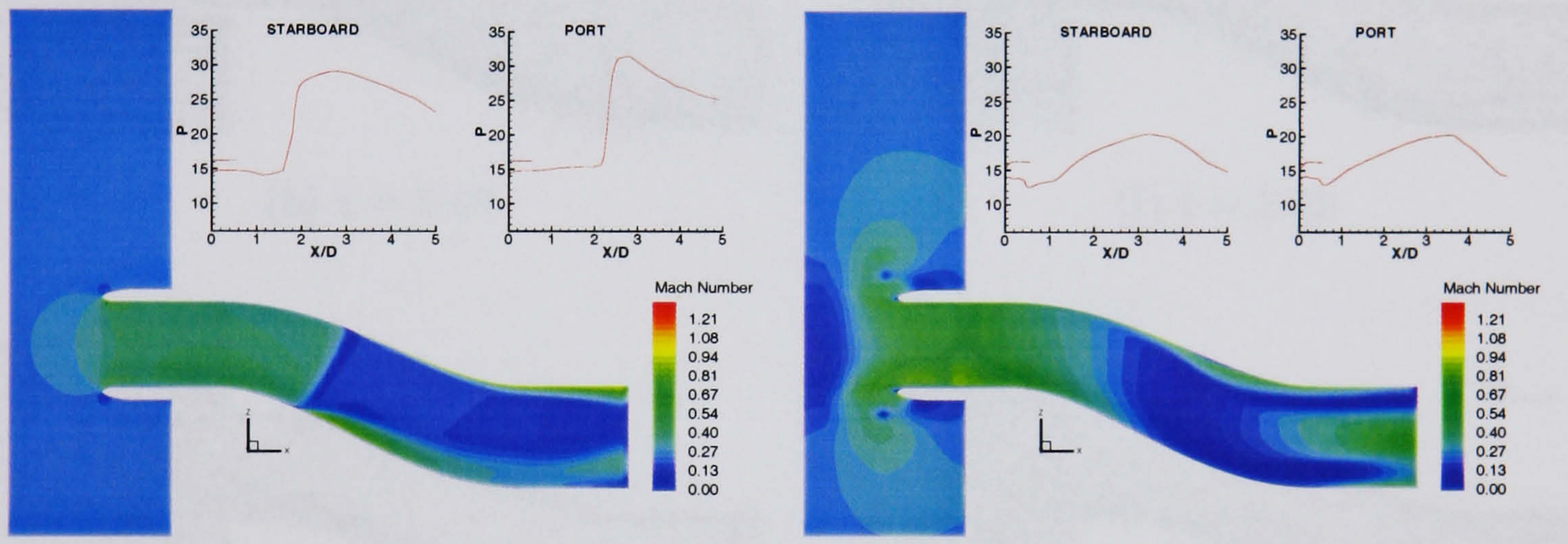

(b) t = 0.62

(e) t = 1.84

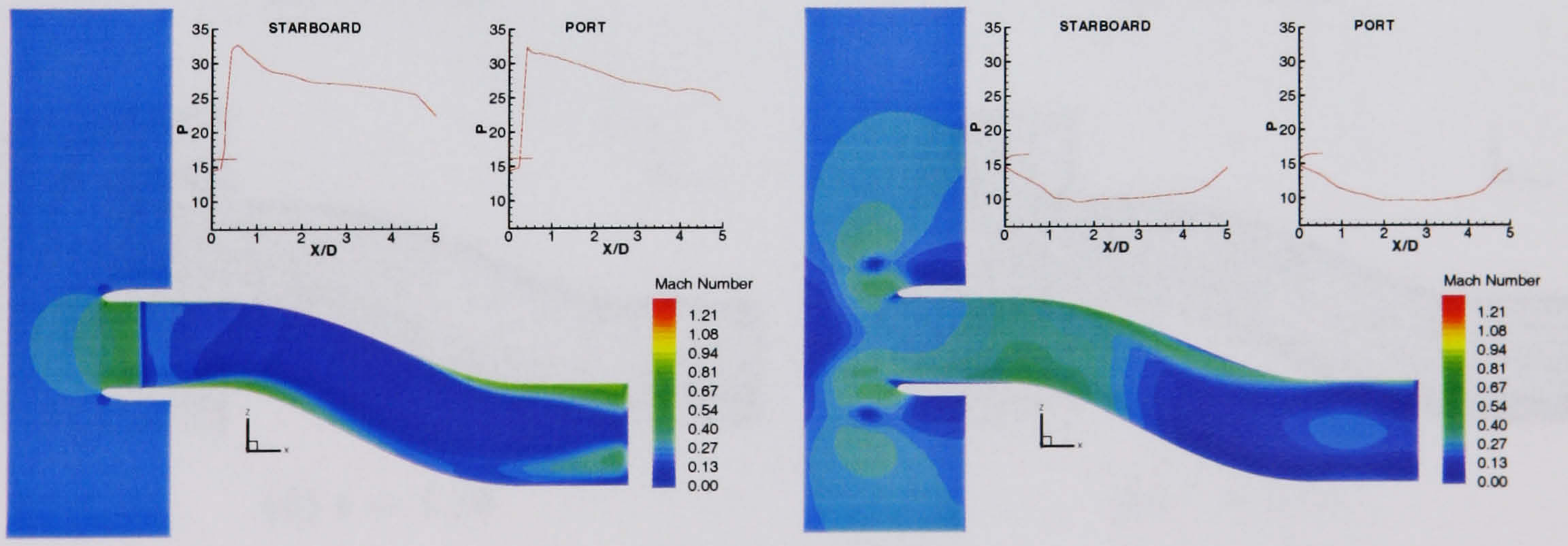

(c) t = 1.00

(f) t = 2.40

Figure 6.26: *LMFR SST calculation, OPR = 2, Surge signature 2 - Symmetry plane Mach number and pressure traces*

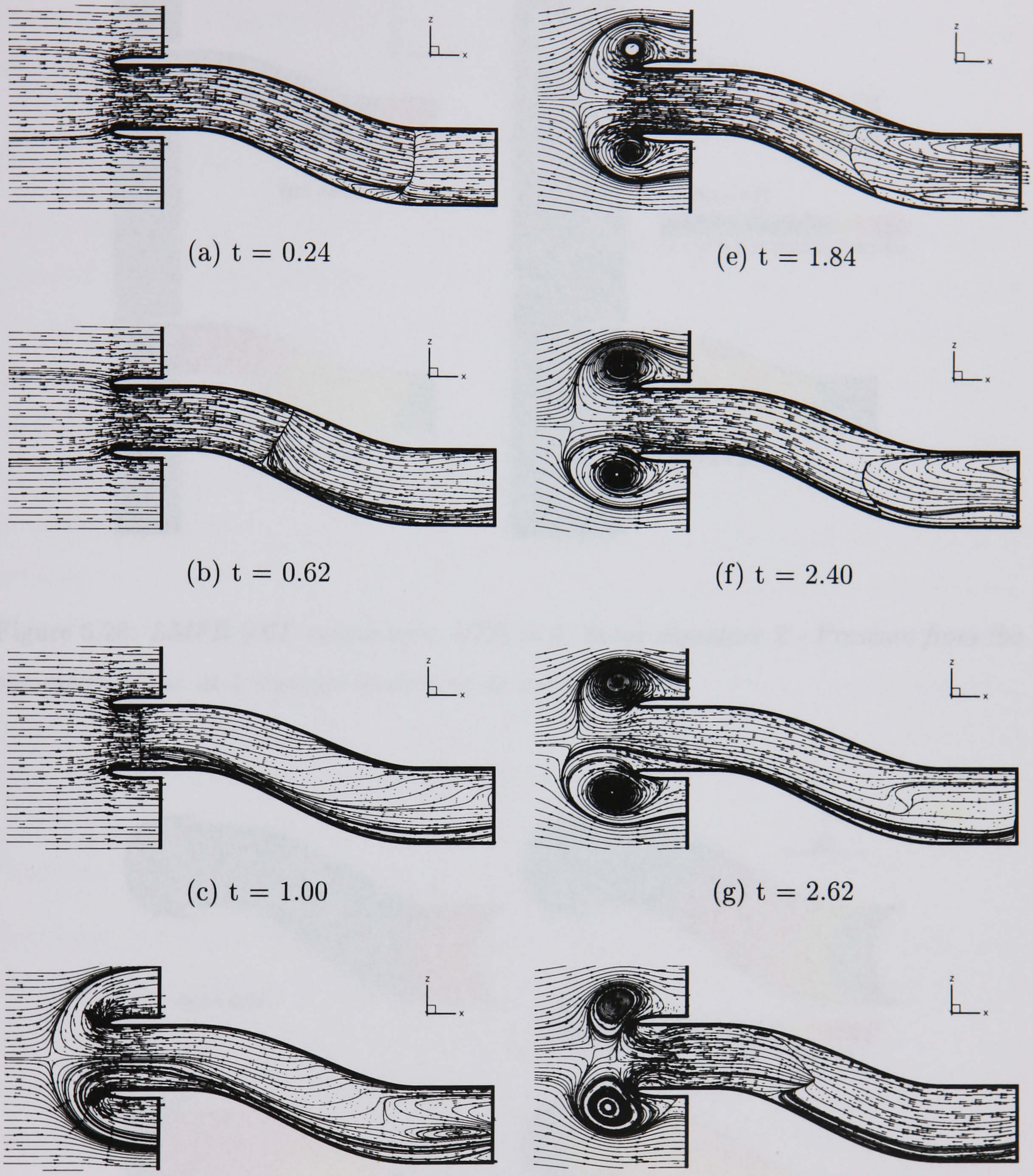

(a) t = 0.24

(e) t = 1.84

(b) t = 0.62

(f) t = 2.40

(c) t = 1.00

(g) t = 2.62

(d) t = 1.26

(h) t = 3.26

Figure 6.27: *LMFR SST calculation, OPR = 2, Surge signature 2 - Symmetry plane streamlines*

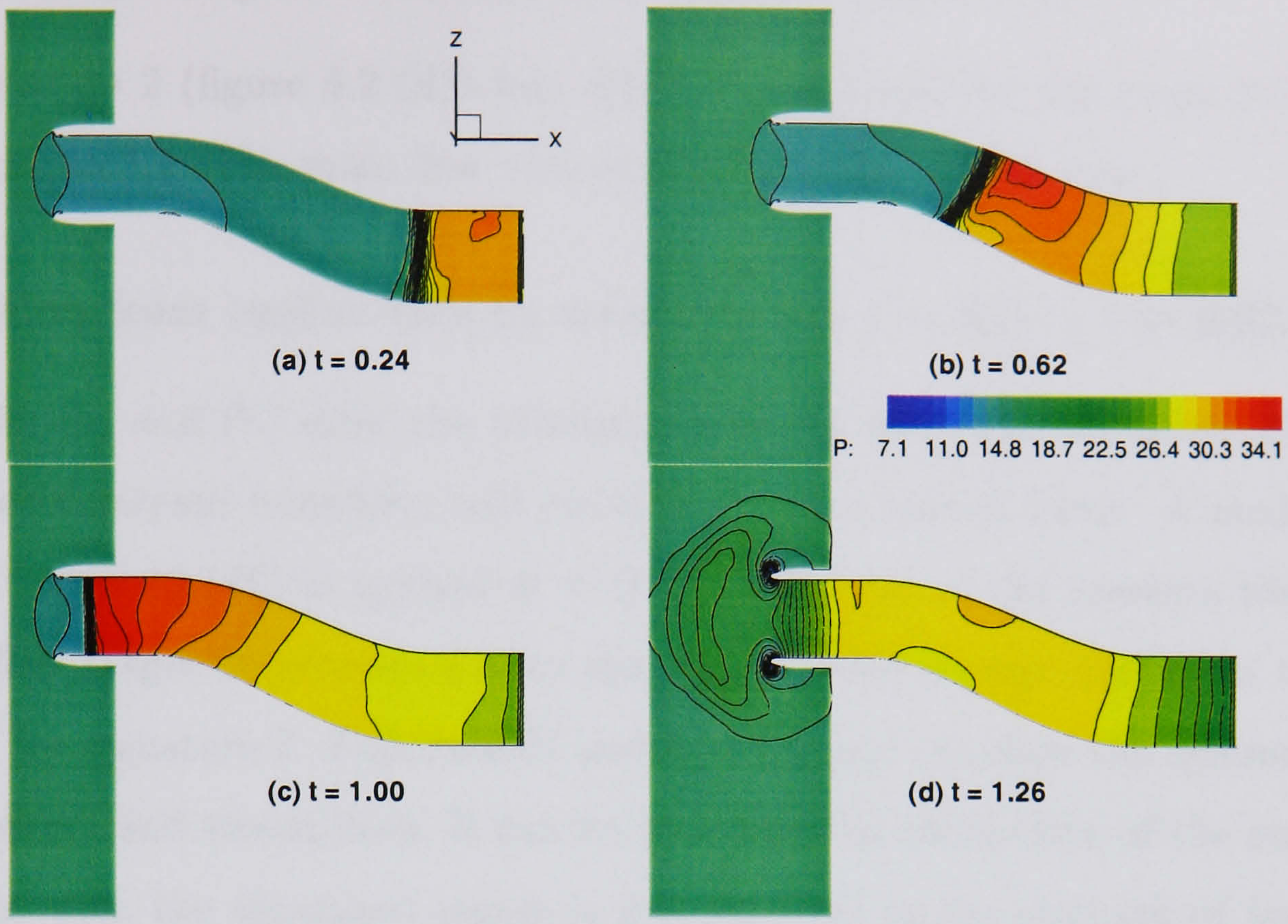

Figure 6.28: *LMFR SST calculation, OPR = 2, Surge signature 2 - Pressure from the symmetry plane at 4 instants leading up to surge exit*

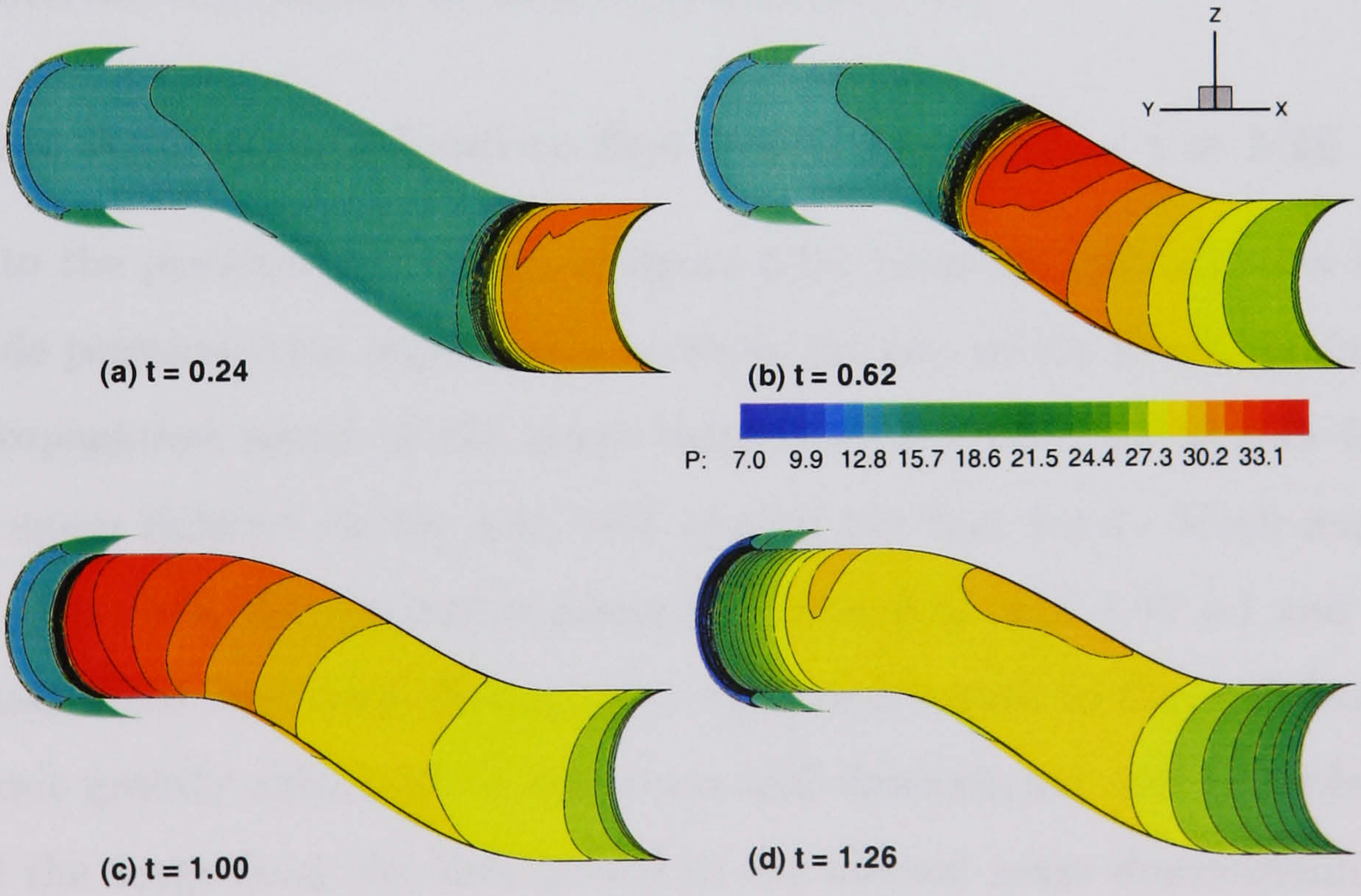

Figure 6.29: *LMFR SST calculation, OPR = 2, Surge signature 2 - Pressure from the duct wall at 4 instants leading up to surge exit*

6.7.2 Surge Signature 2 at HMFR, OPR=1.5

Surge signature 2 (figure 6.2 (d)) was applied once more but the peak over-pressure was reduced to 1.5. The mass flow rate applied was the HMFR case.

Propagation from engine face to second bend: t = 0.0 → t = 0.62

Figure 6.30 (a) and (b) show the pressures from the port and starboard side probes near the downstream boundary and extending to the second bend. A peak pressure of 19.719 (1.5 x 13.146) is applied at t=0.05. The form of the pressure time history in the initial stages of propagation to the second bend is very similar to the higher OPR of 2 for signature 2. Figures 6.31 and 6.32 (a) and (b) show the symmetry plane Mach numbers and streamlines. It can be seen that the interaction of the propagating surge front with the separated region is less involved as the strength of the surge is reduced. At t=0.62 it can be see that the surge front has navigated the second bend. Flow reversal in the separated region is enhanced although not to the amount seen in section 6.4. Figures 6.33 and 6.34 (a) and (b) show that a strong pressure gradient develops towards the port side as the front propagates through the second bend. The general trends are very similar to those seen in section 6.4.

Propagation from second bend to first bend: t = 0.62 → t = 1.26

Returning to the pressure probe data in figure 6.30, plots (c) and (d) show starboard and port side pressure data respectively between the two intake bends. It can be seen that the propagation speed of the surge front is slower than for section 6.4. Peak pressure is again induced on the port side around the first bend. Mach number and streamline plots from the symmetry plane in figures 6.31 and 6.32 (c) and (d) show that the surge front continues through the separated region to the first bend. Flow reversal is not greatly enhanced at this stage and downstream and towards the port side behind the surge front the flow is still in the normal sense downstream. Figures 6.33 and 6.34 (c) and (d) show that the surge front reaches the second bend at around t=1.26. The pressure gradient becomes stronger on both the port and starboard sides however the peak pressure remain localised towards the port side wall.

Propagation from first bend to freestream: t = 1.26 onwards

From figure 6.30 (d) and (e) it can be seen that the pressure front exits the duct at about t=1.2. The pressure front at this stage is very abrupt, as seen with previous signatures and cases. Following the expulsion of the surge wave the pressure begins to recede downstream towards the engine face boundary. A reflection of the original surge expulsion is again felt that begins to propagate up throw the duct. This reflection exits the duct at t=4.4. Mach number contours and streamlines from the symmetry plane show that no flow spillage occurs out of the duct after the surge front exits and flow seems to recover to resemble steady state flow shortly after surge exit.

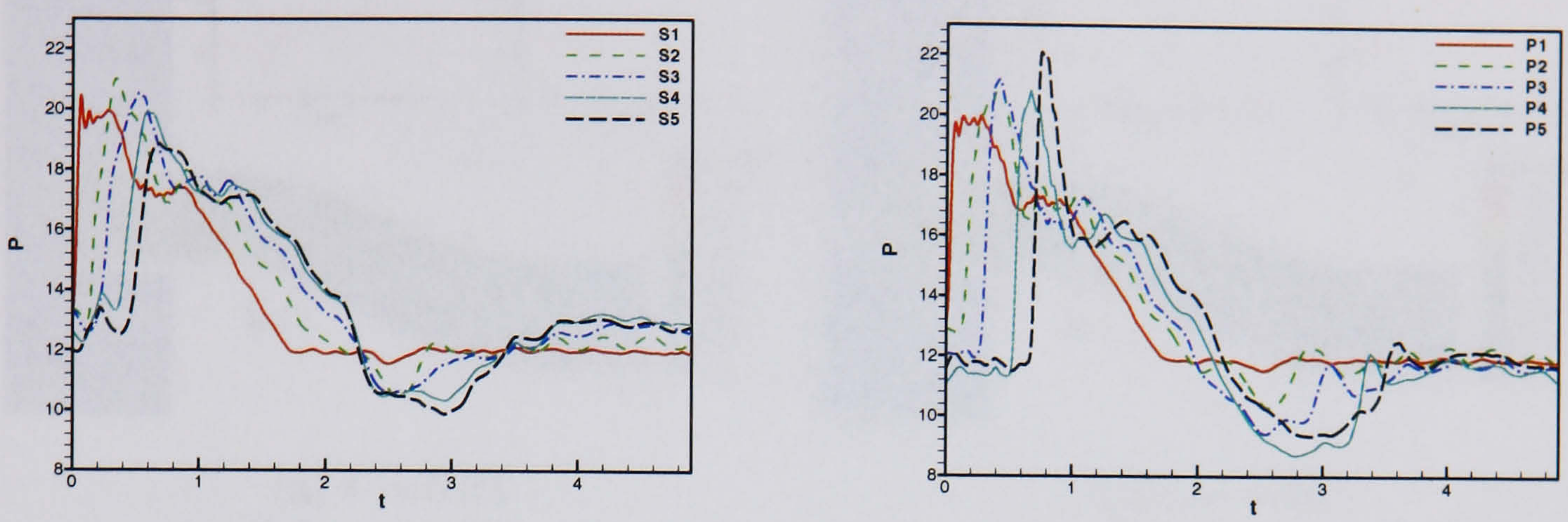

(a) Starboard probes 1 - 5

(b) Port probes 1 - 5

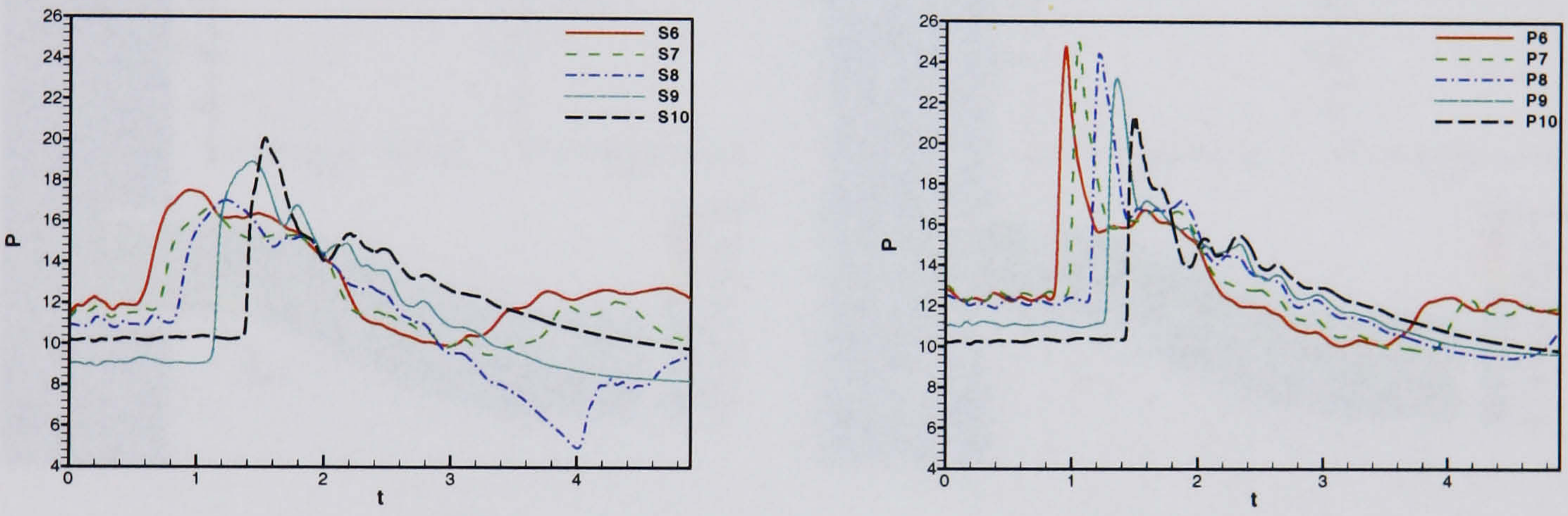

(c) Starboard probes 6 - 10

(d) Port probes 6 - 10

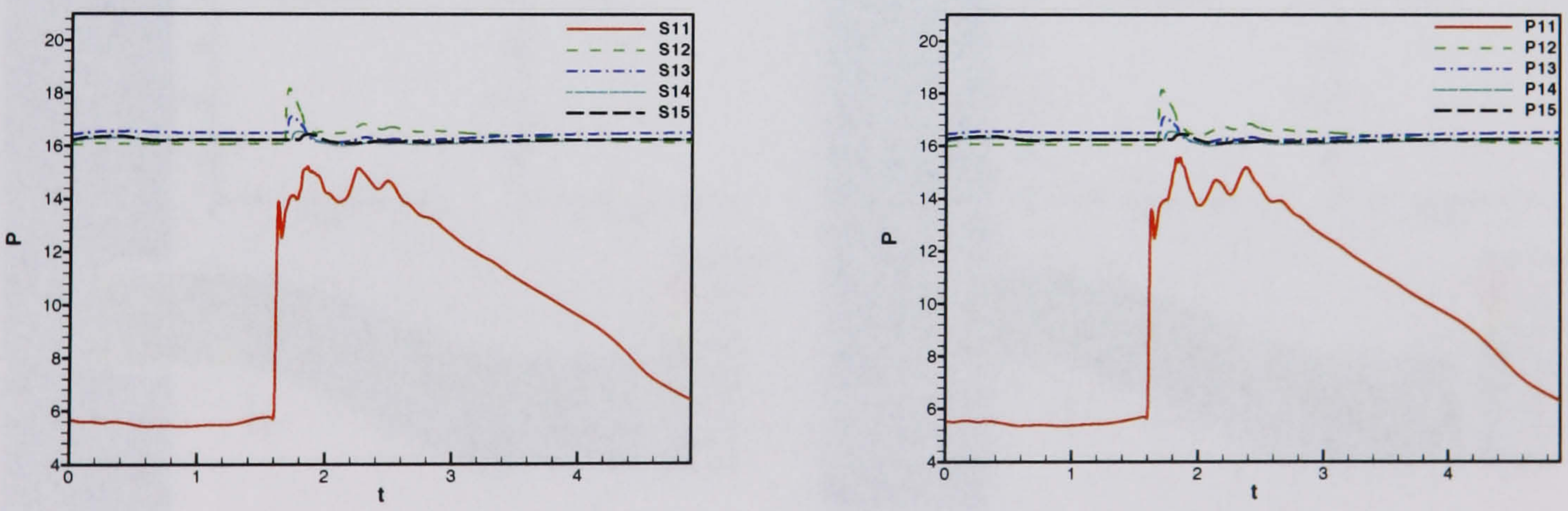

(e) Starboard probes 11 - 15

(f) Port probes 11 - 15

Figure 6.30: *HMFR SST calculation, OPR = 1.5, Surge signature 2 - Symmetry plane probe data*

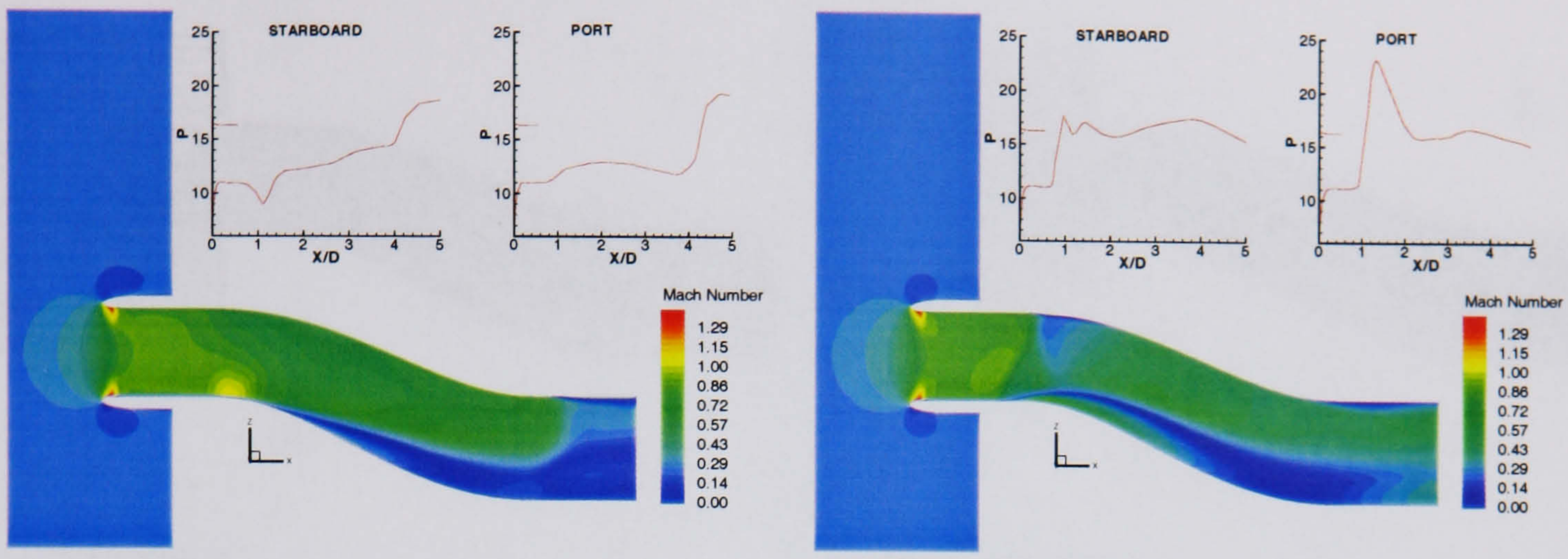

(a) t = 0.24

(d) t = 1.26

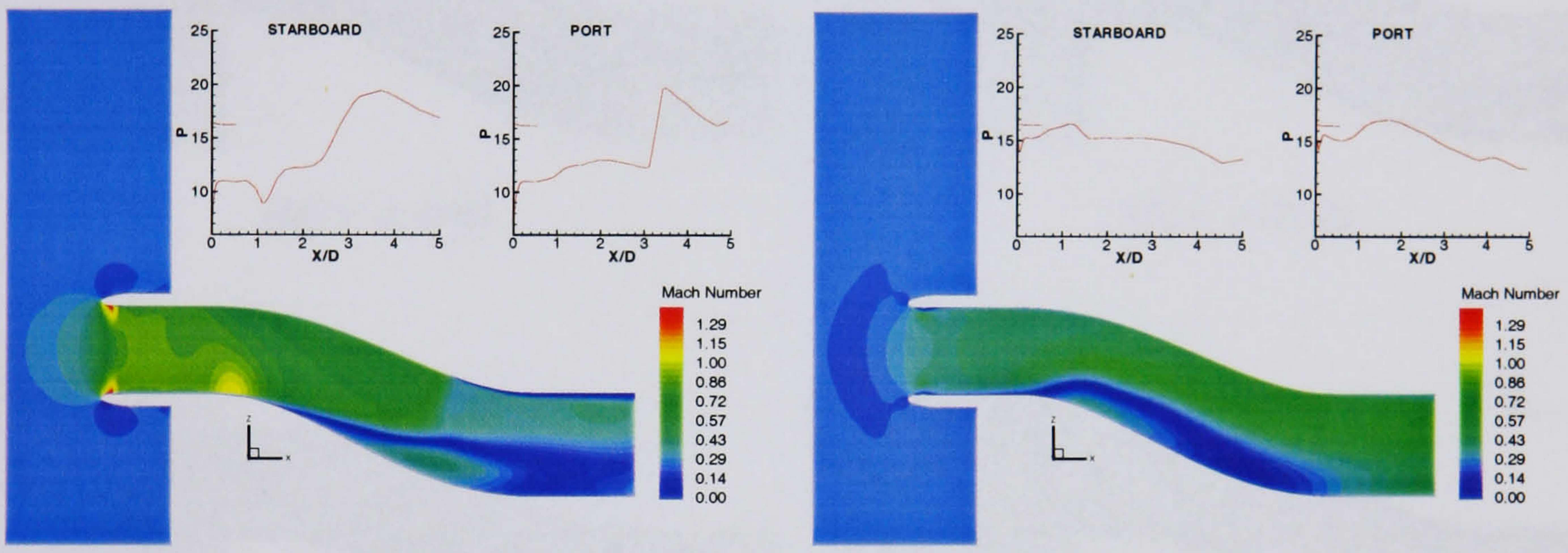

(b) t = 0.62

(e) t = 1.84

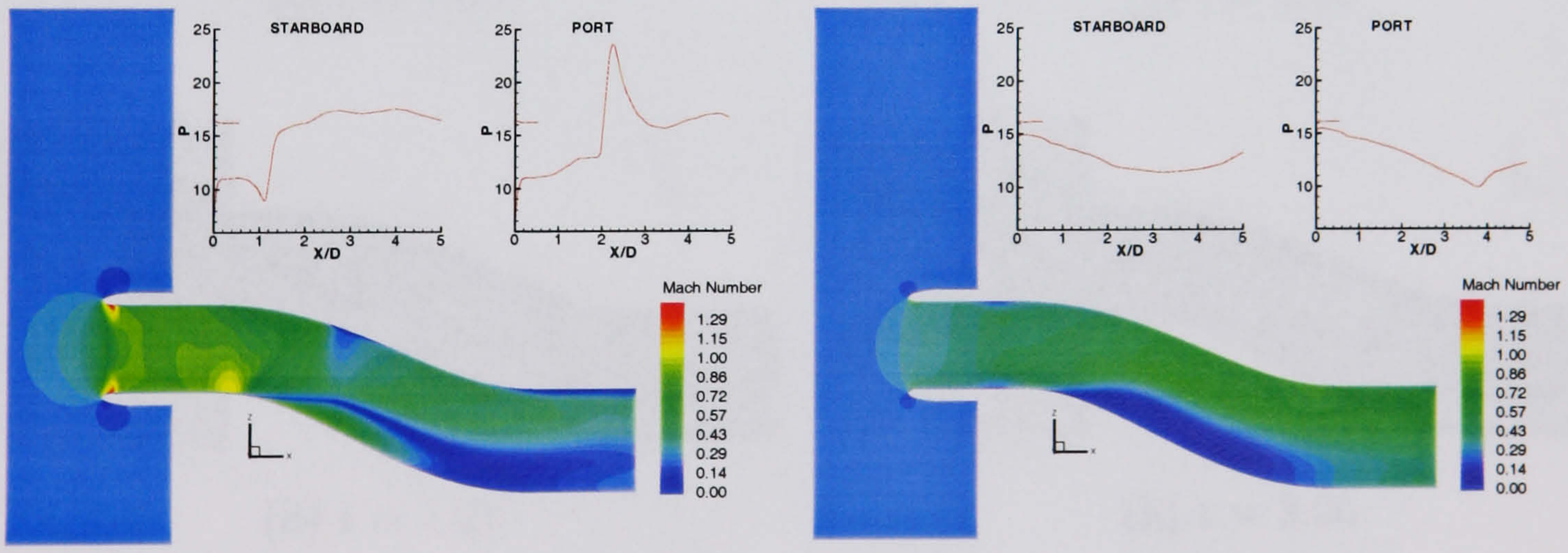

(c) t = 1.00

(f) t = 2.40

Figure 6.31: *HMFR SST calculation, OPR = 1.5, Surge signature 2 - Symmetry plane Mach number and pressure traces*

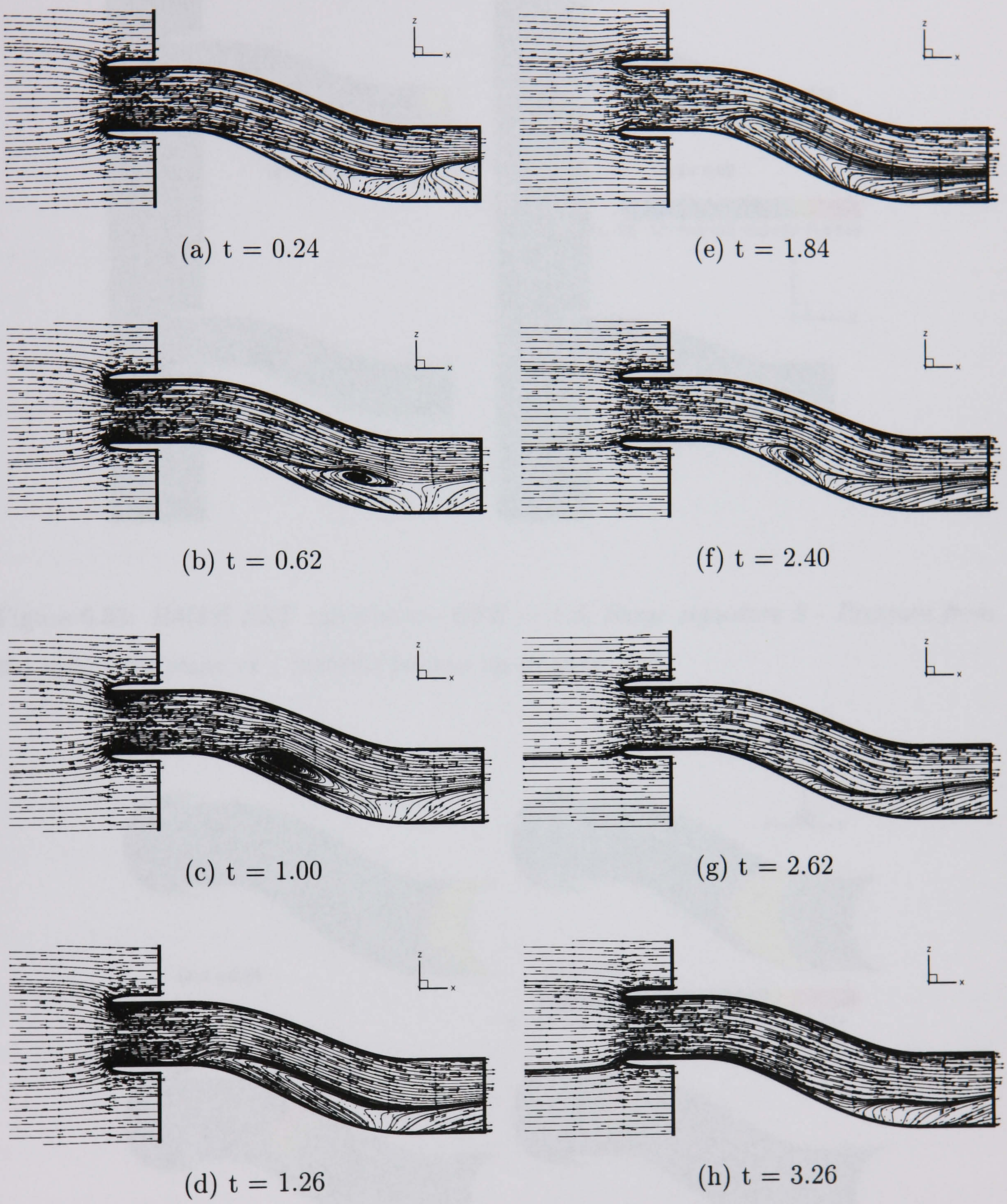

(a) t = 0.24

(e) t = 1.84

(b) t = 0.62

(f) t = 2.40

(c) t = 1.00

(g) t = 2.62

(d) t = 1.26

(h) t = 3.26

Figure 6.32: *HMFR SST calculation, OPR = 1.5, Surge signature 2 - Symmetry plane streamlines*

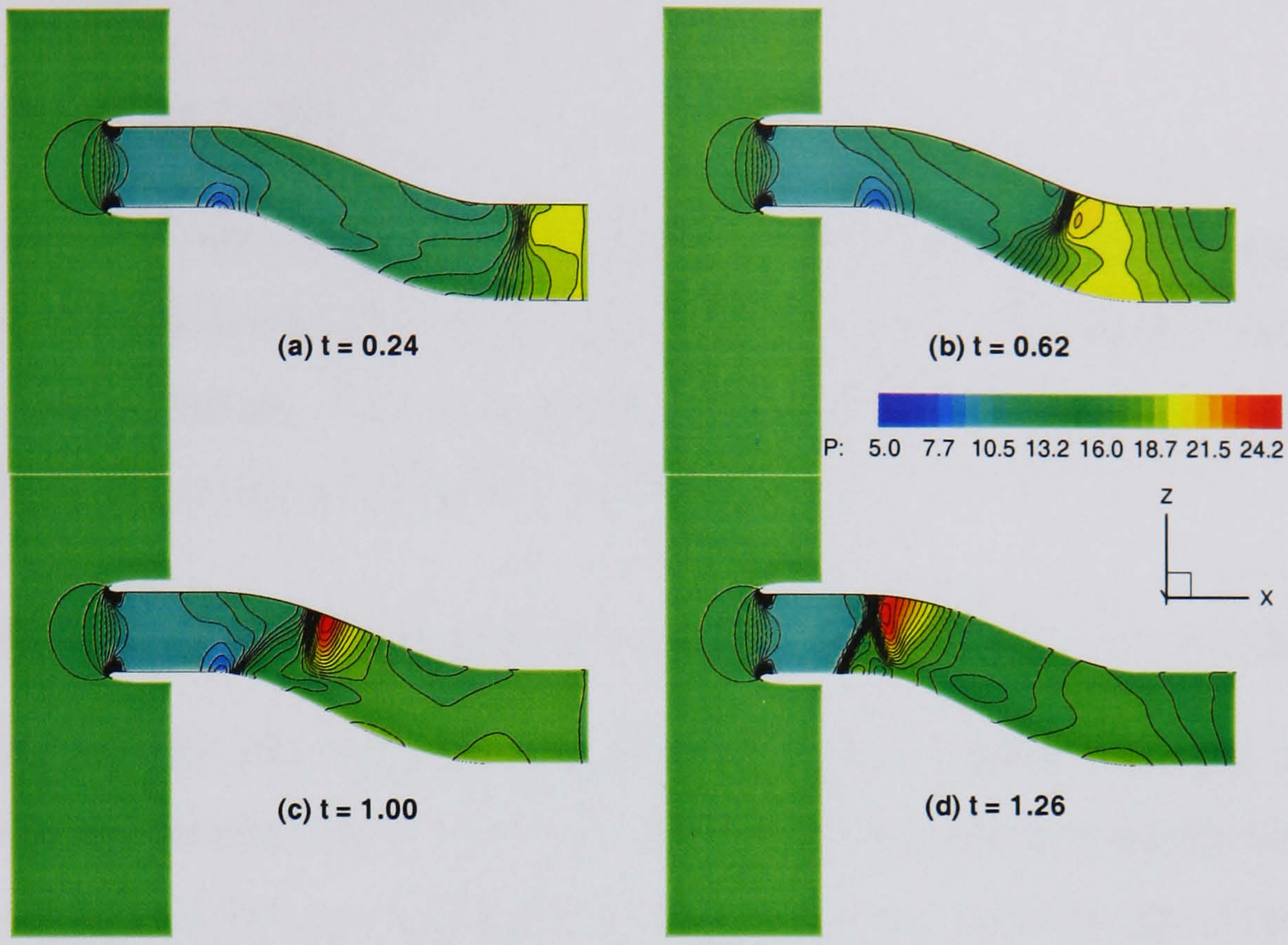

Figure 6.33: *HMFR SST calculation, OPR = 1.5, Surge signature 2 - Pressure from the symmetry plane at 4 instants leading up to surge exit*

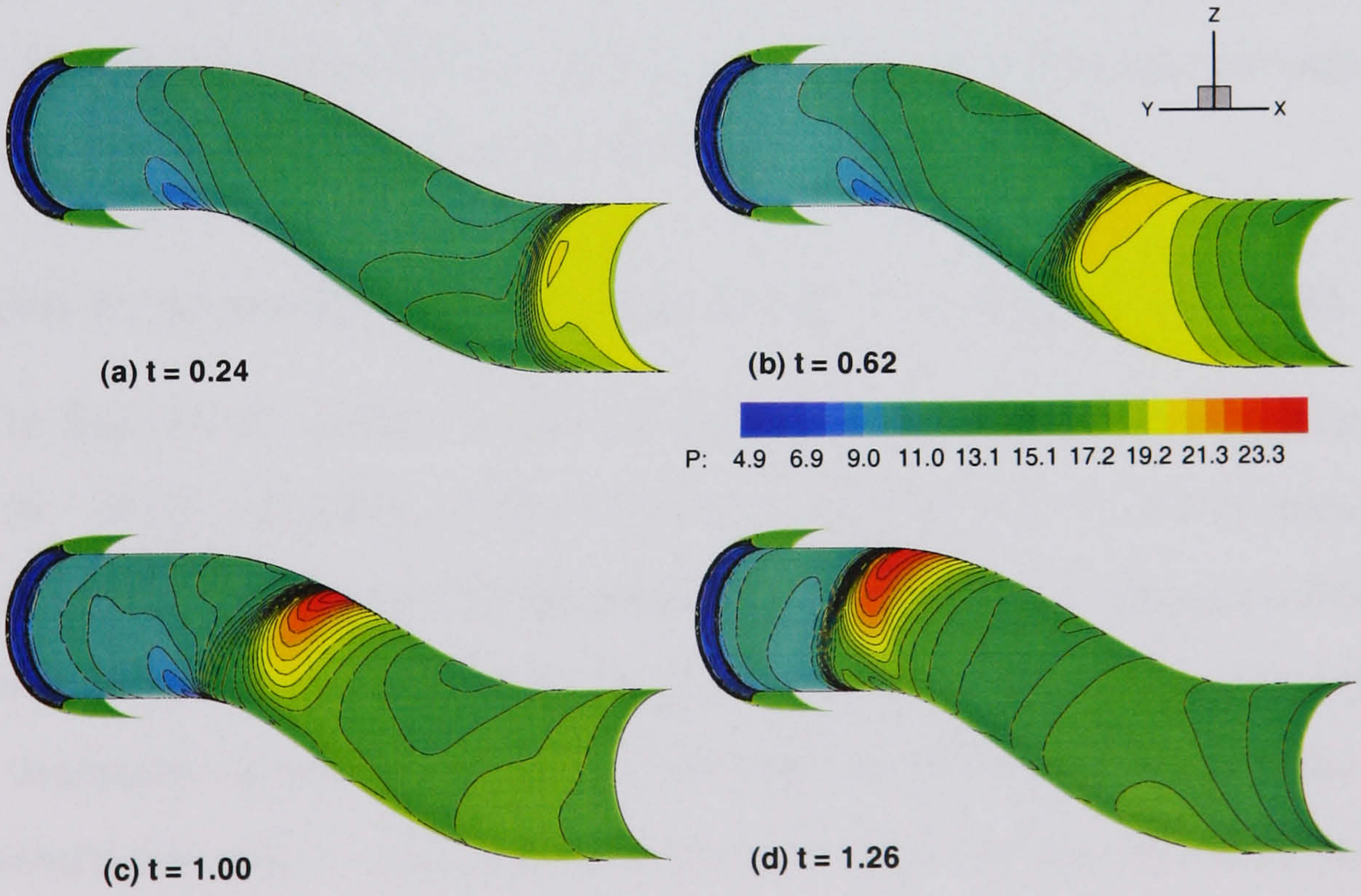

Figure 6.34: *HMFR SST calculation, OPR = 1.5, Surge signature 2 - Pressure from the duct wall at 4 instants leading up to surge exit*

6.8 Surge at Incidence

6.8.1 Yaw at -30^o

Surge signature 1 was applied to the M2129 case at an intermediate angle of -30^o of yaw as this was considered to be representative of an occurrence. The high mass flow case was examined. The analysis is again split up into segments relating to the progression of the surge propagation, as follows.

Propagation from engine face to second bend: $t = 0.0 \rightarrow t = 0.60$

Figure 6.35 (a) and (b) show pressure histories from probes from the downstream boundary to the second bend. It can be seen that the surge propagates to the second bend at t=0.5. The pressure gradient is again stronger on the port side of the duct. The pressure levels are similar to those seen for the 0^o surge case in section 6.3 upstream of the surge front.

Mach number isoline contours and streamlines in figures 6.36 and 6.37 (a) and (b) are similar to the zero degree case downstream. The main effects of the intake at incidence are felt upstream of the second bend. Pressure from the symmetry plane and wall in figures 6.38 and 6.39 (a) and (b) again show the stronger pressure gradient develop on the port side at the second bend.

Propagation from second bend to first bend: $t = 0.60 \rightarrow t = 1.00$

Returning to figure 6.35, plots (c) and (d) show the pressure probes between the two intake bends. With reference to the 0^o case in section 6.3 it can be seen that the main difference is a much higher peak pressure of almost 39 on the port side. On the starboard side the pressure is actually slightly lower, probably due to upstream effects as the flow separates from the cowl lip on the starboard side. It should also be noted on the starboard side that a pressure oscillation develops behind the initial surge front.

Figures 6.36 and 6.37 (c) and (d) show that the interaction of the surge front with the secondary flow creates a slightly stronger secondary flow. As the surge propagates through the second bend the recirculation moves with it. At t=1.3 it can be seen that there are two distinct regions of circulating flow and this may explain the secondary peaks in the pressure trace that appear behind the surge front on the starboard side after the surge exits, as discussed below.

Finally, figures 6.38 and 6.39 (c) and (d) show a strong localised area of pressure towards the port side on the wall. The surge front is more advanced on the starboard side cowl region because of the separation from the lip in this location.

Propagation from first bend to freestream: t = 1.0 onwards

Pressure probe data in Figure 6.35 (e) and (f) show that the surge front exits the duct at about t=1.2 on the starboard side and t=1.4 on the port side. On the starboard side there are two subsequent distinct peaks following the initial surge expulsion. These peaks are thought to arise from the development of two distinct circulating regions as the surge propagates through the separated region prior to expulsion. Reflection of these two peaks can be seen on the pressure trace at probe S10. On the port side the surge front exits at t=1.5 when the peak pressure is 40.2. This is the maximum pressure reached for this case. A reflection of the main surge front is felt at the downstream and this in turn exits the duct at around t=4.4.

Figures 6.36 and 6.37 show that the peak Mach number is induced on the starboard side wall cowl region just before the surge exits the duct and is actually a flow reversal from the propagation of the recirculating region behind the surge front. The surge exits the duct and strong spillage is felt out of the duct, particularly towards the starboard side once more, that extends into the freestream.

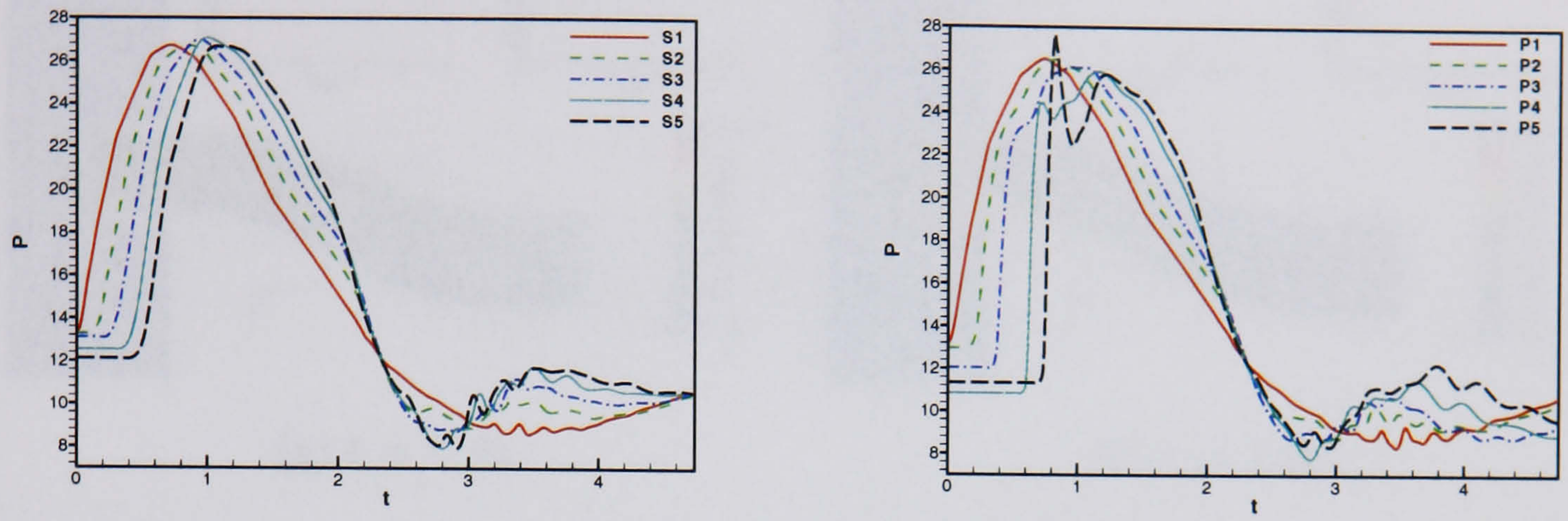

(a) Starboard probes 1 - 5 (b) Port probes 1 - 5

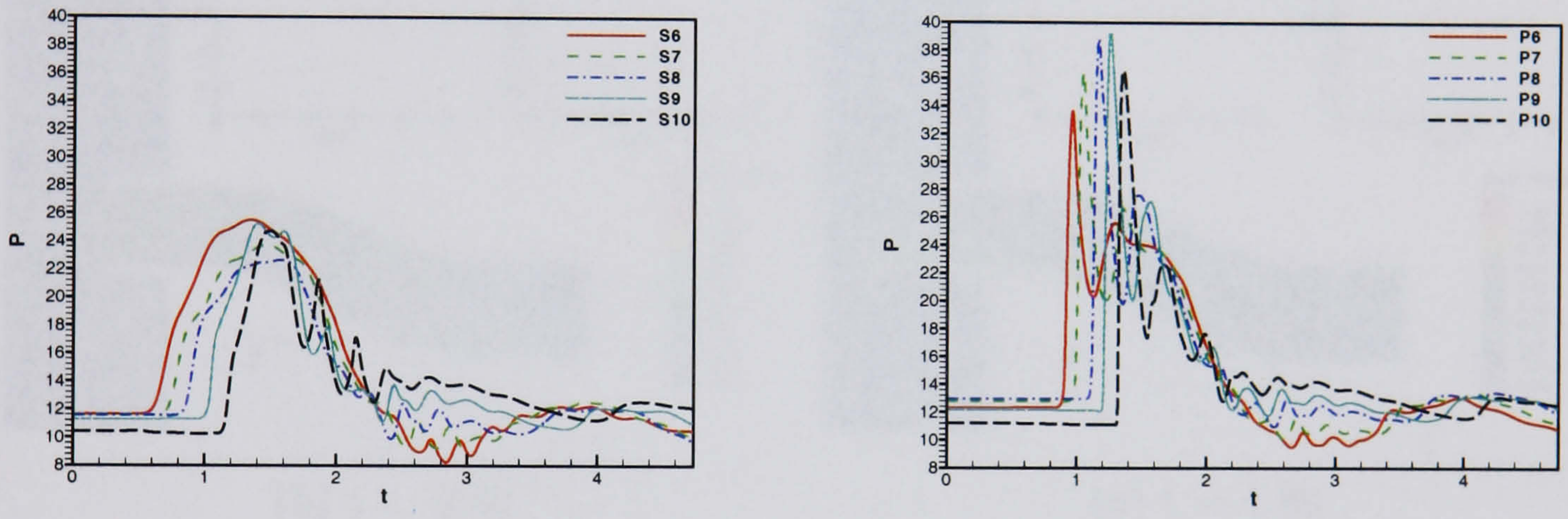

(c) Starboard probes 6 - 10 (d) Port probes 6 - 10

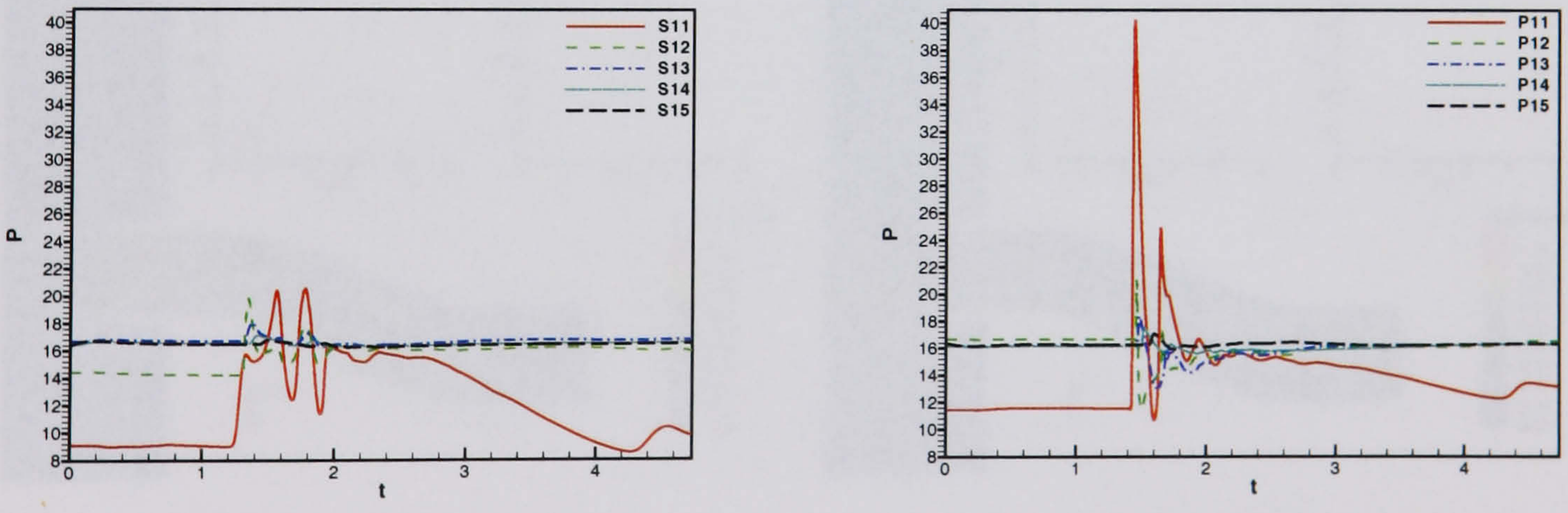

(e) Starboard probes 11 - 15 (f) Port probes 11 - 15

Figure 6.35: *HMFR SST calculation, OPR = 2, Surge signature 1, -30 degrees yaw - Symmetry plane probe data*

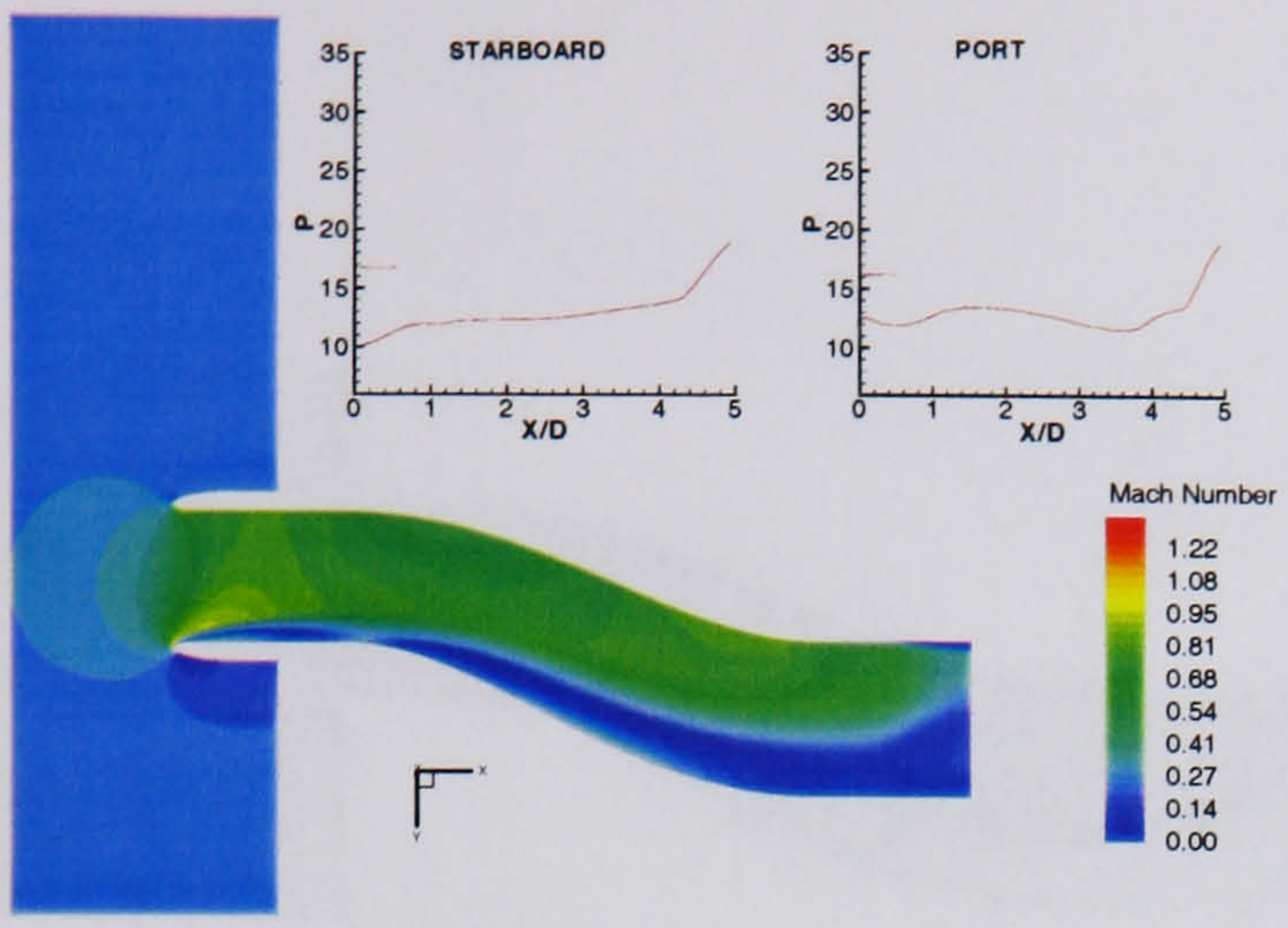

(a) t = 0.20

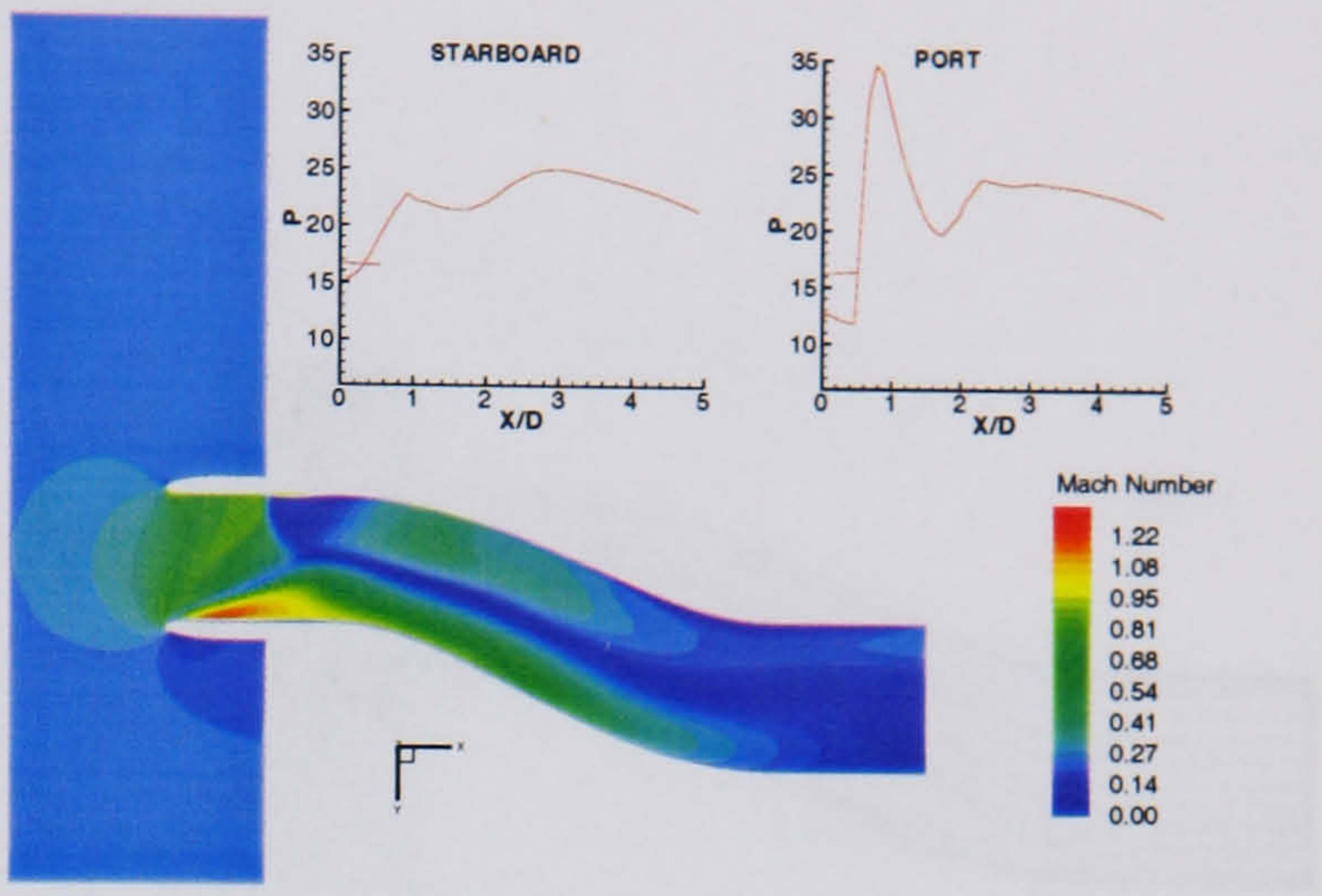

(d) t = 1.30

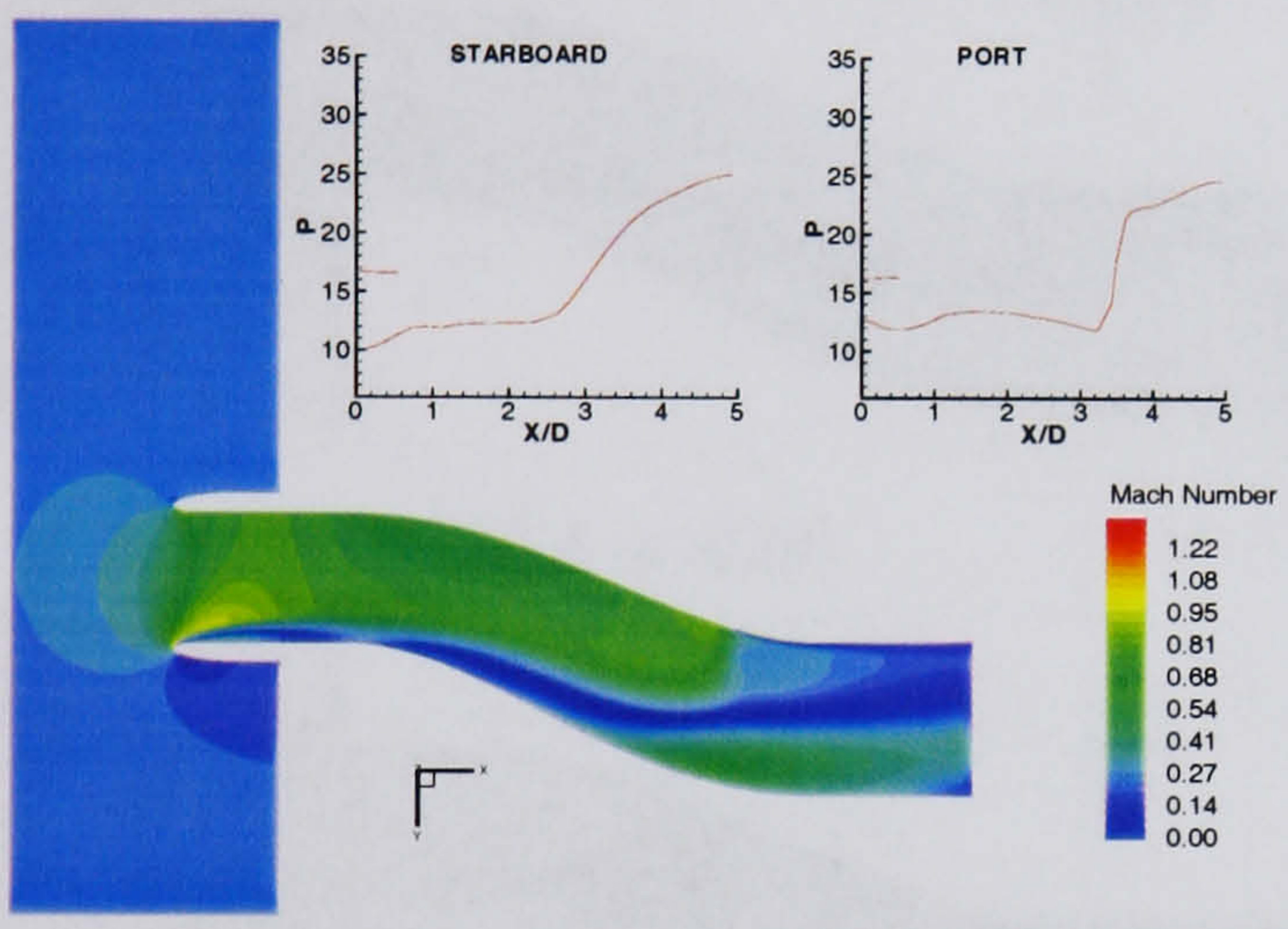

(b) t = 0.60

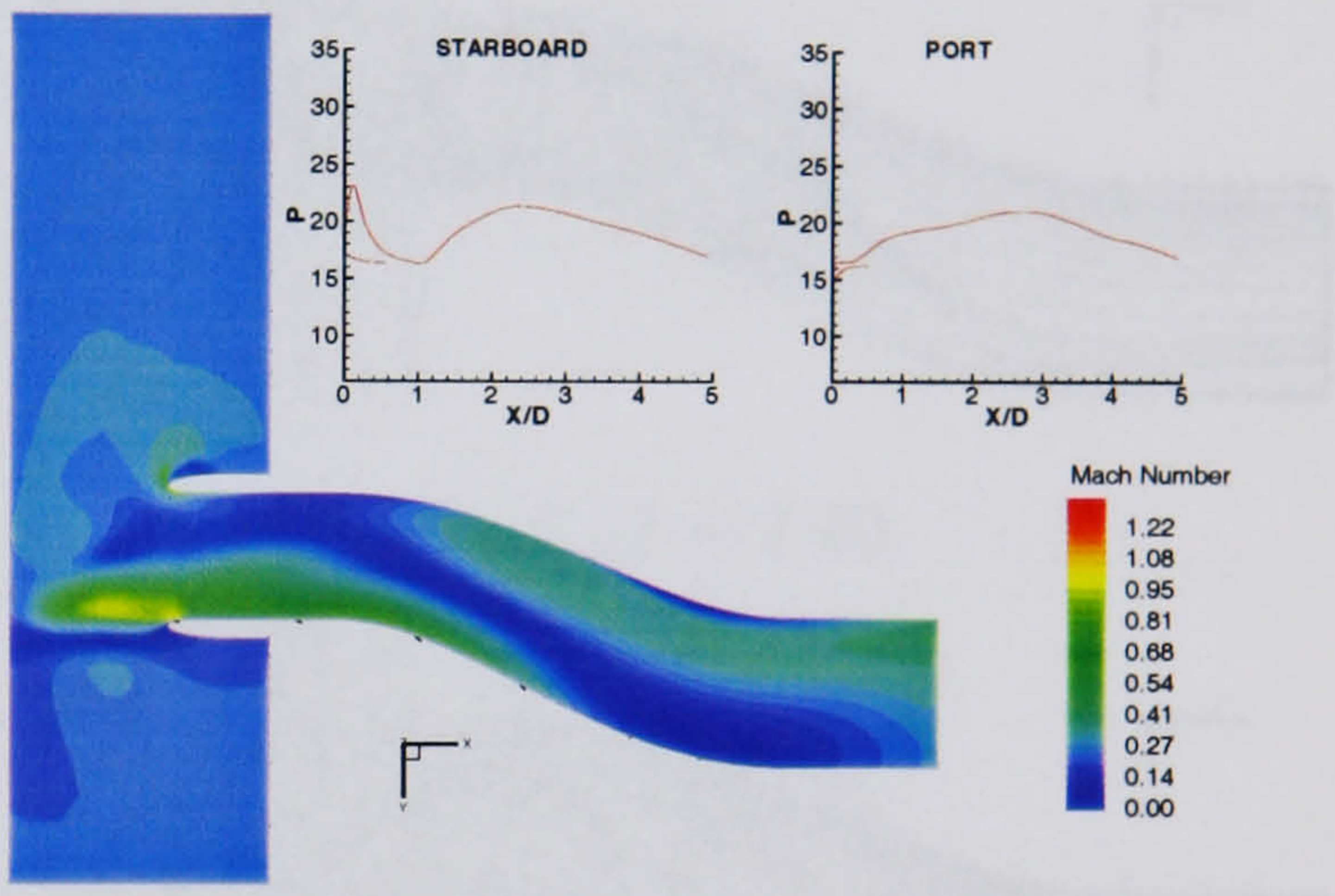

(e) t = 1.80

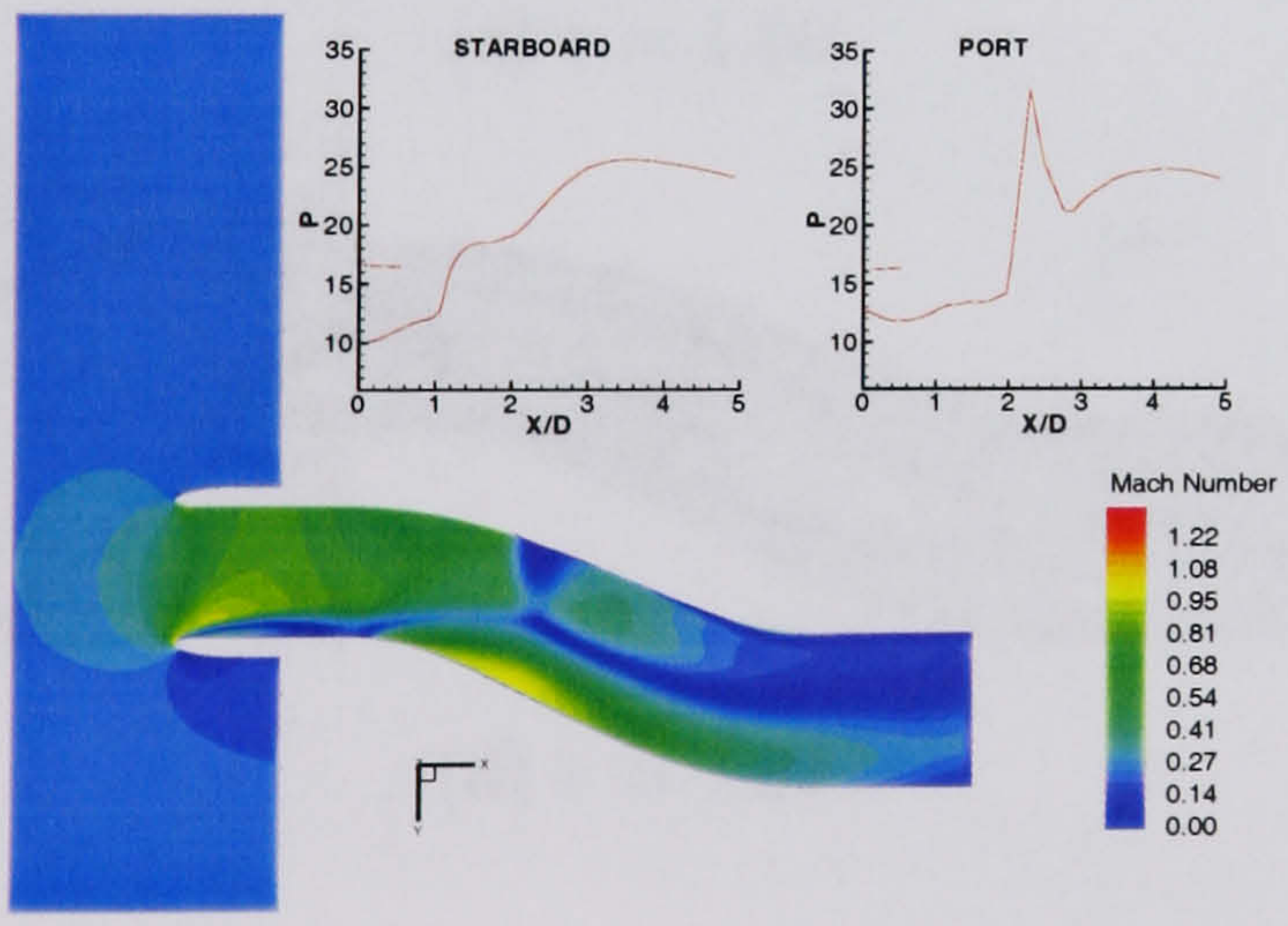

(c) t = 1.00

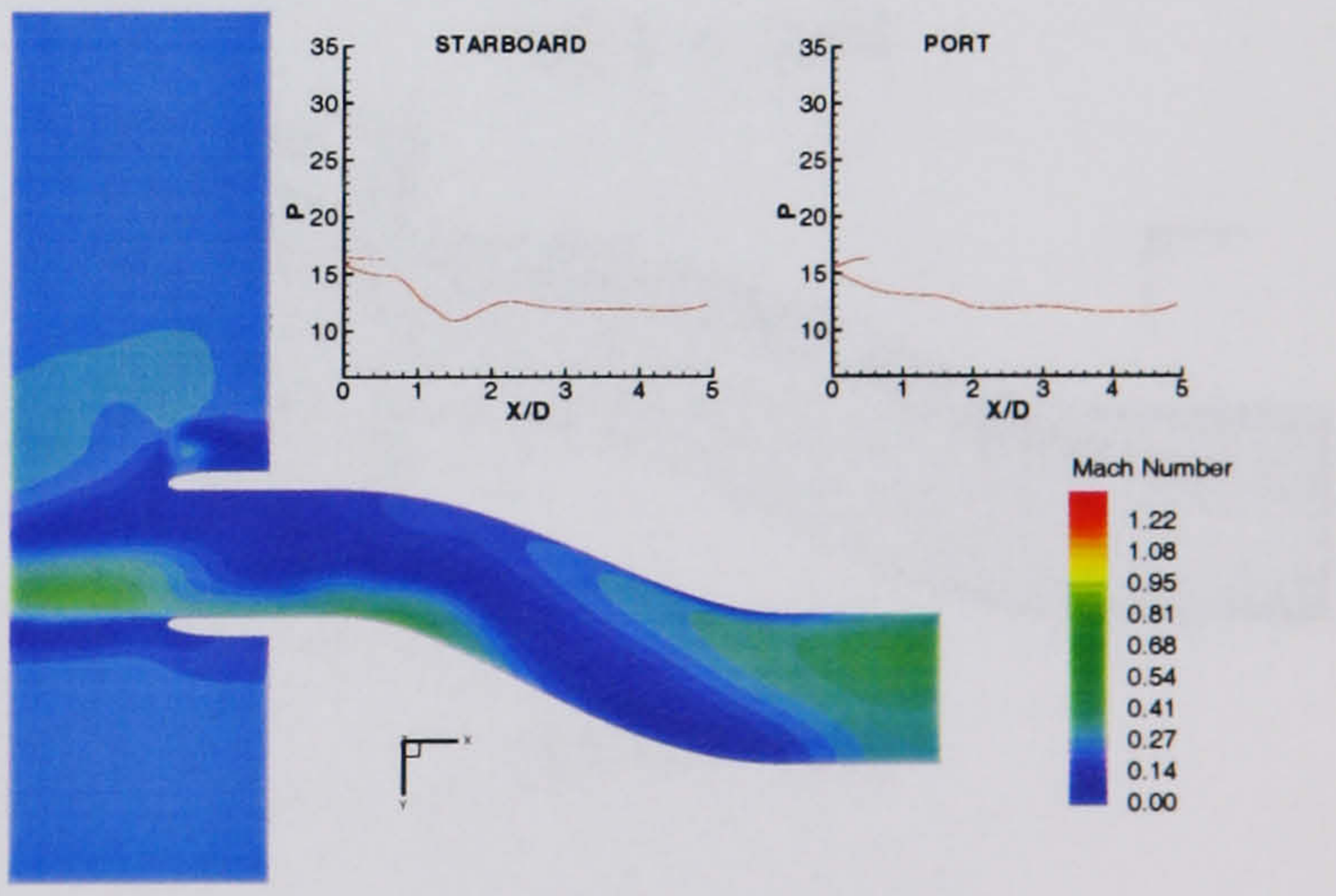

(f) t = 2.40

Figure 6.36: *HMFR SST calculation, OPR = 2, Surge signature 1, -30 degrees yaw - Symmetry plane Mach number and pressure traces*

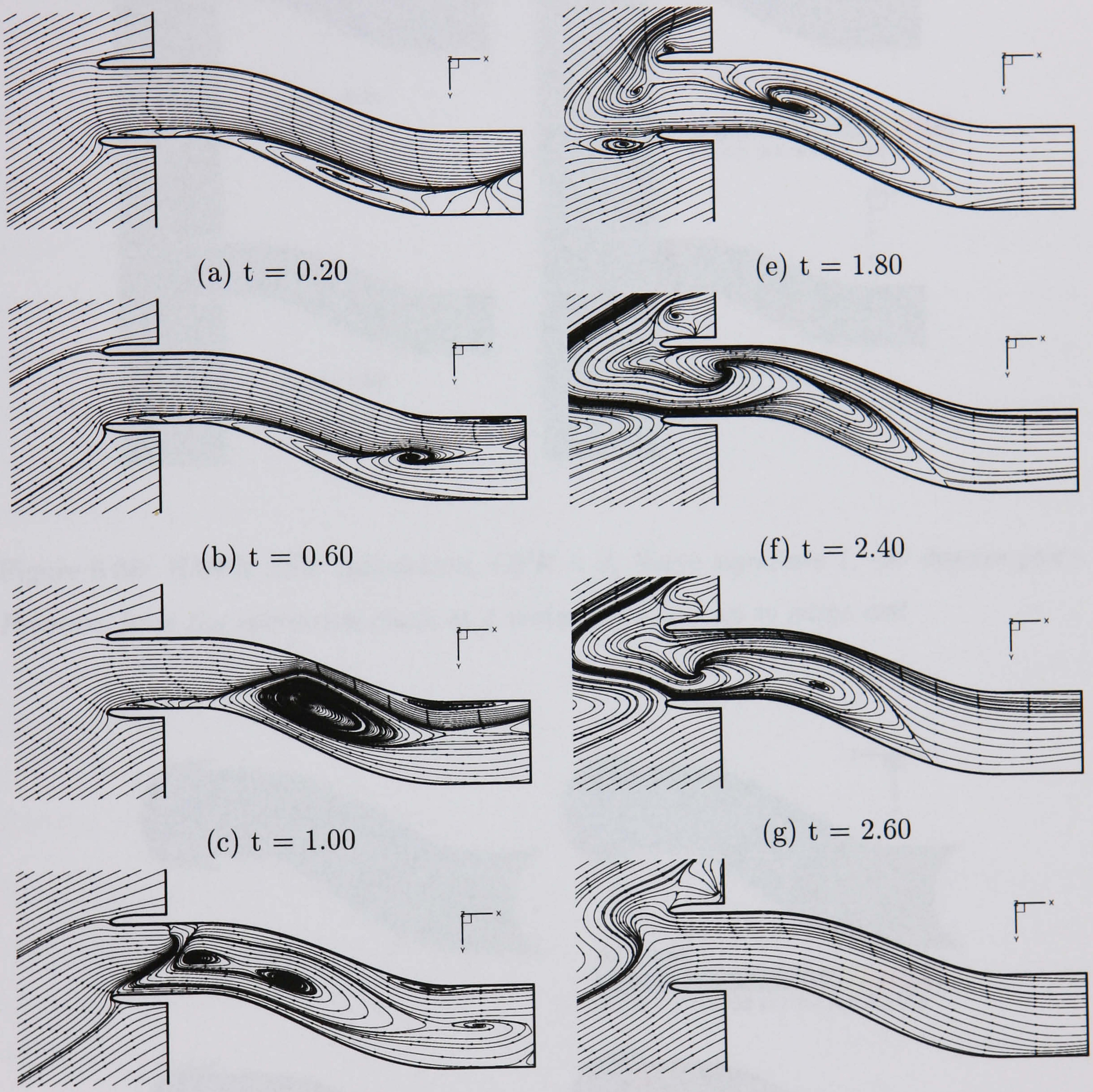

(a) t = 0.20

(e) t = 1.80

(b) t = 0.60

(f) t = 2.40

(c) t = 1.00

(g) t = 2.60

(d) t = 1.30

(h) t = 3.30

Figure 6.37: *HMFR SST calculation, OPR = 2, Surge signature 1, -30 degrees yaw - Symmetry plane streamlines*

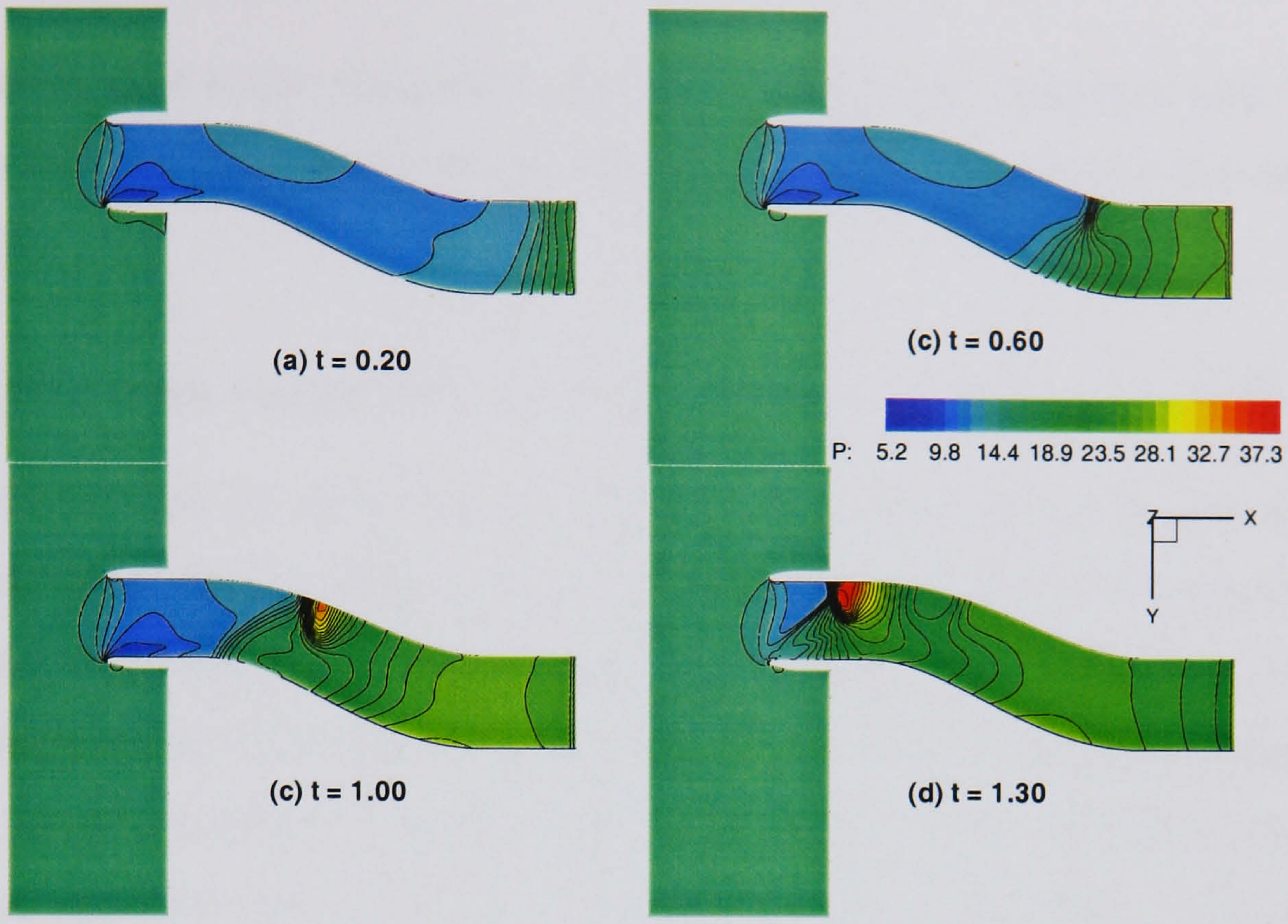

Figure 6.38: *HMFR SST calculation, OPR = 2, Surge signature 1, -30 degrees yaw - Pressure from the symmetry plane at 4 instants leading up to surge exit*

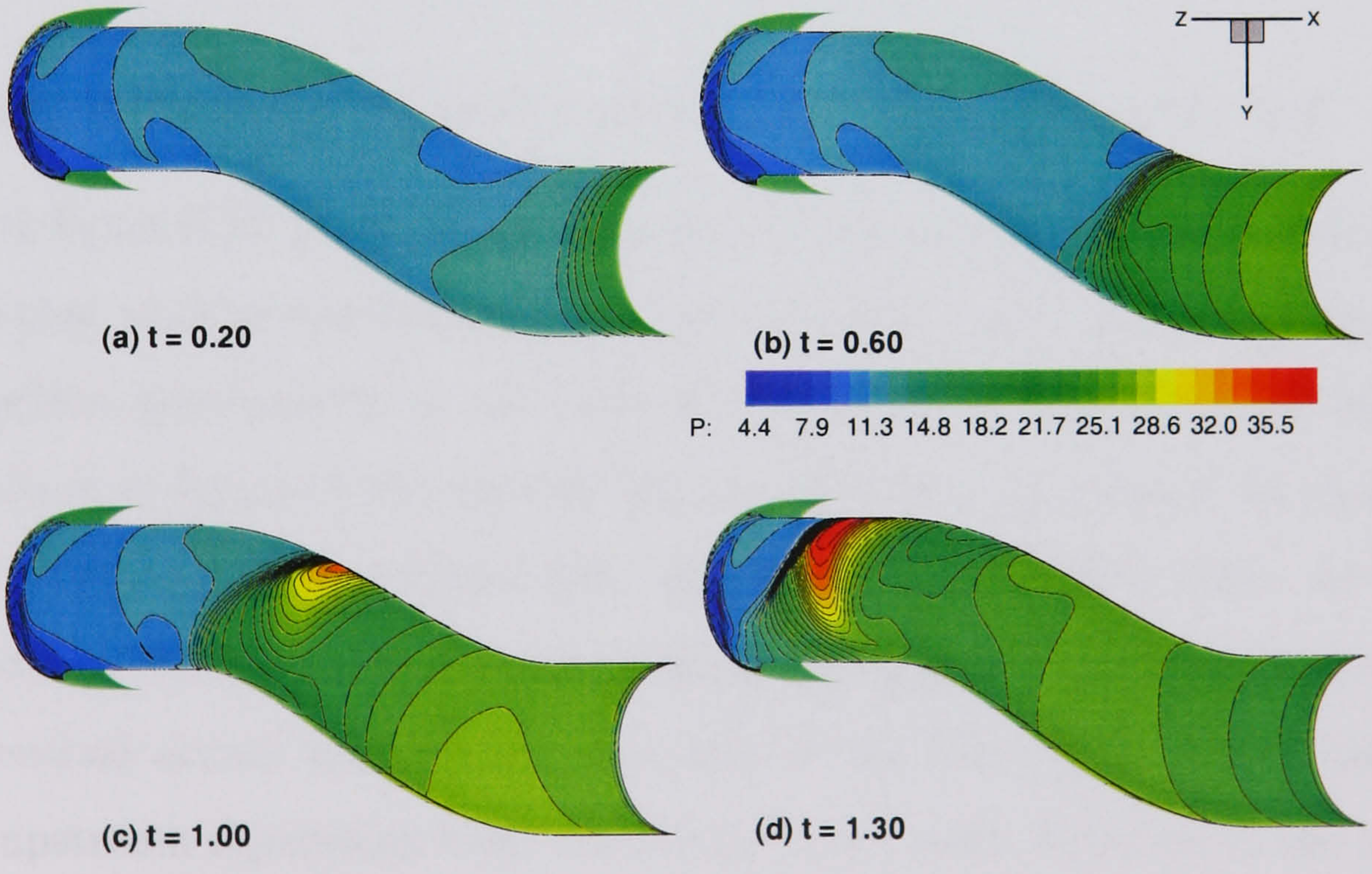

Figure 6.39: *HMFR SST calculation, OPR = 2, Surge signature 1, -30 degrees yaw - Pressure from the duct wall at 4 instants leading up to surge exit*

6.8.2 Yaw at $+30^o$

As the yawing case is not symmetric, yaw at $+30^o$ has been examined also. The same high mass flow case has been used and signature 1 has been applied at the downstream boundary.

Propagation from engine face to second bend: $t = 0.0 \rightarrow t = 0.60$

Figure 6.40 (a) and (b) show pressure histories from starboard and port side probes respectively from the downstream boundary to the second bend. The general form of the pressure data from these locations is similar to the 0^o case once more. The pressure gradient increases as the surge front approaches the second bend, particularly on the port side, as seen previously. Figures 6.41 and 6.42 show that the Mach contours and streamlines are very similar to the 0^o case. The steady-state effects of incidence are mainly upstream where there is separation of the flow from the port side cowl lip and the extent of the secondary flow from the starboard side first bend is also smaller. Wall and symmetry plane pressure in figures 6.43 and 6.44 (a) and (b) show that the surge front is more uniform in terms of pressure gradient at t=0.6 as the effects of the intake offset are reduced at positive angles of yaw.

Propagation from second bend to first bend: $t = 0.60 \rightarrow t = 1.0$

Returning to figure 6.40, plots (c) and (d) cover probes between the two intake bends. It can be seen that peak pressures from these probes on both sides of the duct are generally reduced slightly, particularly on the port side. Examining Mach number isocontours and streamlines in figures 6.41 and 6.42 (b) and (c), this can perhaps be explained by the separated flow on the starboard side originating at the intake cowl. As the surge front approaches the first bend the recirculating region is transported upstream behind it. Flow reversal occurs towards the port side in the low energy region that results due to the upstream separation from the inboard port cowl. Pressure in the symmetry plane and wall in figures 6.43 and 6.44 (c) show that pressures are lower than for the 0^o case and there is evidence that the peak pressure is developing towards the centre of the duct wall, between the port and starboard sides, behind the surge front.

Propagation from first bend to freestream: t = 1.0 onwards

Figure 6.40, plots (e) and (f) show the probes in the cowl region. It can be seen that the peak pressure for this case occurs as the surge exits the duct on the starboard side. The peak pressure is abrupt and drops off rapidly. On the port side the pressure is lower than for the 0^o case and following the initial surge front exit at t=1.4 there follows further peaks. This is similar to the -30^o case on the starboard side. After the surge exits the duct the pressure drops off downstream until there is a slight increase at the engine boundary at around t=3.4 relating to the reflection of the original surge exiting the intake.

Figures 6.41 and 6.42 (c) and (d) show that the interaction of the propagating surge front with the secondary flow region from the starboard side first bend further results in the circulating flow region moving upstream. On the port side, as the surge front propagates through the separated region from the port cowl lip, the flow circulation is enhanced here too. This may be the cause of the peaky nature of the surge pressure history as it exits the duct. The pressure from the symmetry plane and duct wall in figures 6.43 and 6.44 (d) show that the peak pressure at t=1.4 is concentrated more in the centre of the duct wall cowl.

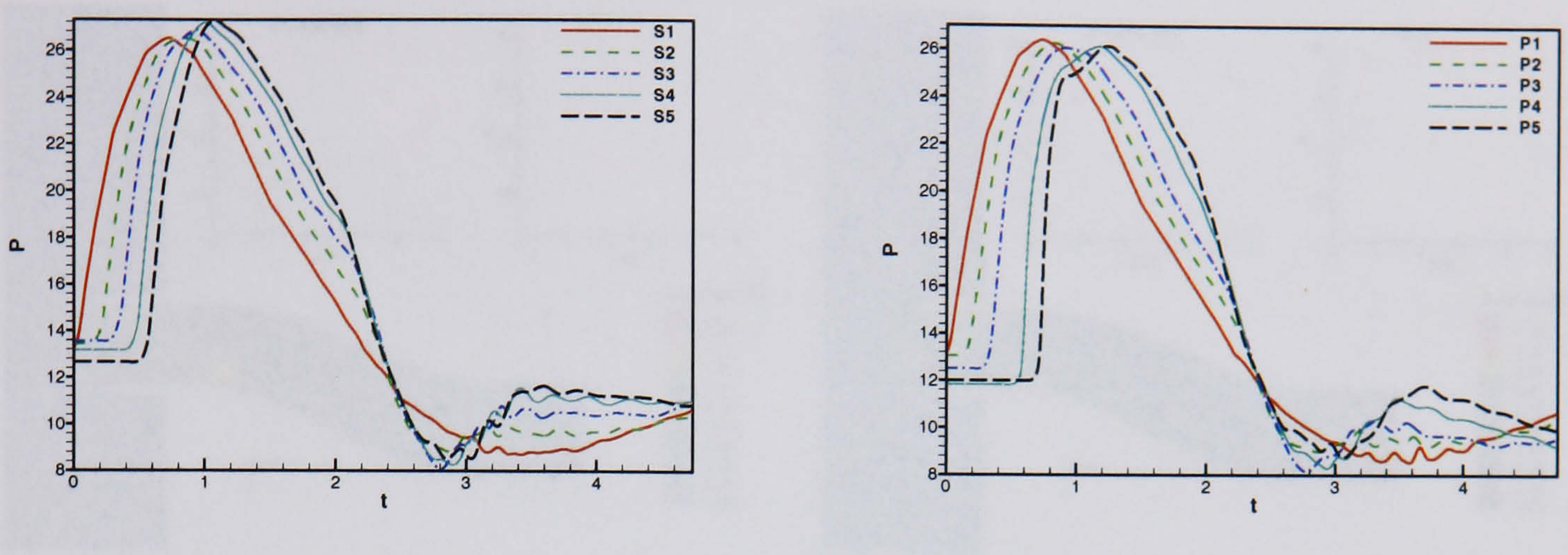

(a) Starboard probes 1 - 5

(b) Port probes 1 - 5

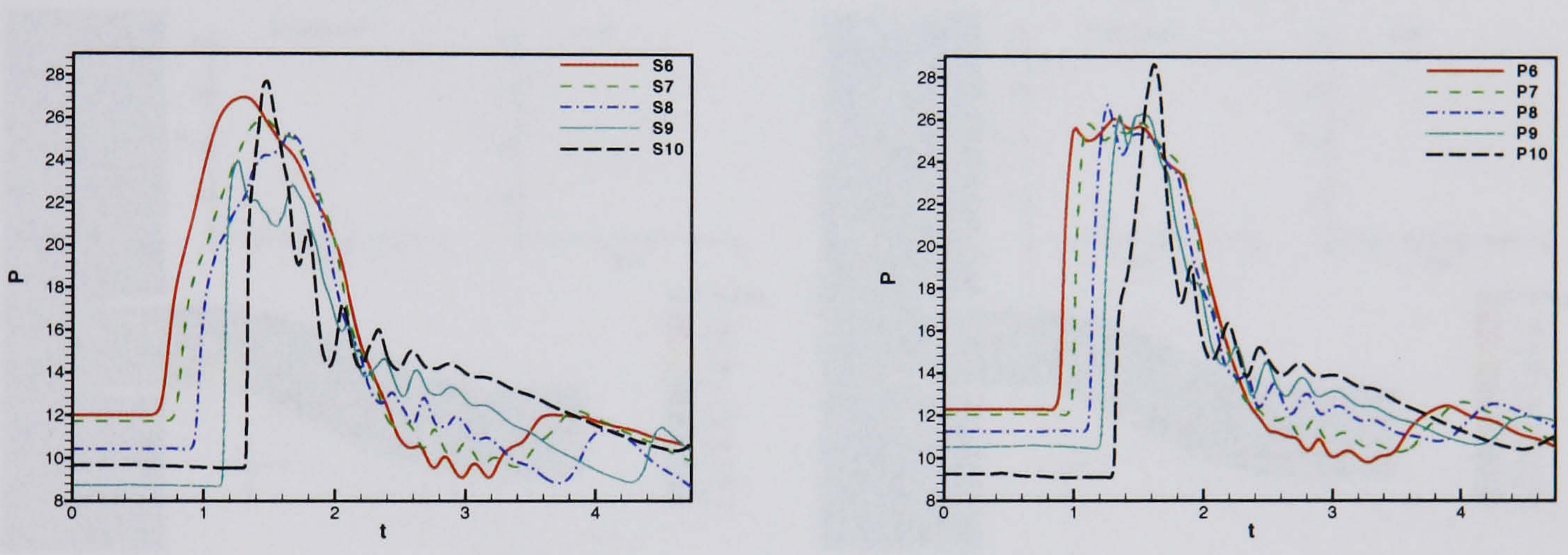

(c) Starboard probes 6 - 10

(d) Port probes 6 - 10

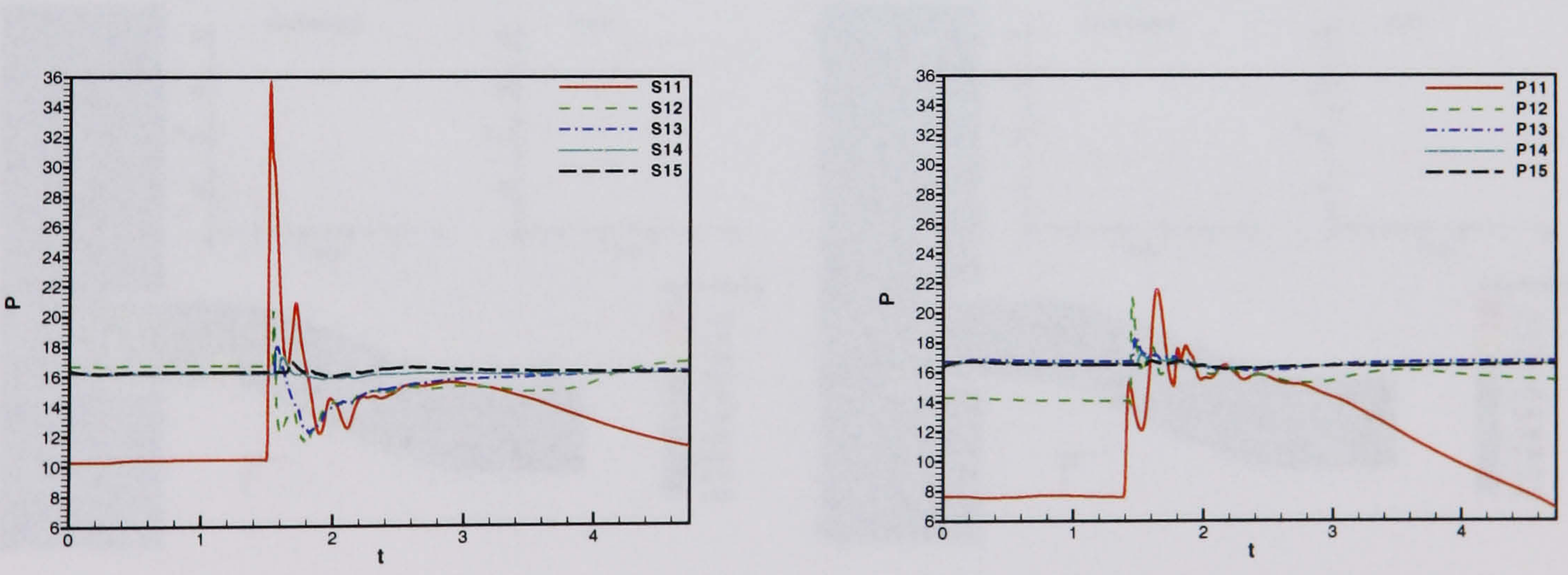

(e) Starboard probes 11 - 15

(f) Port probes 11 - 15

Figure 6.40: *HMFR SST calculation, OPR = 2, Surge signature 1, +30 degrees yaw - Symmetry plane probe data*

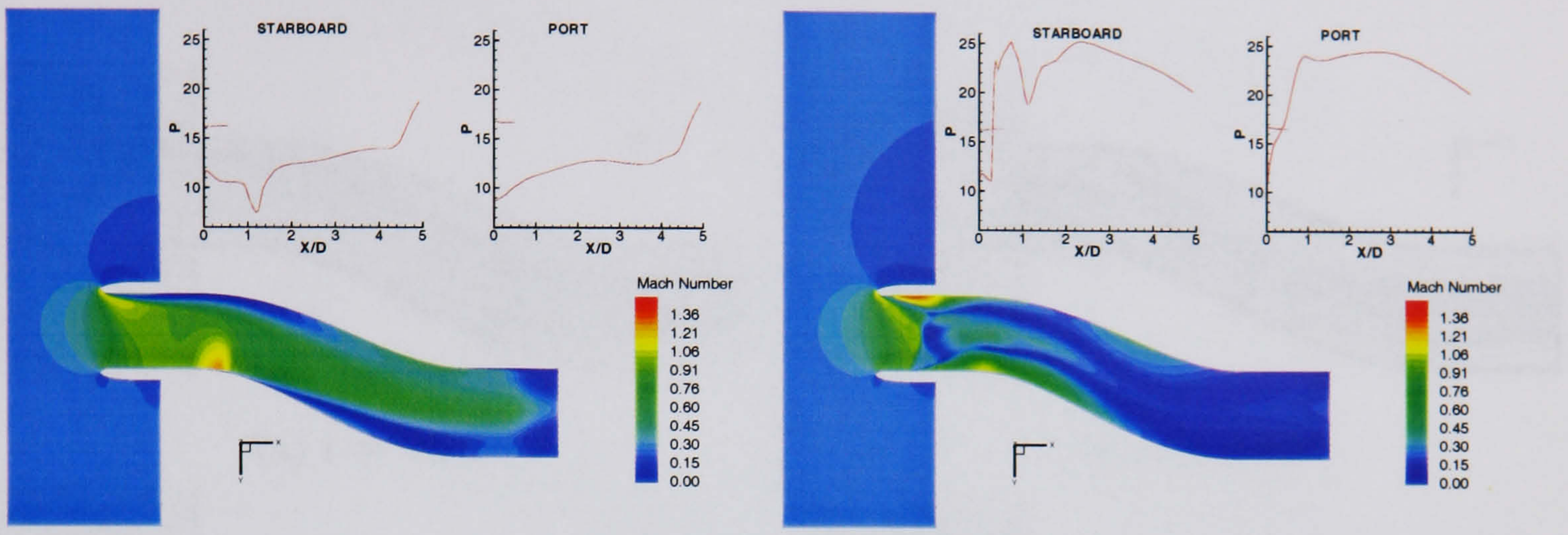

(a) t = 0.20

(d) t = 1.40

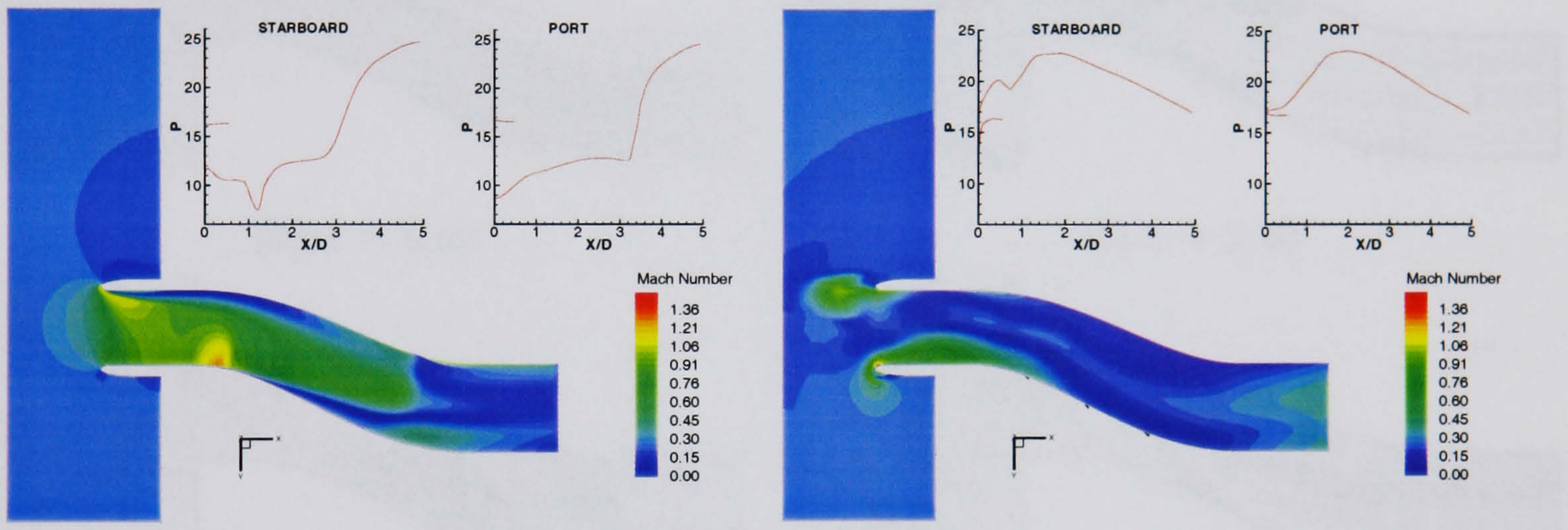

(b) t = 0.60

(e) t = 1.80

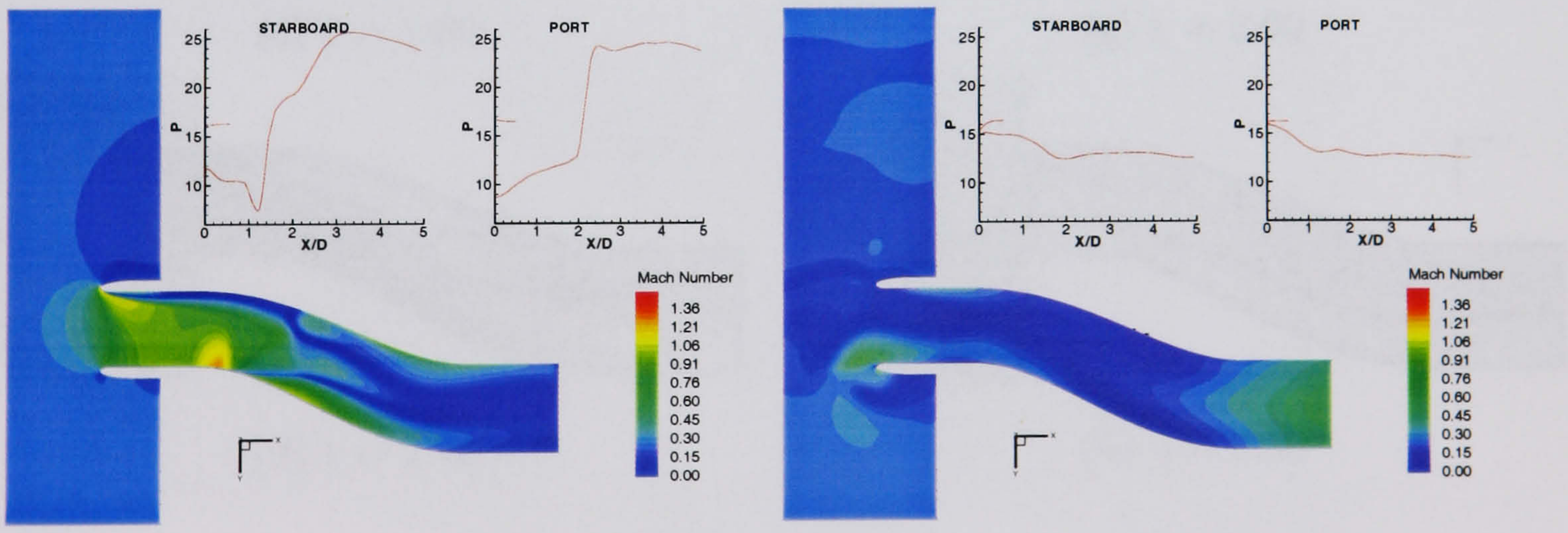

(c) t = 1.00

(f) t = 2.40

Figure 6.41: *HMFR SST calculation, OPR = 2, Surge signature 1, +30 degrees yaw - Symmetry plane Mach number and pressure traces*

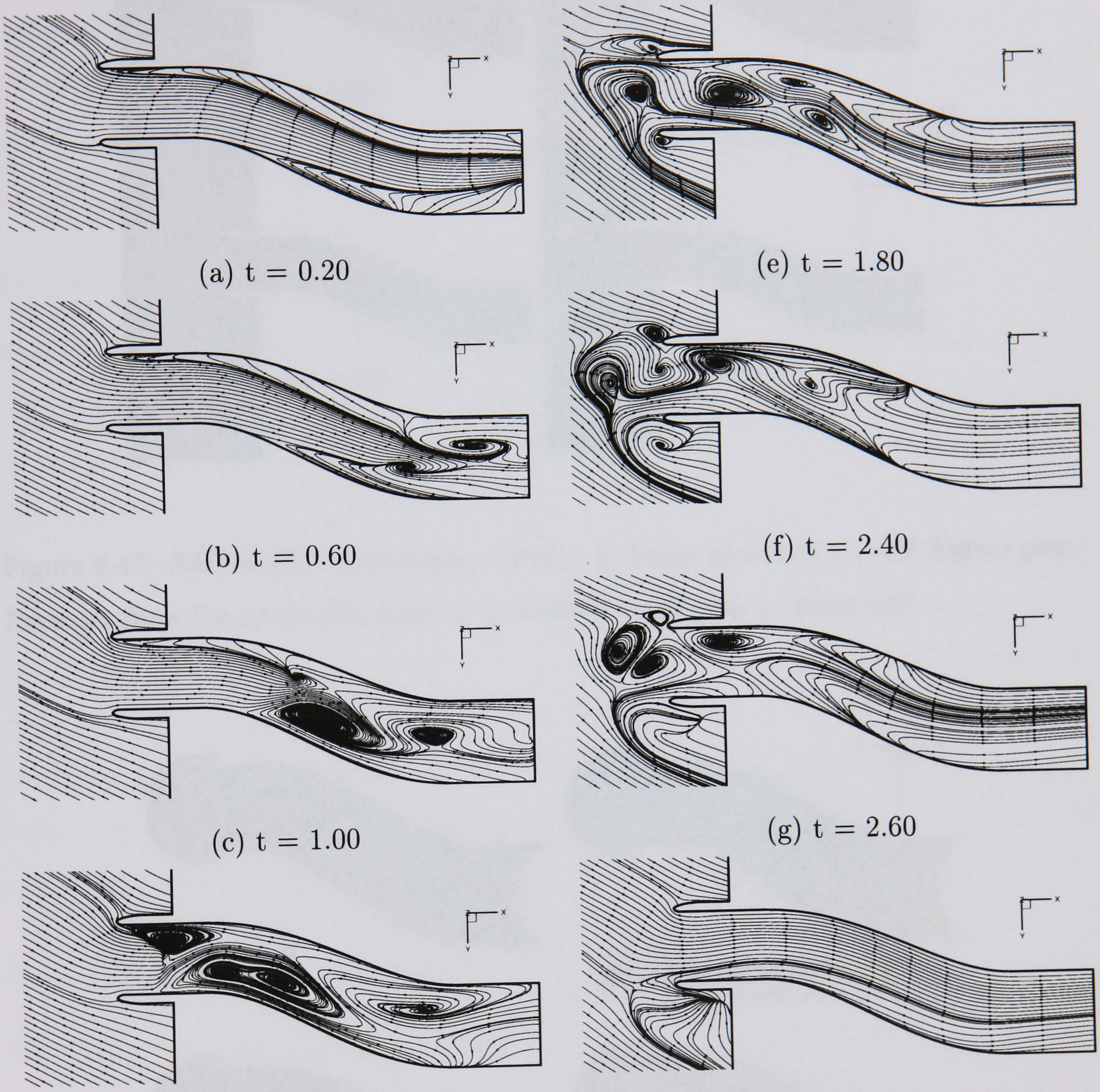

(a) t = 0.20

(e) t = 1.80

(b) t = 0.60

(f) t = 2.40

(c) t = 1.00

(g) t = 2.60

(d) t = 1.40

(h) t = 3.30

Figure 6.42: *HMFR SST calculation, OPR = 2, Surge signature 1, +30 degrees yaw - Symmetry plane streamlines*

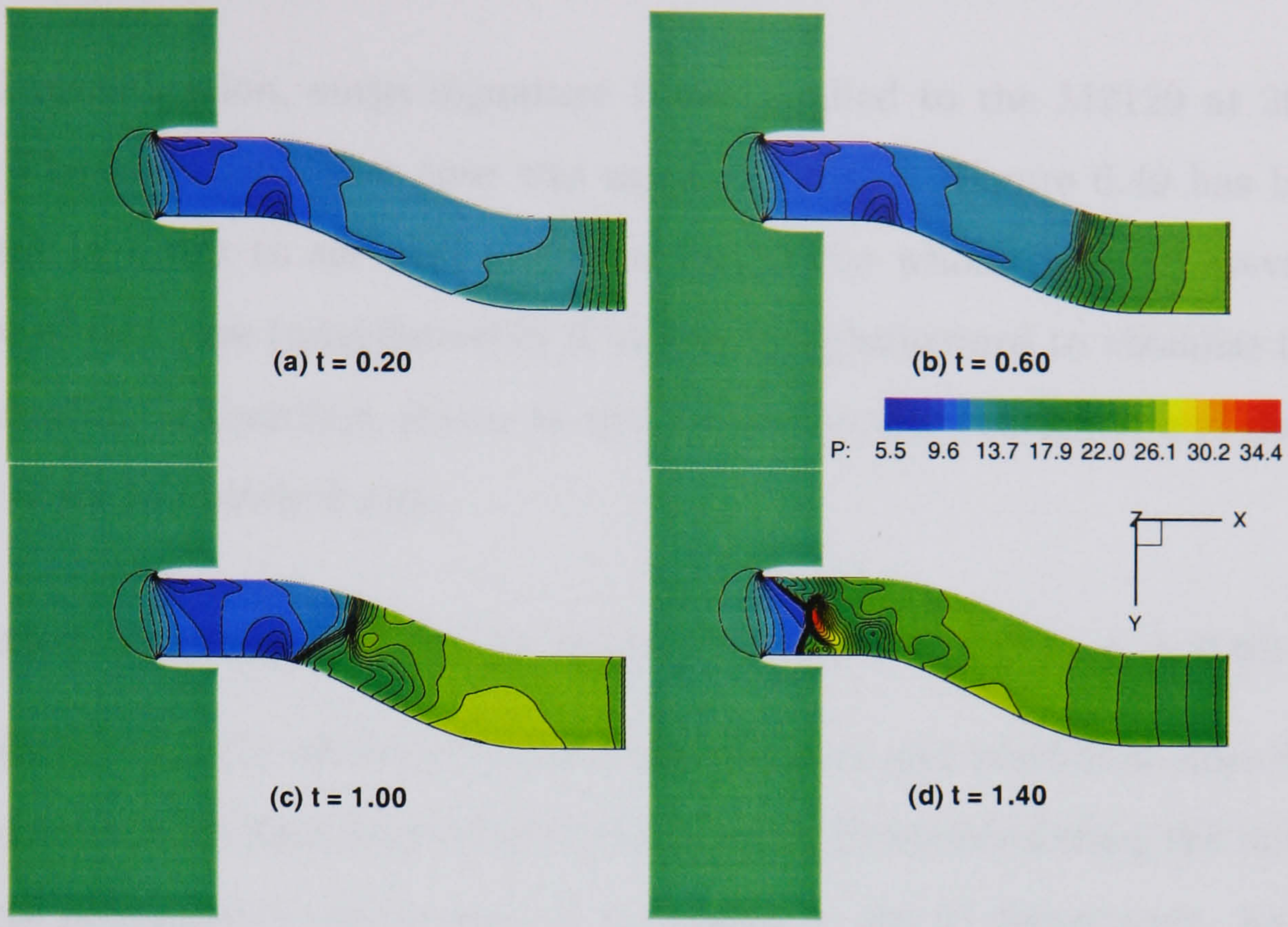

Figure 6.43: *HMFR SST calculation, OPR = 2, Surge signature 1, +30 degrees yaw - Pressure from the symmetry plane at 4 instants leading up to surge exit*

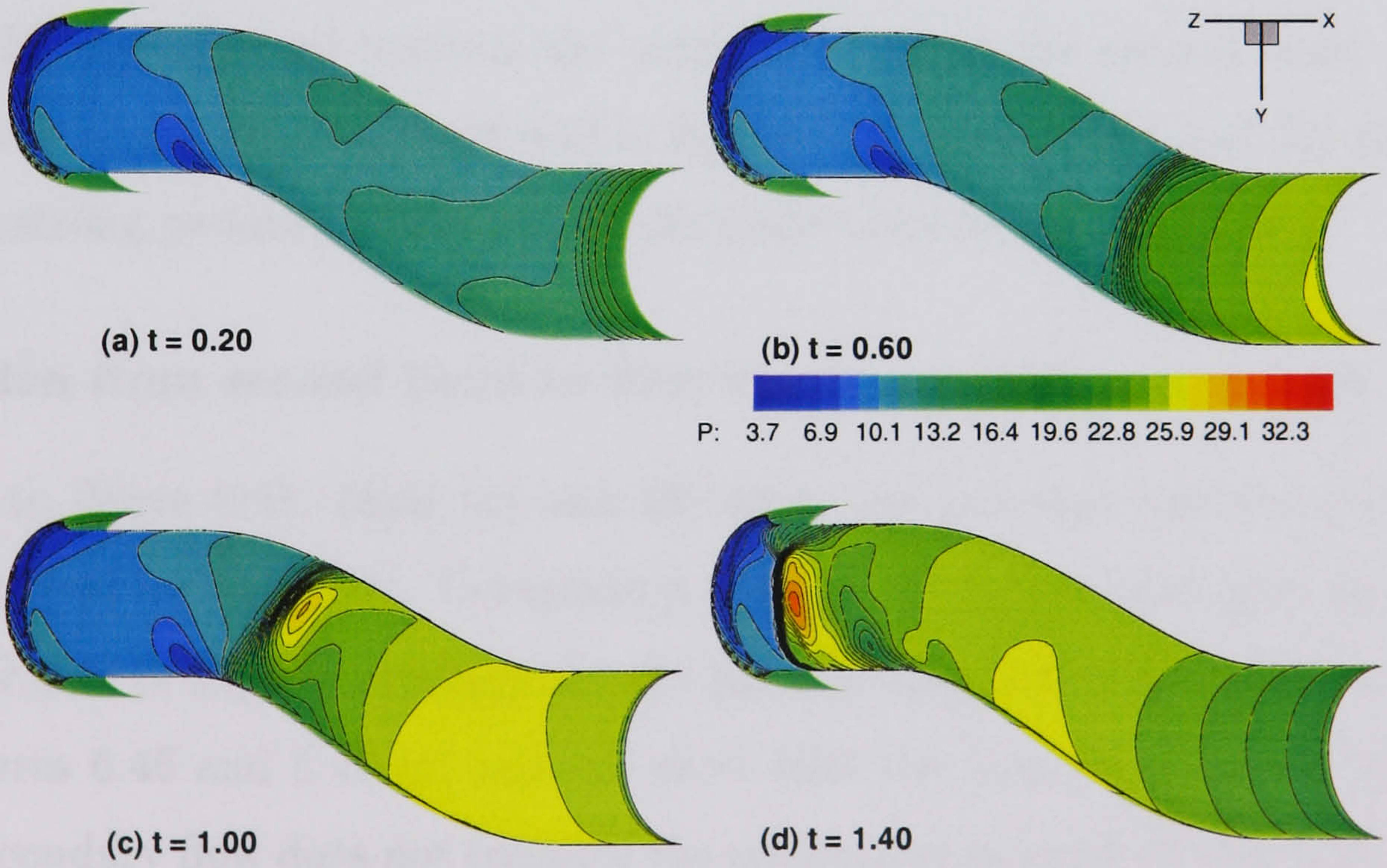

Figure 6.44: *HMFR SST calculation, OPR = 2, Surge signature 1, +30 degrees yaw - Pressure from the duct wall at 4 instants leading up to surge exit*

6.8.3 Pitch at $+30^o$

As a final investigation, surge signature 1 was applied to the M2129 at 30^o degrees of pitch. The high mass flow case was again examined. Figure 6.49 has been made transluscent in order to see wall pressures round the whole duct. However, due to the nature of this case (unsymmetric) it is less straightforward to visualise than other cases. Attention is therefore drawn to the animation CD contained and described in appendix C for the pitched case.

Propagation from engine face to second bend: $t = 0.0 \rightarrow t = 0.60$

Figure 6.45 (a) and (b) shows pressure from the port and starboard sides for probes from the downstream boundary to the second bend. Pressures during the initial stages of the surge propagation can be seen to be similar to the 0^o degree case. As the surge approaches the second bend the pressure gradient increases, particularly on the port side. The main differences are expected to occur upstream due to the effects of the separation from the inboard cowl lip. Figures 6.46 and 6.47 (a) and (b) show symmetry plane Mach numbers and streamlines. Here differences from previous cases are minimal. As the surge reaches the second bend the front interacts with the secondary flow and enhances the flow reversal towards the starboard side at the second bend. Pressure data from the symmetry plane and wall in figures 6.48 and 6.49 (a) and (b) shows more clearly the strong pressure gradient that develops towards the port side.

Propagation from second bend to first bend: $t = 0.60 \rightarrow t = 1.00$

Returning to figure 6.45, plots (c) and (d) show the pressure histories from probes between the two intake bends. Comparison with the 0^o degree case show the pressure on the port side is slightly stronger for the pitched case and again peaks at the first bend. Figures 6.46 and 6.47 (c) and (d) show that the interaction of the surge front with the secondary flow does not enhance the circulation as much in this case. Pressure from the symmetry plane and wall in figures 6.48 and 6.49 (c) show that a high pressure builds behind the surge front on the port side. On the starboard side the surge front has advanced further upstream and has reached the second bend.

Propagation from first bend to freestream: t = 1.0 onwards

Finally, returning to figure 6.45, plots (e) and (f) show pressure histories from probes in the cowl region. It can be seen that the surge front exits the port and starboard sides of the duct at t=1.42 approximately. Following the expulsion of the surge front the pressure in the duct recedes. A reflection of the surge front expulsion is felt at the downstream boundary at approximately t=3.2. This in turn propagates up the intake towards the duct cowl and is similar in strength to previous cases.

Plot (d) onwards from figures 6.46 and 6.47 shows that following the expulsion of the surge from duct spillage is induced on the starboard side but is not as strong as for previous cases. Pressure from the symmetry plane and wall in figures 6.48 and 6.49 (d) show that the peak pressure for the case appears to occur towards the port side wall at the first bend.

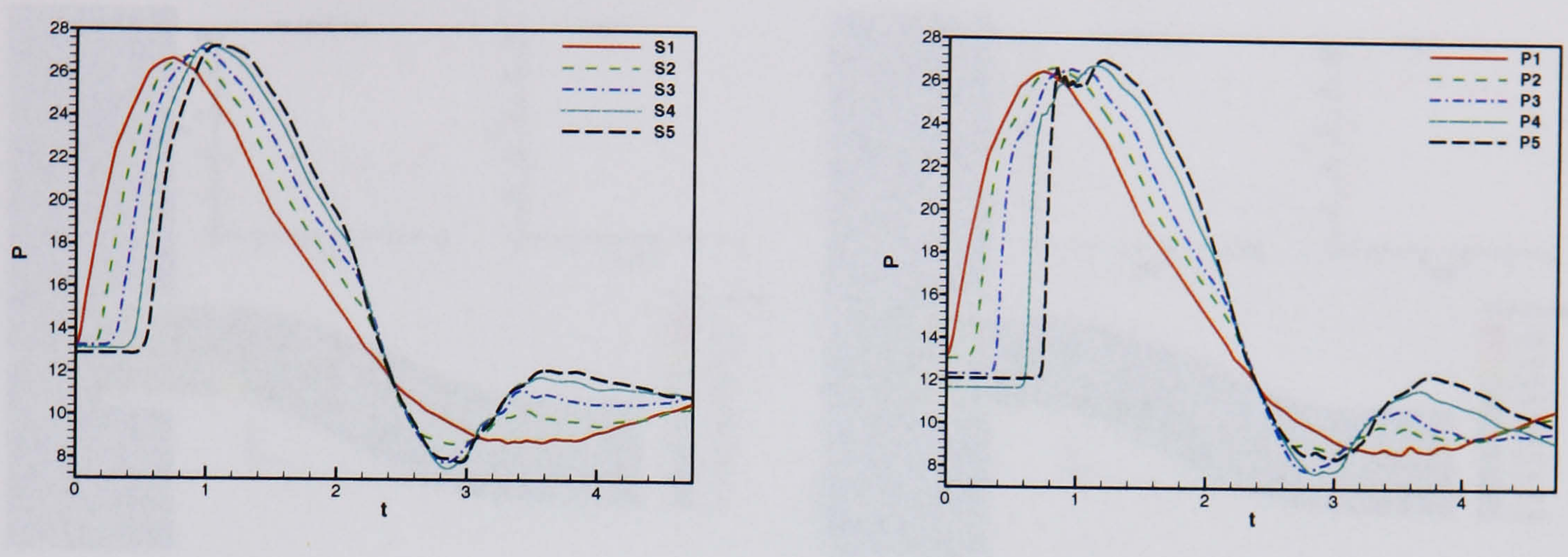

(a) Starboard probes 1 - 5

(b) Port probes 1 - 5

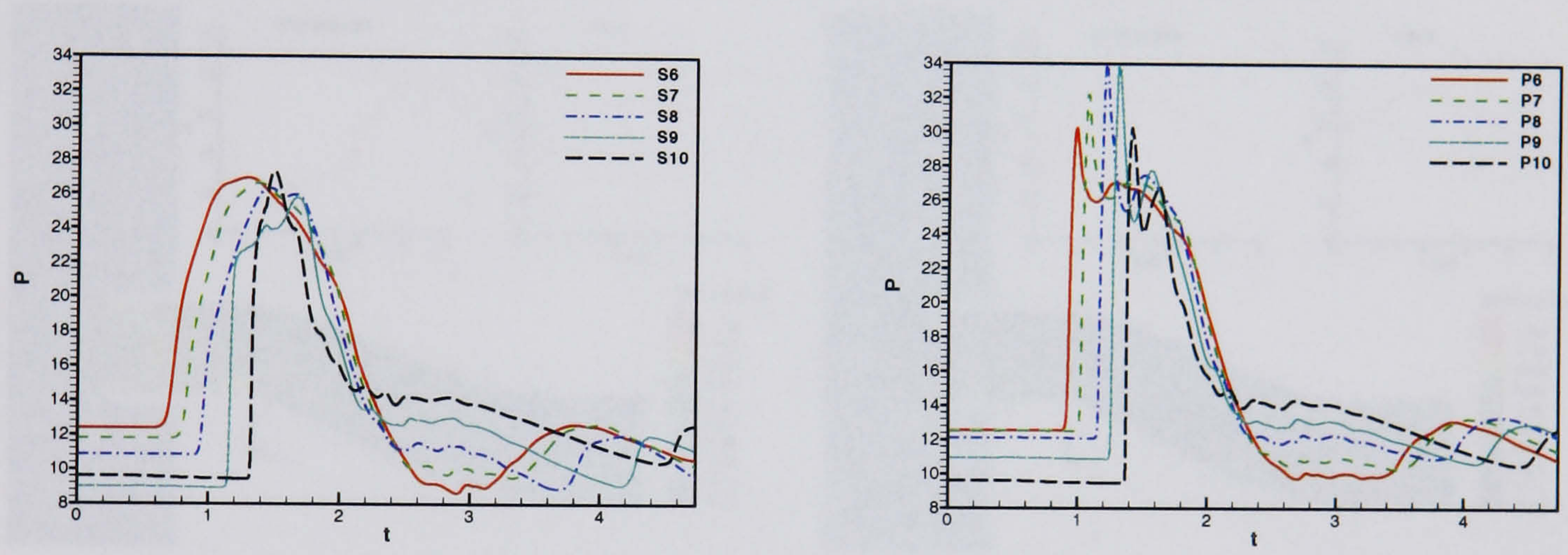

(c) Starboard probes 6 - 10

(d) Port probes 6 - 10

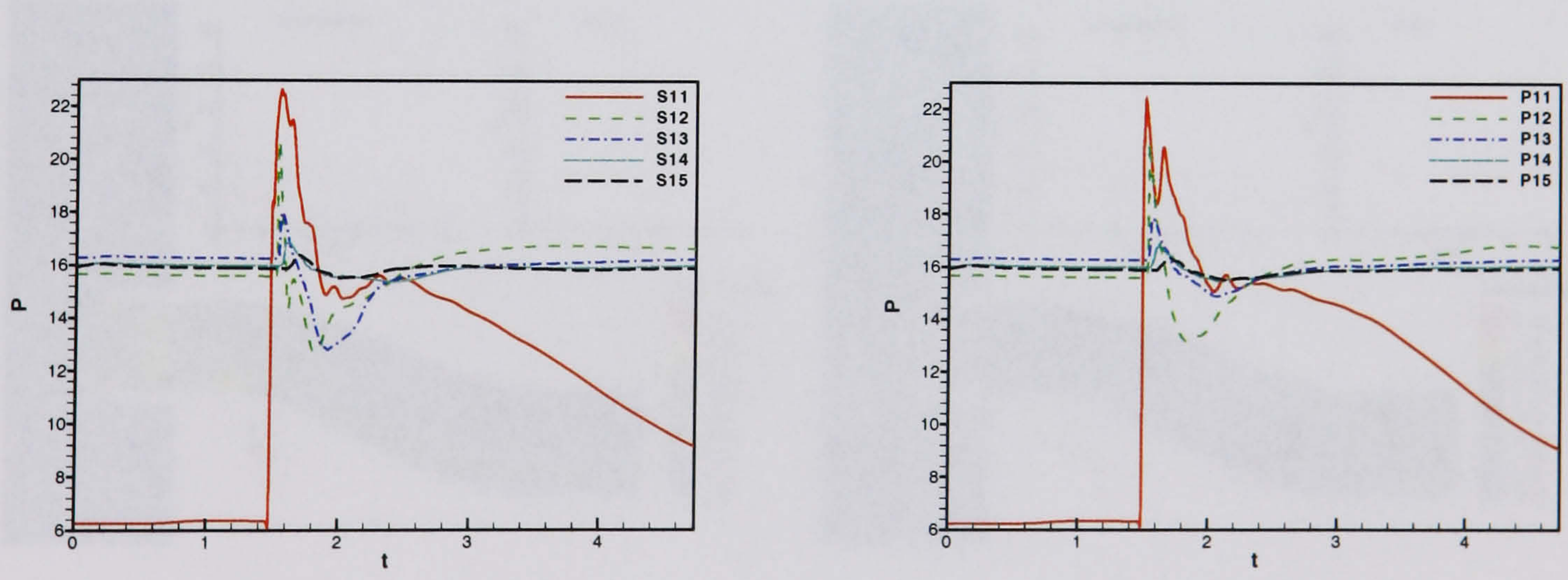

(e) Starboard probes 11 - 15

(f) Port probes 11 - 15

Figure 6.45: *HMFR SST calculation, OPR = 2, Surge signature 1, +30 degrees pitch - Symmetry plane probe data*

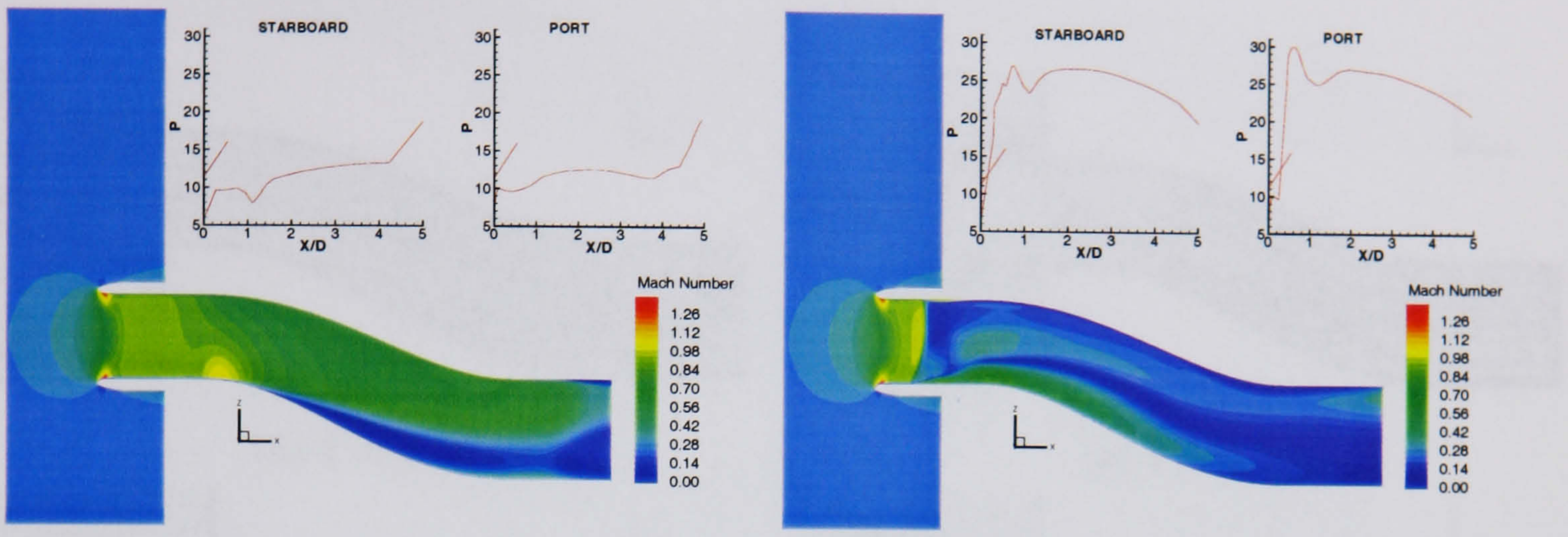

(a) t = 0.20

(d) t = 1.40

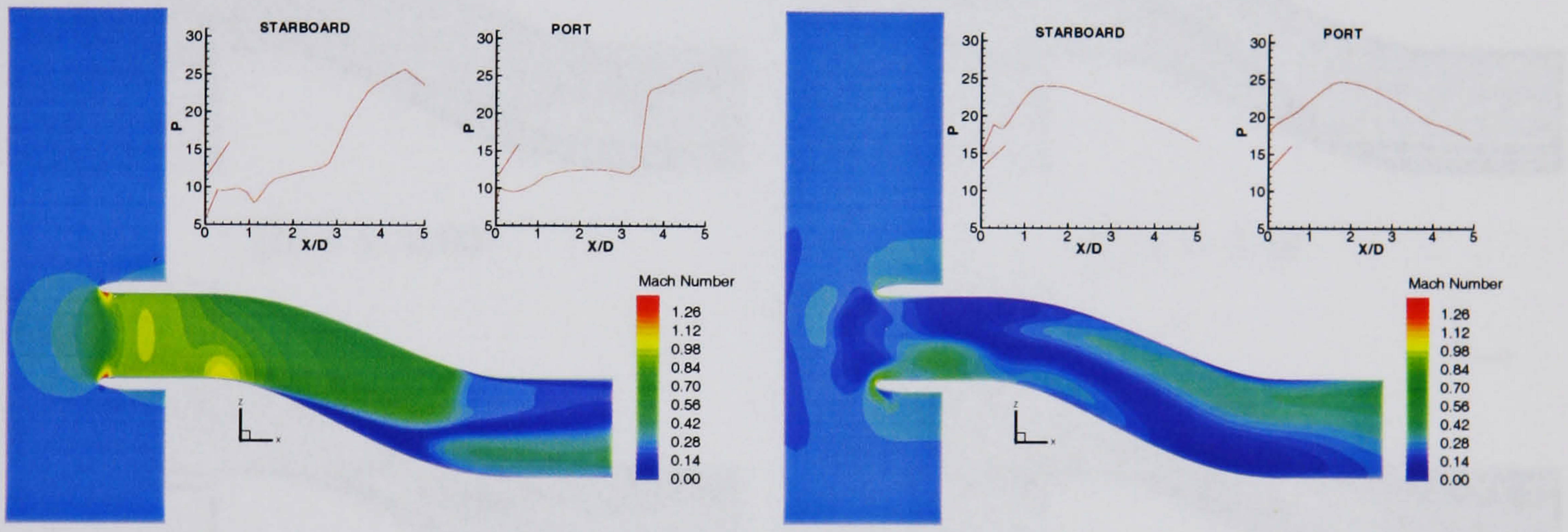

(b) t = 0.60

(e) t = 1.80

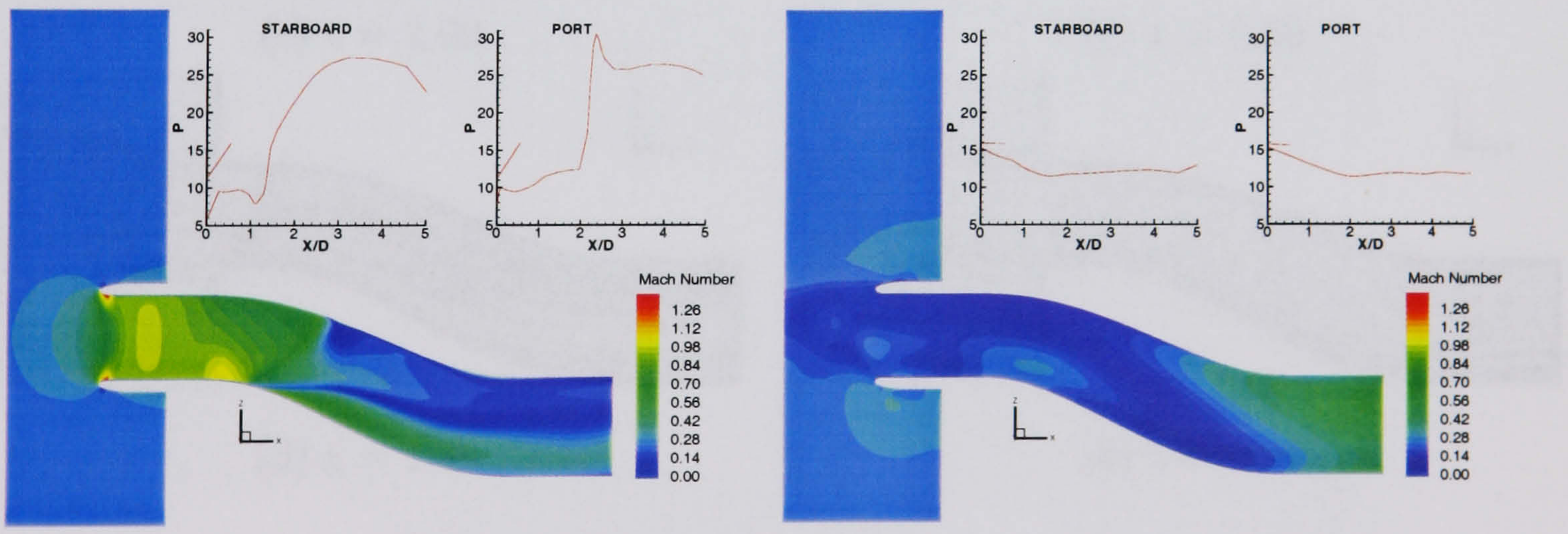

(c) t = 1.00

(f) t = 2.40

Figure 6.46: *HMFR SST calculation, OPR = 2, Surge signature 1, +30 degrees pitch - Symmetry plane Mach number and pressure traces*

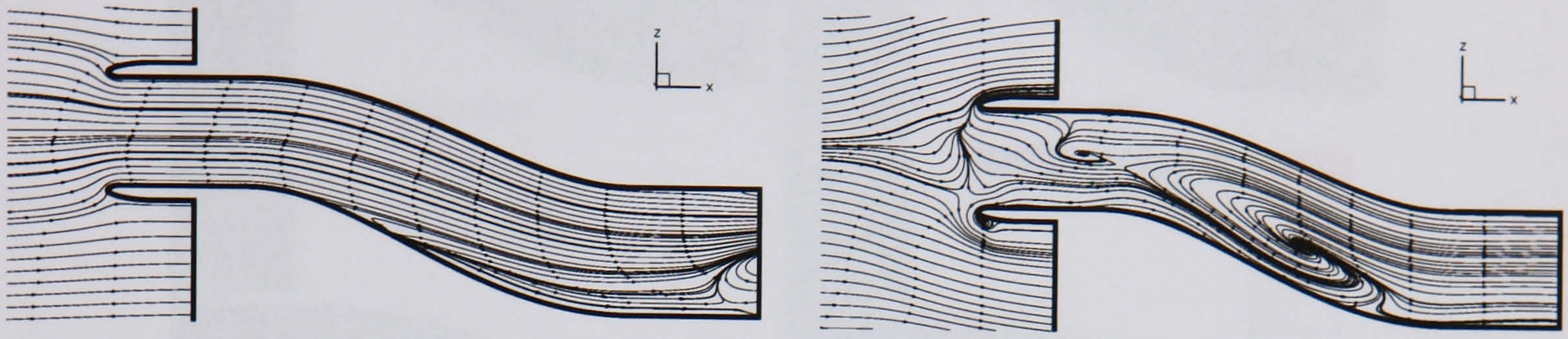

(a) t = 0.20 (e) t = 1.80

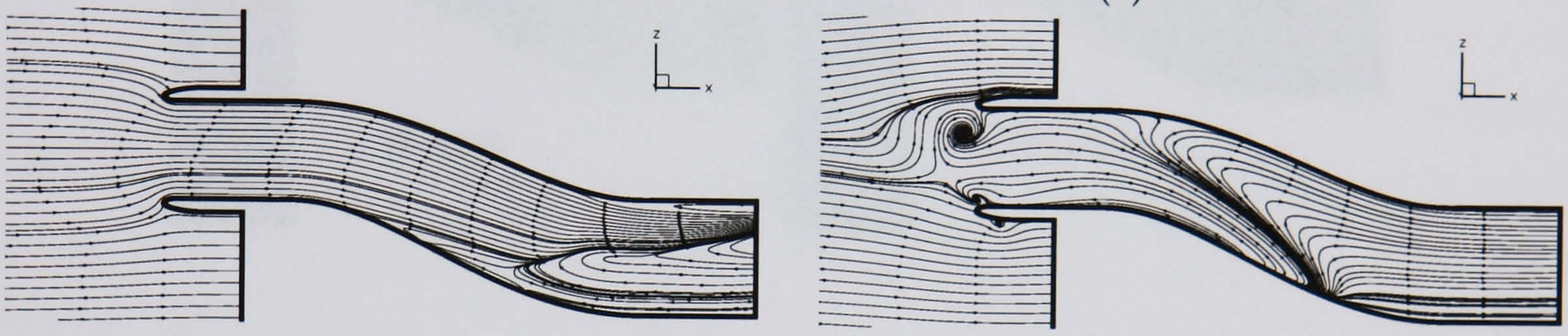

(b) t = 0.60 (f) t = 2.40

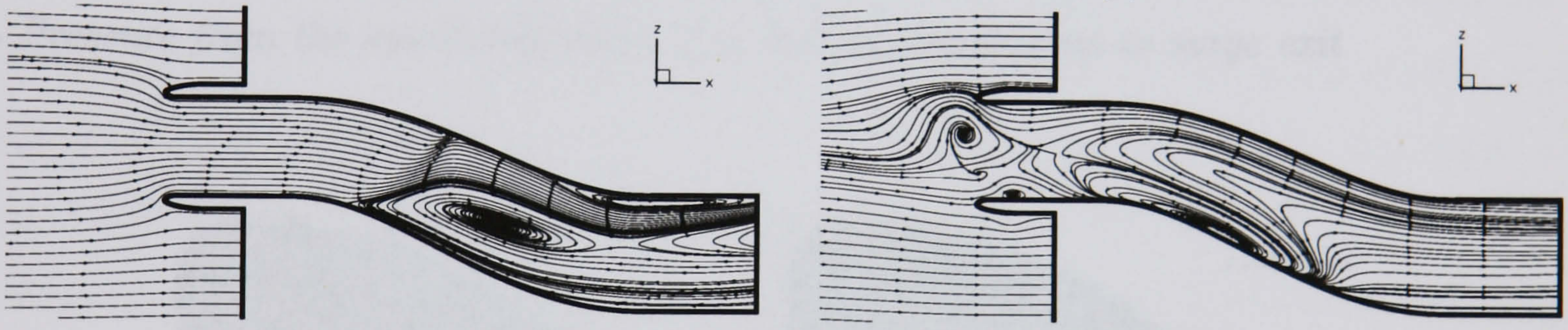

(c) t = 1.00 (g) t = 2.60

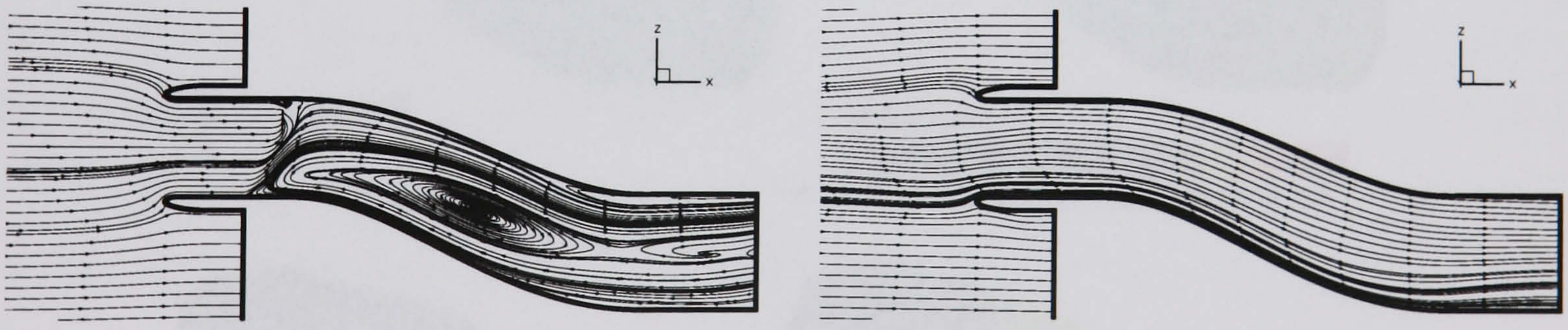

(d) t = 1.40 (h) t = 3.30

Figure 6.47: *HMFR SST calculation, OPR = 2, Surge signature 1, +30 degrees pitch - Symmetry plane streamlines*

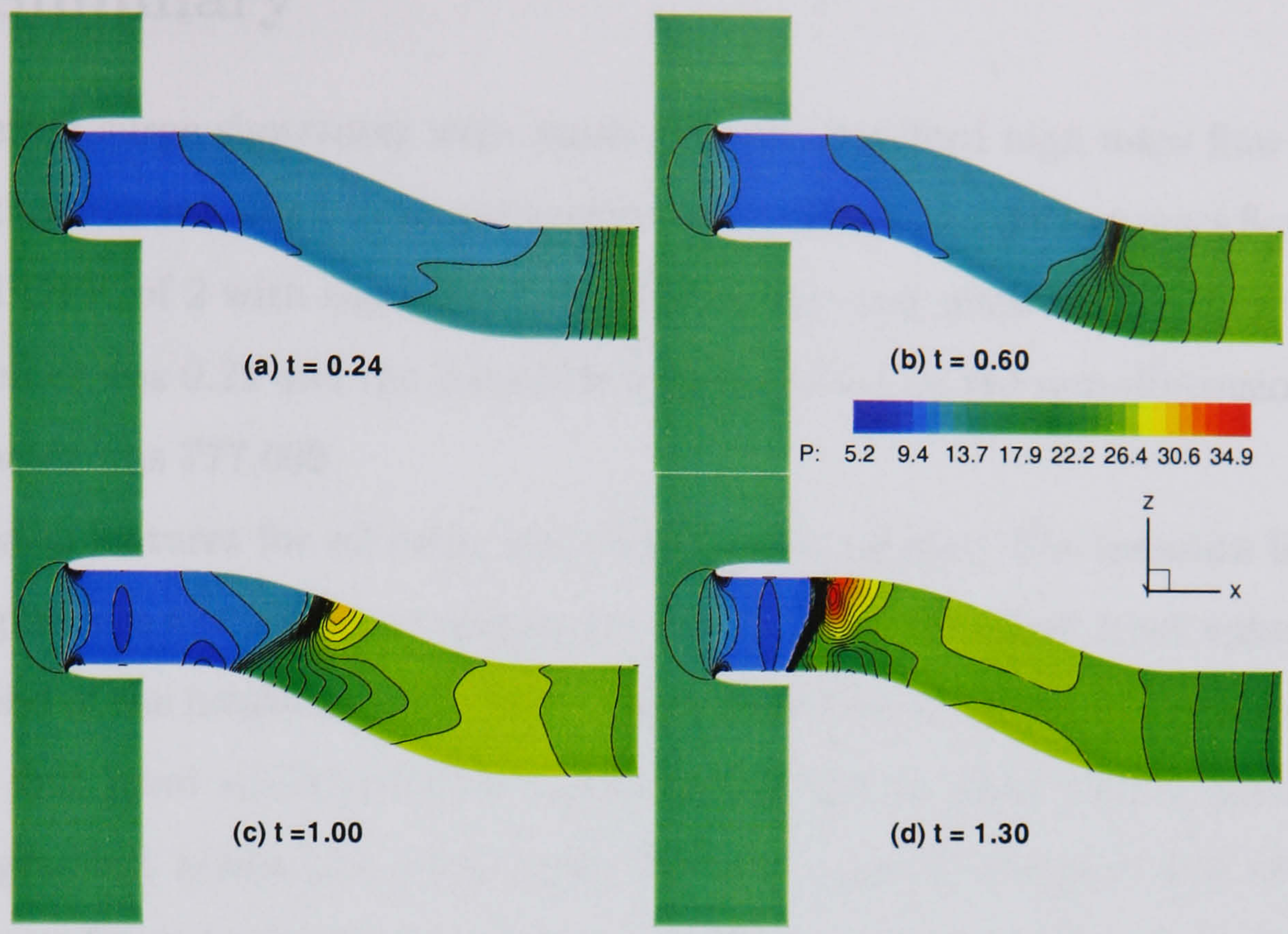

Figure 6.48: *HMFR SST calculation, OPR = 2, Surge signature 1, +30 degrees pitch - Pressure from the symmetry plane at 4 instants leading up to surge exit*

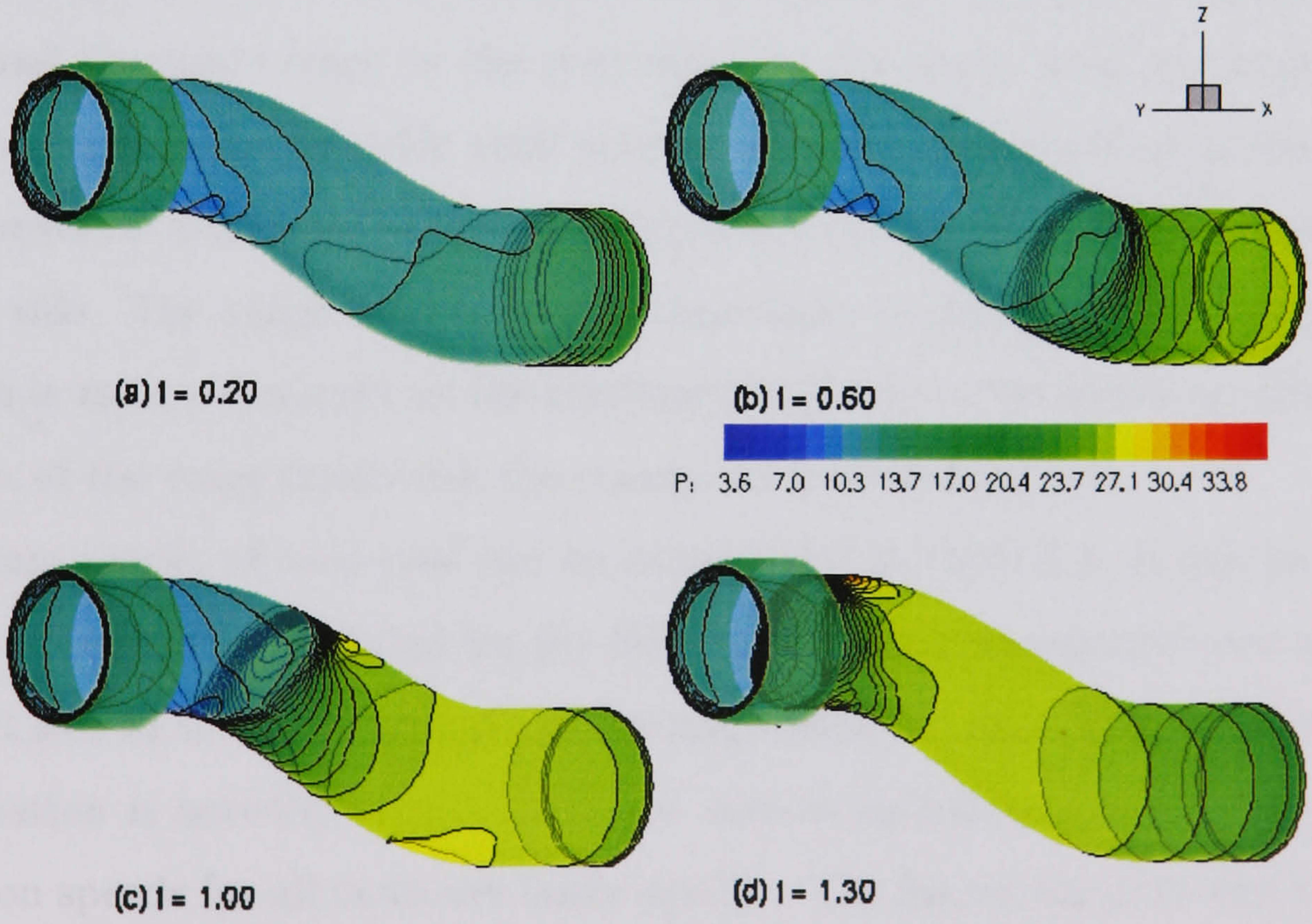

Figure 6.49: *HMFR SST calculation, OPR = 2, Surge signature 1, +30 degrees pitch - Pressure from the duct wall at 4 instants leading up to surge exit*

6.9 Summary

Four different surge signatures were applied to the standard high mass flow case. The investigation was extended to an application of signature 2 to the low mass flow case and a reduced OPR of 2 with signature 1 applied to yaw and pitch at 30°. The freestream Mach number was 0.21 and the Reynolds number based on the non-dimensional engine face diameter was 777,000.

The basic features for all cases were found to be similar. The pressure front forms at the engine face and begins to propagate upstream. As the surge front approaches the second bend of the intake an interaction begins with the natural steady-state separation from the first bend starboard side. This has the initial effect that a much stronger pressure gradient across the surge front develops towards the port side of the duct. As the surge front navigates the second bend and moves into the section of the duct between the two bends the interaction with the secondary separated flow continues. The recirculation in this region increases in size and strength and moves upstream behind the surge front. The surge front on the port side is much more abrupt and propagates slightly slower than on the starboard side. Peak high pressures begin to build behind the surge front on the port side. As the surge front navigates the first intake bend there is considerable peak pressure behind the surge front on the port side and flow reversal associated with the recirculating flow has further increased on the starboard side. The surge front then exits and there is spillage of the flow out of the duct. This is most prominent on the starboard side due to the knock on effects of the interaction of the surge front with the steady-state secondary flow.

The main results of each case can be summarised in table 6.1. It can be seen that the highest pressure is generated for the HMFR surge case at negative yaw and occurs on the port side at the cowl highlight as the surge exits the duct. The pressure recorded in this location is actually over 3 times the normal operating pressure for this case. Propagation speeds for all cases are fairly similar. The fastest surge to exit the duct is signature 2 at low mass flow conditions. This is probably because signature 2 features the most rapid rise to applied peak pressure at the downstream boundary. It also exits slightly faster than signature 2 at the high mass flow conditions as the low mass flow case features less secondary flow and is thus more similar to surge in a straight pipe.

Signature and test conditions	Surge exit time (t)	Peak over -pressure (OPR)
Sig. 1, HMFR, OPR=2	1.45	2.518
Sig. 2, HMFR, OPR=2	1.2	2.655
Sig. 3, HMFR, OPR=2	1.3	2.647
Sig. 4, HMFR, OPR=2	1.9	2.115
Sig. 2, LMFR, OPR=2	1.1	2.493
Sig. 2, HMFR, OPR=1.5	1.6	1.856
Sig. 1, yaw -30^o, HMFR, OPR=2	1.4 (port), 1.2 (starboard)	3.058
Sig. 1, yaw +30^o, HMFR, OPR=2	1.4 (port), 1.5 (starboard)	2.678
Sig. 1, pitch 30^o, HMFR, OPR=2	1.44	2.708

Table 6.1: *Summary of surge conditions, peak pressures, and exit times*

For all surges examined, the expulsion of the initial surge front led to a reflection that travelled down the intake duct and was recorded at the downstream boundary. This in turn then propagates up the intake and exits. The strength of the reflection is small compared to the initial surge front.

Peak pressures for all the surge signatures and cases examined have been found to be considerably in excess of stagnation values and will induce loads on the aircraft structure. A determination of the maximum loads is crucial in the structural design process. Indeed design loads in aircraft intakes are set by peak pressures associated with surge and are currently determined by empirical techniques in general. However there is evidence that peak over-pressure predictions have have been incorrect. The F107A aircraft sustained major structural damage as a result of an engine surge (Marshal [35]). With modern compact ducts and serpentine ducts, new techniques are required to predict peak over-pressures. Experimental simulation of surge is not straightforward but would be of great value. The information in this chapter offers a comparatively cheap estimation of peak pressures that might be experienced during surge. Pressure/time histories determined in the present work could be used in conjunction with a structural modelling package to determine intake loads. Re-design or attenuation measures could then be addressed.

Chapter 7

Conclusions

The primary aim of this work has been to investigate various flows in the Royal Aircraft Establishment intake model 2129 (M2129). This has been accomplished computationally using the University of Glasgow CFD group's in-house code. RANS computations have been made employing one and two-equation turbulence closures.

7.1 Validation of the AGARD Test Cases

A comprehensive investigation of the steady through flow problem has been done. The cases looked at have been examined previously, in particular in an AGARD report [12], and they served as suitable for validation. High and low mass flow cases were examined, initial focus being on the low mass flow case. The freestream Mach number was fixed at 0.21 and the Reynolds number, based on the non-dimensional engine face diameter, was 777,000.

A grid independence study on a coarse (204,980 points), medium (401,000 points), and fine (830,000 points) grid showed that the solutions were grid independent for both the high and low mass flow cases for all turbulence models used and the medium grid was chosen for subsequent analysis.

The HMFR case was challenging as the engine demand is sufficient to generate supersonic flow within the intake. A comparison of the different turbulence models showed two very different flow regimes that occurred in the intake cowl region. The SA and $k-\omega$ models predicted a complex shock reflection pattern that does not appear in experiments and previous computations. Downstream of the first bend the flow recovers for all turbulence models and the results compare well with previous solutions and experiments.

An examination of the flow through the boundary layer in the cowl region shows that the SST model predicts a small pocket of shock induced separation. The boundary layer profile also indicates a more laminar type profile. The SA and $k-\omega$ models had greater near wall associated velocities. The SST model also predicts the strongest secondary flow, characterised by low total pressure patterns at the engine face and a dip in the pressure trace on the starboard side between the two intake bends. The SA model also predicts strong secondary flow though not quite to the extent of the SST model. Although the $k-\omega$ model does predict secondary flow, there is no pronounced dip in the pressure trace along the duct wall.

There are two different sets of computational solutions available for comparison. ARA computations do not predict this shock reflection and compare well with SST results. Dornier computations show signs of shock reflection and certainly predict supersonic flow in the entire region upstream of the first bend and are comparable with the current $k-\omega$ model results. There is also a set of alternative experimental data and the pressure levels here match much better with the $k-\omega$ and SA current solutions.

Although all flow regimes are very different with the current results, namely in the cowl region, the SST model predicts the closest comparison with ARA experimental data which is considered to be the primary set of experimental data. Increased confidence in the SST results can be found after a review of section 2.1.2 where it was predicted that the SST model would perform better due to its improved abilities in simulating separated adverse pressure gradient flow. In the low mass flow case it was also found that the SST model performs the most satisfactorily when compared with experiential data. This further increases confidence in the current SST results for the HMFR case.

The LMFR RANS results compare well with previous results and show a fair comparison with experiment. Secondary flow is evident although there are discrepancies with the starboard static pressure readings between the two bends. However this has also been encountered in previous computations and the accurate prediction of secondary flow for this case is known to be challenging. It was found that an improvement in the prediction of the secondary flow was gained by using the SA and more especially the SST turbulence models. This was highlighted by low total pressure at the engine face and also a dip in the local static pressure trace along the starboard side wall between the two bends.

Overall the confidence in the SST results is greatest and this model is used in further studies in the present work looking at intakes at incidence and surge. This is justified as this validation study showed the model consistently offers the closest comparison with primary experimental and computational data. Further confidence is gained as a review of the turbulence models in section 2.1.2 indicated the improved abilities of the SST model in flows with separation and adverse pressure gradients. A further set of experimental data with more detailed flowfield examination and transitional information would help to clarify a number of issues raised with the other models however.

7.2 AGARD Test Cases at Incidence

Intake flow at incidence was then investigated. The intake was studied for both pitch and yaw angles ($\pm 15^o, \pm 30^o, \pm 45^o$) and at the same low and high mass flow rates examined in the validation study in chapter 3. From the results of that validation study, RANS calculations with the SST turbulence model were preferred.

Positive angles of yaw for the HMFR case showed that, as the angle increased, the effect of the offset in the duct was diminished. This led to a minimum distortion coefficient at 30^o. At 45^o separation occurred on the port side inner cowl region leading to a poorer total pressure distribution across the compressor face. Swirling secondary flow is maintained in all cases as the flow remains attached in the cowl region starboard side.

Increasing the negative angles of yaw for the HMFR case had the effect of increasing the effect of the offset. Separation occurs on the starboard side inner cowl region at -30^o and -45^o. At -45^o the flow does not re-attach prior to the first bend with the effect that secondary flow generation is destroyed. In general pressure recovery and distortion get worse as the negative yaw angle is increased.

For positive angles of yaw at LMFR, increasing the angle again has the effect of decreasing the effect of the offset. Thus, as the angle increases the distortion coefficient decreases. However the pressure recovery does get poorer. A strong favourable pressure gradient develops on the starboard side inner cowl while an adverse pressure gradient develops on the outer starboard cowl surface and separation occurs.

Negative angles of yaw at LMFR again have the effect of increasing the effect of the offset. At -30^o separation occurs from the inner starboard surface but re-attaches prior to the first bend. Thus secondary flow generation still occurs although not as strongly as for the -15^o case. At -45^o the separation from the starboard side lip does not re-attach prior to the first bend and so secondary flow generation is destroyed. There is also considerable separation and recirculation from the outer port side cowl surface.

The pitched calculations are unsymmetric and negative and positive angles are identical halving the number of simulations required over the yawing calculations. Considering first the HMFR case, as pitch angle is increased the pressure recovery decreases. The distortion coefficient is poorest at 15^o but improves by 45^o as the low pressure has affected a majority of the engine face. This is because there is considerable separation from the inner cowl surface upstream.

LMFR pitching calculations show similar trends to the HMFR results. Pressure recovery gets poorer as the angle of pitch is increased. Distortion is harder to predict and is poorest at 30^o. At 45^o it again improves as considerable cowl lip separation occurs upstream leading to large regions of low total pressure at the engine face.

There is current interest in highly compact ducts and flow control to manage poor distortion and pressure recovery metrics (Hamstra et al. [79], Anderson et al. [80]). Highly compact ducts have more severe offsets and thus greater separation and consequent distortion. Hamstra found that microvane flow control can reduce the distortion by 50% in some cases while increasing the pressure recovery by around 5%. Examining the M2129 at incidence, particularly for negative angles of yaw is similar to increasing the offset. Active control using micro air-jets (microjets) would perhaps increase efficiency during pitched and yawed situations.

7.3 Validation of the Unsteady Surge Problem

Unfortunately there was no surge experimental data available for validation for the M2129 intake at the time of writing. Consequently other sources of validation had to be sought.

It was decided that a useful introduction to the unsteady problem would be the inviscid shocktube problem, the solution of which is available analytically. A simple constant cross-section two chamber shocktube was modelled with a pressure ratio between the two chambers held at 100. The boundary between the two chambers was removed and the consequent unsteady problem modelled. It was found that the shock propagation speeds determined from the solution and from the analytic equation matched well. Some problems arose in solving the contact discontinuity region when the computed solution is compared with the exact solution. Peaks and over-predictions occurred and these problems are well known from previous works. The use of a different limiter (for example the Superbee limiter) is one method of solving this problem.

Further, experimental data was obtained from the RMCS for a simple surge in a straight constant radius circular test section. Experimental measurements were based on ten pressure probes located in a straight working section of pipe. Steady flow was blown through the pipe and then a non-instantaneous valve closure instigated a surge wave that propagated upstream past the pressure transducers. Computational modelling of surge in a straight pipe showed similar results to those obtained in experimental data. Experimental data was perhaps slightly low and this could possibly be attributed to the non-instantaneous closure of the valve (instantaneous closure is assumed in the computations). Others errors are reported in the determination of the calculation of the wave speed as background noise was high making curve fitting difficult. However it was not possible to quantify the scale of the possible errors. Analytic equations for determining wave propagation speeds (water hammer theory and equations devised by Kirkov [44]) were also used and comparisons were reasonable although such equations also assume an instantaneous valve closure.

There then followed a convergence study on the M2129 for a surge signature applied at the downstream boundary. There are many causes of surge and it is not an aim of this work to simulate the initiation. The focus instead was the modelling of the propagation of a surge wave through the intake. A single surge signature featuring a sinusoidal rise to peak over-pressure was used for the convergence study. A grid dependence study found that a grid density of 542,714 grid points for RANS computations was sufficient to capture the solution satisfactorily. A time step of 0.0005 was found to be satisfactory to capture the rise time of all the signatures used. Typical calculations using a grid density of 542,714 grid points and a time step of 0.0005 on 8 processors led to calculation times of 140 WCH.

7.4 Surge Simulation Results

Four different surge signatures were applied to the standard high mass flow case. The surge investigation was also extended to an application of signature 2 to the low mass flow case and a reduced OPR of 1.5. This was then extended by looking at signature 1 applied to yaw and pitch at 30^o. The cases examined can be summarised as follows.

Signature 1 has a gradual rise to peak pressure. Despite this there forms a sharp rise to peak pressure as the surge front navigates the second and then first bends of the intake. There is complex interaction of the surge front with the separated region from the first bend starboard side. This leads to a peak pressure of about 32 that develops towards the port side of the duct wall at the second bend as the surge passes and is around three times the normal operating pressure in this location. The surge front exits the duct at a reduced time of approximately 1.5. Following the surge exit to freestream a reflection is felt back at the downstream boundary at around $t = 3$. This reflection then starts to propagate up the intake duct but gets damped out as it progresses.

Signature 2 has a much sharper rise to peak compared to signature 1. Consequently the pressure isolines associated with the surge front are more tightly packed sooner. Peak pressures induced are slightly higher than for signature 1 but again occur on the port side at the first bend as the surge front passes this location and is due to the interaction of the propagating surge front with the steady-state separated region. When the surge exits a reflection is experienced at downstream boundary that also propagates up the intake and exits to freestream.

The form of signature 3 is very similar to signature 2 in that they both feature a rapid rise time to peak OPR. Consequently the time that the surge front exits the duct, and the pressure histories from the probes throughout the duct are very similar. However the peak pressure for this case is not as severe as for signature 2, as the peak pressure is not applied as fast, nor is it held for as long. After the surge exits there is again a reflection that is felt back at the engine face. This coincides with a sharp rise to normal operating pressure (OPR=1) which is a feature of the current signature. This has the effect that the consequent propagation of the reflected wave is stronger than witnessed for signature 2.

Signature 4 features a much slower rise to peak in comparison to previous signatures. The pressure gradient of the surge front increases however as the surge front propagates through the duct. By the time the surge front exits the duct at t=1.9 the surge front is abrupt, as seen for the previous signatures. Peak pressure induced is much lower for this case, the peak being about 27 at the port side first bend and also at the downstream boundary as this is around the maximum pressure that is applied here for an OPR of 2.

Surge signature 2 was applied for the LMFR case. Less complex aerodynamic flows inside the duct are induced as the surge front propagates through. This appears to be because the LMFR steady case has less steady state separation and recirculation from the starboard side first bend. This has the effect that as the surge front propagates up through the duct, it remains fairly uniform across the whole duct and is similar to what may be expected in a duct without considering an offset. Peak pressures are greater than previously experienced as the low mass flow case has a higher applied pressure at the downstream boundary.

Surge signature 2 at a reduced OPR of 1.5 shows similarities to signature 2 at an OPR=2. The surge front is naturally not as strong and takes longer to propagate but there is a similar interaction of the propagating surge front with the secondary flow region. Peak pressures are reduced but are again focused on the port side first bend as the surge front propagates through. After the surge front has exited the duct there is no spillage out of the duct as seen in the previous cases. A reflection is again felt downstream that propagates out of the intake.

Surge signature 2 at -30^o of yaw leads to much stronger peak pressure being developed on the port side. Peak pressures on the starboard side tend to be reduced when compared with the 0^o case. As the surge propagates through the steady state separated region from the first bend starboard side the circulating region travels upstream behind the surge front and two distinct circulating regions develop. These appear to cause secondary pressure peaks on the starboard side after the main surge front has exited. A weaker reflection of the main surge again develops that exits the duct at approximately t=4.4.

Surge at positive yaw at 30^o for signature 2 is in many ways similar to the reverse of -30^o. The maximum peak pressure occurs on the starboard side duct highlight, just before the surge front exits. The propagation of the surge front through the duct leads to complex interaction with the secondary flow off the starboard side first bend. Due to the orientation of the intake with the freestream there is separation of the flow from the inner port side cowl and as the surge front propagates through this, the recirculating flow flow reversal is enhanced.

Surge at 30^o of pitch for the high mass flow case for signature 2 is non-symmetric and makes visualisation of the results less straightforward. The peak pressure for this case appears to occur on the port side first bend just after the surge front passes. The propagation of the surge front through the duct enhances the secondary flow circulation and leads to flow spillage from the starboard side after the surge exits the duct. This spillage is not as strong as seen in previous cases however.

The highest pressure for the HMFR surge at -30^o of yaw occurs on the port side at the cowl highlight as the surge exits the duct. The pressure recorded in this location is actually over 3 times the normal operating pressure for this case. Propagation speeds for all cases are fairly similar. The fastest surge to exit the duct is signature 2 at low mass flow conditions. This is probably because signature 2 features the most rapid rise to applied peak pressure at the downstream boundary. It exits slightly faster than signature 2 at the high mass flow conditions also as the low mass flow case features less secondary flow and is thus more similar to surge in a straight pipe.

In all surges examined the expulsion of the initial surge front led to a reflection that travelled back down the intake duct and was recorded at the downstream boundary. This in turn then propagates up the intake and exits. The strength of the reflection is small compared to the initial surge front.

7.5 Implications of Surge in Intakes

Sharp surge pressure waves produce loads in the intake structure. Pressure peaks have been found to be considerably in excess of freestream stagnation values before relief is obtained at the entrance of the intake after the surge front exits. Estimates of the maximum loads or over-pressures are essential for determining intake structural requirements. A primary problem facing a structural designer is the prediction of maximum overall pressure levels reached during surge. There is evidence that, even fairly recently, maximum over-pressure predictions have not been correct. The F107A aircraft sustained major structural damage during a flight test as a result of engine surge (Marshall [35]).

Future engine-intake designs have goals of good aerodynamic performance and survivability statistics while reducing structural weight and consequently reducing costs. In order to address these goals new design methods must evolve that allow weight to be minimised yet still maintain the necessary margins of structural safety. Design loads for intake structures are set by peak pressures associated with engine surge. These peak pressures are usually determined from empirical techniques. However with current serpentine shaped ducts and highly compact concept ducts, new techniques are required to predict intake surge peak loads for such ducts. Experimental simulation of surge propagation behaviour and data acquisition is difficult and full-scale measured events are scarce prohibiting in-depth analysis.

Chapter 6 now offers a comparatively cheap estimation of peak pressure levels that can be expected as a result of simplified surge signatures being applied at the downstream engine face boundary of the M2129 intake duct. A course of future work proposed would therefore be to use the pressure histories recorded in the duct, in conjunction with structural modelling packages, to determine such intake loads. From this re-design or attenuation strategies could then be proposed.

A point that should be remembered is that the type of surge being modelled here is in effect a cold surge. No attempt has been made to model a hot surge. In the case of a hot surge there are further issues to be considered such as hot gas ingestion problems. This can have the consequence of a reduction in thrust or a reduction in engine stability. In November 2002 a Eurofighter Typhoon DA6 was flying at 45,000 feet at a speed of Mach 0.7. While stabilising the aircraft to perform a flight test both engines suffered a surge that resulted in a double engine flame out. The aircrew attempted to recover the situation but were unable to re-light the engines resulting in them having to abandon the aircraft and eject to safety.

Consideration should also be given to the implications of surge in intakes that are not offset. In such circumstances a more uniform surge front can be expected, akin to that predicted for the LMFR case in the current work. Peak pressure may not be localised at predictable points as found in the current work where peak over-pressures tended to occur on the first bend port side wall. Instead they would be thought to depend much more on the factors such as cowl lip separation due to hard aircraft manoeuvres. Consideration must also be given to over-pressure damage resulting from surge on crucial components of the aircraft engine. On one of the proto-type Concorde aircraft the ramps forming part of the intake control mechanism were destroyed when the engine surged. The solution to the problem was reported to be partly aerodynamic and the intake was redesigned to attenuate the peak pressures encountered.

Finally some further discussion will be made on the effects of cyclic surge as opposed to pop surge that has been simulated in the present work. Both types are of interest in relatively long types of duct such as the M2129. Whereas the pop surge is characterised by a single large amplitude pressure pulse lasting in the order of 0.1 seconds, a'cyclic' surge is a repeatable pattern of pressure pulses. This type of surge is also known as 'lock-in' surge and often requires the shutting down of the engine to terminate the process in flight. Cyclic surge is illustrated in figure 7.1. It can be seen that the pressure rise increases for a reduction in mass flow in a compressor forming the unstalled characteristic line seen in the graph as the solid line. However a point is reached where any further reduction in mass flow leads to a definite change in the flow pattern. The mass flow becomes a function of time and the entire compressor changes from being stalled to unstalled in an essentially phased fashion. In some cases the process is so violent that mass flow is reversed out of the intake during the left hand leg of the process. It is anticipated that peak pressure in such a case of cyclic surge would be in excess of peak pressures predicted in the current work although further work would be required to confirm this. In the case of cyclic surge a revision of the grid domain would also be necessary.

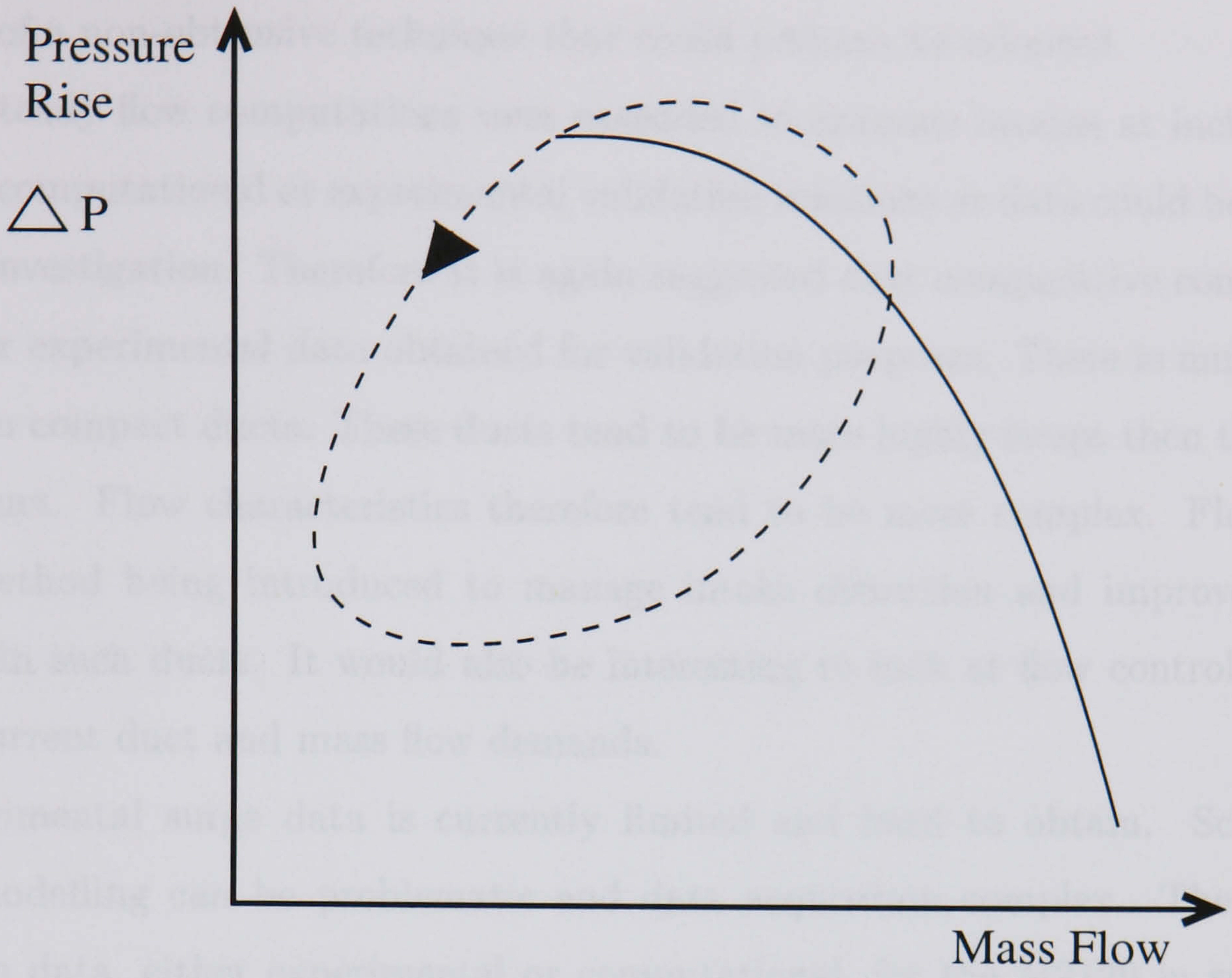

Figure 7.1: *Pressure rise - mass flow characteristics during cyclic surge*

7.6 Suggestions for Future Work

In summary, the M2129 intake has been examined for a variety of flow regimes. A comprehensive validation study found some interesting results. The steady validation study was extended to examine intakes at incidence. Finally, an unsteady intake aerodynamic problem was addressed by investigating the propagation of surge waves following the application of a representative surge signature.

For the steady validation in chapter 3, a further set of comprehensive experimental data would help clarify some of the issues raised. Experimental data for this case has so far been limited to total pressure data across the downstream engine face obtained from a rake of pressure probes. Upstream, static pressure taps on the port, starboard, and top and bottom walls offer limited information. The flow in such intakes is highly three-dimensional and little information can be determined on the characteristics of the flow away from the duct walls. Non-obtrusive techniques such as PIV would offer a useful insight. Liquid crystal techniques would also be interesting as they have been found to be useful in experiments in capturing surface shear stress which is a challenging quantity to predict using computational techniques. Pressure sensitive paint is another example of a non-obtrusive technique that could perhaps be adopted.

The steady flow computations were extended to examine intakes at incidence. No previous computational or experimental validation solutions or data could be found for such an investigation. Therefore it is again suggested that comparative computations be run, or experimental data obtained for validation purposes. There is much current interest in compact ducts. These ducts tend to be more highly swept then the current M2129 duct. Flow characteristics therefore tend to be more complex. Flow control is one method being introduced to manage intake distortion and improve pressure recovery in such ducts. It would also be interesting to look at flow control measures for the current duct and mass flow demands.

Experimental surge data is currently limited and hard to obtain. Scaled wind tunnel modelling can be problematic and data acquisition complex. There was no validation data, either experimental or computational, for the M2129 in surge. The suggestion is again put forward of computational and experimental work to be done for this case and compared with the current work for comprehensive validation purposes. Further data would also possibly aid in the development of an empirical rule to aid intake designers. Another course of further work would be to investigate redesign or attenuation measures to reduce the peak over-pressures predicted in the current surge work.

An overall suggestion for future work would be the consideration of a more realistic, representative engine face boundary condition. The current work imposes a constant and uniform pressure at the downstream boundary to simulate engine demand. This imposed pressure is then altered to a predetermined time varying pressure representing a surge signature to simulate engine surge. Although this method has been found to be adequate for the steady validation calculation, a more advanced technique would undoubtedly be beneficial. This would be particularly true for the surge calculations as the imposed signature is applied uniformly across the whole engine face. In practice an engine surge is rarely uniform and may only effect a small portion of the engine face. An engine face model that could take this into account and even be used to attempt to predict the onset of surge would be of greater benefit.

As mentioned previously the surge modelling in the present work is based on the application of a representative pressure time history. This type of surge is known as a pop surge as discussed in section 5.4. No effort was made in the current work to attempt to simulate cyclic or 'lock-in' surge. It is anticipated that such surge cases would require considerable effort and merit a more comprehensive study. A suggestion is made for future work in this area. As previously discussed anticipated peak pressures are expected to be in excess of those found in the current work and so it would be of great interest to further this work to examine the effects of resonance in the case of cyclic surge.

References

[1] J.D.Anderson, Jr. Computational Fluid Dynamics - The basics with applications. *McGraw-Hill International Editions*, Mechanical Engineering Series, ISBN 0-07-113210-4, 1995.

[2] G.C.Paynter. CFD Status for supersonic inlet design analysis. *AIAA Conference Paper*, 94-0465, 1994.

[3] R.H.Barnard and D.R.Philpott. Aircraft Flight: A description of the physical principles of aircraft flight. *Longman Scientific and Technical*, Harlow, England, ISBN 0-582-00338-5, 1989.

[4] R.H.Barnard and D.R.Philpott. Fundamentals of aerodynamics. *John Wiley and Sons*, ISBN 0-07-100767-9, 1991.

[5] B.W.McCormick. Aerodynamics, aeronautics and flight mechanics. *John Wiley and Sons*, ISBN 0-471-11087-6, 1995.

[6] B.R.Munson, D.F.Young, and T.H.Okiishi. Fundamentals of fluid mechanics. *Longman Scientific and Technical*, Harlow, England, ISBN 0-471-51746-1, 1989.

[7] E.L.Goldsmith and J.Seddon. Practical intake aerodynamic design. *Blackwell Scientific Publications*, ISBN 0-632-03103-4, 1993.

[8] E.L.Goldsmith and J.Seddon. Intake aerodynamics. *Blackwell Scientific Publications*, ISBN 0-632-04963-4, Second edition, 1999.

[9] D.S.Miller. Internal flow systems. *BHRA*, Fluid Engineering Series 5, 1978.

[10] J.D.Mattingly. Elements of gas turbine propulsion. *McGraw-Hill, Inc. International*, International Edition, ISBN 0-07-114521-4, 1996.

[11] W.J.Dardis and E.R.Mayhew. An acceptance process for the evaluation of inlet distortion. *AIAA Conference Paper*, 92-3918, 1992.

[12] Fluid Dynamics Panel Working Group 13. Test case 3 - subsonic/transonic circular intake. *AGARD*, Advisory Report 270, 1991.

[13] N.E.May. The prediction of intake/S-bend diffuser flow using various two-equation turbulence model variants, including non-linear eddy viscosity formulations. *ARA*, Contractor Report M316/1, March 1997.

[14] N.E.May, C.J.Peace, and C.A.McHugh. An investigation of two intake/S-bend diffuser geometries using the SAUNA CFD system - phase 1. *ARA*, Memo 386, July 1993.

[15] N.E.May. The prediction of intake/S-bend diffuser flow using the SAUNA CFD system with two-equation turbulence models. *ARA*, Contractor Report M268/5, November 1995.

[16] P.E.H.Abrahamsen, B.A.Pettersson-Reif, L.Saetran, and J.B.Fossdal. Air intake studies: Experimental measurements and computational modelling. *RTO AVT Symposium on Missile Aerodynamics*, Sorrento, Italy, May, 1998.

[17] L.D.Kral. Recent experience with different turbulence models applied to the calculation of flow over aircraft components. *Progress in Aerospace Sciences*, 34:520–529, 1998.

[18] B.H.Anderson, D.R.Reddy, and K.Kapoor. A comparative study of full Navier-Stokes and reduced Navier-Stokes analyses for separating flows within a diffusing inlet S-duct. *AIAA Conference Paper*, 93-2154, 1993.

[19] G.J.Harloff, C.F.Smith, J.E.Bruns, and J.R.DeBonis. Navier-Stokes analysis of three-dimensional S-ducts. *Journal of Aircraft*, 30(4):526–533, 1993.

[20] C.E.Towne and E.F.Schum. Application of computational fluid dynamics to complex inlet ducts. *AIAA Conference Paper*, 95-0035, 1985.

[21] G.Zhang and D.N.Assanis. 3-D turbulent subsonic compressible flow predictions using high-order schemes and comparison with measurements. *ASME Journal*, 3:165–173, 1996.

[22] B.J.Wendt and B.A.Reichert. Vortex ingestion in a diffusing S-Duct inlet. *Journal of Aircraft*, 33(1):149–154, 1996.

[23] G.J.Harloff, B.A.Reicherrt, and S.R.Wellborn. Navier-Stokes analysis and experimental data comparison of compressible flow in a diffusing s-duct. *AIAA Conference Paper*, 92-2699, 1992.

[24] K.P.M.Saterskog, B.G.Ullbrand, N.H.Olofsson, and T-A.Gronland. Applied CFD analysis of flow distortion in the SAAB 105 inlet. *AIAA Conference Paper*, 95-0035, 1995.

[25] E.A.Van Deusen and V.R.Mardoc. Distortion and turbulence interaction: A method for evaluating engine and inlet compatibility. *AIAA Conference Paper*, 70-632, 1970.

[26] A.Ytterstrom and E.Axelson. Hammershock calculations in the air intake of JAS 39 Gripen, using dual timestepping. *AIAA Conference Paper*, 99-3113, 1999.

[27] T.Hsieh, A.B.Wardlaw Jr., P.Collins, and T.Coakley. Numerical investigation of unsteady inlet flowfields. *AIAA Journal*, 25(1):75–80, 1987.

[28] D.Causon and D.Ingram. Numerical simulation of engine surge in a twin side-by-side intake system. *The Aeronautical Journal*, October:365–370, 1997.

[29] B.D.Goble, S.King, J.Terry, and M.Schoop. Inlet hammershock analysis using a 3-D unsteady Euler/Navier-Stokes code. *AIAA Conference Paper*, 96-2547, 1996.

[30] D.N.Miller and J.W.Hamstra. Enlisting CFD to fight hammer shock in jets. *ASME Journal*, International Gas Turbine and Aeroengine Congress and Exposition, Birmingham, 1996.

[31] R.A.Mays. Inlet dynamics and compressor surge. *Journal of Aircraft*, 8(4):219–226, 1971.

[32] I.O.Hindash, R.H.Bush, and R.R.Cosner. Computational modeling of inlet hammershock wave generation. *AIAA Conference Paper*, 90-2005, 1990.

[33] P.J.Evans and P.P.Truax. YF-16 induction system design loads associated with engine surge. *Journal of Aircraft*, 12(4):205–209, 1975.

[34] K.W.Lotter, P.A.Mackrodt and R.D.Scherbaum. Engine surge simulations in wind-tunnel model inlet ducts. *ICAS*, 88-4.11.4, 1988.

[35] F.L.Marshall. Prediction of inlet duct overpressures resulting from engine surge. *Journal of Aircraft*, 10(5):274–278, 1973.

[36] J.Auzins. Measurement and correlation of structural response to inlet hammershock phenomena on an F-14 airplane. *Grumman Aerospace Corporation*, Calverton, New York, 1972.

[37] W.Luber and J.Becker. The impact of dynamic loads on the design of military aircraft. *Daimler Benz Aerospace AG*, Military Aircraft MT2, Munich, Germany, 1996.

[38] D.R.Bellman and D.L.Hughes. The flight investigation of pressure phenomena in the air intake of an F-111A airplane. *AIAA Conference Paper*, 69-0488, 1969.

[39] F.W.Burcham and D.L.Hughes. Analysis of in-flight pressure fluctuations leading to compressor surge in a F-111A airplane for Mach numbers to 2.17. *AIAA Journal*, 70-0264.

[40] J.Becker, H.Bergmann, and W.Luber. Dynamic hammershock effects on the air intake design of supersonic aircraft. *Deutsche Aerospace AG*, Military Aircraft, Ottobrunn, Germany, 1994.

[41] T.Breuer and S.Servaty. Stall inception and surge in high-speed axial flow compressors. In *Loss Mechanisms and Unsteady Flows in Turbomachines*, pages 26/1–26/17. AGARD CP-571, 1996.

[42] W.T.Cousins, M.G.Jones, and T.L.Belling. Surge and stall characteristics of axial-centrifugal compressors: The enhancement to engine stability. In *Loss Mechanisms and Unsteady Flows in Turbomachines*, pages 29/1–29/13. AGARD CP-571, 1996.

[43] W.J.Borys and W.C.Moffatt. Rotating stall in turbojet engine compressors. In *Loss Mechanisms and Unsteady Flows in Turbomachines*, pages 25/1–25/11. AGARD CP-571, 1996.

[44] A.P.Kirkov, R.H.Soeder, and J.E.Moss. Investigation of the stall hammershock at the engine inlet. *Journal of Aircraft*, 12(4):198–204, 1975.

[45] B.S.Baldwin and H.Lomax. Thin layer approximation and algebraic model for separated turbulent flow. *AIAA Conference Paper*, 78-257, 1978.

[46] L.Davidson. Reynolds stress transport modelling of shock-induced separated flow. *Journal of Computers and Fluids*, 24(3):253–268, 1995.

[47] P.Batten, T.J.Craft, M.A.Leschziner, and H.Loyau. Reynolds-stress-transport modeling for compressible aerodynamics applications. *AIAA Journal*, 37(7):785–797, 1999.

[48] C.G.Speziale. On non-linear $K - l$ and $K - \epsilon$ models of turbulence. *Journal of Fluid Mechanics*, 178:459–475, 1987.

[49] T.J.Craft, B.E.Launder, and K.Suga. Development and application of a cubic eddy-viscosity model of turbulence. *International Journal of Heat and Fluid Flow*, 17(2):108–115, 1996.

[50] T.R.Gatski. Prediction of airfoil characteristics with high order turbulence models. *Technical Memorandum 110246*, NASA, 1996.

[51] R.Aabid, C.Rumsey, and T.Gatski. Prediction of non-equilibrium turbulent flows with explicit algebraic stress models. *AIAA Journal*, 33(11):2026–2031, 1995.

[52] R.Aabid, J.H.Morrison, T.B.Gatski, and C.G.Speziale. Prediction of aerodynamic flows with a new explicit algebraic stress model. *AIAA Journal*, 34(12):2632–2635, 1996.

[53] S.B.Pope. A more general effective-viscosity hypothesis. *Journal of Fluid Mechanics*, 72(2):331–3402, 1975.

[54] C.G.Speziale and T.Ngo. Numerical solution of turbulent flow past a backward-facing step using a non-linear $k - \epsilon$ model. *International Journal of Engineering Sciences*, 26:1099–1112, 1988.

[55] R.Rubinstein and J.M.Barton. Nonlinear Reynolds stress models and the re-normalization group. *Physics of Fluids*, 2(8):1472–1476, 1990.

[56] V.Yakhot and S.A.Oorszag. Re-normalization group analysis of turbulence: I. Basic theory. *Journal of Scientific Computing*, 1(1):3–51, 1986.

[57] S.A.Orszag, V.Yakhot, W.S.Flannery, and F.Boysan. Re-normalization group modelling and turbulence simulations. In R.M.So and C.G.Speziale, editor, *Near Wall Turbulent Flows*, pages 155–183. Elsevier, 1993.

[58] T.H.Shih, J.Zhu, and J.L.Lumley. A realizable reynolds stress algebraic equation model. *NASA*, Technical Memorandum 105993, 1993.

[59] D.D.Apsley and A.Leschziner. A new low-Re non-linear two-equation turbulence model for complex flows. In *Eleventh Symposium on Turbulent Shear Flows*, pages 25–30, 1997.

[60] Y.TJiang, M.Damodaran, and K.H.Lee. High-resolution finite volume computation of turbulent transonic flow past an airfoil. *AIAA Journal*, 35(7):1134–1142, 1997.

[61] T.J.Craft, B.E.Launder, and K.Suga. A non-linear eddy-viscosity model including sensitivity to stress anisotropy. In *Proceedings of the 10th Symposium on Turbulent and Shear Flows*, pages 19–24, 1995.

[62] G.Barakos and D.Drikakis. Investigation of non-linear eddy-viscosity turbulence models in shock-boundary layer interaction. *AIAA Journal*, 38(3):461–469, 2000.

[63] D.Sofialidis and P.Prinos. Development of a non-linear strain-sensitive $k - \omega$ turbulence model. In *Proceedings of the 11th Symposium on Turbulent Shear Flows*, pages 89–94, 1997.

[64] S.Fan, B.Lakshminarayana, and M.Barnett. Low-Reynolds-number $k - \epsilon$ model for unsteady turbulent boundary-layer flows. *AIAA Journal*, 31(10):1777–1784, 1993.

[65] D.C.Wilcox. Turbulence modeling for CFD. *DCW Industries, Inc.*, La Canada, California, ISBN 0-9636051-0-0, 1994.

[66] P.R.Spalart and S.R.Allmaras. A one-equation turbulence model for aerodynamic flows. *AIAA Conference Paper*, 92-0439, 1992.

[67] F.R.Menter. Zonal two equation kappa-omega turbulence models for aerodynamic flows. *AIAA Conference Paper*, 93-2906, 1993.

[68] J.E.Bardina, P.G.Huang, and T.J.Coakley. Turbulence modelling validation, testing, and development. *NASA*, Technical Memorandum 10446, 1997.

[69] K.J.Badcock, M.Woodgate, K.Stevenson, B.E.Richards, M.Allan, G.S.L.Goura, and R.Menzies. Aerodynamics studies on a Beowulf cluster. In P. Wilders et al., editor, *Parallel Computational Fluid Dynamics Practices and Theory*, pages 39–46, May 2002.

[70] D.Feszty, K.J.Badcock and B.E.Richards. Numerical simulation of the hysteresis phenomenon in high speed spiked body flows. *AIAA Conference Paper*, 2000-0141, 2000.

[71] M.T.Arthur, F.Brandsma, N.Ceresola and W.Kordulla. Time accurate Euler calculations of vortical flow on a delta wing in pitching motion. *AIAA Conference Paper*, 99-3110, 1999.

[72] J.Henderson, K.J.Badcock and B.E.Richards. Understanding subsonic and transonic open cavity flows and suppression of cavity tones. *AIAA Conference Paper*, 2000-0658, 2000.

[73] Warwick science park innovation centre. *ICEM CFD Engineering*, URL: http://www.icemcfd.co.uk.

[74] D.W.Mayer, G.C.Paynter, I.S.Chang and W.L.Chow. Boundary conditions for unsteady supersonic intake analysis. *AIAA Journal*, 32(6):1200–1206, 1994.

[75] J.Chung, G.L.Cole. Comparison of compressor face boundary conditions for unsteady CFD simulations of supersonic inlets. *AIAA Conference Paper*, 95-3590, 1995.

[76] C.H.Sieverding. Distortion induced engine instability. *Agard Lecture Series 72*, North Atlantic Treaty Organisation, 1974.

[77] H.W.Liepmann and A.Roshko. Elements of gasdynamics. *Galcit Aeronautical Series*, John Wiley and Sons, Inc., 1957.

[78] Private communications, 2001. DERA, Bedford, U.K.

[79] J.W.Hamstra, D.N.Miller, P.P.Truax, B.A.Anderson, and B.J.Wendt. Active inlet flow control technology demonstration. *The Aeronautical Journal*, pages 473–479, October 2000.

[80] B.H.Anderson and J.Gibb. Application of computational fluid dynamics to the study of vortex flow control for the management of inlet distortion. *AIAA Conference Paper*, 92-3177, 1992.

[81] D.R.B.Webb and K.H.Heron. The effect of engine surge on intake-structure loads. *The Royal Aircraft Establishment*, Technical Report 79067, 1979.

[82] J.K.Wright. Shocktubes. *Methen and co. Ltd.*, 1961.

[83] K.J.Badcock. Application of numerical methods to transient compressible flow. *Ph.D. Thesis*, St. Catherine's College, University of Oxford, 1992.

[84] I.I.Glass and J.Gordon Hall. Handbook of supersonic aerodynamics. *NAVARD Report*, Section 18 - Shocktubes Bureau of Naval Weapons, volume 6, 1959.

[85] C.Hirsch. Numerical computation of internal and external flows: Volume 2 - Computations for Inviscid and Viscous Flows. *John Wiley and Sons Ltd.*, ISBN 0-471-92351-6, 1990.

[86] D.A.Anderson, J.C.Tannehill, and R.H.Pletcher. Computational fluid mechanics and heat transfer. *Series in Computational Methods in Mechanics and Thermal Sciences*, Hemisphere, New York, 1984.

[87] S.Osher and S.Chakravarthy. Upwind schemes and boundary conditions with applications to Euler equations in general geometries. *Journal of Computational Physics*, 50:447–481, 1983.

[88] O.Axelsson. Iterative Solution Methods. *Cambridge University Press*, 1994.

[89] K.J.Badcock, X.Xu, L.Dubuc, and B.E.Richards. Preconditioners for high speed flows in aerospace engineering. *Numerical Methods for Fluid Dynamics*, Institute for Computational Fluid Dynamics, Oxford, U.K., volume 5, pages 287-294, 1996.

[90] F.Cantariti, L.Dubuc, B.Gribben, M.Woodgate, K.J.Badcock, and B.E.Richards. Approximate Jacobians for the solution of the Euler and Navier-Stokes equations. *Aerospace Engineering Report*, University of Glasgow, Glasgow, UK, number 5, 1997.

[91] A.Jameson. Time dependent calculations using multigrid, with applications to unsteady flows past airfoils and wings. *AIAA Conference Paper*, 91-1596, 1991.

Appendix A

The Three-Dimensional Model Equations

A.1 Introduction

The three-dimensional model equations are presented here in conservative form. A full derivation from first principles can be found in numerous text books such as Anderson [1]. The following is a modification of the theory guide to the two-dimensional version of PMB.

The conservative form of the governing equations is convenient for applications in computational fluid dynamics due to the fact that continuity, energy, and momentum equations are expressed by the same generic equation helping to simplify the logic in a computer program.

A.2 Non-dimensional form

In a three-dimensional Cartesian coordinate system, the non-dimensional form of the equations may be written as

$$\frac{\partial \mathbf{W}}{\partial t} + \frac{\partial(\mathbf{F}^i - \mathbf{F}^v)}{\partial x} + \frac{\partial(\mathbf{G}^i - \mathbf{G}^v)}{\partial y} + \frac{\partial(\mathbf{H}^i - \mathbf{H}^v)}{\partial z} = 0. \tag{A.1}$$

Here the vector $\mathbf{W}$ is the vector of conserved flow variables and is sometimes referred to as the solution vector. It can be written as:

$$\mathbf{W} = \begin{pmatrix} \rho \\ \rho u \\ \rho v \\ \rho w \\ \rho E \end{pmatrix} . \qquad (A.2)$$

In the above ρ is the density, u, v and w are the components of velocity given by the Cartesian velocity vector $\mathbf{U} = (u, v, w)$. Finally E is the total energy per unit mass.

When deriving the Navier-Stokes equations, the conservative form is obtained using a control volume that is fixed in space as opposed to moving with the fluid. Consequently, we are forced to consider the flux of energy, mass and momentum into and out of the control volume. The flux vectors $\mathbf{F}$, $\mathbf{G}$, and $\mathbf{H}$ consist of inviscid (^{i}) and viscous ($^{\nu}$) diffusive parts. These are written in full as

$$\mathbf{F}^{i} = \begin{pmatrix} \rho u \\ \rho u^2 + p \\ \rho u v \\ \rho u w \\ \rho u H \end{pmatrix}$$

$$\mathbf{G}^{i} = \begin{pmatrix} \rho v \\ \rho v u \\ \rho v^2 + p \\ \rho v w \\ \rho v H \end{pmatrix} \qquad (A.3)$$

$$\mathbf{H}^{i} = \begin{pmatrix} \rho w \\ \rho w u \\ \rho w v \\ \rho w^2 + p \\ \rho w H \end{pmatrix}$$

$$\mathbf{F}^{\nu} = \frac{1}{Re}\begin{pmatrix} 0 \\ \tau_{xx} \\ \tau_{xy} \\ \tau_{xz} \\ u\tau_{xx} + v\tau_{xy} + w\tau_{xz} + q_x \end{pmatrix}$$

$$\mathbf{G}^{\nu} = \frac{1}{Re}\begin{pmatrix} 0 \\ \tau_{xy} \\ \tau_{yy} \\ \tau_{yz} \\ u\tau_{xy} + v\tau_{yy} + w\tau_{yz} + q_y \end{pmatrix} \tag{A.4}$$

$$\mathbf{H}^{\nu} = \frac{1}{Re}\begin{pmatrix} 0 \\ \tau_{xz} \\ \tau_{yz} \\ \tau_{zz} \\ u\tau_{xz} + v\tau_{yz} + w\tau_{zz} + q_z \end{pmatrix}.$$

The stress tensor components are written as

$$\begin{aligned}
\tau_{xx} &= -\mu\left(2\frac{\partial u}{\partial x} - \frac{2}{3}\left(\frac{\partial u}{\partial x} + \frac{\partial v}{\partial y} + \frac{\partial w}{\partial z}\right)\right) \\
\tau_{yy} &= -\mu\left(2\frac{\partial v}{\partial y} - \frac{2}{3}\left(\frac{\partial u}{\partial x} + \frac{\partial v}{\partial y} + \frac{\partial w}{\partial z}\right)\right) \\
\tau_{zz} &= -\mu\left(2\frac{\partial w}{\partial z} - \frac{2}{3}\left(\frac{\partial u}{\partial x} + \frac{\partial v}{\partial y} + \frac{\partial w}{\partial z}\right)\right) \\
\tau_{xy} &= -\mu\left(\frac{\partial u}{\partial y} + \frac{\partial v}{\partial x}\right) \\
\tau_{xz} &= -\mu\left(\frac{\partial u}{\partial z} + \frac{\partial w}{\partial x}\right) \\
\tau_{yz} &= -\mu\left(\frac{\partial v}{\partial z} + \frac{\partial w}{\partial y}\right),
\end{aligned} \tag{A.5}$$

and the heat flux vector components are written as

$$\begin{aligned}
q_x &= -\frac{1}{(\gamma-1)M_\infty^2}\frac{\mu}{Pr}\frac{\partial T}{\partial x} \\
q_y &= -\frac{1}{(\gamma-1)M_\infty^2}\frac{\mu}{Pr}\frac{\partial T}{\partial y} \\
q_z &= -\frac{1}{(\gamma-1)M_\infty^2}\frac{\mu}{Pr}\frac{\partial T}{\partial z}.
\end{aligned} \tag{A.6}$$

Here γ is the specific heat ratio, Pr is the Prandtl number, T is the static temperature, and M_∞ and Re are the freestream Mach number and Reynolds number, respectively. The various flow quantities are related to each other by the perfect gas relations

$$\begin{aligned} H &= E + \frac{p}{\rho} \\ E &= e + \frac{1}{2}\left(u^2 + v^2\right) \\ p &= (\gamma - 1)\,\rho e \\ \frac{p}{\rho} &= \frac{T}{\gamma M_\infty^2}. \end{aligned} \tag{A.7}$$

Finally, the molecular viscosity μ is evaluated using Sutherland's law,

$$\frac{\mu}{\mu_0} = \left(\frac{T}{T_0}\right)^{3/2} \frac{T_0 + 110}{T + 110}, \tag{A.8}$$

where μ_0 is a reference viscosity at a reference temperature T_0. These can be taken as $\mu_0 = 1.7894\text{x}10^{-5}$ kg/(m.s) with $T_0 = 288.16$ K. It is stressed that the quantities presented here have been non-dimensionalised as discussed in chapter 2. The procedure used is as follows

$$x = \frac{x^*}{L^*}, \qquad y = \frac{y^*}{L^*}, \qquad t = \frac{t^*}{L^*/V_\infty^*},$$

$$u = \frac{u^*}{V_\infty^*}, \qquad v = \frac{v^*}{V_\infty^*}, \qquad \mu = \frac{\mu^*}{\mu_\infty^*},$$

$$\rho = \frac{\rho^*}{\rho_\infty^*}, \qquad p = \frac{p^*}{\rho_\infty^* V_\infty^{*2}}, \qquad T = \frac{T^*}{T_\infty^*}, \qquad e = \frac{e^*}{V_\infty^{*2}}. \tag{A.9}$$

A.3 Reynolds-averaged form

In order to study turbulence one must solve the full N-S equations (called Direct Numerical Simulation - DNS). However these calculations are very large and are currently only possible when examining Reynolds numbers several orders less than those in real applications - Wilcox [65]. Rather than attempt to solve the time evolution of the conserved variables, a somewhat less ambitious method is to calculate the Reynolds averaged form.

The Reynolds-averaged form of the Navier-Stokes equations permits turbulent flow to be considered efficiently. The development is not presented here. It is merely noted that fundamental to this approach is the consideration of the flow variables as consisting of two components, a time averaged component and a turbulent fluctuation. For example, density, pressure, and velocity components are decomposed as

$$\rho = \bar{\rho} + \rho', \qquad p = \bar{p} + p', \qquad u = \bar{u} + u', \qquad v = \bar{v} + v', \qquad w = \bar{w} + w'.$$

The quantities k (the turbulent kinetic energy), μ_T (the eddy viscosity) and Pr_T (the turbulent Prandtl number) are introduced via the important Boussinesq assumption in an attempt to model the fluctuating-variable stress terms arising from the Reynolds averaging. For a complete discussion of this subject see Anderson et al. [86]. The Reynolds-averaged form of the Navier-Stokes equations are identical to those presented in appendix A.2, except for the stress tensor and heat flux vector components shown below. The variables should be considered as mean flow quantities (superscripts are dropped for clarity).

The turbulent nature of the flow is modelled via μ_T and k and a closure hypothesis or turbulence model, for example the SA model (see appendix B.1), the $k - \omega$ model (see appendix B.2), or the the SST model (see appendix B.3).

$$
\begin{aligned}
\tau_{xx} &= -\left(\mu+\mu_T\right)\left(2\frac{\partial u}{\partial x}-\frac{2}{3}\left(\frac{\partial u}{\partial x}+\frac{\partial v}{\partial y}+\frac{\partial w}{\partial z}\right)\right)+\frac{2}{3}\rho k \\
\tau_{yy} &= -\left(\mu+\mu_T\right)\left(2\frac{\partial v}{\partial y}-\frac{2}{3}\left(\frac{\partial u}{\partial x}+\frac{\partial v}{\partial y}+\frac{\partial w}{\partial z}\right)\right)+\frac{2}{3}\rho k \\
\tau_{zz} &= -\left(\mu+\mu_T\right)\left(2\frac{\partial w}{\partial z}-\frac{2}{3}\left(\frac{\partial u}{\partial x}+\frac{\partial v}{\partial y}+\frac{\partial w}{\partial z}\right)\right)+\frac{2}{3}\rho k \\
\tau_{xy} &= -\left(\mu+\mu_T\right)\left(\frac{\partial u}{\partial y}+\frac{\partial v}{\partial x}\right) \\
\tau_{xz} &= -\left(\mu+\mu_T\right)\left(\frac{\partial u}{\partial z}+\frac{\partial w}{\partial x}\right) \\
\tau_{yz} &= -\left(\mu+\mu_T\right)\left(\frac{\partial v}{\partial z}+\frac{\partial w}{\partial y}\right)
\end{aligned}
\tag{A.10}
$$

$$
\begin{aligned}
q_x &= -\frac{1}{(\gamma-1)M_\infty^2}\left(\frac{\mu}{Pr}+\frac{\mu_T}{Pr_T}\right)\frac{\partial T}{\partial x} \\
q_y &= -\frac{1}{(\gamma-1)M_\infty^2}\left(\frac{\mu}{Pr}+\frac{\mu_T}{Pr_T}\right)\frac{\partial T}{\partial y} \\
q_z &= -\frac{1}{(\gamma-1)M_\infty^2}\left(\frac{\mu}{Pr}+\frac{\mu_T}{Pr_T}\right)\frac{\partial T}{\partial z}.
\end{aligned}
\tag{A.11}
$$

A.4 Curvilinear form

The model equations are written in curvilinear (ξ,η,ζ) form to facilitate use on curvilinear grids of arbitrary local orientation and density. A space transformation from the Cartesian co-ordinate system to the local coordinate system must then be introduced

$$\begin{aligned} \xi &= \xi\,(x,y,z) \\ \eta &= \eta\,(x,y,z) \\ \zeta &= \zeta\,(x,y,z) \\ t &= t. \end{aligned}$$

The Jacobian determinant of the transformation is given by

$$J = \frac{\partial(\xi,\eta,\zeta)}{\partial(x,y,z)}.$$

The equation A.1 can then be written as

$$\frac{\partial \hat{\mathbf{W}}}{\partial t} + \frac{\partial(\hat{\mathbf{F}}^i - \hat{\mathbf{F}}^v)}{\partial \xi} + \frac{\partial(\hat{\mathbf{G}}^i - \hat{\mathbf{G}}^v)}{\partial \eta} + \frac{\partial(\hat{\mathbf{H}}^i - \hat{\mathbf{H}}^v)}{\partial \zeta} = 0, \tag{A.12}$$

where

$$\begin{aligned} \hat{\mathbf{W}} &= \frac{\mathbf{W}}{J} \\ \hat{\mathbf{F}}^i &= \frac{1}{J}\left(\xi_x \mathbf{F}^i + \xi_y \mathbf{G}^i + \xi_z \mathbf{H}^i\right) \\ \hat{\mathbf{G}}^i &= \frac{1}{J}\left(\eta_x \mathbf{F}^i + \eta_y \mathbf{G}^i + \eta_z \mathbf{H}^i\right) \\ \hat{\mathbf{H}}^i &= \frac{1}{J}\left(\zeta_x \mathbf{F}^i + \zeta_y \mathbf{G}^i + \zeta_z \mathbf{H}^i\right) \\ \hat{\mathbf{F}}^v &= \frac{1}{J}\left(\xi_x \mathbf{F}^v + \xi_y \mathbf{G}^v + \xi_z \mathbf{H}^v\right) \\ \hat{\mathbf{G}}^v &= \frac{1}{J}\left(\eta_x \mathbf{F}^v + \eta_y \mathbf{G}^v + \eta_z \mathbf{H}^v\right) \\ \hat{\mathbf{H}}^v &= \frac{1}{J}\left(\zeta_x \mathbf{F}^v + \zeta_y \mathbf{G}^v + \zeta_z \mathbf{H}^v\right). \end{aligned} \tag{A.13}$$

The expressions for the inviscid fluxes can be simplified somewhat by defining

$$\begin{aligned} U &= \xi_x u + \xi_y v + \zeta_z w \\ V &= \eta_x u + \eta_y v + \zeta_z w \\ W &= \zeta_x u + \zeta_y v + \zeta_z w. \end{aligned} \tag{A.14}$$

The inviscid fluxes can then be written as

$$\hat{\mathbf{F}}^i = \begin{pmatrix} \rho U \\ \rho u U + \xi_x p \\ \rho v U + \xi_y p \\ \rho w U + \xi_z p \\ \rho U H \end{pmatrix}$$
$$\hat{\mathbf{G}}^i = \begin{pmatrix} \rho V \\ \rho u V + \eta_x p \\ \rho v V + \eta_y p \\ \rho w V + \eta_z p \\ \rho V H \end{pmatrix} \qquad (A.15)$$
$$\hat{\mathbf{H}}^i = \begin{pmatrix} \rho W \\ \rho u W + \zeta_x p \\ \rho v W + \zeta_y p \\ \rho w W + \zeta_z p \\ \rho W H \end{pmatrix}.$$

The derivative terms found in the viscous fluxes are evaluated using the chain rule, for example

$$\frac{\partial u}{\partial x} = \xi_x \frac{\partial u}{\partial \xi} + \eta_x \frac{\partial u}{\partial \eta} + \zeta_x \frac{\partial u}{\partial \zeta}.$$

The evaluation of the metrics of the transformation is clearly important and is described in full in Anderson et al. [86].

A.5 Steady State Solver

The Navier-Stokes equations are discretised using a cell-centred finite volume approach. The computational domain is divided into a finite number of non-overlapping control-volumes, and the governing equations are applied to each cell in turn. Also, the Navier-Stokes equations are re-written in a curvilinear co-ordinate system which simplifies the formulation of the discretised terms since body-conforming grids are adopted here. The spatial discretisation of equation A.12 leads to a set of ordinary differential equations in time,

$$\frac{d}{dt}\left(\mathbf{W}_{i,j,k}V_{i,j,k}\right) = -\mathbf{R}_{i,j,k}\left(\mathbf{W}\right), \qquad (A.16)$$

where $\mathbf{W}$ and $\mathbf{R}$ are the vectors of cell conserved variables and residuals respectively. The convective terms are discretised using Osher's upwind scheme (Osher et al. [87]) for its robustness, accuracy, and stability properties. MUSCL variable extrapolation is used to provide second-order accuracy with the Van Albada limiter to prevent spurious oscillations around shock waves. Boundary conditions are set by using ghost cells on the exterior of the computational domain. In the farfield ghost cells are set at the freestream conditions. At solid boundaries the no-slip condition is set for viscous flows, or ghost values are extrapolated from the interior (ensuring the normal component of the velocity on the solid wall is zero) for Euler flow.

The integration in time of equation A.16 to a steady-state solution is performed using an implicit time-marching scheme by

$$\frac{\mathbf{W}^{n+1}_{i,j,k} - \mathbf{W}^{n}_{i,j,k}}{\Delta t} = -\frac{1}{V_{i,j,k}}\mathbf{R}_{\mathbf{i,j,k}}\left(\mathbf{W}^{n+1}_{i,j,k}\right), \qquad (A.17)$$

where $n+1$ denotes the time $(n+1) * \Delta t$. Equation A.17 represents a system of non-linear algebraic equations and to simplify the solution procedure, the flux residual $\mathbf{R}_{\mathbf{i,j,k}}\left(\mathbf{W}^{\mathrm{n+1}}_{\mathbf{i,j,k}}\right)$ is linearised in time as follows,

$$\begin{aligned}
\mathbf{R}_{\mathbf{i,j,k}}\left(\mathbf{W}^{n+1}\right) &= \mathbf{R}_{\mathbf{i,j,k}}\left(\mathbf{W}^{n}\right) + \frac{\partial \mathbf{R}_{\mathbf{i,j,k}}}{\partial t}\Delta t + O(\Delta t^2) \\
&\approx \mathbf{R}_{\mathbf{i,j,k}}{}^{n}\left(\mathbf{W}^{n}\right) + \frac{\partial \mathbf{R}_{\mathbf{i,j,k}}}{\partial \mathbf{W}_{\mathbf{i,j,k}}}\frac{\partial \mathbf{W}_{\mathbf{i,j,k}}}{\partial t}\Delta t \\
&\approx \mathbf{R}_{\mathbf{i,j,k}}{}^{n}\left(\mathbf{W}^{n}\right) + \frac{\partial \mathbf{R}_{\mathbf{i,j,k}}}{\partial \mathbf{W}_{\mathbf{i,j,k}}}\Delta \mathbf{W}_{\mathbf{i,j,k}}, \qquad (A.18)
\end{aligned}$$

where $\Delta \mathbf{W}_{\mathbf{i,j,k}} = \mathbf{W}_{\mathbf{i,j,k}}{}^{n+1} - \mathbf{W}_{\mathbf{i,j,k}}{}^{n}$. Equation A.17 now becomes the following linear system

$$\left[\frac{V_{i,j,k}}{\Delta t}\mathbf{I} + \frac{\partial \mathbf{R_{i,j,k}}}{\partial \mathbf{W_{i,j,k}}}\right] \Delta \mathbf{W_{i,j,k}} = -\mathbf{R}^{n}_{i,j,k}\left(\mathbf{W^{n}}\right). \tag{A.19}$$

The complexity of a direct method to compute a linear system is of the order of $\mathcal{N}^3$, which becomes prohibitive when the total number of equations, $\mathcal{N}$, becomes large. On the other hand, iterative techniques such as Conjugate Gradient (CG) methods are capable of solving large systems of equations more efficiently in terms of time and memory. CG methods find an approximation to the solution of a linear system by minimising a suitable residual error function in a finite-dimensional space of potential solution vectors. Several algorithms, such as BiCG, CGSTAB, CGS, and GMRES, have been tested (see Badcock et al. [89]) and it was concluded that the choice of method is not as crucial as the preconditioning. The current results use a Generalised Conjugate Gradient method - see Axelsson [88].

A Krylov subspace algorithm is used to solve the linear system. The preconditioning strategy is based on a Block Incomplete Lower-Upper (BILU) factorisation (Axelsson [88]) since it appears to be the most promising and has the same sparsity pattern as the Jacobian matrix (BILU(0)) - i.e. the sparsity pattern of the Lower and Upper matrices is defined with respect to the sparsity of the unfactored matrix for simplicity. Furthermore the BILU(0) factorisation is decoupled between blocks to improve parallel efficiency and this approach does not seem to have a major impact on the effectiveness of the preconditioner as the number of blocks increases.

Implicit schemes require particular treatment during the early stages of the iterative procedure. The usual approach in starting the method is to take a small CFL number and to increase it later on. However, it was found that smoothing out the initial flow doing some explicit iterations, and then switching to the implicit algorithm was equally efficient. In the present method a specified number of forward Euler iterations are executed before switching to the implicit scheme.

The formulation leads to a Jacobian Matrix with a number of non-zero entries per row. Trying to reduce the number of non-zero entries would have several advantages. First, the memory requirements are lowered. Second, the resolution of the linear system by the GCG method is faster in terms of CPU-time since all the matrix-vector multiplications involved require less operation counts. Finally, the linear system is easier to solve since the approximate Jacobian matrix is more diagonally dominant. A full discussion of the Jacobian formulation is given in Cantariti et al. [90].

The steady state solver for the turbulent case is formulated and solved in an identical manner to that described above for the mean flow. The eddy-viscosity is regarded calculated from the latest values of k and ω (for example) and is used to advance the mean flow solution and then this new solution is used to update the turbulence solution, freezing the mean flow values. An approximate Jacobian is used for the source term by only taking into account the contribution of the dissipation terms $\hat{\mathbf{D}}_k$ and $\hat{\mathbf{D}}_\omega$ i.e. no account of the production terms is taken on the left hand side of the system. This approach has a stability advantage as described in Wilcox [65].

A.6 Unsteady State Solver

The formulation is described for the turbulent case. The laminar and inviscid cases represent a simplification of this.

Following the pseudo-time formulation (Jameson [91]), the updated mean flow solution is calculated by solving the steady state problems

$$\mathbf{R}^*_{i,j,k} = \frac{3\mathbf{w}^{n+1}_{i,j,k} - 4\mathbf{w}^{n}_{i,j,k} + \mathbf{w}^{n-1}_{i,j,k}}{2\Delta t} + \mathbf{R}_{i,j,k}(\tilde{\mathbf{w}}^{k_m}_{i,j,k}, \tilde{\mathbf{q}}^{k_t}_{i,j,k}) = 0 \qquad \text{(A.20)}$$

$$\mathbf{Q}^*_{i,j,k} = \frac{3\mathbf{q}^{n+1}_{i,j,k} - 4\mathbf{q}^{n}_{i,j,k} + \mathbf{q}^{n-1}_{i,j,k}}{2\Delta t} + \mathbf{Q}_{i,j}(\tilde{\mathbf{w}}^{l_m}_{i,j,k}, \tilde{\mathbf{q}}^{l_t}_{i,j,k}) = 0. \qquad \text{(A.21)}$$

Here $k_m, k_t, l_m,$ and l_t give the time level of the variables used in the spatial discretisation. Here the grid is moved rigidly but if grid deformation was required then time varying areas would be required in the expression for the real time derivative in equations A.20 and A.21. If $k_m = k_t = l_m = l_t = n+1$, then the mean and turbulent quantities are advanced in real time in a fully coupled manner. However, if $k_m = l_m = l_t = n+1$, and $k_t = n$, then the equations are advanced in sequence in real time, i.e. the mean flow is updated using frozen turbulence values and then the turbulent values are updated using the latest mean flow solution. This has the advantage that the only modification, when compared with the laminar case, to the discretisation of the mean flow equations is the addition of the eddy viscosity from the previous time step. The turbulence model only influences the mean flow solution through the eddy viscosity and so any two equation model can be used without modifying the mean flow solver. Hence, the implementation is simplified by using a sequenced solution in real time. However, the uncoupling could adversely effect the stability and accuracy of the real time stepping, with the likely consequence of limiting the size of the real time step that can be used.

Equations (A.20) and (A.21) represent a coupled nonlinear system of equations. These can be solved by introducing an iteration through pseudo time, τ, to the steady state, as given by

$$\frac{\mathbf{w}_{i,j}^{n+1,m+1} - \mathbf{w}_{i,j}^{n+1,m}}{\Delta\tau} + \frac{3\mathbf{w}_{i,j}^{k_m} - 4\mathbf{w}_{i,j}^{n} + \mathbf{w}_{i,j}^{n-1}}{2\Delta t} + \mathbf{R}_{i,j}(\tilde{\mathbf{w}}_{i,j}^{k_m}, \tilde{\mathbf{q}}_{i,j}^{k_t}) = 0 \tag{A.22}$$

$$\frac{\mathbf{q}_{i,j}^{n+1,m+1} - \mathbf{q}_{i,j}^{n+1,m}}{\Delta\tau} + \frac{3\mathbf{q}_{i,j}^{l_t} - 4\mathbf{q}_{i,j}^{n} + \mathbf{q}_{i,j}^{n-1}}{2\Delta t} + \mathbf{Q}_{i,j}(\tilde{\mathbf{w}}_{i,j}^{l_m}, \tilde{\mathbf{q}}_{i,j}^{l_t}) = 0. \tag{A.23}$$

where the $m-th$ pseudo-time iterate at the $n+1th$ real time step are denoted by $\mathbf{w}^{n+1,m}$ and $\mathbf{q}^{n+1,m}$ respectively. The iteration scheme used only effects the efficiency of the method and hence we can sequence the solution in pseudo time without compromising accuracy. For example, using explicit time stepping we can calculate $\mathbf{w}^{n+1,m+1}$ using $k_m = n+1, m$ and $k_t = n+1, m$ and $\mathbf{q}^{n+1,m+1}$ using $l_m = n+1, m+1$ and $l_t = n+1, m$. For implicit time stepping in pseudo time we can use $k_m = l_m = l_t = n+1, m+1$ and $k_t = n+1, m$. In both of these cases the solution of the equations is decoupled by freezing values but at convergence the real time stepping proceeds with no sequencing error. It is easy to recover a solution which is sequenced in real time from this formulation by setting $k_t = n$ throughout the calculation of the pseudo steady state. This facilitates a comparison of the current pseudo time sequencing with the more common real time sequencing. In the code the pseudo steady-state problems are solved using the implicit steady state solver described in detail in section A.5.

Appendix B

One and two-equation turbulence models

A brief description of the turbulence models implemented in PMB are presented. Conversion to curvilinear form has been covered in section A.4 and the application to the turbulence models represents a continuation of this. The original formulation of the equations is presented.

B.1 The Spalart-Allmaras (SA) Turbulence Model

The Spalart-Allmaras turbulence model [66] is a 1-equation model (inspired by the Baldwin-Lomax turbulence model [45]) and is defined as follows.

Eddy Viscosity Function

$$\nu_T = \tilde{\nu} f_{v1} \tag{B.1}$$

where

$$f_{v1} = \frac{\chi^3}{\chi^3 + c_{v1}^3}, \quad \chi \equiv \frac{\tilde{\nu}}{\nu}. \tag{B.2}$$

Convective Transport Equation of the Eddy Viscosity

$$\frac{D\tilde{\nu}}{Dt} = c_{b1}\tilde{S}\tilde{\nu} + \frac{1}{\sigma}[\nabla.((\nu + \tilde{\nu})\nabla\tilde{\nu}) + c_{b2}(\nabla\tilde{\nu})^2] - c_{w1} f_w \left[\frac{\tilde{\nu}}{d}\right]^2. \tag{B.3}$$

where

$$\tilde{S} \equiv S + \frac{\tilde{\nu}}{\kappa^2 d^2} f_{v2}, \quad f_{v2} = 1 - \frac{\chi}{1 + \chi f_{v1}}, \qquad \text{(B.4)}$$

and

$$f_w = g \left[\frac{1 + c_{w3}^6}{g^6 + c_{w3}^6} \right]^{1/6}, \quad g = r + c_{w2}(r^6 - r), \quad r \equiv \frac{\tilde{\nu}}{\tilde{S} \kappa^2 d^2}.$$

Closure Coefficients

$$c_{b1} = 0.135, \quad \sigma = 2/3, \quad c_{b2} = 0.622, \quad \kappa = 0.41,$$

$$c_{w1} = 2.762, \quad c_{w2} = 0.3, \quad c_{w3} = 2, \quad c_{v1} = 7.1,$$

$$c_{w1} = 2.762, \quad c_{w2} = 0.3, \quad c_{w3} = 2, \quad c_{v1} = 7.1. \qquad \text{(B.5)}$$

B.2 The k - ω Turbulence Model

The k-ω turbulence model of Wilcox [65] can be written as follows in non-dimensional form.

Eddy Viscosity

$$\mu_T = \rho k / \omega. \qquad \text{(B.6)}$$

Turbulence Kinetic Energy

$$\rho \frac{\partial k}{\partial t} + \rho \mathbf{V}.\nabla k - \frac{1}{Re} \nabla . \left[\left(\mu + \sigma^* \mu_T \right) \nabla k \right] = P_k - \beta^* \rho k \omega. \qquad \text{(B.7)}$$

Specific Dissipation Rate

$$\rho \frac{\partial \omega}{\partial t} + \rho \mathbf{V}.\nabla \omega - \frac{1}{Re} \nabla . \left[\left(\mu + \sigma \mu_T \right) \nabla \omega \right] = P_\omega - \beta \rho \omega^2. \qquad \text{(B.8)}$$

Closure Coefficients

$$\alpha = 5/9, \qquad \beta = 3/40, \qquad \beta^* = 9/100, \qquad \sigma = 1/2, \qquad \sigma^* = 1/2. \tag{B.9}$$

In the above relations the production terms of k and ω, P_k and P_ω respectively, are

$$P_k = \mu_T P - \frac{2}{3}\rho k S \tag{B.10}$$

$$P_\omega = \alpha \frac{\omega}{k} P_k, \tag{B.11}$$

and

$$\begin{aligned} P &= \left[\left(\nabla \mathrm{V} + \nabla \mathrm{V}^T \right) : \nabla \mathrm{V} - \frac{2}{3} \left(\nabla . \mathrm{V} \right)^2 \right] && \text{(B.12)} \\ S &= \nabla . \mathrm{V}. && \text{(B.13)} \end{aligned}$$

The equations as shown above use the same non-dimensional quantities as in chapter 2, with the addition of

$$k = \frac{k^* Re}{U_\infty^{*2}}, \qquad \omega = \frac{\omega^* L^*}{U_\infty^*}, \qquad \mu_T = \frac{\mu_T^*}{\mu_\infty^*}. \tag{B.14}$$

The equations for k and ω can be written in a curvilinear form analogous to that used for the mean flow equations in appendix A.4.

B.3 The Shear Stress Transport (SST) Turbulence Model

The SST turbulence model of Menter [67] is defined as follows.

Eddy Viscosity

$$\mu_T = \frac{\rho k / \omega}{max\left[1; \Omega F_2 / \left(a_1 \omega\right)\right]}, \qquad a_1 = 0.31. \tag{B.15}$$

In turbulent boundary layers the maximum value of the eddy viscosity is limited by forcing the turbulent shear stress to be bounded by the turbulent kinetic energy times a_1. This effect is achieved an auxiliary function F_2 and an absolute value of the vorticity, Ω. This auxiliary function is defined as a function of the wall distance (y) as

$$F_2 = \tanh\left[\left(\max\left[2\frac{\sqrt{k}}{0.09\omega y}; \frac{500\mu}{\rho y^2\omega}\right]\right)^2\right]. \tag{B.16}$$

Turbulence Kinetic Energy

The two transport equations of the model are defined below with a blending function F_1 for the model coefficients of the original ω and ϵ model equations. The transport equation is given by

$$\rho\frac{\partial k}{\partial t} + \rho\mathbf{V}.\nabla k - \frac{1}{Re}\nabla.\left[\left(\mu + \sigma^*\mu_T\right)\nabla k\right] = P_k - \beta^*\rho k\omega. \tag{B.17}$$

Specific Dissipation Rate

$$\begin{aligned}\rho\frac{\partial \omega}{\partial t} + \rho\mathbf{V}.\nabla \omega - \frac{1}{Re}\nabla.\left[\left(\mu + \sigma_\omega\mu_T\right)\nabla \omega\right] &= P_\omega - \beta\rho\omega^2 \\ &+2\left(1 - F_1\right)\frac{\rho\sigma_{\omega 2}}{\omega}\nabla k\nabla\omega.\end{aligned} \tag{B.18}$$

Closure Coefficients

The function F_1 is designed to blend the model coefficients of the original $k-\omega$ model in boundary layer zones with the transformed $k-\epsilon$ model in free-shear layer freestream zones. This function takes the value of one on no-slip surfaces and near one over a large portion of the boundary layer, and goes to zero at the boundary layer edge. This auxiliary blending function, F_1, is defined as

$$F_1 = \tanh\left[\left[\min\left(\max\left[\frac{\sqrt{k}}{0.09\omega y}; \frac{500\mu}{\rho y^2\omega}\right]; \frac{4\rho\sigma_{\omega 2}k}{CD_{k\omega}y^2}\right)\right]^4\right], \tag{B.19}$$

where

$$CD_{k\omega} = \max\left[\frac{2\rho\sigma_{\omega 2}}{\omega}\nabla k\nabla\omega; 10^{-}20\right].$$

Here, $CD_{k\omega}$ stands for cross-diffusion in the $k - \omega$ model. The constants are

$$a_1 = 0.31, \quad \beta^* = 0.09, \quad \kappa = 0.41. \tag{B.20}$$

The model coefficients β, γ, σ_k, and σ_ω denoted with the symbol ϕ are defined by blending the coefficients of the original $k - \omega$ model, denoted as ϕ_1, with those of the transformed $k - \epsilon$ model, denoted ϕ_2.

$$\phi = F_1 \phi_1 + (1 - F_1)\phi_2,$$

where

$$\phi = [\sigma_k, \sigma_\omega, \beta, \gamma], \tag{B.21}$$

with the coefficients of the original models defined as

- Inner model coefficients

$$\sigma_{k1} = 0.85, \quad \sigma_{\omega 1} = 0.5, \quad \beta_1 = 0.075,$$

$$\gamma_1 = \beta_1/\beta^* - \sigma_{\omega 1}\kappa^2/\sqrt{\beta^*} = 0.553. \tag{B.22}$$

- Outer model coefficients

$$\sigma_{k2} = 1.0, \quad \sigma_{\omega 2} = 0.856, \quad \beta_2 = 0.0828,$$

$$\gamma_2 = \beta_2/\beta^* - \sigma_{\omega 2}\kappa^2/\sqrt{\beta^*} = 0.440. \tag{B.23}$$

Appendix C

Flow Visualisation Animation Sequences

The CD attached to the back cover of this thesis contains movie sequences for all the surge signatures and cases examined. All the movies are in a concatenated raster meta-file format (RM) that can be visualised with AMTEC's flow visualiser 'Framer'. This package is freely available for most platforms and has been included on the CD. The directories on the CD are logically structured and contain 'readme' files to facilitate the location of all the files. The reader is strongly encouraged to use these movies as they are a great aid in the understanding of the unsteady surge problem.

GLASGOW
UNIVERSITY
LIBRARY

THESIS CONTAINS

VIDEO CD DVD TAPE CASSETTE